Aline Léon
Editor

GREEN ENERGY AND TECHNOLOGY

Hydrogen Technology

Mobile and Portable Applications

Springer

Green Energy and Technology

Aline Léon (Ed.)

Hydrogen Technology

Mobile and Portable Applications

With 322 Figures and 50 Tables

Springer

Editor
Dr. Aline Léon
Institut für Nanotechnologie
Forschungszentrum Karlsruhe
D - 76021 Karlsruhe
Germany
aline.leon@int.fzk.de

ISBN: 978-3-540-79027-3 e-ISBN: 978-3-540-69925-5

Springer Series in Green Energy and Technology ISSN 1865-3529

Library of Congress Control Number: 2008930266

Cover design: WMXDesign GmbH, Heidelberg

Printed on acid-free paper

9 8 7 6 5 4 3 2 1

springer.com

Our thoughts go to the memory of
Prof. Tapan Bose who passed away during
the publication process

Acknowledgements

I would like to acknowledge Prof. Hahn for his advice and support to realize this project with Springer. Thanks are also due to Dr. Christoph Baumann from Springer for his support. I would like to thank all the authors for their participation, contribution, and effort in the achievement of this project. My deep gratitude goes to Dr. Oliver Kircher and Prof. Jacques Huot for their comments, suggestions, and help in the realization of this book. I thank Dr. Jérôme Perrin for his advice to include the portable application. Enormous thanks go to Ms. Maike Schroeder for her help in improving the linguistic quality of all the manuscripts. I would like also to thank Emile and Sébastien for their help. Last, but not least, a special thank goes to Andreas for his support and help in finishing this book.

Contents

List of Contributors

Holger Braess
BMW Group, Knorrstrasse 147, 80788 Munich/Germany,
e-mail: Holger.Braess@bmw.de

Tapan Bose
Hydrogen Engine Center Canada, Trois-Rivières, (Qc) G9A 5H7, Canada

Wolfgang Breitung
Institute for Nuclear and Energy Technologies (IKET), Forschungszentrum Karlsruhe, P.O. Box 3640, D-76021 Karlsruhe, Germany,
e-mail: breitung@iket.fzk.de

Matthias Bronold
Samsung SDI Germany GmbH, European Research Center, Ostendstr. 1–14, 12459 Berlin, Germany, e-mail: matthias.bronold@samsung.com

Brigitte Décamps
Institut de Chimie des Matériaux Paris-Est, UMR 7182, CNRS, Paris 12, 94320 Thiais, France, e-mail: brigitte.decamps@csnsm.in2p3.fr

Ulrich Eberle
GM Fuel Cell Activities, Hydrogen & Fuel Cell Research Strategy (Europe), IPC MK-01, 65423 Rüsselsheim, Germany, e-mail: ulrich.eberle@de.opel.com

Michael Felderhoff
Max-Planck Institut für Kohlenforschung, 45470 Mülheim an der Ruhr, Germany,
e-mail: felderhoff@mpi-muelheim.mpg.de

Maurizio Fermeglia
ICS UNIDO – Area Science Park – 34100 Padriciano – Trieste – Italy; University of Trieste – DICAMP-MOSE – Piazzale Europa 1, 34127 Trieste – Italy,
e-mail: EMaurizio.Fermeglia@dicamp.units.it

Maximilian Fichtner
Institut für Nanotechnologie, Forschungzentrum Karlsruhe, P.O. Box 3640, D-76021, Karlsruhe, Germany, e-mail: fichtner@int.fzk.de

Ekkehard Füglein
NETZSCH-Gerätebau GmbH, Wittelsbacherstraße 42, 95100 Selb, Germany, e-mail: ekkehard.fueglein@netzsch.com

Robert Hahn
Fraunhofer-Institut Zuverlaessigkeit und Mikrointegration (IZM), Gustav-Meyer-Allee 25, D-13355 Berlin, Germany, e-mail: robert.hahn@izm.fraunhofer.de

Rittmar von Helmolt
GM Fuel Cell Activities, Hydrogen & Fuel Cell Research Strategy (Europe), IPC MK-01, 65423 Rüsselsheim, Germany, e-mail: rittmar.dr.von.helmolt@de.opel.com

Stanko Hočevar
Laboratory of Catalysis and Chemical Reaction Engineering, National Institute of Chemistry, SI-1000 Ljubljana, Slovenia, e-mail: stanko.hocevar@ki.si

Ted Hollinger
Hydrogen Engine Center, Algona, Iowa 50511/USA, e-mail: thollinger@hydrogenenginecenter.com

Jacques Huot
Institut de Recherche sur l'Hydrogène, Université du Québec à Trois-Rivières, 3351 des Forges, PO Box 500, Trois-Rivières (Qc) G9A 5H7, Canada, e-mail: jacques.huot@uqtr.ca

Jens Oluf Jensen
Department of Chemistry, Building 207, Technical University of Denmark, DK-2800 Lyngby, Denmark, e-mail: joj@kemi.dtu.dk

Oliver Kircher
BMW Group, Knorrstrasse 147, 80788 Munich/Germany, e-mail: oliver.kircher@bmw.de

Hidetoshi Kusumi
Toyota Motor Corporation, 1, Toyota-cho, Toyota, Aichi, 471-8571 Japan, e-mail: kusumi@hidetoshi.tec.toyota.co.jp

Qingfeng Li
Department of Chemistry, Building 207, Technical University of Denmark, DK-2800 Lyngby, Denmark, e-mail: lqf@kemi.dtu.dk

Aline Léon
Institut für Nanotechnologie, Forschungszentrum Karlsruhe, P.O. Box 3640, D – 76021 Karlsruhe, Germany, e-mail: aline.leon@int.fzk.de

Eric Leroy
Institut de Chimie des Matériaux Paris-Est, UMR 7182, CNRS, Paris 12, 94320 Thiais, France, e-mail: eric.leroy@icmpe.cnrs.fr

Teresa Malyshev
International Energy Agency, 9, rue de la Fédération, 75015 Paris,
e-mail: teresa.malyshev@iea.org

Friedel Michel
Air Liquide Deutschland GmbH, Germany,
e-mail: friedel.michel@airliquide.com

Alan Niedzwiecki
Quantum Fuel Systems Technologies Worldwide Inc., 17872 Cartwright Road,
Irvine, California 92614 USA, e-mail: aniedzwiecki@qtww.com

Jérôme Perrin
Renault Technocentre, Department of Research, Advanced Studies, and Material
(DREAM), 78288 Guyancourt, France, e-mail: jerome.perrin@renault.com

Jörg Rothe
Institut für Nukleare Entsorgung, Forschungszentrum Karlsruhe, P.O. Box 3640,
D-76021 Karlsruhe, Germany, e-mail: rothe@ine.fzk.de

Dieter Schild
Institut für Nukleare Entsorgung, Forschungszentrum Karlsruhe, P.O. Box 3640,
D-76021 Karlsruhe, Germany, e-mail: dieter.schild@ine.fzk.de

Magnus H.Sørby
Department of Physics, Institute for Energy Technology, P.O. Box 40, N-2027
Kjeller, Norway, e-mail: magnuss@ife.no

Neel Sirosh
Quantum Fuel Systems Technologies Worldwide Inc., 17872 Cartwright Road,
Irvine, California 92614 USA, e-mail: nsirosh@qtww.com

William Summers
Department of Energy, Savannah River National Laboratory, Aiken, SC
29808, USA, e-mail: william.summers@srnl.doe.gov

Ken Tanoue
Toyota Motor Corporation, 1, Toyota-cho, Toyota, Aichi, 471-8571 Japan,
e-mail: k-tanoue@toyota-turbine.co.jp

Mathilde Weber
Air Liquide R&D Center, 1 chemin de la porte des Loges, Les Loges en Josas,
BP126, 78354 Jouy en Josas Cedex, France,
e-mail: mathilde.weber@airliquide.com

Hiromichi Yanagihara
Toyota Motor Europe NV/SA, Hoge Wei 33B, Zaventem, 1930 Belgium,
e-mail: hiromichi.yanagihara@toyota-europe.com

Introduction

Aline Léon

In the last years, public attention was increasingly shifted by the media and world governments to the concepts of saving energy, reducing pollution, protecting the environment, and developing long-term energy supply solutions. In parallel, research funding relating to alternative fuels and energy carriers is increasing on both national and international levels. Why has future energy supply become such a matter of concern?

The reasons are the problems created by the world's current energy supply system which is mainly based on fossil fuels. In fact, the energy stored in hydrocarbon-based solid, liquid, and gaseous fuels was, is, and will be widely consumed for internal combustion engine-based transportation, for electricity and heat generation in residential and industrial sectors, and for the production of fertilizers in agriculture, as it is convenient, abundant, and cheap. However, such a widespread use of fossil fuels by a constantly growing world population (from 2.3 billion in 1939 to 6.5 billion in 2006) gives rise to the two problems of oil supply and environmental degradation.

The problem related to oil supply is caused by the fact that fossil fuels are not renewable primary energy sources: This means that since the first barrel of petroleum has been pumped out from the ground, we have been exhausting a heritage given by nature. As a consequence, the production of oil will reach a maximum and then, when about half of the oil will have been exhausted, it will begin to gradually fall to zero [1, 2]. It is worth noting that estimated reserves, although they differed strongly in recent studies, have only a minor effect on the time scale of this process [1]. It is rather influenced by our rate of consumption. And worldwide demand still is increasing (in the transportation sector, for example, the number of vehicles increased from 47 million in 1939 to 800 million in 2006) and will continue to increase with the growth of the world population and the fact that the developing and threshold countries wish to reach the same level of comfort as in industrialized countries.

Aline Léon
Institut für Nanotechnologie, Forschungszentrum Karlsruhe, P.O. Box 3640, D – 76021 Karlsruhe, Germany, e-mail: aline.leon@int.fzk.de

A. Léon (ed.), *Hydrogen Technology*,

Therefore, the supply of conventional oil will be unable to keep up with the demand at a certain point. Several studies and analyses indicate that the global production of conventional oil will reach its peak before or around 2010 [1, 2]. According to the medium-term oil market report by the International Energy Agency, the spare capacity of oil will decrease from currently 3 Mb oil per day to below 1 Mb oil per day in 2012 [3]. Thus, the growing demand from 2012 onwards cannot be fulfilled. From an economic point of view, this implies an increase of the oil price that consumers are already facing, as displayed in Fig. 1. As stated by British Petroleum, however, there has not been any physical shortage of either oil or gas so far, although energy prices have increased [4]. From the political perspective, this results in the problem of secure energy supply due to the unequal geographical repartition of the resources. Indeed, most of the industrialized countries nowadays are dependent on countries where the political situation is unstable.

The environmental degradation problem is due to the fact that burning fossil fuels produces carbon monoxide (poisonous gas), nitrogen oxides (main source of urban smog), and unburned hydrocarbons (main source of urban ozone) and carbon dioxide (greenhouse gas). Due to the increasing number of vehicles and power plants, the concentration of CO_2 in the atmosphere continuously increased from 277 ppm in 1850 to 379 ppm in 2004. In addition to the pollution, there is strong evidence that CO_2 emission is responsible for the rise of the global average temperature of the planet observed, as displayed in Fig. 2 [5, 6]. It has been noted that the top 10 warmest annual average global temperatures (recorded since 1860) have occurred since 1990. The ultimate effect of man-made climate change is unknown, but seems to be responsible for the heatwaves, hurricanes, and other natural disasters that occurred more frequently in the last years. In addition, the process of transporting and storing oil has a big impact on the environment when oil spills, pipeline explosions or well fires occur.

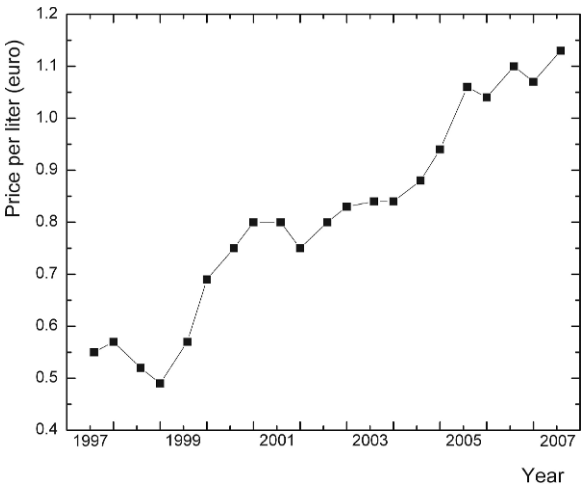

Fig. 1 Evolution of the price of diesel fuel at the pump in Germany

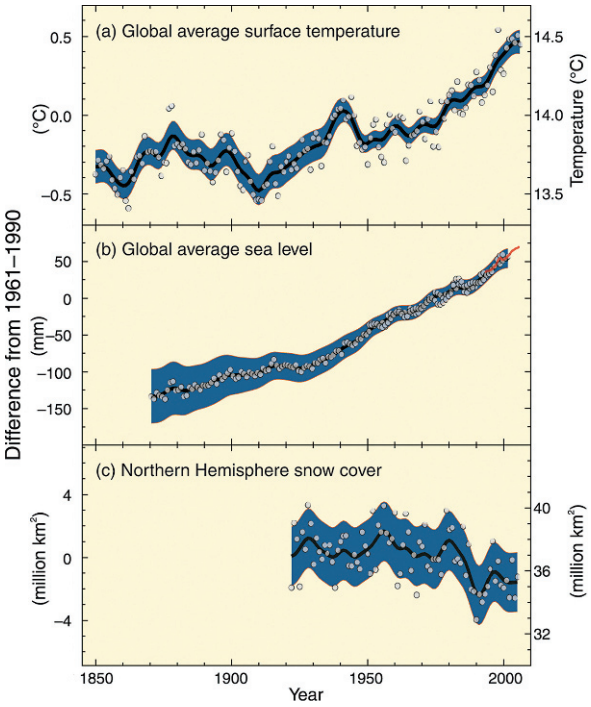

Fig. 2 Observed changes in (a) global average surface temperature; (b) global average sea level from tide gauge (*blue*) and satellite (*red*) data; and (c) Northern Hemisphere snow cover for March–April. All differences are relative to corresponding averages for the period 1961–1990. *Smoothed curves* represent decadal averaged values while *circles* show yearly values. The *shaded areas* are the uncertainty intervals estimated from a comprehensive analysis of known uncertainties (a and b) and from the time series (c) [6]

As a consequence of the problems of energy supply and environmental degradation, the world will have to reduce its fossil fuel consumption rate, build more efficient and that consumes less power plants, use hybrid technology in the transportation sector, and/or find renewable substitutes in the transportation and other sectors. These may be non-conventional oil and gas, renewable energy (solar, hydro, wind, biomass), and nuclear energy, including fission and fusion (which might be a source in the future). Nowadays, electricity is the most used energy carrier. Figure 3 summarizes the current pathways of grid electricity production from chemical fuels. The time sequences I–IV indicate the evolution of competing technologies. The fuel cell, which is an electrochemical device that combines hydrogen fuel with oxygen, produces electric power, heat, and water only. Therefore, the fuel cell technology and hydrogen as an alternative energy carrier are considered the ultimate goal of a secure energy supply and a clean environment. Unlike electricity, hydrogen can be stored for a long period of time. Hydrogen and electricity have the remarkable property of being complementary and exchangeable thanks to the technology of the fuel cell and electrolysis.

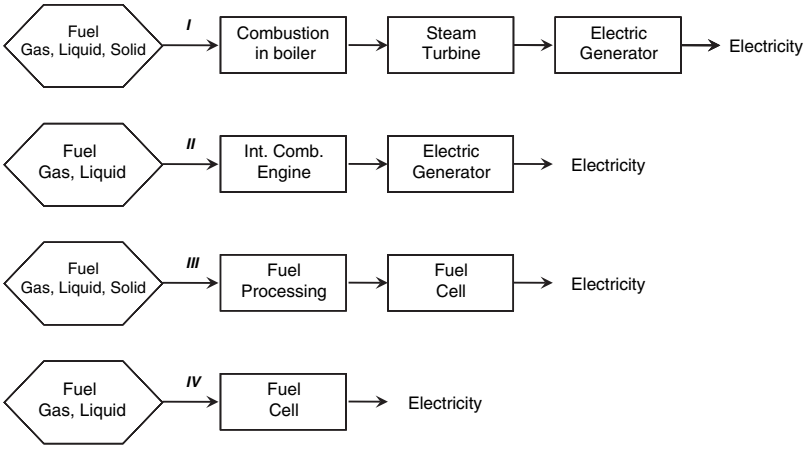

Fig. 3 The time sequence (I–IV) of competing technologies for electricity generation based on chemical fuels

However, in an all-fuel-cell-vehicle scenario for the year 2050, 112 million *t* H_2 would be required annually. A number of technical problems remain to be solved, which range from hydrogen production to transport, on-board vehicle storage, storage for the generation of electricity, etc. The development of adequate on-board energy storage units, for example, is a major economic and technological barrier to the introduction of hydrogen vehicles. The cost factor is a barrier, although technologies exist for production, delivery, and conversion. It is worth noting that none of the alternative solutions will be as convenient and cheap as oil has been. That is why it is now important to further develop existing hydrogen technologies from the testing phase to applications suitable for economically efficient everyday use. Furthermore, education is needed to enhance public acceptance of hydrogen.

Finally, these technologies should be made available to developing countries. Otherwise, these countries will increasingly turn to the 'dirty' fuel to meet their energy demand (for example, British Petroleum published that the consumption of coal rose by 11% in China in 2006 alone) and counteract the effort made by the industrialized countries to reduce pollution.

In this context, the present book with articles written by internationally recognized academic researchers and industry scientists is aimed at providing the state of the art of mobile and portable applications, the focus being on hydrogen as a potential energy carrier of the future.

The book will consist of five parts as follows:

Part I will summarize the cycle of hydrogen from its production, storage, transport, distribution, and conversion to electricity production by the fuel cell.

Presently, three energy sources are available to produce hydrogen. They comprise fossil fuels (although it is not a carbon-free process), nuclear energy, and renewable sources (in particular water electrolysis, wind energy, solar energy, and biomass).

For each case, the process will be described, followed by an analysis of the costs and environmental impact.

For the development of the future hydrogen economy, a safe and efficient means of storing hydrogen will be required in mobile, portable, and stationary applications. The different storage approaches that are currently of interest include the storage of hydrogen as compressed hydrogen gas (CGH_2), cryogenic liquid hydrogen (LH_2), and solid storage (SSH_2). After a description of the CGH_2 characteristics, compression of the gas using mechanical and non-mechanical compressors will be outlined. Then, the characteristics of LH_2 and the liquefaction principle of hydrogen will be presented. Industrial plants by Linde and Air Liquide will be described. Subsequently, solid storage (SSH_2) by reversible storage systems (including high-surface-area adsorbants, classical hydrides, and advanced storage materials) and irreversible systems (including chemical hydrides and organic cycle compounds) will be considered. It should be noted that an additional promising storage technology currently under investigation is the cryo compressed hydrogen ($cCGH_2$), which expands the hydrogen storage portfolio.

Widespread use of hydrogen as an energy carrier will require a transmission and distribution network. At present, compressed hydrogen is transported in cylinders and pipelines, liquid hydrogen by cryogenic trucks. These transportation modes will be described. Then, bulk storage in natural underground stores (caverns, depleted underground natural gas formation) and underground storage in tanks as a buffer between production facilities and fluctuation in demand will be highlighted. Finally, a high-pressure filling station installed by Air Liquide will be described.

Fuel cells play an important role as devices which convert the energy stored in hydrogen into the form of electricity. They can be used for large-scale power generation in central power plants as well as for small-scale electricity generators. Herein, the technical principle of a fuel cell will be given, followed by the description of its construction from the single cell to the system. Then, existing fuel cells, namely, alkaline, phosphoric acid, proton exchange, molten carbonate, and solid oxide fuel cells, will be presented.

Part II will outline the state of the art of mobile applications. The transport sector is currently considered to be one of the major drivers of the introduction of hydrogen, as this sector is 95% dependent on oil worldwide. Moreover, automotive industry aims at reducing CO_2 emissions from vehicles. To date, five technologies have emerged, which promise to have this potential. These are the clean diesel, the internal combustion engine (ICE) running with hydrogen, the battery-driven electric vehicle, the hybrid vehicle, and the fuel cell vehicle. In this part the status of these technologies will be highlighted.

First, the challenges and requirements of automobile industry will be introduced. Current fuel alternatives, namely, synthetic fuels, biofuels, compressed or liquefied natural gas, liquefied petroleum gas, batteries, and hydrogen, will be described and their potentials for substituting gasoline or diesel fuel will be analyzed and discussed. Then, hydrogen will be considered as the best mobile energy carrier from today's point of view and the general requirements made on a hydrogen-powered car will be presented. Finally, use of hydrogen in the transport sector

will be described and analyzed with particular attention being paid to consumer requirements.

This analysis will be followed by the presentation of existing technologies for the future. These include:

- Hydrogen-powered ICE which is an important mid-term technology on the way towards hydrogen economy. This technology has been introduced by BMW.
- Hybrid technology which is a combination of an electric motor with a battery and an internal combustion engine with gasoline to ensure the propulsion of a vehicle. This technology has been implemented by Toyota.
- Fuel cell vehicles which use hydrogen and the proton exchange membrane fuel cell to produce electricity to propel vehicles equipped with an electric motor.

Hydrogen-powered ICE or fuel cell vehicles need to be supplied with hydrogen at a certain pressure, flow rate, and within prescribed temperature limits. Hence, the fuel should in principle be stored on-board in a storage system which will safely accept hydrogen during refueling, store it with a minimum loss, and deliver it when needed by the power train. To date, most prototype vehicles have stored hydrogen in composite tanks at high pressure, while some store liquid hydrogen at temperatures between 20 and 30 K. So far, only a limited number of demonstration vehicles with metal hydrides and chemical hydrides have been conceived. Therefore, the high-pressure tank and cryogenic reservoirs will be presented in this book, from the requirements to their principles, designs, validations of the system, and safety to the challenges for commercialization.

The public which usually is not experienced in handling hydrogen will accept this technology only if a safety level comparable to that of current gasoline vehicles can be achieved. This will require a systematic investigation of the hydrogen behavior under normal operating conditions, in case of component malfunctions, in the event of vehicle collisions, and under service/repair conditions. This section will first outline the motivations of safety investigations, followed by an analysis of hydrogen accidents. Then, the analysis procedure of accident involving H_2 based on a three-dimensional numerical simulation of hydrogen distribution and different hydrogen combustion modes will be described and applied to investigate the release of hydrogen from a car parked in a residential garage. Finally, safety issues related to hydrogen vehicles and hydrogen infrastructure will be presented.

Part III will focus on the state of the art of portable applications. Hydrogen microsystems for portable power are of interest, because they will be one of the easiest ways of introducing hydrogen to the public via the young generation. The main challenge remains the cost.

The first section will be dedicated to describing the principle and performance of existing technologies for portable applications. These are batteries (currently, the best performance is achieved by a lithium-based rechargeable battery), photovoltaic portable modules, and portable fuel cells. Finally, the Li-ion battery and the portable fuel cell will be compared.

The second section will concentrate on the development of micro fuel cells in order to achieve higher energy densities compared to batteries. Present research focuses on the direct liquid fuel cell (using methanol, ethanol or formic acid), PEM fuel cells (with hydrogen generated from reformed methanol, reversible storage alloys, chemical hydrides or water-reactive alloys), and the bio-fuel cell (using alcohols, organic acids, glucose). Here, only the first two systems will be considered. It will be pointed out that the key challenge in this field is how to miniaturize the different parts of a portable fuel cell as well as the water management.

The third section will outline the challenges for industry. After a description of a direct methanol fuel cell, the basic challenges will be presented in terms of performance, reliability, durability, and infrastructure.

Part IV will be dedicated to the development of new hydrogen storage materials with properties suitable for technical applications. Despite intensive research, no approach exists that can meet the technical requirements. This chapter will cover the different tools necessary to develop new materials, from their synthesis to their characterization.

Chemical or mechanical synthesis of hydrogen storage materials will be described first. Then, the experimental methods and devices necessary for determining the kinetic and thermodynamic properties of the material will be reviewed. Finally, advanced tools to characterize the hydrogen storage properties of materials will be described. These include X-ray diffraction and powder neutron diffraction for structural analysis, scanning and transmission electron microscopy for imaging as well as X-ray photoelectron spectroscopy and X-ray absorption spectroscopy for surface and bulk analysis. These tools are necessary to gain fundamental knowledge in order to design new materials with the required properties.

Part V will conclude this book by giving the perspectives from the scientific, environmental, political, and economic points of view.

References

1. Colin C. Campbell and Jean H. Laherrère, *The End of Cheap Oil*, Scientific American, March 1998
2. The Association for Study of Peak Oil, ASPO, Statistical review of world oil and gas, 2002
3. International Energy Agency, Medium term oil market report, July 2007
4. http://www.bp.com/statisticalreview
5. Hadley centre report, Climate change, rivers, and rainfall, December 2005, (http://www.metoffice.com/research/hadleycentre/pubs/brochures/B2005/COP11.pdf)
6. Intergovernmental panel on climate change (http://www.ipcc.ch/pdf/assessment-report/ar4/syr/ar4_syr.pdf)

Part I
Hydrogen Cycle

Chapter 1
Introduction

Aline Léon

Hydrogen, the lightest of all gases, is abundant on earth in combination with oxygen as water, with carbon as hydrocarbons, and in all living organisms. Hydrogen is a secondary energy carrier that can be obtained from any primary energy source and used in mobile, stationary and portable applications. Unlike electricity, hydrogen, once produced, can be stored in large quantities for long periods of time. The clean hydrogen cycle as displayed in Fig. 1.1 consists of producing hydrogen from renewable energy, then of storing it, and transporting it to the end consumer, where it can be converted into electricity using a fuel cell. Most of the techniques for this cyclic process are presently available. However, they are not yet cost-competitive with fossil fuel technologies. This is one of the main reasons why the use of hydrogen is not so widespread, despite some remarkable properties.

Part I of this book will present the cycle of hydrogen from its production to its storage, transport, distribution, and conversion into electricity via the fuel cell.

Today, three energy sources are available to produce hydrogen. They comprise fossil fuels, renewable energy, and nuclear energy. In the next decades, fossil fuels will remain the major source of hydrogen production, although it is not a carbon-free process. Therefore, the production process from coal and natural gas will be described with the sequestration of CO_2 being taken into account as well. Hydrogen production without any release of carbon from nuclear energy and renewable sources (in particular from water electrolysis, wind energy, solar energy, and biomass) will be discussed. In each case, the description of the process will be followed by an analysis of the cost issue and the environmental impact.

For the development of the future hydrogen economy, a safe and efficient means of storing hydrogen will be required in mobile, portable, and stationary applications. However, physical and thermodynamic properties of hydrogen pose the greatest technological challenges to its storage. After a short description of the purification technology of hydrogen, the different storage approaches that are currently

Aline Léon
Institut für Nanotechnologie, Forschungszentrum Karlsruhe, P.O. Box 3640, D – 76021 Karlsruhe, Germany, e-mail: aline.leon@int.fzk.de

A. Léon (ed.), *Hydrogen Technology*,

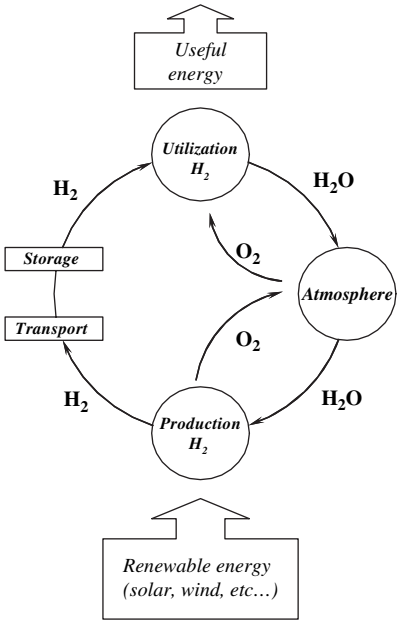

Fig. 1.1 Clean hydrogen cycle

of interest will be described in this chapter. These are the storage of hydrogen as compressed hydrogen gas (CGH_2), cryogenic liquid hydrogen (LH_2) and solid storage of hydrogen (SSH_2). Following the description of their characteristics, the compression process of the gas and the liquefaction process of hydrogen will be first presented. Then, solid storage (SSH_2) by reversible storage systems (including high-surface-area adsorbants, classical hydrides, and advanced storage materials) and irreversible systems (including chemical hydrides and organic cycle compounds) will be highlighted.

To a widespread use of hydrogen as an energy carrier, the transmission and distribution infrastructure is of importance. At present, mature pathways include the transport of compressed hydrogen in cylinders and cryogenic trucking of liquid hydrogen. Therefore, hydrogen distribution by gas pipelines will be described by giving an overview of the existing network, followed by the pipeline characteristics. Then, the delivery by compressed gas trailers and liquid hydrogen transportation will be presented. Any large-scale hydrogen distribution system is associated with the problem of bulk storage to provide for a buffer between production facilities and fluctuation in demand. The most widely studied options are natural underground storage (caverns and depleted underground natural gas formation) and underground storage in tanks. Both options will be then described. Finally, an overview of hydrogen filling stations for vehicles will be given, followed by a description of a high-pressure filling station installed by Air Liquide.

Fuel cells play an important role in the hydrogen energy concept as devices which extract the energy stored in hydrogen in the form of electricity. Fuel cells have high utilization efficiencies, are clean and quiet. They are versatile and can be used for

large-scale power generation in central power plants as well as for small-scale electricity production. In contrast to a battery, they can run infinitely in principle to the extent they have been filled up with a fuel. The technical principle of a fuel cell and the cell performance will be described first, followed by construction from the single cell to the system. Then, the electrolyte, electrodes, cells, stacks, and systems of alkaline, phosphoric acid, proton exchange, molten carbonate, and solid oxide fuel cells shall be presented. The advantages and challenges will be discussed for each type of fuel cell.

Chapter 2
Hydrogen Production

Stanko Hočevar and William Summers

List of Abbreviations

atm	atmosphere, pressure unit
ANL	Argonne National Laboratory, Argonne, IL, USA
ATR	Autothermal reforming
AWEA	American Wind Energy Association
CAD	Computer-aided design
CBS	Bacterium Rubrivivax gelatinosus CBS
CdTe	Cadmium telluride
CIS	Copper indium diselenide
CIS	Commonwealth of Independent States,
CH2	Compressed hydrogen
C/H	Carbon to hydrogen ratio
CRD	Conservation Reserve Program

Stanko Hočevar
Laboratory of Catalysis and Chemical Reaction Engineering, National Institute of Chemistry, SI-1000 Ljubljana, Slovenia, e-mail: stanko.hocevar@ki.si

William Summers
Department of Energy, Savannah River National Laboratory, Aiken, SC 29808, USA,
e-mail: william.summers@srnl.doe.gov

A. Léon (ed.), *Hydrogen Technology*,

CPOx	Catalytic partial oxidation
CO_2	Carbon dioxide
EIA	Energy Information Administration, US Government
ETH	Eidgenössische Technische Hochschule Zürich, Switzerland
EPA	Environmental Protection Agency
EU	European Union
EU HFP	European Union Hydrogen and Fuel Cell Technology Platform
EVA	Ethylvinylacetate
FCV	Fuel cell vehicle
FGD	Flue gas desulfurization
GREET	Greenhouse gases, Regulated Emissions, and Energy use in Transportation (GREET), software package, Argonne National Laboratory, Argonne, IL, USA
GHG	Greenhouse gases
H/C	Hydrogen to carbon ratio
HCP	Hydrogen from Coal Program
HHV	Higher heating value
HTE	High-temperature electrolysis
HTS	High-temperature shift
HyS	Hybrid sulfur
H/C	Hydrogen to carbon ratio
HHV	Higher heating value
HTE	High-temperature electrolysis
HTS	High-temperature shift
HyS	Hybrid sulfur
H/C	Hydrogen to carbon ratio
ICEV	Internal combustion engine vehicle
IGCC	Integrated gasification combined cycle
ITM	Ion transport membrane
KOH	Potassium hydroxide
Kg/SD	Kilogram per stream day
kWe	Kilowatts of electric power
LBST	Ludwig-Bölkow-Systemtechnik GmbH, Ottobrunn, Germany
LCA	Life cycle assessment
LEBSs	Low-emission boiler systems
LH_2	Liquid hydrogen
LHV	Lower heating value
LTS	Low-temperature shift
MEA	Membrane-electrode assembly
MIT	Massachusetts Institute of Technology, Boston, USA
NEG Micon	NEG Micon A/S, Denmark, manufacturer of wind turbine technology
NIMBY	Not In My Backyard
NO_x	Nitrogen oxides
NREL	National Renewable Energy Laboratory, Department of Energy, US
O&M	Operation & maintenance
OECD	Organization for Economic Cooperation and Development
PEMFC	Proton exchange membrane fuel cell
PFBC	Pressurized fluidized-bed combustion
PMS	Production management scenario
POx	Partial oxidation
PSA	Pressure swing adsorption
PV	Photovoltaic
R&D	Research & development
SDE	Sulfur dioxide depolarized electrolyzer

SIC	Sulfur-iodine cycle
SMR	Steam-methane reforming
SO_x	Sulfur oxides
TTW	Tank to wheel
UN	United Nations
USDA	US Department of Agriculture
US DOE	United States Department of Energy
WGS	Water gas shift

2.1 Introduction

Historically speaking, the "natural" tendency for new technologies to use chemical fuels with a higher energy content coincides with the fuels having an always higher H/C ratio: Wood, coal, oil, natural gas. Eventually, it may be concluded: The most potent fuel among the chemical fuels is hydrogen and it is natural that mankind moves towards using it in the near future. Fortunately, it is the most abundant element on earth and in the universe and it is also the cleanest fuel – the product of hydrogen combustion is water.

Pure hydrogen as the strongest chemical fuel allows to suppress CO_2 and particulate emissions almost completely (depending on the process of hydrogen production) and to lower the NO_x emissions (depending on the energy conversion system used).

However, hydrogen is not only the strongest chemical fuel, it also serves as an *energy carrier (vector)*. Hydrogen can be produced in several different ways, as can be seen in Fig. 2.1, and then used for energy transfer over short and long distances or for the onsite conversion of energy into electricity and heat. Obviously, interest focuses on those ways of hydrogen production that are *sustainable* (like biomass) or, even better, *renewable* (like solar, wind, geothermal, hydro, etc.). Two

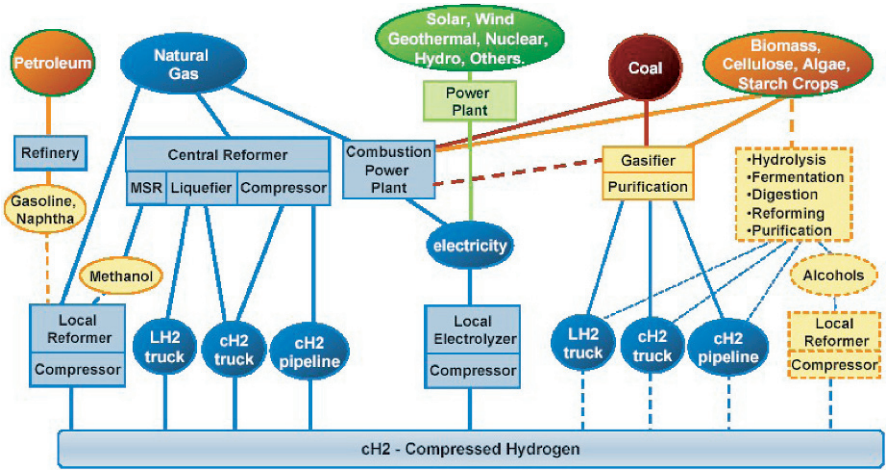

Fig. 2.1 Pathways of hydrogen production from non-renewable, sustainable, and renewable primary energy sources

basic options exist for producing hydrogen. One way is to separate the hydrogen from hydrocarbons through processes referred to as reforming or fuel processing. The second way to produce hydrogen is from water using the process of electrolysis to dissociate water into its separate hydrogen and oxygen constituents. Electrolysis technologies that have been in use for decades both dissociate water and capture oxygen and/or hydrogen primarily to meet the industry's chemical needs. Electrolysis also played a critical role in life support (oxygen replenishment) in space and submarine applications over the past decades.

In the following sections some technologies for hydrogen production from fossil, sustainable, and renewable primary energy sources will be presented, the emphasis lying on pure hydrogen production processes.

2.2 Production from Fossil Fuels

Hydrogen is currently produced on an industrial scale by steam reforming of natural gas. Most of the hydrogen made from fossil fuels is presently used in the fertilizer, petroleum, and chemical industries. Natural gas resources will suffice for several decades, such that their use will be extended to meet the hydrogen needs in the medium term. The world gas production is expected to double between 2000 and 2030. The resources of natural gas are abundant and expected to increase by around 10%. However, regional disparities of gas resources and production costs will modify the regional gas supply pattern by 2030. Indeed, about one third of the total gas production will originate from the Commonwealth of Independent States (CIS), while the remaining production is projected to be almost equally shared by the OECD countries, the Middle East, and the other gas producers in Latin America and Asia.

Another source which is envisaged to be exploited to generate hydrogen is coal. In fact, coal resources are enormous and will not limit coal supply by 2030. The world coal production is expected to double between 2000 and 2030, with a significant increase in Africa and Asia. This latter continent is projected to cover more than half of the total coal production by 2030. Compared to natural gas, however, this resource generates approximately twice as much CO_2 per amount of hydrogen produced. Nevertheless, the development of an economically efficient and safe CO_2 sequestration method will enable coal to play a significant role in hydrogen generation.

The *proved* coal resources worldwide would be sufficient for 155 years of reserve to production ratio, while the *proved* natural gas reserves would be enough for 55 years of reserve to production ratio [1].

2.2.1 Hydrogen from Coal

Coal is a viable option for producing hydrogen in very large, centralized plants, once the demand for hydrogen will be large enough to support an associated distribution

infrastructure. Some countries and regions have enough coal to generate all of the hydrogen that the economies will need for more than 200 years. Moreover, a substantial coal infrastructure exists already and commercial technologies for converting coal into hydrogen are available from several licensors. In addition, the costs of producing hydrogen from coal are among the lowest, and technology improvements needed to reach the future cost targets have been identified. Coal is considered to play a significant role in hydrogen generation in the medium term, due to its general availability and its low costs.

If coal will be a major source for future hydrogen production, the current production and delivery infrastructure capacities would have to be increased from today's annual use of H_2 produced from coal (11.7 million tons per year) by more than a factor of four in order to meet the 2050 hydrogen demand [2]. It should be noted that such an increase in production will not be without any detrimental effects on the environment. Indeed, extracting more coal to produce hydrogen will have a number of environmental impacts, such as land disturbance, soil erosion, dust, biodiversity impacts, waste piles, abandoned mines, etc., which remain to be considered.

Once coal has been extracted, it needs to be moved from the mine to the power plant or other place of use. Bulk coal transportation occurs by railway, trucks are used for local transport. For economic reasons, however, most of the world's coal is consumed in power plants located near coal mines to avoid long-distance transportation. More than 60% of the coal used for power generation worldwide are consumed within 50 km distance from the mine site.

The major drawback of using coal to produce H_2 is that the resulting CO_2 emission is larger compared to any other way of generating hydrogen. On a net energy basis, coal combustion produces 80% more CO_2 than the combustion of natural gas and 20% more than residual fuel oil which is another widely used fuel for power generation [3]. Using current technology, the CO_2 emission is about 19 kg CO_2 per kilogram of hydrogen produced from coal, while it amounts to approximately 10 kg CO_2 per kilogram of hydrogen from natural gas. Prior to the widespread use of coal to generate hydrogen, it is therefore required to develop carbon sequestration techniques that can handle very large amounts of CO_2.

2.2.1.1 Conventional Combustion Process of Coal

Conventional coal-fired power generation uses a combustion boiler that heats water to make steam which, in turn, is used to drive an expansion steam turbine and generator. So far, numerous designs of coal combustion boilers have been developed. Among them, the most modern and efficient one is the supercritical-pressure steam generator. It uses pulverized coal, produces supercritical (high-pressure/high-temperature) steam, and operates at "supercritical pressure".

Such a plant, as displayed in Fig. 2.2, operates at pressures higher than 220 bar, such that boiling stops, as the boiler has no water – steam separation. In contrast

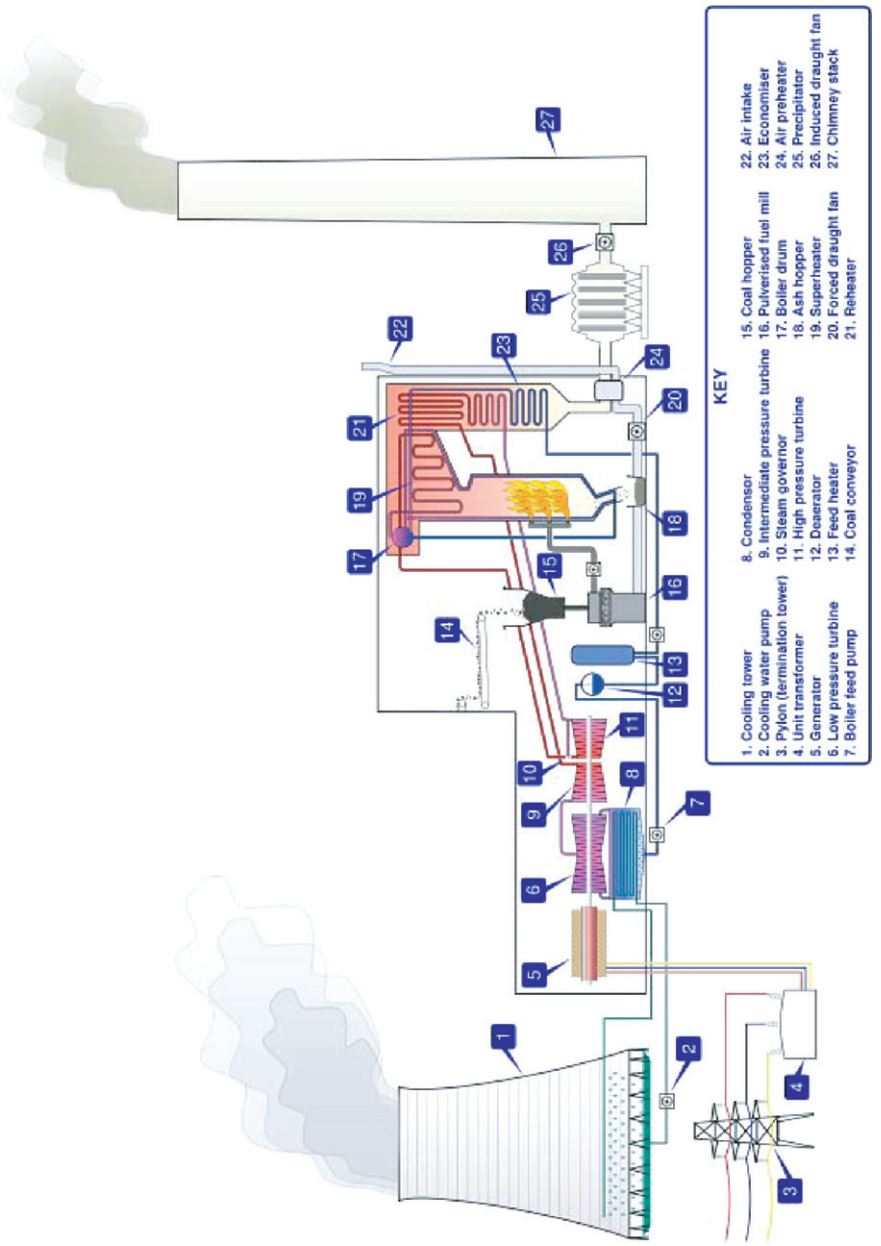

Fig. 2.2 A coal-fired thermal power station

to a "subcritical boiler", no steam bubbles are generated in the water, because the pressure is above the "critical pressure". The pressure drops below the critical point in the high-pressure turbine and the steam enters the generator's condenser. This device is more efficient than the"combustion boiler", as it uses slightly less fuel and GHG production is decreased. Overall efficiencies typically are in the range of 36–40%.

The main pollutants resulting from conventional coal combustion are sulfur oxides SO_x, nitrogen oxides (NO_x), particulates, CO_2, and mercury (Hg). SO_x is minimized by the use of coal with lower sulfur content as well as by flue gas desulfurization (FGD) processes. The control of other emissions still is technologically demanding and costly, especially when the old coal-fired plants are reconstructed. Although emissions from coal-fired plants are of concern to various bodies—national and international-, the production of electricity and heat from fossil fuels makes up a large share in the national energy mix for many countries around the globe. Greenhouse gases (GHG, mainly CO_2, CH_4, N_2O, hydrofluorocarbons, perfluorocarbons, and SF_6) and particulate emissions are considered on highest level by the UN Framework Convention on Climate Change.

Although it has been used for power generation for decades, this conventional combustion technique is not suitable for producing hydrogen. New processes for the generation of power and/or hydrogen are favored, such as the integrated gasification combined cycle (IGCC) power generation involving conversion instead of combustion, because they efficiently reduce the pollutants [4].

2.2.1.2 Integrated Gasification Combined Cycle (IGCC)

Clean coal technologies use alternative ways of converting coal in order to reduce plant emissions and to increase the plant's thermal efficiency. In turn, the overall cost of electricity is lowered compared to conventional conversion. The goal is to reach thermal efficiencies in the range of 55–60% (higher heating value [HHV]) [5]. Systems which are under development for coal conversion include:

- Low-emission boiler systems (LEBSs)
- High-performance power systems (HIPPSs)
- Integrated gasification combined cycle systems (IGCC)
- Pressurized fluidized-bed combustion systems (PFBC)

Of these systems, the integrated gasification combined cycle (IGCC) only is of interest for hydrogen production, as it uses a different conversion process that significantly reduces the emissions compared to the three other systems.

Gasification systems typically involve partial oxidation of coal with oxygen and steam in a high-temperature and elevated-pressure reactor. The short reaction proceeds in a highly reducing atmosphere that creates a synthesis gas (syngas) which is a mixture of predominantly CO and H_2 with some steam and CO_2 This syngas can be further shifted to increase the H_2 yield. The gas can be cleaned in conventional ways to recover elemental sulfur (or to produce sulfuric acid). It is easy to

isolate a highly concentrated CO_2 stream for disposal (underground in abandoned mines, underwater in the deep sea, chemically bound, etc.). The use of high temperature/pressure and oxygen also minimizes NO_x production. The slag and ashes discharged at the bottom of the reactor are used to encapsulate heavy metals in an inert, vitreous material currently used for road filling. The high temperature also prevents the production of organic materials, and more than 90% of the mercury are removed in syngas processing. Syngas produced by today's gasification plants is used in a variety of applications, often at a single facility. These applications include:

- Syngas used as feedstock for the production of chemicals and fertilizers
- Syngas converted into hydrogen for processing in refineries
- Production and generation of electricity by burning the syngas in a gas turbine and additional heat recovery using a combined cycle.

Existing gasification plants are of either air-blown or oxygen-blown design. Air-blown designs save the capital costs and operation expenses of air separation units. However, the dilution of the combustion products with nitrogen makes the separation in particular of CO_2 a much more complex task. In addition, the extra inert nitrogen volume passed through the plant significantly increases the vessel size and the costs of downstream equipment. In contrast to this, oxygen-blown designs do not need additional nitrogen. Once the sulfur compounds have been removed from the syngas, a high-purity stream of CO_2 only is left, which can be separated easily and cheaply. As CO_2 capture and sequestration will be applied in future hydrogen generation plants, only oxygen-blown designs will be considered for practical purposes [6]. Figure 2.3 displays a flowchart of such an IGCC power plant.

Most gasification plants produce syngas for chemical production and often for steam. IGCC plants then burn the syngas to produce power. The generation of multiple products is one of the strengths of the gasification system. Relatively few gasification plants are dedicated to producing hydrogen only (or any other single product). The future large-scale hydrogen generation plant will likely generate some amounts of power because of the advantages of multiple products generation.

There are several hundred gasification plants in operation that run on a variety of feedstocks. These include residual oils from refining crude oil, petroleum coke, and, to a lesser extent, coal. The syngas generated is typically used for subsequent chemicals manufacture; power generation by IGCC systems is a more recent innovation that was demonstrated successfully in the mid-1980s and has been operated commercially since the mid-1990s. Hence, gasification is a well-proven commercial process technology, and several companies offer licenses for its use.

All technology needed to produce hydrogen from coal is commercially proven and in operation today. Designs of hydrogen and power co-production facilities have already been made available. It is estimated that a gasification plant producing hydrogen only today would be able to deliver hydrogen to the plant gate at a cost of about 0.96 US$/kg H_2 with no CO_2 sequestration. If CO_2 capture would be required as well, costs would amount to 1.03 US$/kg H_2. These costs refer to hydrogen production at very large, central station plants, from which it will be distributed through pipelines.

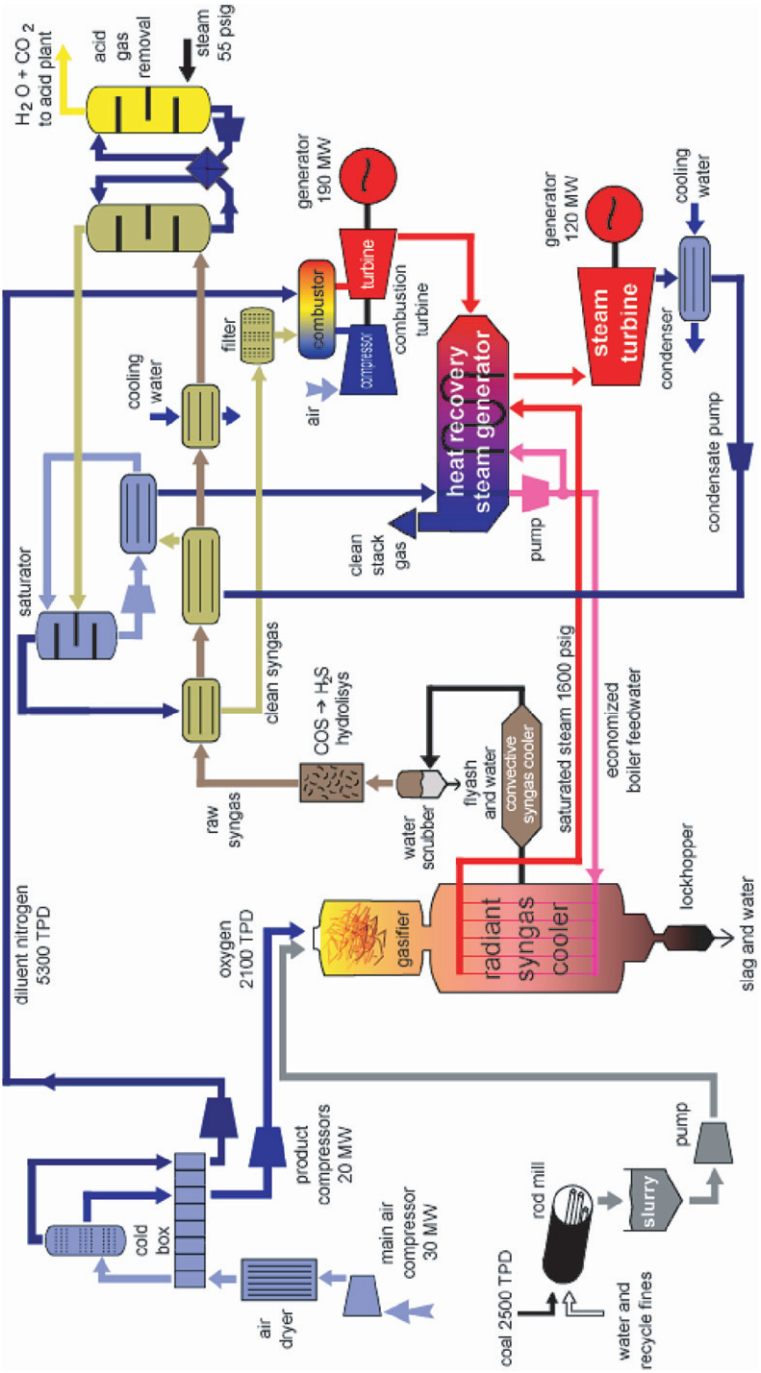

Fig. 2.3 Flowchart of an IGCC power plant utilizing the heat recovery steam generator (HRSG)

At these plants, a single gasifier can produce more than 2.83 million m^3 H_2/day. A typical installation would include two to three gasifiers.

However, improved technologies currently under development will continue to drive down the costs and increase the efficiency of these facilities. Hydrogen-from-coal plants combine a number of technologies, including oxygen supply, gasification, CO shift, sulfur removal, and gas turbine technologies. All of these technologies are being further developed, such that the plant's balances of capital and operation costs and thermal efficiency will be improved significantly. Examples of these pending technology advances are:

- Ion transport membrane (ITM) technology for air separation (oxygen supply)
- Gasifier technology (feedstock preparation, conversion, availability)
- Warm gas cleaning
- Gas turbines for both syngas and hydrogen
- CO_2 capture technology
- New, lower-cost sulfur removal technology
- Slag handling improvements [7].

These new technologies and the concept of integrating them in an operating plant are in a very early development phase and will require a long time to verify the true potential and to reach commercialization. In case of success, the estimated hydrogen production costs can be reduced to 0.77 US$/kg.

Economic efficiency of producing hydrogen from coal is somewhat different from the use of other fossil fuels. The capital costs incurred per kilogram of produced hydrogen are higher for coal plants, but the raw material costs per kilogram of produced hydrogen are lower. In other words, coal is inexpensive, but the coal gasification plant is expensive. If the coal price would change by 25%, hydrogen costs would change by 0.05 US$/kg only. If the costs of the plant would change by 25%, however, hydrogen costs would change by 0.16 US$/kg. This should lead to a very stable cost of hydrogen production that will even be lowered by future technology improvements.

CO_2 emissions result from the carbon in the coal. The emissions depend on the type and the quality of the coal. For standard coal composed of 2% sulfur and 27.9 MJ/kg, approximately 18.8 kg CO_2 are emitted per kilogram of hydrogen produced. If the plant is equipped with a CO_2 capture system, the amount of CO_2 released is estimated to be reduced by as much as 80 to 90% (the exact amount depends on capital efficiency and cost-benefit analysis). Although the economic efficiency of hydrogen production from coal varies with the quality of the coal gasified, any coal can be gasified to produce hydrogen. The main effects of a variable coal quality on hydrogen production are the amount of by-products produced (primarily slag and elemental sulfur) and the capital costs (mostly due to the amount of additional inert material in the coal that has to be handled). For a gasification plant producing a maximum amount of hydrogen from coal, the varying feed coal quality is estimated to produce a variation of less than 15% in the amount of CO_2 generated per ton of hydrogen produced. The lower-quality coals (with a lower C/H ratio) generate lower amounts of CO_2 per ton of hydrogen. Other effects of coal quality are less significant.

2.2.1.3 International Programs for Zero-Emission Coal-Fueled Facilities

The US DOE goal of the Hydrogen from Coal Program (HCP) is to have an operational, zero-emission coal-fueled facility in 2015 that co-produces hydrogen and electricity with 60% overall efficiency. Apart from the DOE's Hydrogen from Coal Program, two other significant DOE coal R&D programs Vision 21 and FutureGen are being pursued. The new coal-based power systems that are being developed under the Vision 21 and FutureGen programs aim at combining a power plant with sequestration systems.

Very similar 2015 targets are envisioned in the recent EU Hydrogen & Fuel Cell Technology Platform document "Implementation Plan – Status 2006" [8], according to which the coal-to-hydrogen gasification technologies – with carbon capture and storage – are considered to be the predominant production technologies in the medium term.

In reforming/partial oxidation coal-to-hydrogen production processes special emphasis is put on R&D of hydrogen purification technologies and fuel processing catalysts.

2.2.2 Hydrogen from Natural Gas

Compared to other fossil fuels, natural gas is a cost-effective feed for producing hydrogen, because it is widely available, easy to handle, and has a high hydrogen-to-carbon ratio which minimizes the formation of carbon dioxide (CO_2) as a by-product.

2.2.2.1 Steam Reforming, Partial Oxidation, Autothermal Reforming

Primary ways of converting natural gas, mostly methane, into hydrogen involve a reaction with either steam (steam reforming), oxygen (partial oxidation), or both simultaneously (autothermal reforming). The following reactions take place:

$$CH_4 + 2H_2O \rightarrow CO_2 + 4H_2$$
$$CH_4 + O_2 \rightarrow CO_2 + 2H_2$$

In practice, the hydrogen produced contains a mixture of carbon monoxide (CO), carbon dioxide (CO_2), and unconverted methane (CH_4). Therefore, further processing is required to purify the gas. The reaction of CO with steam (water-gas shift) over a catalyst produces additional hydrogen and CO_2, and after purification, high-purity hydrogen (H_2) is recovered [9]. In most cases, CO_2 is vented into the atmosphere today, but there are options of capturing it for subsequent sequestration.

Steam-methane reforming is widely used worldwide to generate both synthesis gas and hydrogen. The gas produced is used to make chemicals, such as ammonia and methanol, to refine petroleum, metals, and electronic materials, and to process

food components. More than 40 million tons per year (t/yr) H_2 (110 million kg/day) are produced using SMR. Today, hydrogen is also produced by partial oxidation and ATR.

Steam-Methane Reforming (SMR)

Worldwide production of hydrogen is about 50 million tons per year [10], and over 80% of this production is accomplished by steam-methane reforming (SMR) which will be discussed below.

Figure 2.4 displays the four basic steps of steam-methane reforming. First, natural gas is treated catalytically with hydrogen to remove sulfur compounds. Then, the desulfurized gas is reformed by mixing it with steam and passing it over a nickel-on-alumina catalyst to produce CO and hydrogen. This step is followed by a catalytic water-gas shift reaction to convert the CO into hydrogen and CO_2. As a final step, the hydrogen gas is purified. If the by-product CO_2 has to be sequestered, a separation process has to be added to capture it. The reforming reactions are as follows:

$$\begin{aligned} CH_4 + H_2O &\rightarrow CO + 3H_2 \\ CO + H_2O &\rightarrow CO_2 + H_2 (\text{water-gas shift reaction}) \\ \text{Overall: } CH_4 + 2H_2O &\rightarrow CO_2 + 4H_2 \end{aligned}$$

The reaction of natural gas with steam to form CO and H_2 requires a large amount of heat (206 kJ/mol methane). In current commercial plants this heat is added using fired furnaces containing tubular reactors filled with the catalyst.

Partial Oxidation (POX)

Partial oxidation (POX) of natural gas with oxygen is carried out in a high-pressure, refractory-lined reactor. In this process the "desulfurized" gas is combined with air before the partial oxidation reaction takes place to produce CO and hydrogen. The ratio of oxygen to carbon is controlled thoroughly in order to maximize the yield of CO and H_2 while maintaining an acceptable level of CO_2 and residual methane as well as minimizing the formation of soot. Downstream equipment is provided to remove the large amount of heat generated by the oxidation reaction, to shift the CO to H_2, to remove CO_2 which could be sequestered, and to purify the hydrogen product. Of

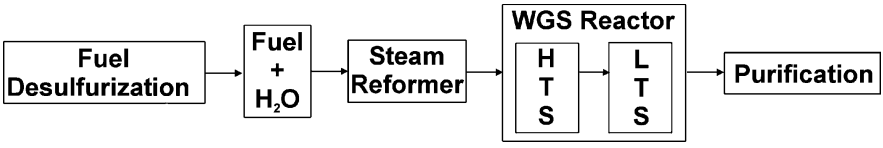

Fig. 2.4 Hydrogen generation process by steam reforming of a fuel (WGS = Water-gas shift, HTS = High-temperature shift, LTS = Low-temperature shift)

course, this process requires a source of oxygen, which is provided by including an air separation system. Alternatively, air can be used instead of oxygen, although the hydrogen produced has to be recovered from nitrogen and other gases using palladium diffusion membrane. POX can also be carried out in the presence of an oxidation catalyst. In this case, the process is called catalytic partial oxidation (CPOX).

Autothermal Reforming (ATR)

As already stated, SMR is highly endothermic and commercially tubular reactors are used to achieve the heat input required. A possibility to supply this heat input is to use the partial combustion of methane by autothermal reforming (ATR), where oxygen and steam are used in the conversion process. The reformer consists of a ceramic-lined reactor with a combustion zone and a downstream fixed-bed catalytic SMR zone. The heat generated in the combustion zone is directly transferred to the catalytic zone by the flowing reaction gas mixture, thus providing the heat needed for the endothermic reforming reaction. Today, ATR is used primarily for very large conversion units. There are several other design concepts that combine direct oxygen injection and catalytic conversion, including secondary reforming.

Hydrogen Purification for PEM Fuel Cells

In the future hydrogen economy various types of fuel cells will play a crucial role as energy transformers. For these devices, the requirements regarding hydrogen purity are quite high, especially for the low-temperature PEM fuel cells. The concentration of CO in the hydrogen fuel stream, for instance, must not be higher than 10 ppm when a Pt catalyst is used on the anode side, and it must not exceed 100 ppm in the case of a Pt/Ru catalyst. For mobile or portable applications working with PEMFC systems, the fuel processor has to be compact and lightweight. In order to achieve these goals, the final step of downstream hydrogen purification is catalytic preferential oxidation instead of the bulkier pressure swing adsorption. Figure 2.5 displays a general diagram of fuel reforming to produce high-purity hydrogen for PEM fuel cells.

In general, the development of fuel processors on different scales for energy conversion with fuel cells has triggered the R&D of chemical reactor engineering in both up-scale and down-scale direction, as shown in Fig 2.6. The reactors are designed to cover the power range from mW to several hundreds of kW, i.e. in the span of 7 to 8 orders of magnitude!

The vast commercial experience based on this manufacturing capacity has led to many improvements of the technology, the objective being to reduce costs and to increase efficiency. Perhaps, the most important element is the tubular reactor in which the SMR reaction takes place. Progress has led to higher tube wall temperatures, better control of carbon formation, and feedstock flexibility. This, in turn, has resulted in lower steam-to-carbon ratios and improved efficiency. The water-gas shift unit has also been improved. Now, one-step shift can be employed to replace the former two-step operation at different temperatures. Finally, purification of the

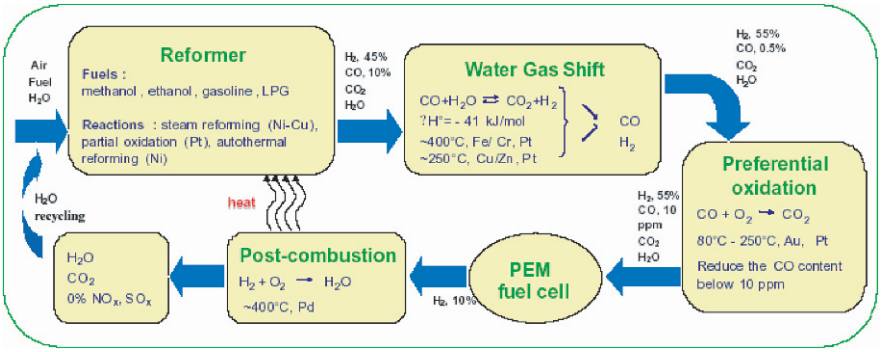

Fig. 2.5 General scheme of fuel reforming for the production of hydrogen to be used in low-temperature PEMFCs

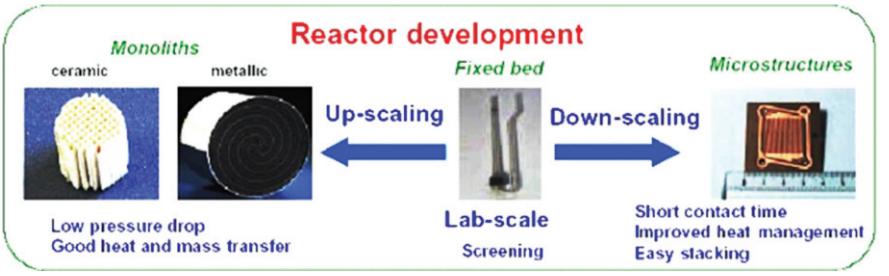

Fig. 2.6 Fuel processor development for hydrogen production in fuel cell applications

hydrogen product has been simplified by using pressure swing adsorption (PSA) to remove methane, carbon oxides, and trace impurities in a single step. While designs today do not generally include CO_2 capture, the respective technology is available. Using a commercial selective absorption process, CO_2 could be recovered for subsequent sequestration.

2.2.2.2 Available Commercial Plants

Progress has also been achieved in designing and building larger SMR plants. Currently, single-train commercial plants of up to 480,000 kg H_2 per day exist and even larger plants can be constructed using multiple trains. Furthermore, units delivering quantities as small as 300 kg/day are being built. Figure 2.7 displays photos of such a commercial small-scale SMR plant which uses components of fixed design, one of the elements of mass production (see, for instance, http://www.mahler-ags.com/de/wasserstoff/hydroform-c.htm). In many cases, the units built are unique, with specific features to meet the requirements of a site, application, or customer.

Partial oxidation utilizing natural gas is fully developed and used commercially. For economic reasons, commercial units today use feeds of lower value than natural gas, such as coal, coke, petroleum residues, or other by-products. However, natural

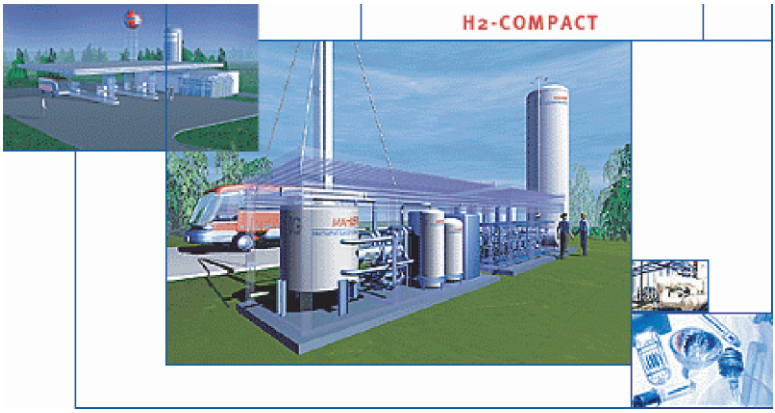

Fig. 2.7 Small-scale SMR plant for hydrogen generation in the range between 107 and 214 kg/day

gas is the feed preferred for POX from the technical point of view and can be used to generate hydrogen competitively.

Currently, oxygen-blown ATR with natural gas is used in very large units that generate a mixture of CO and H_2 for the Fischer-Tropsch process or methanol synthesis. This is partly attractive, because the units can produce the hydrogen-to-carbon monoxide ratio needed in the synthesis step. Since the heat of reaction is added by combustion with oxygen, the catalyst can be incorporated as a fixed bed that can be scaled up to achieve further benefits of a larger plant size in both the ATR and the oxygen plant. ATR also offers benefits when CO_2 capture is included. The optimum separation technology for this design recovers CO_2 at 3 bar, which, in turn, reduces the costs of compression to pipeline pressure (75 bar).

In summary, all three processes (SMR, POX, and ATR) are mature technologies today for the conversion of natural gas into hydrogen. SMR is the less expensive one compared to POX and ATR. However, this is not true for very large units, where ATR has this advantage. SMR also is more efficient when including the energy for air separation. POX has the advantage of being applicable to lower-quality feeds, such as petroleum coke, but this is not directly relevant to natural gas conversion.

2.2.2.3 Distributed Generation from Natural Gas

For distributed generation, the cost of sequestration appears prohibitive [4]. Release of carbon dioxide from distributed generation plants during the transition to a hydrogen economy may be a necessary consequence, unless an alternative, such as hydrolysis with electricity from renewable resources becomes sufficiently attractive or R&D significantly improves the distributed natural gas production systems.

Distributed hydrogen generation from natural gas could be the lowest-cost option during the transition phase. However, it has never been achieved in a manner that meets all of the special requirements of this application. The principal challenge is to develop a hydrogen appliance with a demonstrated capability of being produced

in series and operated reliably and safely in service stations with periodic inspection by non-trained personnel only (station attendants and consumers).

The capability for mass production is needed in order to meet the demand during the transition period (thousands of these units would be needed) and minimize manufacturing costs. These units need to be designed to maximize operating efficiency, to include the controls, "turndown" capability, and to meet using the required hydrogen storage system the variable demand for hydrogen over 24 hours. They also must be designed to meet the hydrogen purity requirements of fuel cells. Steam reforming process technology is available for this application and companies have already provided one-of-a-kind units in the size range of interest.

The possibility to use partial oxidation or autothermal reforming for the distributed generation of hydrogen will depend on the development of new paths to recover oxygen from air or to separate the hydrogen product from nitrogen. This is necessary, as conventional, cryogenic separation of air will become increasingly expensive while the unit size will be scaled down. In contrast to this, membrane separations appear amenable to this application and may provide the means for producing small and efficient hydrogen units.

2.2.2.4 Economic Efficiency of Hydrogen Production

Given the current interest in possibilities of a hydrogen economy and the current commercial need for hydrogen, significant effort focuses on improving natural gas conversion into hydrogen. Improved catalysts, materials of construction, process simplification, new separation processes, and reactor concepts that can improve the integration of steam reforming and partial oxidation are investigated as well as catalytic partial oxidation. Since steam reforming and partial oxidation are mature technologies, the primary improvement options will be to develop designs for specific applications that are cost-effective and efficient.

Several thousand distributed generators will be needed for hydrogen economy, and it should be possible to lower the cost of these generators significantly by the mass production of a generation "appliance." Such appliances may be further improved by tailoring the design to the fueling application. For example, hydrogen would likely be stored at roughly 400 bar. To the extent the conversion reactor pressure can be increased, hydrogen compression costs would be reduced and efficiency improved. For distributed generators incorporating POX or ATR, suitable cost-effective hydrogen purification methods have to be developed. Alternatively, the oxygen may be recovered with membranes, which will lower the costs. Other concepts are being studied at the moment. They comprise new or modified ways of providing the endothermic heat of steam reforming or utilizing the heat of reaction in partial oxidation.

In the following section plant sizes of 1,200,000 kg per stream day (kg/SD), 24,000 and 480 kg/SD will be investigated for hydrogen production from natural gas. For each plant size, two possibilities will be considered, with the current case representing what can be done today with modern technology and the future case

representing what might be possible in the future. The future case for the 480 kg/SD plant includes the estimated benefits of mass production. Moreover, options for the two larger plants include CO_2 sequestration and compression of H_2 to pipeline pressure (75 atm) SS. The sequestration option was not included for the smallest plant, since the costs of collecting CO_2 from distributed plants were considered to be too high, as 4.40 US$/kg H_2 have to be added.

Table 2.1 displays the economic data of the conversion of natural gas into hydrogen for these three different plants. As can be seen, current investments vary from 411 US$ to 3847 US$/kg/SD as plant size is decreased from 1.2 million to 480 kg/SD. While the improved technology in the future will lower the investment by 20 to 48%, plant size will have a more pronounced effect. For the two larger plants, the implementation of CO_2 capture will increase the investment by 22 to 35%.

Hydrogen cost in the largest plant without CO_2 capture is 1.03 US$/kg with current technology and 0.92 US$/kg with future technology. This cost increases to 1.38 and 1.21 US$/kg in a medium-sized plant, and to 3.51 and 2.33 US$/kg in the smallest plant. CO_2 capture adds 11 to 21%, depending on the scenario. Moreover, the overall thermal efficiency of the largest plant will vary from 72.3 to 77.9% without CO_2 capture and from 61.1 to 68.2% with CO_2 capture. Efficiency of the smallest plant is 55.5 to 65.2%. Without capture, the CO_2 emissions are 8.8 to 12.1 kg CO_2 per kilogram hydrogen. Capture lowers these emissions to 1.3 to 1.7 kg CO_2 per kilogram of hydrogen. These emissions and thermal efficiency estimates include the effects of generating the required electricity offsite in state-of-the-art power generation facilities of 65% efficiency at 0.32 kg CO_2/kWh of electricity.

The DOE states that its goal by 2010 is to reduce the cost of the distributed production of hydrogen from natural gas and/or liquid fuels to 1.50 US$/kg (delivered, untaxed, without sequestration) at the pump, based on a natural gas price of 3.8 US$/GJ. Analysis indicates that this goal will be very difficult to achieve for the distributed hydrogen plants and likely require additional time. The possible future case of distributed generation taking into account the estimated benefits of mass production of SMR units yields a hydrogen cost of 1.88 US$/kg with 3.8 US$/GJ of natural gas. Achievement of the DOE goal would require additional thermal efficiency improvements and investment reductions. The goal could be met, if, for example, the SMR thermal efficiency was further increased to 70 or 80% (excluding the compression of the hydrogen product to storage pressure). In addition, the SMR investment could be cut by 35% when including the benefits of mass production. It is also important to note that the cost estimates are based on the assumption that distributed generators operate throughout the year at 90% design capacity. As a consequence, units would have to operate at or near design capacity 24 hours a day. Otherwise, the cost of hydrogen from such units would be higher than calculated. Achieving a 90% capacity factor would require careful integration of the design rate of the hydrogen generator, hourly demand variations at fueling stations, and onsite storage capability.

Future costs of hydrogen from small hydrogen plants are subject to considerable uncertainties which are even further increased by the need for a high reliability and safe operation with infrequent attention by relatively non-trained operators (i.e. customers and station attendants).

Table 2.1 Economic data of the conversion of natural gas into hydrogen

	Plant Size (kilograms of hydrogen per stream day [SD]) and Case					
	1,200,000[PTU*a*UTP]		24,000[PTU*b*UTP]		480[PTU*c*UTP]	
	Current	Possible Future	Current	Possible Future	Current	Possible Future
Investment (no sequestration) $/kg/SD	411	297	897	713	3847	2001[PTU*d* UTP]
Investment (with sequestration), $/kg/SD[PTU*e*UTP]	520	355	1219	961	–	–
Total H_2 cost (no sequestration), $/kg	1.03[PTU*f*UTP]	0.92[PTU*f*UTP]	1.38[PTU*f*UTP]	1.21[PTU*f*UTP]	3.51[PTU*g*UTP]	2.33[PTU*g*UTP]
Total H_2 cost (with sequestration), $/kg[PTU*e*UTP]	1.22[PTU*f*UTP]	1.02[PTU*f*UTP]	1.67[PTU*f*UTP]	1.46[PTU*f*UTP]	–	–
CO_2 emissions (no sequestration), kg/kg H_2	9.22	8.75	9.83	9.12	12.1	10.3
CO_2 emissions (with sequestration), kg/kg H_2	1.53	1.30	1.71	1.53	–	–
Overall thermal efficiency (no sequestration), %[PTU*h*UTP]	72.3[PTU*a*UTP]	77.9[PTU*a*UTP]	46.1	53.1	55.5	65.2
Overall thermal efficiency (with sequestration), %[PTU*e*UTP, PTU*h*UTP]	61.1	68.2	43.4	49.0	–	–

[PT*a*TP]Includes compression of the hydrogen product to pipeline pressure of 75 atm.
[PT*b*TP]Includes liquefaction of H_2 prior to transport.
[PT*c*TP]Includes compression of H_2 to 400 atm for storage/fueling vehicles.
[PT*d*TP]Includes estimated benefits of mass production.
[PT*e*TP]Includes capture and compression of CO_2 to 135 atm for pipeline transport to sequestration site.
[PT*f*TP]Based on natural gas at 4.27 US$/GJ.
[PT*g*TP]Based on natural gas at 6.17 US$/GJ.
[PT*h*TP]Based on lower heating values for natural gas and hydrogen; includes hydrogen generation, purification, compression, and energy imported from outside as well as distribution and delivery.

Hydrogen cost when using steam-methane reforming is sensitive to the price of natural gas. Based on current technology cases, an increase in the natural gas price from 2.37 US$ to 6.17 US$/GJ will increase hydrogen cost by 97% in a 1.2 million kg/SD plant and by 68% in a 24,000 kg/SD unit. For the 480 kg/SD unit, an increase from 4.27 US$ to 8.06 US$/GJ will raise the hydrogen cost by 28%. These figures underline the importance of focusing research on improving efficiency in addition to reducing investment.

2.2.2.5 Natural Gas and Methane Emissions

Natural gas is lost into the atmosphere during the production, processing, transmission, storage, and distribution of hydrogen. Since methane, the major component of natural gas, has a global warming potential of 23 [11], this matter deserves discussion.

Methane is produced primarily in biological systems by the natural decomposition of organic waste. Methane emissions include those from agriculture and the decomposition of animal wastes. The Environmental Protection Agency (EPA) estimates that 70% of methane emissions result from human activities and the remainder from natural processes. Less than 20% of the total global emissions of methane are related to fossil fuels, including natural gas operations. The EPA reports that 19% of the anthropogenic emissions of methane in 2000 came from natural gas operations. Of these, 25% originated from the distribution of natural gas within cities, primarily to individual users [12].

As already pointed out, the use of hydrogen-powered cars would significantly increase natural gas consumption. However, this increase would not necessarily increase losses from the natural gas system.

2.2.2.6 Outlook

There are several advantages in generating hydrogen from natural gas. Feedstock availability is quite high, since natural gas is available in most populated areas and an extensive pipeline distribution system for natural gas already exists in Europe. Furthermore, extensive commercial experience exists and natural-gas-to-hydrogen conversion technology is widely used commercially throughout the world. Moreover, optimization of large plants has reached an advanced stage. If centralized, large-scale natural gas conversion plants are built, CO_2 can be captured for subsequent sequestration. Using small distributed hydrogen generators, however, separation and capture of CO_2 probably will not be economically feasible. Small-scale reformers at fueling stations most likely will be implemented during the transition period, if policies will be adopted to stimulate a transition to hydrogen for light-duty vehicles.

The major drawbacks of natural gas are that it is a non-renewable, limited resource and increasing amounts will have to be imported in the future to meet EU

market needs—which will be opposite to the goal of improving the EU's supply security. Moreover, natural gas prices fluctuate and are very sensitive to seasonal demand. This variability becomes even more important knowing that SMR economics are sensitive to the natural gas price (see above).

Distributed generation of hydrogen from natural gas in fueling facilities might be the lowest-cost option for hydrogen production during the transition period. However, the future cost of this option is uncertain, given the technical and engineering uncertainties as well as the special requirements of the EU program, as development is advanced by contract research organizations.

Distributed generation of hydrogen is envisaged to meet two particular requirements:

(1) Mass production of thousands of generating units with the latest technology improvements in order to meet the demand, minimize the costs, and improve efficiency.
(2) Unit designs and operating procedures that ensure a reliable and safe operation of these appliances with periodic surveillance by relatively non-trained personnel only (station attendants and consumers).

In contrast to this, centralized generation of hydrogen in one-of-a-kind, medium-sized, and large plants is practiced widely. As a result, an extensive commercial experience is available in this area. Given the commercial market for hydrogen, suppliers will continue to search for ways to improve the technology and make it even more competitive for medium- and large-scale plants.

According to the EU HFP programme, research of distributed generation will include demonstration of a "low-cost, small-footprint plant" [8]. The requested designs would involve concomitant engineering that would create designs for manufacturing engineering to guide research and to prepare for the mass production of the appliance. A system design will also be developed for a typical fueling facility, including the generation appliance, compression, high-pressure storage using the latest storage technology, and dispensers. With today's technology, such ancillary systems cost 30% as much as the reformer. It is believed that these costs can be reduced by over 50% and that efficiency may be improved by system integration and the incorporation of the latest technology. Compression and high-pressure storage are examples of systems for which significant improvements are expected.

The EU HFP program has been launched to stimulate the development of newer concepts, such as membrane separation coupled with chemical conversion. Currently, there is only a little, if any market for mass-produced hydrogen appliances. Therefore, it is advisable that EU HFP should stimulate the development of these devices. Primary challenges are the development and demonstration of two features:

(1) A mass-produced hydrogen appliance suitable for distributed generation in fueling stations and
(2) a complete hydrogen system for fueling stations, which is capable of meeting a variable hydrogen demand on a 24-hour basis.

With further research and development, the unit capital cost of a typical distributed hydrogen plant producing 480 kilograms of hydrogen per day (kg/d) might be reduced from 3847 to 2000 US$/kg/d, and the unit cost of hydrogen might be reduced from 3.51 to 2.33 US$/kg. These hydrogen unit costs are based on a natural gas price of 6.17 US$/GJ; a change in the natural gas price of plus or minus 1.90 US$/GJ would change the hydrogen cost by about 12% with current technology. Improved plants could reduce the estimated CO_2 emissions from 12.1 to 10.3 kg per kilogram of hydrogen, and overall thermal efficiencies might improve from 55.5 to 65.2%, in either case without sequestration.

2.3 Hydrogen from Nuclear Energy

Nuclear energy is a viable option for producing large quantities of hydrogen without greenhouse gases being generated or favorable renewable energy conditions or large land areas being needed. Since nuclear reactors are by nature very concentrated sources of energy, large centralized hydrogen production plants can be constructed on relatively small land areas with flexible siting requirements. Similar to coal-based hydrogen plants, nuclear hydrogen plants will require a hydrogen delivery infrastructure to connect the centralized production facilities with distributed users, such as hydrogen refueling stations for automobiles. The lack of a current hydrogen infrastructure may be overcome in the near future, if nuclear hydrogen plants were first used to supply hydrogen to large industrial users, such as oil refineries, fertilizer (ammonia) plants, large plants processing tar sands and hydrogen, or synfuel plants. In this case, hydrogen from nuclear plants would replace hydrogen produced by natural gas steam reforming in most cases. The capacity of a typical nuclear hydrogen plant would be in the range of 200–800 tons hydrogen per day, which is comparable to the requirements of the large industrial hydrogen users listed above. Figure 2.8 displays an example of a “nuclear hydrogen future”.

There are several ways of producing hydrogen from nuclear energy. Nuclear reactors may be used to generate electricity which, in turn, could be used to power water electrolyzers to produce hydrogen. Since low-temperature electrolysis is a proven, commercial process, this approach to hydrogen production from nuclear energy could be used today. In fact, since nuclear energy currently supplies a significant amount of electricity in many countries, any electrolyzer running on grid-based electricity is actually producing “nuclear hydrogen”. The largest cost factor of hydrogen generated by conventional electrolysis is the cost of electricity, and in many cases, nuclear power plants produce low-cost electricity compared to other generating sources. According to the Nuclear Energy Institute in the U.S., the current generating cost for existing nuclear plants (not including the capital cost-carrying charges) is less than 2.0 cents per kilowatt-hour, which is about the same as coal-based electricity and less than half of that of oil or natural gas plants. However, electricity from new nuclear power plants will be more expensive due to the capital investments required. A recent study [13] estimated the cost of electricity

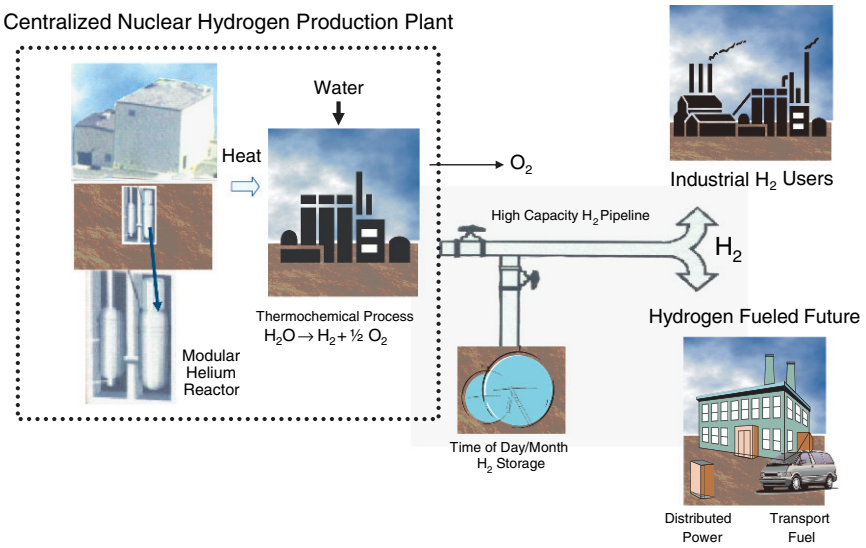

Fig. 2.8 A future hydrogen supply system using nuclear energy

from new light-water nuclear plants to be 4.0 to 6.7 cents per kilowatt-hour, depending on a number of factors, including capital costs, construction time, and the capital cost.

However, even with electricity at 5 cents per kilowatt-hour, electrolysis is a relatively expensive means of producing hydrogen. At 70% efficiency, a water electrolyzer requires about 53 kWh of electricity per kilogram of hydrogen produced. Therefore, the cost of electricity alone amounts to $2.65/kg. Including capital cost of the electrolyzer and OM costs, hydrogen costs in excess of $3.50/kg result. Moreover, this is a fairly inefficient process, since the overall efficiency of hydrogen production would be about 23%, if the electricity was generated at 33% efficiency as in the current light-water nuclear reactors. Although hydrogen produced by this method would be expensive compared to current transportation fuels, nuclear plants combined with conventional electrolysis may still be a viable approach, if future transportation costs will increase significantly or carbon limits will be imposed due to global warming concerns.

In the longer term, the most attractive hydrogen production means using nuclear energy will be those that utilize high temperatures or efficient electricity from an advanced nuclear reactor to produce hydrogen from water. These advanced reactors are known as generation IV nuclear reactors and they are designed to be more efficient, safer, and more economical than the current version of light-water reactors. The high-temperature helium gas-cooled reactors are the most developed type, and first demonstration plants are expected to be built in the next 10 years. They are of modular design, typically 400–600 MW(th) per reactor, and can be installed in underground silos to enhance safety. When utilizing a refractory type of

nuclear fuel, they are passively safe, meaning that natural forces are sufficient to prevent the temperatures from reaching the melting point of the fuel and creating a runaway reaction. Helium-cooled nuclear reactors operate at very high temperature, and they are capable of delivering process heat in the temperature range of 800–1000°C. This is ideal for the most promising high-temperature water splitting processes. The high-temperature heat can also be used to generate electricity in a Brayton gas turbine cycle, thus increasing the nuclear plant's electricity generation efficiency to 45–48%, compared to 33% for conventional light-water reactors.

Two main approaches have emerged as leading contenders for high-temperature water splitting using heat from advanced nuclear reactors: Thermochemical cycles and high-temperature (steam) electrolysis (HTE). HTE is based on the use of solid oxide fuel cell technology. Since the electrolyzers operate at high temperature (800–1000°C), a portion of the energy needed for water dissociation can be supplied in the form of thermal energy rather than electricity. This may result in a significant increase in hydrogen production efficiency. Even with the high electricity generation efficiency of gas-cooled reactors, the overall hydrogen generation efficiency using low-temperature water electrolysis is 32–35% only. By combining the high-temperature reactor with an HTE, the overall hydrogen generation efficiency can be increased to 45–50%.

Perhaps, the most compelling technology for generating hydrogen with nuclear energy is thermochemical water splitting. Thermochemical cycles produce hydrogen through a series of coupled chemical reactions, some endothermic and some exothermic. Energy is input in the form of heat (or heat plus smaller amounts of electricity for hybrid cycles). The net result is the production of hydrogen and oxygen from water at a much lower temperature than direct thermal decomposition of water. All the process chemicals are fully recycled, and the only consumable is water. Typically, a high-temperature endothermic reaction step is necessary, requiring thermal energy in the temperature range of 750–1000°C. Thermochemical cycles were investigated from the late 1960s through the mid-1980s, but most development activities were stopped as nuclear power fell out of favor. Over 200 cycles using different combinations of chemical reactions have been identified in literature, although many have been found to be unworkable, to have parasitic side reactions that reduce efficiency, or to require excessive temperatures. Thermochemical cycle technology still is in a relatively early stage, and only a few cycles have been demonstrated on the laboratory scale. Although there is still uncertainty about the outcome of the R&D, there also is the potential for significant process improvement based on more recent advances in materials and chemical process technology over the past two decades.

Figure 2.9 displays the most developed thermochemical cycle, the sulfur-iodine cycle. In this cycle iodine and sulfur dioxide are added to water, forming hydrogen iodide and sulfuric acid in an exothermic reaction. Under proper conditions, these compounds are immiscible and can be separated easily. The sulfuric acid can be decomposed at about 850°C, releasing the oxygen and recycling the sulfur dioxide. Hydrogen iodide can be decomposed at about 350°C, releasing hydrogen

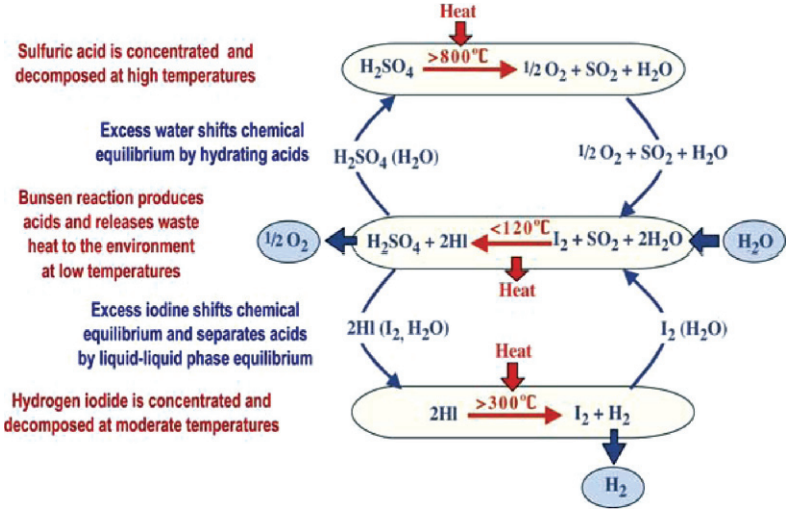

Fig. 2.9 The sulfur-iodine thermochemical water splitting cycle [14]

and recycling iodine. The net reaction is the decomposition of water into hydrogen and oxygen. The whole process requires water and high-temperature heat only and releases hydrogen, oxygen, and low-temperature heat. All reagents are recycled without any routine release of effluents. Figure 2.10 shows a simple schematic representation of the process.

A complete laboratory-scale system of the S-I cycle has been operated successfully at low pressure in Japan, producing up to ~50 normal liters/hour of hydrogen. A laboratory-scale S-I cycle test loop working under prototypical pressure and temperature conditions is now under construction in the U.S. by General Atomics,

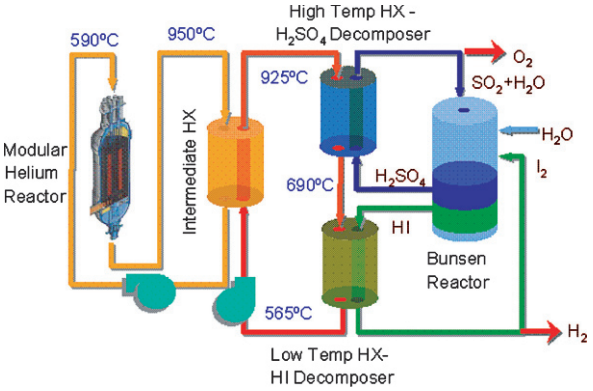

Fig. 2.10 Schematic representation of the sulfur-iodine cycle [14]

Sandia National Laboratory, and the French national laboratory CEA. [15]. The loop is designed to produce 100–200 normal liters/hour of hydrogen. Commercialization of this process is planned to catch up with that of the high-temperature gas-cooled reactors by 2017–2020. Overall process efficiency is expected to be approximately 46%. When coupled to a modular helium reactor, the cost of hydrogen production is estimated to be $3.00/kg without any emissions of CO_2 [14].

A second leading thermochemical cycle is the hybrid sulfur (HyS) process which was originally developed by the Westinghouse Electric Company in the 1970s. The HyS process is a variant of sulfur-based thermochemical cycles, and it utilizes the same high-temperature sulfuric acid decomposition step as the S-I cycle to form sulfur dioxide and liberate oxygen. Instead of using other thermochemical reactions to produce hydrogen and/or regenerate reactants, however, the HyS process uses a sulfur dioxide depolarized electrolyzer (SDE). As a result, only hydrogen, oxygen, and sulfur species are involved in the process chemistry. This greatly simplifies material considerations and minimizes chemical separation steps. The two-step HyS cycle consists of the following chemical reactions:

$$H_2SO_4 \Leftrightarrow SO_2 + H_2O + \frac{1}{2}O_2 \text{ thermochemical}, 800 - 900^\circ C$$
$$2H_2O + SO_2 \Leftrightarrow H_2SO_4 + H_2 \text{ electrochemical}, 100 - 120^\circ C$$

The electrolyzer oxidizes sulfur dioxide to form sulfuric acid at the anode and reduces protons to form hydrogen at the cathode. The presence of SO_2 at the anode of the electrolyzer greatly decreases the reversible cell potential for electrolysis. Whereas direct electrolysis of water has a reversible cell potential of 1.23 volts at 25°C, the reversible potential for SO_2 anode-depolarized electrolysis is 0.158 volts only (a theoretical 87% reduction in electric energy requirements). The research objectives are to achieve practical cell voltages of 0.5 to 0.6 volts at current densities of 500 mA/cm^2.

The major processing operations necessary for hydrogen production using the HyS process are shown in Fig. 2.11. Since HyS is a hybrid thermochemical cycle, energy input in the form of both electricity and thermal energy is required. For a commercial nuclear hydrogen plant, approximately 38% of the nuclear reactor's thermal output would be directed to electricity production and 62% to provide process heat. Recent flowchart analysis and optimization led to calculated overall thermal process efficiencies of 52–54% on a higher heating value basis [16].

The cost of hydrogen from thermochemical cycles depends primarily on the capital cost of the nuclear reactor, the capital cost of the hydrogen plant, and the overall efficiency of converting nuclear heat into hydrogen. Estimates for mature, large centralized plants using gas-cooled nuclear reactors and the HyS thermochemical cycle reveal hydrogen production costs of $2.00/kg or less. This may be competitive with hydrogen from natural gas steam reforming plants, if the cost of natural gas exceeds about $5.00 per million Btu and/or limitations or taxes are imposed due to the gas plant's carbon dioxide emissions.

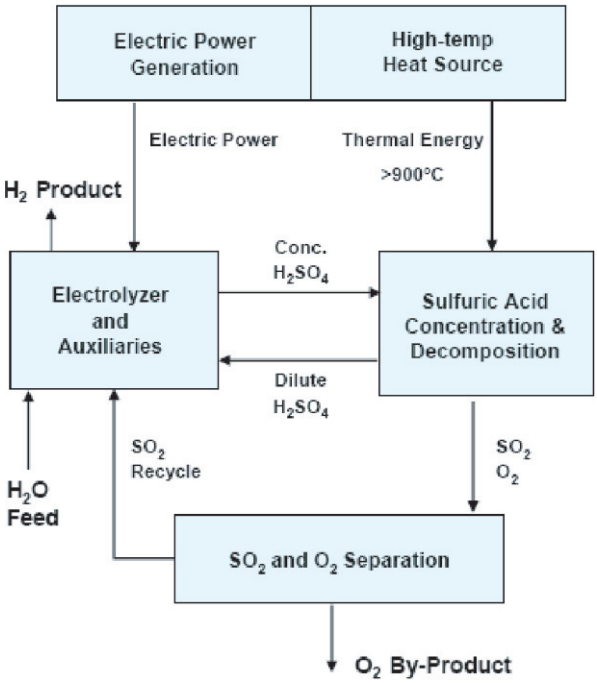

Fig. 2.11 Flowchart of the hybrid sulfur process

2.4 Production from Renewable Sources

The production of hydrogen from renewable energy sources is often stated to be the long-term goal of a mature hydrogen economy [17]. The development of cost-effective renewable technologies should clearly be a priority in the hydrogen program, especially since considerable progress will be required before these technologies will reach the levels of productivity and economic viability needed to compete effectively with the traditional alternatives. Thus, basic research in the area of renewable energy needs to be extended, and the development of renewable hydrogen production systems accelerated.

2.4.1 Hydrogen from Water Electrolysis

Hydrogen can be produced from water using the process of electrolysis to dissociate water into its separate hydrogen and oxygen constituents. Electrolysis technologies that have been in use for decades both dissociate water and capture oxygen and/or hydrogen, primarily to meet the needs of chemical industry. Electrolysis also played a critical role in life support (oxygen replenishment) in space and submarine applications over the past decades.

2.4.1.1 Why is Electrolysis of Interest?

Production of hydrogen by electrolysis generally consumes considerably more energy per unit hydrogen produced than hydrogen produced from hydrocarbons. Nonetheless, electrolysis is of interest as a potential source of hydrogen energy for several reasons, as will be discussed below.

- Water (and the hydrogen it contains) is more abundant than hydrocarbons are. Depletion and geopolitical concerns related to water generally are far less serious compared to those related to hydrocarbons. Furthermore, there are geographical regions around the world where hydrocarbons (especially natural gas, the predominant source of hydrogen reformation) simply are not available. In such areas hydrogen obtained from water may be the only practical means of providing hydrogen.
- The net energy costs of producing hydrogen by electrolysis must be seen in an economic context. Electrolysis may be a means of converting low-cost energy sources (e.g. coal) into much higher-value energy sources to replace gasoline or other transport fuels.
- Electrolysis is considered to be a potentially cost-effective means of producing hydrogen on a distributed scale and at costs appropriate to meet the challenges of supplying the hydrogen needed by the early generations of fuel cell vehicles. Electrolyzers are compact and may be situated at existing fueling stations.
- Electrolysis represents a path towards hydrogen production from renewably generated electrical power. From the energy point of view, electrolysis literally is a way to transform electricity into fuel. Thus, electrolysis is the means of linking renewably generated power to transport fuel markets. Currently, renewable solar, wind, and hydro power, by themselves, are producing electricity only.
- Electrolyzers operating together with power-generating devices (including fuel cells) represent a new architecture for markets of distributed energy storage. Various electrolyzer suppliers are developing products that can generate hydrogen when primary electricity is available, then store it, and use this hydrogen for subsequent regeneration into electricity when needed. For example, several firms are involved in developing backup power devices that operate in the 1 to 20 kilowatts (kW) range for up to 24 hours, well beyond the capacity of conventional batteries. The same concept is being applied directly to renewable sources, creating the means to produce power-on-demand from inherently intermittent renewables.

Finally, electrolysis may play a role in regenerative braking on vehicles. Electrolyzers and hydrogen have the appropriate scale and functionality to become part of the distributed generation marketplace, as the costs of electrolyzers will fall with time.

2.4.1.2 Electrolysis with a Solid Polymer and Liquid Electrolyte

Current electrolysis technologies are divided into two basic categories:

(1) Solid polymer electrolyte (which provides for a solid electrolyte) [17]
(2) Liquid electrolyte, most commonly potassium hydroxide (KOH)

In both technologies water is introduced into the reaction environment, where it is dissociated by an electric current. The resulting hydrogen and oxygen are then separated by an ion-conducting membrane into two separate physical streams.

Solid polymer or proton exchange membranes were developed in the 1950s and 1960s by General Electric and other companies in order to support the U.S. space program. A proton exchange membrane (PEM) electrolyzer literally is a PEM fuel cell operating in the reverse mode, as displayed in Fig. 2.12. Indeed, when water is fed into the PEM electrolyzer cell, hydrogen ions are drawn into and through the membrane, where they recombine with electrons to form hydrogen atoms. Hydrogen gas is channeled separately from the cell stack and captured. Oxygen gas remains behind in the water. As this water is recirculated, oxygen accumulates in a separation tank and can then be removed from the system.

Electrolyzers equipped with a liquid electrolyte typically use a caustic solution to perform similar functions as a PEM electrolyzer. In such systems oxygen ions migrate through the electrolytic material, leaving hydrogen gas dissolved in the water stream. This hydrogen is extracted readily from the water, when it is directed into a separating chamber.

In history KOH systems were used in larger-scale applications than PEM systems. The Electrolyzer Corporation of Canada (now Stuart Energy) and the electrolyzer division of Norsk Hydro built relatively large plants (100 kg/hour and larger) to meet fertilizer production needs at locations around the globe, where natural gas is not available to provide hydrogen for the process.

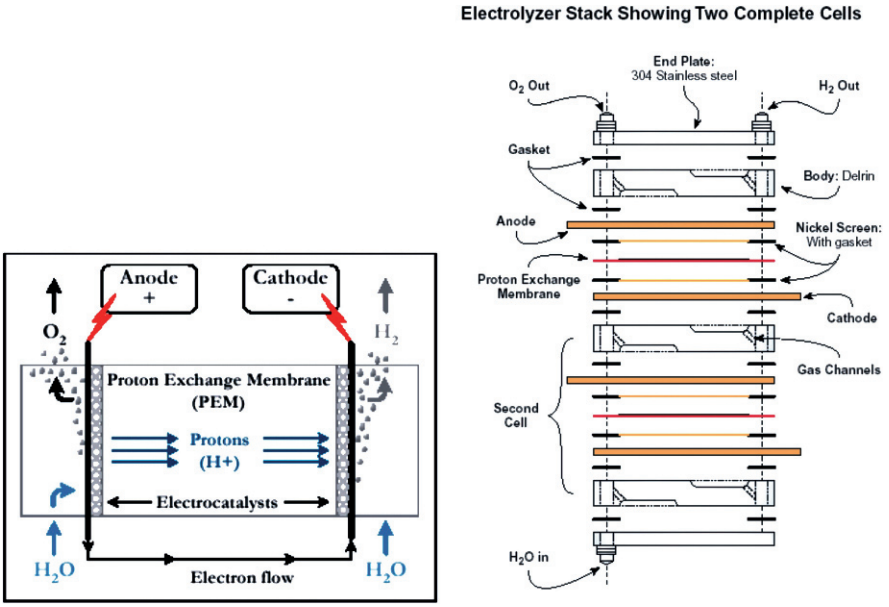

Fig. 2.12 Schematic representation of PEM electrolyzer functioning (left) and cross-section of the PEM electrolyzer stack (right)

Today, the all-inclusive costs of producing hydrogen using a PEM and a KOH electrolyte are roughly comparable. Reaction efficiency tends to be higher for KOH systems, because the ionic resistance of the liquid electrolyte is lower than the resistance of current PEM membranes. The reaction efficiency advantage of KOH systems over PEM systems, however, is compensated by higher purification and compression requirements, especially for a small-scale plant (1 to 5 kg/hour).

Proton exchange membranes, whether operating in the electrolysis mode or fuel cell mode, have a higher efficiency at lower current density. There is a 1:1 relationship in electrolysis between the rate of hydrogen production and the current applied to the system. The energy required at the theoretical efficiency limit of any water electrolysis process is 39.4 kWh per kilogram. PEM electrolyzers operating at low current density may approach this efficiency limit. However, the quantities of hydrogen produced at low current density are small, resulting in very high capital costs per unit hydrogen produced. Cell stack efficiencies drop to 75% when current densities rise to the range of 10,000 amps per square meter. As previously stated, the electrochemical efficiency of KOH systems is higher over a broader range of current densities. But this higher reaction efficiency is balanced at least in part by higher compression and purification costs as well as by higher costs associated with managing the liquid electrolyte itself.

2.4.1.3 Commercial Electrolyzers

At present, electrolyzers are commercially viable in selected industrial gas applications only and in various non-commercial military and aerospace applications (see, for instance, http://www.claind.it/sito/prodotti/hydrogen-generators/index.php or http://www.teledynees.com/). Commercial applications include the above-mentioned remote fertilizer markets, on which natural gas feedstock is not available. The other major commercial market for electrolysis today is the distributed or "merchant" industrial hydrogen market. This merchant market involves hydrogen delivery by truck in various containers. Large containers are referred to as tube trailers. An industrial gas company will deliver a full tube trailer to a customer and take the empty trailer back for refilling. Customers with smaller-scale requirements are served by cylinders that are delivered by truck and installed by hand.

The hydrogen generator installation costs range between 30,000 and 400,000 €, and depend on the hydrogen production capacity (from 0.5 to 30 Nm^3/h), delivery pressure (up to 15 bar), and hydrogen purity (99.7 or 99.999%). In general, the smaller the quantities of hydrogen required by a customer are, the higher is the all-inclusive cost. Tube trailer customers (e.g. semiconductor, glass, or special metal manufacturers) pay an amount in the range of about 12 US$/kg H_2. Cylinder customers (e.g. laboratories, research facilities, and smaller manufacturing companies) pay at least twice the tube trailer price. The value of hydrogen on distributed chemical markets today is much higher than the value of hydrogen used as fuel. The price of hydrogen will have to be in the 2.00 US$/kg range to compete with conventional fuels for transportation.

It will take significant cost reduction and efficiency improvement efforts for electrolytic hydrogen to compete on vehicle fueling markets. Nonetheless, a number of stationary energy-related applications for electrolytic hydrogen are beginning to materialize. These smaller, but higher-value energy applications deserve attention and support, as they will advance the practical development of hydrogen from electrolysis for future, larger-scale fueling markets.

Power-on-demand from inherently intermittent renewables is another interesting application of electrolysis. Off-grid, renewable-based systems need electricity at night or when the wind does not blow. The value difference between electricity when available and when needed is often great enough to use batteries to fill this gap. When the amount and duration of stored energy become large in relation to battery functionality, an electrolyzer-hydrogen regenerative system may be a lower-cost solution, as it will eventually enhance the use of renewables for meeting off-grid energy needs.

2.4.1.4 Cost of Hydrogen from Electrolysis

The current technology may provide an electrolyzer-based fueling facility which produces hydrogen at a rate of 480 kg/day or 20 kg/hour. This plant would be able to refuel 120 cars per day, assuming an average of 4 kg per car. Electrolyzer systems of this scale are expected to operate with an overall efficiency of 63.5% lower heating value [LHV], including all parasitic loads other than compression. The electrolyzer can generate hydrogen at an internal pressure in the 10 bar range. Consequently, supplementary compression is required for automotive application in order to raise the pressure to the range of 400 bar. In this case, an additional electrical requirement associated with compression must be fulfilled. If assuming that 2.3 kW/kg/hour are needed, then about 5% are added to the plant's electrical consumption. As a consequence, the overall efficiency is dropping down to about 59%. Today, a plant of this scale would consist of a solid polymer electrolyzer only. With additional development, however, PEM technology is expected to achieve a comparable scale.

The cost of hydrogen from electrolysis is dominated by the cost of electricity and the capital cost recovery for the system. Another factor – operation and maintenance expenses (O&M) – may add 3 to 5% to the total annual costs. The electrochemical efficiency of the unit, coupled with the price of electricity, determines the variable cost. The total capital cost of the electrolyzer unit, including compression, storage, and dispensing equipment, is the basis of fixed-cost recovery.

Regarding capital cost recovery, the cost of the 480 kg/day system, excluding compression and dispensing, is assumed to be around 1000 US$/kW input. The total cost of a system on this scale would be around 2.5 million US$. Since it is anticipated that electrolysis technology scales with an 85% factor, smaller-scale systems, with somewhat higher unit costs, are feasible. For example, a facility with half of the above capacity of hydrogen production and fueling of 60 cars per day would cost about $1.25 million, plus a 15% scaling factor. The scalability of electrolysis is

one of the important factors for its likely use in early-stage fuel cell vehicles. The electrochemical efficiency of electrolysis is essentially independent of scale.

The total cost of electrolytic hydrogen from currently available technology reaches a 14% capital cost recovery factor and has to include the total cost (variable, capital, and O&M) associated with the fueling facility. The cost of grid electricity delivered is assumed to be 7 cents/kWh. Total costs in this case are in the range of \$6.50/kg of H_2 produced.

2.4.1.5 Research Priorities

The research priorities that may improve the efficiency and/or reduce the cost of future electrolysis fueling devices are:

- To reduce the ionic resistance of the membrane.
- To reduce other (parasitic) system energy losses.
- To reduce current density, higher temperatures.
- To optimize a number of components and the overall operating system to reduce the cost. Volume manufacturing and pricing are also important cost factors.

It is likely that PEM electrolysis is subject to the same basic cost reduction drivers as the fuel cells. Cost breakthroughs which all promise to lower the cost per unit of production are:

(1) Catalyst formulation and loading.
(2) Bipolar plate/flow field.
(3) Membrane setup and durability.
(4) Volume manufacturing of subsystems and modules by third parties.
(5) Overall design simplifications.
(6) Scale economies (within limits).

The electrolyzer capital costs may fall by a factor of 8, from \$1000/kW in the near term to \$125/kW over the next 15 to 20 years, contingent on similar cost reductions of fuel cells. This reduction seems to be feasible when considering the claims made by fuel cell developers, according to which they can decrease the cost of fuel cells to \$50/kW from today's nearly \$5000/kW.

At present, technologies beyond PEM are deemed to offer a higher overall efficiency by significantly increasing the temperatures and employing optimized design concepts. As an example, solid oxide fuel cell technology operates at much higher temperatures than PEM technology does and therefore it may be a source of advanced electrolyzer performance. Figure 2.13 displays a schematic representation of a high-temperature solid oxide electrolyzer. In such a case, efficiencies moving towards 95% may be possible, but it will take probably at least five and perhaps 10 years until solid oxide systems operating at 500 to 1000°C will be available in the future. Moreover, solid oxide systems imply a significantly larger scale than PEM systems, because they have to be equipped with a thermal management system. Solid oxide electrolyzers may be scalable down to gas station duty, but this

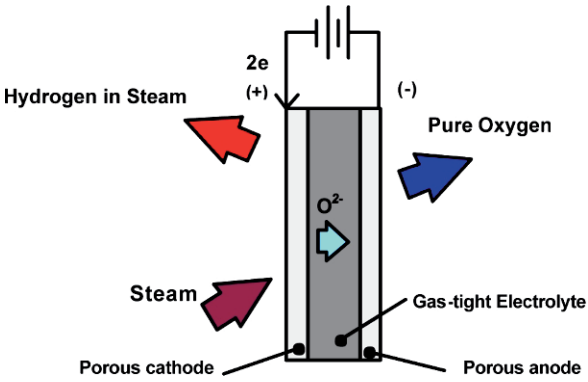

Fig. 2.13 High-temperature solid oxide electrolyzer operation scheme

still remains to be proved. Clearly, PEM systems may be scaled appropriately for distributed refueling duty.

Further advances in electrolysis technology will be based on solid oxide electrolyzer/hydrocarbon hybrids. The hybrid concept will enhance the efficiency of the high-temperature electrolysis process by using the oxidation of natural gas as a means of intensifying the migration of oxygen ions through the electrolyte and, thus, reducing the effective amount of electric energy required to transport the oxygen ion. The concept appears to offer the potential for a significantly improved net electrochemical efficiency. However, it relies on a number of technical breakthroughs in solid oxide technology and eventually requires the supply of a separate stream of methane or another combustible fuel in addition to water and electricity.

Assessment of electrolysis improvements mainly focuses on PEM-based technologies rather than on advanced concepts. It is intended to present a vision for the future that is based on today's technology and does not rely on new technological breakthroughs that, should they occur, would only enhance the cost and performance.

All in all, improvements of electrolyzer performance will be due to three advancements:

(1) Improved electrochemical efficiency – efficiency gains from 63.5 to 75% system efficiency (LHV) could be reachable.
(2) System costs – as stated above, the system capital costs may be reduced by a factor of eight, from $1000 to $125/kW, driven largely by the same cost factors that also will have to be addressed by fuel cell developers, if fuel cells are supposed to enter the transportation market.
(3) Compressor performance and cost will be improved as a result of a variety of emerging hydrogen energy alternatives. These alternatives may bring hydrogen to significantly higher volumetric energy densities than those attained today with hydrogen compression only. For instance, nanocrystalline Mg alloys may have a volumetric density as high as 11.1 moles of hydrogen per cm^3 in comparison with the volumetric density of liquid hydrogen of 7.0 moles of hydrogen per cm^3 (see http://www.gkss.de/Themen/W/WTP/Hydrogen.html).

Variable costs (electricity) will fall as a result of improved electrochemical efficiency. The biggest change will result from the large drop of capital costs, which will directly lead to lower capital cost per unit of production. This, along with lower compression costs, will reduce the all-inclusive costs of hydrogen from $6.58/kg using current technology to $3.94/kg in case of future improvements. Each 1 cent reduction in the price of electricity will reduce the cost of electrolytic hydrogen fuel by 53 cents/kg or more than 8% per penny. Effective utilization of electrolysis as a fueling option will require the cooperation of utilities and decision-making bodies.

2.4.1.6 Environmental Impact

The environmental impact of the use of electrolysis to produce hydrogen depends on the source of electricity. The electrolysis process as such produces little, if any CO_2 or other greenhouse gas emissions. Electrolyzers contain no combustion devices and the only input to the process other than electricity is pure water. However, a relationship exists between emissions and electrolysis. Any pollution associated with electricity consumed by the electrolyzer needs to be taken into account. As stated previously, electrolysis claims to create a path for converting renewable power into fuel. The low capacity factors of renewables (other than geothermal and hydro power), however, will make an economic all-renewables case very difficult to implement. Electricity from nuclear plants also is without any greenhouse gas emissions, but the prospects of additional nuclear plants are uncertain at best.

Power from the grid is assumed to be based on the grid's average mix. With today's grid mix, about 17.6 kg CO_2 are emitted per kilogram of hydrogen. As the portfolio of energy resources used to supply electric power will change in the future, the amount of CO_2 emitted to produce 1 kg H_2 could either increase or decrease.

2.4.1.7 Outlook

Electrolysis may be particularly well suited to meet the early-stage fueling needs of a fuel cell vehicle market. Electrolyzers may be scaled down reasonably well; the efficiency of the electrolysis reaction is independent of the size of the cell or cell stacks involved. Moreover, the balance of plant costs is also fairly scalable. The compact size of electrolyzers allow for the plants to be placed at or near existing fueling stations. Finally, electrolyzers can use existing water and electricity infrastructures to a considerable extent, thus avoiding the need for a new pipeline or surface hydrogen transport infrastructure.

Electrolyzers typically operate with grid quality power. Hence, new power control and conditioning equipment will have to be developed for electrolyzers to operate efficiently from renewable sources. A good efficiency in converting renewable power into hydrogen may be achieved, as electrolyzers require direct current and renewables generate direct current. Consequently, there will not be any losses associated with ac/dc conversion.

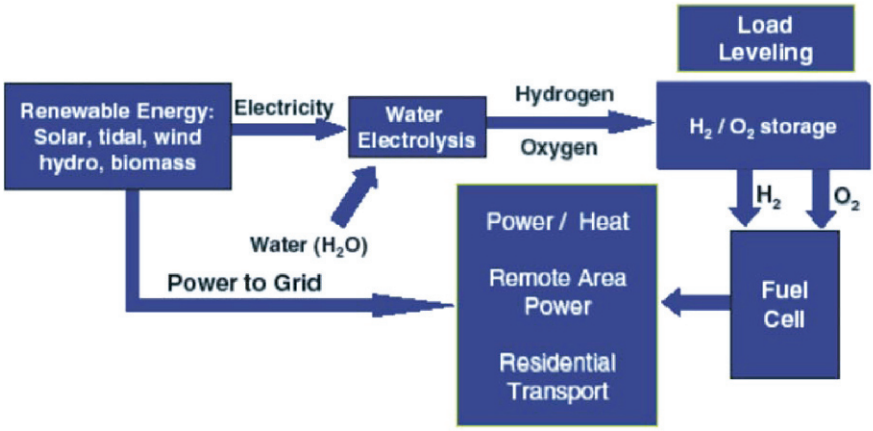

Fig. 2.14 Concept diagram for demonstrating electrolysis technology in a sustainable energy cycle for remote-area power supply

Electrolysis cells have been scaled successfully from 9 to 150 cm^2 active area with very little loss in hydrogen generation efficiency. Test stations to test stacks at up to 5 kW H_2 capacity and pressures of 20 bar have been constructed with multiple levels of safety redundancy. The system design allows for an unattended safe operation of stacks for extended periods. Stacks of varying dimensions and hydrogen generation capacities have been built and tested, some for periods exceeding 1500 hours at a current density of 1 A cm^{-2}. An efficiency of up to 87% initially at 1 A cm^{-2} has been achieved by an optimization of the interface, catalyst, MEA fabrication, fluid/current flow, and stack design. The largest stack tested to date has a hydrogen generation capacity of 11 l/min and an oxygen generation capacity of 5.5 l/min. Operation has been demonstrated in a thermally self-sustaining mode from cold start, with water and electricity as the only inputs. Temperatures exceeding 80°C can be achieved easily at a current density of 0.8 A cm^{-2} or higher [17].

There is a big market for small-scale distributed hydrogen generation. Due to its fast response time, startup/shutdown characteristics, and ability to accept large variations in load, PEM electrolysis technology has the potential for being coupled to intermittent sources of renewable electricity with minimal power electronics. As hydrogen allows for a flexible energy storage over a long duration, the PEM electrolyzer technology will be particularly suited for remote-area power supply in a sustainable energy cycle, as represented by the concept diagram (cf. Fig. 2.14).

2.4.2 Hydrogen from Wind Energy

Of all the renewables currently on the drawing boards, wind is deemed to have the highest potential in the near and medium term for use as an excellent source of

production of pollution-free hydrogen. Using the electricity generated by the wind turbines, water is electrolyzed into hydrogen and oxygen. The prerequisites for its successful development and deployment are threefold: (1) Further reduction of the cost of wind turbine technology and the cost of the electricity generated by wind, (2) reduction of the cost of electrolyzers, and (3) optimization of the wind turbine-electrolyzer with the hydrogen storage system.

2.4.2.1 History

While wind energy had been one of humanity's primary energy sources for transporting goods, milling grain, and pumping water for several millennia, its use as an energy source began to decline as industrialization took place in Europe and then in America. This decline was gradual at first, as the use of petroleum and coal, both cheaper and more reliable energy sources, became widespread. Then, it fell more sharply, as power transmission lines were extended into most rural areas of industrialized countries. The oil crises of the 1970s, however, triggered renewed interest in wind energy technology for grid-connected electricity production, water pumping, and power supply in remote areas, thus promoting the industry's rebirth. In 2002, grid-connected wind power in operation surpassed 31,000 MW worldwide.

Since the mid-1970s, the unit size of commercial machines has grown steadily. In the mid-1970s, the typical size of a wind turbine was 30 kW. By 1998, the largest units installed had a capacity of 1.65 MW. Now, turbines with an installed power of 2 MW have been introduced on the market and machines of more than 3 MW are being developed. The trend towards larger machines is driven by the demand side of the market that wishes to utilize economies of scale and to reduce the visual impact on the landscape per unit of installed power, and expects that the offshore potential will be growing.

Larger turbines, more efficient manufacture, and careful siting of wind machines have brought the installed capital cost of wind turbines down from more than $2500/kW in the early 1980s to less than $1000/kW today at the best wind sites. However, the on-stream capacity factor for wind generally is in the range of 30–40%, which raises the effective cost. Cost decrease is primarily due to improvements in wind turbine technology, but also a result of the general increase in the wind farm size, which benefits from economies of scale, as fixed costs can be related to a larger generating capacity. As a result, wind energy currently is one of the most cost-competitive renewable energy technologies, and in some places it is beginning to compete with new fossil fuel generation [18].

In the early 1980s, the United States accounted for 95% of the world's installed wind energy capacity. The U.S. share has since dropped to about 16% in 2006. Other countries dramatically increased their capacity in the mid-1990s, while the U.S. capacity essentially stagnated until 1999, when more than 600 MW of new capacity were installed in a rush to beat an expiring production tax credit for utility-scale projects [19]. The year 2006 confirmed the rise in importance of the world wind energy market with, according to the first estimates available, 13.394 MW vs.

Table 2.2 Installed wind power capacity worldwide at the end of 2006 (in MW)

Geographic area	2005	2006	Added capacity in 2006*
European Union	40,490	48,042	7553
Rest of Europe	397	489	92
Total Europe	40,887	48,531	7645
United States	9149	11603	2454
Canada	684	1451	767
Total North America	9833	13,054	3221
India	4434	6053	1619
Japan	1150	1128	22
China	1260	1699	439
Other Asian Countries	254	324	70
Total Asia	7098	9204	2106
Rest of the World	1417	1839	422
Total World	59,235	72,628	13,394

* *Decommissioned wind farms are deducted from the figures.*
Sources: EurObserv'ER 2007 (European Union figures)/AWEA 2007 for the United States, Wind Power Monthly 2007 (others).

a 11.746 MW market in 2005, as shown in Table 2.2. Europe remained the principal region in the world for wind turbine installations, with a 57.1% market share in 2006, followed by North America (24.0%) and Asia (15.7%). World wind power capacity is now established at 72.628 MW. Wind power today is part of the energy mix of more than 60 countries, not only in practically all of the developed countries, but also in more and more of the developing ones. India already has a 6.053 MW installed capacity (+1.619 MW compared to 2005) and ranks in fourth place behind Germany, Spain, and the USA. China enters the top ten (in eighth place) with 1.699 MW installed (+439 MW compared to 2005). The USA confirmed their status as a major wind sector power supplier. According to the AWEA (American Wind Energy Association), a 2.454 MW market and 11.603 MW installed capacity were reached in 2006. This market is expected to exist for at least two more years thanks to the American government's decision to extend the production tax credit period until 31 December 2008, that is to say, 1 year longer than initially planned [20].

Estimates show that U.S. wind resources could provide more than 10 trillion kWh [2], which includes land areas with wind class 3 or above (corresponds to wind speeds greater than 7 meters per second [m/s] [15.7 mph] at a height of 50 m) within 20 miles of existing transmission lines and excludes all urban and environmentally sensitive areas. This is over 4 times the total electricity currently generated in the United States. In the DOE's *Hydrogen Posture Plan* [21], wind availability is estimated to be 3250 GW, equivalent to the above capacity factor of 35%. In 2002, installed wind capacity was about 5 GW generating 12.16 billion kWh, corresponding to a capacity factor of 29% [22].

2.4.2.2 Technical Principle

The main technical parameter determining the economic success of a wind turbine system is its annual energy output, which, in turn, is determined by parameters, such as average wind speed, statistical wind speed distribution, distribution of occurring wind directions, turbulence intensities, and roughness of the surrounding terrain. Of these, the most important and sensitive parameter is the wind speed, which increases exponentially with height above ground. The power in the wind is proportional to the third power of the momentary wind speed. As accurate meteorological measurements and wind energy maps become more commonly available, wind project developers can more reliably assess the long-term economic performance of wind farms.

Recent technical advances made wind turbines more controllable and grid-compatible and reduced the number of components, making them more reliable and robust. The technology is likely to continue to improve. Such improvements will include an enhanced performance at variable wind speeds to capture the maximum amount of wind according to local wind conditions and a better grid compatibility. These advances may result from a better turbine design (Fig. 2.15) and optimization of rotor blades, more efficient power electronic controls and drive trains, and better materials. Furthermore, economies of scale and automated production may continue to reduce costs [23].

Wind technology does not have any fuel requirements, contrary to coal, gas, and petroleum technologies. However, both the equipment costs and the costs of special characteristics, such as intermittence, resource variability, competing demands for land use, and transmission and distribution availability, may add substantially to the costs of generating electricity from wind. Table 2.3 gives the usual wind classification at 50 m height and the associated theoretical wind power. Wind turbines are

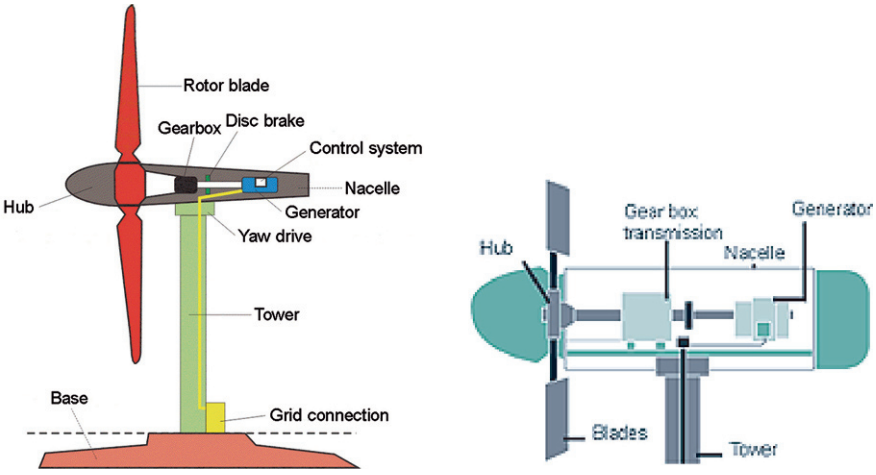

Fig. 2.15 Wind turbine installation and its cross-section

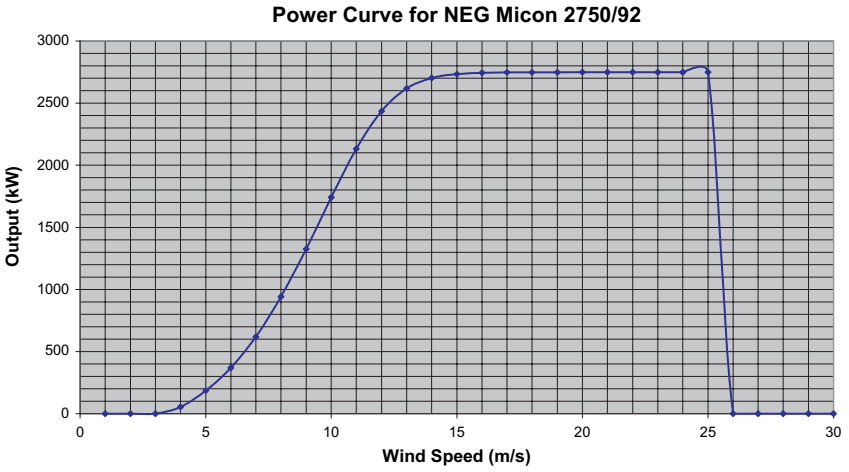

Fig. 2.16 Power curve of the NEG Micon 2750/92 wind turbine

usually built on wind fields of class 4 and higher. From this table and Fig. 2.16, it is obvious that the wind power increases with the cube of the wind speed.

The NEG Micon 2750/92 is used to demonstrate the conversion of wind energy into electrical energy. The specifications of this wind turbine are listed below. The power curve ($P_{curve}(V)$) is given in Fig 2.16.

NEG Micon 2750/92 specifications:
Maximum capacity = 2750 kW
Rotor diameter = 92 m
Hub height = 70 m
Cut-in speed = 3 m/s
Cut-out speed = 25 m/s

For wind resources to be useful for electricity generation and/or hydrogen production, the site must have the following characteristics:

(1) Sufficiently powerful winds
(2) Location near existing distribution networks
(3) Economic competitiveness with alternative energy sources

Table 2.3 Standard Wind Classification for the U.S. at 50 m

Wind Class	Resource Potential	Wind Speed (m/s)	Wind Power (W/m^2)
1	None	0–5.6	0–200
2	Marginal	5.6–6.4	200–300
3	Fair	6.4–7.0	300–400
4	Good	7.0–7.5	400–500
5	Excellent	7.5–8.0	500–600
6	Outstanding	8.0–8.8	600–800
7	Superb	8.8–11.9	800–2000

While the technical potential of wind power to fulfill the need for energy services is substantial, the economic potential of wind energy will remain dependent on the cost of wind turbine systems as well as on the economic efficiencies of alternative options.

Wind energy has some technical advantages, apart from being both a clean and secure energy source, when compared with conventional fossil fuel generation and some other renewable energy sources. First, it is modular, which means that the generating capacity of wind farms can be expanded easily, since new turbines can be manufactured and installed quickly; this is not the case for either coal-fired or nuclear power plants. Furthermore, a repair of one wind turbine does not affect the power production of all the others. Secondly, the energy generated by wind turbines at good wind sites can pay for the materials used to manufacture them in as little time as 3 to 4 months [24].

Despite these advantages, wind's biggest drawback continues to be its intermittence and mismatch with demand, an issue for both electricity generation and hydrogen production [25]. The best wind sites often are not in close proximity to populations with the greatest energy needs, as in the U.S. Midwest; this problem makes such sites potentially impractical for onsite hydrogen production, owing to the high costs of storage and long-distance hydrogen distribution. On the other hand, if hydrogen storage and distribution were to become more cost-effective, potentially large quantities of relatively cheap hydrogen could be produced at remote, high-quality wind sites and distributed around the country.

2.4.2.3 Cost Issue

Worldwide, the cost of generating electricity from wind has fallen by more than 80%, from about 38 cents/kWh in the early 1980s to a current value for good wind sites located in the United States of 4 to 7 cents/kWh, with average capacity factors close to 30%. The current federal production tax credit of 1.8 cents/kWh for wind-generated electricity lowers this cost to below 3 cents/kWh at the best wind sites. This is a cost decrease by an order of magnitude in two decades. Analysts generally forecast that costs will continue to drop significantly, as the technology improves further and the market grows around the world [24], though some do not (e.g. the EIA). For possible future technologies, it is assumed that the cost of electricity generated using wind turbines will decrease to 4 cents/kWh (including transmission costs). This assumption is based on a wind turbine capital cost of $500/kW, total capital costs of $745/kW, and a capacity factor of 40%. The expectation is that wind turbine design will be refined and economies of scale will accrue. While these values can be considered optimistic [21], others predict even lower values, given successful technology advancement and supportive policy conditions [22].

In the future, costs will be reduced by multiple advancements and further improvements in turbine design and optimization of rotor blades, more efficient power controls and drive trains, and improvements in materials. The improvements in ma-

terials are expected to facilitate increased turbine height, leading to a better access to the higher-energy wind resources available at these greater heights. The desire of new U.S. vendors to participate in wind energy markets will increase competition, leading to an overall optimization and lower cost of the wind turbine system.

2.4.2.4 Wind Technology and H_2

Hydrogen production from wind power and electrolysis is a particularly interesting proposition, since, as just discussed, wind power is the economically most competitive of all renewable sources, with electricity prices of 4 to 5 cents/kWh at the best wind sites (without subsidies). This means that wind power can generate hydrogen at lower costs than any of the other renewable options available today. Since hydrogen from wind energy can be produced close to where it will be used, there will be a clear role for it to play in the early years of hydrogen infrastructure development, especially as it is believed that a hydrogen economy is most likely, at least initially, to develop in a distributed manner.

Wind-electrolysis hydrogen production systems are currently far from being optimized. For example, the design of wind turbines to date has been geared to electricity production, not hydrogen. To optimize for a better hydrogen production, power control systems integrated between the wind turbine and electrolyzer will have to be analyzed to tailor hydrogen storage to the wind turbine design. Furthermore, a system may be desgined to co-produce electricity and hydrogen from wind. Under the right circumstances, this could be more cost-effective and provide for a broader system use, thus facilitating wind hydrogen system deployment [24].

For distributed wind-electrolysis hydrogen generation systems in the USA, it is estimated that by using today's technologies, hydrogen can be produced at good wind sites (class 4 and above) for approximately \$6.64/kg H_2 without a production tax credit, with grid electricity being used as backup for when the wind is not blowing. A system is considered that uses the grid as backup to alleviate the capital underutilization of the electrolyzer with a wind capacity factor of 30%. It assumes an average cost of electricity generated by wind of 6 cents/kWh (including transmission costs), while the cost of grid electricity is pegged at 7 cents/kWh, a typical commercial rate. This hybrid hydrogen production system has pros and cons. It reduces the cost of producing the hydrogen, which would be \$10.69/kg H_2 without grid backup, but it is also associated with CO_2 emissions from what would otherwise be an emission-free hydrogen production system. The CO_2 emissions are a product of using grid electricity; they are 3.35 kg C per kilogram of hydrogen.

In the future, the wind-electrolysis hydrogen system could be optimized substantially. The wind turbine technology could improve and, in turn, reduce the cost of electricity to 4 cents/kWh with an increased capacity factor of 40%, as discussed previously. Moreover, the electrolyzer cost could come down substantially and its efficiency might be increased, as described in Chap. 10. The combination of the increase in capacity factor and the reduction in the capital cost of the electrolyzer as well as in the cost of wind-generated electricity results in eliminating the need

for using grid electricity (price still pegged at 7 cents/kWh) as a backup. The wind machines and the electrolyzer are assumed to be made large enough that sufficient hydrogen can be generated during those 40% of the time the wind turbines are assumed to provide electricity. Due to the assumed reductions in the cost of the electrolyzer and of wind turbine-generated electricity, this option now is less costly than using a smaller electrolyzer and purchasing grid-supplied electricity when the wind turbine is not generating electricity. Hydrogen produced in this manner from wind without grid backup is estimated to cost \$2.85/kg H_2, while it is \$3.38/kg H_2 for the alternative system with grid backup. Furthermore, the advantage of the hydrogen production system being now CO_2 emission–free is added.

Electricity systems have evolved so that they can now deliver power to consumers with a high efficiency by a highly integrated system that aggregates supply and demand. Wind power benefits from this level of aggregation of this system. Numerous utility studies have indicated that wind can be absorbed readily into an integrated network until the wind capacity accounts for about 20% of maximum demand. Beyond this, changes to operational practice would likely be needed. Practical experience, as wind penetrates to higher levels, will continue to provide a better understanding of these system integration issues. The degree to which grid compatibility and integration will influence the future hydrogen production from wind needs to be better understood.

2.4.2.5 Environmental Impact

Hydrogen produced from wind power has some obvious environmental advantages. It does not generate any solid, radioactive, or hazardous wastes; it does not require water; and it is essentially emission-free, producing no CO_2 or climate pollutants, such as NO_x and SO_2. In addition, it is a domestic source of energy. Thus, it addresses the main aspects driving the present move towards a hydrogen economy – environmental quality and energy security. But wind power is not problem-free.

Indeed, wind energy, although considered an environmentally sound energy option, does have several negative environmental aspects connected to its use. These include acoustic noise, visual impact on the landscape, impact on bird life, shadows caused by the rotors, and electromagnetic interference influencing the reception of radio, TV, and radar signals. In practice, the noise and visual impacts appear to cause most problems for siting projects. Noise impacts have been reduced by progress in aero-acoustic research providing design tools and blade configurations that are much quieter. With careful siting, the impact on bird life appears to be a minor problem. Avoiding habitats of endangered species and major migration routes in the siting of wind farms will largely eliminate this problem.

A growing and often intractable problem involves land use issues, particularly the "not in my backyard" phenomenon (i.e. NIMBY). In densely populated countries where the best sites on land are occupied, there is an increasing public resistance,

making it impossible to realize projects at acceptable cost. This is one of the main reasons why countries, such as Denmark and the Netherlands, are concentrating on offshore projects, despite the fact that they are expected to be less technically and economically favorable than good land sites. In countries, such as the United Kingdom and Sweden, offshore projects are being planned not because of scarcity of suitable land sites, but because preserving the landscape is such an important national value – though there is also growing resistance to offshore wind projects for the same reason, as seen for a recently proposed wind project off Cape Cod in the United States.

2.4.2.6 Outlook

Wind energy has some very clear advantages as a source of hydrogen. It fulfills the two main motivations that are propelling the current push towards a hydrogen economy, namely, reducing CO_2 emissions and reducing the need for hydrocarbon imports. In addition, it is the most affordable renewable technology deployed today, with expectations that costs will continue to decline. Since renewable technologies effectively address two of the major public benefits of a move to a hydrogen energy system and wind energy is closest to practical utilization with the technical potential to produce a sizable percentage of future hydrogen, it deserves continued, focused attention in the hydrogen economy development programs.

Although wind technology is the most commercially developed of the renewable technologies, it still faces many barriers to deployment as a hydrogen production system. There is a need to develop optimized wind-to-hydrogen systems. Partnerships with industry are essential in identifying the R&D needed to help advance these systems to the next level.

2.4.3 Hydrogen from Solar Energy

Solar energy holds the promise of being inexhaustible. If harnessed, it can cover all of the energy needed in the foreseeable future. It is clean and environmentally friendly. It converts solar energy into hydrogen without the emission of any greenhouse gas. Due to its distributed nature of power production, it contributes to national security.

There are certain challenges associated with the use of solar energy. The intermittent nature of sunshine, on both a daily and a seasonal basis, presents a number of challenges. A backup system or a storage system for electricity/hydrogen is needed for the periods when sunshine is not available and power demand exists. Furthermore, this intermittent availability means that 4 to 6 times more solar modules have to be installed than the peak watt rating would dictate. This intermittency also implies that a significant decrease in the module cost is required. Another challenge is to ensure that no toxic materials are discharged during the fabrication and over the

complete life cycle of the solar cell. Such questions have been raised in the context of cadmium-containing solar cells, and public perception in such cases will play a key role.

It has been estimated that solar energy has the potential of meeting the energy demand of the human race well into the future. One of the methods of recovering solar energy is through the use of photovoltaic (PV) cells. Upon illumination with sunlight, PV cells generate electric energy. Commercial PV modules are available for a wide range of applications. However, they represent a miniscule contribution to electric power production worldwide. The current cost of electricity from a PV module is 6 to 10 times the cost of electricity from coal or natural gas. Therefore, if PV electricity was to be used to produce hydrogen, the cost would be significantly higher than if fossil fuels were used. The key to solar energy to be used on a large scale for electricity or hydrogen production is cost reduction. This would require a number of advancements of current technology.

2.4.3.1 Silicon, Thin-Film Technologies

Approximately 85% of the current commercial PV modules are based on single-crystal or polycrystalline silicon. The single-crystal or polycrystalline silicon cells generally are of 10 to 15 centimeters (cm) in dimension [26, 27]. They are either circular or rectangular. In a module, a number of cells are soldered together. Each cell is capable of providing a maximum output of 0.6 volts (V), with the total module output approaching 20 volts. The output current of each cell in bright sunlight generally is in the range of 2–5 amps. The single-crystal silicon cells are made from wafers obtained by continuous wire sawing of single-crystal ingots grown by the Czochralski process. Similarly, a large portion of the polycrystalline silicon cells are made from ingots obtained by directional solidification of silicon in a mold. The wafer thickness generally is in the range of 250–400 microns. It is worth noting that nearly half of the silicon is wasted as "kerf" loss during cutting.

Polycrystalline silicon cells are also made from silicon sheet or ribbon grown by other techniques [27]. This process avoids the costs associated with the cutting of silicon ingots into wafers. The silicon wafers or ribbons are then further processed to develop *p-n* junctions and wire contacts. The array of cells is laminated using glass and transparent polymer, called ethylvinylacetate (EVA), to provide the final PV module. The modules are known to have a long lifetime (10- to 25-year warranty by manufacturers). The current technology gives about 18% cell efficiency and 15% module efficiency.

A second type of PV technology is based on deposition of thin films. PV cells are prepared by deposition of amorphous as well as microcrystalline silicon using a variety of techniques, including plasma-enhanced chemical vapor deposition, hot wire chemical vapor deposition, and so on. Polycrystalline thin-film compounds based on groups II-VI of the periodic table, such as cadmium telluride (CdTe), and group I-III-VI ternary mixtures, such as copper-indium-diselenide (CIS), have been used to make thin-film solar cells [28]. The thickness of deposited layers is much less than 1 micron.

As compared with crystalline silicon solar cells, the thin-film technology potentially has a number of significant advantages in manufacturing:

(1) Lower consumption of materials
(2) Fewer processing steps
(3) Automation of processing steps
(4) Integrated, monolithic circuit design, assembly of individual solar cells to final modules is no longer necessary
(5) Fast roll-to-roll deposition [29]

It has been estimated that for crystalline silicon solar cells, the complete process involves more than two dozen separate steps to prepare and process ingots, wafers, cells, and circuit assemblies before a module is complete [29]. On the other hand, thin-film module production requires only half as many process steps, with simplified materials handling.

Thin-film technology appears to hold greater promise for cost reduction, which led to research by several laboratories over the past two or three decades (Fig. 2.17). Cell efficiencies as high as 21.5% were reported for copper-indium (gallium)-diselenide (CIGS) [28]. Similarly, a high efficiency of 16.5% was reported for CdTe research cells. Amorphous silicon is deposited by using silane ($SiHB_{4B}$) and hydrogen mixtures. In laboratory-scale cells of amorphous silicon, the highest efficiencies obtained are about 12%.

A big challenge for thin-film solar cells is to overcome the large drop in efficiency from the laboratory-scale cell to that of a real module. For example, commercial modules of CdTe and CIGS have efficiencies in the range of 7–12% (as compared with laboratory-scale cell efficiencies of 16.5 and 21.5%). Similarly, commercial amorphous silicon modules have efficiencies of less than 10% [30]. The drop in efficiency with increasing cell size is substantial. Attempts are being made to increase the efficiency of amorphous and microcrystalline silicon cells by making dual and triple junction cells [31]. This change leads to multiple layers, each having

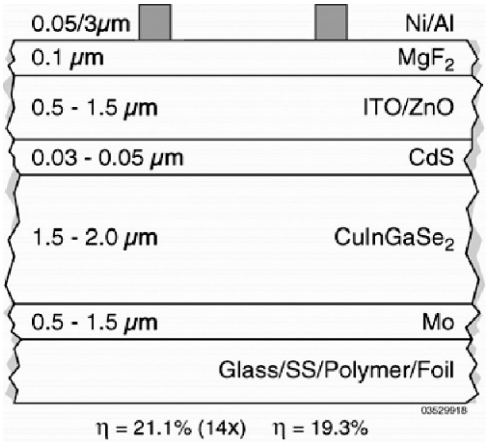

Fig. 2.17 Thin-film CIS solar cell structure

a different optimum band gap. However, the deposition of multiple layers increases the processing steps and, hence, the cost. A final note is that amorphous silicon modules, when exposed to sunlight, undergo light-induced degradation, thereafter operating at a lower, stabilized efficiency [30].

In spite of its promise, thin-film technology has been unable to reduce the cost of solar modules, owing to low deposition rates that have led to a low capital utilization of expensive machines. The yields and throughputs have been low. These plants need better inline controls. Recently, some corporations shut down their thin-film manufacturing facilities due to manufacturing problems. Obviously, easier and faster deposition techniques leading to reproducible results are needed. Also, deposition techniques are required that would not result in a substantial drop in efficiency from laboratory scale to module scale.

Today, there is no clear "winner technology." More than a dozen firms produce solar modules. Even the largest of these firms do not have world-class, large-scale production facilities (greater than 100 MW_p of solar modules per year). This size limitation does not allow for economy-of-scale benefits in solar cell production. Many companies use multiple technologies.

2.4.3.2 Cost Issue

The current cost of solar modules is in the range of \$3–\$6 per peak watt (W_p). For solar cells to be competitive with the conventional electricity production technologies, the module cost must come down below \$1/W_p. Nowadays, the installed cost is about \$3.285/W_p, the electricity cost is estimated to be about \$0.319/kWh. For a futuristic case with all expected technology and production advances, the anticipated installed cost of \$1.011/ W_p will lead to electricity cost of \$0.098/kWh. While this target is attractive for electricity generation, hydrogen is not produced at competitive cost.

Energy is consumed in the manufacture of solar modules. It has been estimated by NREL that for a crystalline silicon module, the payback period of energy is about 4 years. For an amorphous silicon module, this period currently is about 2 years, with the expectation that it will eventually be less than 1 year.

Various developments are likely to improve the economic competitiveness of solar technology, especially for thin-film technology. The current research on microcrystalline silicon deposition techniques is leading to higher efficiencies. Techniques leading to higher deposition rates at moderate pressures are being developed [32]. Better barrier materials to eliminate moisture ingress in the thin-film modules will prolong the module's life span. Robust deposition techniques will increase the yield from a given type of equipment. Inline detection and control methods will help to reduce the cost. Some of these advances will require creative tools and methods.

It is believed that installed costs of roughly \$1/ W_p are achievable. Material costs are quite low, but substrate material, expensive coating equipment, low utilization of equipment, and labor-intensive technology lead to high overall costs. It is expected that in the next decade or two, improvements in these areas have a potential to bring

the cost much below $1/W_p$. World-class plants with economies of scale will further contribute to the lowering of cost. For crystalline silicon wafer-based technology, the raw material costs by themselves are almost $1/W_p$. However, improvements in operating efficiency, the cost of raw materials, and reduced usage of certain materials are expected to bring overall cost close to $1/W_p$.

Regarding production costs, all of the technologies discussed convert solar energy into electricity and use the electricity to generate hydrogen through the electrolysis of water. Since PV cells produce dc currents, the electric power can be used directly for electrolysis. As discussed in the section above on electrolyzers, considerable cost reductions are anticipated, which will lower the cost of hydrogen from solar cells. These cost reductions will be particularly valuable for solar cell electricity, because the low usage factor associated with PV modules also contributes to the low usage of electrolyzers. This, in turn, has a high impact on the cost of the hydrogen produced.

For example, the hydrogen cost for the future optimistic case is calculated to be $6.18/kg. For this case, the cost of the installed PV panels, including all general facilities, is estimated to amount to $1.011/W_p$. It is used in conjunction with an electrolyzer that is assumed to take advantage of all advancements made in the fuel cell. The PV part is responsible for $4.64/kg and the electrolyzer for $1.54/kg. Compared with this, the cost of hydrogen from a future central coal plant at the dispensing station is estimated to be $1.63/kg, including carbon tax. This cost implies that for a PV electrolyzer to compete in the future with a coal plant, either the cost of PV modules must be reduced by an order of magnitude or the electrolyzer cost must drop substantially from $125/kW. The low utilization of the electrolyzer capital is responsible for such a high value. It has been proposed to use electricity from the grid to run the electrolyzer when solar electricity is unavailable. This use will increase the availability of the electrolyzer. However, for solar to play a dominant role in the hydrogen economy in the long term, it cannot rely on power from the grid to supplement equipment utilization. While electricity at $0.098/kWh from a PV module can be quite attractive for distributive applications where electricity is used directly, its use in conjunction with electrolysis to produce hydrogen certainly is not competitive with the projected cost of hydrogen from coal.

2.4.3.3 Novel Concepts

Dye-Sensitized Solar Cell

A concept proposed is the dye-sensitized solar cell, also known as the Grätzel cell [33]. Figure 2.18 displays a schematic representation of the Grätzel dye-sensitized solar cell. A dye is incorporated in a porous inorganic matrix, such as TiO_2, and a liquid electrolyte is used for positive charge transport. Photons are absorbed by the dye and electrons are injected from the dye into *n*-type titania nanoparticles. The titania nanoparticles fuse and carry electrons to a conducting electrode. The dye gets its electron from the electrolyte, and the positive ion of the electrolyte moves to the

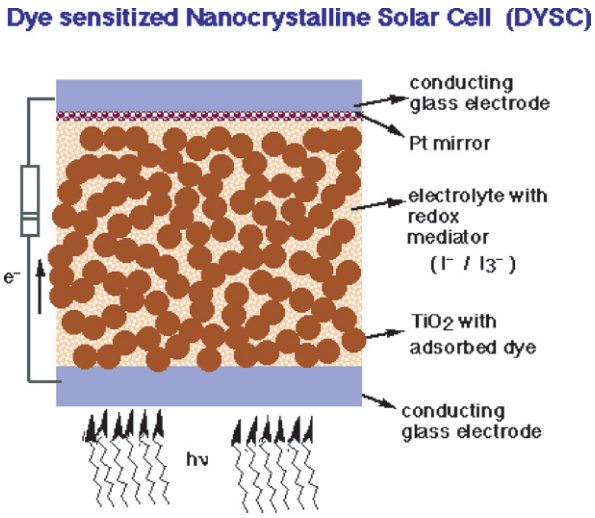

Fig. 2.18 Principle of the Grätzel dye-sensitized solar cell

other electrode [34]. This type of cell has a potential to be less expensive. However, the current efficiencies are quite low, and the stability of the cell in sunlight is very poor. Therefore, research is needed to improve the performance of these cells.

Hybrid Solar Cell

Another area of intense research is the integration of organic and inorganic materials on the nanometer scale in hybrid solar cells. The current advancement in conductive polymers and the use of such polymers in electronic devices and displays gives reason for optimism. The nano-sized particles or rods of suitable inorganic materials are embedded in the conductive organic polymer matrix. Once again, the research is in the early phase and the current efficiencies are quite low. However, the production of solar cells based either solely on conductive polymers or on hybrids with inorganic materials has a large potential to provide low-cost solar cells. It is hoped that thin-film solar cells of such materials would be cast at a high speed, resulting in low cost.

Photoelectrochemical Cell

Research is being performed to create photoelectrochemical cells for the direct production of hydrogen [34]. In this method light is converted to electrical and chemical energy. The technical challenge lies in the fact that energy from two photons is needed to split one water molecule. A solid inorganic oxide electrode is used to absorb photons and provide oxygen and electrons. The electrons flow through an external circuit to a metal electrode, and hydrogen is liberated at this electrode. The candidate inorganic oxides are $SrTiO_3$, $KTaO_3$, TiO_2, SnO_2, and Fe_2O_3. When successful, such a method promises to directly provide low-cost hydrogen from solar energy.

As regards the production costs, it seems that a photoelectrochemical device, in which all functions of photon absorption and water splitting are combined in the same equipment, may have a better potential for hydrogen production at reasonable costs. However, it is instructive to do a quick "back of the envelope" analysis of the acceptable cost of such a system. It is assumed that cost per peak watt for a photoelectrochemical device is the same as that for the possible future PV modules. It is further assumed that this energy is recovered as hydrogen rather than electricity. Therefore, a recovery of 39.4 kWh corresponds to a kilogram of hydrogen. This implies that 4729 kWe of solar plants will produce about 576 kg/day of hydrogen (assuming an annual capacity factor of 20%). At the total cost of $0.813 million per year, this gives $3.87/kg of hydrogen! This cost is still too high when compared with that of hydrogen from coal or natural gas plants. Photoelectrochemical devices should recover hydrogen at an energy equivalent of $0.4 to $0.5/$W_p$. This cost challenge is similar to that for electricity production from solar cells.

2.4.3.4 Outlook

Large-scale use of solar energy for hydrogen economy will require research and development efforts on multiple fronts. In the short term, there is a need to reduce the cost of thin-film solar cells. This reduction will require the development of silicon deposition techniques that are robust and provide for high throughput rates. New deposition techniques at moderate pressures with microcrystalline silicon structures for higher efficiencies are needed. Inline detection and control and the development of better roll-to-roll coating processes can lead to reductions in the manufacturing costs. Increased automation will also contribute to decreasing the cost. Issues related to a large decrease in efficiency from small laboratory samples to the module level should be addressed. In the short run, thin-film deposition methods may potentially benefit from a fresh look at the overall process from the laboratory scale to the manufacturing scale. Research in this area is expensive. Some additional centers for such research in academia with industrial alliances could be beneficial. It will be necessary to establish multidisciplinary teams from different engineering disciplines for such studies.

In the middle to long term, organic-polymer-based solar cells promise to be suitable for mass production at low cost. They might be cast as thin films at very high speeds using known polymer film casting techniques. Currently, the efficiency of such a system is quite low (in the neighborhood of 3 to 4% or lower), and stability in sunlight is poor. However, due to the tremendous development in conducting polymers and other electronics-related applications, it is anticipated that research in such an area has a high potential for success.

Similarly, the search for a stable dye material and better electrolyte in dye-sensitized cells (Grätzel cells) has a potential to lead to lower-cost solar cells. There is a need to increase the stable efficiency of such cells; a stable efficiency of about 10% could be quite useful.

In the long run, the success of directly splitting water molecules by using photons is quite attractive. Research in this area could be very fruitful.

2.4.4 Hydrogen from Biomass (and by Photobiological Processes)

Two basic pathways of molecular hydrogen production by biological processes are currently being considered:

(1) Via photosynthetically produced biomass, followed by subsequent thermochemical processing
(2) Via direct photobiological processes without biomass as intermediate

The first process is well-known and intensely studied, while the second still is in the early research stage. Their common features are the capturing and conversion of solar energy into chemical energy, mediated by photosynthetic processes. In both cases, solar energy serves as the primary energy source for the production of molecular hydrogen by biological processes. In contrast to processes using fossil fuels as primary energy sources, biological processes do not involve the net production of CO_2.

2.4.4.1 Biomass from Photosynthesis

In photosynthesis as carried out by plants, cyanobacteria, and microalgae, solar energy is converted into biomass in commonly occurring ecosystems at an overall thermodynamic efficiency of about 0.4% [35]. This low efficiency is due to the molecular properties of the photosynthetic and biochemical machinery as well as to the ecological and physico-chemical properties of the environment. Of the incident light energy, only about 50% are photosynthetically useful. This light energy is used at an efficiency of about 70% by the photosynthetic reaction center and converted into chemical energy, which is converted further into glucose as the primary CO_2 fixation end product at an efficiency of about 30%. Of this energy, about 40% are lost due to dark respiration. Because of the photo inhibition effect and the non-optimal conditions in nature, a further significant loss in efficiency is observed when growing plants in natural ecosystems. Therefore, common biomass collected from natural ecosystems contains about 0.4% of the primary incoming energy only. Although higher yields (in the 1 to 5% range) have been reported for some crops (e.g. sugarcane), the theoretical maximal efficiency is about 11%.

Generally, two types of biomass resources can be considered in the discussion on renewable energy feedstock:

(1) Primary biomass, such as energy crops, including switch grass, poplar, and willow
(2) Biomass residues

It should be noted that the term primary is used when derived from wood or processed agricultural biomass, secondary when derived from food, fiber-processing by-products, or animal waste, and tertiary when derived from urban residues.

Today, about 4% of total energy use in the United States are based on the use of biomass, mainly in the form of forest residues. At a cost of $30 to $40/t, the available biomass can be estimated to be between 220 and 335 million dry tons per year. This biomass consists mainly of urban residues, sludge, energy crop, and wood and agricultural residues. A significant fraction of this biomass, especially forest residues, is already used by directly industry or in other competing processes, such as energy generation. However, if all of this theoretically available biomass could be converted into hydrogen, the annually available amount would be of the order of 17 to 26 million t H_2. In an all-fuel-cell-vehicle scenario in the year 2050, 112 million t H_2 would be required annually. Considering this demand and the competing demands for other uses of biomass, the currently available biomass is insufficient to satisfy the entire demand in a hydrogen economy, and new sources for biomass production would need to be considered.

Bioenergy Crops, Switch Grass

Primary biomass in the form of energy crops is expected to have the most significant quantitative impact on hydrogen production for use as transportation fuel by 2050. Estimates of energy that can potentially be derived from energy crops to produce biomass by 2050 range between 45 and 250 exajoules (EJ) per year. Bioenergy crops are currently not produced as dedicated bioenergy feedstock in the United States. Therefore, crop yields, management practices, and associated costs are based on agricultural models rather than on empirical data [36].

In the most aggressive scenario for a hydrogen economy as considered in the USA, a land area between 280,000 and 650,000 square miles is required to grow energy crops in order to support 100% of a hydrogen economy. The magnitude of this demand for land becomes obvious when comparing these figures with the currently used crop land area of 545,000 square miles in the United States. Consequently, bioenergy crop production would require a significant redistribution of the land currently dedicated to food crop production and/or the development of a new land source under the U.S. Department of Agriculture's (USDA's) Conservation Reserve Program (CRP).

Although bioenergy crops can be grown in all regions of the United States, regional variability in productivity, rainfall conditions, and management practices limit energy crop farming to states in the Midwest, South, Southeast, and East [36]. Considering all crop land used for agriculture as well as crop land in the CRP, pasture, and idle crop land [37], two management scenarios for profitable bioenergy crop production can be derived:

(1) One to achieve high biomass production (production management scenario, or PMS)
(2) The second to achieve high levels of wildlife diversity (wildlife management scenario, or WMS).

The production management scenario would produce about 188 million tons of dry biomass annually, which would be equivalent to 15 million tons of H_2. This would require 41.8 million acres of crop land, of which about 56% would be from currently used crop land, 30% from the CRP, and 13% from idle crop land and pasture. The crop would be exclusively switch grass.

In the wildlife management scenario, 96 million dry tons (dt) of biomass (equivalent to 7.6 million t H_2) would be produced on 19.4 million acres of crop land. These 19.4 million acres would be made up by about 53% from currently used crop land, 42% from the CRP, and 4% from idle crop land and pasture. Land from the CRP would become a significant source for farming biomass crops.

The CRP sets aside environmentally sensitive acres under 10- to 15-year contracts. Appropriate management practices must be developed before CRP lands are used. Environmental impacts of various management practices must be examined to ensure that there is no substantial loss of environmental benefits, including biodiversity, soil and water quality. It is conceivable that a farming scenario alternating between agricultural crops and bioenergy crops on existing agricultural and CRP lands could be developed. It should be noted that those unproven cases were not considered in this analysis [38].

Cost Issue

Bioenergy crop production is considered profitable at $40/dt and could compete with currently grown agricultural crops [36]. Based on assumed yields, management practices, and input costs, switch grass is the least expensive bioenergy crop to produce on a per dry ton basis. Production costs (farm gate costs) for switch grass are estimated to range from $30/dt to $40/dt, depending on the management scenarios [37]. Adding processing and delivery costs would result in an approximate delivered biomass price in the order of $40 to $50/dt, respectively. Using thess feedstock costs as well as current and projected gasifier efficiencies (50% versus 70%), the future costs per kilogram of hydrogen produced from biomass and delivered to the vehicle can amount to about $3.60. In this scenario a reduction in biomass cost was assumed to be achieved by increasing the crop yield per hectare by 50%, which presents significant technical challenges.

The profitability of bioenergy crop farming will vary with given field and soil types [36]. Notably, the price per dry ton of bioenergy crop is predicted to increase with the total biomass produced. A shift of crop land use from traditional agricultural crops to bioenergy crops will also result in higher prices for traditional crops. Because of land ownership, management, and crop establishment, biomass production by energy crop production will be more expensive than using residue biomass. Additionally, regional variation in the availability of residue biomass, such as in woody areas in the northeastern United States, could make hydrogen production from biomass competitive in such regions in the short term. However, such operations would be restricted to selected regions in the United States. In a long-term sustainable scenario, it would require biomass production at the same rate as its

consumption. It is unlikely that such localized operations would contribute significantly to the needed H_2 supply.

Environmental Impact

In the overall process of biomass production and gasification, no net CO_2 is generated, except for the CO_2 released from fossil fuels used for (1) harvesting and transportation of biomass, (2) operation of the gasification systems, and (3) electricity as well as for (4) production and delivery of fertilizers in an advanced biomass system. Biomass handling alone is estimated to consume about 25% of the total capital costs of operation of a mid-size biomass gasification plant. Furthermore, biomass production requires, in addition to land (see above), about 1000 to 3000 t of water per ton of biomass as well as nutrients in the form of nitrogen (ammonia), phosphorus (phosphate), sulfur, and trace metals. Profitable future hydrogen production from biomass will require energy crops with increased growth yields, which translate into increased need for fertilizers, energy for production of fertilizers, and potentially water. As is the case with the production of food crops, erosion, nutrient depletion of the soil, and altered water use practices could result in potentially significant environmental impacts as a consequence of farming activities. These effects need to be considered carefully.

H_2 from Gasification/Pyrolysis of Biomass

Current technologies for converting biomass into molecular hydrogen include gasification/pyrolysis of biomass coupled to subsequent steam reformation (Fig. 2.19) [36]. The main conversion processes are:

(1) Indirectly heated gasification
(2) Oxygen-blown gasification
(3) Pyrolysis
(4) Biological gasification (anaerobic fermentation)

Biomass gasification has been demonstrated on a scale of 100 tons of biomass per day. Only a small, 10 kg/day of H_2 pilot biomass plant is in operation, and no empirical data on the operation, performance, and economic efficiency of a full-scale biomass-to-hydrogen plant are available. The thermodynamic efficiencies of these processes are currently around 50%. Considering the low energy content of biomass, between 0.2 and 0.4% of the total solar energy available is converted into molecular hydrogen.

Biomass gasifiers are designed to operate at low pressure and are limited to midsize-scale operations. As a consequence, biomass is heterogeneous, its production localized, and the cost is relatively high to gather and transport biomass. Therefore, current biomass gasification plants are associated inherently with unit capital costs that are at least 5 times as high as those for coal gasification and operate at a lower efficiency [39].

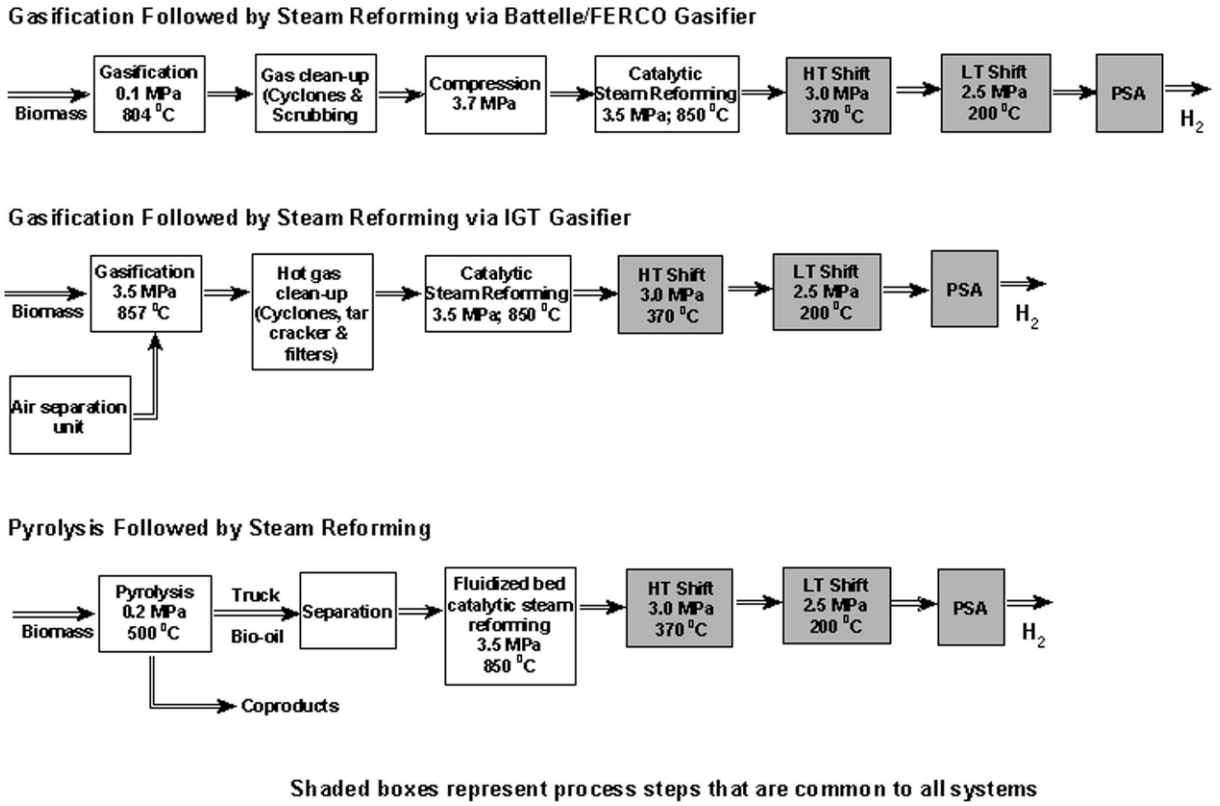

Fig. 2.19 Biomass gasification/pyrolysis processes for H_2 production

Co-production (biorefinement) of, for example, phenolic adhesives, polymers, waxes, and other products with hydrogen production from biomass is being discussed in the context of plant designs to improve the overall economic efficiency of biomass-to-hydrogen conversion [36]. The technical and economic viability of such co-production plants is yet unproven.

Several major technical challenges are associated with biomass gasification/pyrolysis. They include variable efficiencies, tar production, and catalyst attrition [36]. The moisture content as well as the relative composition and heterogeneity of biomass can result in a significant deactivation of the catalyst. Recent fundamental research identified a new, potentially inexpensive class of catalysts for aqueous-phase reforming of biomass-derived polyalcohols [40]. In contrast to residue biomass, the use of bioenergy crops as biomass for gasification is advantageous, as its composition and moisture content are predictable, and the gasification process can be optimized for the corresponding crop.

Using anaerobic fermentation to convert biomass into hydrogen, a maximum of about 67% of the energy content (e.g. of glucose) can be recovered theoretically in hydrogen [40]. Considering the currently known fermentation pathways, a practical efficiency of biomass conversion into hydrogen by fermentation is between 15 and 33% (4 mol H_2/mol glucose), although this is only possible at a low hydrogen partial pressure. However, more efficient fermentation pathways could be conceived and would require significant bioengineering efforts. These values compare with a biomass gasification efficiency of around 50%. The impurity of the hydrogen from biomass may be of concern, as fuel cell operations require relatively high-grade quality.

In the past the process of biomass gasification received most of the attention. Gasification technology using biomass, typically wood residues as feedstock, was adapted from coal gasification, and a few small-scale prototypes of biomass gasification plants have been built. However, no mid-size gasification facility exists to date that converts biomass into hydrogen, and no empirical data are available on the operation, performance, and economic efficiency of a mid-size biomass-to-hydrogen plant, as assumed in the economic model. The assumptions made for the analysis of current technology consist of modular combinations based on existing technical units for coal gasification (shell gasifier, air separation unit, traditional shift), without considering the variability in chemical composition and moisture content of typical biomass. An overall gasification efficiency of 50% is assumed. In another scenario analyzed 100% of the H_2 demand would need to be met by biomass-derived hydrogen, acknowledging that a mix of different primary energy sources is more likely in a possible future scenario. As the relative proportion of such mixes of primary feedstock is unknown, only the simplified case was considered.

Estimation of the economic efficiency of future technology for biomass-to-hydrogen conversion using gasification is more problematic and much more uncertain because of the necessary extrapolations. The following assumptions were made for a mid-size plant:

(1) Advanced biomass gasifiers can be developed and will use newly developed technology, such as fluidized catalytic cracking
(2) Biomass gasifiers can be modified to produce a CO and H_2 syngas, as does coal gasification
(3) Biomass gasification will operate at an overall efficiency of about 70%
(4) Through genetic engineering and other breeding methods, the growth yield of switch grass can be increased by 50%

It was also assumed that the future biomass will be derived from bioenergy crops at a price of $50/dt, as opposed to coming from less expensive biomass residues, although it is possible that a mixture of bioenergy crops and residues could be used for future gasifications. With these assumptions, the current price per kilogram of hydrogen delivered at the vehicle of $7.04 could be reduced to about $3.60 in the future. Analysis shows that two factors mainly contribute to the high price: The high capital charges for gasification and the high biomass costs.

2.4.4.2 H_2 from Photobiological Processes

In recent years, fundamental research on hydrogen production by photosynthetic organisms received significant attention. In photosynthesis water is oxidized photobiologically to molecular oxygen and hydrogen in order to satisfy the organism's need to build biomass from CO_2. This notion has prompted the idea of reengineering this process to directly release those equivalents as molecular hydrogen. Such direct production of molecular hydrogen probably is the thermodynamically most efficient use of solar energy in biological hydrogen production (theoretically about 10 to 30%), because it circumvents inefficiencies in the biochemical steps involved in biomass production as well as those involved in biomass conversion into hydrogen, as discussed above. The photosynthetic formation of molecular hydrogen from water is thermodynamically feasible even at high hydrogen partial pressure. However, such biological capability does not occur in any known organism; thus, it will require substantial metabolic engineering using new approaches in molecular biotechnology. In a variation of this approach, electron flow from the photosynthetic reaction center could be coupled to nitrogenase, which also releases H_2. Another mode of hydrogen production discussed in the context of photosynthetic H_2 production is dark fermentation mediated by photosynthetic microorganisms. In all cases, the reducing equivalents for producing hydrogen are derived from water, which is abundant and inexpensive.

The hybrid system shown in Figs. 2.20 and 2.21 is directed to the use of waste organic matter as a source of fuel for electrical power generation. Thus, this system can address two major environmental issues: Waste disposal and power generation. The ballasted gasifier converts biomass into a gas stream that generates electricity using a combination of fuel cell systems. A biological system in the form of the anaerobic bacterium R. gelatinosus CBS, which enzymatically reforms CO and H_2O to H_2 and can sequester CO_2, could both remove environmentally harmful greenhouse gases from the gas stream and generate additional H_2 for power generation. The

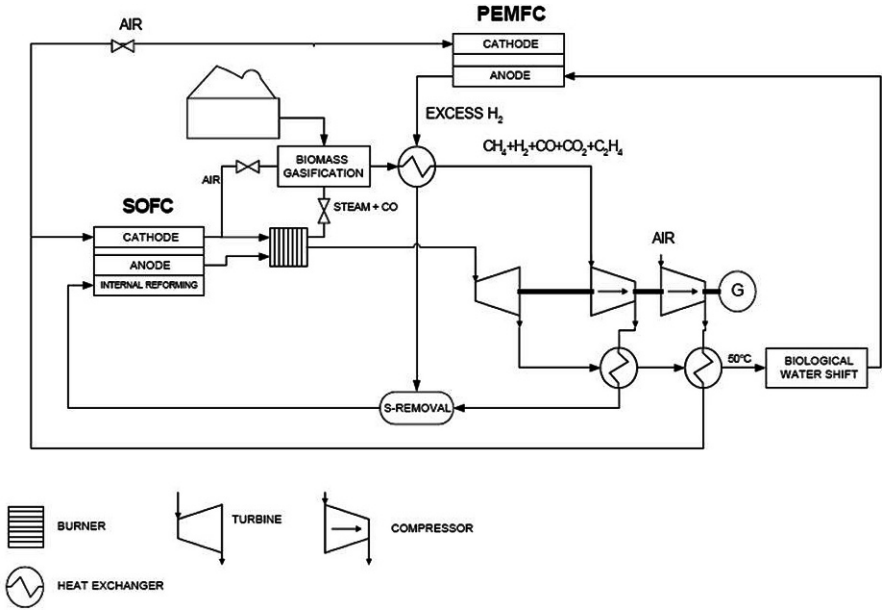

Fig. 2.20 Schematic diagram of a high-pressure biomass gasifier with biological *gas reformer*

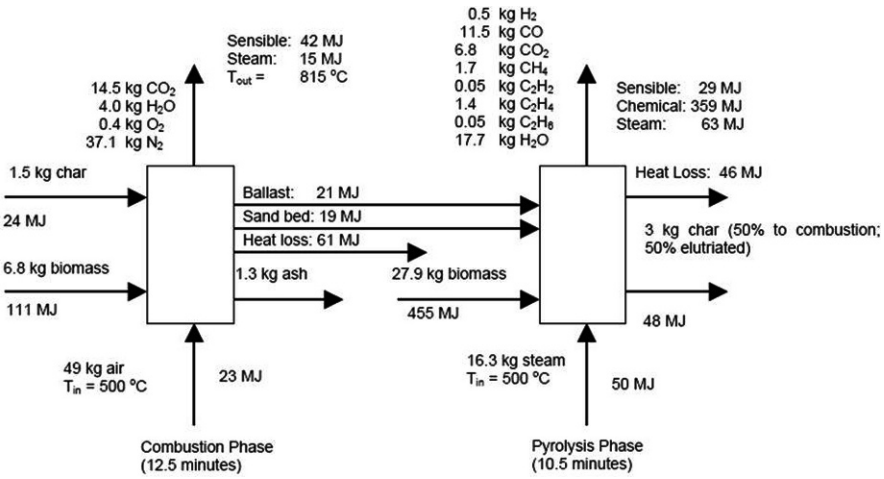

Fig. 2.21 Mass and energy balances of the ballasted gasifier

integrated system of gasifier, biological shift reactor, and fuel cell results in higher output power per unit of biomass than that of a simpler power system consisting of a gasifier and fuel cell [41].

Since the primary energy of all biological processes for hydrogen production is renewable solar energy, all other technologies using solar energy, including pho-

tovoltaic and other newer processes, such as thin-film technology, are competing for (land) surface area. Wind energy indirectly is solar energy. Currently, the solar-to-electrical conversion efficiency of newer photoelectric processes is 15 to 18%, compared with 0.4% for bulk biomass formation and about 10%, potentially, for direct hydrogen production by photosynthetic organisms. As solar energy harvesting technologies are competing for land use with each other and with other societal activities, such as farming, housing, and recreation, the overall efficiency of a solar energy conversion process will be a key to its economic viability.

2.4.4.3 Outlook

Hydrogen production from biomass is an attractive technology, as the primary energy is solar (i.e. "renewable"), without any net CO_2 being released (except for the transport). When coupled to CO_2 capture and sequestration on a larger technical scale, this technology might be the most important means to achieve a net reduction of atmospheric CO_2. Furthermore, different forms of biomass (bioenergy crops, residues, including municipal waste, etc.) could be used in different combinations.

The current concept of biomass-to-hydrogen conversion is subject to several limitations. Biomass conversion into hydrogen is intrinsically inefficient, and only a small percentage of solar energy is converted into hydrogen. Moreover, in order to contribute significantly to a hydrogen economy, the quantity of biomass that needs to be available necessitates the farming of bioenergy crops. Bioenergy crops obtained by farming, however, will be intrinsically expensive. Residue biomass is less expensive, but more variable and heterogeneous in composition, thus making the gasification process less efficient. In addition, significant costs are associated with the collection and transportation of dispersed, low-energy-density bioenergy crops and residues. Most importantly, large-scale biomass production would also pose significant demand on land, nutrient supply, water, and the associated energy for increased biomass production. The environmental impact of significant energy crop farming is unclear, but it can be assumed to be similar to that in crop farming and include soil erosion, significant water and fertilizer demand, eutrophication of downstream waters, and impact on biological diversity. Biomass production is also sensitive to seasonal variability as well as to vagaries of weather and to diseases, with significant demands regarding the storage of biomass in order to compensate for the anticipated fluctuations. Public acceptance of growing and using potentially genetically engineered, high-yield energy crops also is unclear. In addition, competing uses of biomass for purposes other than hydrogen production will determine the price of biomass. Overall, it appears that hydrogen production from farmed and agriculture-type biomass by gasification/pyrolysis will only be marginally efficient and competitive.

Biomass gasification could play a significant role in meeting the goal of greenhouse gas mitigation. It is likely that both in the transition phase to a hydrogen economy and in the steady state, a significant fraction of hydrogen might be derived from coal. In co-firing applications with coal, biomass can provide up to 15% of the total

energy input of the fuel mixture. The greenhouse gas mitigation can be addressed by co-firing biomass with coal to reduce the losses of carbon dioxide into the atmosphere that are inherent to coal combustion processes (even with the best-engineered capture and storage of carbon). Since growth of biomass fixes atmospheric carbon, its combustion leads to no net addition of atmospheric CO_2 even if vented. Thus, co-firing of biomass with coal in an efficient coal gasification process, providing the opportunity for capture and storage of CO_2, could lead to a net reduction of atmospheric CO_2. The co-firing fuel mixture, being dilute in biomass, places lower demands on biomass feedstock. Thus, cheaper, though less plentiful, biomass residue could supplant bioenergy crops as feedstock. Use of residue biomass also would have a much less significant impact on the environment than farming of bioenergy crops.

Photobiological hydrogen production is a much more efficient process and requires nutrients to a lesser extent than biomass-to-hydrogen conversion. The objective is to engineer a (micro) organism that catalyzes the light-mediated cleavage of water with the concomitant production of hydrogen at high rates and high thermodynamic efficiency. This process does not take place in naturally occurring organisms at an appreciable rate or scale. While this approach has much potential, there are also major challenges. Substantial bioengineering efforts have to be undertaken to engineer microorganisms with a robust metabolic pathway, including improved kinetics for hydrogen production and efficiencies in light energy conversion and hydrogen production, before a pilot-scale photobiological system could be evaluated. This requires long-term, fundamental research on a significant funding level. Moreover, inexpensive, large-scale reactor systems need to be designed that minimize the susceptibility to biological contamination. In addition, the public perception of the use and possible concerns regarding the potential "escape" of genetically engineered microorganisms need to be addressed.

2.5 Conclusions

Comparing different technologies for hydrogen production is a complex matter and, therefore, a matter of serious disputes. In the case of hydrogen production, an infinite number of possible fuel pathways exist (see Fig. 2.5 at the beginning of this chapter). It has to be assessed which one of these possible pathways is the most suitable one from the complex point of view of global economics, national economics, environmental issues, health issues, etc. At the moment, no integral tools exist that would take into account all these aspects and give the answer. However, there are many prestigious institutions in the world working on these issues and developing new, more and more complex tools to deal with these problems. Among them are ETH Zürich, MIT, ANL, LBST, etc. The most popular methods used are the life cycle assessment methods.

Life cycle assessment (LCA) is a tool that provides a comprehensive analysis of the environmental impact caused by a product during its life cycle, comprising its

production, use, and disposal. Environmental impact is mainly caused by the consumption or/and transformation of materials and energies. Therefore, LCA looks at material flows, energy use, and associated emissions. Costs are usually not an issue within the LCA. But on the other side, costs certainly form the basis for decision-making in business. Consequently, numerous efforts are undertaken to implement LCA with economic parameters. LCA has to cope with a number of difficulties:

- Relevant data are uncertain and may vary to some extent
- Data are not available in some cases
- Some technologies considered are still under development
- It is not always clear, where to draw the boundary for the analysis
- There is practically an infinite number of possible fuel pathways
- Fortunately, only few pathways make sense (which already is a result of an LCA)

Despite the theoretical and practical limitations of LCA, this is the best method to assess and compare different energy systems. LCA is always a work in progress, due to innovations in the segments of the production chain. However, it enhances our understanding of energy systems and gives orientation where to look for the more sustainable solutions.

Life cycle assessment of hydrogen fuel has to analyze material flows, energy flows, and emissions. In the following paragraph two different approaches to LCA of hydrogen fuel will be presented, both for the use of hydrogen as a fuel in vehicles. Since this is one of the most desirable uses of hydrogen and, at the same time, the most demanding one, it will fit very well to the scope of this book.

The material flows, energy flows, and emissions are caused by:

1. The production of the fuel supply infrastructure and of the vehicles
2. The production of the hydrogen fuel
3. The use of the fuel (hence, the vehicle has to be included in the analysis!)
4. The dismantling and disposal of supply infrastructure and vehicles

Topics 2 and 3 are addressed in Well-To-Tank (WTT) and Tank-To-Wheel (TTW) analyses. A comprehensive LCA should also investigate topics 1 and 4. Often, this is not done due to difficulties in data collection and/or due to a presumption that these effects are of minor importance.

The first approach is based on three technologies for hydrogen production that are considered: Traditional hydrogen production via natural gas reforming and the use of two renewable technologies (wind and solar electricity generation) to produce hydrogen through the electrolysis of water. The gasoline used in conventional transportation is considered to be obtained by standard crude oil processing and distillation (see Fig. 2.22). Economic and environmental indicators are introduced to compare different technologies for gasoline and hydrogen production and utilization in vehicles.

Based on life cycle assessments of hydrogen production technologies [42], a method was proposed to obtain an objective criterion to measure sustainable

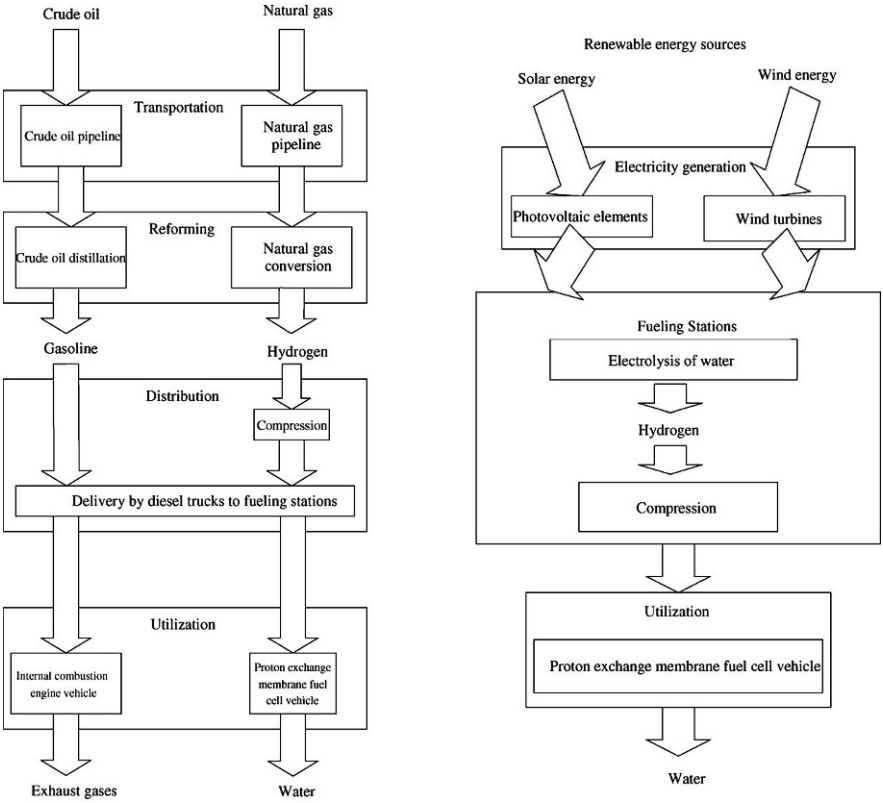

Fig. 2.22 Principal technological steps in utilizing fossil fuels and solar and wind energies in transportation

Table 2.4 Sustainability indexes for different hydrogen production technologies and its use in PEMFC vehicles

Hydrogen production technology	Sustainability index for air pollution reduction	Sustainability index for greenhouse gas emission reduction
Hydrogen–Natural Gas	0.113	– 0.271
Hydrogen–Wind	0.081	–0.036
Hydrogen–Solar	–0.069	–0.250

development in order to assess hydrogen production technologies for the utilization of hydrogen as an ecologically benign fuel in PEMFC vehicles. The results indicate that a decrease of the environmental impact (air pollution and greenhouse gas emission reduction) as a result of hydrogen use as a fuel is accompanied by a decline in the economic efficiency (as measured by capital investment effectiveness) (see Table 2.4).

An optimal strategy of introducing competing environmentally benign technologies can be chosen taking into account the relationship between environmental and economic criteria in the form of sustainability indexes. From the estimations obtained, it is concluded that hydrogen production from wind energy via electrolysis is more consistent with a sustainable development in terms of greenhouse gas emission mitigation and that traditional natural gas reforming is more favorable for air pollution reduction [43].

The second approach is based on greenhouse gas regulated emissions and energy use in transportation (GREET) software and has been used to analyze the fuel life cycle. Also here, the life cycle of the fuel consists of obtaining the raw material, extracting the fuel from the raw material, transporting, and storing the fuel as well as using the fuel in the vehicle. Four different methods of obtaining hydrogen were analyzed; using coal and nuclear power to produce electricity and extraction of hydrogen through electrolysis and via steam reforming of natural gas in a natural gas plant and in a hydrogen refueling station.

The analysis carried out [44] shows (Table 2.5) that the FCV is a better choice than ICEV, except for hydrogen production using coal as the primary energy source. No matter whether hydrogen is extracted via steam reforming of natural gas or the use of electricity from nuclear power, the energy consumption by a today's FCV is 50% lower than that of an ICEV. The total carbon dioxide emission is 77% lower in an FCV compared to an ICEV, if hydrogen is extracted from steam reforming of natural gas. If hydrogen is extracted via the use of electricity from nuclear power, the emissions are lowered and are 87% lower compared to an ICEV. However, if hydrogen was extracted by electrolysis via coal, the energy consumption of an FCV is 19% higher compared to an ICEV and the emissions are 50% higher than those of an ICEV. It is similar for future vehicles: If hydrogen is extracted via steam reforming of natural gas or the use of electricity from nuclear power, the energy consumption by an FCV is 27% lower than that of an ICEV. The total carbon dioxide emission is 37% less for an FCV when hydrogen is extracted from steam reforming of NG. When hydrogen is extracted from electricity via nuclear power, the emissions of the future FCV will be 77% lower compared to the future ICEV. Again, if hydrogen was to be extracted using electrolysis via coal, the energy consumption of the FCV is 62% higher compared to an ICEV and the total carbon dioxide emissions are 98% higher than those of an ICEV.

The well-to-wheel efficiency of a fuel cell vehicle run by hydrogen obtained from natural gas is 21%, while the well-to-wheel efficiency of an internal combustion engine vehicle run by conventional gasoline is 13.8%. This is due to the fact that the FCV vehicle is much more efficient during the pump-to-wheel stage. Indeed, the FCV pump-to-wheel efficiency is 36%, while the ICEV pump-to wheel efficiency is 17.1%. Even though the capital cost of an FCV is estimated to be higher than the cost of an ICEV by around CAD$ 6500, the higher FCV efficiency will compensate for this difference with lower operating costs. Therefore, the cost of the FCV is expected to be lower than that of the ICEV over their entire lifetime.

Table 2.5 Total energy consumption and total emissions (future vehicle)

Method	Fuel Life Cycle (GJ)	Total CO_2 (ton)	Vehicle Life Cycle (GJ)	Total CO_2 (ton)	Total Energy in Life Cycle (GJ)	Total CO_2 (ton)	Energy (%)	Emissions (%)
Hydrogen extracted from water by electrolysis, with coal as a basis, and used in refuelling stations	1512.87	139.41	147.12	15.12	1659.98	154.53	62	98
Hydrogen extracted from NG in a power plant and distributed to refueling stations	575.11	32.49	147.12	15.12	722.23	47.61	−30	−39
Hydrogen extracted from NG in the refueling station	606.94	34.43	147.12	15.12	754.06	49.55	−27	−37
Hydrogen extracted from water by electrolysis from nuclear power and distributed to refueling stations	597.29	2.97	147.12	15.12	744.41	18.09	−27	−77
Conventional gasoline extracted from petroleum and distributed to refueling stations	882.98	62.96	143.19	15.10	1026.17	78.06	0	0

References

1. Fossil fuel. (2006, November 13). In *Wikipedia, The Free Encyclopedia*. Retrieved 10:13, November 20, 2006, from http://en.wikipedia.org/w/index.php?title=Fossil_fuel &oldid=87453991.
2. IEA Energy Technology Essentials, ETE 05, OECD/IEA, April 2007.
3. *International Energy Outlook 2001*, http://www.eia.doe.gov/oiaf/archive/ieo01/index. html.
4. *The Hydrogen Economy: Opportunities, Costs, Barriers, and R&D Needs, Chapter 8*, Committee on Alternatives and Strategies for Future Hydrogen Production and Use, National Academy of Engineering, Board on Energy and Environmental Systems, The National Academies Press, Washington, DC, 2004, http://books.nap.edu/openbook.php record_id=10922&page=R2.
5. http://en.wikipedia.org/wiki/Fossil_fuel_power_plant#Fuel_processing.
6. M. C. Carbo, D. Jansen, W. G. Haije, and A. H. M. Verkooijen, *Advanced Membrane Reactors for Fuel Decarbonisation in IGCC: H2 or CO2 separation*?, Presented at the Fifth Annual Conference on Carbon Capture and Sequestration, 8–11 May 2006, Alexandria VA, U.S.A.
7. P. Middleton, H. Solgaard-Andersen, and T. Rostrup-Nielsen, *Hydrogen Production with CO2 Capture Using Membrane Reactors*, Joint Industry CO2 Capture Project (CCP), Digital Business, April 2003.
8. https://www.HFPerope.org/hfp/ip_consultation.
9. S.-T. Lin, Y.-H. Chen, C.-C. Yu, Y.-C. Liu, and C.-H. Lee, *Modelling an experimental methane fuel processor*, Journal of Power Sources 148 (2005) 43–53.
10. C. Forsberg, *Hydrogen Futures, Nuclear Energy, and Separations*, Plenary Lecture at 13th Symposium on Separation Science and Technology for Energy Applications, Oak Ridge National Laboratory, Gatlinburg, Tennessee, October 27–30, 2003.
11. The Intergovernmental Panel on Climate Change (IPCC) has defined the global warming potential as follows: "An index describing the radiative characteristics of well-mixed greenhouse gases that represents the combined effect of the differing times these gases remain in the atmosphere and their relative effectiveness in absorbing outgoing infrared radiation. This index approximates the time-integrated warming effect of a unit mass of a given greenhouse gas in today's atmosphere, relative to that of carbon dioxide".
12. Environmental Protection Agency (EPA), "Current and Future Methane Emissions from Natural Sources." Available online at http://www.epa.gov/ghginfo/reports/curr.htmUT. Accessed on December 10, 2003.
13. J. Deutch and E. Moniz, *"The Future of Nuclear Power"*, Massachusetts Institute of Technology Interdisciplinary Study, July, 2003. http://web.mit.edu/nuclearpower/
14. P. Pickard, *"Sulfur-Iodine Thermochemical Cycle"*, Project PD20, 2007 DOE Hydrogen Program Review, May 16, 2007. http://www.hydrogen.energy.gov/annual_review07_proceedings.html
15. K. Schultz, C. Sink, P. Pickard, S. Herring, J. O'Brien, B. Buckingham, W. Summers, and M. Lewis, *"Status of the US Nuclear Hydrogen Initiative"*, Paper 7530, Proceedings of ICAPP 2007, Nice, France, May 13–18, 2007.
16. W. Summers, M. Gorensek, and J. Weidner, *"Hybrid Sulfur Cycle Flowsheets for Hydrogen Production from Nuclear Energy"*, Paper 182g, Proceedings of AIChE 2006 Spring Meeting, Orlando, Florida, April 26, 2006. http://www.aiche-ned.org/conferences/aiche2006spring/session_182/AICHE2006spring-182g-Gorensek.pdf
17. S. P. S. Badwal, S. Giddey, and F. T. Ciacchi, *Hydrogen and oxygen generation with polymer electrolyte membrane (PEM)-based electrolytic technology*, Ionics 12 (2006) 7–14.
18. J. A. Turner, *A realizable renewable energy future*, Science **285** (1999) 687–689; 1493–1493.
19. Global Wind Energy Market Report, American Wind Energy Association, March 2004; http://www.awea.org/resources/resource%5Flibrary/#DocumentsandReports.

20. Renewable Energy Trends 2003. With Preliminary Data For 2003. Energy Information Administration, U.S. Department of Energy, Washington, DC 20585, July 2004, http://tonto.eia.doe.gov/FTPROOT/renewables/062803.pdf.
21. K. S. Cory, S. Bernow, W. Dougherty, S. Kartha, and E. Williams, *Analysis of Wind Turbine Cost Reductions: The Role of Research and Development and Cumulative Production*, Presented at AWEA's WINDPOWER '99 Conference, Burlington, VT, 22 June 1999 http://www.tellus.org/energy/publications/awea9_amy.pdf.
22. EurObservER, Wind Energy Barometer, February 2007.
23. Hydrogen Posture Plan. An Integrated Research, Development, and Demonstration Plan, U.S. Department of Energy, February 2004; http://www1.eere.energy.gov/ hydrogenandfuelcells/pdfs/hudrogen_posture_plan.pdf.
24. L. J. Fingersh, *Optimized Hydrogen and Electricity Generation from Wind*, National Renewable Energy Laboratory, NREL/TP-500-34364, Golden, Colorado 80401–3393, June 2003, http://www.nrel.gov/docs/fy03osti/34364.pdf.
25. T. B. Johansson, H. Kelly, A. K. N. Reddy, and R. H. Williams (eds.). *Renewable Energy: Sources for Fuels and Electricity*. Washington, D.C.: Island Press, 1993.
26. M. D. Archer and R. Hill (eds.), *Clean Electricity from Photovoltaics, Series on Photoconversion of Solar Energy*, Vol. 1, Imperial College Press, London, 2001.
27. M. A. Green, *Photovoltaic principles*, Physica E 14 (2002) 11–17.
28. H. S. Ullal, *Polycrystalline Thin Film Photovoltaic Technologies: Progress and Technical Issues*, NREL/CP-520-36241, August 2004, accessible at www.nrel.gov/ncpv/thin_film/docs/nrel_partnership_ullal_pv_sec_2004_status.doc.
29. R. D. Wieting, *CIS manufacturing at the MW scale*, Proceedings of the 29th IEEE Photovoltaic Specialists Conference, New Orleans, USA, May 18–22, (2002). 478–483.
30. A. Shah, P. Torres, R. Tscharner, N. Wyrsch, and H. Keppner, *Photovoltaic technology: the case for thin-film solar cells*, Science, 285 (1999) 692–698.
31. J. Yang, A. Banerjee, and S. Guha, *Triple-junction amorphous silicon alloy solar cell with 14.6% initial and 13.0% stable conversion efficiencies*, Applied Physics Letters, 70 (22) (1997) 2975–2977.
32. B. Schroeder, *Status report: solar cell related research and development using amorphous and microcrystalline silicon deposited by HW(Cat)CVD*, Thin Solid Films 430 (2003) 1–6.
33. B. O'Regan and M. Grätzel, *A low-cost, high-efficiency solar cell based on dye-sensitized colloidal TiO_2 films*. Nature, 353 (1991) 737–740.
34. M. Grätzel, *Photoelectrochemical cells*, Nature, 414 (2001) 332–344.
35. D. O. Hall and K. K. Rao, *Photosynthesis*. 6th edn. Cambridge, U.K.: Cambridge University Press; 1999.
36. T. A. Milne et al., *Hydrogen from Biomass: State of the Art and Research Challenges*, Report No. IEA/H2/TR-02/001, NREL, Golden, CO, 2002.
37. D. De La Torre Ugarte, M. E. Walsh, H. Shapouri, and S. P. Slinsky, *The Economic Impacts of Bioenergy Crop Production on US Agriculture*, USDA, Washington, DC, 2003.
38. D. J. A. Johansson and Ch. Azar, *A scenario based analysis of land competition between food and bioenergy production in the US*, Presented at Climate Change Mitigation Measures in the Agro-Forestry Sector and Biodiversity Futures, 16–17 October 2006–ICTP, Trieste, Italy, *Accepted for publication in Climatic Change*.
39. P. L. Spath, J. M. Lane, M. K. Mann, and W. A. Amos, *Update of Hydrogen from Biomass – Determination of the Delivered Cost of Hydrogen*, NREL, Golden, Colorado, Midwest Research Institute, Battelle, Bechtel, 2001.
40. J. Woodward, M. Orr, K. Cordray, and E. Greenbaum, *Efficient Production of Hydrogen from Glucose-6-Phosphate*, Oak Ridge National Laboratory; Proceedings of the 2000 DOE Hydrogen Program Review NREL/CP-570-28890.
41. W. Merida, P.-C. Maness, R. C. Brown, and D. B. Levin, *Enhanced hydrogen production from indirectly heated, gasified biomass, and removal of carbon gas emissions us-*

ing a novel biological gas reformer, International Journal of Hydrogen Energy 29 (2004) 283–290.
42. Economic input–output life cycle assessment, Green design initiative, Carnegie Mellon University. Available online at http://www.eiolca.net, Accessed on 14 December 2004.
43. M. Granovskii, I. Dincer, and M. A. Rosen, *Environmental and economic aspects of hydrogen production and utilization in fuel cell vehicles*, Journal of Power Sources 157 (2006) 411–421.
44. N. Zamel and X. Li, *Life cycle analysis of vehicles powered by a fuel cell and by internal combustion engine for Canada*, Journal of Power Sources 155 (2006) 297–310.

Chapter 3
Hydrogen Storage

Aline Léon

List of Abbreviations

CGH_2	Compressed Hydrogen
CUTE	Clean Urban Transportation Europe
EU	European Union
LH_2	Liquid Hydrogen
SSH_2	Solid Storage of Hydrogen

Aline Léon
Institut für Nanotechnologie, Forschungszentrum Karlsruhe, P.O. Box 3640, D – 76021 Karlsruhe, Germany, e-mail: aline.leon@int.fzk.de

A. Léon (ed.), *Hydrogen Technology*,

3.1 Introduction

For the development of the future hydrogen economy, a safe and efficient means of storing hydrogen is required in mobile, portable, and stationary applications. Cars represent the ultimate market for manufacturers of hydrogen storage systems, although they pose some of the greatest challenges to commercialization due to their relatively small size, the necessity for a vast fuelling infrastructure, and public acceptance. In addition, performance and reliability are high and the cost issue is critical. Indeed, for a successful application of hydrogen as an energy carrier, hydrogen should be stored safely for variable periods of time, as efficiently as gasoline. At the same time, simple handling and low costs should be ensured. However, the unusual physical and thermodynamic properties of hydrogen today pose the greatest technological challenges to its penetration in the market as an energy carrier.

The phase diagram of hydrogen, Fig. 3.1, indicates that the three phases coexist at a temperature of 13.803 K. The solid phase exists below 14 K. The liquid phase is present from the triple point up to the critical point. The boiling temperature of hydrogen at 1 bar is around 20 K. Above the critical point (T_c = 32.976 K and P_c = 12.928 bar), the liquid – vapor equilibrium ceases to exist. Therefore, hydrogen is in the gas phase at normal pressure (1 bar) and temperature (298.15 K).

Under normal conditions, the density of the gas is 0.08238 Kg/m^3 [1]. For 5 kg of hydrogen, this implies a volume of around 60 m^3 and an energy content of 600 MJ = 166.65 kWh. For the same weight and energy content, the gasoline volume

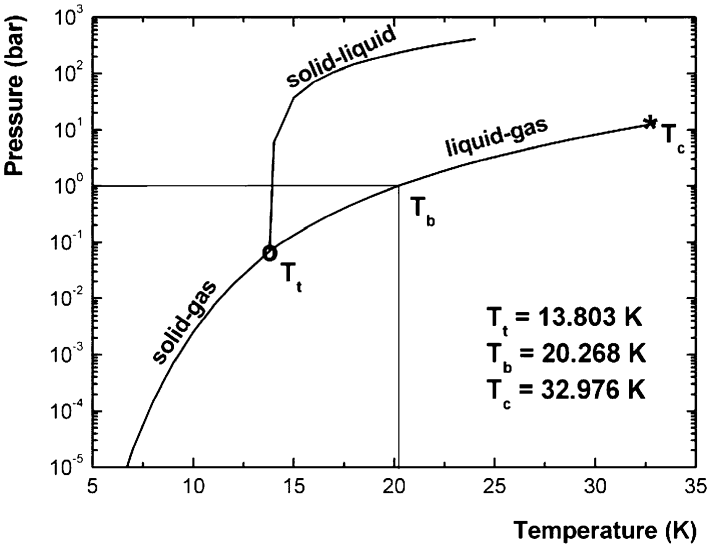

Fig. 3.1 Phase diagram of p-H_2. T_t represents the triple point (T_t = −259.347°C, P_t = 0.0704 bar), T_b the boiling point (T_b = −252.882°C, P_b = 1 bar), and T_c the critical point (T_c = −240.174°C, P_c = 12.928 bar) [1]

is 0.019 m^3. In view of these numbers, it is clear that for efficient storage, hydrogen density should be increased by reducing the volume taken by the gas under normal temperature and pressure conditions. As a consequence, the "usual state" of hydrogen has to be changed in order to store it efficiently. This can be accomplished by increasing the pressure, decreasing the temperature below the critical temperature or by reducing the repulsion interaction between hydrogen molecules by binding them with another material. Thus, the following three main options emerged:

1. Compressed hydrogen storage (CGH_2).
2. Cryogenic hydrogen storage (LH_2).
3. Solid storage of hydrogen (SSH_2).

The properties that are of importance in the use of hydrogen in the storage tank, in pipelines, and at the fuelling station are the flow of hydrogen, its composition, density, specific volume, specific heat,[1] conductivity,[2] viscosity, enthalpy, entropy, Joule–Thomson coefficient,[3] and the velocity of sound in the gas.[4]

An outline of the requirements to guide current research and development and to achieve commercially viable hydrogen storage technologies is given by the U.S. DOE hydrogen storage system performance targets [2]. These targets are not based on a particular method or technology for storing hydrogen, but on equivalency to current gasoline storage systems in terms of weight, volume, cost, and other operating parameters. The ultimate goal is the implementation of hydrogen-powered fuel cell vehicles with a performance comparable or superior to today's gasoline vehicles. Translating vehicle performance requirements into storage system's needs resulted in the DOE hydrogen storage system targets. The storage system should include all the hardware (i.e. tank, valves, regulators, piping, mounting brackets, insulation, thermal management, and any other balance of plant components) in addition to the storage media and a full charge of hydrogen. Among others, the most important targets to be fulfilled by any storage system are the gravimetric and volumetric capacity, the refueling time (which depends on the thermodynamics of the materials and the thermal management for heat removal), and the minimum full flow rate.

Following a short description of the purification technology of hydrogen, this chapter will present various storage approaches that are currently of interest. They include the storage of hydrogen as compressed hydrogen gas (CGH_2) and cryogenic liquid hydrogen (LH_2). Then, solid storage (SSH_2) will be considered in the form of reversible and irreversible storage systems.

3.2 Purification of Hydrogen

The raw gas obtained by the methods described in Part I, Chapter 2 is delivered at various pressures and grades. Consequently, hydrogen has to be purified before compression, liquefaction or storage in a chemical form. The acceptable level of impurities for compression is around 4 ppm, whereas for liquefaction it should be below 1 ppm. This is to avoid any clogging of the different components in a liquefier (i.e. at 20 K, all the other elements except for He are solid).

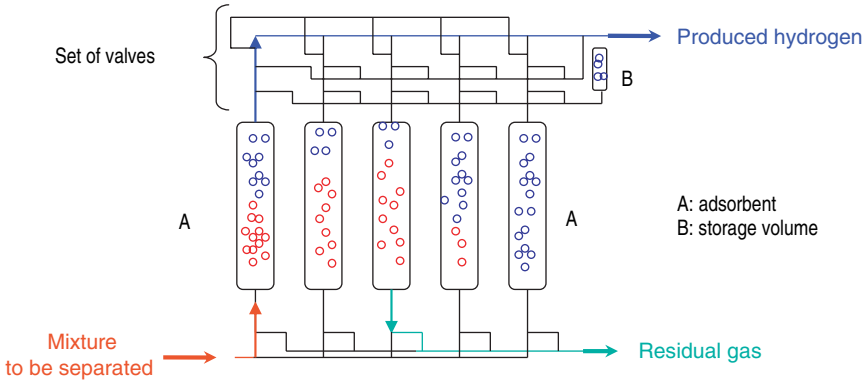

Fig. 3.2 Schematic diagram of a PSA unit with 5 adsorbents for hydrogen purification [3]

Purification of a gas can be performed by several techniques, such as separation by permeation, adsorption, absorption, distillation or by partial condensation [3]. For hydrogen the most common industrial technique is adsorption using a pressure-swing adsorption system (PSA) combined with or replaced by permeation or distillation processes. Figure 3.2 displays a typical system for hydrogen, which is composed of 5 adsorbents (the number of adsorbents actually depends on the extraction efficiency required), volumes for storage and for the stabilization of flow, and a set of valves. The process consists of feeding the raw gas under a certain pressure into the adsorbents (examples: Aluminates, silica gels, active charcoal, etc. in the form of stones, balls, sticks), where the heaviest constituents like CO_2, H_2O, CH_4, CO, Ar, and N_2 get captured while hydrogen passes through. The adsorbents are regenerated in several steps by decreasing the pressure and hydrogen reflux. At the outlet of this unit, hydrogen is purified to an impurity level of approximately 4 ppm. Further purification to an impurity level below 1 ppm is carried out using low-temperature adsorbents at liquid nitrogen temperature.

When hydrogen is produced by an electrolysis of water, traces of oxygen are removed in a "deoxo", a reactor working at a temperature around 700 K with palladium as catalyst. Oxygen has to be removed not only to avoid the blocking of the piping and heat exchangers, but also for safety reasons to avoid the formation of an explosive mixture when the liquefier is warmed up.

3.3 Compressed Hydrogen (CGH_2)

3.3.1 Characteristics of CGH_2

Figure 3.3 displays the volumetric density of n-H_2 (normal hydrogen) as a function of the pressure at three different temperatures [1]. It can be seen that hydrogen density does not increase linearly with increasing pressure. A hydrogen density of

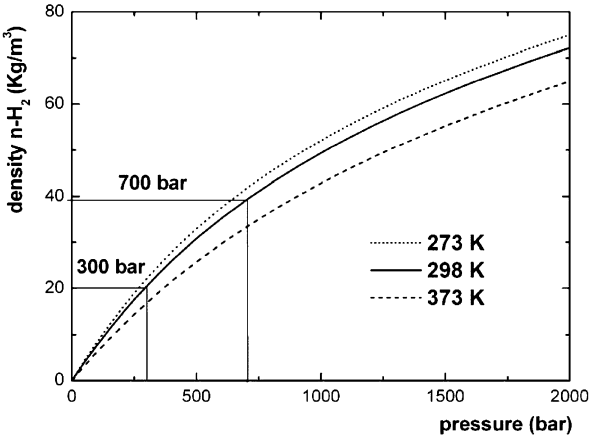

Fig. 3.3 Evolution of the volumetric density of n-H_2 as a function of pressure at three different temperatures [1]

20 Kg/m^3 is reached at 300 bar. The volumetric density can be increased to around 40 up to 70 Kg/m^3 by compressing the gas to a pressure of up to 700 or 2000 bar, respectively. However, 2000 bar is technically not feasible. Nowadays, a pressure of 350 bar is the standard and 700 bar is the current target value. High-pressure storage allows reducing the storage volume for 5 kg of hydrogen from 60 m^3 to 0.25 and 0.125 m^3 at a pressure of 1, 300, and 700 bar, respectively. The decrease of the storage volume from 300 to 700 bar is not as drastic as the decrease resulting when varying the pressure from 1 to 300 bar. Hence, another increase in internal pressure will not result in any significant breakthrough in volumetric density.

3.3.2 Hydrogen Compressors

A hydrogen compressor is a mechanical device that increases the pressure of the gas by reducing its volume. However, the low molar weight of hydrogen (M = 2.016 g/mol^{-1}) requires the use of a volumetric compressor instead of a centrifugal compressor in order to gain efficiency. Moreover, the energy used to compress a gas does not only produce a pressure increase, but also generates heat. Compression work usually is calculated using the appropriate gas state and energy equations with two common approximations, adiabatic (isentropic) and isothermal compression.

In the adiabatic case, the process is assumed to take place without any heat exchange between the compressed gas and the environment and without variations of entropy. Under these conditions, the amount of work needed to raise the gas pressure from P_1 to $P_2 (P_1 < P_2)$ is given by:

$$W_{\Delta S \to 0, ideal} = \frac{\gamma}{\gamma - 1} R T_1 \left[\left(\frac{P_2}{P_1} \right)^{\gamma/(\gamma-1)} - 1 \right] \tag{3.1}$$

where T_1 is the temperature of hydrogen at P_1 and γ is the specific heat ratio of the gas (C_p/C_v) that is assumed to be independent of temperature. For an adiabatic process, PV^{γ} is constant throughout compression. A correction factor, η_a is introduced to account for the irreversibility of an actual process.

For isothermal compression, the temperature of the gas is considered constant during the process. The compression work calculated under this assumption varies depending on whether ideal gas or real gas models are applied. The actual compression work will usually range between the theoretical conditions of isothermal and isentropic compression, which represent a lower and upper limit of compression work, respectively.

Generally, the compressed gas has to be cooled down after each stage to make compression less adiabatic and more isothermal. Hence, hydrogen typically is compressed in several stages. Important design parameters of a compressor are the inlet pressure and temperature, the discharge pressure, the required flow rate, the volume to fill, the start and end pressure, and the time allowed to fill the volume. Hydrogen compressors are expensive due to the materials used, their sizes, and their high maintenance costs of wear parts (e.g. valves, rider bands, piston rings). Moreover, compression is energy-intensive. At an inlet pressure of 20 bar and an outlet pressure of 70 bar with an adiabatic efficiency around 70 to 80%, for example, the compression energy required is between 0.6 and 0.7 kWh/kg. If the gas has to be compressed from 7 bar to 500 bar, the adiabatic efficiency is around 50 to 70% and compression energy is between 2.6 kWh/kg and 3.5 kWh/kg [4].

Types of compressors include mechanical piston and diaphragm compressors, non-mechanical compressors, such as the solid-state hydrogen compressor, and the electrochemical hydrogen compressor. Their properties and characteristics will be described shortly below.

3.3.2.1 Mechanical Compressors

These devices are used for filling vehicle tanks rapidly, moving gas between storage vessels, and unloading the gases from high-pressure tube trailers.

Piston Compressor

Figure 3.4 displays a single-stage piston compressor C12-40-7000LX/SS by Hydro-Pac, Inc. [5]. This compressor was designed for operation at a discharge pressure of 850 bar and inlet pressure of 350 bar. The capacity is around 430 kg/h at an inlet pressure of 350 bar and a motor size of 30 kW. Such a hydrogen gas compressor costs around US$98,800 [5].

The piston compressor is an electro-hydraulically driven, non-lubricated, liquid-cooled, single-stage unit, including an electric motor, hydraulic pump, hydraulic oil reservoir, high-pressure gas intensifier, and intensifier shifting mechanism. The two major components are the intensifier and the fluid-power drive. As obvious from the

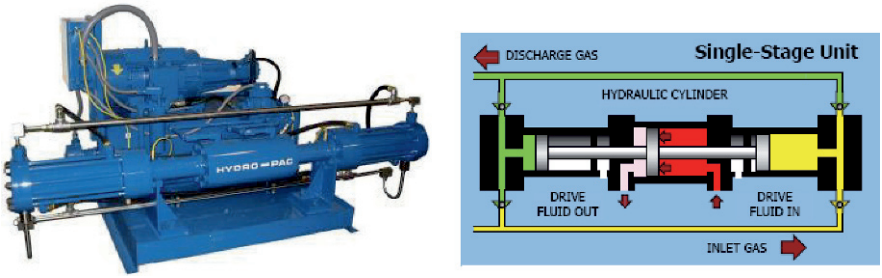

Fig. 3.4 Hydro-Pac hydrogen compressor model C12-40-7000LX for compression of hydrogen up to 80 MPa (800 bar), 30 kW (left). Single-stage unit with an inlet pressure of 35–40 MPa (350–400 bar) (right) [5]

schematic diagram of the single-stage unit, the intensifier contains a hydraulic drive cylinder in the center that is coupled by tie rods with two single-stage gas cylinders on either side. The fluid power drive provides the intensifier with pressurized hydraulic fluid. During operation, the gas fills the cylinder. Then, the force of the hydraulic pressure acts on the hydraulic piston compressing the gas in the first cylinder. Once compression is completed, the four-way valve redirects the hydraulic fluid and the piston assembly moves in the opposite direction. The special features of such a system are non-contamination of the compressed gas (using a non-lubricated design and isolated chamber for the fluid power and the compressed gas), the variable inlet pressure (using a high inlet pressure allows maximizing the compressor output), the near-isothermal compression due to the long, slow compression stroke (this allows reducing the power consumption), and reliability (the compressor has been used for thousands of hours in critical application).

Piston-metal Diaphragm Compressor

In this case, the gas from the piston and related components is isolated by a set of metal diaphragms as shown in Fig. 3.5 [6]. The piston moves a column of hydraulic fluid, which in turn moves the diaphragm set and displaces the gas to be compressed. As a consequence, the process is more isentropic than adiabatic, thus allowing to achieve a higher compression ratio. The deflection and inherent stresses of the metal diaphragms are controlled by a carefully designed cavity contour. This compressor compresses gases without any contamination of the process media or leakage of the gas into ambient air. Its service life is around 40,000 hours of continuous operation without any diaphragm or spare parts replacement. Under the EU project CUTE, three fully automated compressor systems were manufactured. This pilot compressor is self-contained and amenable to plug-and-play installation by the end user. Such a compressor has been installed in a wind park near Athens, Greece, Fig. 3.6, where hydrogen is produced by a water electrolyzer of 25 kW, which is supplied by a 500 kW gear-less, synchronous, multi-pole Enercon E40 wind turbine.

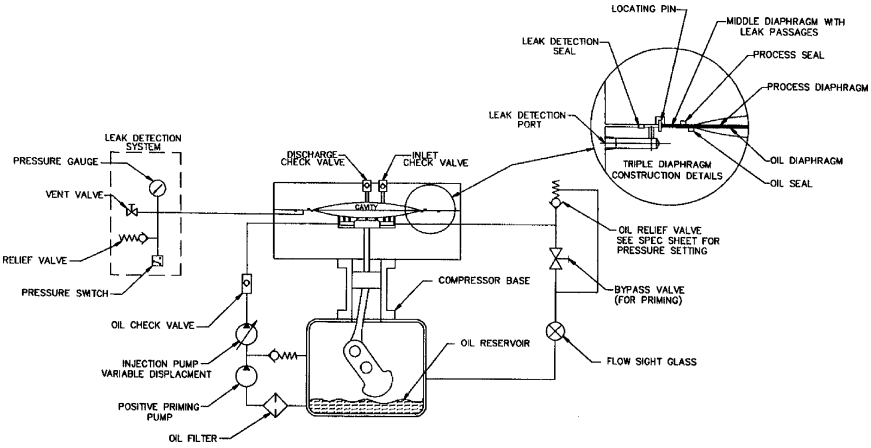

Fig. 3.5 Schematic diagram of a triple metal diaphragm compressor designed by PDC [6]

The compressor is used for filling high-pressure hydrogen cylinders. The compressor has a single-stage configuration with a maximum inlet pressure of 18 bar and a maximum outlet pressure of 400 bar and a flow of 5 Nm^3/h. The compressor is powered by a 7.5 kW electric motor at 1450 rpm. The size is 1245 × 1014 × 1778 mm, total weight amounts to 907 kg. The compressor equipped with piping, accessories, instrumentation, heat exchangers, etc. costs around US$60,000 [6].

Fig. 3.6 Wind farm near Athens, Greece, equipped with a PDC compressor [6]

3.3.2.2 Non-mechanical Compressor

These types of compressors have several advantages over mechanical hydrogen compressors, including smaller size, lower capital, operating, and maintenance costs, and the absence of moving parts, which eliminates problems related to wear, noise, and intensity of energy usage. Moreover, they can supply high-purity hydrogen.

Metal Hydride Compressor

The metal hydride compressors are thermally powered systems that use the properties of reversible metal hydride alloys to compress hydrogen without contamination. A wide range of pressures and pressure ratios can be obtained by selecting suitable alloys. The operating principle of the hydride compressor is based on heat and mass transfer in the reaction bed during absorption and desorption processes.

The selection of an adapted metal hydride alloy is important to reach the desired performance of the compression cycle. The thermodynamic (i.e. the enthalpy ΔH and the entropy ΔS obtained from the pressure-composition-temperature isotherm and the Van't Hoff plot), thermal (i.e. the specific heat C_p which controls the temperature increase produced by the addition of a given quantity of heat and the effective thermal conductivity λ which controls the diffusion of heat through the porous material), and kinetic (i.e. reaction rate which controls the flow of hydrogen) properties of the selected material should be characterized in detail in order to optimize compressor operation. Moreover, the materials should possess the properties listed below:

- Large hydrogen storage capacity.
- Good kinetic behavior for fast hydrogen flow from the compressor.
- High compression ratio in order to fill up a cylinder in a single-stage compression.
- Small hysteresis loss to ensure a high working compression ratio at convenient operating temperature.
- Good anti-poisoning and anti-aging characteristics.
- Wide and flat plateau pressures.

In addition, knowledge of metal hydride reactor heat and mass transfer characteristics is of importance for the design of hydride compressor. More details on the reactor design can be found elsewhere [7, 8, 9].

A single-stage thermal compressor is composed of a module filled with a reversible metal hydride alloy. Figure 3.7 displays the operation of the hydride compressor, which comprises four processes:

1. Hydrogen is absorbed into the alloy bed at low temperature (T_i) and at low pressure (P_i).
2. The module is subsequently heated from (T_i) to a higher temperature (T_f) with compression.
3. Compressed hydrogen is released at high temperature (T_f) and high pressure (P_f).
4. The module is cooled down from (T_f) to (T_i).

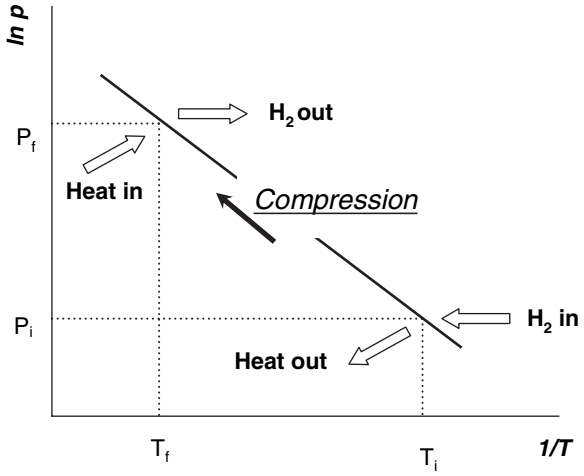

Fig. 3.7 Operation of a single-stage hydrogen compressor (Van't Hoff plot)

The pressure increases exponentially with increasing temperature. Hence, large pressure increases may be caused by moderate temperature increases only. An example is the $Mm_{1-x}Ca_xNi_{5-y}Al_y$ alloy (where Mm is mixed metal) which takes up industrial hydrogen at 2 MPa (20 bar) and 20°C and gives ultra-pure hydrogen at 10 MPa (100 bar) and 95°C with hot water only being used as a source of heat [10].

To obtain higher pressures, a multi-stage thermal compressor is used, which consists of several modules connected in series. Each module contains a different metal hydride alloy and hydrogen is successively absorbed into and desorbed out of several hydride beds [9, 11]. The driving force exerted by a variation in temperature and the difference of enthalpy between alloys of the coupled module gradually increases the exit pressure from one stage to the next one. An example is the double-stage compressor in which an AB_5 type alloy is used as the low-pressure stage alloy and an AB_2 as the high-pressure alloy to compress industrial grade hydrogen at a pressure of around 2 MPa to ultra-pure hydrogen with a pressure of up to 45 MPa [9]. Figure 3.8 displays the thermodynamic principle of the above double-stage compressor. The Van't Hoff plots corresponding to the absorption and desorption of the two alloys are represented. Point 1 represents the absorption of hydrogen by the AB_5 alloy and the removal of the heat produced by cool water. Then, the hydride bed is heated with 99°C hot water and hydrogen at a pressure around 10.5 MPa is produced, as indicated by point 2. This hydrogen is subsequently fed into the high-pressure-stage compressor (point 3), which is cooled by 20°C water. The AB_2 alloy absorbs hydrogen rapidly due to the fact that the pressure from the low-compressor stage is higher than the hydriding plateau pressure of the AB_2 alloy. This hydride bed is heated with 99°C hot water and high-purity hydrogen at 45 MPa is released (point 4).

The metal hydride compressor operates by cycling between two temperatures. Therefore, its energy needs mainly consist in heating and cooling resources. Hot

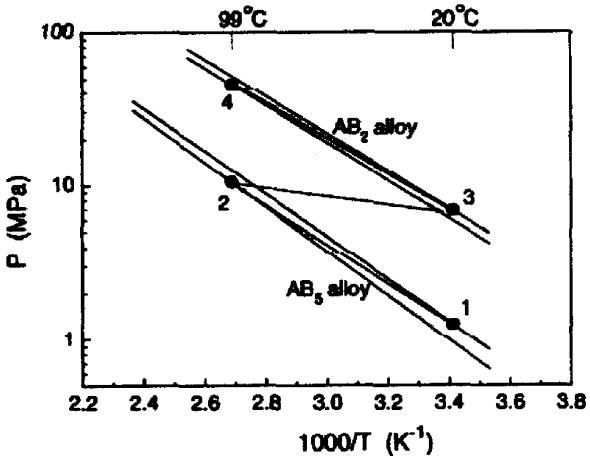

Fig. 3.8 Thermodynamic principle of a double-stage hydrogen compressor [9]

fluids or electric heating of the beds may provide for the compression energy. Thermal compression is not based on the adiabatic process and thermal efficiency can be calculated as follows:

$$\eta = \frac{W}{Q} = \frac{W}{Q_1 + Q_2} \tag{3.2}$$

where $W = \mathrm{f}(P_{\mathrm{eq}})$ is the compression work from T_{i} to T_{f}. The equilibrium pressure is estimated by the Van't Hoff equation as

$$\ln P_{\mathrm{eq}} = \frac{\Delta S}{R} - \frac{\Delta H}{RT} + f_{\mathrm{hysteresis}} + f_{\mathrm{slope}} \tag{3.3}$$

Q in Eq. (3.2) represents the total energy used to compress n mol of hydrogen. Q_1 is the energy used to heat the hydride from T_{i} to T_{f} and Q_2 the thermal energy that makes the hydride release hydrogen. For a double-stage compressor $Q_1 = [(m_I C_{pI} + m_{II} C_{pII})(T_f - T_i)]$, where m and C_{p} are the weight and the specific heat of the hydrogen storage alloys I and II, respectively, and $Q_2 = [n(\Delta H_I + \Delta H_{II})]$, where n is the molar number of compressed hydrogen.

Electrochemical Compressor

This type of compressor is used when a small quantity of hydrogen has to be compressed to high pressure, because it is more efficient than the mechanical compressor in this regime [12]. The working principle is based on an electrochemical cell, Fig. 3.9, composed of an anode, a membrane electrode assembly (MEA), and a cathode [13]. When a potential difference is applied, the hydrogen at a pressure P_{a} is oxidized to H^+ at the anode. These ions are transported through the membrane to the cathode, where they are reduced to hydrogen at a pressure $P_{\mathrm{c}} > P_{\mathrm{a}}$, if the cathode

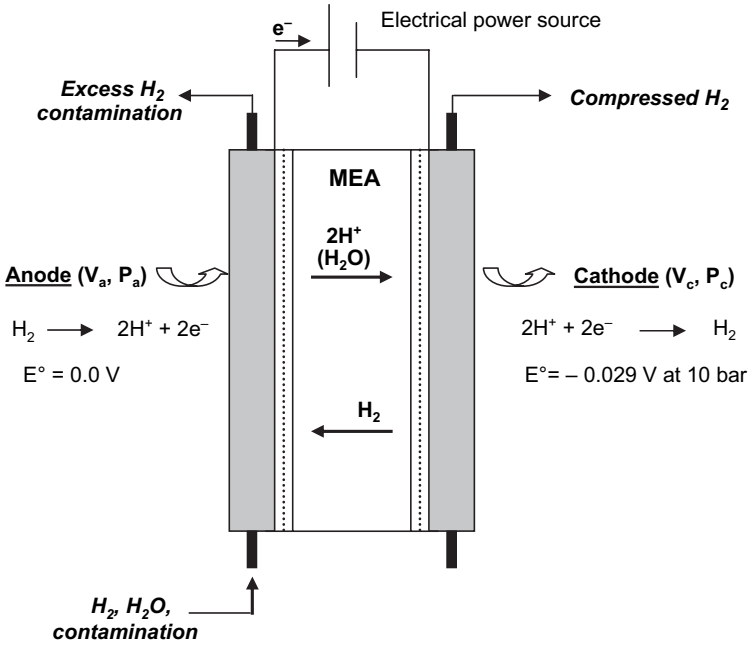

Fig. 3.9 Principle of the electrochemical hydrogen compressor [13]

compartment is hermetically sealed. A multi-stage electrochemical hydrogen compressor incorporates a series of membrane electrode assemblies (MEAs). It should be noted that the process is selective for hydrogen, as the inert gas components cannot pass the membrane.

With an electrochemical compressor, hydrogen can be compressed from ambient pressure to 16 MPa for example [14]. A main parameter that affects the efficiency of such a compressor is the humidification of the membrane. In fact, the membrane has to be saturated with water to have a good ionic conductivity (i.e. protons are only transported, if they cross the membrane in the hydrated form). Therefore, diffusion studies are carried out using different membranes to determine the relationship between membrane thickness and diffusion rate [13]. Research relating to membrane materials which can work as a proton conductor without any further humidification at ambient temperature has shown that a single MEA film of hydrogen sulfated fullerenol $[C_{60}(OSO_3H)_n(OH)_n]$ can be used to compress hydrogen up to 1 MPa [15].

3.3.3 Storage of CGH_2

Once hydrogen is compressed, the next important factor for application is to have a high volume of hydrogen carried per unit weight of the container. Consequently,

use of such a high pressure of hydrogen implies an appropriate ultra-lightweight material for the construction of the storage cylinders and the compressors, which can withstand the applied pressure and resist the effects of hydrogen embrittlement[5] and has a low hydrogen permeability. Progress achieved in both the materials of construction and manufacturing technology increased the technical efficiency of the cylinders from 0.05 m^3/kg (500 kg vessel made of wrought iron for a gas capacity of 25 m^3) in 1880 to around 0.13 m^3/kg (low-alloy steels with the addition of 1% Cr and 0.2% Mo) in the mid-1960s [16]. Nowadays, technical efficiency is 0.70 m^3/kg for a 110 kg vessel made of three layers of composite materials. Gas capacity amounts to 77 m^3 [16]. The state of the art of current compressed gas tanks, including design requirements and safety features, is described in more detail in Part II, Chap. 8a by Sirosh and Niedzwiecki from Quantum Technologies Inc. [17].

3.3.4 Outlook

Storage of hydrogen as a compressed gas is close to technical feasibility. Compressed storage is of interest to small city cars and large vehicles. The major difficulty is the volume needed to store the hydrogen and the energy required for the compression of the gas. Therefore, research is going on to improve the storage cylinders by optimizing materials and to develop design principles and an efficient method to compress hydrogen. In addition, special seals and/or tolerance standards are investigated to achieve high pressures. New approaches, including guided rotor compressors and linear compressors, are pursued. At the moment, the critical issue for an accelerated market penetration is the cost of hydrogen compression and storage cylinders.

3.4 Liquid Hydrogen (LH_2)

A second method to increase the density of hydrogen is to decrease the temperature of the gas at a constant pressure to obtain the liquid phase. The normal hydrogen, n-H_2, which corresponds to the equilibrium mixture at room temperature, is a gas composed of 75% o-H_2 (ortho-hydrogen) and 25% p-H_2 (para-hydrogen). The ortho- and para-hydrogen are the two isometric forms of the hydrogen molecule depending on the relative orientation of the nuclear spin of the individual atoms [1]. The molecules with a parallel nuclear spin, called ortho-hydrogen, o-H_2, are on a higher energy level than the molecules with an anti-parallel nuclear spin, called para-hydrogen, p-H_2 (stable state). The percentage of ortho–para concentrations in the mixture at equilibrium is temperature-dependent as displayed in Fig. 3.10. When the temperature decreases, a conversion takes place slowly to 100% p-H_2, which is the stable phase at 20 K. The conversion reaction from the n-H_2 to the p-H_2 state is a reversible and exothermic reaction that occurs without breaking the H–H bond.

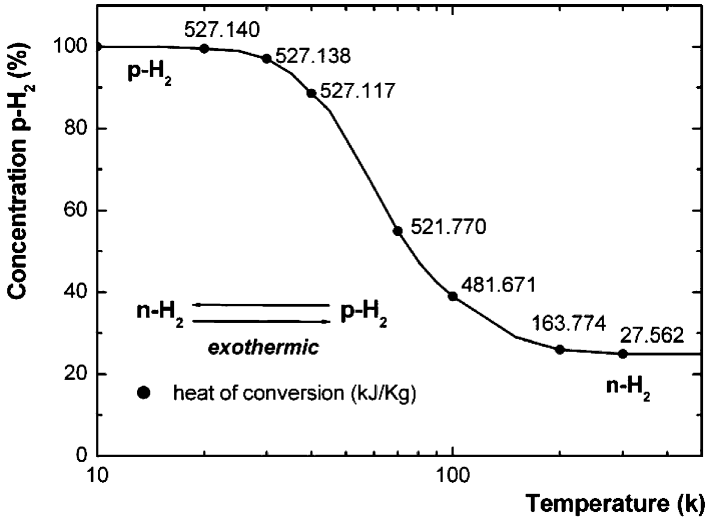

Fig. 3.10 Evolution of the concentration of p-H_2 at equilibrium as a function of the temperature. The heat of conversion is given in kJ/kg [1]

3.4.1 Characteristics of Liquid Hydrogen

As shown in Fig. 3.11, the density of liquid hydrogen is around 80 kg/m^3 at 22 K and a pressure of 4 bar. Hence, liquid hydrogen needs less storage volume than the gas (one liquid hydrogen container can substitute approximately 7 to 8 CGH_2 trailers). That is why liquid hydrogen is of interest, although the unusual properties of hydrogen described below impose several technological constraints to the liquefaction process and cryogenic storage.

The boiling temperature of hydrogen is 20 K at 1 bar. At this temperature, natural gas and other gases are solid. Consequently, hydrogen should be purified to a level below 1 ppm before its liquefaction in order to avoid any clogging of the heat exchangers, which in turn will decrease the overall efficiency of the liquefier.

Hydrogen has a peculiar Joule–Thomson effect inversion temperature of around 190 K at a pressure below 50 bar. As a consequence, a process other than a Joule–Thomson expansion has to be used to cool hydrogen from 300 to 190 K.

The vaporization enthalpy of hydrogen is very low. Hence, an excellent thermal insulation is required in the coldest part of the liquefier as well as in the storage vessel to minimize the loss by vaporization.

The molar weight of hydrogen is 2.016 g/mol, which is 14 times less than that of nitrogen. Consequently, the kinetic energy of hydrogen at a certain pressure and temperature is 14 times smaller than that of nitrogen. Hence, use of the volumetric piston compressor is recommended instead of a centrifugal compressor.

The conversion from n-H_2 to p-H_2 is naturally a slow and exothermic reaction, where the heat of conversion is temperature-dependent as can be seen in Fig. 3.10. It

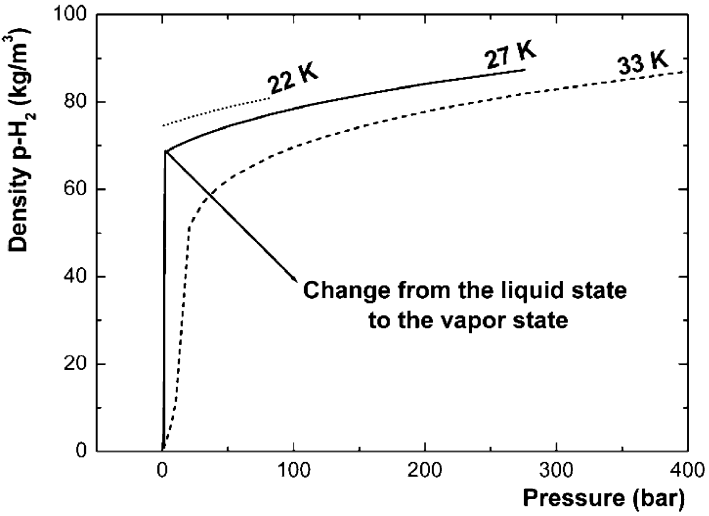

Fig. 3.11 Evolution of the density of liquid hydrogen as a function of pressure at three different temperatures

increases non-linearly when the temperature decreases, from 27.562 kJ/kg at 300 K to 527.140 kJ/kg at 20 K [18]. At 20 K, the heat of conversion from n-H_2 to p-H_2 (around 527 kJ/kg) is higher than the heat of vaporization of n-H_2 (454 kJ/kg). This implies that the reaction has to be accelerated and cooled in order to minimize the reversibility of the reaction. Therefore, exothermic conversion takes place with a catalyst and the most common one is iron oxide $Fe(OH)_3$ obtained from the reaction of NaOH with $FeCl_3$. The exothermic catalytic conversion may be of adiabatic, isothermal or continuous type [19].

- In the *adiabatic conversion* the catalyst is installed in a container, where the hydrogen is flowing. As a consequence, the hydrogen temperature increases during the conversion and it has to be cooled down again.
- In the *isothermal conversion* the catalyst is installed in a container maintained at a constant temperature by a cryogenic liquid at its boiling temperature. The heat released during the conversion of hydrogen then vaporizes the cryogenic liquid.
- In the *continuous conversion* the catalyst is integrated in the heat exchanger, where the hydrogen is flowing. This allows for a constant removal of the conversion heat released. Thus, the hydrogen remains close to the ortho–para equilibrium at every temperature.

Each of these modes can be integrated in the design of a liquefier. However, the continuous conversion mode has the best efficiency.

The liquefaction cycles are based on two thermodynamic expansion processes:

1. Isenthalpic expansion or Joule–Thomoson expansion which is performed using a valve.

2. Imperfect isentropic expansion or an expansion with energy extraction using an expansion turbine or an expander. In this case, no liquid is formed at the end of the expansion.

Perfect adiabatic conditions are not feasible in an LH_2 storage reservoir, implying that losses due to heat flux can only be minimized, but not avoided.

3.4.2 Liquefaction of Hydrogen

Dewar (British) was the first to realize the liquefaction of hydrogen in 1898. Subsequently, Prof. Linde (German) conceived the first liquefier by compression in 1900. Later, Claude (French), founder of Air Liquide, improved this machine.

Hydrogen gas has to be cooled down from 300 to 20 K taking into account its particular physical properties, such as the low boiling temperature, the low Joule–Thomson effect inversion temperature, the slow exothermic ortho–para conversion, the large variation of heat conversion with temperature, and the internal heat leaks. As a consequence, the design of an efficient liquefier (i.e. high product yield with low energy cost) depends on the selection of an optimized liquefaction cycle and equipment.

3.4.2.1 Design of a Liquefier

The liquefaction process of hydrogen combines the effect of cooling with an adiabatic expansion of the gas. The hydrogen gas should be purified first to an impurity level below 1 ppm and compressed to 20 bar (as the optimum pressure to liquefy hydrogen is above the critical pressure), before it is delivered to the inlet of the liquefier. The main components of a liquefier are:

- Compressors.
- Heat exchangers.
- Turbines to decrease the temperature of hydrogen and to extract some energy that would be lost.
- Expanders to provide cooling at various points of the cycle.
- Intercoolers to remove the heat between the different stages of compression.
- Pumped liquid nitrogen or hydrogen bath to supply extra cooling to the heat exchangers.
- A Joule–Thomson expansion valve to produce some liquid.

All cryogenic equipment should be enclosed by a single cold box with a vacuum and multi-layer insulation in order to minimize evaporation loss. Moreover, most of these components are made of high-strength materials, such as Cr and Mo steel, in order to withstand the low operating temperatures and resist hydrogen embrittlement and permeability.

The simple liquefaction system is based on a pre-cooling of the gas using a nitrogen cycle (from 300 to 80 K) in series with an ortho–para converter (from 80 to 30 K) and a Joule–Thomson valve for expanding the gas at 20 K to produce liquid hydrogen.

An optimization of the liquefier, known as a Claude cycle, is obtained by separating the cooled gas from the liquid and returning it to a 2-(or 3, 4)stage compressor via the heat exchanger [19]. A schematic diagram based on a two-stage compressor Claude system is displayed in Fig. 3.12. The cycle comprises the main line to liquefy hydrogen as described above and two compressors in series. The first compressor pressurizes the return gas from Joule–Thomson expansion and the vapors generated by the storage of liquid hydrogen. The second one compresses to a pressure of 50 bar the outlet gas from the first one and the flux from the expansion turbines.

The efficiency of the liquefier η is the ratio between the theoretical work W_{th} required and the real work W_r. The theoretical work includes the energy necessary to cool hydrogen from ambient temperature to 20 K, the heat due to the phase transformation, and the heat of conversion from n-H_2 to p-H_2. The ideal work for the liquefaction of hydrogen from 300 K at 1 bar to 20 K at 1 bar is equal to an electric energy requirement of 3.9 kWh/kg. This energy is decreased to 2.8 kWh/kg, if the feed hydrogen gas is compressed to a pressure of 30 bar. In addition, the real work

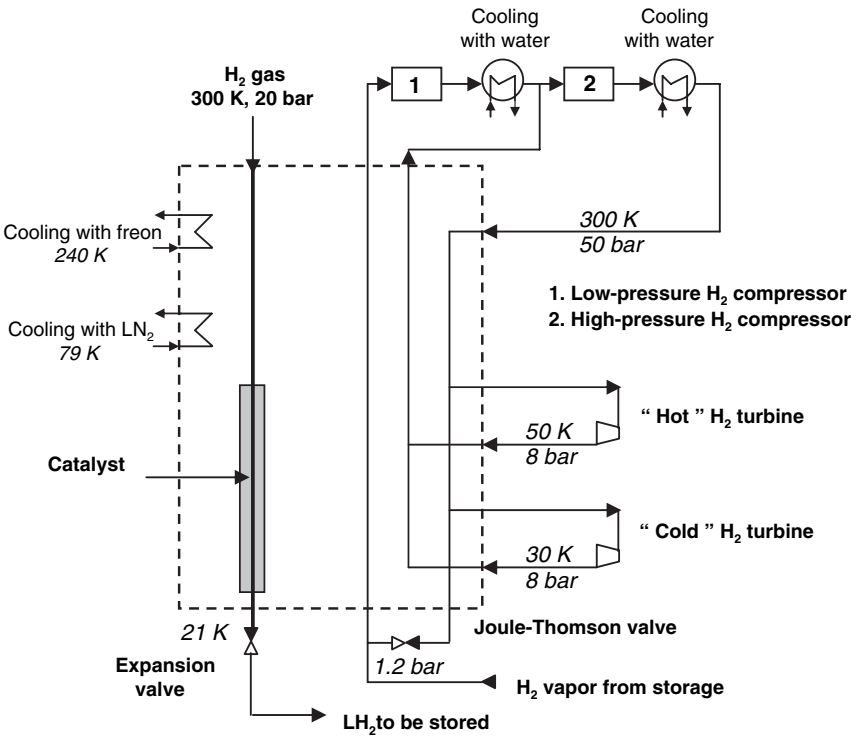

Fig. 3.12 Schematic diagram of hydrogen refrigeration based on the Claude cycle [19]

depends on the thermal insulation of the liquefier, the efficiency of the heat exchangers, and the compressors. Hence, the efficiency of a liquefaction plant increases with its size and, hence, production rate.

3.4.2.2 Industrial Liquefiers

Large-scale hydrogen liquefaction plants are based on the Claude cycle, where hydrogen is used as the refrigerant. Existing plants differ in design by the number of turbines and compressors used as well as by the type of converter used to carry out the exothermic conversion. Ten hydrogen liquefaction plants are located in North America with a capacity ranging from 5.4 tons/day to 32 tons/day [3]. There are only three hydrogen liquefaction plants in Europe. Air Liquide owns and operates one liquefier in Waziers, France. The second one is operated by Air Products in Rozenburg, Netherlands, and the third one by Linde in Ingolstadt, Germany. The hydrogen liquefaction capacities of the three liquefiers are 10.5, 5.4, and 4.4 tons/day, respectively. Total capacity in Europe presently is 20 tons/day equivalent to 230,000 Nm^3/day or 84 million Nm^3/year. In addition, Linde will build another liquefier which will have a daily tonnage of 5.7 tons in Leuna. The industrial liquefiers by Linde and Air Liquide will be described briefly below.

Liquefier by Linde

The hydrogen liquefier in Ingolstadt (Germany) designed by Linde is located on the site of a refinery which supplies hydrogen-rich raw gas (H_2 concentration is around 86%) [20]. Figure 3.13 displays the schematic diagram of the liquefaction process. The raw gas is supplied at around 3300 Nm^3/h, with the pressure varying between 9 and 14 bar. The raw gas is first compressed to 20 bar and then purified in a pressure-swing adsorption system to an impurity level of about 4 ppm. After purification, the hydrogen can be passed to the high-pressure line (where it is compressed to 225 bar using a piston compressor) or the liquefaction line.

The liquefaction line is designed for a capacity of 2000 Nm^3/h and based on a Claude cycle. The liquefier is composed of one adsorber, six plate-type heat exchangers, two ortho/para $Fe(OH)_3$ catalysts outside of the heat exchanger, one LN_2 bath with catalyst, one LH_2 bath with catalyst, three expansion turbines, two Joule–Thomson valves, and two compressors. All cryogenic equipment is enclosed in a single cold box. Prior to refrigeration, the hydrogen is first purified to an impurity level below 1 ppm using a low-temperature adsorber. Then, three temperature levels are applied:

1. Up to 80 K using liquid nitrogen.
2. From 80 to 30 K using expansion turbines.
3. From 30 to 20 K using Joule–Thomson expansion valves.

Ortho/para hydrogen conversion is accomplished using two adiabatic converters and two isothermal converters with liquid nitrogen and hydrogen baths. Moreover, work is extracted from the cycle gas by three expansion turbines arranged in series.

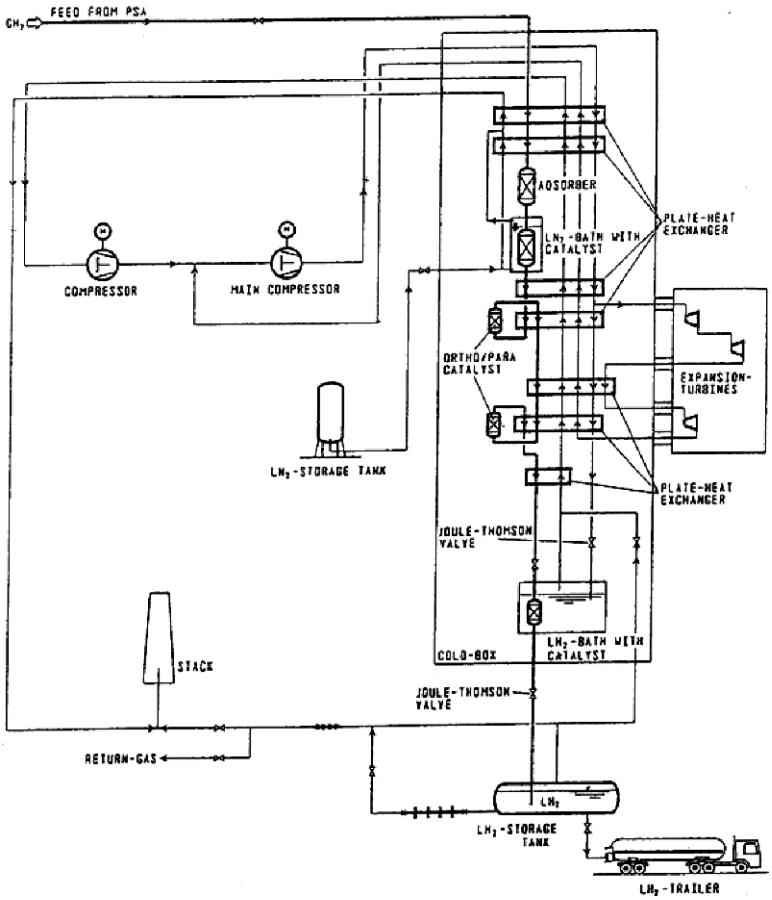

Fig. 3.13 Schematic diagram of the hydrogen liquefier by Linde [20]

The daily output is 4.4 tons and the produced LH_2 is stored in a vacuum-insulated 270 m^3 tank with a loss of 0.3% per day. Considering the whole liquefaction process and taking into account a specific production energy of 0.4 kW/h for the liquid nitrogen, the specific energy per liter LH_2 is 0.9 kWh, which corresponds to a thermodynamic efficiency of about 33% of that of an ideal Carnot cycle with four-stage ortho–para conversion.

Liquefier by Air Liquide

Air Liquide owns one hydrogen liquefier cycle in Kourou for the rocket test facilities ARIANE IV and V [19]. This liquefier uses hydrogen produced by catalytic reforming of methanol at 600 K according to the following reaction:

$$CH_3OH + H_2O \rightarrow CO_2 + 2H_2$$

The hydrogen produced is first purified to an impurity level below 1 ppm. Then, it is cooled and liquefied in three steps as follows:

1. From 300 to 230 K using mechanical refrigeration.
2. From 230 to 80 K using a nitrogen cycle.
3. From 80 to 20 K using a hydrogen cycle.

The nitrogen cycle comprises one N_2 compressor and a N_2 turbine. The hydrogen cycle is composed of two H_2 compressors in series and two H_2 turbines. Heat exchange between 300 and 20 K is performed in vacuum-brazed aluminum plate fin exchangers. Exothermic catalytic conversion is performed by continuous conversion. All pieces of cryogenic equipment are enclosed in a single cold box with vacuum and multi-layer insulation.

The liquefaction capacity is 2.3 tons per day and the liquid hydrogen is stored in several reservoirs of 323 m^3 with a daily loss of less than 0.3%. The efficiency of the liquefier is around 40%.

3.4.3 Liquid Hydrogen Storage

The liquid hydrogen supplied by the liquefier has a high purity and high storage density. Typically, the LH_2 is stored in a dual-walled stainless steel vessel with vacuum super-insulation between the inner and the outer vessel consisting of several highly reflective radiation shields separated by an appropriate spacer material in order to minimize losses due to radiation, convection, and conduction heat, as perfect adiabatic conditions are not feasible [21, 22]. The storage tank will always have intrinsic heat leaks which can be minimized, but not avoided. As a consequence, hydrogen always evaporates after filling the tank. Thus, the ratio between liquid and gas (part of the liquid evaporates to gas) changes and this leads to a pressure increase. From a certain pressure, gas is released. From this point, the temperature inside stays the same until all the gas has evaporated. These heat leaks only depend on the temperature difference between the inside and outside of the vessel. They are an intrinsic feature of the vessel and depend on the quality, capacity, and the shape of the tank only.

Evaporation rate is proportional to the surface to volume ratio and a linear function of the total heat flux. Therefore, evaporation losses can be decreased by increasing the volume of the tank (the best shape actually is a sphere). Losses are in the order of 0.3% per day for a vacuum-insulated 320 m^3 tank, whereas they amount to 5% per day for a 102 l cryogenic vehicular tank with a total heat entry of 1.7 W. A more detailed description of the cryogenic tank, from the requirements to the design in mobile application, can be found in Part II, Chap. 8b by Michel from Air Liquide.

3.4.4 Liquefaction Cost

The total investment costs (i.e. building construction cost, components cost, engineering, overhead and administration, start-up expenses, etc.) of a liquefaction plant

with a capacity of 150 tons/day, for example, is around US$200,000,000 [23]. The liquefaction process is very energy–intensive, as typical unit powers are in the order of 12.5 to 15 kWh/kg. The liquefaction costs of a large-scale liquid hydrogen plant primarily depend on the energy costs

The liquefaction of hydrogen gas needs energy which cannot or only partly be re-covered in the re-vaporization process. Hence, liquefaction energy is a loss of the overall system and it should be minimized. The prime cost factor for large systems is power consumption which is related to the basic efficiency of the selected cycle and the efficiency of the different components like compressors, heat exchangers, and expanders. Energy analysis indicates that the higher the hydrogen is compressed at ambient temperature, the lower is the power needed for the cooling from 80 to 30 K. In addition, conversion should take place in the continuous mode in order to have the smallest irreversibility. The compressor is the most important part with respect to both cost and its ability to influence the overall performance of the system [24]. It was demonstrated that several stages of compression with intermediate cooling are required to minimize the power consumption. Another component of importance is the heat exchanger which should be compact with a counterflow configuration and an operating pressure around 25 bar [24].

An innovative conceptual design of a large-capacity hydrogen liquefier proposed by Quack indicates that a thermodynamic efficiency in the order of 60% can be reached with a power requirement of 7 kWh/kg [25]. The proposed liquefier is designed in the following way:

- Hydrogen gas is compressed from 1 to 80 bar in 5 stages with a pressure ratio per stage of about 2.4. The overall power consumption can be reduced by using intercoolers cooled with water in the first stage and a propane refrigerator.
- The ortho–para conversion is carried out in the continuous equilibrium mode with two main heat exchangers.
- Cooling from 300 to 73 K is proposed to be performed with a helium/neon mixture as refrigerant instead of the "classical" nitrogen cycle.
- Cooling from 73 to 25 K is performed with a helium–neon cycle using 6 expanders.
- Cooling from 25 K to storage conditions is carried out by expansion of the hydrogen stream from 80 to 1 bar. The flash gas is compressed by a cold compressor to a pressure level, where it can be condensed by the helium cycle. At the outlet of this condenser, a simple throttling process is used to obtain the saturated liquid at 1 bar.

It should be noted that if the pressure of the feed hydrogen is around 20 bar instead of 1 bar as selected in this design with a storage pressure of 3 bar, the total power requirement of the liquefier would decrease to around 5 kWh/kg.

To summarize, large-scale plants have to be built to decrease capital cost. Further research is needed with respect to new compression and expansion technologies with high-speed centrifugal compressors with titanium wheels as proposed by Quack and possibly expanders to decrease energy consumption [25]. Materials development is required to lower the cost of the high-efficiency insulation of

the storage vessels. New approaches to low-temperature refrigeration, which are still in the research and development stage, include cooling by magnetic refrigeration. The active magnetic refrigeration (AMR) is based on the magneto-calorific effect of the materials used close to their transition temperature. This means that the absorption and release of the heat occur by the change of temperature due to the adiabatic magnetization/demagnetization of the material [26, 27, 28, 29, 30, 31]. The main advantage of this process is that the energy loss is close to zero during the adiabatic magnetization/demagnetization cycles compared to the classical compression/expansion process.

3.4.5 Outlook

Cryogenic liquid hydrogen has a much higher volumetric density than gaseous hydrogen, resulting in lower transport and storage costs. Nowadays, liquefaction technology is safe, reliable, and produces daily tonnage quantities. However, for the use of liquid hydrogen on a large scale, an increase in liquefier efficiency is required to reduce energy costs, since current liquefaction technology is costly and presently consumes more than 30% of the stored energy. This implies an optimization of liquefaction cycles and equipment to produce large volumes of liquid hydrogen with low energy requirements. Components subject to optimization include compressors, turbine expanders, and heat exchangers.

Moreover, research relating to lightweight materials for the tanks and the reduction of the daily loss due to thermal heat needs to be continued. Current research also focuses on active or passive cooling systems to increase the stand-by time before evaporation losses occur.

3.5 Solid Storage of Hydrogen (SSH_2)

Hydrogen stored in a solid-state material has potential advantages compared to compressed or liquid hydrogen storage in terms of volumetric density (it requires one third of the volume of a pressurized hydrogen gas tank at 345 bar) and safety (heat is required to deliver hydrogen), technology, and available resources.

The parameters which are of importance to hydrogen storage are the gravimetric and volumetric densities on the system basis. Furthermore, hydrogen uptake and release should be reversible. Finally, the net energy has to be taken into account. This includes the energy needed to manufacture the storage system, to produce and to store it. The technical requirement defined for a standard car is that 5 kg of hydrogen shall be stored to have a range of 500 km. This means that only hydrides with the highest possible gravimetric hydrogen storage capacities are viable for potential commercial automotive application. Moreover, the temperature and pressure during

operation shall be in the range from 20 to 358 K and 0 to 6 bar, respectively, in order to match the operating conditions of the fuel cell. Other important requirements are:

- A relatively low desorption temperature compatible with a PEM fuel cell.
- Relatively fast kinetics of hydrogen desorption.
- The filling time should not exceed 5 minutes.
- Cycling stability.
- Low density of hydride.
- Low hydride price.

Although huge numbers of compounds were investigated in the last years, no system has been found so far that would be able to fulfill all requirements. Hence, new approaches had to be pursued. One is to modify the properties of the known materials by atomic substitution, addition of dopants, by using nanoscale materials instead of bulk material (as nanostructurization was found to improve the kinetic properties of the material), etc.

Current research focuses on reaching the volumetric and gravimetric capacity targets, meeting the energy and temperature requirements for hydrogen release, fulfilling the appropriate charging and discharging rate of hydrogen (i.e. good kinetics), and understanding the fundamental mechanism of the hydrogenation/dehydrogenation reaction. The materials investigated may be divided into reversible and irreversible storage systems. Both of them may be considered on-board storage systems. The difference is that the irreversible system is regenerated off-board.

3.5.1 Reversible Storage Systems

Reversible storage system means that the material may be refilled, recharged with gaseous hydrogen on-board the vehicle. In practice, two basic mechanisms may be considered for hydrogen storage:

1. Physisorption which implies the adsorption of molecular hydrogen by the material.
2. Chemisorption which implies the dissociation of hydrogen molecules and subsequent chemical bonding of H atoms by integration in the lattice of a metal, alloy or by formation of a new chemical compound.

In the following sections, selected compounds will be presented for these two approaches, which are of interest for hydrogen storage in solid-state materials.

3.5.1.1 Hydrogen Storage by Physisorption

Physical adsorption is based on weak Van der Waals forces between the adsorbate molecules and the adsorbent. The interaction energy for molecular hydrogen

typically is between 1 and 10 kJ/mol. The order of magnitude of the interaction depends on the nature of the gas molecule and on the adsorbing material.

As a consequence of the low adsorption energy involved in the physisorption process, physical adsorption is completely reversible and fast refueling is possible without the problem of heat management. However, higher hydrogen storage capacities can be obtained at lower temperature only, typically at 77 K. Different classes of materials, such as active charcoal, nanostructured carbon [32, 33, 34, 35], zeolites [33, 36], and metal organic framework [37, 38, 39, 40, 41], have been investigated for hydrogen storage by adsorption at low temperature. Among the examples presented below are carbon nanostructures and the metal organic framework, as they are the most promising systems.

Nanostructured Carbon

A great variety of carbon nanostructures exists, such as activated carbon, carbon nanofibers, multi-walled carbon nanotubes (MWCNT) and single-walled carbon nanotubes (SWCNT), carbon nanohorns, etc. They all consist of benzene-like carbon hexagons with sp^2-hybridized carbon atoms, but they differ from each other in the way these hexagons are arranged in the material. By different synthetic procedures and treatments of carbon materials, it is possible to design a nanostructure with the desired surface area and pore density.

The hydrogen storage capacity is measured volumetrically with a Sievert's type apparatus at room temperature (RT) and 77 K. Figure 3.14 displays the kinetics of hydrogen uptake at 77 K and at RT. At 77 K, a type I adsorption isotherm (or Langmuir isotherm), characteristic of microporous solids is observed [35]. The isotherm exhibits two regions with an increase in hydrogen uptake at low pressure followed by a horizontal plateau at high pressure. The initial increase depends on the heat of

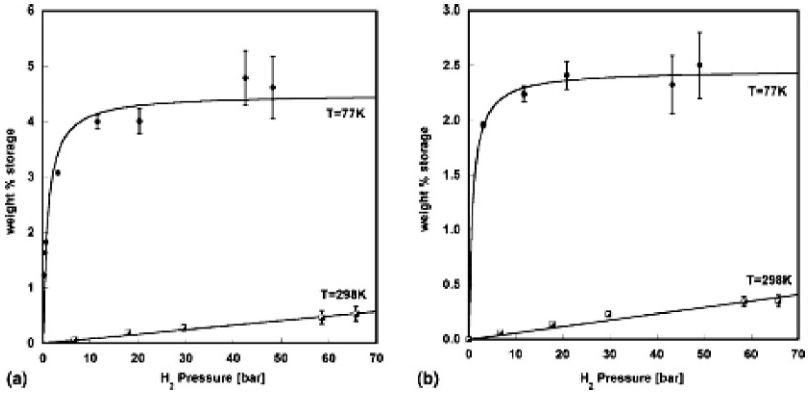

Fig. 3.14 Hydrogen adsorption isotherms at room temperature and at 77 K fitted with a Henry type and a Langmuir type equation, respectively, (a) for activated carbon, (b) for purified SWCNTs [35]

adsorption, while the plateau is independent of the interaction energy and reflects the complete coverage of the adsorbent's surface. At RT, a linear Henry type isotherm is observed. The storage capacity is very low, indicating that only a fractional coverage takes place with the formation of a highly diluted monolayer.

The hydrogen storage capacity is based on the local interaction between hydrogen molecules. It has been shown that the hydrogen storage capacity almost is a linear function of the specific surface area at room and at low temperature [33, 35]. By developing microporous materials with a large specific surface area, it is therefore possible to increase the storage capacity. Moreover, it has been demonstrated that a correlation exists between the microporous volume and the adsorption storage capacity [35, 42, 43]. To identify the whole microporosity range, carbon materials are characterized by N_2 adsorption isotherms at 77 K to determine the total volume of micropores smaller than 2 nm in size and by CO_2 adsorption at 273 K for micropores smaller than 0.7 nm in size. The linear relation found between the hydrogen adsorption capacity and CO_2 micropore volume suggests that the presence of a homogeneous narrow microporosity (≤ 0.7 nm) is of importance to hydrogen adsorption [35, 42]. Hence, carbon materials ideal for hydrogen storage should possess a high specific surface area as well as a high microporosity with a small pore dimension.

However, the amount of hydrogen adsorbed by the best carbon material (labeled Activated Carbon I, obtained from the reaction of coke with KOH) with an SSA of 2564 m^2/g, an average pore diameter of 1.18 nm, and a pore volume of 0.75 cm^3/g for pores with a radius less than 0.65 nm is limited to 0.54 wt.% H_2 at 298 K and 65 bar of hydrogen and to 4.4 wt.% at saturation and 77 K [35, 36].

Metal Organic Framework (MOF)

Metal organic frameworks with an SSA between 2500 and 4000 m^2/g are a new class of microporous materials which reach the highest theoretical SSA value for carbon material of about 2600 m^2/g. These materials are composed of metal oxide groups connected to each other by a rigid structure. They are the lightest known crystalline materials with densities down to 0.21 g/cm^3. These materials allow for the design of a network with the metal centers and pore dimensions desired.

To date, hundreds of different MOFs have been synthesized with a great variety of network topologies [37, 38, 39]. The most famous porous structure is MOF-5 [37, 38] displayed in Fig. 3.15. It consists of Zn_4O clusters at the corners of a cube and connected to each other with benzene-1,4-dicarboxylate $O_2C–C_6H_4–CO_2$ as ligand to give an extended 3D cubic framework and, hence, a crystalline solid with interconnected pores of 0.8 nm aperture width and 1.2 nm pore diameter. Different metal centers like Mn^{2+}, Ni^{2+}, Mg^{2+}, Cu^{2+} have been investigated as well as various pore dimensions by varying the nature of the ligand, e.g. naphthalene-2,6-dicarboxylate, 4,5,9,10-tetrahydropyrene-2,7-dicarboxylate. For MOF-5, reliable measurements made by different laboratories indicate that the maximum uptake of hydrogen is 4.5–5.2 wt.% at 77 K and 50 bar of hydrogen pressure [40]. For room

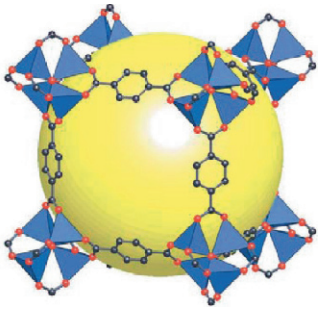

Fig. 3.15 MOF-5 structure [38]

temperature, the adsorption capacity of MOF-5 is less than 0.2 wt.% at pressures up to 67 bar. The highest value reported is 7 wt.% at 77 K for MOFs having a specific surface area of 3000–4700 m^2/g [44, 45].

Neutron powder diffraction of this material revealed that at low-concentration loadings, the ZnO_4 cluster is responsible for most of the adsorption, while the organic linker plays a secondary role only [46]. Inelastic neutron scattering (INS) revealed that a site in the corner of the pore, on the inorganic cluster, ought to be the preferred binding site for hydrogen at low loadings. At higher-loadings, INS indicates the existence of well-defined multiple binding sites for hydrogen within the cavities of MOF-5, with some of these being associated with the organic linking group [47]. A detailed analysis performed by using materials with the same inorganic cluster ZnO_4 and different organic linkers indicates that the binding of hydrogen at the inorganic cluster sites is affected by the nature of the organic link due to differences in their electronic structures [47].

The hydrogen storage capacity of this material is determined by the heat of adsorption (i.e. interaction energy of H_2 molecules) and the specific surface area. Moreover, the interaction of the hydrogen molecules also depends on the pore size, as the presence of small micropores produces an increased adsorbate-adsorbent interaction. At present, the great challenge with this material is to develop new MOFs with an optimum pore size without decreasing the specific surface area.

3.5.1.2 Hydrogen Storage by Chemisorption

The general mechanism of absorption of hydrogen gas by a metal consists in the physisorption of H_2 molecules on the surface, followed by the dissociative chemisorption of individual H atoms. Then, the H atoms diffuse away from the surface into periodic sites (often interstitial) in the metal crystal lattice. Once in the crystal lattice, H atoms can take the form of a random solid solution or an ordered hydride structure with distinct bonding to metal atoms and high volumetric packing density. A fundamental drawback of this method is the necessity to split or recombine the hydrogen molecules and to form chemical bonds with the material. This makes a thermal management of the storage necessary in order to supply or remove the heat

of reaction. Details of the thermodynamic and kinetic properties of hydrides can be found in Part IV, Chap. 16a by J. Huot.

Several compounds have been studied and investigated for hydrogen storage. Their list and a summary of their properties can be found at http://hydpark.ca.sandia.gov [48]. Here, selected examples will be presented, including classical hydrides like $LaNi_5H_6$ and MgH_2, and advanced storage materials of complex hydrides like alanates and amides or boronates destabilized by partial substitution with Mg.

Classical Hydrides

Metallic hydrides are divided into several types. The most widely studied systems are of the following types:

- A (Mg, V, Ti, …)
- AB (FeTi, …)
- A_2B (Mg_2Ni, Mg_2Cu, …)
- AB_2 ($ZrCr_2$, …)
- AB_5 ($LaNi_5$, …)

where A and B represent that element that is strongly and weakly forming the hydride, respectively. Metallic hydrides are classified either according to the nature of the bond between the metal and hydrogen or according to the temperature at which the decomposition occurs. In the first case, it is distinguished between ionic hydrides, metallic hydrides, and covalent hydrides. In the second case, high-temperature hydrides (MgH_2, …) and low-temperature hydrides ($LaNi_5H_6$, …) are distinguished.

La-Ni System

The classical AB_5 hydrides are based on $LaNi_5$. The hydriding properties of this material were first reported by Van Vucht et al. in the 1970s [49]. The intermetallic compound is synthesized by induction melting of the pure elements under vacuum or argon atmosphere, followed by annealing at 1073–1473 K [50]. $LaNi_5$ crystallizes in the hexagonal structure of a $CaCu_5$ type (space group *P6/mmm* with La in 1a (0 0 0) and Ni in 2c (1/3 2/3 0) and 3 g (1/2 0 1/2)) [50].

Hydrogen can be absorbed into and desorbed from $LaNi_5$ at nearly atmospheric pressures and 25°C. Absorption/desorption pressure hysteresis is small and the plateaus are rather flat. The enthalpy of formation of $LaNi_5H_6$ is −30.9 kJ/mol H_2 and the desorption plateau pressure at 25°C is 1.6 atm. The hydrogen storage capacity of this compound is 1.4 wt.% [51]. The capacity loss observed when cycling was commonly attributed to the decomposition of the alloy into lanthanum oxides or hydroxides and nickel particles.

$LaNi_5$ has very useful properties, but is rather expensive due to the expensive elemental La. Consequently, this element was substituted first by the low-cost rare earth alloy mixed metal (Mm). The most common (Mm) has the following composition (Ce (48–50 wt.%), La (32–34 wt.%), Nd (13–14 wt.%), Pr (4–5 wt.%), other

rare earths (1.5 wt.%). Compared to $LaNi_5$, however, the absorption/desorption isotherms of $MmNi_5$ at 25°C exhibit high pressures of up to 100 atm and hysteresis as can be seen in Fig. 3.16 [52]. As a consequence, other elements were used to partly substitute Mm and Ni in $MmNi_5$ like $Mm_{1-x}A_xNi_5$ (A = Ca, Y, Zr, etc.), $MmNi_{5-y}B_y$ (B = Co, Al, Mn, Fe, Cu, Si, Ti, etc.) or $Mm_{1-x}A_xNi_{5-y}B_y$. These substitutions allow modifying the thermodynamic properties (equilibrium pressure and capacity) of the corresponding hydrides. However, a reduction of the storage capacity and a change of the equilibrium pressure are observed in all cases. Study of the logarithm of the plateau pressure as a function of the intermetallic compound cell volume for various $La_{1-x}A_xNi_{5-y}B_y$ at room temperature has shown a linear dependence [53]. As the cell volume can be changed by substitutions, this property allows the plateau pressure of the compound to be adapted to the needs of the application by substituting a proper amount of nickel with other elements like Al or Mn.

AB_5 hydrides and mostly their substitutional derivatives are commercially used in nickel-metal hydride (Ni-MH) batteries. The negative electrode is composed of agglomerated powders of AB_5 alloys, the electrolyte is a concentrated solution of KOH in a small quantity, and the positive electrode is the conventional $NiOOH/Ni(OH)_2$ ($E^0 = +0.49\,V$) electrode. More details about the electrochemical performance, cycle life as well as a comparison with different battery families can be found elsewhere [54].

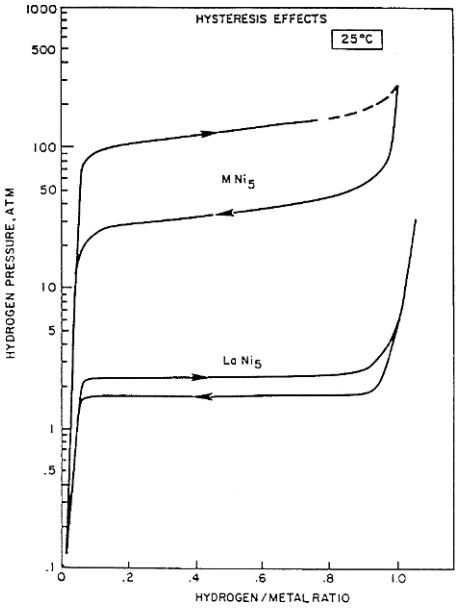

Fig. 3.16 25°C absorption/desorption isotherms for $LaNi_5$ and $MmNi_5$ [52]

Mg-based Compounds

Magnesium was considered as a very promising element due to its high storage capacity (7.5 wt.% H) and its low cost. Magnesium absorbs gaseous hydrogen at a temperature above 280°C and a hydrogen pressure above or equal to 10 bar. It is a reversible reaction which is exothermic upon the formation of the hydride and endothermic upon decomposition. The volume expansion occurring during the transformation of the metal to the hydride is in the order of 15%. Magnesium hydride possesses a high thermodynamic stability and very slow kinetics. As a consequence, the focus moved to magnesium alloys (mainly Mg_2Ni, Mg_2Cu, Mg-$LaNi_5$) which exhibit improved sorption properties, but a decrease in the hydrogen storage capacity [55, 56]. In the 1990s, introduction of ball milling allowed improving drastically the hydrogen absorption/desorption kinetics of pure magnesium. Indeed, ball-milled nanocrystalline magnesium (grain size smaller than 50 nm) could absorb 6 wt.% hydrogen in 120 minutes at 300°C under a hydrogen pressure of 10 bar. Under the same conditions, microcrystalline magnesium (grain size 1 μm) does not absorb any hydrogen [57].

Magnesium hydride can be obtained either by a direct synthesis of the elements at high pressure and a temperature higher than 280°C, by reactive ball milling of magnesium powder (99.9% purity, 100 mesh) at room temperature under a hydrogen pressure of 2 atm [58] or by indirect methods using organic solvents [59, 60] or the ion implantation technique [61]. The β-phase of magnesium hydride crystallizes in the tetragonal structure. The space group is *P4/mnm* and the lattice parameters are $a = 4.5168$ Å and $c = 3.0205$ Å with the atomic positions of Mg in (0, 0, 0) and (1/2, 1/2, 1/2) and H in ± (X, X, 0) and ± (X + 1/2, 1/2–X, 1/2) with $X = 0.306$ [62]. In this rutile-type structure each hydrogen atom is in planar coordination with three magnesium atoms. The magnesium atoms are octahedrally coordinated to six hydrogen atoms. The length of the Mg–H bond is 1.95 Å and the H–H distances are 2.49 and 2.76 Å [63, 64]. The β-phase is the stable phase of magnesium hydride. Two metastable phases exist: The γ-MgH_2 phase (obtained by transformation of the β-MgH_2 under high compressive stress) and the δ-MgH_2 phase (obtained by transformation of the β-MgH_2 under high pressure (2.5 to 8 GPa) and high temperature (650 to 800°C)) [65].

Magnesium hydride is a compound which is thermodynamically stable, as the decomposition temperature is around 587 K at a hydrogen pressure of 2.3 bar [66]. The enthalpy and entropy of this compound have been determined by volumetric or gravimetric measurement and using the Van't Hoff diagram. As can be seen in Table 3.1, there is a large scattering of the values of the enthalpy of magnesium hydride formation. In 1999 (by means of a TG-DSC performed under 1 bar of Ar and at a heating rate varying from 1 to 5 K/min), Bogdanovic et al. determined an average enthalpy of desorption of $\Delta_d H(683\,\mathrm{K}) = 74.05 \pm 1.3\,\mathrm{kJ/mol\ H_2}$ from 14 measurements using a calorimetric method [72]. This implies that a quarter of the energy stored is released as heat during the formation of MgH_2 (exothermic reaction) and should be provided to the system in order to desorb hydrogen (endothermic reaction).

Table 3.1 Enthalpy and entropy values for the formation of magnesium hydride

Enthalpy kJ $(mol\ H_2)^{-1}$	Entropy $J.K^{-1}$ $(mol\ H_2)^{-1}$	Ref.
−74		[63]
−74.4	135	[66]
−77.4	135	[67]
−70	126	[68]
−85	137	[69]
−80.9		[70]
−74.7		[71]

The reaction between magnesium and gaseous hydrogen should be initiated first by heating the metal to high temperature under vacuum at helium or hydrogen pressure. This is the so-called activation process. In literature, the activation procedure is controversial, as some authors note that magnesium could absorb hydrogen without any treatment [73, 74, 75], while some others suggest that the activation is necessary in the case of magnesium [76, 77]. In general, the formation of magnesium hydride follows a nucleation and growth mechanism. As already stated, hydriding/dehydriding of magnesium is very slow. Therefore, numerous attempts were made to increase the hydrogenation rate and decrease the desorption temperature by modifying several parameters on which the kinetics is highly dependent, such as the shape of the material, the size of the particle, the state of the surface, the thickness of the oxide layer, the presence of impurities, the presence of precursors or additives, etc. To date, the fastest kinetics has been obtained with nanometric powder. Moreover, the hydrogenation rate has been improved by using Pd as catalyst. Indeed, magnesium powder ball-milled with Pd (less than 1 wt.%) absorbs 6 wt.% of hydrogen in 60 minutes at 300°C under a hydrogen pressure of 10 bar without any activation procedure, while 120 minutes were necessary for a powder without palladium [57]. The hydrogenation rate can be further improved by using additives like metals (Ti, Nb, Fe, Co, Ni, Al) [78, 79], non-metals (C, Si) [80], a mixture of metals and non-metals [81], transition metallic oxides (TiO_2, V_2O_5, MnO_2) [82], intermetallic compounds ($LaNi_5$, FeTi) [83, 84] or mixtures of intermetallics. A review of Mg-based compounds was published by Selvam et al. [85] and Khrussanova [86]. A review of the Mg/Ni system can be found in the paper by Orimo and Fujii [87].

Magnesium hydride is commercially available as a powder, the dehydrogenation/hydrogenation reaction of which also is slow. As in case of magnesium, the kinetics has been improved by ball milling and by doping with a catalyst or an additive. The fastest kinetics has been obtained with the systems ($MgH_2 + 5$ at.% V) [88] and $MgH_2/(TiO_2)0.01$ [89]. The first system reached 5.5 wt.% H_2 in 500 seconds at 200°C under a hydrogen pressure of 10 bar, the second 6 wt.% H_2 in 300 seconds at 300°C under a hydrogen pressure of 8.4 bar. It was found that the dehydrogenation rate at temperatures between 473 and 573 K was limited by nucleation and two-dimensional growth with an activation energy of 69.5 kJ/mol. At higher temperature, the reaction is interface-controlled with a two-dimensional growth of the forming Mg phase [90]. Structural studies of this system suggest a gateway model,

where hydrogen coming out of magnesium hydride flows through niobium to leave the material [91]. Further improvement has been obtained by doping MgH_2 with 0.5 mol.% Nb_2O_5. About 7 wt.% of hydrogen were desorbed within 150 seconds at 300°C under a hydrogen pressure of 0.85 MPa [92]. By doping MgH_2 with 1 mol.% Nb_2O_5 by ball milling, Hanada et al. obtained a compound that could absorb more than 5 wt.% of hydrogen at 1 MPa and room temperature [93]. In a recent review paper, Dornheim et al. [94] discussed the role of particle size, fine microstructure, and catalysts. They showed that additives have many favorable effects, such as pinning of grain boundaries, enhancement of hydrogen diffusion, and increases in nucleation rate. Tests in an industrial-size tube vibration mill showed the feasibility of production of hydride-based storage materials on a larger scale.

Advanced Storage Materials

The classical hydrides suffer from a low gravimetric density due to the relatively high mass of the metal atoms. Consequently, the focus of research has moved to systems consisting of light elements, such as Li, Be, B, Na, Mg, Al, Si, K, and Ca. Of these, hydrides from elemental beryllium have been eliminated due to its high toxicity. Among the examples that will be described below are the so-called alanates and the amides or boronates destabilized by partial substitution with Mg. An overview of the progress achieved with these materials is given in the recent review by Orimo et al. [95].

Alanates

Alanates are ternary, salt-like compounds and belong to the so-called "complex hydrides". Most of the alanates were found to be thermodynamically or kinetically stable at room temperature; they are soluble in many organic solvents and important reducing agents in chemical synthesis. Several alanate compounds like $LiAlH_4$ (10.54 wt.% H) [96, 97], $NaAlH_4$ (7.41 wt.% H) [see below], $KAlH_4$ (5.71 wt.% H) [98], $Mg(AlH_4)_2$ (9.27 wt.% H) [99], and $Ca(AlH_4)_2$ (7.84 wt.% H) [100] have been synthesized and investigated with respect to hydrogen storage.

Of these candidates, sodium alanate, $NaAlH_4$, is the one which has been most widely studied due to its favorable thermodynamic properties which allow for a reversible hydrogen exchange at temperatures around 100°C and its commercial availability [101]. However, hydrogen exchange with the pure compound is kinetically inhibited. These kinetic barriers were first lowered by using transition-metal precursors which were added to the alanate by wet impregnation [102, 103]. Since then, the decomposition reaction has been made reversible under moderate temperature and pressure conditions. Figure 3.17 displays the scheme of the thermal dissociation of pure and catalyzed sodium alanate. The pure, macrocrystalline $NaAlH_4$ melts at 186°C. Then, the melt starts to decompose and release hydrogen at around 240°C, forming the hexahydride Na_3AlH_6 and elemental Al as solid decomposition products. Pure Na_3AlH_6 decomposes at a temperature above 300°C and releases H_2, so

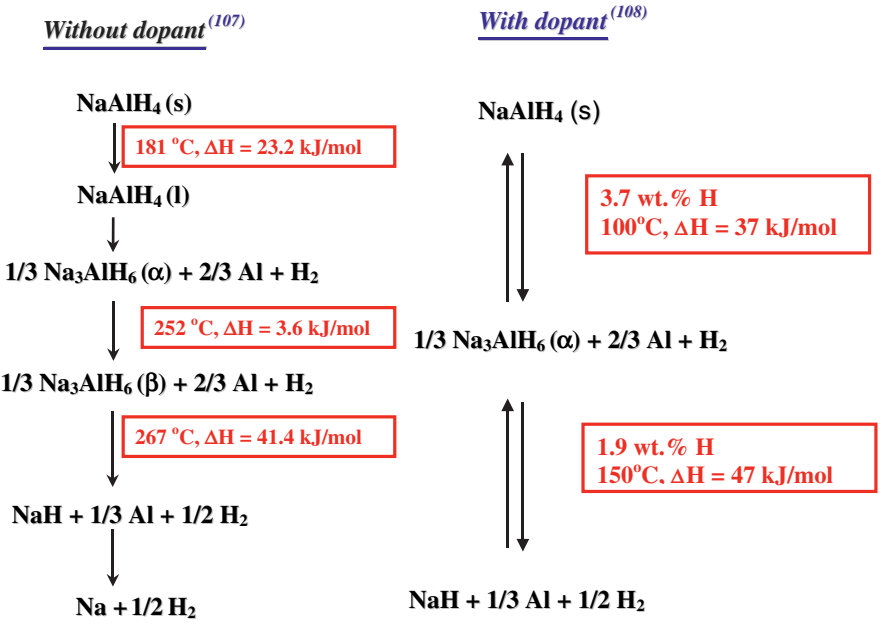

Fig. 3.17 Schematic diagram of the thermal decomposition of pure and doped sodium alanate

that a mixture of two solid phases, NaH and Al, is obtained. The last step is the decomposition of NaH to the elements, which occurs at a temperature above 450°C. Therefore, this step is not considered for practical purposes.

As can be seen, the scheme of a doped sample exhibits significant differences. At first, the reaction is made reversible and from the first two steps, a reversible hydrogen capacity of 5.6 wt.% is expected. The thermal decomposition of doped $NaAlH_4$ occurs without the melting of the sample. The enthalpy values of 37 and 47 kJ/mol for the first and second step, respectively, were obtained from equilibrium data using the Van't Hoff method. Equilibrium pressures of 1 bar H_2 are reached at 33°C for the first step and at 110°C for the second step. Figure 3.18 displays the crystal structure of $NaAlH_4$ and Na_3AlH_6. The space group of $NaAlH_4$ is I 41/a with the lattice parameters of a = 5.0119 Å, b = 5.0119 Å, c = 11.3147 Å and atomic positions Al (0, 0.25, 0.625), Na (0, 0.25, 0.125), and H (0.2372, 0.3836, 0.5469) [104].

Numerous transition and rare-earth metal catalysts have been investigated as precursors in order to lower the kinetic barriers of $NaAlH_4$ [105, 106]. Ti-based precursors and, recently, a Ce-based precursor were found to have the best catalytic properties [106, 107, 108, 109]. Moreover, a concentration ranging from 2 to 5 mol.% of Ti or Ce on the basis of $TiCl_3$, Ti_{13}.6THF, or $CeCl_3$ has been shown to be a good compromise between the catalytic activity and the loss of storage capacity. The storage material is obtained by adding the precursor to the Na alanate either by wet impregnation or by ball milling. A more detailed description of these

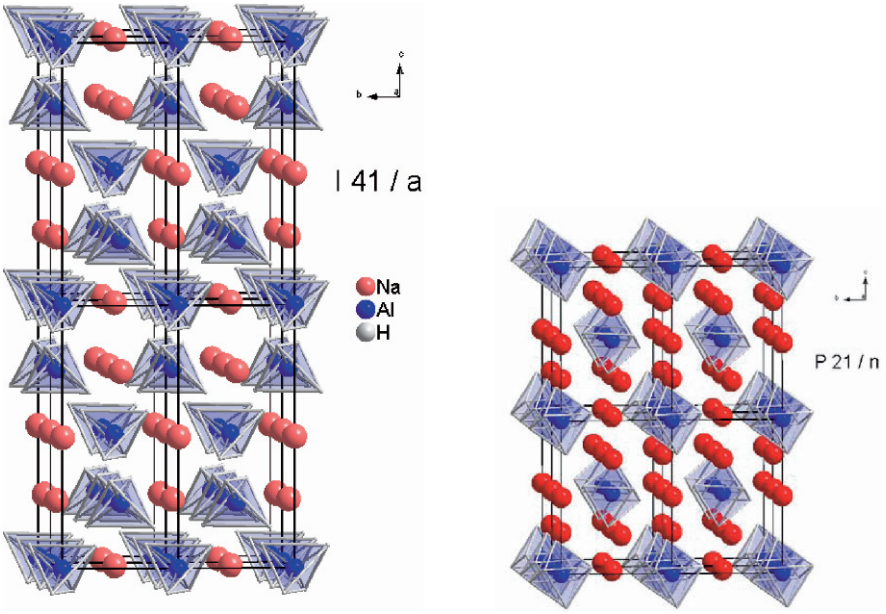

Fig. 3.18 Structure of $NaAlH_4$ (space group I 41/a, lattice parameters $a = 5.0119$ Å, $b = 5.0119$ Å, $c = 11.3147$ Å, atomic positions Al(0, 0.25, 0.625), Na(0, 0.25, 0.125), H(0.2372, 0.3836, 0.5469)) and Na_3AlH_6 (space group P 21/n, lattice parameters $a = 5.408$ Å, $b = 5.538$ Å, $c = 7.757$ Å, atomic positions Al(0, 0, 0), Na_1(0, 0, 0.5), Na_2(−0.00129, 0.46129, 0.25008), H_1(0.0918, 0.0352, 0.2207), H_2(0.2220, 0.3283, 0.5454), H_3(0.1649, 0.2689, 0.9500)

processes can be found in Part IV, Chap. 15 by Felderhoff. The mechanical alloying has proved to be most efficient in terms of superior kinetic properties. Therefore, this method is widely used to prepare the storage material.

The kinetics of the decomposition reaction of pure sodium alanate and sodium alanate doped with 5 mol.% of Ti on the basis of $TiCl_3$ or Ti_{13}·6THF is compared in Fig. 3.19. The decomposition of purified $NaAlH_4$ that has been ball-milled for 30 min and held at 170°C results in the release of the theoretical amount of 5.6 wt.% of hydrogen. The decomposition of the doped material is highly dependent on the nature of the dopant. In fact, 4.5 wt.% of H_2 are released within 700 seconds from sodium alanate doped with Ti colloid, whereas 8000 seconds are needed to reach this state of the reaction when using the $TiCl_3$-doped sample. The differences between the three materials are drastic. In addition to differences in kinetics, the reversible hydrogen storage capacities differ as well.

The effect of the milling time and cycling under hydrogen on the absorption/desorption kinetics as well as the storage capacity are illustrated for $NaAlH_4$ doped with 5 mol.% Ti from Ti_{13} · 6THF in Figs. 3.20 and 3.21. Decomposition measurements were performed at 150°C under a residual hydrogen pressure of 0.3 bar, absorption was done at 100°C under a hydrogen pressure of 100 bar. Figure 3.21 shows the amount of hydrogen released with desorption time for the

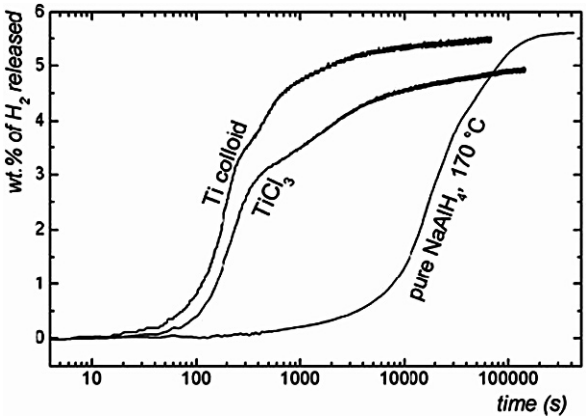

Fig. 3.19 Isothermal decomposition kinetics of the first desorption of pure $NaAlH_4$ held at 170°C and of Na-alanate doped with 5 mol.% Ti on the basis of $TiCl_3$ or Ti_{13}·6THF held at 150°C and under a residual hydrogen pressure of 0.3 bar [114]

first (labelled a1d) and the ninth (labelled a9d) dehydrogenation cycle of samples ball-milled for 2 minutes (labelled bm2), 30 minutes (labelled bm30), and 180 minutes (labelled bm180). As can be seen, 5 wt.% H_2 are released in the first desorption cycle within 500 s, 2000 s, and 10,000 s for the samples (bm180), (bm30), and (bm2), respectively. The difference in the desorption times of samples (bm180) and (bm30) mainly results from the kinetics of the second step of the reaction, which

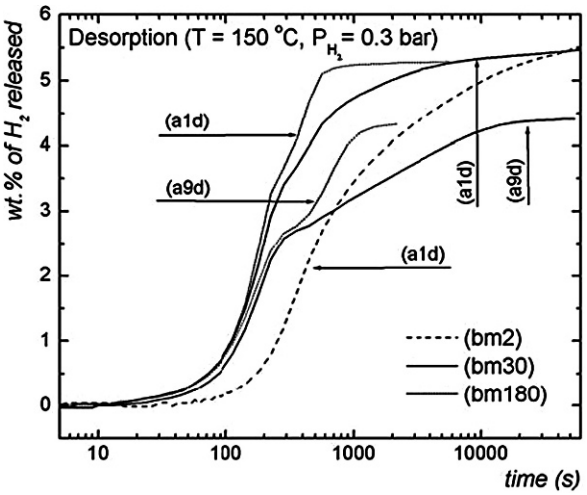

Fig. 3.20 Desorption kinetics of Na-alanate doped with 5 mol.% Ti on the basis of Ti_{13}·6THF at 150°C and a residual pressure of 0.3 bar hydrogen. The first and ninth cycles are presented for samples (bm30) and (bm180). Only the first cycle is shown for sample (bm2) [114]

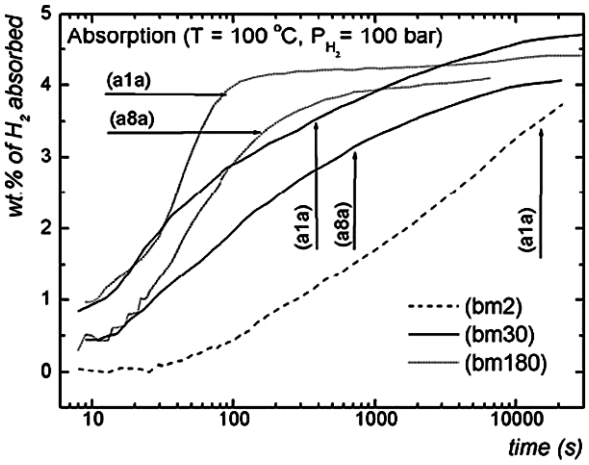

Fig. 3.21 Kinetics of the absorption of Na-alanate doped with 5 mol.% Ti on the basis of Ti_{13}·6THF at 100°C and a hydrogen pressure of 100 bar. The first and ninth cycles are presented for samples (bm30) and (bm180). Only the first cycle is shown for sample (bm2) [114]

is slower in sample (bm30) than in sample (bm180). In the subsequent cycles, the kinetics of both samples decreases and from the fourth cycle, the desorption kinetics does not change significantly. For all samples, 5.5 wt.% of H_2 are released after the first decomposition. Then, the storage capacity decreases continuously and reaches a value of 4.5 wt.% H_2 after 4 cycles for samples (bm180) and (bm30).

Figure 3.21 displays the absorption curves of the first cycle for sample (bm2) and those of the first and ninth absorption cycles for samples (bm30) and (bm180). As for the desorption, kinetics of absorption is faster for sample (bm180) than for sample (bm30). In the first cycle, the sample (bm180) has absorbed 3.5 wt.% of H_2 within 60 s, whereas the sample (bm30) has absorbed 2.5 wt.% only. The absorption kinetics and storage capacity do not change in the first two cycles, while subsequent cycles decrease the kinetics and the amount of hydrogen absorbed by the sample.

Kinetic studies of the different absorption and desorption steps have revealed that the transformation kinetics follows a sigmoidal behavior [110]. The absorption and desorption steps can be fitted with a good agreement by a nucleation and growth model according to the Johnson–Mehl–Avrami theory. It has been shown that transport in the solid is the rate-determining process. This means that diffusion of NaH and Al limits the reaction rate when the hexahydride phase is formed during absorption.

Recent studies on the atomic scale [111, 112, 113] elucidated the state of the dopant in different stages of the dehydrogenation/rehydrogenation reaction. A comparison of the behaviors of the Ti-based precursor-doped materials revealed that most of the Ti species do not remain at the surface upon milling and subsequent cycling, irrespective of the Ti-based precursor used to activate the reversible decomposition reaction of Na alanate [114]. Furthermore, the chemical state of Ti is relevant to the desorption/absorption reaction rate and the storage capacity.

Reduction of Ti species to the metallic state upon ball milling (as occurring for $TiCl_3$) [112, 113, 114] or during the first absorption reaction (as occurring for the Ti colloid precursor) [114] promotes the formation of small bimetallic entities between Ti and Al. The local environment resulting after several cycles under hydrogen consists of small clusters composed of Ti, surrounded by about 10 Al atoms at 2.80 ± 0.02 Å and a small Ti contribution (around 1 atom) at 3.88 ± 0.02 Å. The formation of this nano-scale Ti-Al alloy was correlated with the decrease of the hydrogen storage capacity and the desorption/absorption reaction rate [114]. Considering the structure of $NaAlH_4$, XRD analysis by Rietveld refinement indicates that the Bragg positions and the lattice parameters of Ti-doped sodium alanate are preserved [115]. From the refinement of the site occupation factors, the substitution of Ti on the Na site can be excluded. As concerns the substitution of Ti in the Al site, the refinement does not allow a clear statement to be made as for the Na site. Furthermore, there is no vacancy formation in Ti colloid-doped sodium alanate. In situ neutron diffraction experiments performed using uncatalyzed and $TiCl_3$-catalyzed $NaAlH_4$ indicated that the reaction products TiAlx and NaCl induce grain refinement, while maintaining the small particle size for the decomposition products, high H vacancy densities, and H-D exchange in the catalyzed sample [116].

Some new insights into the reaction have been gained, but the physical and chemical processes involved in hydrogen release and uptake are not yet fully understood. There are still open questions concerning the state of the catalysts as well as the relationships between the structure and the characteristic properties observed with this material. How does the catalyst really work and decrease the thermal activation process? What is physically and chemically happening during cycling?

Combined Systems

A new way to store hydrogen by using lithium nitrides has been proposed by Chen et al. [117, 118]. The decomposition of Li_3N leads to the formation of a mixture of lithium amide and lithium hydride according to the following reaction:

$$Li_3N + 2H_2 \leftrightarrow LiNH_2 + 2LiH$$

However, it is more suitable to start with lithium amide in order to increase the reversible capacity. In this case, the decomposition of lithium amide leads to the formation of lithium imide and ammonia at 380°C as follows:

$$2LiNH_2 \leftrightarrow Li_2NH + NH_3$$

It has been shown that a 1:1 ball-milled LiH-$LiNH_2$ releases around 5–8 wt.% of H_2 within 3 hours at 210°C. The kinetics was further enhanced to 45 minutes by adding 1mol% of $TiCl_3$ as catalyst. As the temperature is too high for practical application, intensive research started with respect to the destabilization of LiH-$LiNH_2$ by the partial substitution of Li by other elements [119]. Among the different mixtures studied, only the 1:2 MgH_2-$LiNH_2$ mixture shows a good reversibility with a drop of the storage capacity to 4.5 w.% according to:

$$2LiNH_2 + MgH_2 \leftrightarrow Li_2Mg(NH)_2 + 2H_2.$$

Partial substitution of lithium by magnesium lowers the reaction temperature [120], as the reaction enthalpy calculated using the Van't Hoff law is −39 kJ/mol H_2 for the ball-milled 1:2 MgH_2-$LiNH_2$ mixture, while it ranges from −45 to −65 kJ/mol H_2 for the decomposition of $LiNH_2$. Further improvement was achieved by the ball-milled 2:1 LiH-$Mg(NH_2)_2$ mixture with the hydrogen storage capacity reaching 5.6 wt.% and a good reversibility in the 200–220°C temperature range. However, one problem of the lithium/nitrogen system is the presence of ammonia in the reactions, as less than 0.1 ppm only is allowed to prevent the poisoning of the PEM fuel cell [2].

Lithium boron hydride is another attractive candidate for hydrogen storage due to its high hydrogen capacity (18.4 wt.%). However, $LiBH_4$ with an enthalpy estimated to about −70 kJ/mol is too stable for any practical application. An interesting concept is to use a stable boride (MgB_2, AlB_2) to decrease the heat of formation of boron hydrides [121]. This method was proposed by Vajo et al. [121, 122] and independently by Barkhordarian et al. [123]. In this scheme, the formation of the dehydrogenated alloy MgB_2 can reduce the hydrogenation/dehydrogenation enthalpy by 25 kJ/mol H_2 compared with pure $LiBH_4$ and the system is reversible according to the following reaction:

$$LiBH_4 + \frac{1}{2}MgH_2 \leftrightarrow LiH + \frac{1}{2}MgB_2 + 2H_2$$

Still, the kinetics is too slow, although a catalyst like $TiCl_3$ is used, and the temperature in the range of 315–400°C is too high for any practical applications.

3.5.2 Irreversible Storage Systems

These systems may offer options with high energy densities and potential ease of use, especially if the storage medium is in the liquid form that will allow minimizing the need for infrastructure changes and eliminate the need for large, special containers. In this approach the spent medium should be removed from the vehicle and regenerated with hydrogen either at the fueling station or at a centralized processing facility, as most reactions are irreversible. Therefore, off-board regenerative hydrogen storage technologies may be considered only, if an efficient recycling of the by-products is achieved.

3.5.2.1 Chemical Hydrides

The elements that are of interest in the composition of the hydrides for regenerative off-board storage of hydrogen are Li, Na, Mg, and B. The hydrogen contained in this system can be recovered by two reactions that are exothermic and irreversible:

1. Thermal decomposition of the hydride, where the storage material undergoes a chemical decomposition caused by thermal energy.

2. Hydrolysis of the hydride, where the storage material reacts with H_2O, a proton-containing reactant, according to the following reaction:

$$MH_n + nH_2O \rightarrow nH_2 + M(OH)_n$$

Simple Hydrides (LiH, NaH, MgH_2, CaH_2)

The hydrolysis of MgH_2 takes place as follows:

$$MgH_2 + 2H_2O \rightarrow Mg(OH)_2 + 2H_2$$
$$\Delta H^o = -140.5\,\text{kJ/mol}\,H_2$$

Taking into account the weight of water, a hydrogen storage capacity of 6.5 wt.% of hydrogen may be reached by this system. If the water from the fuel cell is redirected to the chemical hydride, then the yield increases to 15.4 wt.% [124]. The product of the reaction is environmentally benign, but should be regenerated off-board. It has been shown that nanocrystalline magnesium hydride (obtained by ball milling of the polycrystalline material for 20 hours) exhibits a higher conversion rate and a faster kinetics compared to the conventional material. Indeed 54% of the theoretical capacity are released by the polycrystalline material after 20 hours, while 74% are achieved by the nanocrystalline MgH_2 for the same time. After 10 hours of the reaction, however the hydrolysis rate also decreases for the nanocrystalline material due the formation of a passivation layer. The performance of this material was improved by adding a third metallic element, such as Ca or Li. A significant improvement was achieved with the nanocomposite MgH_2-Ca 20 at.% milled for 10 hours. Indeed, the hydrolysis reaction was completed in only 4 hours and showed the fastest kinetics compared to MgH_2-Ca 5 at.% milled for 10 hours.

The advantage of the hydrolysis reaction with these hydrides is that they do not require any catalyst and they possess a high reactivity. However, safety is a concern and most of the time, it is required to use a slurry or encapsulation technology.

Boron Hydrides (MBH_4 with M = Li, Na, K)

Hydrogen is generated from these compounds by hydrolysis rather than by thermal decomposition because of the high temperature required and the formation of alkali metal in gaseous form that are very corrosive and dangerous in the last step of the decomposition process. Decomposition by reaction with water occurs according to the following equation:

$$MBH_4 + xH_2O \rightarrow (MBO_2, x - 2H_2O) + 4H_2$$

where x depends on the nature of the metal, the temperature, and the composition of the solution.

As can be seen, the metaborates formed bind water and this results in a decrease of the real gravimetric density of the system. Of the three boron hydrides, the reaction of sodium boron hydride solutions is the one studied most by several research groups and companies in the world. Millennium Cell was the leader in developing sodium boron hydride-based energy sources [125].

In the ideal case the catalyzed hydrolysis process of $NaBH_4$ can be written as follows:

$$NaBH_4(aq) + 2H_2O \rightarrow NaBO_2(aq) + 4H_2 + \text{heat}$$
$$\Delta rH = -67\,\text{kJ/mol}\,H_2,\ \text{Pt or Ru-based supported catalyst}$$

The hydrolysis of $NaBH_4$ produces 7.3 or 21.2 wt.% depending on whether the water is taken or not taken into account, respectively [126]. Gaseous hydrogen is produced as needed by pumping the fuel over the catalyst or by stopping the pumping of the fuel. Sodium boron hydride is non-flammable, non-explosive, and easy to transport. It is stored at ambient pressure and temperature. Moreover, the reaction that generates the hydrogen is a low-temperature reaction at about 60–80°C. There is no side reaction or volatile by-product. As the reaction is exothermic, there is no need to supply external heat for the reaction to occur. The hydrogen delivered is pure and humidified. The waste borax $NaBO_2$ is water-soluble and environmentally benign. It can be disposed of or recycled to $NaBH_4$ on a special site by adding hydrogen and using an appropriate catalyst. A schematic diagram of the on-demand hydrogenation cycle using $NaBH_4$ for portable fuel cells can be found in Part III, Chap. 12 by Hahn.

The major disadvantages are the cost and the storage in liquid form which is not stable in the long term. In addition, the system capacity should be increased and the energy requirement for regeneration should be lowered. Therefore, novel approaches to an energy-efficient conversion of borates to boron hydride are required.

3.5.2.2 Organic Cycle Compounds

In these compounds hydrogen is stored covalently in an organic liquid carrier, mainly cyclic alkane. A potential advantage is that such a liquid carrier is easily transportable and does not require any water on-board as a co-reactant. In addition, the use of a new type of liquid fuel would not need a major change in today's gasoline infrastructure.

Hydrogen from these compounds is released by interaction with a heated catalyst to form unsaturated aromatic compounds. Hence, dehydrogenation of alkane is an endothermic process, whereas catalytic hydrogenation can be performed at a relatively high temperature, but moderate hydrogen pressure of 7 bar.

Decalin, Methylcyclohexane, *N*-ethyl Carbazole

Liquid cyclic hydrocarbons, such as decalin ($C_{10}H_{18}$) and methylcyclohexane (C_7H_{14}) have been studied, as they can release around 6 to 7 wt.% of hydrogen

according to equations. However, a special high-temperature reactor, such as a membrane reactor [127] or isothermal tubular reactor [128], has to be designed. Moreover, a platinum-based or other noble metal catalyst is required to enhance the kinetics of hydrogen evolution. In addition, the generated hydrogen has to be purified most of the time.

$$C_{10}H_{18} \rightarrow C_{10}H_8 + 5H_2 \text{ (7.3 wt.\% of } H_2) \text{ 262°C, Pt/C or Pt-W/C catalyst}$$
$$C_7H_{14} \rightarrow C_7H_8 + 3H_2 \text{ (6.1 wt.\% of } H_2) \sim 375°C, \text{ Pt/}Al_2O_3 \text{ catalyst}$$

To overcome these difficulties, Air product [129] investigated the properties of larger hydrocarbons, mainly polycyclic aromatic compounds and other pi-conjugated molecules, to find a more stable aromatic compound. Taking into account the results of thermodynamic calculations, which indicated that extended polycyclic aromatic hydrocarbons, where one C atom is substituted by one N atom, could lower the enthalpy of dehydrogenation, they selected and investigated the properties of *N*-ethyl carbazole [130]. This compound has a gravimetric hydrogen storage capacity of about 5–7 wt.% and a volumetric capacity of 0.050 kg/l. The enthalpy of dehydrogenation is around 50 kJ/mol H_2. Figure 3.22 displays the hydrogen evolution from *N*-ethyl carbazole after 3 cycles. Dehydrogenation/hydrogenation was carried out with catalysts based on Pd or Ru. Dehydrogenation was performed under a hydrogen pressure of 1 bar and a temperature ramp from 25 to 200°C, the hydrogenation reaction at 170°C under a hydrogen pressure of 82 bar. As can be seen, around 5.5 wt.% of hydrogen can be released in 2 hours and no purification step is necessary. However, the low gravimetric density of this compound calls for the characterization and development of other carbazoles to meet the DOE targets.

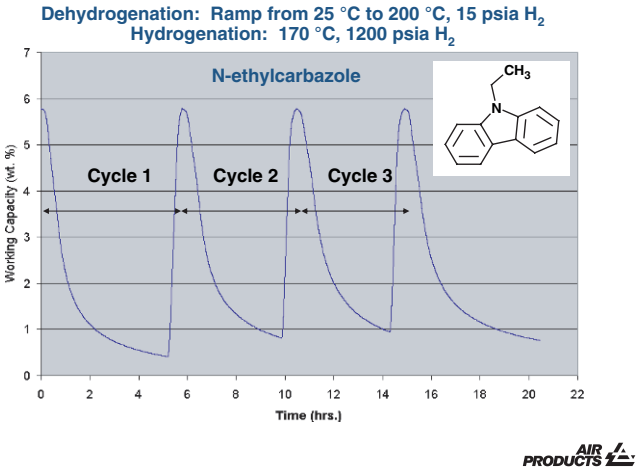

Fig. 3.22 Cyclic desorption of hydrogen from *N*-ethyl carbazole [2]

HYDRNOL™

Recently, a company from the United States, Asemblon [131], proposed a liquid carrier which stores the hydrogen at ambient temperatures and pressure. The company has named its proprietary liquid carrier HYDRNOL™, a hydrocarbon-based organic molecule [132]. The Asemblon system consists of four components, the liquid fuel HYDRNOL, the hydrogen release module (which consists of microchannels, a packed bed made of embedded nano-sized catalysts on porous substrates, and nanosprings), the spent fuel recovery module, and the hydrogenation module. In a vehicle, hydrogen is liberated upon demand from HYDRNOL which comes in contact with a hot, high-surface-area catalyst. The depleted HYDRNOL is collected, removed, and transported to a remote site for catalytic hydrogenation.

3.5.3 Outlook

Materials-based approaches, such as solid-state materials or liquids, require less volume than pressurized or cryogenic systems. In addition, safety of on-board vehicular storage of hydrogen is increased, because a tank rupture would not result in large energy releases. Despite extensive effort, however, no material has been found so far, which fulfills the requirements of mobile applications. Hence, new concepts as well as multi-disciplinary approaches are being pursued in order to both increase the reversible storage capacity and the kinetics of hydrogen exchange of systems with suitable thermodynamic properties. On the other hand, metal hydride can be used in limited stationary applications, where weight is not a critical factor and where waste heat is available at the appropriate temperature for hydrogen release.

3.6 Conclusions

Unlike electricity, hydrogen can be stored for long periods of time without significant losses. The three main options that have emerged are compressed hydrogen storage, cryogenic storage, and solid storage. Figure 3.23 displays the actual status of hydrogen storage systems. The compressed hydrogen storage and cryogenic storage are technically available, whereas the third one is still subject of research. As can be seen, none of the current vehicular hydrogen storage systems meets the combined gravimetric, volumetric, and cost targets for either 2010 or 2015. A solution which may be promising is the combination of different storage modes. For example, a tank working under moderate pressure (200 bar) and at low temperature (e.g. liquid nitrogen) allows reaching a storage density close to the 700 bar tank without the technological inconvenience at such a pressure.

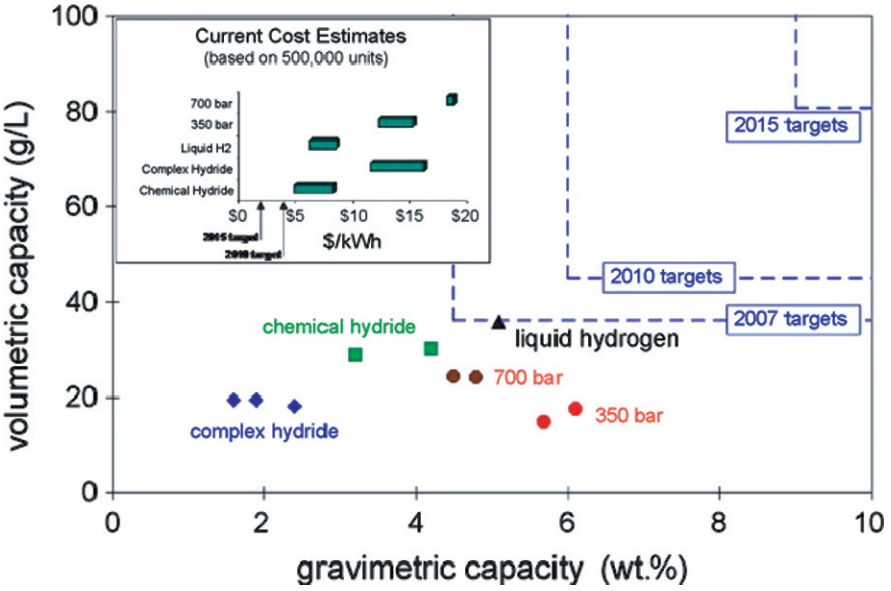

Fig. 3.23 Current status of hydrogen storage systems and cost [2]

A great challenge for future generations of hydrogen-powered vehicles is then the development of lightweight storage systems with conformable tank shapes that can be adapted to the space available in various vehicle structures.

Notes

1. The heat capacity (specific heat) at constant pressure is defined as $C_p = \left(\frac{\partial H}{\partial T}\right)_p$, where H is the enthalpy. The heat capacity at constant volume is $C_V = \left(\frac{\partial U}{\partial T}\right)_V$, where U is the internal energy, T is temperature, and V is the specific volume.
2. The thermal conductivity coefficient relates the transfer of heat through a material via molecular interaction to a temperature gradient across the material.

$$q = -\lambda \times \text{grad}T$$

where q is the heat flux (heat per unit area per unit time), grad T is the temperature gradient, and λ is the thermal conductivity coefficient.

3. A Joule–Thomson (JT) expansion is an isenthalpic expansion of the gas. The Joule–Thomson coefficient μ represents the drop of the temperature in a JT expansion of a real gas. μ is defined according to the following equation:

$$\mu = -C_p^{-1}\left(\frac{\partial H}{\partial P}\right)_T = \left(\frac{\partial T}{\partial P}\right)_H$$

For certain values of pressure, the coefficient μ is equal to zero. This point is called the inversion point of the Joule–Thomson effect. If the initial temperature of the gas is below the JT

effect inversion temperature, then the gas is cooled during the expansion. Conversely, the gas is warmed during expansion, as it is the case for hydrogen and helium at room temperature.

A Joule–Thomson valve is a component through which a gas is allowed to expand adiabatically, resulting in lowering its temperature.

4. The speed of sound in a gas is defined as follows:

$$c = \sqrt{\gamma \cdot \frac{P}{\rho}}$$

where γ is the isentropic expansion factor (this is the ratio of specific heats of a gas at a constant-pressure to a gas at a constant-volume(C_p/C_v)), p is the pressure and ρ is the density.

5. Hydrogen embrittlement is the process by which various metals, most importantly high-strength steel, become brittle and crack following exposure to hydrogen.

References

1. Encyclopédie des gaz, Air Liquide, Division scientifique, Amsterdam, Elsevier (1976)
2. S. Satyapal, J. Petrovic, C. Read, G. Thomas, and G. Ordaz, "The U.S. department of energy's national hydrogen storage project: Progress towards meeting hydrogen-powered vehicle requirements", Catalysis Today 120 (2007) 246
3. P. Petit, "Séparation et liquéfaction des gaz", Techniques de l'Ingénieur, traité Génie des procédés, Volume J3 600
4. R. Drnevich, "Hydrogen delivery: liquefaction and compression", Strategic initiatives for hydrogen delivery workshop, May 7 (2003)
5. http://www.hydropac.com/
6. http://www.pdcmachines.com/
7. P. Muthukumar, M.P. Maiya, and S.S. Murthy "Experiments on a metal hydride based hydrogen compressor", International Journal of Hydrogen Energy, 30 (2005) 879
8. F. Laurencelle, Z. Dehouche, and J. Goyette, T.K. Bose "Integrated electrolyser-metal hydride compression", International Journal of Hydrogen Energy, 31 (2006) 762
9. X. Wang, R. Chen, Y. Zhang, C. Chen, and Q. Wang "Hydrogen storage alloys for high-pressure suprapure hydrogen compressor", Journal of Alloys and compounds, 420 (2006) 322
10. M. Au and Q. Wang "Rare earth-nickel alloy for hydrogen compression", Journal of Alloys and compounds, 201 (1993) 115
11. Z. Dehouche, N. Grimard, F. Laurencelle, J. Goyette, and T.K. Bose, "Hydride alloys properties investigations for hydrogen sorption compressor", Journal of Alloys and compounds, 399 (2005) 224
12. B. Rohland, K. Eberle, R. Ströbel, J. Scholta, and J. Garche, "Electrochemical hydrogen compressor", Electrochimica Acta, 43(24) (1998) 3841
13. R. Ströbel, M. Oszcipok, M. Fasil, B. Rohland, L. Jörissen, and J. Garche, "The compression of hydrogen in an electrochemical cell based on a PE fuel cell design", Journal of Power Sources, 105 (2002) 208
14. S. Porter, "Hydrogen generation from electrolysis", Proton Energy Systems, May 23 (2005)
15. R. Maruyama, "Electrochemical hydrogen storage into $LaNi_5$ using a fullerene-based proton conductor", Electrochemical and Solid-State Letters, 5(5) (2002) A89
16. R.S. Irani, Material Research Society Bulletin (2002) 680
17. http://www.qtww.com/
18. G.E. McIntosh, "Hydrogen liquefiers since 1950", Advances in Cryogenic Engineering: Transactions of the Cryogenic Engineering Conference – CEC, Volume 49 (2004) 9

19. J. Gallarda, “Liquéfaction de l’hydrogène”, Techniques de l’Ingénieur, traité Génie des procédés, J3, 603
20. M. Bracha, G. Lorenz, A. Patzelt, and M. Wanner, “Large-scale hydrogen liquefaction in Germany”, International Journal of Hydrogen Energy, 19(1) (1994) 53
21. J. Wolf, “Liquid – Hydrogen Technology for Vehicles”, Material Research Society Bulletin (2002) 684
22. G. Krainz, G. Bartlok, P. Bodner, P. Casapicola, Ch. Doeller, F. Hofmeister, E. Neubacher, and A. Zieger, “Development of Automotive Liquid Hydrogen Storage Systems”, Advances in Cryogenic Engineering: Transactions of the Cryogenic Engineering Conference – CEC, 49 (2004) 35
23. B. Kelly, “Liquefaction and pipeline costs”, Hydrogen Delivery Analysis Meeting, May 2007, Columbia, Maryland, USA
24. M.T. Syed, S.A. Sherif, T.N. Veziroglu, and J.W. Sheffield, “An economic analysis of three hydrogen liquefaction systems”, International Journal of Hydrogen Energy, 23(7) (1998) 565
25. H. Quack, “Conceptual design of a high efficiency large capacity hydrogen liquefier”, Advances in Cryogenic Engineering: Proceedings of the Cryogenic Engineering Conference, 47 (2002) 255
26. K. Ohira, K. Nakamichi, and H. Furumoto, “Experimental study on magnetic refrigeration for the liquefaction of hydrogen”, Advances in Cryogenic Engineering, 45 (2000) 1747
27. A.J. DeGregoria, L.J. Geuling, J.F. Laatsch, and J.R. Rowe, “Test results of an active magnetic regenerative refrigerator”, Advances in Cryogenic Engineering, 37, Part B (1992) 875
28. C.B. Zimm, E.M. Ludeman, M.C. Severson, and T.A. Henning, “Materials for regenerative magnetic cooling spanning 20 K to 80 K”, Advances in Cryogenic Engineering, 37, Part B (1992) 883
29. K.A. Gschneidner, Jr., H. Takeya, J.O. Moorman, V.K. Pecharsky, S.K. Malik, and C.B. Zimm “New magnetic refrigeration materials for the liquefaction of hydrogen”, Advances in Cryogenic Engineering, 39, Part B (1994) 1457
30. K.A. Gschneidner, Jr., V.K. Pecharsky, and S.K. Malik, “The $(Dy_{1-x}Er_x)Al_2$ alloys as active magnetic regenerators for magnetic refrigeration”, Advances in Cryogenic Engineering, 42 (1996) 475
31. M.A. Richard, A.M. Rowe, and R. Chahine, “Magnetic refrigeration: Single and multimaterial active magnetic regenerator experiments”, Journal of Applied Physics, 95(4) (2004) 2146
32. A. Zuettel, P. Sudan, Ph. Mauron, T. Kiyobayashi, Ch. Emmenegger, and L. Schlapbach, “Hydrogen storage in carbon nanostructures”, International Journal of Hydrogen Energy, 27 (2002) 203
33. M.G. Nijkamp, J.E. Raaymakers, A.J. van Dillen, and K.P. deJong, “Hydrogen storage using physisorption-materials demand”, Applied Physics A, 72 (2001) 619
34. E. Poirier, R. Chahine, P. Bénard, D. Cossement, L. Lafi, E. Melançon, T.K. Bose, and S. Désilets, “Storage of hydrogen on single-walled carbon nanotubes and other carbon structures”, Applied Physics A, 78 (2004) 961
35. B. Panella and M. Hirscher, “Hydrogen adsorption in different carbon nanostructures”, Carbon, 43 (2005) 2209
36. M Hirscher and B. Panella “Large surface area nanostructures for hydrogen storage”, Annales de Chimie Science des Matériaux, 30(5) (2005) 519
37. M. Eddaoudi, J. Kim, N. Rosi, D. Vodak, J. Wachter, M. O’Keeffe, and O.M. Yaghi, “Systematic design of pore size and functionality in isoreticular MOFs and their application in methane storage”, Science, 295 (2002) 469
38. O.M. Yaghi, M. O’Keeffe, N.W. Ockwig, H.K. Chae, M. Eddaoudi, and J. Kim, “Reticular synthesis and the design of new materials”, Nature, 423 (2003) 705
39. J.L.C. Roswell, A.R. Milward, K.S. Park, and O.M. Yaghi, “Hydrogen sorption in functionalized metal-organic framework”, Journal of the American Chemical Society, 126 (2004) 5666
40. B. Panella and M. Hirscher, “Hydrogen physisorption in metal-organic porous crystals”, Advanced Materials, 17(5) (2005) 538
41. M Hirscher and B. Panella, “Hydrogen storage in metal-organic frameworks”, Scripta Materialia, 56 (2007) 809

42. N. Texier-Mandoki, J. Dentzer, T. Piquero, S. Saadallah, P. David, and C. Vix-Guterl, “Hydrogen storage in activated carbon materials: Role of nanoporous texture”, Carbon, 42 (2004) 2735
43. R. Gadiou, S. Saadallah, T. Piquero, P. David, J. Parmentier, and C. Vix-Guterl, “The influence of textural properties on the adsorption of hydrogen on ordered nanostructured carbons”, Microporous and Mesoporous Materials, 79 (2005) 121
44. A.G. Wong-Foy, A.J. Matzer, and O.M. Yaghi, “Exceptional H_2 saturation uptake in microporous metal-organic frameworks”, Journal of the American Chemical Society 128 (2006) 3494
45. D.J. Collins and H.-C. Zhou, “Hydrogen storage in metal-organic frameworks”, Journal of Material Chemistry, 17 (2007) 3154
46. T. Yildirim and M.R. Hartman, “Direct observation of hydrogen adsorption sites and nanocage formation in metal-organic frameworks”, Physical Review Letters, 95 (2005) 215504
47. J.L.C. Roswell, J. Eckert, and O.M. Yaghi, “Characterization of H_2 binding sites in prototypical metal-organic frameworks by inelastic neutron scattering”, Journal of American Chemical Society, 127 (2005) 14904
48. G. Sandrock and G. Thomas, “The IEA/DOE/SNL on-line hydride databases”, Applied Physics A, 72(2) (2001) 153
49. J.H.N. Van Vucht, F.A. Kuijpers, and H.C.A.M. Bruning, Philips Research Report, 25 (1970) 133
50. R. Cerny, J.M. Joubert, M. Latroche, A. Percheron-Guégan, and K. Yvon, Journal of Applied Crystallography, 33 (2000) 997
51. C. Lartigue, A. Percheron-Guégan, J.C. Achard, and F. Tasset, Journal of the Less Common Metals, 75 (1980) 23
52. G. Sandrock, “Hydrogen-metal systems” in Hydrogen Energy System, Y. Yürüm (ed.), Kluwer Academic Publishers, Netherlands (1995) 135
53. F. Cuevas, J.M. Joubert, M. Latroche, and A. Percheron-Guégan, “Intermetallic compounds as negative electrodes of Ni/MH batteries”, Applied Physics A, 72 (2001) 225
54. J.M. Joubert, M. Latroche, and A. Percheron-Guégan, “Metallic hydrides II: Materials for electrochemical storage”, Material Research Society Bulletin September (2002) 694
55. G. Liang, “Synthesis and hydrogen storage properties of Mg-based alloys”, Journal of Alloys and Compounds, 370 (2004) 123
56. J.J. Reilly, “Synthesis and properties of useful metal hydrides”, in Hydrides for energy storage, A.F. Andresen and A.J. Maeland (eds), Pergamon press, Oxford (1978) 301
57. A. Zaluska, L. Zaluski, and J.O. Ström-Olsen, “Nanocrystalline magnesium for hydrogen storage”, Journal of Alloys and Compounds, 288 (1999) 217
58. Y. Chen and J.S. William, “Formation of metal hydrides by mechanical alloying” Journal of Alloys and Compounds, 217 (1995) 181
59. H. Imamura, M. Kawahigashi, and S. Tsuchiya “Exceptionally active magnesium for hydrogen storage: Solvated magnesium clusters formed in low temperature matrices”, Journal of the Less Common Metals, 95 (1983) 157
60. B. Bogdanovic, “Magnesium hydride: A homogeneous-catalysed synthesis and its use in hydrogen storage”, International Journal of Hydrogen Energy, 9 (1984) 937
61. A. Altmann and T. Schober, “Hydrides in Mg and Ti produced by hydrogen ion implantation”, Scripta Metallurgica and Materialia, 25(3) (1991) 723
62. A.S. Pedersen, “Magnesium (Beryllium) and alkaline earth (calcium, strontium and barium) hydrides”, in Solid State Phenomena, E.A. Lewis and A. Aladjem (eds), Scitec Publications volume 49–50 (1996) 46
63. H. Ellinger, C.E. Holley, B.B. McInteer, D. Pavone, R.M. Potter, E. Staritsky, and W.H. Zachariasen, “The preparation and some properties of magnesium hydride”, Journal of American Chemical Society, 77 (1955) 2647
64. W.H. Zachariasen, CE. Holley, and J.F. Stamper, “Neutron diffraction study of magnesium hydride”, Acta Crystallographica, 16 (1963) 352

65. A. San-Martin and F.D. Manchester, “The H-Mg (Hydrogen-Magnesium) system”, Bulletin of Alloy Phase diagrams, 8(5) (1987) 431
66. J.F. Stamper, Jr., C.E. Holley, Jr., and J.F. Suttle, “The magnesium-hydrogen system”, Journal of American Chemical Society, 82 (1960) 3504–3508
67. B. Tanguy, J.L. Soubeyroux, M. Pezat, J. Portier, and P. Hagenmuller, “Amélioration des conditions de synthèse de l’hydrure de magnésium à l’aide d’adjuvants”, Material Research Bulletin, 11, (1976) 1441–1448
68. A.S. Pedersen, J. Kjøller, B. Larsen, B. Vigeholm, and J.A. Jensen, “Magnesium for hydrogen storage”, International Journal of Hydrogen Energy, 8 (1983) 205–211
69. L. Belkbir, E. Joly, and N. Gerard, “Comparative study of the formation-decomposition mechanisms and kinetic in $LaNi_5$ and magnesium reversible hydride”, International Journal of Hydrogen Energy, 6 (1981) 2145–2156
70. B. Bogdanovic, A. Ritter, B. Spliethoff, and K. Straβburger, “A process steam generator based on the high temperature magnesium hydride/magnesium heat storage system”, International Journal of Hydrogen Energy, 20 (1995) 811–822.
71. G. Friedlmeier and M. Groll, “Experimental analysis and modelling of the hydriding kinetics of Ni-doped and pure Mg”, Journal of Alloys and compounds, 253–254 (1997) 550–555,
72. B. Bogdanovic, K. Bohmhammel, B. Christ, A. Reiser, K. Schlichte, R. Vehlen, and U. Wolf, “Thermodynamic investigation of the magnesium-hydrogen system”, Journal of Alloys and compounds, 282 (1999) 84–92
73. B. Vigeholm, J. Kjøller, and B. Larsen, “Magnesium for hydrogen storage”, Journal of the Less Common Metals, 74 (1980) 341–350
74. B. Vigeholm, “Magnesium as an energy material”, Proceedings – World Magnesium Conference, Proceedings – 41st World Magnesium Conference, London, pp. 59–63
75. A. Zaluska, L. Zaluski, and J.O. Ström-Olsen, “Nanocrystalline magnesium for hydrogen storage”, Journal of Alloys and Compounds, 288 (1999) 217–225
76. A.S. Pedersen, J. Kjøller, B. Larsen, and B. Vigeholm, “On the hydrogenation mechanism in magnesium I”, in Hydrogen energy progress V, Proceedings of the 5th World Hydrogen Energy Conference, Toronto 15–20 July 1984, ed. by T.N. Veziroglu and J.B. Taylor, Pergamon Press, New-York, pp. 1269–1277
77. C.P. Chen, B.H. Liu, Z.P. Li, and J. Wu, “The activation mechanism of Mg-based hydrogen storage alloys”, Zeitschrift fur Physikalisch Chemie B, 181 (1993) 259–267
78. E. Ivanov, I. Konstanchuk, A. Stepanov, and V. Boldyrev “Magnesium mechanical alloys for hydrogen storage”, Journal of the Less Common Metals, 131 (1987) 25–29
79. S. Bouaricha, J.P. Dodelet, D. Guay, J. Huot, S. Boily, and R. Schulz, “Hydriding behavior of Mg-Al and leached Mg-Al compounds prepared by high-energy ball milling”, Journal of Alloys and Compounds. 297 (2000) 282–293
80. H. Imamura, S. Tabata, Y. Takesue, Y. Sakata, and S. Kamazaki, “Hydriding-dehydriding behavior of magnesium composites obtained by mechanical grinding with graphite carbon”, International Journal of Hydrogen Energy, 25 (2000) 837–843
81. M. Khrussanova, J.-L. Bobet, M. Terzieva, B. Chevalier, D. Radev, P. Peshev, and B. Darriet, “Hydrogen storage characteristics of magnesium mechanically alloyed with $YNi_{5-x}Al_x$ (x = 0, 1 and 3)”, Journal of Alloys and Compounds, 307 (2000) 283–289
82. P. Wang, A.M. Wang, H.F. Zhang, B.Z. Ding, and Z.Q. Hu, “Hydrogenation characteristics of Mg-TiO_2 (rutile) composite”, Journal of Alloys and Compounds, 313, (2000) 218–223
83. M. Terzieva, M. Khrussanova, and P. Peshev, “Hydriding and dehydriding characteristics of Mg-$LaNi_5$ composite materials prepared by mechanical alloying”, Journal of Alloys and Compounds, 267 (1998) 235–239
84. G. Liang, S. Boily, J. Huot, A. Van Neste, and R. Schulz, “Hydrogen absorption properties of a mechanically milled Mg-50 wt.% $LaNi_5$ composite”, Journal of Alloys and Compounds, 268, (1998) 302–307
85. P. Selvam, B. Viswanathan, C.S. Swamy, and V. Srinivasan, “Magnesium and magnesium alloy hydrides”, International Journal of Hydrogen Energy, 11(3) (1986) 169–192
86. M. Khrussanova, “Metal alloy hydrides for hydrogen storage”, Bulgarian Academy of Science, 19(3), (1986) 358–373

87. S. Orimo and H. Fujii, "Materials science of Mg-Ni-based new hydrides", Applied Physics A, 72(2) (2001) 167–186
88. G. Liang, J. Huot, S. Boily, A. Van Neste, and R. Schulz, "Hydrogen storage properties of the mechanically milled MgH_2-V nanocomposite", Journal of Alloys and Compounds, 291, (1999) 295–299
89. W. Oelerich, T. Klassen, and R. Bormann, "Metal oxides as catalysts for improved hydrogen sorption in nanocrystalline Mg-based materials", Journal of Alloys and Compounds, 315 (2001) 237–242
90. G. Liang, J. Huot, S. Boily, and R. Schulz, "Hydrogen desorption kinetics of a mechanically milled MgH_2 + 5at.% V nanocomposite", Journal of Alloys and Compounds, 305 (2000) 239.
91. J.F. Pelletier, J. Huot, M. Sutton, R. Schulz, A.R. Sandy, L.B. Lurio, and S.G.J. Mochrie, "Hydrogen desorption mechanism in MgH_2 – Nb nanocomposite", Physical review B, 63 (2000) 521
92. G. Barkhordarian, T. Klassen, and R. Bormann, Scripta Materialia, 49 (2003) 213
93. N. Hanada, T. Ichikawa, S. Hino, and H. Fujii, "Remarkable improvement of hydrogen sorption kinetics in magnesium catalyzed with Nb_2O_5", Journal of Alloys and Compounds, 420 (2000), 46–49
94. M. Dornheim, N. Eigen, G. Barkhordarian, T. Klassen, and R. Bormann, Advanced Engineering Materials, 8(5) (2006) 377–385
95. S.I. Orimo, Y. Nakamori, J.R. Eliseo, A. Züttel, and C.M. Jensen, "Complex Hydrides for Hydrogen Storage", Chemical Reviews, 107 (2007) 4111–4132
96. J. Chen, N. Kuriyama, Q. Xu, H.T. Takeshita, and T. Sakai, "Reversible hydrogen storage via titanium-catalyzed $LiAlH_4$ and Li_3AlH_6", Journal of Physical Chemistry B, 105 (2001) 11214–11220
97. H. Morioka, K. Kakizaki, S.-C. Chung, and A. Yamada, "Reversible hydrogen decomposition of $KAlH_4$", Journal of Alloys and Compounds, 353 (2003) 310–314
98. M. Fichtner, O. Fuhr, and O, Kircher, "Magnesium alanate – a material for reversible hydrogen storage?", Journal of Alloys and Compounds, 356–357 (2003) 418–422
99. M. Mamatha, B. Bogdanovic, M. Felderhoff, A. Pommerin, W. Schmidt, F. Schüth, and C. Weidenthaler, "Mechanochemical preparation and investigation of properties of magnesium, calcium and lithium-magnesium alanates", Journal of Alloys and Compounds, 407 (2006) 78–86
100. http://www.albemarle.com/Products_and_services/Fine_chemicals/
101. P. Claudy et al., "Etude du comportement thermique du tetrahydroaluminate de sodium $NaAlH_4$ et de l'hexahydroaluminate de sodium Na_3AlH_6 de 298 a 600 K", Thermochimica Acta, 8 (1980) 75
102. B. Bogdanovic and M. Schwickardi, "Ti-doped alkali metal aluminium hydrides as potential novel reversible hydrogen storage materials", Journal of Alloys and Compounds, 253–254, (1997) 1–9
103. B.C. Hauback, H.W. Brinks, C.M. Jensen, K. Murphy, and A.J. Maeland, "Neutron diffraction structure determination of $NaAlD_4$", Journal of Alloys and Compounds, 358 (2003) 142–145
104. D.L. Anton, "Hydrogen desorption kinetics in transition metal modified $NaAlH_4$", J. Alloys and Compounds, 356 (2003) 400
105. B. Bogdanovic, G. Sandrock, "Catalized complex Metal Hydrides", MRS bulletin, 712 (2002)
106. M. Fichtner, O. Fuhr, O. Kircher, and J. Rothe, "Small Ti clusters for catalysis of hydrogen exchange in $NaAlH_4$", Nanotechnology, 14 (2003) 778
107. B. Bogdanovic, M. Felderhoff, S. Kaskel, A. Pommerin, K. Schlichte, and F. Schüth, "Improved hydrogen storage properties of Ti-doped sodium alanate using titanium nanoparticles as doping agents", Advanced Materials, 15 (2003) 1012
108. B. Bogdanovic, M. Felderhoff, A. Pommerin, F. Schüth, and N. Spielkamp, "Advanced hydrogen storage materials based on Sc-, Ce-, and Pd-doped $NaAlH_4$", Advanced Materials, 18 (2006) 1198

109. O. Kircher and M. Fichtner, "Hydrogen exchange kinetics in $NaAlH_4$ catalyzed in different decomposition states", Journal of Applied Physics, 95(12) (2004) 7748
110. A. Léon, O. Kircher, J. Rothe, and M. Fichtner, "Chemical state and local structure around titanium atoms in $NaAlH_4$ doped with $TiCl_3$ using X-ray absorption spectroscopy", The Journal of Physical Chemistry B, 108 (2004) 16372
111. J. Graetz, J.J. Reilly, J. Johnson, A.Y. Ignatov, and T.A. Tyson, "X-ray absorption study of Ti-activated sodium aluminum hydride", Applied Physics Letters, 85 (2004) 500
112. M. Felderhoff, K. Klementiev, W. Grünert, B. Spielthoff, B. Tesche, J.M. Bellosta von Colbe, B. Bogdanovic, M. Härtel, A. Pommerin, F. Schüth, and C. Weidenthaler, "Combined TEM-EDX and XAFS studies of Ti-doped sodium alanate", Physical Chemistry Chemical Physica, 6 (2004) 4369
113. A. Léon, O. Kircher, J. Röthe, S. Dieter, and M. Fichtner, "Evolution of the local structure around Ti atoms in $NaAlH_4$ doped with $TiCl_3$ or small Ti clusters ($Ti_{13}^{\cdot} \cdot 6THF$) by ball milling", Journal of Physical Chemistry B, 110 (2006) 1192
114. P. Canton, M. Fichtner, C. Frommen, and A. Léon "Synchrotron X-ray studies of Ti-doped $NaAlH_4$", Journal of Physical Chemistry B, 110 (2006) 3051
115. S. Singh, S.W.H. Eijt, J. Huot, W.A. Kockelmann, M. Wagemaker, and F.M. Mulder, "The $TiCl_3$ catalyst in $NaAlH_4$ for hydrogen storage induces grain refinement and impacts on hydrogen vacancy formation", Acta Materialia 55 (2007) 5549
116. P. Chen, Z. Xiong, J. Luo, J. Lin, and K.L. Tan, "Interaction of hydrogen with metal nitrides and imides", Nature, 420 (2002) 302–304
117. P. Chen, Z. Xiong, G. Wu, Y. Liu, J. Hu, and W. Luo, Scripta Materialia, 56 (2007) 817
118. H. Fujii and T. Ichikawa, "Recent development on hydrogen storage materials composed of light elements", Physica B, 383 (2006) 45–48
119. W. Luo, "($LiNH_2$ – MgH_2): A viable hydrogen storage system", Journal of Alloys and Compounds, 381 (2004) 284–287
120. G.L. Soloveichik, "Metal borohydrides as hydrogen storage materials", Materials Matters, 2 (2007) 11–14
121. J.J. Vajo, S.L. Skeith, and F. Martens, "Reversible storage of hydrogen in destabilized $LiBH_4$", Journal of Physical chemistry B, 109 (2005) 3719–3722
122. J.J. Vajo and G.I. Olson, "Hydrogen storage in destabilized chemical systems", Scripta Materialia, 56 (2007) 829
123. G. Barkhordarian, T. Klassen, M. Dornheim, and R. Bormann, "Unexpected kinetic effect of MgB_2 in reactive hydride composites containing complex borohydrides", Journal of Alloys and Compounds, 440 (2007) L18–L21
124. J. Huot, G. Liang, and R. Schulz, "Magnesium-based nanocomposites chemical hydrides", Journal of Alloys and Compounds, 353 (2003) L12
125. S.C. Amendola, "Process for synthesizing borohydride compounds", US patent 6524542 (2003)
126. http://www.millenniumcell.com
127. P. Ferreira-Aparacio, I. Rodriguez-Ramos, and A. Guerrero-Ruiz, "Pure hydrogen production from methylcyclohexane using a new high performance membrane reactor", Chemical Communications 2002(18) (2002) 2082
128. G. Bustamante, Y. Swesi, I. Pitault, V. Meille, and F. Heurtaux, "A hydrogen storage an transport mean", Proceedings International Energy Congress and Exhibition IHEC (2005) Turkey
129. http://www.airproducts.com
130. A. Cooper and G. Pez, "Development of new carbon-based sorbent systems for an effective containment of hydrogen", DOE Annual Merit Review Presentation (2005), available at: http://www.hydrogen.energy.gov/annual_progress05_storage.html
131. http://wwww.asemblon.com
132. E.D. Naeemi, D. Graham, and B.F. Norton, "Introducing HYDRNOL TM: Organic liquid storage for hydrogen", Sigma Aldrich, 2(2) (2007) 23

Chapter 4
Hydrogen Transport and Distribution

Mathilde Weber and Jérôme Perrin

List of abbreviations

ASTM	American Society for Testing Materials
CUTE	Clean Urban Transport for Europe
D	nominal outside diameter of a pipe
FRP	fibre-reinforced polymer
GH_2	gaseous H_2
H_2	Hydrogen
ISO	International 0rganization for Standardization
LH_2	liquid H_2

Mathilde Weber
Air Liquide R&D Center, 1 chemin de la porte des Loges, Les Loges en Josas, BP126, 78354 Jouy en Josas Cedex, France, e-mail: mathilde.weber@airliquide.com

Jérôme Perrin
Renault Technocentre, Department of Research, Advanced Studies, and Material (DREAM), Guyancourt, France, e-mail: jerome.perrin@renault.com

A. Léon (ed.), *Hydrogen Technology*,

MIG	gas metal arc welding
MOP	Maximum operating pressure
Nm^3	stands for 'normal' m^3 under standard pressure and temperature conditions
SMR	steam-methane reforming
T	nominal wall thickness of a pipe
TIG	tungsten inert gas welding
YS	Minimum yield strength

4.1 Introduction

The successful development of the future hydrogen transmission and distribution infrastructure is critical to a widespread use of hydrogen as an energy carrier.

Hydrogen delivery infrastructure is related to the hydrogen production site (centralised or not) and its transportation to the end-use station. At present, mature pathways include the transport of compressed gaseous hydrogen in cylinders and cryogenic trucking of liquid hydrogen. The components needed for the transmission and distribution are pipelines, compressed gas tube trailers and cylinders, or cryogenic trucks, railcars, and ships. Depending on the degree of hydrogen penetration in the market, a certain capital cost of pipelines will be necessary to build the estimated million km of distribution pipelines and thousand km of high- and medium-pressure transmission pipelines.

As a result of its lower molecular weight and viscosity, hydrogen flows more than two times faster than natural gas in a pipeline under the same conditions of pipe diameter and pressure drop. Due to the lower heating value, however, such a hydrogen pipeline carries about 30% less energy than its natural gas counterpart. As a consequence, hydrogen pipelines need to operate at higher pressures to achieve comparable energy transport capacities or they have to be of large diameter. A special issue to be taken into account with hydrogen is its fast diffusion through most materials and seals, which in turn may cause severe degradation of steels, etc ….

Any large-scale hydrogen distribution system also is associated with the problem of bulk storage to provide a buffer between production facilities and fluctuation in demand. The most widely studied options are underground caverns and depleted underground natural gas formation.

The following sections will focus on the hydrogen distribution infrastructure from pipeline distribution for large industrial needs to local distribution via truck transport with or without on-site hydrogen production. Then, underground bulk storage as well as hydrogen refuelling stations for vehicles will be described.

4.2 Hydrogen Distribution by Gas Pipelines

To meet the increasing hydrogen demand by industrial customers, the capacities of hydrogen production are increasing, existing networks are expanding, and new networks are being developed. Praxair, as an example, doubled its capacity in 2002

in Texas and Louisiana and Air Products has developed distribution pipelines in Canada, Brazil, and South East Asia.

The distribution of hydrogen by pipelines actually is the most economic way to supply large amounts of gas. With the development of hydrogen use in large industry processes, several networks of pipelines have been developed in specific areas. These pipelines connect H_2 producers and industrial users. They could also supply hydrogen energy users through filling stations delivering either compressed or liquefied hydrogen.

4.2.1 Overview of World Pipeline Networks

The major actors of hydrogen transportation and distribution are Air Liquide, Air Products, Linde, and Praxair. The length of the hydrogen pipeline network is estimated to be around 1600 km in Europe and 900 km in North America. In the USA, most pipelines are located along the Gulf coast (Texas and Louisiana) where large quantities of hydrogen are consumed at refineries and in chemical manufacture. Tables 4.1 and 4.2 give a list of the main pipeline network in Europe and North America and their operators, respectively [1, 2]. Figure 4.1 displays part of the pipeline network around the world from Air Liquide, Linde, and Praxair.

Figure 4.1a displays the Air Liquide hydrogen pipeline network in Benelux, France, and Germany. The one in Germany is the first hydrogen pipeline which was

Table 4.1 Hydrogen pipelines in Europe

Operator	Network	Length (km)	Country	Length (km)
			Netherlands	187
	North Europe	949	Belgium	613
	Dunkerque	14		
	France East	37	France	303
Air Liquide	France Centre East	57		
	France South East	42		
	Le Havre	4		
	Ruhr	240	Germany	240
	Monthey	2	Switzerland	2
	Priolo	6	Italy	6
	sub-total	1351	sub-total	1351
	Leuna-Bitterfeld	135	Germany	135
Linde	Teesside	35	United Kingdom	35
	sub-total	170	sub-total	170
	Rozenburg/Rotterdam	70	Netherlands	70
Air Products	Teesside	5	United Kingdom	5
	Porto Marghera	2	Italy	2
	sub-total	57	sub-total	77
Else	Stenungsund	18	Sweden	18
TOTAL		1596		1596

Table 4.2 Hydrogen pipelines in North America

Operator	Network	Length (km)
	Texas and Louisiana (Gulf coast)	100 + 55
Air Liquide	Edmonton (Canada)	3
	Pennsylvania	3
	Louisiana (Baton Rouge-New Orleans)	210
Air Products	Texas/Gulf coast	390
	California	21
	Canada	10
	Texas and Louisiana	482
Praxair	California	< 10
	Indiana	< 10
	Alabama	< 10
Else	Canada (Shell Canada Ltd.)	/
	Amuav (Venezuela)	/

built in 1938 in the Ruhr area. This 240 km long pipeline still is under operation nowadays and about fourteen production sites are connected to the pipeline which has an estimated capacity of 250 million Nm^3 of hydrogen per year (Nm^3 stands for 'normal' m^3 under standard pressure and temperature conditions). The pipeline was initially established to transport by-product hydrogen generated during acetylene production to Hiberna, a company involved in coal processing. This pipeline system has made by-product hydrogen much more marketable. The hydrogen producers currently connected to the Air Liquide pipeline with their net supply are Bayer AG (Krefeld, Leverkusen), Degussa AG (Lülsdorf, Marl), and Ruhrkohle Bergbau AG (Bottrop) [1].

Figure 4.1c displays the pipeline network operated by Linde. Linde Gas AG owns and operates a hydrogen pipeline system in the eastern German chemical industry region with a total length of 135 km. This pipeline system links the Linde sources at Leuna to hydrogen consumers at different locations, such as the Total refinery at Spergau, and incorporates a Linde filling station for trailers.

Figure 4.1e displays Air Products' major worldwide hydrogen pipeline systems. The two most extensive networks, linking production sources to consumers, are located in the US West Gulf Coast (southeast Texas through southwest Louisiana) and the eastern Louisiana Gulf Coast (Baton Rouge through New Orleans). Air Products owns and operates other hydrogen pipeline networks in California, Canada, the Netherlands, the United Kingdom, Thailand, and Singapore (totalling 15 km in Asia)

As can be seen, the potential of hydrogen as a new energy carrier leads to the development of the hydrogen pipeline network [1]. Within the "Zero Regio" European project, for instance, Linde installed a 900 bar hydrogen pipeline (of 1" diameter) over a distance of 1.7 km in the Frankfurt, Rhine-Main area. In addition, Sapio (Air Products group) proposes to build a pipeline in Arezzo (Etruria). Moreover, within the "Hydrogen Park" project in Porto Marghera (Venetia), a new hydrogen pipeline shall be built underground through an urban area.

(a)

(b)

(c)

Fig. 4.1 Main hydrogen pipelines in the world. (**a**) Air Liquide hydrogen pipelines in Benelux, France, and Germany (Ruhr area). (**b**) Air Liquide hydrogen pipelines on the Gulf coast (USA). (**c**) Linde hydrogen pipelines in Germany. (**d**) Praxair hydrogen pipelines on the Gulf coast (USA). (**e**) Air Product hydrogen pipelines on the Gulf coast (USA)

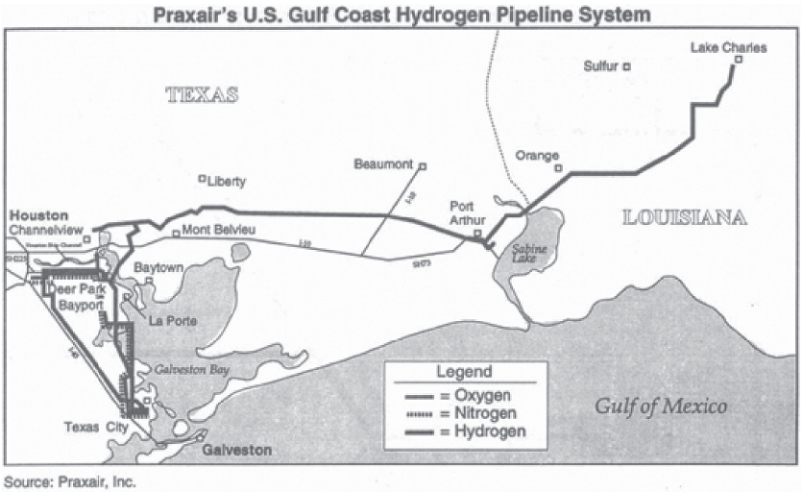

(d)

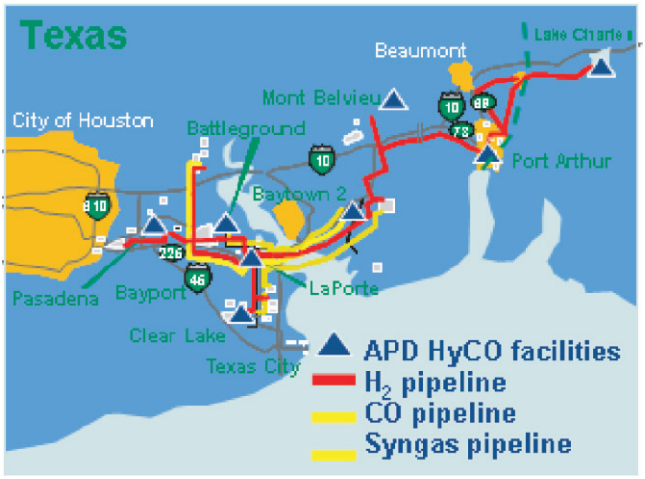

(e)

Fig. 4.1 (continued)

4.2.2 Pipeline Characteristics

Hydrogen is a non-toxic and very volatile gas. However, it is much more flammable than conventional fuels, as the lower and upper flammability limits in air are 4 and 75%, respectively [3]. Hazards due to outdoor release of hydrogen will be reduced quickly to safe levels as a result of the fast dispersion, while indoor hazards will depend on the size and geometry of confinement. Thus, pipeline operations require

careful design, installation, and maintenance procedures. Major hazard studies are often performed in order to assess the consequences of major accidents on the environment. These major hazard studies are required by the authorities in some parts of the world, as in Europe, where the SEVESO Directive applies.

The operating pressure of hydrogen pipelines generally is lower than 100 bar (most commonly between 40 and 70 bar) and the diameter of the pipelines usually ranges from 10 to 300 mm. Pipeline construction involves extensive welding for making pipes and connecting pipes. The pipelines are classified either as seamless pipes which are made by hot working and piercing solid billets of steel or welded pipes which are made by bending plates into a tube form and welding along the seam [3]. Then, the pipes are transported to site and welded in-situ along their circumference using TIG, MIG, or laser beam methods. It is extremely important that the welded joints are free from defects and excessive residual stresses. For this purpose, post-weld X-ray inspection of the weld is carried out. Once the pipes have been checked, an external coating is applied by brushing or spraying in order to protect the pipes against corrosion. Moreover, an internal coating can be used in order to reduce hydrogen permeation (see Sect. 2.1) at high working pressure. Once the line has been completed and its interior has been cleaned from sand, dirt, and welding debris, it can be tied-in to origin and destination pipes. However, pipe connections as well as valves and compressor stations are the main causes of leaks. Before the pipeline can go into operation, it therefore has to be pressure-tested by hydro testing (water is most frequently used) and then dried with air before use.

The exploitation of a pipeline network requires compressor stations, as the by-product hydrogen generally is available at low pressure. Hydrogen compressors feeding the pipeline system are usually found at locations where crude hydrogen is purchased or produced. The compressors are expensive and require a high maintenance. Actually, they are not installed, if another alternative is possible. For instance, when hydrogen is produced using natural gas (steam-methane reforming), the natural gas feedstock can be compressed and the production plant operated at a higher pressure. Other compressors, such as booster stations along the pipelines, may be necessary to compensate for the pressure decrease due to friction. However, when pipelines are relatively short (i.e., shorter than 100 km), the pressure at the entrance usually is high enough to avoid the need for intermediate booster stations along the pipelines. It should be noted that due to the low density of hydrogen, elevation losses do not induce a significant pressure decrease along the pipeline.

4.2.2.1 Pipeline Flow Capacity and Operating Pressure

The pipeline flow capacity is related to the customer's requirements, the construction (pipe diameter, changes in elevation along the pipeline path), and the properties of the gas (viscosity, molecular weight, pressures losses due to friction). Once a pipeline has been designed and built, its capacity can still be increased either by looping or the addition of compressors at intermediate points along the path. However, the pipeline capacity is limited by its maximum allowable pressure which will

depend on the pipe characteristics (diameter, thickness, material) and its location. The maximum operating pressure (*MOP*) can be calculated according to the following equation:

$$MOP = \frac{2.YS.t}{D}.C \tag{4.1}$$

where *YS* represents the minimum yield strength of the pipe material (given by the manufacturer's specifications), *D* the nominal outside diameter of the pipe, *t* the nominal wall thickness of the pipe, and *C* is a design factor determined using international specifications (ISO, ASTM, …). The latter takes into account the material used, the gas, the temperature, and other design or material factors (location, longitudinal joint factor, etc …). Further specifications generally apply depending on the type of fluid transported. For environmental and safety reasons, most pipelines are buried, as this offers the best protection against external impacts.

4.2.2.2 Pipeline Materials

Physical Properties

Most pipelines for gas transportation are made of low-carbon and low-alloy steels. They are composed of iron (98 to 99 wt.%), carbon (up to 0.30 wt.%), and manganese (0.30 to 1.5 wt.%), with a small amount of other alloying elements, such as molybdenum, vanadium, and titanium. These steels combine economic affordability with an adequate range of physical properties, such as strength, toughness, ductility, and weldability.

- Strength is a property of materials usually defined as minimum yield strength, *YS*, which is the minimum level of stress before permanent deformation. Strength depends on the chemical composition of the steel and on the thermomechanical treatment during manufacturing.
- Fracture toughness is related to the resistance of the material to crack propagation under tensile stress.
- Ductility is the ability of the material to deform permanently before failure.
- Weldability is a key feature of the steels, as the weldability of steel decreases as it strength increases.

Steels are sensitive to corrosion and can be protected against it by a cathodic protection system. For buried pipes, it consists in applying an electric current through the soil between the pipeline (cathode) and metal blocks (anode) buried at regular intervals and a certain distance from the line. As a result, the blocks are corroded preferably. It should be noted that this system has a low power requirement and can be fed by solar energy produced *in-situ* [3].

The maximum operating pressure of a pipeline network is proportional to the strength of steel and to the wall thickness of the pipe. High-strength steels would thus present the advantage of higher operating pressure or thinner walls, but they are much more sensitive to hydrogen embrittlement.

Hydrogen Embrittlement

Hydrogen embrittlement results from adsorption and diffusion of hydrogen in steel. Gaseous hydrogen may indeed adsorb on a surface, dissociate there in the atomic form, and diffuse in steel, leading to a decrease of the crack initiation energy. For the most brittle steels, fracture occurs at the grain boundary as a result of the decrease of the energy of cohesion between grains [4, 5]. Hydrogen embrittlement is thus characterised by a loss of ductility on slow application of strain and may yield severe cracking of the material. Ultimately, the material may break after some time when subjected to a stress level well below the yield strength of the steel.

The susceptibility of steels to this effect increases with increasing content of carbon and manganese. Indeed, these two components facilitate the formation of the hard martensite phase which is more sensitive to hydrogen embrittlement [3]. The steels used for hydrogen pipelines thus contain low amounts of carbon and manganese, $\leq$1–1.2 and $\approx$ 0.2 wt%, respectively, and are characterised by a low strength (yield strength < 290 MPa) (corresponds to API 5LX grades 42 or 52). It should be noted that in a pipeline network, the compatibility of the materials must not only be assessed for the pipes, but also for valves, compressors, manifolds, and metering units.

Due to this materials issue, the operating pressure of hydrogen pipelines generally is lower than 100 bar. Higher operating pressures can be achieved using austenitic steels. However, their costs prohibit large-scale transportation.

Future Developments

As regards the development of hydrogen as an energy carrier, the development of the hydrogen pipeline network has become a key issue. A hydrogen pipeline carries about 30% less energy compared to a natural gas pipeline due to the lower heating value of hydrogen (about one third of that of natural gas). As a consequence, there is a renewed interest in the research for new pipeline materials compatible with hydrogen and their use at higher operating pressure. New steels, for example, are tested within the Naturalhy European project [3].

Research also concentrates on polymeric coatings for steel pipes and fibre-reinforced polymer pipelines (FRP). FPR pipelines are composed of a polymeric tube that is impermeable to hydrogen and wrapped with glass, aramid or carbon fibres. The tube is finally coated with a polymeric layer. Such pipelines could be used up to 70 or 250 bar depending on the design and materials [6]. They are considered to be a feasible alternative to steel pipelines in terms of performance and cost (especially lower installation costs as compared to steel pipes).

Another alternative for the expansion of the hydrogen pipeline network would be to use the existing natural gas network. The natural gas network indeed is much more important than the existing hydrogen network (1,850,000 km (90% for distribution) compared to 1500 km for hydrogen in 2003 in EU25). Many projects (Nordic H_2 program, Naturalhy…) are then concerned with the adaptation of the

natural gas network to the transportation of hydrogen, pure or mixed with natural gas. In addition to materials issues (pipe, seal, valves, …), the efficiency of existing compressor stations for natural gas (multi-stage centrifugal compressors) limits the hydrogen content in mixtures with natural gas to 10–15% [3]. Consequently, higher hydrogen contents would require major investments for different components, such as compressors, pipe materials, design of pipeline.

4.3 Hydrogen Delivery by Fleet

Large customers from refineries, chemical industries, or steel- and glass-making are preferably supplied by large on-site H_2 production plants or by hydrogen pipelines, while smaller-scale industrial gas applications (typically when the consumption remains smaller than 1000 Nm^3 per hour) are supplied either by small on-site H_2 production units, by trailers, or cylinders. In Europe, the total volume of this industrial hydrogen supplied by trailers or cylinders is estimated to amount to 425 million Nm^3 in 2006, whereas the total hydrogen market, including large industries, is at least three times larger in volume. Nevertheless, altogether, this remains a small fraction of the total hydrogen production capacity that is estimated to amount up to 89 billion Nm^3 [3, 7].

The first step to address this market is to purify and package the gas at first-level gas stations, from which trailers depart to serve customers or second-level cylinder filling centres. These gas stations may have their own on-site production, but more often, they use either the excess capacity of an SMR source dedicated to a large customer or the by-product hydrogen from a chloro-alkali plant or a naphtha cracker, sometimes via a pipeline.

4.3.1 Delivery by Compressed Gas Trailers

Delivery of compressed hydrogen in seamless steel vessels by trucks is the most common way for short distances (< 200 km) and small quantities (up to about 300 kg). The steel employed for the vessels must be compatible with hydrogen (see Sect. 6.2.).

Figure 4.2 displays the steel tube trailers or cylinder trailers at 200 bars or 300 bars, which can carry from 2000 to 6200 Nm^3 of H_2. This corresponds to a theoretical H_2 weight capacity between ~180 kg and ~540 kg, whereas the empty truck weighs ~ 40 tons. The best performance with ~540 kg is reached when using bundles of light-weight type II composite cylinder bottles. Nevertheless, the effective capacity of compressed hydrogen gas trucking never is 100% due to the imposed pressure equalisation of the customer tank.

The total fleet transporting compressed gaseous hydrogen in Europe can be estimated from the fleet of Air Liquide which has more than 350 CGH_2 tube trailers

Fig. 4.2 Two types of compressed gas hydrogen trailers operated by Air Liquide in Europe: tube trailer carrying 2000 to 3000 Nm^3 of H_2 (depending on the numbers of tubes) and type II composite cylinder trailers carrying 6200 Nm^3 of H_2 (540 kg)

in operation across Europe. Taking into account the Air Liquide market share for industrial hydrogen in Europe, the total number of compressed gaseous hydrogen trailers in Europe may well be estimated to be close to one thousand.

4.3.2 Liquefied Hydrogen Transportation

In terms of hydrogen weight capacity, delivery in liquefied form is over six times more efficient than using compressed gas delivery. For instance, a super-insulated liquid hydrogen truck of 40 tons can carry about 3500 kg of liquefied hydrogen, which corresponds to a weight efficiency of 7.5 wt%. Linde, as an example, has liquid hydrogen trucks with volumetric capacities of 15,000, 41,000, and 53,000 litres, which can transport 1000, 2900, and 3750 kg of hydrogen, respectively. The cost of handling and transport liquid hydrogen by trucks, railway or ship is lower than that of an equivalent quantity of compressed-gas hydrogen. However, as hydrogen is generally used in its gaseous form, delivery of liquefied hydrogen requires the expense of cryogenic technology for the customer and the producer.

The liquid hydrogen business has been developed most extensively in North America. The first liquid hydrogen plants were built in the USA to supply the American Space Program. Several plants were built in Canada where quite inexpensive energy was available for the liquefaction process. In Europe, the largest part of hydrogen is delivered in gaseous form, whereas the delivery of liquefied hydrogen makes up 7% of the world capacity only (world capacity is estimated to exceed 270 tons per day). There are three hydrogen liquefaction plants in Europe (total capacity 20 tons/day): one operated by Air Liquide in Waziers, France (10 tons/day), one by Air products in Rozenburg, Netherlands (5 tons/day), and one by Linde in Ingolstadt, Germany (4.4 tons/day) [3].

4.4 Underground Storage of Hydrogen

With recent developments of hydrogen technology, hydrogen storage facilities are being developed and investigated to regulate hydrogen consumption and production. The most widely studied options for storing large quantities of gaseous hydrogen

are underground depleted gas fields, aquifers, and/or caverns. Another option is underground storage in buried tanks either in compressed gas form or in liquid form. These different options will be described and illustrated in the following sections.

4.4.1 Natural Underground Storage

Underground storage of hydrogen and synthetic gas (H_2-CO) mixes is not a new concept. A major study of underground storage of gaseous hydrogen was conducted in 1979 by the Institute of Gas Technology (now known as Gas Technology Institute, GTI) in the USA [8]. Over the last decades, there were several examples of underground storage of pure hydrogen or synthetic gas H_2-CO mixtures [9]. Praxair is presently constructing a large underground hydrogen storage facility to enable "peak shaving" of its hydrogen production. This facility, located in Texas, will use a salt cavern and be the first of its kind in the gas industry. Connected to the Praxair's hydrogen pipeline network which serves large areas in Texas and Louisiana, it will significantly increase the on-demand availability of hydrogen during periods of peak demand. This peak-shaving system is envisaged to be brought on line in 2007 [7].

Gas can be stored in depleted oil or gas fields. Figure 4.3(a) displays the schematic representation of a depleted fossil oil or gas well, with the porous rock structures having the following features:

– a stratum of porous rock, usually sand or sandstone, at a depth of 150–900 m below the surface,
– an impervious cap rock of adequate thickness,
– a suitable geological structure, usually dome-shaped.

Such storage facilities tend to be extremely large; they can store volumes of gas exceeding 10^9 Nm^3. The pressures may be up to 40 atm. The porosity of the sandstone or sand must be sufficiently high to provide a reasonable void space to yield an economically acceptable storage volume. The permeability must be high enough to provide for an adequate rate of inlet flow (injection) and outlet transmission injection (withdrawal). On the other hand, the cap rock structure must be reasonably

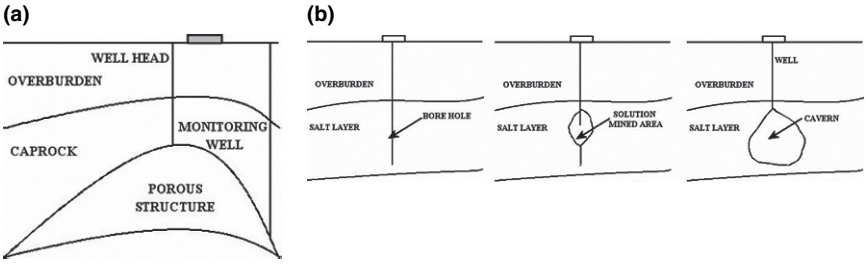

Fig. 4.3 **(a)** Schematic representation of a depleted fossil oil or gas well, or aquifer. **(b)** Schematic representation of the solution-mining of a salt cavern: 1) initial bore hole, 2) solution mining in process 3) final solution-mined cavern [10]

impermeable, if it is to contain the gas. An important point to note regarding the performance of the cap rock structure is the mechanism involved in sealing the top of the underground reservoir, either a depleted field or an aquifer. Water fills all the voids of the cap rock structure and can be expelled only by sufficiently high pressure to overcome the capillary resistances (the threshold pressure of the cap rock). Below this incremental pressure, the cap rock will act as an effective barrier to the passage of any gas. This mechanism is independent of the nature of the gas. Therefore, hydrogen in underground storage will behave much like natural gas as far as the integrity against leakage is concerned.

During exploitation, a minimum base gas or "cushion gas" has to be maintained, which is the volume of gas intended as permanent inventory in the storage reservoir to maintain adequate pressure and delivery rates throughout the withdrawal season.

A second option is the storage in rock and salt caverns, voids like excavated rock caverns or mines or solution-mined salt caverns as displayed in Fig. 4.3(b) Single salt caverns may have a size around 50 10^6 m^3, whereas hard rock caverns would be one tenth of this size. Unlike depleted field and aquifer storage systems, cavern storage involves large open, void spaces to be filled with gas. A more complex structural analysis is therefore required to establish feasibility. For example, if the pressure in the cavity is allowed to drop significantly below ambient pressure, a collapsing stress situation is created, which might result in the loss of structural integrity of the storage volume. An approach considered is to replace the gas drawn off by water, such that the cavity pressure is maintained. Of course, there is no cushion gas requirement in this hydraulically compensated scheme, and the delivery pressure is constantly equivalent to the hydraulic head. The disadvantage of storage in salt caverns is that the working fluid must be saturated brine and its surface storage is complicated due to many environmental constraints.

4.4.2 Underground Storage in Tanks

Underground storage may also consist in burying compressed gas or liquid hydrogen tanks that are usually placed at ground level, in order to save ground space. Of course, this option should only be applied for smaller hydrogen quantities (typically 10^3 to 10^4 Nm^3) and at a much smaller depth (typically a few metres) than direct gas storage in caverns.

Nevertheless, the challenge of local storage of hydrogen in future hydrogen vehicle refuelling stations has triggered a new interest and proposals for this option. Indeed, when referring to the largest existing gasoline fuelling stations in Europe – which are scaled to refill several hundreds up to one thousand cars per day with a local storage capacity corresponding to two days of consumption – the equivalent hydrogen refuelling stations in the future should be able to store up to 10 tons of hydrogen. This corresponds to a volume of the order of several 10^5 Nm^3, or 250 m^3 at 700 bars, or 140 m^3 of liquid hydrogen [7].

4.4.2.1 Compressed Gas Tanks

Presently, the largest manufactured compressed hydrogen tanks in the world (about 15,000 m^3) can be pressurised up to 12–16 bar only. Individual metallic cylindrical tanks at 200–300 bar can be scaled up to ~ 1000 litres (inner water volume) each for hydrogen transport in tube trailers where currently about 15 tubes are bundled together.

Large-volume high-pressure gas tanks made of carbon fibre-reinforced composite vessels are presently being developed for CNG or H_2 by a few companies. For example, Lincoln Composites has already manufactured type IV vessels with a plastic liner at 7000 psi (483 bar) for small-size hydrogen refuelling stations (50 kgH_2/day); the company is presently working on a new tank with a plastic liner at 5000 psi (350 bar), approximately 1.08 metres in diameter, 11.5 metres in length, and a storage volume of approximately 8700 litres (water volume).

Although a compressed gas storage installation is usually placed outdoors, on or above ground level, it may be buried to save ground space and also to provide improved protection from external impacts, such as radiation from adjacent fires or damage caused by explosions. However, this alternative is rarely used, because it makes inspection of the vessels and interconnection of pipes more difficult and requires preventative measures to prevent corrosion. Nevertheless, to overcome the difficulty of inspection and pipe interconnection, it has been proposed to place the tanks in a basin and submerge them afterwards in a liquid, such as water, so that tank protection from heating and explosion is compatible with an easy inspection simply by lowering the water level in the basin. Alternatively, the tank may be placed in a protection system consisting of a sack that contains the tank and a gas-permeable material arranged in such a manner that it constitutes a layer around the tank [11]. Figure 4.4 displays the sack, a material which is impermeable to water and gas.

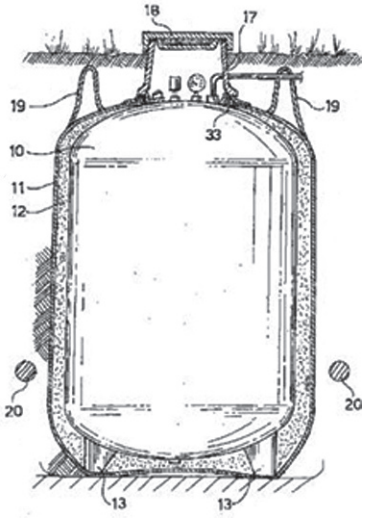

10: tank

11: sack

12: gas-permeable material

13: supporting means

17: access pit

18: removable cover

19: handles

20: device for cathodic protection

33: lightening cable

Fig. 4.4 Gas tank with protection system for underground installation [11]

4.4.2.2 Liquid Tanks

At present, the technology of liquid hydrogen storage is state of the art thanks to extensive applications in space propulsion. Liquid hydrogen tanks for long-term storage have a double vacuum perlite insulation. Common stationary tanks have capacities ranging from 1500 litres (approx. 1100 Nm^3 or 100 kg H_2) up to 75,000 litres (~60,000 Nm^3 or ~5 tons of H_2) with radii of 1.4 to 3.8 m and heights from 3 m up to 14 m. The largest tank belongs to NASA and is located at Cape Canaveral. This tank has an outer spherical diameter of 20 m, a storage volume of about 324,000 Nm^3 (about 270 tons liquid H_2), and its evaporation rate is below 0.03% per day, allowing for a storage period of several years.

The benefits of underground liquid H_2 stationary storage may be summarised as follows:

i) it decreases land usage and footprint,
ii) it reduces potential hazards (vandalism, fire, and vehicle impact),
iii) it has an inherent spill containment [7].

Currently, there are only a few examples of liquid H2 tanks placed in a room underground or buried underground.

The first example is the liquid H_2 tank of the bus refuelling station operated by BP in London within the HyFleet-CUTE project. Figure 4.5 displays the cryogenic tank manufactured by Air Liquide for BOC, which is placed in a basement, with a technical room for operators separated from the main body of the tank for safety reasons [10, 12]. The second example is the concept proposed by Linde [13] for future hydrogen filling stations offering both liquid H_2 and compressed gaseous H_2. Figure 4.6 displays the schematic diagram of the underground liquid H_2 storage concept which was applied in the construction of a hydrogen refuelling station for BMW in Munich in 2007.

The last example, Fig. 4.7, is the concept proposed and developed by Air Products for the Shell Hydrogen refuelling station in Washington DC. The originality

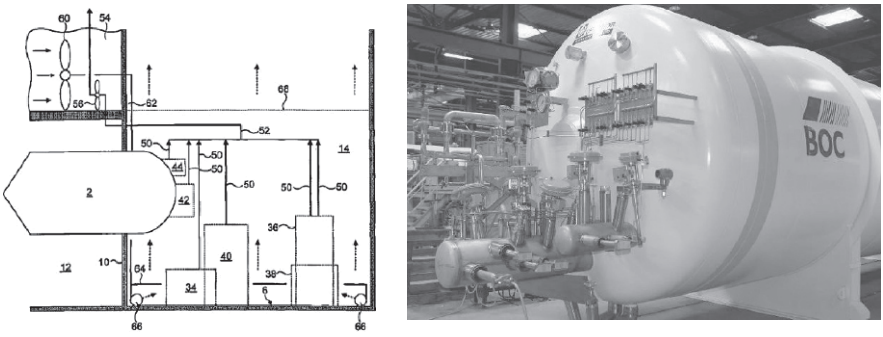

Fig. 4.5 Underground storage of the liquid H_2 tank in the BP hydrogen refuelling station located in London. The picture of the tank is from Cryolor (tank manufacturer, subsidiary of Air Liquide) and the schematic drawing of the installation is taken from [11]

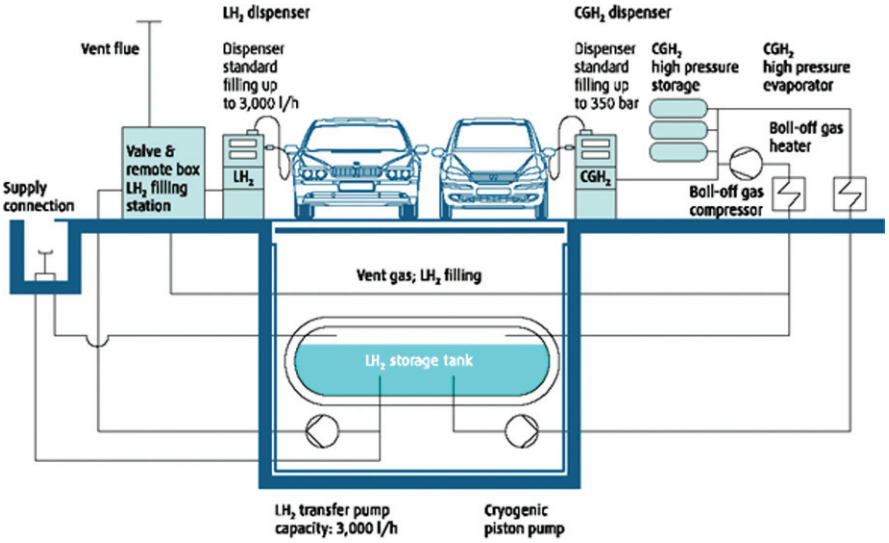

Fig. 4.6 Linde concept for future hydrogen filling stations for GH_2 and LH_2 with underground storage tanks

of this solution is that all connections are accessible at ground level after the tank has been slid vertically into a cylindrical cavity. This concept applies for storage volumes from 1500 up to 9000 gallons (~ 400 up ~ 2400 litres) of LH_2, equivalent to 27–167 kg, or 320–1920 Nm^3 of H_2, and the boil-off rate is less than 3% per day.

Fig. 4.7 Air products underground LH_2 tank installed at the shell hydrogen refuelling station in Washington DC in 2004

4.5 Hydrogen Filling Stations for Vehicles

With respect to the development of hydrogen energy for vehicles, there is a need for new filling stations devoted to large public use and filling procedures adapted to this new market as well as safety issues. Hydrogen fuel for vehicles has to be competitive by offering autonomy and an energy density on board in the same range than the classical fuels. Hydrogen fuel can be stored on board in liquid or gaseous form in light-weight tanks.

Below, an overview of the filling stations will be given, followed by the issues relating to compressed gas hydrogen filling for vehicles.

4.5.1 Overview

Hydrogen refuelling stations have been developed worldwide for demonstration purposes, for example under the CUTE (Clean Urban Transport for Europe) project. In 2007, there are about 180 existing or planned stations in the world (www.h2stations.org). Today, the new projects are more oriented towards infrastructure development, such as the hydrogen "highways" projects in the United States, Canada or Norway. More than half of these stations have on-site hydrogen production and more than one third are based on renewable energy sources, such as wind or photovoltaic energy, to supply an electrolyser or reforming biogas. Most of these stations deliver compressed gas at 35 MPa (350 bar), while some of them have already been upgraded to 70 MPa (700 bar) [1].

4.5.2 High-Pressure Filling

The understanding of filling procedures has become a key issue to achieve 35 and 70 MPa filling of tanks with hydrogen. Such high pressures are needed to achieve a correct energy density on board. In addition, the filling has to be fast enough to be competitive with classical fuels. For public acceptance reasons, the refuelling time target is of great importance and the objective today is to refuel a passenger car in less than four minutes (target for compressed gas refuelling within the European STORHy project) [14].

The thermodynamics of filling have been described [15], but refer to classical filling for industrial gas (metallic tanks, 200 bar, slow or medium-speed fillings). On the other hand, fast filling of type III (fine metallic liner wrapped with fibres) or type IV (fine polymeric liner wrapped with fibres) vessels (more details on these vessels can be found in Chap. 8a of this book) is closer to adiabatic compression because of time reduction and lower thermal conductivity of the walls. The compression effect during filling induces a temperature increase in the tank, which depends on the filling rate, volumes, and thermal properties of the tank walls. In order to reach the targeted mass of hydrogen despite the inherent heating, an overpressure

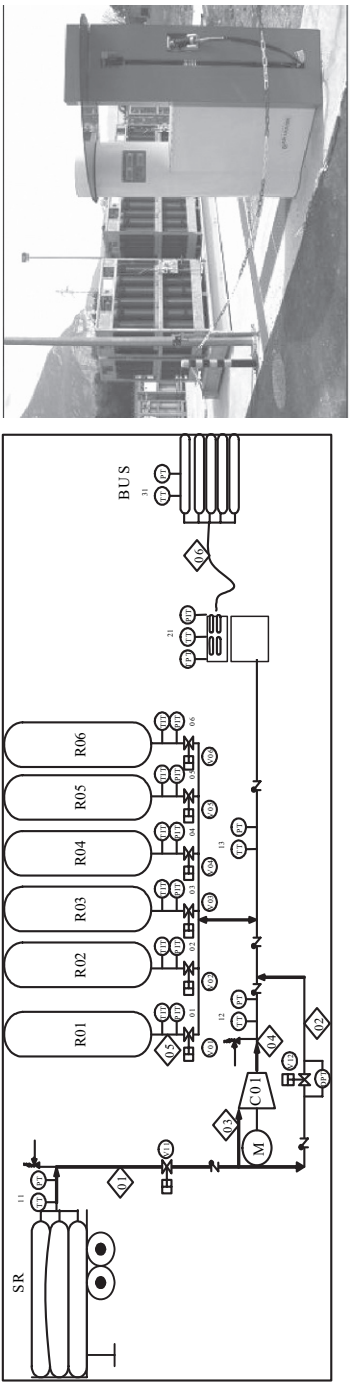

Fig. 4.8 Air Liquide H_2 station diagram

is necessary. However, this overpressure is limited by the mechanical properties of the vessels given by the maximum operating pressure which equals 1.25 times the service pressure.

Hence, three risks can be identified in case of fast filling. These are overheating, overpressure, and overfilling, which consist in filling the tank at low temperature and exposing it to a higher temperature. Hence, filling steps should be controlled appropriately to ensure safety by remaining within the operating window of tanks, namely, −40 to 85°C, and to perform an optimised filling [16, 17].

Air Liquide installed the first H_2 refuelling station in Sassenage, France in 2002. Figure 4.8 displays the schematic diagram of the station. This station is designed to fill three buses per day with compressed hydrogen gas at 350 bar. High-pressure buffers at 420 bar allow for a fast filling of the buses by pressure equilibrium. This station was equipped with six independent buffers which are recompressed by a membrane compressor from a 200 bar tube trailer which supplies hydrogen to the station. Hydrogen is charged through a dispenser developed by AIR LIQUIDE DTA (Advanced Technologies Division) and the transferred mass is controlled by a Coriolis type flow meter. Several pressure and temperature sensors allow for a complete control of the station. Figure 4.9 displays the evolution of several parameters with time during filling at 350 bar. For comparison, the simulated data obtained by using an accurate simulation tool to predict the average gas temperature and the required filling conditions are presented as well. This software was developed to avoid overheating and develop a safe filling procedure (simulation tool developed by Air Liquide [16, 17]. Such predictive algorithm may be an alternative to filling controlled by real-time hydrogen mass management, as the communication between the vehicle and the station is not easy to manage.

Figure 4.10(a) displays the Air Liquide station which has been optimised for 700 bar filling and used for demonstration at the Bibendum challenge in Paris in

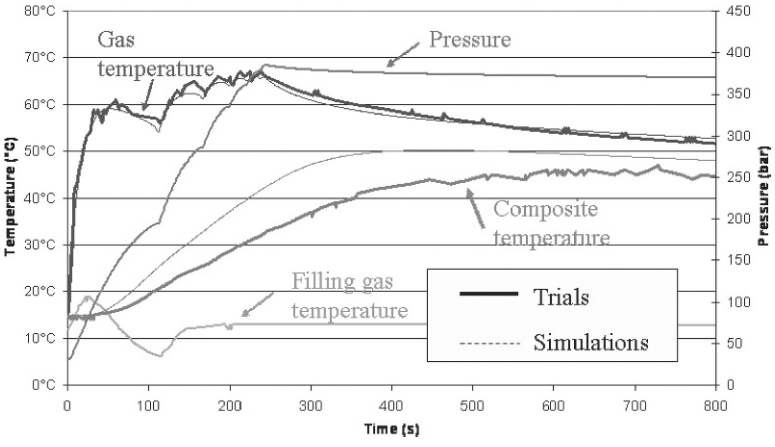

Fig. 4.9 Evolution of gas temperature, pressure, composite temperature (outer layer), and filling gas temperature as a function of time; recorded at the Air Liquide filling station (filling speed 87 bar/min). Comparison between experiment and simulation [17]

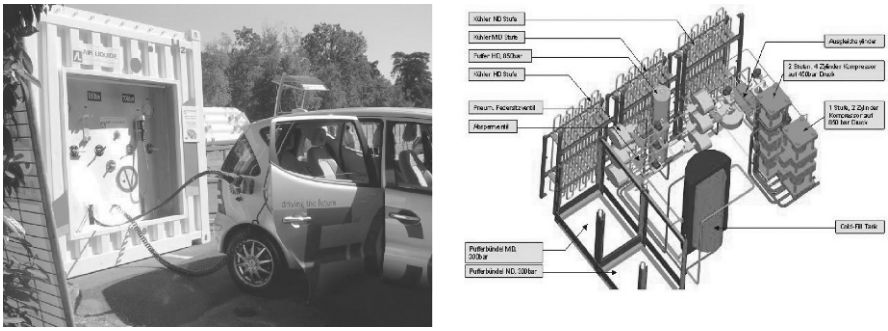

Fig. 4.10 AirLiquide (**a**) and Linde (**b**) 700 bar filling stations

2006. Figure 4.10(b) displays the first working 700 bar station which was designed by Linde at the Opel test centre in Germany for one vehicle per day. The filling scheme in this case includes 2 buffers at 300 bar, a tank at 850 bar, and two hydraulic boosters at 450 and 850 bar. The compressed hydrogen is cooled to −20°C before injection into the vehicle tanks to limit overheating, which is also known as cold filling procedure. More details can be found under the following link (www.linde-gas.com).

The next steps for hydrogen refuelling stations will be to develop filling procedures reliable and compatible with public expectations, namely, fast and safe for a correct energy density on board.

4.6 Conclusion

Most of the technologies for transportation and distribution of gases are already mastered by industrial gas and natural gas companies. Industrial gas companies are used to hydrogen, but mainly for industrial customers, while natural gas companies are used to deliver natural gas both to industries and for individual usage.

Hydrogen energy infrastructure should combine the industrial and individual delivery with safe, cost-effective, and energy-efficient solutions to distribute large quantities of hydrogen for stationary and mobile applications.

In terms of cost, the DOE objective for 2017 sets hydrogen delivery from the point of production to the point of use in vehicles or stationary power units to less than 1 $ per kilogram of hydrogen delivered [18]. In order to fulfil this goal, R&D efforts are still needed to improve performances of pipes, cylinders, storages, and filling stations. An even more important factor is a better understanding of the roadmap for hydrogen energy deployment.

As for any logistic problem, a cost-effective and optimised decision requires a clear definition of timing and quantities in order to connect optimally sources and delivery points. Transient solutions can be achieved with truck delivery for small and medium quantities with some flexibility, but large pipe investments are long-term decisions requiring guarantees of quantities and stability of the demand.

References

1. Perrin J. *Hydrogen distribution infrastructure*. Roads2HyCom WP2 (2006).
2. Suresh B., Schlag S., and Inoguchi Y. *Hydrogen marketing research report*. Chemical Economics Handbook—SRI Consulting, Reference 743.5000 A (2004).
3. Castello P., Tzimas E., Moretto P., and Peteves S. D. *Techno-economic assessment of hydrogen transmission & distribution systems in Europe in the medium and long term*. The Institute for Energy, Petten, European Commission, JRC, Reference EUR 21586 EN (2005).
4. Brass A. M., Chene J., and Coudreuse L. *Fragilisation des aciers par l'hydrogène : étude et prévention. Fragilisation des aciers par l'hydrogène : mécanisme*. Techniques de l'Ingénieur M175 et M176 (2000).
5. Barthelemy H. *Compatibility of metallic materials with hydrogen-Review of the present knowledge*. WHEC (2006).
6. Smith B., Eberle C., Frame B., Blencoe J., Anovitz L., and Mays J. *New materials for hydrogen pipelines*. DOE Hydrogen Program 2005, Progress Report (2005).
7. Perrin J. *On-site storage and distribution: underground hydrogen storage*. Roads2HyCom WP2 (2006).
8. Foh S., Novil M., Rockar E., and Randolph P. *Underground hydrogen storage*. Final Report, Institute of Gas Technology, Chicago, Issued as BNL 51275 (1979).
9. Panfilov M., Gravier G., and Fillacier S. *Underground storage of H_2 and H_2-CO_2-CH_4 mixtures*. Proceedings of the 10th European Conference on the Mathematics of Oil Recovery (ECMOR), Amsterdam (2006).
10. Stone H. B. J., Veldhuis I., and Richardson R. N. *An investigation into large-scale hydrogen storage in the UK*. Proceedings International Hydrogen Energy Congress and Exhibition IHEC (2005).
11. Poillucci G. *Gas tank with protection system for underground installation*. European Patent EP1435481 B1 (2003).
12. Roach J. *Liquefied gas storage installation*. European Patent Application EP1631768 A1 (2004).
13. Trill, R. and Wolf J. *Filling station for hydrogen*. European Patent EP 1360084 B1 (2006).
14. Pregassame S., Barth F., Allidieres L., and Barral K. *Hydrogen refuelling station: filling control protocols development*. WHEC Proceedings (2006).
15. Eriksson R. *AGA AB "Théorie du remplissage-gaz simples" Symposium Bouteilles à gaz*. Industrial Gas Committee (1985).
16. Werlen E., Pisot P., Barral K., and Renault P. *Thermal effects related to H_2 fast filling in high pressure vessels depending on vessels types and filling procedures: modelling, trials and studies*. Proceedings European Energy Conference (2003).
17. Pregassame S., Barral K., Allidieres L., Charbonneau T., and Lacombe Y. *Operation feedback of hydrogen filling station*. Hydrogen and Fuel Cells 2004 Conference and Trade Show (2004).
18. Freedom car and Fuel Partnership *Hydrogen Delivery technology roadmap*. DOE Hydrogen Fuel Cells and Infrastructure Program (2007).

Chapter 5
Fuel Cells

Jens Oluf Jensen and Qingfeng Li

Jens Oluf Jensen
Department of Chemistry, Building, Technical University of Denmark, Lyngby, Denmark, e-mail: joj@kemi.dtu.dk

Qingfeng Li
Department of Chemistry, Building 207, Technical University of Denmark, DK-2800 Lyngby, Denmark, e-mail: lqf@kemi.dtu.dk

A. Léon (ed.), *Hydrogen Technology*,

List of Abbreviations

AC	Alternating current
AFC	Alkaline fuel cell
ATR	Autothermal reforming
DC	Direct current
DMFC	Direct methanol fuel cell
HHV	Higher heating value
ICE	Internal combustion engine
LHV	Lower heating value
MCFC	Molten carbonate fuel cell
MEA	Membrane electrode assembly
OCV	Open circuit voltage
PAFC	Phosphoric acid fuel cell
PBI	Polybenzimidazole
PEMFC	Proton exchange Membrane fuel cell (or simply polymer fuel cell)
PFSA	Perfluorosulphonic acid
POX	Partial oxidation
ppm	Parts per million
PROX	Preferential oxidation
PTFE	Polytetrafluoroethylene (Teflon)
SOFC	Solid oxide fuel cell
SR	Steam reforming
YSZ	Yttria-stabilised zirconia

5.1 Introduction

Fuel cells play a central role in the hydrogen energy concept, namely, as devices which efficiently extract the energy stored in hydrogen in the form of electricity. There are other means for doing that, e.g. via direct combustion in internal combustion engines, but fuel cells have a potential for being more efficient, more silent, and wider scalable. Moreover, fuel cells are not restricted to a future hydrogen society, but can be applied today already when fuelled by natural gas via a reformer or directly in high-temperature cells. Micro fuel cells fuelled by methanol are close to commercialization on the vast market of portable electronics.

The present introduction to fuel cells is by no means comprehensive. First of all, the aim is to provide ground to ease the understanding of the fuel cells' role

in the hydrogen energy systems. A deeper understanding of fuel cells involves a broad range of scientific disciplines like electrochemistry, catalysis, materials science, mechanics, and fluid dynamics. For readers who want to work with or develop fuel cells or components for fuel cells, reference is made to the extensive literature on the topic. Besides the original scientific publications, a large number of monographs are available. A well written introduction addressing a diverse technical audience is "Fuel cell systems explained, 2nd ed." by Larminie & Dicks [1]. For a more detailed treatment, see "Fuel cell handbook" [2]. This recent four-volume work is probably the most comprehensive one on most technical aspects of fuel cells. The latest news and development can be found on the web. Some recognized sites are: "*www.fuelcelltoday.com*", *www.hyweb.de*, and "*www.fuelcells.org*". The latter comprises, among many other things, a list of fuel cell books.

5.2 What is a Fuel Cell?

A fuel cell is an electrochemical cell, i.e. a device in which a chemical process is coupled directly to an electric current. In some cases, the current drives a chemical process, in others, the chemical process creates an electrical current. The best known example of such a cell is a battery. In a battery chemical energy is converted into electrical energy on demand. The fuel cell is doing the same thing, but the fundamental difference is that while all chemical energy is stored in the battery, the energy is supplied continuously to the fuel cell as fuel. This means that a fuel cell, in contrast to a battery, can run infinitely – at least in principle. The cells can be divided into the four categories as shown in Table 5.1.

The conventional pathway for generating electrical energy from a fuel is through combustion, a heat engine and a generator. See Fig. 5.1. In a car or a diesel generator the combustion device and the heat engine are integrated in the same unit (the engine), but in a power plant each conversion step is separate. The fuel cell is able to convert the chemical energy of the fuel directly into electrical energy. This is one of the principle advantages of the fuel cell. In both cases, however, a significant amount of the energy is converted into waste heat.

Many chemical substances can serve as fuel. In all cases energy is released when they react with oxygen from the air. In all these processes the fuel is oxidized, i.e. electrons are transferred to oxygen. Let us consider the simplest fuel (which also is the easiest converted in a fuel cell), namely, hydrogen. When hydrogen is combusted

Table 5.1 The four categories of electrochemical cells

	Galvanic cell (Chemistry makes electricity)	**Electrolysis cell** (Electricity makes chemistry)
Internal reactants	Battery	Rechargeable battery
External reactants	Fuel cell	Electrolyser

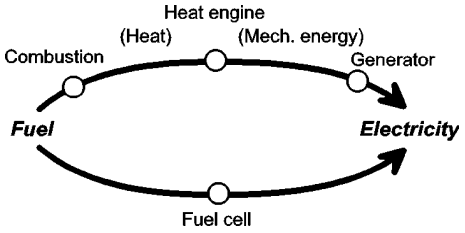

Fig. 5.1 The two pathways for the production of electrical power from a fuel

with oxygen, water is formed, and during the reaction, one electron is transferred from each hydrogen atom to the oxygen atom. The energy state of the electron is lower in oxygen and the energy difference is released as heat. The reaction can be understood as visualised in the reactions 1–3, although this is mechanistically incorrect.

$$H_2 \rightarrow 2H^+ + 2e^- \tag{5.1}$$

$$\frac{1}{2}O_2 + 2e^- \rightarrow O^{2-} \tag{5.2}$$

$$2H^+ + O^{2-} \rightarrow H_2O \tag{5.3}$$

The overall process is

$$H_2 + \frac{1}{2}O_2 = H_2O + \text{heat} \tag{5.4}$$

The trick in fuel cells is to make the electron work for us on the way to the oxygen. To do this, the reduction process (electron donation by hydrogen) and the oxidation process (electron reception by oxygen) must be separated. The two processes are restricted to take place on two separate electrodes. On one side, the negative electrode is located, where hydrogen is oxidized and on the other side is the positive electrode, where oxygen is reduced. The electrons released from hydrogen can be led away to an external electrical circuit, in which they will perform electrical work before they are returned to oxygen via the other electrode. It is a general convention in electrochemistry that the electrode at which an oxidation process takes place is named the anode. The cathode is the other electrode, where the reduction process takes place.

In a first approach, the system should now work, but when the electrodes are separated, the end product water cannot be formed. Instead, hydrogen ions H^+ (protons) are accumulated on the negative electrode and oxygen ions O^{2-} (oxide ions) on the positive electrode. The accumulated charge builds up a potential that immediately stops the process. To overcome this fundamental problem, a charge balance must be maintained and this is done by an electrolyte placed in the gap between the electrodes. An electrolyte is an ion conductor, i.e. a medium that allows for the transport of ions. In the hydrogen/oxygen cell the electrolyte can be a proton conductor or oxide ion conductor. In both cases, the ions on the electrodes can combine and form water. This can also be understood as the closing of the electrical circuit. The full cycle with a proton-conducting electrolyte is sketched in Fig. 5.2. It is crucial that the electrolyte is a good ion conductor and an insulator when it comes to electrons to avoid a short cell.

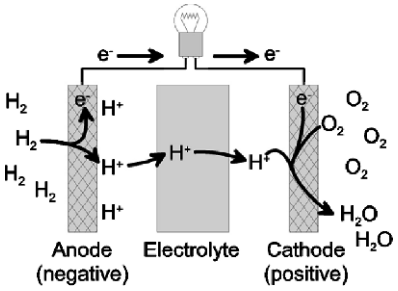

Fig. 5.2 Schematic representation of a fuel cell with a proton-conducting electrolyte

Typical classical electrolytes are aqueous solutions of salts, acids or bases, but when it comes to fuel cells, solid ion conductors like special polymers or ion-conducting ceramics also are among the most successful electrolytes. Different electrolytes commonly used in fuel cells will be described in the paragraphs on fuel cell types below.

5.3 Energy Conversion in a Fuel Cell

5.3.1 The Energies Involved

The energy content of a fuel is normally defined as the higher heating value (HHV), i.e. the full amount of heat that is released, if the fuel is combusted with oxygen. Reactants and products are to be in their standard state at 25°C and 1bar. For hydrogen the reaction is

$$H_2(g) + \frac{1}{2}O_2(g) = H_2O(l) \tag{5.5}$$

The product H_2O is in the liquid state, but in many cases, it is more relevant to consider water in its vapour (gaseous) state. Therefore, the lower heating value (LHV) is defined similarly, but with the difference that water is in the vapour state. All species are still at 25°C and 1 bar (water as a vapour under these conditions is a hypothetical state). The lower heating value is smaller by the heat of condensation of the water compared to the higher heating value. The values for hydrogen can be found in Table 5.2.

Table 5.2 Higher and lower heating values (ΔH) of hydrogen in its standard state, i.e. at 25°C, 1 bar. Free energy of combustion (ΔG) is included

Hydrogen (25°C, 1 bar)	Higher heating values (HHV)	Lower heating values (LHV)
Enthalpy of combustion (ΔH)	−285.8 kJ/mol H_2	−241.8 kJ/mol H_2
Free energy of combustion (ΔG)	−237.1 kJ/mol H_2	−228.6 kJ/mol H_2

The enthalpy (ΔH) is the maximum heat that can be released from the process and this is the reason behind the name "heating value". The maximum work (or electrical energy) that can be extracted is the Gibbs free energy (ΔG). ΔG, the maximum work, determines theoretical reversible cell voltage, E_{rev}, because the voltage is a measure of the energy at which the current is delivered. Like ΔG is the maximum work, E_{rev} is the maximum cell voltage of a fuel cell. It can be calculated by

$$E_{rev}(T) = \frac{-\Delta G(T)}{nF} \tag{5.6}$$

where F is Faraday's constant, the molar charge (95 485 C/mol), and n the number of electrons transferred. For a hydrogen-powered fuel cell at 25°C, the reversible cell voltage is 1.23 V. For hydrogen, ΔG is smaller than ΔH and while ΔH is almost independent of temperature, ΔG decreases with temperature as can be seen in Fig. 5.3.

5.3.2 The Conversion Efficiency

The maximum electrical energy available from a hydrogen-powered fuel cell is thus ΔG and the maximum total energy converted is ΔH. Consequently, the maximum efficiency, $\eta_{\max}$, is

$$\eta_{\max} = \frac{\Delta G(T)}{\Delta H(25°C)} \tag{5.7}$$

As ΔG decreases with temperature, while ΔH is practically constant (Fig. 5.3), it is clear that the maximum efficiency decreases with temperature. As a first approach, this seems to be a strong argument against fuel cells with high working temperature, but in reality fuel cells are not able to perform with maximum efficiency. What matter more are the different losses that are always experienced with real fuel cells.

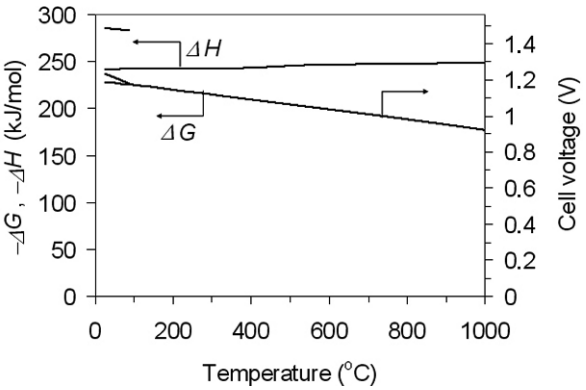

Fig. 5.3 Key energies and the calculated cell voltage as functions of temperature. The enthalpy (ΔH) and the free energy (ΔG) of combustion of hydrogen are plotted on the primary y-axis. Note that both curves split below 100°C to reflect water formation in both liquid and gaseous states. On the secondary y-axis, the calculated cell voltage is plotted (proportional to ΔG)

These losses (described in Sect. 5.4 The Cell Performance) are generally reduced at high temperatures and the net effect instead is a higher overall efficiency.

It is often stressed that fuel cells are more efficient than heat engines like internal combustion engines. Any device that produces mechanical work (or electrical work) from the heat from a fuel is limited by Carnot's law which states that the maximum efficiency, $\eta_{\max}$, is

$$\eta_{Max} = \frac{T_h - T_l}{T_h} \tag{5.8}$$

where T_h is the high temperature at which heat is available and T_l is the low temperature (e.g. ambient temperature or cooling water). The rationale behind this law is entropy preservation for the flow of heat from a high temperature to a low temperature. It is well known that the total entropy must always increase for any process to take place. In the ultimate (hypothetical) case, entropy is just preserved. In the case of a fuel cell, entropy preservation (practically an increase) is also dictated, but not coupled to heat flows, and the Carnot limitation therefore does not apply to fuel cells. Instead, the entropy restriction is introduced via the general relation between ΔH and ΔG:

$$\Delta H = \Delta G + T\Delta S \tag{5.9}$$

where ΔS is the entropy change of the process.

The Carnot efficiencies based on selected T_l are plotted in Fig. 5.4 together with fuel cell efficiencies. It can be seen that the fuel cells' maximum efficiency crosses the Carnot efficiency at high temperatures depending on the T_l chosen. However, this should not lead to strong conclusions, as none of the systems attains its maximum efficiency.

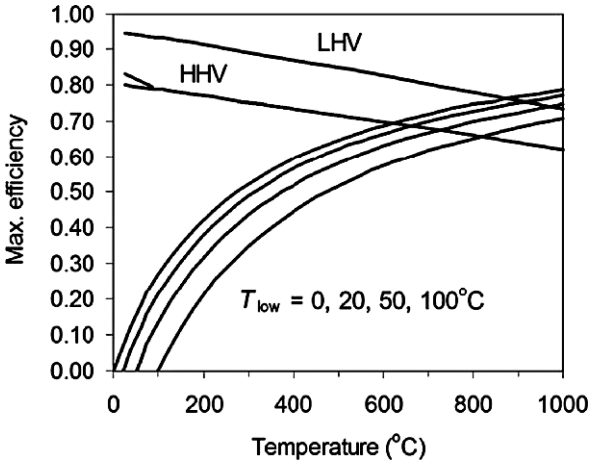

Fig. 5.4 The maximum theoretical electrical efficiency as a function of the working temperature. The curves' labels HHV and LHV are for a fuel cell with reference to the higher and lower heating values, respectively. The rainbow-shaped curves are Carnot efficiencies for any heat engine with the higher temperature, T_h, on the primary axis and the lower temperature, T_l, indicated as 0, 20, 50, and 100°C in the same order. Unit efficiency corresponds to 100%

The performance of any fuel cell is visualised by the characteristic polarisation curve that is a plot of the cell voltage as a function of the load, i.e. the current or the current density. The latter is the cell current divided by the electrode cell area to be more general and to facilitate comparison of cells of different size.

Polarisation curves may be very different, but they normally have the same characteristic shape as displayed in Fig. 5.5. The reason for this S-shape will be explained in Sect. 5.4 The cell performance. Here, it is used to show that the fuel cell conversion efficiency can be read directly from it. The product of corresponding values of voltage and current (or current density) is the electrical power (or power density), i.e. energy per second. The maximum voltage calculated from $\Delta G(T)$ (equation (5.6)) is the upper limit for any polarisation curve. However, as the HHV is generally used as the reference for the energy content of a fuel, an efficiency calculation should be based on the HHV. Even though the full HHV cannot be converted into electricity, a hypothetical cell voltage can be calculated from equation (5.6), replacing $\Delta G(T)$ by ΔH (the HHV). This gives 1.48 V (if LHV is used, the voltage is 1.25 V) and this voltage is named the thermoneutral voltage, because a cell operating at this voltage (not possible for a fuel cell) would convert all fuel energy into electricity without any heat formation*. At this hypothetical voltage, the cell would perform at 100% electrical efficiency with reference to the HHV, as all fuel energy is harvested as electricity.

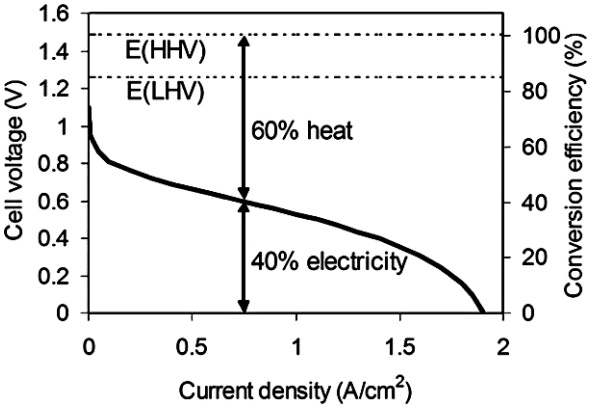

Fig. 5.5 A polarisation curve of a fuel cell (solid curve). The thermoneutral voltages based on either HHV or LHV (both hypothetical) are plotted as dotted lines. An arbitrarily working point is chosen at about 0.6 V and 0.75 A/cm2. The voltage corresponds to 40% of thermoneutral voltage and the remaining 60% are released as heat. The electrical conversion efficiency is thus 40%. If a similar calculation is done based on the LHV, then the conversion efficiency will be 48%

*The term "thermoneutral potential" is used more often in relation with electrolysers, because they operate at voltages higher than 1.23 V and therefore also at 1.48 V. Electrolysers are fundamentally endothermic (heat-consuming) and at 1.48 V, the energy corresponding to the difference in delivering the current at 1.23 and 1.48 V is converted into heat through irreversible losses. This amount just fits the heat demand from the cell.

The proportionality between cell voltage and ΔH or ΔG makes it straightforward to read the conversion efficiency directly from the polarisation curve. This is done on the secondary Y-axis in Fig. 5.5. It can be seen that as the cell voltage decreases with increasing load, the conversion efficiency decreases following the same pattern. This is a fundamental difference to an internal combustion engine (ICE) which has its maximum efficiency at a rather high load. A practical consequence of this is that a fuel cell vehicle is superior to an ICE vehicle in city traffic with limited load, while on a highway, the difference in efficiency is not that pronounced.

It must be stressed that the practical efficiency depends on the entire system. Parasitic losses are introduced by the components surrounding the fuel cell, the "balance of plant". Such components are air compressors, blowers, power converters, pumps in the heat management circuit, control devices, etc.

Some of the energy dissipated as heat can in some cases be reclaimed via a heat engine. This is only practical for high-temperature fuel cells like MCFC and SOFC, and this process is Carnot limited. Intuitively, it may appear like the fuel energy is extracted twice, but in fact, only a fraction (around one half) of the energy is converted into heat and subsequently passed through the heat engine. Moreover, some of the high temperature heat will be consumed for heating air and fuel. Anyway, by combining the two processes, a higher overall efficiency can be obtained. The maximum total conversion efficiency of such a combined process can also be derived from Fig. 5.4. An SOFC working at 800°C has a maximum fuel cell efficiency of about 65%. The heat (35%) is converted in the heat engine with a maximum efficiency of 73% (lower temperature chosen: 25°C) and the overall maximum efficiency is then $65\% + 0.73 \cdot 35\% = 90\%$. All losses as well as the heat for gas preheating are omitted in the calculation.

5.4 The Cell Performance

In order to understand the performance characteristics of a fuel cell, some electrochemical principles are useful. Electrochemistry deals with oxidation and reduction. When a species increases its oxidation state, it is oxidized and when it reduces its oxidation state, it is reduced. An electrode at which an oxidation takes place is called an anode, and if reduction takes place, it is a cathode. Similarly, any electrochemical oxidation process, like hydrogen oxidation, to positive hydrogen ions (protons) is called an anodic process (anode, oxidation). The reverse process (reduction of protons to hydrogen) is called cathodic (cathode, reduction). In a fuel cell the hydrogen electrode is the anode and the air electrode is the cathode, as shown in Fig. 5.2.

The shape of the polarisation curve (the current – potential curve) is well understood and a lot of information can be derived from it. In electrochemistry the term "polarisation" means that the electrode(s) changes its potential as a function of the current. Several different mechanisms account for parts of the conversion losses in the cells and each results in a so-called overpotential (or overvoltage). The sum

of these overpotentials (which might be either positive or negative) is the overall overvoltage at any current density that can be read from the polarisation curve, i.e. as the potential difference between the cell voltage and the reversible voltage (the latter: 1.23 V at 25°C). Despite the fact that the actual cell voltage is lowered the difference to the reversible potential is still called an overpotential.

The polarisation curve begins at the open circuit voltage (OCV, the voltage measured with zero current), which according to theory so far, should be the reversible voltage or potential, i.e. 1.23 V at 25°C*, and slightly lower at higher temperatures. The OCV is sometimes said to be the same as the reversible potential, but this is not correct. The reversible potential is established from thermodynamics, while the OCV is what is actually measured with zero current in the external circuit. The reversible potential of an electrode is determined by the *Nernst* equation which can be found in many textbooks. The reversible voltage is the difference between the two reversible electrode potentials.

The general experience is that OCV is somewhat lower than the reversible potential. Several factors influence this deviation. The electrode (especially the air electrode) may not be in total equilibrium and side reactions in the form of corrosion processes or reactions of minor impurities may result in a so-called mixed potential. The side reaction may also be due to trace amounts of reactants from the other electrode diffusing through the electrolyte to react on the opposite electrode. This phenomenon is called crossover and especially pronounced for direct methanol fuel cells. The polarisation curve is very steep just after OCV, and a somewhat simplified explanation of the voltage depression is that oxygen at the cathode (or hydrogen at the anode) is converted to a small extent just enough to balance the current from the parasitic processes. This way, the electrode is not effectively at zero current and the OCV attains a value as if it was measured a bit further down the polarisation curve. The OCV depression has no practical influence on the cell performance at practical current densities, but if it is much larger than expected for the fuel cell system studied, it can be taken as an indication of internal leaking causing an unnaturally high crossover rate.

5.4.1 Activation Losses

The polarisation curve can be split up into 3 main parts, each explained by individual mechanisms. See a, b, and c in Fig. 5.6. The first one (a) is the initially strongly curved part which reflects losses in the electrochemical process. It is called *activation losses* or *charge transfer losses*. Activation losses (activation polarisation) appear on both electrodes and are the sum of the two contributions that can be seen on the overall polarisation curve of the cell. If the contribution from one cell alone shall be extracted, a reference electrode of known fixed potential must be inserted

*The reversible voltage of 1.23 V is exact, provided that all reactants and products (H_2, O_2, and H_2O) are in their standard state each with unit activity. This means that the gases are at partial pressures of 1 bar and that water is liquid.

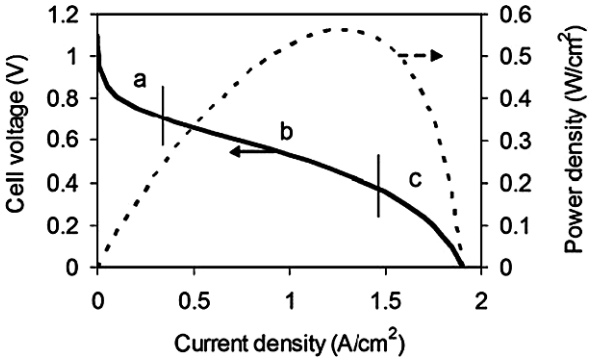

Fig. 5.6 The same polarisation curve as in Fig. 5.5 (solid line). Three overvoltage regimes are labelled: (**a**) the charge transfer-controlled part, (**b**) the ohmic part, and (**c**) the mass transport-limited part. The dotted curve is the power density

into the system. This is standard in electrochemical experiments in the laboratory, but references are normally not applied in full-size fuel cells. Generally, the major fraction of the activation losses (especially in low-temperature cells) is attributed to the cathode (the oxygen electrode). This is because the oxygen reduction process is much slower than the hydrogen oxidation process.

A catalyst always enhances the charge transfer process. Otherwise, the performance would be extremely poor. Catalytic efficiency is quantified by the *exchange current density*, i_0. In equilibrium at the reversible potential, no net current is measured, but in dynamic equilibrium the two opposite electrochemical processes occur simultaneously at equal rates (hydrogen oxidation and proton reduction in case of the hydrogen electrode). The size of each of these currents is the exchange current. A good electrode has a high exchange current density. When normalised to current *density*, the true catalyst area or the geometrical electrode area can be chosen. The catalyst area is more fundamental, but rather ill-defined and rarely known. Instead, the geometrical electrode area is normally used. This is also most practical, when the exchange current density is linked to the current density of the cell at load. The exchange current density depends on several factors, like the catalyst material, the available and active catalyst surface area, the electrode morphology, and contaminations on the catalyst surface (poisoning).

The activation polarisation of an individual electrode is described by the *Butler-Volmer* equation

$$i = i_0 \left[\exp\left(\frac{-\alpha n F}{RT} \Delta E_{\text{act}} \right) - \exp\left(\frac{(1-\alpha) n F}{RT} \Delta E_{\text{act}} \right) \right] \tag{5.10}$$

where i = current density, i_0 = exchange current density, α = charge transfer coefficient, n = no. of electrons (= 2 for di-hydrogen, H_2), F = Faraday's constant (the molar charge = 96485 C/mol), ΔE_{act} = polarisation or activation overvoltage, R = the gas constant (8.314 J/molK), and T = absolute temperature (K). The charge

transfer coefficient, α, is a dimensionless quantity that will be explained later. The value typically is close to 0.5.

The expression (5.10) is exponential with i_0 as the pre-factor. At the reversible potential of the electrode, the activation overvoltage, ΔE_{act}, is zero and both exponential functions are unity corresponding to both anodic and cathodic currents of the size of i_0. The total current density, i, is then zero.

Let us look at the negative electrode of the fuel cell (the anode, hydrogen electrode). The first exponential function describes the cathodic reaction (reduction, i.e. $2H^+ + 2e^- = H_2$) and the second exponential function describes the anodic reaction (oxidation, e.g. $H_2 = 2H^+ + 2e^-$). When the electrode is polarised with a positive overpotential, i.e. to a higher potential, the first exponential function becomes smaller and loses significance, while the second exponential function increases and becomes dominant. The net current is negative (electrons are "produced" at the electrode and sent out through the wire) and it is an anodic current (the electrode process is fuel oxidation). This is actually what happens when the cell is working.

It is important to notice that both the anodic and cathodic processes in equation (5.10) take place at the same electrode. In the examples given above, the hydrogen electrode was chosen. At the air electrode, analogue cathodic (oxygen reduction) and anodic (oxide oxidation) reactions take place, and equation (5.10) can be applied in the same form for the positive air electrode. In this case, the first exponential function prevails when the electrode is polarised negatively. The current is then positive and electrons are consumed. It is a cathodic current originating from oxygen reduction at the electrode. All together, the potentials of the two electrodes move closer to each other and, thus, the overall cell voltage becomes smaller than the reversible voltage.

The *charge transfer coefficient*, α, is also called the *symmetry factor* for the reasons given below. When an electrode is polarised positively ($\eta > 0$), the oxidation process requires less activation energy to proceed. Consequently, the anodic current will increase as compared to the exchange current, and the second exponential of equation (5.10) increases. At the same time the cathodic current represented by the first exponential decreases. The physical reason in brief is that for this reaction, the activation energy increases, leading to a lower rate of the cathodic current. The symmetry factor, α, describes how the effect of a polarisation is divided into contributions to the anodic and the cathodic current, respectively (one increasing, one decreasing). The value of α must be between 0 and 1, and it is often close to 0.5.

In some literature the sign convention is different and the Butler-Volmer expression is written as

$$i = i_0 \left[\exp\left(\frac{\alpha n F}{RT} \Delta E_{act} \right) - \exp\left(\frac{-(1-\alpha) n F}{RT} \Delta E_{act} \right) \right] \tag{5.10a}$$

i.e. with opposite signs inside the exponentials. This way, an anodic current becomes positive and cathodic negative. It is just a matter of definition. However, anodic always means oxidative. In this context, only the form (5.10) of the Butler-Volmer equation will be applied.

In the Butler-Volmer equation the current is a function of voltage. For the polarisation curve, it is convenient the other way around. To be able to find the reverse function $\eta(i)$, it is easiest to look at the cases where either the anodic or the cathodic current dominates. This is when $|i| >> i_0$, practically when $i > 10\,\mathrm{mA/cm^2}$ (geometric area). In case of a cathodic net current, the Butler-Volmer equation can be approximated as

$$i = i_0 \exp\left(\frac{-\alpha n F}{RT}\Delta E_{\mathrm{act}}\right) \tag{5.11}$$

which can be rearranged into

$$\Delta E_{\mathrm{act}} = -\frac{RT}{\alpha n F}\ln\left(\frac{i}{i_0}\right) \text{ (cathodic)} \tag{5.12}$$

The assumed cathodic current is positive and it is evident from (5.12), that it results in a negative overvoltage, i.e. if we use this model on a fuel cell's cathode, a lowering of the electrode potential is expected.

This was for the cathodic current of an electrode. Similarly, the anodic overvoltage of an electrode is

$$\Delta E_{\mathrm{act}} = \frac{RT}{(1-\alpha)nF}\ln\left(\frac{-i}{i_0}\right) \tag{5.13}$$

The anodic current is negative and results in a positive overvoltage. Applied to a fuel cell, it brings the anode potential up or closer to the cathode potential, i.e. the cell voltage decreases.

So far, a single electrode has been treated. When looking at the whole fuel cell, the net current is always anodic at the anode and cathodic at the cathode. The current which must be always the same at both electrodes is now defined as either negative or positive depending on the electrode considered. This is awkward when looking at the whole cell, and in this case, the current will be defined as positive throughout the cell. With a positive current, the sign of i in equation (5.13) must change to positive:

$$\Delta E_{\mathrm{act}} = \frac{RT}{(1-\alpha)nF}\ln\left(\frac{i}{i_0}\right) \text{ (anodic)} \tag{5.14}$$

In the fuel cell the total activation overvoltage is the sum of the cathodic and anodic contributions, i.e. the equations (5.12) and (5.14). Note that all symbols in (5.12) refer to values at the cathode, while all symbols in (5.14) refer to values at the anode. As both expressions have the same logarithmic form, they can, with reasonable approximation, be merged to one as:

$$\Delta E_{\mathrm{act}} = \frac{RT}{\alpha n F}\ln\left(\frac{i}{i_0}\right) \text{ (the cell)} \tag{5.15}$$

Note that in (5.15) the values of α and i_0 differ from those in equation (5.12) and (5.14). α will still be close to 0.5 and i_0 will be close to the smaller of the two i_0 values. Note also that (5.15) is only valid for $|i| >> i_0$.

5.4.2 Ohmic Losses

The next part of the polarisation curve in Fig. 5.6 is close to linear. The activation overvoltage is only changing slightly here and the major contribution is the Ohmic resistance in the system. Wherever a current flows – electric or ionic – a proportional voltage drop is the consequence. It simply follows Ohm's law like any wire or resistor. The main contribution to Ohmic resistance normally comes from the electrolyte, and the slope of the linear part of the polarisation curve can give a good estimate of the electrolyte resistance (units: Volt/Ampere = Ohm). Like the current, Ohmic resistance can also be normalised to the areas as *area-specific resistance* (not resistance density). To keep the Ohmic resistance low, a thin electrolyte is desired. However, it is a trade-off between resistance on one side and mechanical stability and durability on the other. The ohmic loss, E_r, is

$$\Delta E_r = I \cdot R = i \cdot r \tag{5.16}$$

where $R(\Omega)$ is the total resistance and r is the area-specific resistance (Ωcm^2).

5.4.3 Mass Transport Losses

The third regime begins, where the curve in Fig. 5.6 bends downwards. Here, the rapid voltage decay is a result of limited mass transport. The reactants simply cannot reach the electrode fast enough to keep up the reaction. The catalyst is starved and "sees" only the reactants at partial pressures that are smaller by orders of magnitude than during low current densities. Moreover, the product is similarly accumulated and both facts drive the reverse reaction working against the desired one. The result is a steep voltage drop as a function of the current density. In extreme cases, the cell voltage may fall below zero and the cell is said to be reversed. Actually, the process is not reversed before the voltage passes – 1.23 V, which is needed for the reverse process, namely, electrolytic splitting of water. The term "cell reversal" is thus meant for the change of polarity, and it may be harmful to many fuel cells. It can be avoided easily in single cells by a proper voltage control. In stacks, however, where many cells are connected in series, the other cells can easily force the current through the malfunctioning cell without any clear impacts on the overall voltage. The best way to avoid cell reversal in stacks is to keep track of the individual cell voltages. A typical reason for cell reversal in low-temperature cells is that water is condensed in some gas channels, thus blocking the mass transport.

As the mass transport limitation depends highly on electrode morphology (thickness, porosity, pore sizes, resistance to flooding, etc.), it is difficult to develop a simple general model like for charge transfer and ohmic resistance. Instead, empirical or semi-empirical expressions are often used. An example is given in equation (5.16), where ΔE_{mt} is the overvoltage resulting from the mass transport limitation.

$$\Delta E_{\mathrm{mt}} = -\frac{RT}{nF}\ln\left(1-\frac{i}{i_l}\right) \tag{5.17}$$

i_l is the limiting current density, i.e. the largest current possible in the system determined by the highest possible transport rates. The term is obviously insignificant for current densities much smaller than the limiting current density. As the limiting current density is approached, this negative contribution to the polarisation curve increases fast. Strictly speaking, equation (5.17) should be set up for each electrode, but in practice, the one with the smallest i_l will dominate.

All contributions can now be merged to one equation (5.18). With suitable values, it describes a polarisation curve with a shape similar to the ones in Figs. 5.5 and 5.6.

$$\begin{aligned} E &= E_{\mathrm{rev}} - \Delta E_{\mathrm{act}} - E_r - E_{\mathrm{mt}} \\ &= E_{\mathrm{rev}} - \frac{RT}{\alpha nF}\ln\left(\frac{i}{i_0}\right) - ir - \frac{RT}{nF}\ln\left(1-\frac{i}{i_l}\right) \end{aligned} \tag{5.18}$$

The physical consequence of the overvoltages described above is that part of the fuel energy is converted into heat. This heat is shown for an arbitrary working point in Fig. 5.5.

5.5 The Construction and System

5.5.1 Single Cells and Stacks

The single cell is the smallest operational unit. It consists of electrodes with an electrolyte in between as already shown in Fig. 5.2. The electrolyte may either be a solid ion conductor or a liquid kept in place inside an inert matrix or a similar physical separator to avoid a short circuit. The electrodes are built of different layers with different functions. Figure 5.7 shows the principle of a typical electrode construction. The electrode is based on a macroporous substrate which provides the mechanical strength. The whole electrode is porous to allow the hydrogen or oxygen to reach the catalysts near the electrolyte. The catalyst layer is between the substrate and the electrolyte. It is microporous in order to form as many three-phase areas as possible. The three-phase area is where the gas phase, the electrolyte, and the electrode (with the catalyst) meet. All these phases are indispensable for carrying out the reaction, as gases, ions, and electrons take part. Often, a microporous layer forms the transition between the macroporous substrate and the catalyst layer. The electrode serves several purposes apart from keeping the catalyst in place. It must be electronically conducting to provide the pathway for the electrons from the process. Similarly, it must remove the process heat which is mostly produced at the catalyst (activation and mass transport losses) or in the electrolyte (Ohmic loss). The strongest electrode with the best conductance for both electrons and heat is obtained with a rather dense structure, but the requirement for easy gas permeation calls for a structure as

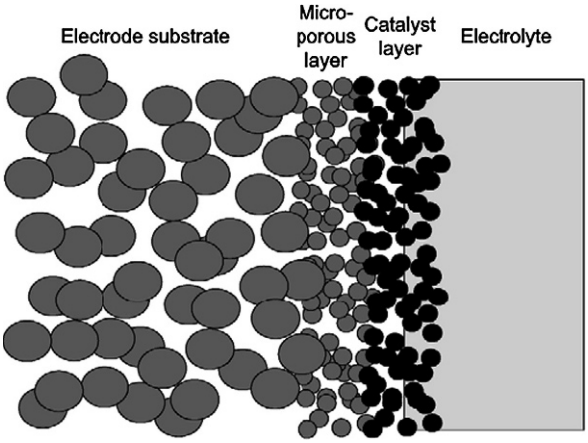

Fig. 5.7 Cross-section of a fuel cell electrode in contact with the electrolyte. On the right side of the electrolyte, the other electrode is placed as a mirror image of the one displayed

open as possible. Moreover, in case of a liquid or liquid-containing electrolyte, the different layers need to interact differently with the electrolyte. The catalyst layer must be hydrophilic to stay in good contact with the electrolyte, while the layers behind must be hydrophobic to avoid leaching out of the electrolyte. For cells working below the boiling point of water, the hydrophobic layers also help prevent accumulation of liquid water, which might block the pores. It should now be obvious that the electrodes are very sophisticated and their successful manufacture requires skills and experience.

Before the cell can work, proper gas channels must be fitted. Figure 5.8 shows a single cell with gas channel plates. In most cases, both fuel and air are led to the electrodes via such gas channels which also provide a pathway out for the produced water.

For most applications, the available voltage of 0.5–0.7 V is not practical. In addition, optional power electronics used to stabilise or convert the voltage are not very

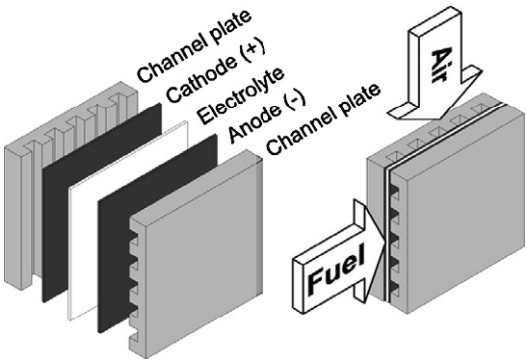

Fig. 5.8 The anatomy of a single cell with gas channels

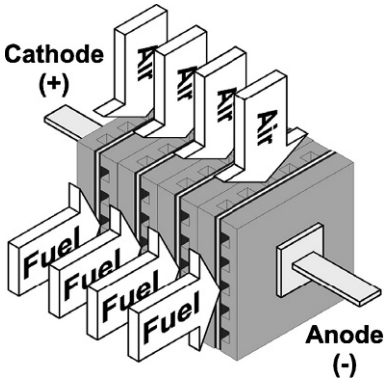

Fig. 5.9 A fuel cell stack of four cells

efficient at voltages below 1 V. Therefore, many cells are coupled in series to form a fuel cell stack with a higher overall voltage. Another advantage is that a more compact construction is obtained, if a number of flat cells are placed on top of each other. This is visualised in Fig. 5.9. The channel plates of two adjacent cells are generally manufactured as one unit, called a bipolar plate, because it connects to a positive and a negative electrode at the same time. Another name for the bipolar plate is *interconnect*.

In the figure the gas manifolds are missing. They can either be external or internal. External manifolds are clamped on the stack sides, while internal manifolds are integrated in the bipolar plates. It can be imagined that if the bipolar plates in Fig. 5.9 are slightly larger than the electrodes, gas manifolds can be built in with common channels along the stacking direction leading to tube connections in the end plates which close the stack.

5.5.2 Fuel Processing

The ultimate fuel for any fuel cell is pure hydrogen. With hydrogen the best performance and fuel utilisation is obtained. However, due to the lack of a hydrogen infrastructure and in some cases impractical storage techniques, other fuels must be considered in the near and medium terms. A whole range of fuels, including natural gas, methanol, ethanol, gasoline, and diesel, is of interest, as they can be converted into hydrogen via a reforming process. There are different ways of doing this, but the general idea is that the hydrogen in the organic fuel is extracted by reaction with water. The carbon forms carbon dioxide.

The most fundamental reforming technique is *steam reforming* (SR). With methane, for example, hydrogen formation proceeds in two steps, of which the first is the *steam reforming reaction*

$$CH_4 + H_2O \rightarrow CO + 3H_2 \tag{5.19}$$

This process is followed by the *water gas shift reaction*, or simply the *shift reaction*

$$CO + H_2O \rightarrow CO_2 + H_2 \tag{5.20}$$

The total reaction is

$$CH_4 + 2H_2O \rightarrow CO_2 + 4H_2 \tag{5.21}$$

Steam reforming is an endothermic (heat-consuming) process (for methane the standard enthalpy of the reaction is +206 kJ/mol). Therefore, the equilibrium is shifted in favour of hydrogen formation when the temperature is increased. Methane reforming is carried out at temperatures of 600–900°C. Also for kinetic reasons, a high temperature is necessary. The shift reaction is an exothermic (heat-producing) process and, thus, low temperatures are desired here to convert as much of the CO as possible. The kinetics is the limiting factor here and normally the process is too slow at temperatures below 200°C. Actually, two shift reactors are often operated in series; a high-temperature shift reactor at about 400°C with a high conversion rate, but with incomplete conversion, followed by a low-temperature shift reactor at 200°C, at which more CO is converted, but at a slower rate.

Two alternative reforming techniques are *partial oxidation* (POX) and *autothermal reforming* (ATR). The challenge to overcome in any case is to supply the heat for the process. In steam reforming the heat is supplied from outside, typically by burning fuel. In the other processes the fuel is burned inside the reaction chamber of the reformer and, thus, the heat evolves where it is needed. In partial oxidation a controlled amount of oxygen (or air) is supplied with the fuel and a partial combustion takes place:

$$CH_4 + 1/2O_2 \rightarrow CO + H_2$$

The partial combustion makes the process exothermic and is often carried out at 1200–1500°C. At these temperatures, a catalyst is not necessary and the resulting advantage is sulphur tolerance. Partial oxidation can, of course, also be carried out at lower temperatures with a catalyst.

Autothermal reforming is like a combination of steam reforming and partial oxidation. Oxygen and water are supplied with the fuel, but the amount of oxygen is only just enough to produce the required amount of heat for a simultaneous steam reforming process.

One or more shift reactors follow both reforming processes and a strict control of the oxygen addition is crucial to avoid overheating which can damage the catalyst or other components.

It is important to convert as much CO as possible, not only to maximise the hydrogen yield, but first of all, because CO is a poison of the catalyst in low-temperature fuel cells. CO adsorbs to catalyst sites in competition with hydrogen. At low temperatures, CO binds strongly to the catalyst, leaving a severely reduced catalyst surface for hydrogen. For polymer fuel cells CO concentrations as low as 20 ppm affect the performance.

The CO concentration after the low-temperature shift reaction is several thousands of ppm, so further CO removal is mandatory. A number of techniques shall be mentioned here without detailed explanation: (1) preferential oxidation (PROX),

where CO is adsorbed on a catalyst and then oxidised by a small amount of oxygen without combusting too much of the hydrogen. (2) Methanation. The reforming process is reversed and CO is converted into methane which is inert to the low-temperature catalyst. (3) Pressure swing adsorption techniques. CO is captured on a large-surface material which is regenerated at lower pressure. (4) Membrane filtration. Palladium and some palladium alloys are highly permeable for hydrogen only. All these techniques add to the system complexity and costs. Moreover, some of them are not easily controlled in a dynamic system with varying load, like in a vehicle. The CO clean-up is often considered the most challenging part of a fuel cell system based on reforming. Today, however, reforming of natural gas almost exclusively produces hydrogen, because it is the cheapest way, even though the CO must be removed.

To sum up, when used with fuel cells, the advantage of reforming is that fuels that are immediately available or easier to store onboard can be used. Methanol is the easiest fuel to reform and the process can be fast and almost complete at temperatures as low as 230°C. At this temperature, no separate shift reactor is needed. The drawbacks of reforming are that the system is more complex, that hydrogen is diluted with CO_2, which limits fuel utilisation, and that an efficient CO clean-up system is mandatory in fuel cells working below 150°C.

5.5.3 Fuel and Air Stoichiometry

Dry air consists of 78% nitrogen, 21% oxygen, and traces of other gases. Moreover, ambient air also contains a varying amount of water. On the way through the cathode compartment, oxygen is consumed, while nitrogen is not. This results in a relative decrease in the oxygen partial pressure and if the flow is adjusted to supply just enough oxygen to produce the electrical current in the cell, the concentration will be zero in the air leaving the cell. In a fuel cell the term *air stoichiometry* means the ratio between the oxygen supplied in the air flow and the oxygen needed theoretically at a fixed current (as calculated from equation 5.2 and Faraday's constant, F). It has the symbol λ. In the example just described, the air stoichiometry is 1.0. It is not possible to run a fuel cell on $\lambda_{air} = 1.0$, because the air partial pressure will be too small near the end of the gas channels, leading to severe mass transport problems. Note that the force driving gas diffusion is a concentration gradient which will approach zero in this case. Moreover, the gas flow resistances through the different cells in real stacks are not strictly equal and this aggravates the situation even more by local starvation. For these reasons, the air stoichiometry rarely is below 2.0 (a flow rate with twice the theoretical amount of oxygen) and sometimes even higher. The drawback of a high air stoichiometry is that more air must be passed through the cells and this requires a larger compressor consuming more of the produced electrical power. The larger flow rate also results in a larger pressure drop in the channels, which again increases the demand on the compressor. In a dynamic system with variable current the air and fuel flow rates must follow the current, because they are both proportional to the current.

If a fuel cell is operated on hydrogen from a reformer, the case is similar, as the fuel gas is a mixture of hydrogen and carbon dioxide (and perhaps some water and carbon monoxide). Also in this case, the solution is to increase the stoichiometry, but the excess fuel is wasted, as it is not converted in the fuel cell. For this reason, fuel stoichiometry is always lower than air stoichiometry and values as low as $\lambda_{fuel} = 1.2$ are possible in a well-engineered system. This means that the fuel flow is in excess of 20%. This 20% excess fuel in the anode off-gas is normally combusted in a catalytic burner, and the resulting heat can then be used for fuel processing. Some fuel cell systems run well at $\lambda_{fuel} = 1.0$, if the fuel is pure hydrogen, but if the fuel cell is operated at temperatures below the boiling point of water, measures like eventual purging must be taken to remove water vapour in order to avoid condensation in the channels or pores.

5.5.4 Fuel Cell Systems

It is repeatedly said that fuel cells produce electricity without any moving parts. This is true for the cell alone, but in most applications the fuel cell needs a quite complex system of auxiliary components like pumps, blowers or compressors. Often, the fuel cell only accounts for a smaller part of the weight and volume of the system. The way the system is constructed depends on the application, the type of fuel cell, and the fuel. In general, all fuel cells need an air blower or a compressor to drive air through the cathode channels at a sufficient rate. An exception is "self-breathing" micro fuel cells in which oxygen from the air is transported to the cathode by natural convection and diffusion. It should be noted that the self-breathing principle is only possible in very small systems with a high surface to volume ratio. If the fuel cell is run on pressurised gases, the performance is better, but the increased efficiency is often compensated by the energy consumption of the air compressor (some of the mechanical energy can be reclaimed by an expander at the cathode exit). The energy used for these peripheral parts is called parasitic losses which may be below 3–5% of the produced energy in a well-engineered system.

Depending on the type, the fuel cell has a certain allowed temperature window for operation. As already mentioned, a large fraction of the fuel energy is converted into heat in the cell. This heat must be removed to avoid overheating. There are two main ways of doing that. The simplest system involves air cooling with a larger air flow either through enlarged cathode channels or through separate cooling channels. The price for the simplicity is that more compression work is needed and that the heat becomes difficult to utilizes, because it is dissipated in a large volume of luke-warm air. Alternatively, a liquid coolant can be applied in separate channels. Then a circulating pump and one or more heat exchangers must be added to the system. With a liquid coolant the heat can be reclaimed at a higher temperature because of the higher heat capacity and heat conductivity compared to air. Higher temperature means higher quality of the heat and higher applicability. Some indicative working temperatures of different fuel cell types are listed in Table 5.3.

Table 5.3 Overview of key characteristics of different fuel cell types. The working temperatures are indicative and can in some cases be varied

	AFC	Low temperature		High temperature	
		PEMFC (DMFC)	PAFC	MCFC	SOFC
Temperature	60–100°C	60–80°C	200°C	650°C	800–1000°C
Electrolyte	Aqueous KOH	Polymer	Phosphoric acid	Molten salt	Solid ceramic
Electrolyte	Alkaline	Acidic	Acidic	Alkaline	-
Conducts	OH^-	H^+	H^+	O^{2-}as CO_3^{2-}	O^{2-}
Catalyst	Noble/non-noble	Noble metal	Noble metal	non-noble	non-noble
Fuel	H_2	H_2	H_2	H_2	H_2
	NH_3	(CH_3OH)		CO	CH_4
				CH_4	CO
					NH_3

During start-up, the minimum working temperature can be achieved from an external heat source possibly via the liquid coolant. Alternatively, a mixture of hydrogen and air can be fed into the cell. This combustible mixture reacts at the electrode catalysts and heat is generated just where it is needed.

If the system involves a reformer, the complexity increases. Several heat exchangers are typically built in for better heat management. Selected mass flows are preheated or cooled. Depending on the temperature, the excess heat from the fuel cells can be used for fuel or water evaporation, steam reforming, preheating of air for the burner, etc. If the temperature of the excess heat from the fuel cell is not high enough to drive a steam reformer, the heat can instead be obtained from a catalytic burner combusting the anode off-gas containing the overstoichiometric fraction of hydrogen. This way, the energy of the unconverted hydrogen is utilised. Power electronics like DC/DC converters are applied when a higher or a more stable voltage is needed. AC current can be produced with a DC/AC converter.

5.6 Fuel Cell Types

Fuel cells are normally named after their electrolytes. In principle, fuel cells can be constructed with any electrolyte, but five electrolytes dominate, each with its own class named after it. The ion conduction mechanism determines the working temperature of the cell. This leads to a division into two temperature categories, namely, low-temperature fuel cells working at up to about 200°C and high-temperature fuel cells working between 650 and 1000°C. The medium-temperature area has not been utilised so far, because no viable electrolyte has been found so far. The low-temperature electrolytes are not thermally stable at higher temperatures and the high-temperature electrolytes typically require a high temperature to gain sufficient conductivity. Numerous molten salts are known at medium temperatures, but none has been successful as a medium-temperature fuel cell electrolyte so far. At present, medium-temperature solid ion conductors are in an early experimental state, but they are likely to play a role in the near future.

The *alkaline fuel cell* (AFC) has an aqueous solution of KOH as electrolyte. The *proton exchange membrane fuel cell* (PEMFC) and the *phosphoric acid fuel cell* (PAFC) both have acidic electrolytes, namely, a special polymer with acidic side chains and phosphoric acid, respectively. The *molten carbonate fuel cell* (MCFC) makes use of a molten carbonate salt and the *solid oxide fuel cell* (SOFC) is built around a solid ceramic oxide ion conductor. A sub-group of the PEMFC is the *direct methanol fuel cell* (DMFC) which is optimised for conversion of methanol. Table 5.3 gives a summary of the main characteristics of these different fuel cell types. In all cases, the starting point was the electrolyte and the rest of the cell has been developed in order to be compatible with it. In the acidic systems, for instance, noble metals are always applied as catalysts, while in the other systems noble metals are not necessary. The different fuel cells will find different uses. In Table 5.4 they are assigned to the most obvious applications.

As there is no fundamental difference between fuel cells and electrolysis cells, it is obvious to consider operating a fuel cell in the reverse mode, i.e. as an electrolyser. In this way, a simple energy storage system can be obtained, in which hydrogen is produced and consumed by the same unit. Volume, weight, and especially costs can be reduced significantly in this way. Such a cell is often referred to as a reversible fuel cell*. Unfortunately, this is not as straightforward as it may sound. Fuel cells are highly optimised devices, and bi-functionality involves compromises. For example, transport of reactants and products is ideally handled differently in the two modes. Furthermore, corrosion is more severe at higher potentials that are to be faced in electrolysis mode. As a consequence, different materials and designs with different advantages and drawbacks are typically used for cells optimised for each of the two modes.

Table 5.4 Typical applications envisaged for the different types of fuel cells. There is no sharp boundary between the applications of each cell type and the table shall only serve as an indicative guide

	Size	Low temperature			High temperature		
		AFC	PEMFC	DMFC	PAFC	MCFC	SOFC
Portable electronics	1–100W			+			
CHP	1–5kW		+		+		+
APU	1–10kW		+		+		+
UPS	1–1000kW		+	+			
Person vehicles	10–100kW		+				
Boats	50–500kW		+				+
Buses/trucks	100–500kW		+				+
Ships	1–50MW				+	+	+
Power stations	10–1000MW				+	+	+
Space	1–10kW	+	+				

*The term “reversible” is erroneous in a chemical sense, because no fuel cell is reversible. They always have irreversible losses. “Reversible” only refers to the fact that the current and the gas flows can be reversed.

Today, the main R&D effort is spent on PEMFC (including DMFC) for small to medium-sized applications and on SOFC for larger applications. The PEMFC is attractive with a high power density and robustness when operated dynamically with frequent start-ups. It is a quite mature system. The SOFC has the potential for the highest conversion efficiency due to the high temperature, and the excess heat can be used for several applications. However, the high temperature also makes the systems impractical for smaller applications. The SOFC is not yet as close to commercialization as the PEMFC. All the systems described in the following sections suffer from high costs and this is an issue that must be – and certainly is – addressed by research groups worldwide.

5.7 Alkaline Fuel Cells (AFC)

The alkaline fuel cell uses aqueous KOH as the electrolyte. The cell reactions are

$$\text{Cathode}: \quad O_2 + 4e^- + 2H_2O \rightarrow 4OH^- \tag{5.22}$$

$$\text{Anode}: \quad 2H_2 + 4OH^- \rightarrow 4H_2O + 4e^- \tag{5.23}$$

$$\text{Overall}: \quad O_2 + 2H_2 \rightarrow 2H_2O \tag{5.24}$$

The working temperature normally ranges from 60°C to 100°C, but operating temperatures as high as 150°C are possible, if the system is pressurised. The vapour pressure of water in the electrolyte is significantly lower than that of pure water due to the high concentration of KOH. The AFC was used in the Apollo space programme (although not exclusively).

5.7.1 Electrolyte and Electrodes

For the alkaline electrolyte aqueous potassium hydroxide (KOH) is used, because it has the highest ionic conductivity of the common alkali metal hydroxides in aqueous solution. The maximum conductivity is measured in a 6-molar concentration (just below 30 wt%). For catalysts both noble and non-noble metals can be used, (platinum or platinum alloys like in PEMFC). The best non-noble anode catalyst is Raney nickel which is a special high-surface-area nickel. It is manufactured from a nickel-aluminium or nickel-zinc alloy, from which the aluminium or zinc is dissolved, leaving behind a highly porous structure. The cathode is typically silver supported on carbon.

5.7.2 Cells, Stacks, and System

AFCs are constructed in two ways. The electrolyte can either be circulating or static. Circulation of the electrolyte might seem to complicate things, but there are certain

advantages related to it. The electrolyte can serve as the heat transfer fluid for both heating and cooling the cells. At the same time, the water management and optimum electrolyte concentration can be controlled and maintained easily from outside the cells. As a consequence, there will be no concentration gradient in the active electrolyte in the cells due to the water formation. Moreover, gas bubbles which are critical to the performance are washed out during the circulation. Finally, the electrolyte can be replaced, if damaged.

5.7.3 Advantages and Challenges

A major advantage of the AFC is the low costs of the components. Both the electrolyte and the catalysts (if not noble) are inexpensive. The oxygen reduction process at the cathode has a low activation overvoltage compared to other low-temperature fuel cells.

The biggest disadvantage of the AFC is that the electrolyte reacts with CO_2 as

$$CO_2 + 2OH^- \rightarrow CO_3^{2-} + H_2O \tag{5.25}$$

The CO_3^{2-} tends to precipitate as K_2CO_3, because K_2CO_3 has a lower solubility than KOH. Even at low concentration, it reaches oversaturation. If this precipitation takes place in the electrode pores, the gas transport is blocked locally and the cell performance goes down. Moreover, K_2CO_3 in solution has a lower conductivity than KOH. The CO_2 reaction is called carbonisation and it is a problem over time, because CO_2 is accumulated from the air passing through the cathode chamber even with the small concentration of 0.03 pct. in the atmosphere.

5.7.4 $NaBH_4$ Fuel Cells

AFCs can be fuelled by $NaBH_4$. $NaBH_4$ is stable in a concentrated KOH solution like the AFC electrolyte. When $NaBH_4$ is passed over a suitable catalyst, hydrogen is released readily. The concept was commercialised by the company Millenium-Cell. In the boron hydride fuel cell this catalyst is the anode catalyst. The reactions are [3]

$$\text{Cathode}: 2O_2 + 4H_2O + 8e^- \rightarrow 8OH^- \tag{5.26}$$

$$\text{Anode}: BH_4^- + 8OH^- \rightarrow B(OH)_4^- + 4H_2O + 8e^- \tag{5.27}$$

$$\text{Overall}: BH_4^- + 2O_2 \rightarrow B(OH)_4^- \tag{5.28}$$

The reversible cell voltage at standard temperature and pressure is 1.64 V which is significantly higher than for a hydrogen-fuelled cell. This proves that the boron hydride is directly converted electrochemically on the anode catalyst and not through hydrogen release and subsequent electrochemical reaction like in a conventional

cell. A drawback of such a system is that the manufacture of $NaBH_4$ is rather energy-consuming and, thus, the round-trip energy efficiency is low. Hence, the use should be restricted to applications in which energy efficiency is not important.

5.8 Phosphoric Acid Fuel Cells (PAFC)

The first commercial fuel cell-based power plant was based on a phosphoric acid fuel cell. It was the PC25, a 200 kW unit manufactured in 1991 by the ONSI Corporation (now UTC Fuel Cells). It is fuelled by natural gas through a reformer also fitted in the same system. The electrolyte is phosphoric acid which is a proton conductor. The cell reactions are

$$\text{Cathode: } O_2 + 4H^+ + 4e^- \rightarrow 2H_2O \tag{5.29}$$

$$\text{Anode : } 2H_2 \rightarrow 4H^+ + 4e^- \tag{5.30}$$

$$\text{Overall: } O_2 + H_2 \rightarrow 2H_2O \tag{5.31}$$

5.8.1 Electrolyte and Electrodes

Acids are generally good proton conductors, but there are at least two more reasons for the success of phosphoric acid as electrolyte. It is among the thermally most stable acids and its vapour pressure is very low. Therefore, it can be used at temperatures up to 200°C, where most other acids either decompose or are too volatile to be confined in the system. Unfortunately, phosphoric acid tends to polymerise at high temperature, beginning with the release of water from a pair of phosphoric acid molecules. However, this process is in chemical equilibrium and counteracted by the water formed in the cell during operation. The acid electrolyte is contained in an inert matrix of typically SiC. The cells are often fitted with an electrolyte reservoir which compensates volume changes due to thermal effects and especially the change of water content during dynamic operation. The reservoir can replenish the electrolyte, as acid is lost with the gas streams over time despite the very low vapour pressure. PAFC is meant for stationary applications with a service life in the order of 40,000 hrs. Due to the contact with the acid, the catalysts must be noble metals (at least, only noble metals have proved to be active and stable enough so far). Platinum or platinum alloys precipitated as nano-clusters on porous carbon are mostly used for both electrodes.

5.8.2 Cells, Stacks, and System

Cells are constructed with the cells separated by graphite-based bipolar plates. Seals are made of PTFE (Teflon) or optionally of the similar FEP. PAFCs typically are fully integrated systems with a steam reformer like the PC25 mentioned above.

5.8.3 Advantages and Challenges

The relatively high operating temperature is an advantage in connection with a reformer system, because the tolerance to CO is high enough to allow un-purified hydrogen directly from the low-temperature shift reactor.

The high working temperature compared to the other low-temperature fuel cells requires more pre-heating during start-up. During shut-down or idle operation, the cathode should not be in contact with air at the operating temperature and open voltage. If the electrodes are above 0.8 V, carbon corrosion and platinum dissolution may take place. During start-up and shut-down, the cathode therefore must be kept under nitrogen protection. PAFC systems are normally meant for continuous operation.

The activation overvoltage at the cathode is large, leading to a lower conversion efficiency compared to what could be expected due to the high working temperature. A reason is that phosphate ions adsorb to the catalyst surface, competing with oxygen on the active sites.

If the cell is operated at high temperature (> 200°C), the water content is very low and the melting point is higher than room temperature. If cooled from this condition, there is a severe risk of freezing damage. The stack should then either be kept at a high enough temperature to ensure a liquid electrolyte (> 50°C) or the electrolyte must be diluted by water vapour during cooling.

5.9 Proton Exchange Membrane Fuel Cells (PEMFC)

The proton exchange membrane fuel cell is the one to which most development activities were devoted in recent years. A strong force driving these activities was the aim of developing fuel cell-based electric vehicles. The low operating temperature, fast start-up, and possibility of a compact construction make it an obvious choice for a lot of applications ranging from portable electronics to vehicles. Other names commonly used for the PEMFC are “polymer fuel cell”, “polymer electrolyte fuel cell (PEFC)”, or “solid polymer electrolyte fuel cell (SPEFC).

5.9.1 Electrolyte and Electrodes

The proton exchange membrane forming the electrolyte is a special plastic with the ability to conduct protons, i.e. hydrogen ions, H^+. Despite its small size, a proton does not easily make its way through a polymer. The small size causes a high charge density and the proton tends to stick to other chemical species. So far, the most successful polymer electrolyte has been perfluorosulphonic acid (PFSA).

PFSA is made of a perfluorinated carbon backbone with side chains ending in sulphonic acid groups $-SO_3H$, as shown in Fig. 5.10. The fluorinated backbone resembles Teflon and has a similar chemical inertness and is highly hydrophobic (water-rejecting). In contrast to this, the sulphonic acid groups are hydrophilic

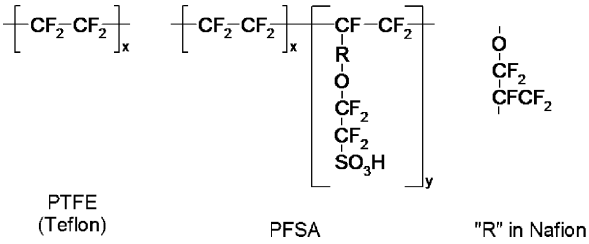

Fig. 5.10 The chemical structure of poly-perfluorosulphonic acid (PFSA), the most frequently applied electrolyte in PEMFC. The side chains may vary, as visualised by "R". The formulations of R for Nafion and poly-tetrafluoroethylene (Teflon) are shown for comparison

(water-loving) and when water is present, they bend towards each other and form local water-containing areas surrounded by hydrophobic areas. These hydrophilic areas are proton-conducting. The sulphonic acid transfers its proton to the water molecules and it is now able to move with or between the water molecules. It may be imagined that the proton might also just jump between adjacent sulphonic acid groups, but it takes a free site to jump to and the distance generally is too long. The water molecules act as proton shuttles and it is actually well known that several water molecules are transported with each proton through the membrane. This number is called the *water drag number* (or *electro-osmotic drag coefficient*) and is typically in the range of 1–3.

An important consequence of this conduction mechanism is that a high water content in the membrane is required to maintain ion conductivity. At low temperatures, say below 50°C, the water produced in the cell often is enough to keep the membrane wet. At higher temperatures, where the drying effect of the cathode air in particular is stronger, water management is needed and the cathode air (and optionally the anode fuel gas as well) is wetted to minimise the drying effect. This water management must be controlled strictly, because excess water may cause condensation and the formation of droplets blocking the electrode channels. The need for a high water content in the membrane limits the temperature to around 80°C. At a higher temperature, the cell must be pressurised to keep up the right water content for a high conductivity.

The catalyst is always made of noble metal, mostly platinum or platinum alloys. Platinum is catalytically active and chemically rather stable in contact with the acidic electrolyte. The non-noble catalysts available for alkaline fuel cells are not stable in an acidic environment. The catalyst is deposited as nano-clusters on a high-surface-area carbon powder. Over the years, the noble metal loading was reduced. As the state of the art today, it is in the range of 0.1–0.5 mg/cm^2.

5.9.2 Cells, Stacks, and System

The PEMFC electrode supports are made of different carbon materials. A highly porous carbon fibre sheet provides for mechanical strength. On the inner side, a

microporous layer is applied. The catalyst may either be applied on the electrode or directly on the membrane before the cell is assembled to an *MEA* (a *Membrane Electrode Assembly*). Bipolar plates are traditionally made of solid graphite and later injection-moulded graphite powder with a resin binder. The latest aim is to use steel to avoid the brittleness of the graphite. Strong steel plates allow for very thin plates and, consequently, for the most compact stack.

As already mentioned, the membrane needs a high water content and PEMFC systems differ from other fuel cell systems by the humidifier. Water management is often accomplished in a heat exchanger-like counter-flow unit, in which the highly humid used air wets the fresh incoming air through a diaphragm.

5.9.3 Direct Methanol Fuel Cells

A special variant of the PEMFC is the *direct methanol fuel cell* (DMFC). As an alternative to a complex system with a reformer, a shift reactor, a CO clean-up unit, and a catalytic burner, it is possible to convert methanol directly in a DMFC. It is basically a cell with the same membrane and the same cathode as a normal PEMFC. On the anode side, the fuel is methanol in aqueous solution, which is circulated via the electrode. When the cell is running, the following electrode reactions take place:

$$\text{Cathode}: 1.5O_2 + 6H^+ + 6e^- \rightarrow 3H_2O \tag{5.32}$$

$$\text{Anode}: CH_3OH + H_2O \rightarrow 6H^+ + CO_2 + 6e^- \tag{5.33}$$

$$\text{Overall}: CH_3OH + 1.5O_2 \rightarrow CO_2 + 2H_2O \tag{5.34}$$

The theoretical open voltage at standard temperature and pressure is 1.21 V and practically identical to that of a hydrogen fuel cell. However, when the cell is working against a load, the voltage is significantly lower than that of a hydrogen PEMFC at same current density (typically about 400 mV lower). This means that the conversion efficiency is correspondingly lower, and for this reason, the DMFC is most suited for smaller applications, where the energy efficiency is not a critical issue.

The reason for the low cell voltage (which actually improved dramatically in recent years) first of all is that the process of methanol oxidation involves a sequence of steps, of which some are slow. The situation is somehow comparable to oxygen reduction at the cathode. This means that there is a large activation overvoltage on both electrodes and the initial part of the polarisation curve shows a steep drop. Another problem is fuel crossover. Methanol resembles water to some extent and is easily soluble in the hydrophilic areas inside the PFSA membrane. When methanol diffuses through the electrolyte, it reacts at the cathode, resulting not only in a loss of fuel, but first of all in a potential depression at the cathode (a mixed potential). To minimise the crossover, a low concentration of methanol is often used (the concentration gradient across the membrane is the force driving crossover diffusion). Methanol concentration commonly is as low as 3 wt.%.

This is a compromise between crossover and reduced methanol activity. A thicker membrane will also reduce crossover, but the internal resistance will increase. Modified or entirely new membranes with lower methanol permeability are subject of extensive research.

The DMFC might well be the first fuel cell to be manufactured in large series on a commercial basis. Methanol as a liquid is easy to store and the energy density of the cell and the storage container is very competitive to batteries, even though the conversion efficiency is far from ideal. Many prototypes have been constructed for laptop PCs and Toshiba has even developed a DMFC for an MP3 player. For such small-scale and trendy applications, a high price per watt is acceptable. Market introduction was announced several times, but has been delayed repeatedly.

5.9.4 Advantages and Challenges

As already mentioned, a key advantage of the PEMFC is the low working temperature which allows for fast start-up, dynamic operation, and frequent shutdown. Numerous materials are available for the construction, e.g. elastomers for sealing. Moreover, the membrane can be very thin and still tight. With very thin liquid electrolytes, there always is a risk of local "holes" leading to gas crossover. In general, PEMFC can be formed into very compact units.

The high costs of platinum are often emphasised as a major disadvantage, and certainly this is true. However, other components (membrane, bipolar plates) are still too expensive for the platinum to be the cost driver. For a strong market penetration of vehicular PEMFC, the noble metal production needs to be increased. The required water management is an engineering challenge which can be dealt with, but which complicates the system.

Other disadvantages are related to the low working temperature. If the cell is fuelled by hydrogen via reforming, it is crucial to keep the CO content extremely low, say less than 20 ppm. The catalyst can be optimised for a higher CO tolerance (platinum-ruthenium alloys are the best for this purpose), but still a CO clean-up to less than 100 ppm is mandatory. The low temperature also complicates proper cooling, as was identified by the automotive industry. Despite the higher efficiency, PEMFC vehicles need a larger cooling radiator than comparable combustion engine vehicles. This is due to the fact that in the fuel cell system most heat is transported out via the circulating coolant, while in the conventional car most of the heat leaves through the exhaust.

5.9.5 High-Temperature PEMFC

The latest breakthrough with PEMFC is the high-temperature membrane. It was reported in 1995 [4] that the polymer polybenzimidazole (PBI, Fig. 5.11) can be doped with phosphoric acid and gain high proton conductivity. PBI is a well-known and highly temperature-resistant polymer. Among other applications, it has already

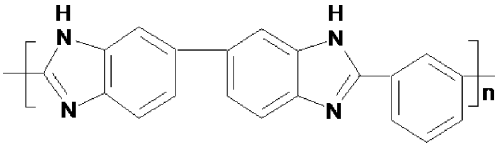

Fig. 5.11 The repeated unit of poly (2,2′-m-(phenylene)-5,5″-bibenzimidazole), PBI. The unprotonated nitrogens in the imidazole rings are basic and can be protonated by the phosphoric acid

been used as fibres for protective garments for firemen and race drivers. It is thermally stable with a glass transition temperature of 430°C. Phosphoric acid is used as dopant because of the thermal stability and a very low vapour pressure, just like for the phosphoric acid fuel cell. The PBI-based fuel cell can be seen as a hybrid between the PEMFC and the PAFC and the practical working temperature ranges from 120 to 200°C [5]. Below 120°C, the conductivity is too low and above 200°C, the acid polymerises too easily, which decreases the conductivity. Moreover, several materials in the cell are not durable above 200°C.

It may sound like an unnecessary complication to raise the working temperature of a PEMFC, but there are several advantages of it. The tolerance to CO is increased by orders of magnitude. While a normal PEMFC at 80°C only tolerates, say 20 ppm CO, a cell with the same platinum catalyst operated at 200°C can tolerate several percents of CO, i.e. 4 orders of magnitude more [6]. Practically, this means that hydrogen from a reformer system needs no CO clean-up apart from a shift reactor. Moreover, the membrane needs no humidification, because the phosphoric acid plays the role of the water in the conventional membrane, namely, it acts as a proton shuttle. This absence of the need for water management actually is a precondition for high-temperature operation at ambient pressure. Other advantages of the high temperature are that cell cooling is easier and can be performed with a small radiator due to the higher temperature difference to the surrounding air. In addition, the excess heat might even be utilised for steam formation in connection with a reformer or for other heating purposes. However, this alternative is not without disadvantages. For instance, the cell voltage is not yet as high as in a good low-temperature PEMFC and the higher working temperature results in longer start-up times. High-temperature PEMFC is an active research field and many alternative high-temperature membrane materials are under development for use as proton conductors [7].

5.10 Molten Carbonate Fuel Cells (MCFC)

The molten carbonate fuel cell is one of the two main high-temperature fuel cells. Ion conduction takes place via a mechanism different to those of the other fuel cells. Oxide ions are transported dressed as carbonate ions in a carbonate melt. To make this possible, carbon dioxide must be supplied with the air on the cathode side and removed with the formed water on the anode side. The half-cell reactions are:

$$\text{Cathode: } O_2 + 2CO_2 + 4e^- \rightarrow 2CO_3^{2-} \tag{5.35}$$

$$\text{Anode : } 2H_2 + 2CO_3^{2-} \rightarrow 2H_2O + 2CO_2 + 4e^- \tag{5.36}$$

$$\text{Overall : } 2H_2 + O_2 + 2CO_2(\text{cathode}) \rightarrow 2H_2O + 2CO_2(\text{anode}) \tag{5.37}$$

The operating temperature is 650–700°C, and MCFCs are always large stationary modules. Several MCFC power generators are in service around the world, but like the other fuel cell types, they still cannot be said to be truly commercial.

5.10.1 Electrolyte and Electrodes

The electrolyte in an MCFC is a molten mixture of lithium and sodium carbonate or of lithium and potassium carbonate. It is contained in a porous matrix of $LiAlO_2$, which is stable in the highly corrosive carbonate melt. The thickness typically is 0.5–1 mm. The liquid electrolyte cannot be kept in place in the separator as hydrophobic electrodes in low-temperature fuel cells do it. Instead, by adjusting the pore sizes to the right capillary forces this can be achieved.

The anode is made of porous structures of a sintered Ni-Al or Ni-Cr alloy. The cathode is lithiated (lithium-doped) nickel oxide. It is prepared in situ from a porous nickel plate that is oxidised by air when the cell is heated. It is lithiated by lithium from the electrolyte and by this process the conductivity increases to a sufficient level. Noble metals are not required for the catalysts.

5.10.2 Cells, Stacks, and System

The bipolar plates in an MCFC are made of nickel or nickel-plated stainless steel. Stacks are developed with internal as well as external manifolds. When internal manifolds are used, the electrolyte is used for sealing.

The working temperature is high enough for steam reforming of hydrocarbons. This is the reason for the multi-fuel capability. Water is formed continuously at the anode from hydrogen and oxide ions carried by the carbonate electrolyte. With this water, steam reforming can be carried out inside the cell as internal reforming. In this way, the overall system and the thermal management are simplified compared to low-temperature fuel cells with external reforming. Internal reforming can take place more specifically in the anode chamber (direct internal reforming) or in a separate compartment that is in direct thermal contact with the cell (indirect internal reforming). The advantage of the latter is that the reforming catalyst is not in contact with the corrosive catalyst.

As a continuous supply of CO_2 is required on the cathode side parallel to CO_2 formation through the reforming process, recycling should be considered. This can be done via a separation process in which part of the CO_2 is extracted from the anode off-gas and fed to the cathode with the air. Alternatively, part of the anode

off-gas which contains fuel rests that need to be burned anyway can be oxidised in a burner and fed to the cathode. In this way, CO_2 is provided.

Typically, all the hot components are integrated in one compartment, called a thermal envelope.

5.10.3 Advantages and Challenges

The advantages are good oxygen kinetics and a high value of the heat produced, both due to the high working temperature. Besides, the temperature allows for internal reforming of hydrocarbon via internal or external reforming. However, MCFCs do not tolerate NH_3 like SOFC does. The system is most suited for use with carbon-containing fuels to keep the CO_2 in the system.

The challenges are corrosion, electrolyte loss, electrode creep and sintering, and precipitation of nickel particles in the electrolyte, resulting in cell shorts. The nickel stems from corrosion of the NiO of the cathode or from the separator plates.

5.11 Solid Oxide Fuel Cells (SOFC)

The solid oxide fuel cell differs from the other cells, because it has an oxygen ion conductor as electrolyte. This electrolyte and the electrodes are ceramic materials. As the ion conduction mechanism involves a movement of oxide ions in a solid crystal lattice, the working temperature must be high, today 800–1000°C. The electrode reactions with hydrogen as the fuel are as follows:

$$\text{Cathode: } O_2 + 4e^- \rightarrow 2O^{2-} \tag{5.38}$$

$$\text{Anode : } 2H_2 + 2O^{2-} \rightarrow +2H_2O4e^- \tag{5.39}$$

$$\text{Overall : } 2H_2 + O_2 \rightarrow 2H_2O \tag{5.40}$$

5.11.1 Electrolyte and Electrodes

The by far most successful electrolyte is yttria-stabilised zirconia (YSZ). Zirconia (zirconium oxide, ZrO_2) has different stable crystal structures at different temperatures. Above 2369°C, the structure is cubic (fluorite structure). Between 2369 and 1127°C, it is tetragonal and below 1127°C, it is monoclinic. The cubic high-temperature phase can be stabilised at lower temperatures by the addition of yttria (Y_2O_3). As long as the additions are small, the structure is preserved, but as a first approach, this induces a charge imbalance, because the Zr^{4+} ions are matched by two O^{2-} ions and the Y^{3+} ions are matched by one and a half O^{2-} ions. Charge balance is a must and as the overall structural arrangement is preserved, the only solution is vacancies, i.e. empty oxide positions. These vacancies are the basis of

ion conductivity, because O^{2-} ions can shift to a neighbouring vacant site. The activation energy for such jumps is high and therefore, temperatures of 800–1000°C are needed to provide for a sufficient conductivity. In this temperature interval the highest conductivity is obtained with 8–10 mole% yttria. At 1000°C, the conductivity is in the order of 0.1 S/cm, at 800°C, it is 0.02 S/cm.

The electrode materials also are advanced ceramics. There are no deposited catalysts. Instead, the construction material also serves as catalyst. This is possible because of the high temperature.

The anode is a composite of nickel and YSZ, called a cermet (a mixture of *cer*amic and *met*al). The nickel acts as the reduction catalyst and provides for electronic conductivity. It is stable due to the reducing environment at the cathode. The YSZ prevents the finely dispersed nickel particles from sintering (which would otherwise be expected at the high temperature) and it also controls the thermal expansion coefficient at levels close to that of the electrolyte. The issue of thermal expansion is crucial in SOFC, because all components are stiff and there are no elastomers available to adapt strain.

The cathode cannot be made in the same way with a metal as electronic conductor, because metals are unstable in the oxidising environment. Instead, an electronically conducting ceramic is applied. Generally, ceramics are known as electrical insulators, but there are many examples of oxides which are good electronic conductors, some even at room temperature. Many of these are oxides with the perovskite structure ABO_3, where A and B are metals. Similarly to the YSZ, partial substitution can be made and both ionic and electronic conductivity can be obtained. Some highly conductive perovskites cannot be used as cathode materials, simply because they react with the electrolyte at the high temperature and form undesired compounds. The state-of–the-art cathode material for SOFC is $La_{1-x}Sr_xMnO_{3-d}$ (lanthanum strontium manganite, LSM). The electronic conductivity depends on x and the temperature, but it is in the order of 200 S/cm at around 1000°C. Another criterion for selecting LSM is that thermal expansion must not differ too much from those of the other components. The subscript "3-d" instead of just "3" in the formula refers to the fact that the oxide is not fully stoichiometric, but contains oxide vacancies due to substitution.

5.11.2 Cells, Stacks, and System

The cells of SOFCs are prepared by stacking layers of electrode material and electrolyte material on top pf each other. While other fuel cells are mostly prepared as compact flat cells, the SOFC cells are manufactured in quite different shapes. The reason is that the stacking and sealing of brittle cells without elastic seals is a challenge. Moreover, the large temperature changes during start-up complicate things.

Siemens-Westinghouse developed tubular cells which are ceramic tubes with a cathode electrolyte and the anode as concentric layers. The long tubes need sealing at one end only, which can be extended into a colder area, where sealing materials do not need to be as temperature-resistant. The cells are connected by nickel felt, and this is possible, because the anode chamber ensures a reducing protective environment outside of the tubes. The tubular design has the drawback that it is not

as compact as a planar plate design. In a planar design the different layers in the cell can be very thin, but at least one of them must be thick enough to provide for mechanical strength. The different designs are referred to as electrolyte-supported or anode-supported depending on which layer is the substrate for the others. In anode-supported cells the electrolyte can be as thin as 10 μm and this is very attractive, since the electrolyte resistance is proportional to the thickness. Planar cells are separated by interconnects with gas channels (the same as the bipolar plates in PEMFCs). At temperatures above 800°C, the interconnect is made of ceramics, but below 800°C, chromium steel plates can be used. The sealing is made of a glass.

5.11.3 Advantages and Challenges

The SOFC technology is challenging and commercial breakthrough is expected later than for PEMFCs. However, there are significant advantages of SOFCs, especially for stationary more or less continuous applications. The high operating temperature results in fast kinetics also at the cathode. Although the ΔG of the fuel cell process decreases with temperature, the fast kinetics more than compensate for this and the SOFC can reach high conversion efficiency in the order of 60% of HHV. Multiple fuels like CO, alkanes, alcohols, and ammonia can be converted in an SOFC, although pre-reforming is required in some cases. The heat produced has a high value due to its high temperature. It can be used in a turbine and, thus, increase the electrical efficiency. The drawbacks may also be attributed to the high temperature and to the brittle nature of the cells. The SOFC has a long start-up time and should preferably run for long periods to avoid the large temperature changes faced when closed down. The temperature changes and gradients can put severe strain on the brittle cells and the sealing. In small systems it may be difficult to maintain the high temperature. Future development is aimed at a lowering the working temperature, extending the lifetime, and reducing costs.

References

1. J. Larminie and A. Dicks. Fuel Cell Systems Explained. 2nd ed. Wiley (2003).
2. W. Vielstich, A. Lamm, and H. A. Gasteiger (eds.). Handbook of Fuel Cell, Vol 1–4. Wiley (2003).
3. Z. P. Li, B. H. Liu, K Arai, and S. Suda. Development of the direct borohydride fuel cell. *J. Alloys Compd*. 404–406, 648–652 (2005).
4. J. S. Wainright, J.-T. Wang, D. Weng, R. F. Savinell, and M. Litt. Acid-doped polybenzimidayoles: A new polymer electrolyte. *J. Electrochem. Soc*. 142, L121. (1995).
5. Q. Li, R. He, J. O. Jensen, and N. J. Bjerrum. PBI-based polymer membranes for high temperature fuel cells-preparation, characterizations and fuel cell demonstrations. *Fuel Cells* 4(3) 147–159 (2004).
6. Q. Li, R. He, J. Gao, J. O. Jensen, and N. J. Bjerrum. The CO poisoning effect in polymer electrolyte membrane fuel cells operational at temperatures upto 200°C. *J. Electrochem. Soc*. 150(12), A1599–A1605 (2003).
7. Q. Li, R. He, J. O. Jensen, and N. J. Bjerrum. "Reviews: Approaches and recent development of polymer electrolyte membranes for fuel cells operational above 100°C". *Chem. Mater*. 15, 4896–4915 (2003)

Part II
State of the Art Mobile Applications

Chapter 6
Challenges and Requirements for Car Industry

Oliver Kircher and Holger Braess

List of Abbreviations

BTL	Biomass to liquid
CcH_2	Cryo-compressed hydrogen
CGH_2	Compressed gaseous hydrogen
CNG	Compressed natural gas
CTL	Coal to liquid
DME	Dimethyl ester
DOE	US Department of Energy
FAME	Fatty acid methyl ester
FC	Fuel cell
GE	Gasoline energy equivalent

Oliver Kircher
BMW Group, Knorrstrasse 147, 80788 Munich, Germany, e-mail: Oliver.Kircher@bmw.de

Holger Braess
BMW Group, Knorrstrasse 147, 80788 Munich, Germany, e-mail: Holger.Braess@bmw.de

A. Léon (ed.), *Hydrogen Technology*,

GGE	Gasoline gallon equivalent
GHG	Green house gas
GTL	Gas to liquid
ICE	Internal combustion engine
LH_2	Liquefied hydrogen
LNG	Liquefied natural gas
LPG	Liquefied petroleum gas
NGL	Natural gas liquids
OECD	Organisation for Economic Cooperation and Development
R&D	Research and development
RME	Rapeseed methyl ester
SCC	Standard cubic centimetre
TES	Transport energy strategy
TNT	Trinitrotoluene

6.1 Status Quo of Existing Car Technologies

The technology of burning gasoline or diesel in cars equipped with an internal combustion engine was developed and established in the 20th century to guarantee individual mobility at comparably low costs that can be afforded by many people in the world. The convenience of gasoline- or diesel-powered cars is well known and appreciated by the customer. The most important ones are:

- Simple storage and filling of gasoline/diesel
- Low costs of a complete storage system to power the engine
- High achievable vehicle ranges of up to 1000 km without re-fuelling due to high volumetric and gravimetric storage density of gasoline/diesel
- Re-fuelling can be easily performed by the customer within a short time
- The power train and storage system have a high reliability and high durability and can be used by the customer with a minor maintenance expenditure only and without any technical restrictions throughout the lifetime of a car

Due to ongoing optimisation of fuel injection, overall efficiencies close to 20 (gasoline cars) and 25% (diesel cars) can be achieved, taking into account all losses between tank and wheel [1]. By applying hybrid technologies and reinforcing the usage of more lightweight materials, overall efficiency can be further improved [2]. However, trade-offs with safety requirements and customer expectations exist, partly compensating for the theoretical efficiencies gains in the past.

In the future these controversial requirements will further increase since it is commonly accepted among researchers, political and industrial leaders that the era of solely hydrocarbon based fuels for mobile applications is about to come to an end for different reasons.

In the first place, according to current estimations, it is predicted that the global production maximum of oil ("oil peak") will occur, when half of all recoverable oil resources have been depleted. For conventional oil this *mid-depletion* point could be reached within the next 10–20 years if current demand continues to grow [3]. Although estimates of global ultimate recoverable conventional oil resources differ strongly in recently published studies, surprisingly, it has only a minor effect

on the point of time of the "oil-peak" [4]. From that point on, the availability of conventional oil will steadily decrease. It is expected that additional oil supply from unconventional sources, such as oil sands or shale oil, will only reduce the slope of the declining world production, but not postpone the oil peak significantly [3]. Hence the moment of when worlds demand for transportation fuel cannot be met any longer will strongly depend on the development of alternatives to fossil fuel and the reduction of fossil fuel consumption. The mid-depletion point of conventional natural gas resources will be reached only a few decades later, which means that oil substitution by natural gas is not a viable long-term alternative[1]. Unconventional natural gas resources such as sub-sea methane hydrates or aquifer gas may offer a long term potential. Due to the lack of feasible production technologies, however, these resources will not be exploited on industrial scale within the next decades [3].

Currently, about 40% of the world's energy demand is covered by oil. Transportation is the largest oil-consuming sector with a share of more than 50% of world's demand [2]. In addition to the geological constraints, the European Hydrogen and Fuel Cell Technology Platform laid its emphasis on three high-level policy objectives to establish a future non-oil-based energy system with hydrogen as backbone [5]:

1. Security of energy supply
2. Climate change
3. Strengthening of the economy in terms of achieving high European added value in the total hydrogen value chain

Since major oil resources are located in political unstable regions, such as the Middle East, the issue of security of supply is gaining importance in the OECD countries. In the US, Japan and EU political support of R&D programmes on alternative fuels has reached a level of more than 500 bn€ of public funding per year [5] in order to achieve a higher degree of independence of both energy availability and energy price distortions.

The predictions for the global warming process in the 21st century lead to the necessity of reducing global CO_2 and other greenhouse gas (GHG) emissions. Recent investigations of global warming estimate a significant increase in the average global temperature by the end of the 21st century, if no measures are taken for a drastic reduction of GHG emissions [6].

6.2 Current Fuel Alternatives and their Potential to Substitute Gasoline and Diesel

Responding to the challenges outlined in the previous section, a variety of technical solutions may be considered. All non-oil-based fuels are classified to be "alternative fuels" and different classes exist. From the automotive point of view, potential impacts on power train technology and (even more importantly) on on-board energy storage justify the following classification:

- Liquid alternative fuels, mainly hydrocarbons such as synthetic fuels and bio-fuels (bio-alcohols, fatty acid methyl esters (FAME))
- Gaseous alternative fuels (e.g. hydrogen, natural gas, LPG)
- Electricity

Considering the primary energy alternatives, it is distinguished between fuels gained from exhaustible energy (from fossil sources or nuclear power) or from renewable energy (solar power, wind, geothermal power, hydroelectric power, biomass) as displayed in Fig. 6.1.

6.2.1 Synthetic Fuels

Synthetic fuel (synfuel) is a collective term for liquid hydrocarbons that are synthesised from syngas via the Fischer-Tropsch or other catalytic processes[2]. While in theory gasoline-type fuels could also be synthesised, the focus of ongoing and future activities clearly lies on high-quality fuels for diesel engines. Shell is currently using natural gas for synfuel production (GTL = "Gas to Liquid") in Malaysia (Bintulu since 1993, capacity 12,500 barrel/d) and Qatar (under construction, capacity 140,000 barrel/d). During the apartheid the South African company Sasol developed a process using coal as feedstock (CTL = "Coal to Liquid"), which will be deployed in China on a large scale, with plans existing for installing a capacity of up to 4 million tons per year until 2010 [7]. Not only fossil primary energies, but also biomass (BTL = "Biomass to Liquid") can be used for synfuel production. However, only pilot plans exist today. A major R&D topic for the

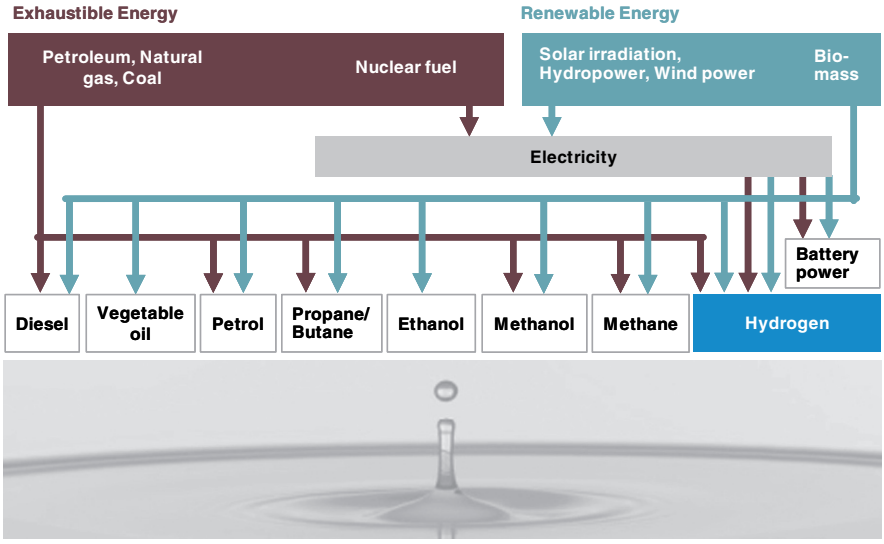

Fig. 6.1 Production of gasoline, diesel, and their alternatives from different energy sources

further up-scaling of the gasification process is the handling of the natural feedstock "biomass" of variable composition and humidity. This requires many more technical efforts than it is the case for natural gas (mainly CH_4) or coal. All these synthetic fuels can be burned in conventional internal combustion engines (ICE) without major modifications being needed. In addition, the existing infrastructure could be used.

As mentioned above GTL and CTL are based on fossil energy sources and thus can only contribute towards the political goal of security of supply but cannot be considered as sustainable fuel alternative for gasoline or diesel. BTL is produced from biomass and, thus, has the potential of reducing CO_2 emissions. However, it does not have the potential of fully substituting gasoline or diesel, due to the need of huge amounts of biomass. According to a recent study, the technical substitution potential for BTL from EU sources is estimated to be 20% by 2020 [8], not taking into account the demand for biomass which will be used by other sectors, such as heat and power generation.

6.2.2 Bio-Fuels

Bio-fuels are fuels which are produced from biomass[3]. The strongest advantage of bio-fuels compared to fossil fuels is the potential for a nearly neutral well-to-wheel CO_2 balance which will be achieved with second generation bio-fuels. First generation bio-fuels, such as rapeseed methyl ester (RME) or ethanol from sugar beet or corn, can only achieve well-to-wheel CO_2 reductions in the order of 30–50% [9]. This is due to fertiliser- and energy-intensive activities in sugar beet or corn farming. Recent Studies [9] indicate that the N_2O emissions from the intense use of fertiliser can even completely countervail the greenhouse gas emission balance of these first generation bio-fuels. Second generation bio-fuels will use lignocellulose feedstock, such as wood residues or farmed wood, which require a significantly smaller fertiliser and energy input.

Bio-fuels can be classified into:

- Bio-fuels for compression ignition engines (diesel)
  - Fatty acid methyl ester (FAME such RME, commonly known as "bio-diesel") produced from plant oils
  - Dimethyl ester (DME[4]) $H_3C–O–CH_3$ produced by gasification of biomass
  - BTL (see section above)
- Bio-fuels for spark ignition engines (Otto)
  - Alcohol produced by the fermentation of sugar beet or corn (ethanol CH_3CH_2OH)
  - Fermentation of lignocellulose or gasification of biomass (methanol CH_3OH).

Bio-diesel and ethanol both can be used in pure form or as a partial substitute of diesel and gasoline. Without any engine modifications, ethanol or bio-diesel currently can be blended with gasoline or diesel up to a content of 5% [10]. Methanol

can be mixed with gasoline or diesel up to a content of 15%, but its high toxicity requires further measures at the filling station to prevent the soil and groundwater from being poisoned. Dimethyl ester is gaseous under standard conditions and has to be stored and burned in the engine under pressure. The fuel supply system is similar to an LPG system.

As for BTL, all other bio-fuels are not considered to have the potential of substituting a high proportion of gasoline or diesel. In Germany for example, half of the technical potential of biomass is used for stationary applications already.

6.2.3 Compressed or Liquefied Natural Gas

Natural gas mostly consists of methane (CH_4) which can be burned in internal combustion engines which slightly reduced CO_2 emissions compared to gasoline (minus 16%) or diesel (minus 13%) [11]. Methane can be stored in liquid form (liquefied natural gas = LNG) or compressed form at typically 250 bar (compressed natural gas = CNG). Like oil, natural gas is a fossil energy source and, hence, a finite resource. As illustrated in Chap. 6.1, natural gas does not have the potential of substituting a significant proportion of future gasoline or diesel demand in the next decades.

6.2.4 Liquefied Petroleum Gas (LPG)

Liquefied petroleum gas (LPG) consists of a mixture of butane and propane with a nominal ratio of 50:50. LPG is produced as by-product either in the production of oil and natural gas[5], in the refining process or in a synthetic process from synthesis gas. Compared to gasoline or diesel, LPG has a minor potential of reducing CO_2 emissions only. Like natural gas, it has a limited availability due to its fossil origin and, hence, no long-term substitution potential for gasoline and diesel.

6.2.5 Battery Electric Storage

Battery techniques developed a lot in recent years, but they are still far away from fulfilling all requirements of suitable energy storage for automotive applications. The stored energy density and the maximum possible driving range are too low. Currently, the highest energy densities achieved with lithium ion batteries reach up to 0.18 kWh/kg and 0.2 kWh/L [12], which is far below automotive requirements (see Table 6.2 and Figure 6.4). Furthermore, a quick recharge according to automotive standards is not possible[6]. Battery electric vehicles definitely have the ability to act a niche as an efficient transportation for short distances in urban areas with overnight recharge in residential garages. With the current status of the technology, however, batteries do not have the potential of fully substituting gasoline or diesel as energy carrier for mobile applications.

6.2.6 Hydrogen

Hydrogen is the simplest and most abundant element in the universe. On earth, however, hydrogen is not available in pure form as primary energy source, but always chemically bound, e.g. in water, hydrocarbons (oil, natural gas, coal, biomass …) or other organic or inorganic compounds and has to be released by the introduction of energy.

Apart from electricity, hydrogen is the only energy carrier which is completely carbon-free and, thus, has great potential of reducing CO_2 emissions, assuming that it is produced from renewable or low- carbon energy sources. Nowadays, hydrogen is mostly produced from exhaustible energy sources. In the future when the world's oil and gas production will decline, it will either be produced from coal or from renewable energy sources (biomass gasification, electrolysis with wind or solar-thermal electricity).

Compared to all other alternatives to gasoline and diesel, the technical fuel substitution potential of hydrogen virtually has no limit. However, it needs to be stated that economic considerations will shape the introduction of hydrogen, too. Total supply costs of liquid hydrogen (without tax) from wind offshore power would be in the order of 1.9 € per litre gasoline equivalent, whereas liquid hydrogen from biomass could be supplied at about 0.8 € per litre gasoline equivalent [9]. Bio-fuels such as RME or ethanol, which already cover 1.4% of EU's fuel supply and will deliver 5.75% by 2010 [13], can currently be produced at slightly lower costs.

To sum up, the development of future fuels will consist of the following two steps:

1. In the short and medium term (until 2020), 2nd generation bio-fuels will allow for a modest reduction of transport-related GHG emissions, due to their limited substitution potential.
2. In the long term (after 2020) only renewable hydrogen will achieve high substitution rates and well-to-wheel CO_2 reductions of 90% and higher.

6.3 General Requirements on Hydrogen Powered Cars

The reasons why hydrogen is currently considered to be the major mid- and long-term alternative to gasoline and diesel were discussed in Chap. 6.2. On the one hand, it can be obtained from both fossil and renewable energy sources and, on the other hand, hydrogen can be converted in both internal combustion engines and fuel cells to power CO_2 emission-free cars. However, hydrogen has totally different properties from gasoline and diesel. From Table 6.1, it can be seen that hydrogen has a much higher gravimetric but a much lower volumetric storage density than gasoline and diesel.

Despite these differences, the performance, costs, and consumer convenience requirements of the storage system are strongly influenced by the properties of the well-known gasoline and diesel storage technology in current cars. For hydrogen

Table 6.1 Energy densities (volumetric and gravimetric) and physical densities of gasoline, diesel, and their potential alternatives

Fuel	Volumetric density [MJ/l]	Gravimetric density [MJ/kg]	Density [g/l]
Gasoline	33.6	44	764
Diesel	35.8	43	833
RME	32.8	37	887
Ethanol	21.1	26.8	789
Methanol	15.7	19.9	787
DME	19.0	28.4	670
CNG 250 bar	9.4	50	188.3
LNG 4 bar	19.6	50	391.7
LPG 4 bar	25.1	46.4	540.9
LH_2 4 bar	7.5	120	62.9
CGH_2 350 bar	2.8	120	23.4
CGH_2 700 bar	4.7	120	39.3

vehicles to enter a mass market, customers will expect a safety level, performance, range, and handling (at least) comparable to conventionally fuelled cars. Based on existing car technologies, the US Department of Energy (DOE) published a roadmap for the requirements on many aspects of future hydrogen-powered vehicles. According to the DOE program *Hydrogen, Fuel Cells & Infrastructure Technologies*, three major obstacles have to be overcome for a commercialisation and market penetration of hydrogen fuel cell vehicles [14]:

1. The on-board hydrogen storage system has to guarantee a minimum vehicle range of 300 miles, while meeting packaging, cost, performance, and safety criteria.
2. The costs of an efficient and safe hydrogen production have to be lowered to be competitive with gasoline while meeting environmental criteria.
3. In the case of fuel cells in combination with an electric motor as power train, fuel cell system costs have to be lowered to a level of 30 $ per kilowatt, while meeting performance and durability criteria.

While obstacles 1 and 2 also hold for hydrogen vehicles powered by internal combustion engines (ICE), obstacle 3 does not longer apply. In the next few years, ICE technologies developed for example by BMW, the Ford Motor Company, Mazda, and MAN (for busses) will solve this problem. In this context, both ICEs[7] and fuel cells in combination with electric motors will exist next to each other in a hydrogen transportation economy. Currently, it is anticipated that a commercialisation of fuel cells in terms of fulfilling costs, performance and durability targets will not happen before 2015–2020 [15]. In the meantime, hydrogen ICEs will be the suitable bridging technology between the fossil fuel age and the upcoming hydrogen age, their efficiency being further improved by a combination with hybrid concepts [16].

Cost-effective and safe production of hydrogen (obstacle 2) may be achieved, in an early phase of hydrogen economy at least, by mixing fossil and renewable

energy sources to produce hydrogen and by granting tax incentives. The price of hydrogen (not including taxes) would be comparable to the price of gasoline (including taxes) when producing hydrogen by a well-balanced mix of fossil feedstock (e.g. natural gas) and renewable energies. A current estimate for liquid hydrogen costs, not including tax, is given in Fig. 6.2. With further market penetration of hydrogen vehicles, the proportion of hydrogen produced with fossil energy resources will be lowered steadily and replaced by renewable energy sources. Increased demand for hydrogen will cause the production costs from renewable energy sources to be decreased.

As regards obstacle 1, however, the current situation is different. Irrespective of the costs, no technology is available at the moment, which can guarantee an adequate vehicle range without major restrictions for the customer. As already discussed in Chap. 6.2, hydrogen has a comparatively good gravimetric density, but a very poor volumetric density. Figure 6.3 illustrates the theoretical amount of storable hydrogen in a 150 litre volume by means of a pressure-density phase diagram for hydrogen. Compressed storage technology of hydrogen (CGH_2) reaches very restricted density of 3.5 kg at 350 bar and, respectively, of 5.9 kg storable hydrogen at 700 bar in a 150 litre volume[8]. Current liquid hydrogen (LH_2) storage technologies at 4 bar storage pressure are characterised by densities of 9.4 kg hydrogen in a 150 litre volume, with the potential of increasing this value to more than 10 kg by reduction of the storage pressure[9]. Further increase in the physical storage capacity will only be possible by somehow combining compressed and liquid storage technology by means of supercritical or cryo-compressed hydrogen (C_cH_2) [17]. At 30 bars, for instance, 10.7 kg of hydrogen can be stored in a 150 litre volume.

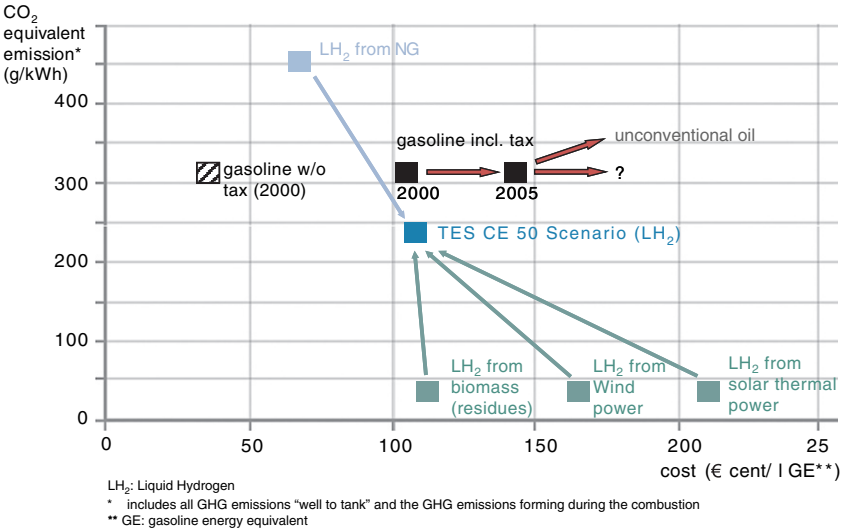

Fig. 6.2 Liquid hydrogen – costs and CO_2 options. Costs of LH_2 do not include tax. (Source [8])

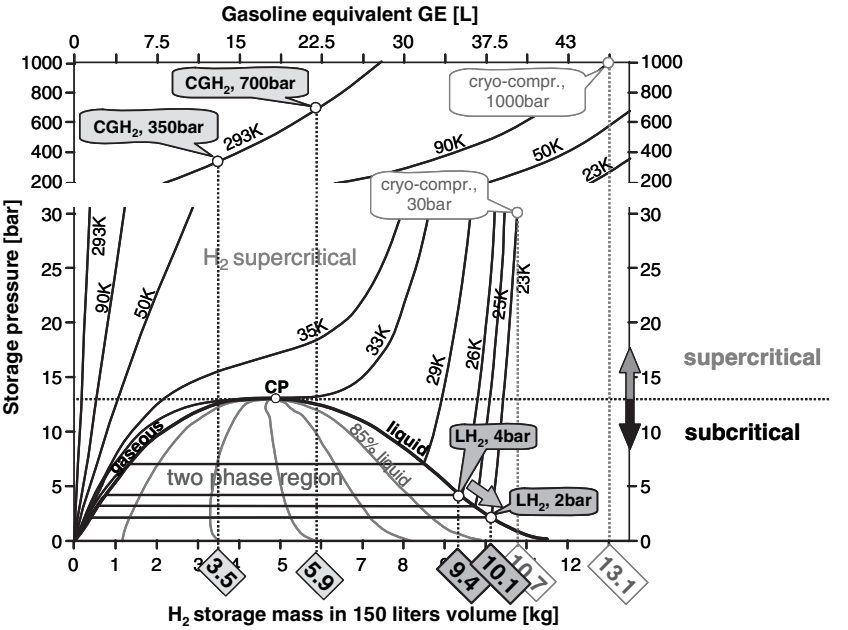

Fig. 6.3 Phase diagram of hydrogen with storage densities based on the mass stored in a 150 litre volume for storage at subcritical and supercritical pressure. (Source [20])

Besides the physical storage of hydrogen, several possibilities of storing hydrogen in condensed matter exist. Among them, storage in metal hydrides, carbon nanostructures, metal organic frameworks, chemical or organic hydrides are being investigated by researchers and engineers as possible alternatives to physical storage of hydrogen. Currently none of these technologies is sufficiently advanced to be a real alternative for road transport.

Selected requirements for on-board storage systems as defined by the DOE for 2007, 2010 and 2015 are listed in Table 6.2. The on-board storage system comprises the tank, valves, pressure regulators, piping, mounting brackets, insulation, heat exchangers, safety devices and any other components necessary, including the amount of hydrogen and any material, such as solid sorbent or liquid, used to store the hydrogen. Presently, the 2007 and 2010 DOE system storage targets can only be met by the physical storage of hydrogen. From Table 6.2, it is clear, however, that the 2015 system storage targets cannot be fulfilled by the physical storage of liquid hydrogen even at the lowest possible storage pressure or by the storage of supercritical hydrogen at a high pressure of several hundred bars. Despite intensive research on alternatives to physical hydrogen storage, a solution to reversibly store hydrogen in solid or liquid host materials in a cost-efficient way with all storage density and charge/discharge performance requirements being met is not in sight. Thus, it is commonly agreed among car producers that the first hydrogen production cars for consumers will be equipped with physical hydrogen storage systems

Table 6.2 Selected US DOE hydrogen storage system performance targets. gge = gasoline gallon equivalent; FC = fuel cell; ICE = internal combustion engine; scc = standard cubic centimetre. (Source [21])

Storage parameter	Units	2007	2010	2015
Gravimetric system storage density	kWh/kg (kg H_2/kg)	1.5 (0.045)	2 (0.06)	3 (0.09)
Volumetric system storage density	kWh/L (kg H_2/L	1.2 (0.036)	1.5 (0.045)	2.7 (0.081)
Storage system costs	$/kWh ($/kg H_2)	6 (200)	4 (133)	2 (67)
Fuel costs	$/GGE	–	2–3	2–3
Durability/operability				
• Operating ambient temperature	°C	−20/50	−30/50	−40/60
• Min/max delivery temperature	°C	−30/85	−40/85	−40/85
• Cycle life (1/4 tank to full)	Cycles	500	1000	1500
• Minimum delivery pressure from tank	Atm (abs)	8 FC/10 ICE	4 FC/35 ICE	3 FC/35 ICE
• Maximum delivery pressure	Atm (abs)	100	100	100
Charging/discharging rates				
• System filling time (5 kg)	Minutes	10	3	2.5
• Minimum full flow rate	(g/s)/kW	0.02	0.02	0.02
• Start time to full flow (20°C)	s	15	5	5
• Start time to full flow (−20°C)	s	30	15	15
• Transient response 10%–90% and 90%–0%	s	1.75	0.75	0.75
Fuel purity	% H_2	99.99% (dry basis)		
Environmental health and safety				
• Permeation & leakage	SCC/h			
• Toxicity	–	Meets or exceeds applicable standards		
• Safety	–			
• Loss of usable H_2	(g/h)/kg H_2 stored	1	0.1	0.05

in liquid or compressed form. In the long term, the cryo-compressed storage of hydrogen at supercritical pressures has the potential to supersede compressed or liquid hydrogen since it combines the advantages of both technologies. Cryo-compressed storage of hydrogen for vehicular applications is a research field which is currently in the early stages and, thus, no further details of this technology will be discussed in the following.

Figure 6.4 shows the system energy storage density of current and future liquid and compressed hydrogen storage systems as well as the energy storage density of complex metal hydrides in comparison with gasoline and diesel. Although hydrogen itself is much lighter than gasoline and diesel, the gravimetric system energy density is very low. Storage vessels designed for compressed or liquefied hydrogen are more complex and peripheral components are far away from automotive standards, thus leading to an increased system weight. Considering this problem and the low volumetric storage density, a major challenge for car industry is the integration of the storage system in the package of the car.

Hydrogen cars operated in various demonstration programmes worldwide were originally designed as gasoline- or diesel-powered cars and modified for the use of hydrogen. Future car concepts will have to be completely new designs, considering the different properties of hydrogen compared to gasoline and diesel. Even in optimised car concepts, liquid hydrogen in cryogenic vessels and compressed gaseous hydrogen in high-pressure cylinders will have severe shape restrictions. The immediate consequence is reduced energy availability in hydrogen-powered cars or a radical different vehicle package[10]. The current estimate is that common storage amounts of 50–80 litres for gasoline will have to be reduced to amounts which correspond to about half the gasoline equivalent for hydrogen cars. To offer

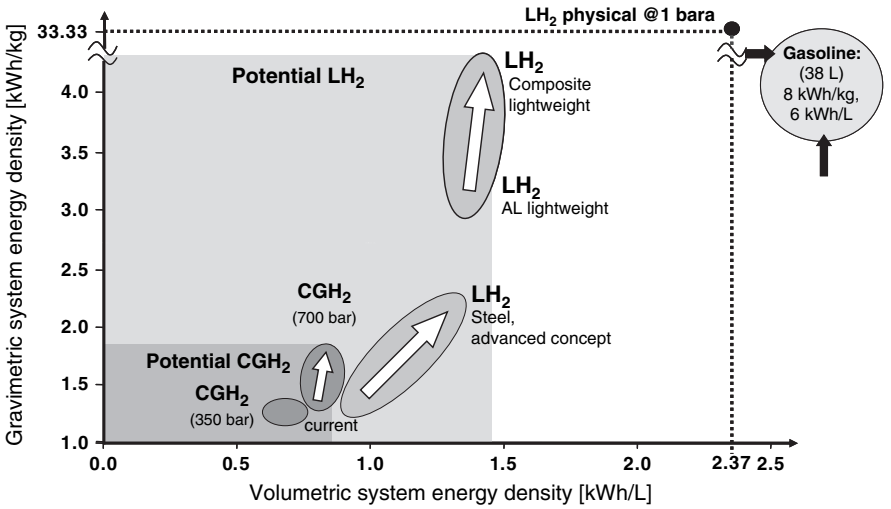

Fig. 6.4 Storage capacity of current and future liquid (LH_2) and compressed (CGH_2) storage systems (values include tank and all auxiliary systems). (Source [20])

a reasonable driving range to the customer, hydrogen cars will have to become more energy-efficient. To increase energy efficiency of the car, the power train unit, heat management, storage system, and the overall control concept will have to be optimised and combined with an intelligent energy management of the car. In hydrogen-powered cars the storage system will be as important as the engine in current gasoline cars.

What people often directly refer to when discussing the marketability of hydrogen cars is the safety aspect. A common idea is that safety of hydrogen cars is a crucial issue, because hydrogen is a flammable and, under certain conditions, explosive gas. At this point, it has to be said that hydrogen is not less safe than gasoline or diesel, but behaves differently. Table 6.3 compares various properties of gasoline and hydrogen. In the first place, hydrogen has several properties like non-toxicity, low density, high diffusivity in air, a high self-ignition temperature, and rather harmless flame behaviour, which make it much easier to handle than gasoline. However, hydrogen has a much broader range for the formation of an ignitable or explosive mixture in air and lower ignition energy[11]. In view of the fact that hydrogen is not detectable by humans, a major focus has to be put on the reliability of a nearly leakage-free[12] performance of the storage system and all hydrogen-carrying components.

In the transition time before hydrogen cars will start to enter a mass market, another major problem for car manufactures will be the missing infrastructure of hydrogen filling stations. From the filling stations operator's point of view a major investment in hydrogen filling stations will not be profitable until a certain number of hydrogen cars will be running on the streets. At present, 227 hydrogen filling stations are planned or already in operation worldwide[13] corresponding to an average of only 2–3 hydrogen cars per station[14]. Hence, the infrastructure providers expect a significant ramp up of the hydrogen vehicle fleet before the network will be further extended. This problem can only be solved by close cooperation between car manufacturers and filling station operators.

The market roll-out is likely to happen in some pilot regions in the US, Europe, and Japan, where a certain number of hydrogen filling stations have to be in

Table 6.3 Properties concerning the safety of hydrogen compared to gasoline

Property	Gasoline	Hydrogen
Density (ratio to density of air)	3.2–4	0.09
Regime of ignitable mixture in air	1–7.6 vol.%	4–75 vol.%
Regime of explosive mixture in air	1.1–3.3 vol.%	18–65 vol.%
Ignition energy	0.24 mJ	0.02 mJ
Self-ignition temperature	220–280°C	585°C
Flame	Broad flame regime, hot radiation	Narrow flame regime, low heat radiation, hardly visible
Flame temperature	2200°C	2045°C
Theoretical explosion energy	44.22 kg TNT/m^3 gas	2.02 kg TNT/m^3 gas
Diffusion coefficient in air	0.05 cm^2/s	0.61 cm^2/s
Toxicity	Toxic	Non-toxic

operation at the beginning. For efficient business, however, a guaranteed amount of hydrogen cars capable of using these filling stations needs to be in operation after a while. On the other hand, certain standards for re-fuelling couplers and the filling process will have to be agreed upon between all parties involved.

6.4 Customer-Driven Requirements on Hydrogen Powered Cars

In Chap. 6.3 a long list of general requirements on hydrogen-powered cars concerning storage density, infrastructure, costs, and marketability was discussed. Finally, it also is the customer who makes certain requirements on *energy availability* and *driving performance*, energy availability, and the driving performance of a car. Thus, *customer benefit* also determines the level of marketability of hydrogen cars.

In this section, typical requirements determining the customer's benefit with respect to hydrogen cars will be discussed. We will see that several properties which are completely natural for gasoline or diesel cars are big challenges for hydrogen cars.

6.4.1 Fast and Convenient Re-Filling

The filling process of current gasoline and diesel cars is easy and straightforward. The fuel is filled at ambient temperature and pressure into the storage vessel of the car. No special treatment for the filling line or the fuel is necessary. For hydrogen cars the filling process becomes more difficult for both liquid and gaseous hydrogen and in particularly for solid storage materials.

As liquid hydrogen has a very low boiling point of around −250°C and a low heat of evaporation, a sophisticated insulation of the filling line on the fuel station side and of the pipe between re-fuelling coupler and storage vessel on the car side has to be implemented in order to minimise boiling losses due to heat flow into the hydrogen. Despite the insulation, the filling line always has to be pre-cooled prior to re-filling and a compromise between fast re-filling and re-filling without gas return to the fuelling station has to be found.

Due to gas heating during the filling of a gaseous compressed storage vessel, there are two basic options for re-fuelling – either filling at a pressure higher than the storage pressure or filling of pre-cooled gas at storage pressure [18]. In the first scenario the storage vessel has to be designed for a pressure higher than the storage pressure[15], with all disadvantages like a higher demand for carbon-fibre materials (and, thus, increased material costs), higher safety requirements, and reduced volumetric system storage density due to increased vessel-wall thickness. The second scenario currently seems to be more practicable. However, due to the cooling of the carbon-fibre vessels during re-filling, durability and reliability against thermal cycling of the vessel may become a critical issue[16].

For solid hydrogen storage materials like metal hydrides the situation is completely different and even more serious. In a typical reversible metal hydride the reaction enthalpy is of the order of 20–40 kJ per mole hydrogen bound to produce feasible dissociation pressures at moderate temperatures[17]. During the recharging process, this amount of energy is released by means of heat. For quick recharging, use of an additional heat exchanger and cooling will be indispensable to prevent overheating of the storage vessel and its auxiliary components[18]. With the use of non-reversible solid or liquid storage materials, this problem could be avoided. In this case, used fuel will be replaced by fresh hydrogen-loaded fuel at the filling station. Currently, several research projects are dealing with the development of suitable off-board rechargeable hydrogen storage materials and strategies for a practicable infrastructure for the re-cycling of used fuel [19].

6.4.2 Driving Range and Driving Dynamics

The maximum cruising range of a car is determined by the amount of stored energy and the overall efficiency of the car. For a customer-viable range of 300 miles or more, 7–10 kg hydrogen will have to be stored to guarantee satisfactory power output in future-generation hydrogen cars. Storing 10 kg of hydrogen – which is equivalent to the energy content of just about 38 litres of gasoline – is a major challenge for a satisfactory integration in the car package. On the other hand, it requires a considerable gain in efficiency of future cars compared to today's gasoline ICE vehicles to offer an acceptable performance and driving range to the customer. If just 5 kg or less hydrogen were stored, limited vehicle properties and a shorter range probably would have to be accepted even in highly efficient future fuel cell vehicles.

Figures 6.3 and 6.4 show that the volumetric storage density of the hydrogen itself and of the hydrogen storage system is crucial to the physical storage of hydrogen. Current LH_2 (CGH_2) storage systems require about 6 (8) times the volume of a gasoline storage system – for the same amount of stored energy. Future perspectives of using advanced vessel designs and materials will allow a reduction of this factor to about 4 for LH_2 storage systems. For CGH_2 storage systems, however, an improvement of volumetric storage density will hardly be possible. While a package-adapted shape of LH_2 storage vessels is feasible within certain boundaries, an alternative to cylindrical geometries will never be possible for high-pressure storage vessels. For currently available reversible solid storage materials, both gravimetric and volumetric storage densities are the critical issues (cf. Fig. 6.4). They do, however, allow the shape of the storage vessel to be adapted to the car package more easily than for physical storage methods. Alternative non-reversible storage materials in liquid form (see the discussion for re-filling) suffer from neither a poor volumetric storage density nor any restriction in the storage vessel shape. However, other restrictions like a low gravimetric storage density exist.

The driving dynamics of hydrogen vehicles powered by internal combustion engines will always exceed those of hydrogen vehicles powered by fuel cells in combination with electric motors. Driving dynamics and a customer-viable range at the same time can only be ensured by a sufficient amount of stored hydrogen, thus making storage at low temperatures in liquid form (or alternatively in cryo-compressed form at supercritical pressures, cf. Fig. 6.3) indispensable to meet these requirements.

6.4.3 Operability Under all Climate Conditions

Depending on the storage and the power train technology, a guaranteed full car operability under extreme climate conditions still is a challenge in some areas, e.g. for cold starts. While internal combustion engines (ICEs) fed by hydrogen do not have any operating restrictions in the automotive operation temperature regime (−40 to +60°C), the situation for cars powered by electric motors in combination with fuel cells is different. For currently available fuel cells, a certain temperature regime is indispensable to guarantee full operability without causing any damage to the susceptible fuel cell membrane.

Among the storage concepts, compressed hydrogen storage does not have any climate-caused restrictions in operability. In a liquid storage system cold start conditions may lead to restrictions in the power supply depending on the hydrogen extraction and control concept[19]. Currently, the development of elaborated extraction and control concepts is under way and there will be no climate-related operating restrictions of liquid hydrogen storage systems in the long term. For solid storage techniques, particularly for metal hydrides, operability under any climate conditions is a crucial issue. Due to the nature and physical properties of metal hydrides, full operability under all climate conditions without any restrictions or additional measures is impossible. Typical reversible metal hydrides like complex aluminium hydride compounds provide an insufficient hydrogen dissociation pressure at low temperatures and have to be heated until engine or fuel cell waste heat can be used. On the other hand, hydrides fulfilling low-temperature requirements reach a dissociation pressure of several hundred bars at high operation temperatures[17] and require storage in high-pressure vessels.

6.4.4 Reliability and Durability

As already mentioned in Chap. 6.3, safety is a major issue in the development of hydrogen-powered cars. From the customer's point of view, hydrogen cars have to be at least as safe as current conventional cars without any restrictions in performance, operability and road capability. As there is little experience and less empirical reference values exist for durability and reliability, new methods have to be developed for safeguarding of hydrogen storage systems. In the long term, car

manufacturers will be able to rely on sufficient statistically relevant data in order to apply an appropriate risk assessment in the design and development phase of hydrogen-powered cars.

6.5 Summary and Outlook

Due to the mid-depletion peak of conventional carbon-based fuel coming within the next decades, dramatic climate change scenarios with ongoing GHG emissions of the industrial countries, and the current political and economic situation, the dependence on carbon-based fuel sources is about to come to an end and these sources will have to be substituted by a sustainable, affordable, technical feasible and (from well-to-wheel) carbon-free fuel alternative.

Many alternatives to gasoline and diesel are currently available. Most of them, however, are either also produced from carbon-based sources (and, thus, only lead to minor reductions in GHG emissions) or do not have potential of fully substituting the energy demand in the transportation sector. They are only complementary pathways of a future fuel roadmap, offering the advantage of short- and medium-term implementation. As regards the long-term substitution potential and the ability to meet projected customer needs, only hydrogen is considered to be a sustainable and low-carbon fuel alternative for the future.

On the way towards a hydrogen-oriented fuel market, all requirements on vehicle performance and customer expectations as discussed in Chaps. 6.3 and 6.4 will have to be met by the car industry in order to develop a business case for hydrogen-powered vehicles. Firstly, the political requirements on security of supply and GHG emission reduction of the transportation sector (see Chap. 6.2) will have to be fulfilled. On the other hand, future consumers will have to be attracted by a performance that is at least comparable to conventional cars.

Notes

1. The static range of oil, i.e. the ratio between oil reserve and current consumption, is calculated to be around 40 years, for natural gas about 65 years, assuming a constant consumption. Source: BP Statistical Review of World Energy, June 2006.
2. Syngas is a common term for the mixture of $CO + H_2$ in chemical industry.
3. According to this definition, synthetic fuels and hydrogen produced from biomass are also bio-fuels.
4. Due to lower viscosity and lacking lubricity, DME requires a significant modification of diesel engines.
5. Production figures of big oil or gas fields are commonly listing the by-products of these gaseous hydrocarbons under the term of NGL (natural gas liquids).
6. To recharge a battery which stores the energy equivalent of about 11 litres of gasoline (100 kWh), the recharging power has to be of the order of 6 MW to recharge the battery within 5 minutes, which is a typical automotive requirement.

7. To gain efficiency, future hydrogen ICEs will probably also be combined with electric motors like conventional hybrid cars nowadays.
8. 1 kg of hydrogen has a heating value of 33.33 kWh, which roughly corresponds to the energy stored in 1 gallon (= 3.78litre) of gasoline.
9. For both fuel cells and internal combustion engines, the power train has to be supplied with a minimum pressure to guarantee the provision of sufficient power under all driving conditions. Further reduction of the storage pressure below about 4 bars requires a pressure build-up unit between storage vessel and power train. Currently, cryogenic pumps for automotive applications are not yet available.
10. Compare, e.g., the Concept Car EDAG Cinema 7D (www.edag.de) presented at the IAA 2005.
11. The ignition energy of 0.24 mJ for gasoline also is very low. Hence, it always has to be assumed for gasoline that the ignition energy is somehow available.
12. Nearly leakage-free in this sense means that small leakages, if occurring, should never and under no operation condition lead to a critical concentration of hydrogen in air.
13. H_2 Filling Stations Worldwide, a web service provided by LBST (www.h2stations.org).
14. The worldwide hydrogen car fleet is estimated to be in the range of some 100 vehicles under operation in demo programmes mainly in the US, Japan, and Europe.
15. To ensure fast re-filling of 5 kg hydrogen below 5 minutes for a 700 bar storage vessel, around 850–875 bars filling pressure have to be applied, see Ref. [18].
16. Assuming an average driving distance between two re-filling processes of 250 km, 600 re-filling cycles result during a typical automotive life cycle of 150,000 km. Applying an appropriate safety factor, several thousand re-filling cycles and the consecutives temperature cycles have to be safeguarded.
17. A good overview of metal hydrides and the relationship between reaction enthalpy and dissociation pressure is given, e.g., in: Andreas Züttel, *Materials for Hydrogen Storage*, Materials Today, September 2003.
18. Assuming a recharging amount of 5 kg hydrogen in 5 minutes for a hydride with 30 kJ/mole reaction enthalpy, an emerging heat power of around 250 kW has to be compensated.
19. Current liquid hydrogen storage vessels are equipped with a heating system and the hydrogen supply to the engine/fuel cell is ensured by heat input and the consecutive pressure increase in the storage vessel.

References

1. Andreas Dildey, *Die PEM-Brennstoffzelle als alternativer PKW-Antrieb*, Dissertation, TU Braunschweig, 2005.
2. JRC/EUCAR/CONCAWE Well-to-Wheels Study, Version 2C, 2007 (http://ies.jrc.ec.europa.eu/wtw.html).
3. "Reserven, Ressourcen und Verfügbarkeit von Energierohstoffen", Bundesanstalt für Geowissenschaften, 2004.
4. Colin C. Campbell and Jean H. Laherrère, *The End of Cheap Oil*, Scientific American, March 1998.
5. Deployment Strategy Report, *European Hydrogen and Fuel Cell Technology Platform*, 2004 (www.hfpeurope.org).
6. See, e.g.: D.A. Stainforth et al., *Uncertainty in predictions of the climate response to rising levels of greenhouse gases*, Nature 433, 403–406;
   Hadley Centre Climate Report, *Uncertainty, Risk and Dangerous Climate Change*, December 2004 (http://www.metoffice.com/research/ hadleycentre/pubs/brochures/B2004/ global.pdf);
   Hadley Climate Change Report, *Climate Change, Rivers and Rainfall*, December 2005 (http://www.metoffice.com/research/ hadleycentre/pubs/brochures/B2005/COP11.pdf); IPCC Fourth Assessment Report, *Climate Change 2007*, November 2007 (http://www.ipcc.ch/ ipccreports/assessments-reports.htm).

7. Alexander's Oil & Gas Connections, volume 11, issue 13, 2006 (www.gasandoil.com).
8. 3rd interim report, TES (Transport Energy Strategy, publication expected by the end of 2006).
9. P.J. Crutzen, A.R. Mosier, K.A. Smith, and W. Winiwarter, *N_2O release from agro-biofuel production negates global warming reduction by replacing fossil fuels*, Atmos. Chem. Phys. 8, 389–395, 2008.
10. European specifications for gasoline fuel EN228 and for diesel fuel EN590.
11. Report of the Alternative Fuels Contact Group, December 2003.
12. ZEV Panel Final Report, *Status and Prospects for Zero Emissions Vehicle Technology*, Report of the ARB Independent Expert Panel 2007, April 13th 2007, http://wwww.arb.ca.gov/msprog/zevprog/zevreview/zev panel reprt.pdf.
13. Communication of the European Commission on an Action Plan for Biomass, COM (2005) 628, final, December 7th 2005.
14. DOE Office of Energy Efficiency and Renewable Energy, Hydrogen, Fuel Cells & Infrastructure Technologies Program Multi-year Research, Development and Demonstration Plan (www.eere.energy.gov/hydrogenandfuelcells/mypp).
15. Deployment Strategy Report, *European Hydrogen and Fuel Cell Technology Platform*, 2004 (www.hfpeurope.org).
16. See, e.g., the approach of Quantum Technologies Inc.: Neel Sirosh, *Hydrogen Internal Combustion Engine Hybrid Electric Vehicle Development*, NHA Annual Hydrogen Conference 2006, Long Beach, 2006.
17. Salvador M. Aceves, Gene D. Berry, Andrew H. Weisberg, Francisco Espinosa-Loza, and Scott A. Perfect, *Advanced Concepts for Vehicular Containment of Compressed and Cryogenic Hydrogen*, WHEC 16, Lyon, 2006.
18. See, e.g.: Sitra Pregassame, Frédéric Barth, Laurent Allidieres, and Katia Barral, *Hydrogen Refuelling Station: Filling Control Development*, WHEC 16, Lyon, 2006; Sitra Pregassame, Friedel Michel, Laurent Allidieres, Philippe Bourgeois, and Katia Barral, *Evaluation of Cold Filling Processes for 70MPa Storage Systems in Vehicles*, WHEC 16, Lyon, 2006.
19. See, e.g.: Alan C. Copper, Karen M. Campbell, and Guido P. Perez, *An Integrated Hydrogen Storage and Delivery Approach Using Organic Liquid-Phase Carriers*, WHEC 16, Lyon, 2006.
20. Tobias Brunner, *Liquid Hydrogen Storage for Passenger Car Application – Roadmap to Mass Market*, Hydrogen Production and Storage Forum, Vancouver (Canada), September 2006.
21. Sunita Satyapal, John Petrovic, George Thomas, Carole Read, and Grace Ordaz, *The U.S. National Hydrogen Storage Project*, WHEC 16, Lyon, 2006.

Chapter 7
Status on Existing Technologies

Chapter 7a
Hydrogen Internal Combustion Engine

Ted Hollinger and Tapan Bose

Ted Hollinger
Hydrogen Engine Center, Algona, Iowa 50511, USA, e-mail: thollinger@hydrogenenginecenter.com

Tapan Bose
Hydrogen Engine Center Canada, Trois-Rivières, (Qc) G9A 5H7, Canada

A. Léon (ed.), *Hydrogen Technology*,

List of Abbreviations

A/F	Air/Fuel Ratio
CAC	Charge Air Cooler
CFI	Central Fuel Injection
CR	Compression Ratio
EQR	Equivalence Ratio
GDP	Gross Domestic Product
HC	Hydrocarbon
HEC	Hydrogen Engine Centre
hp	Horsepower
ICE	Internal Combustion Engine
MFI	Multi-port Fuel Injection
Pt	Platinum
RPM	Rotation per Minute
SFI	Sequential Fuel Injection

In 2002 while preparing the World Hydrogen Energy Conference in Montréal, BMW contacted us to discuss the possibility of organizing a demonstration of their 7 Series hydrogen internal combustion engine car. The proposition was accepted and the demonstration was a great success. Both the attendees of the conference and the general public were impressed by the hydrogen car. In 2003, Ford Motor Company celebrated their 100 years by developing their millennium car which was none other than a hybrid hydrogen internal combustion car. The car was named Model U which is the modern version of Model T of the last century. The question which arises then is why both BMW and Ford are interested in developing a hydrogen internal combustion car? In the present manuscript, it is attempted to answer this question by carefully looking at the advantages and the disadvantages of a hydrogen internal combustion engine.

The earliest [1] attempt at developing a hydrogen engine is credited to Rev. W. Cecil of Britain. In 1820, he presented a paper to the Cambridge Philosophical Society on the application of hydrogen gas to produce power in machinery. The engine developed then was running satisfactorily. Later in the 1860s and 1870s, Otto of Otto Cycle fame used a producer gas in his combustion engine. The producer gas contained more than 50% hydrogen. However, since the development of the carburetor, gasoline has dominated the field of engines.

In recent times, hydrogen became the fuel of choice for rocket engines and launch vehicles. This is mainly because hydrogen contains the highest energy per unit mass among all fuels. More recently, problems related to climate change have generated lots of interest in hydrogen, because the burning of hydrogen in air produces no greenhouse gases, such as CO_2. Moreover, the combustion properties of hydrogen are rather helpful for the use of hydrogen as a fuel in an internal combustion engine.

Ford Motor Company has been the leader in hydrogen ICE technology in the USA. Ford has developed a 6.8 L V10 that runs on hydrogen [2]. This concept has been used in a Ford F450 shuttle bus for airport transportation. The engine was introduced on August 7, 2002, in Dearborn, Michigan by Ted Hollinger, then VP of Ballard Power Conversion Group. This introduction started the hydrogen phase of the long history of the ICE. A quote from Forbes magazine sums it up in the best way. One can read 'what really captured Bill Ford's imagination was a plain old piston engine, just like the ones that his great-grandfather put into Model Ts. But this one would run on hydrogen instead of gasoline, emitting no carbon dioxide. A hydrogen internal combustion engine could be a relatively inexpensive bridge to the hydrogen economy of the future. Fuel cells—a long-promised technology, still unaffordable—would come later. Better yet, only one other company, BMW, is seriously working on a similar hydrogen engine.' [3]

This article is divided into 12 sections. In the first section, we will discuss the properties of hydrogen and its consequences for an internal combustion engine. In the second section, the role of the turbo charger for direct injection and the use of ammonia as hydrogen carrier will be discussed. Exhaust emission, engine controls, and fuel injection system shall be explained in the next three sections. In the subsequent sections, the engine components for hydrogen use will be discussed in detail. In the last five sections, the production of water, hydrocarbon, and NO_x emissions, hydrogen embrittlement, sensors and venting, and future applications will be elaborated.

7a.1 Hydrogen Properties as a Fuel

As transportation fuel, hydrogen offers an immense advantage over fossil fuels. Not only is hydrogen the most prevalent element in the universe, it also provides the best opportunity to create a clean burning fuel that offers little or no harmful emissions.

In the following section, the properties of hydrogen which plays an important role in the combustion process will be described. Then, the consequences of these properties shall be discussed, if hydrogen is used in an engine initially designed to operate on gasoline.

7a.1.1 Properties of Hydrogen

The properties of hydrogen that play an important role in the combustion process are the wide range of flammability, the low ignition energy, the high auto-ignition temperature, the small quenching distance, the high diffusivity, the low density, and the high flame velocity. Table 7a.1 displays a comparison of these properties between gasoline, natural gas, and hydrogen when used in an internal combustion engine.

Table 7a.1 Comparison of the properties involved in the combustion process between gasoline, natural gas, and hydrogen when used in an ICE. Flammability limit simply means that a fuel could be ignited only within the limits given in the table. In the case of hydrogen, we have indicated this to be between 10 and 74% of hydrogen in air

Property	Gasoline	Natural Gas	Hydrogen
◇ *Flammability limits* (ϕ)	0.7–4	0.4–1.6	0.1–7.4[1]
◇ *Laminar flame velocity (m/s)*	0.37–0.43	0.38	1.85
◇ *Octane number*	85–99	> 130	> 140
Adiabatic flame temp. (C)	2306.7	1967.8	2206.7
Auto-ignition temp. (C)	276.7	449.4	584.4
♦ *Stoichiometric volume (%)*	2	9.48	29.53
♦ *Minimum ignition energy (mJ)*	0.24	0.28	0.02
♦ *Quenching distance (mm)*	2	2.1	0.076

◇ Indicates favorable for hydrogen, ♦ Indicates unfavorable for hydrogen

1. ***Wide range of flammability***: Hydrogen can be burnt over a wide range of fuel-air mixing ratios (from 4 to 74%). Since it takes very little hydrogen to burn in air, hydrogen can be combusted on a lean mixture. This makes it possible to have a more complete combustion and fuel economy. The lean mixture may also reduce the temperature of combustion and, thus, produce less nitrous oxide. However, this will result in significant reduction of power and may necessitate the use of a turbo charger to increase the power.
2. ***Low ignition energy***. Hydrogen needs very little energy to ignite. It is about one order of magnitude less than gasoline. This means that hot sources and hot spots in the cylinder could act as sources of ignition, which may lead to premature ignition.
3. ***High auto-ignition temperature***. The auto-ignition temperature of a substance is the lowest temperature at which a chemical will spontaneously ignite in a normal atmosphere without an external source of ignition, such as a flame or spark. This temperature is required to supply the activation energy needed for combustion. The auto-ignition temperature is an important factor for determining the compression ratio. The temperature rise during compression is related to the compression ratio by the following relation:

$$T_2 = T_1(V_1/V_2)^{\gamma-1} \tag{7a.1}$$

where V_1/V_2 = the compression ratio, T_1 = absolute initial temperature, T_2 = absolute final temperature, and γ = ratio of specific heats. However, the final temperature may not exceed the auto-ignition temperature without causing pre-ignition. Thus, the high auto-ignition temperature of hydrogen leads to a higher compression ratio as compared to hydrocarbon fuels. As shown in Chap. 6, the higher the compression ratio, the higher are the thermal efficiencies of the engine.

[1] Although some places give a lower flammability limit of hydrogen to be 4% in air, but in practice hydrogen needs to be about 10% in air for ignition.

Small quenching distance. Quenching distance is defined as a characteristic length scale associated with laminar flame quenching during propagation in a narrow channel or tube. This distance varies inversely with initial pressure and is smaller for gases with higher laminar flame speeds. The quenching of hydrogen is smaller than gasoline. This implies that the chance for backfire is increased with hydrogen compared to gasoline or natural gas

4. ***High diffusivity***. The diffusivity of hydrogen in air is much higher than gasoline. This ensures that if a leak develops, the hydrogen disperses rapidly. Also, it produces a more uniform air-fuel mixture. This is important in the cylinder of an engine to get even "burning" of the fuel.
5. ***Low density***. The low density of hydrogen is a great disadvantage. It necessitates a larger volume for storage and a reduced power output because of the lower energy density.
6. ***High flame velocity***. Hydrogen burns at about 2.83 meters per second versus 0.34 meters per second for gasoline at atmospheric pressure and under stoichiometric conditions. This higher flame velocity requires tighter ignition timing.

7a.1.2 Consequences of these Properties for an ICE

If hydrogen is used as fuel in engines initially designed to operate on gasoline, there are several problems that need to be overcome and changes in the engine design are required. All of the problems are of course associated with the properties of the fuel.

The **low density** of the fuel, for example, is a concern because of the amount of volume it occupies in the cylinder prior to ignition. This increased fuel volume reduces the amount of air that can occupy the cylinder and forces the power output to be reduced. This becomes an even bigger problem knowing that in order to reduce the NO_x emissions to low levels, you must use more air. For instance, if an equivalence ratio (EQR, the ratio of stoichiometric air fuel mixture to the air fuel ratio in question) of 0.4 is required to reduce NO_x to near zero, then 2.5 times as much air is needed and even less power is developed. Fortunately, the **wide range of flammability** allows the air to fuel ratio to become very high and still ignite the mixture. This "lean" mixture is an advantage in the fact that it reduces not only NO_x, but improves also efficiency. This increase in efficiency helps then to improve the output power.

Hydrogen has a very **low ignition energy** requirement. This low ignition energy makes a hydrogen-fueled engine susceptible to pre-ignition. Indeed, any hot spots can cause pre-ignition. Engines that have built up carbon deposits, because they previously ran on gasoline will have pre-ignition problems. Therefore, several design changes are necessary, if hydrogen is used as fuel in an ICE due to its low ignition energy.

The first change concerns the spark plugs. They should be a cold-rated type and they should not be platinum–tipped, because Pt is a catalyst promoting ignition. Cold-rated plugs are designed to cool quickly and therefore avoid the possibility

of acting like a "glow plug" and causing pre-ignition. Fine wire iridium-tipped spark plugs are the preferred type. The new spark plugs should be gapped at about 0.0381 cm, although engines have been run with gaps as small as 0.0178 cm. However, a gap of 0.0635 cm or more is not recommended, although the engine will run correctly.

The second change relates to the ignition system in order that it will not fire on the exhaust cycle. In many of today's modern cars, the coil pack will be designed with one coil of the ignition driving two different spark plugs. One of them is for a cylinder that is firing, while the other is for a cylinder that is exhausting. If the engine's ignition system is designed in this way, then the coil pack is placed with coils that only fire on the ignition cycle. This can be done with two coil packs or with separate coils. If a coil-on-plug system is modified, the two wire coils may be replaced by three wire types. For vehicles equipped with distributors, this is not a problem.

The third change is about the nature of the oil. One should use a synthetic oil to avoid pyrolysis-caused hot spots and, thus, pre-ignition. Pyrolysis is a thermal decomposition process that can destroy the oil and decompose it. To further reduce the possibility of oil causing a problem, a positive crankcase ventilation system with an oil separator needs to be added. Further details can be found later in the manuscript. To reduce the possibility of oil entering the combustion chamber, it is recommended that diamond-like coatings should be applied to the valve seals and that the pistons should be changed to hyper-eutectic barrel-skirted types with a much smaller tolerance than normal. A close monitoring of the hydrocarbons in the exhaust will tell you how successful you have been.

The next problem to face is the **small quenching distance**. This means that hydrogen will burn closer to a given surface than gasoline. For this reason, modern designers have tended to move the top piston ring down slightly to strengthen it. It also means that any small pocket, such as in a spark plug, could be ignited when using hydrogen. Actually, most modern engines will not be really affected by the small quenching distance.

The **high diffusivity** is an advantage, because the hydrogen will quickly disperse in air and will give a much more uniform air-fuel mixture. This means that the mixture will burn more evenly and more completely. The high diffusivity also means that if there is a hydrogen leak, the hydrogen will disperse very rapidly and, thus, eliminate any unsafe condition caused by the leak. Because of hydrogen's high diffusivity, there is no need to worry about "swirl" or other fuel-air mixing techniques.

The **high flame velocity** means that the hydrogen fuel-air mixture will burn much faster than gasoline. Under stoichiometric conditions, it burns about 8.3 times faster than gasoline. This higher flame velocity means that the engine tuning is much more critical. Since the fuel burns faster, there is a need to precisely control the spark timing, because if the timing is too early, all power will be lost. Furthermore, because the fuel burns so fast, the spark can be applied much later. For instance, gasoline timing may ignite the air-fuel mixture to 10° before top dead center and hydrogen may be at or near top dead center. This also means that the spark advance for gasoline-fueled engines will be wrong for hydrogen and must be modified.

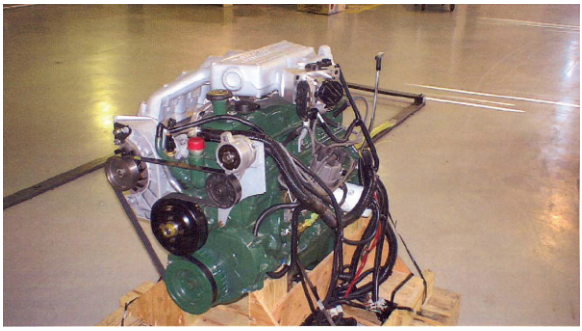

Fig. 7a.1 4.9 liter HEC six cylinder hydrogen internal combustion engine with a compression factor of 13.5:1

Hydrogen has an **octane rating** of about 140. This higher octane rating allows the engine to operate at higher compression ratios than gasoline. The result of increasing the compression ratio is that it also raises the thermal efficiency of the engine and therefore can produce more power. Hydrogen engines will run with 14.5:1 compression ratios. Figure 7a.1 displays an hydrogen internal combustion engine with a compression factor of 13.5:1

7a.2 Overcoming the Larger Cylinder Volume Required by Hydrogen

The original Ford F300 (4.9L) had a power rating of 120 hp with a compression ratio (CR) of 8.3 to 1. With the electronic fuel injection (efi) a long ram intake manifold was used to boost the air flow. The combination with the efi allowed getting 131 hp at a CR of 8.3 to 1. In the following section, the F300 engine will be used as a model to compare the performance with an engine that has been converted to run on hydrogen. In looking at the performance of a hydrogen-fueled engine, one should first decide on the amount of NO_x emissions that will be allowed. Under stoichiometric conditions, the NO_x emission level will be very high. The NO_x emission level can be reduced by running the engine leaner, at a lower equivalence ratio (EQR), and, thus, reducing the combustion temperature, as NO_x does not form below 700°C. To get the NO_x level below 10 ppm, the engine needs to run at an EQR of 0.4 or less. We will look at the performance at an EQR of 0.4, 0.5, 0.7, and 1.0, where 1.0 will only be used for comparison sake.

7a.2.1 Use of a Turbo Charger or Direct Injection

To begin with, hydrogen occupies a lot of space inside the combustion chamber of the engine. The amount of space required is about 29.6% of the available space. Gasoline will only occupy 1 to 2% as a vapor. This means that there is less space

Table 7a.2 Output power (hp)/efficiency (%)

Fuel	CR	EQR = 1	EQR = 0.7	EQR = 0.5	EQR = 0.4	EQR = 0.4 turbo
Gas	8.3:1	120/29.1	–	–	–	–
Gas	9.3:1 efi	138/30.0	–	–	–	–
H_2	9.0:1	130/30.1	94/31.0	69/31.7	56/32.1	125/36.01
H_2	10.0:1	135/31.1	97/32.1	71/32.8	58/33.3	–
H_2	12.0:1	142/32.7	102/33.7	75/34.6	61/35.1	–
H_2	13.2:1	145/33.4	105/34.5	77/35.4	62/35.9	–
H_2	14.5:1	148/34.0	107/35.2	78/36.1	64/36.7	–

for the required air and further details can be found elsewhere [1]. We will use the theoretical thermodynamic efficiency of an Otto cycle engine as our "measuring stick". The formula is

$$n = 1 - (1/CR^{\gamma-1}) \tag{7a.2}$$

where n is the efficiency, CR is the compression ratio, and γ is the specific heat ratio.

Table 7a.2 displays the output power versus the efficiency using gas or hydrogen for different compression ratios and selected lower equivalence ratios. One can see that changing the equivalence and compression ratios makes a huge difference in the output power and the efficiency. Therefore, one method to overcome the low density of hydrogen is to use a turbo charger or a super-charger to force more air into the cylinder. The use of a high compression ratio and turbo charger, combined with a low equivalence ratio can provide the engine builder with a near-gasoline-like performance, while still being able to meet low NO_x emission requirements. Another method is to use direct injection, whereby the hydrogen is forced into the cylinder after the air is already in the cylinder and after the intake valve has closed. The use of liquid hydrogen increases also the amount of air getting into the cylinder. Many aspects of the engine to increase mechanical efficiency can be improved, but this is an incremental approach which helps only, if the engine design is already competitive.

That is why another approach is considered, where the hydrogen's lack of density is accepted and, together with the basics, an engine around hydrogen's unique characteristics is designed. The flame velocity of hydrogen is more than six times faster than gasoline; therefore, the maximum engine speed and/or the maximum cylinder size should not be limited to gasoline engine design limits. For instance, the cylinder bore and stroke could be doubled without sacrificing engine speed. If the cylinder bore size is doubled from 10 to 20 cm, the volume is quadrupled, while only increasing the piston ring surface area by twice. The large bore engine would slightly increase the mechanical efficiency. The engine's footprint would not change significantly, a V-8 engine would give way to a V-4 and an inline 6-cyl would be replaced by a 3-cyl version. The engine cost would not increase too much either, because parts like the cooling system and crankshaft also used with the gasoline versions were designed to handle the higher power associated with that fuel.

HEC is considering manufacturing an engine with a 20 cm bore and a 20 cm stroke as an upgrade to the 10 cm bore and 10 cm stroke engines currently produced. The volume is calculated as pi × radius of bore^2 × stroke. Inserting the proper numbers, one gets 3140 and 25,120 cm^3. This may seem difficult to grasp at first, but hydrogen-fueled engines need larger cubic centimeter cylinders to achieve optimum performance. Diesel engines have gone to larger cylinders to achieve the power levels they needed. Hydrogen engines do not only need the larger cylinders, they also need to operate at higher speeds than the equivalent size diesel would.

7a.2.2 Use of Ammonia as a Hydrogen Carrier

Anhydrous ammonia, NH_3, may hold the key to solving the storage and density issues associated with hydrogen. Ammonia, consisting of one nitrogen and three hydrogen molecules, actually is denser in hydrogen than liquid hydrogen. Furthermore, an infrastructure for distributing and using ammonia is already in place, as it has been widely used as a fertilizer and refrigerator for around 100 years. The relative ease associated with transporting and storing ammonia could further eliminate other issues that impede hydrogen's use as a fuel. The combined use of ammonia places it second only to sulfuric acid among chemicals in annual usage. Ammonia is stored in tanks that are identical to those used by the propane industry except that the valves are changed. Most ammonia is currently made from a reforming process using natural gas; however, it is possible to synthesize ammonia from renewable sources like solar, wind or hydroelectric power. This process involves first using the electrical power to electrolyze water to create hydrogen and then further add nitrogen to create ammonia. In the last several years, researchers showed considerable interest in utilizing ammonia as part of the hydrogen solution. In 2004, a yearly conference began that is devoted entirely to the use of ammonia as a fuel and/or a hydrogen carrier.

7a.2.3 Use of Mixed Gases

One of the uses for hydrogen is to mix it with other gases to reduce the exhaust gas emissions. The best known of these mixtures is hythane which is a combination of natural gas and hydrogen. Mixtures from about 17% hydrogen to 30% have been used. Recently, ammonia was mixed with gasoline [4] and diesel to try to reduce emissions and improve efficiency. Even the mixing of ammonia and hydrogen has been considered. Hydrogen could be injected along with almost any fuel, once modifications were made to the engine to accommodate it. HEC recently developed an engine that features dual injectors for such an application. This trend should continue with multi-fuel or flex-fuel vehicles and equipment becoming more prevalent, as industry continues to try and find ways to make existing fossil fuel run cleaner. Catalytic converters could help reduce the emissions even further.

7a.3 Engine Exhaust Emissions

Table 7a.3 displays the emissions of by-products (HC, CO, NO_x, CO_2, CH_4) from a natural gas and an hydrogen engine. These results indicate that a natural gas engine producing 50 kW would produce 34.85 kg of CO_2 per hour. If the engine ran 1000 hours per year, the results would be 34,850 kg of CO_2 emitted into the atmosphere. The total of all emissions from natural gas is equal to 698.66 g/kW-h, while the total of all hydrogen emissions is 0.083 g/kW-h with $\varphi = 0.4$. This clearly shows why hydrogen is considered as the clean fuel. The difference is 34,850 kg versus 4.15 kg per 1000 hours. That represents a decrease of over 8000 times, and natural gas is considered clean compared to gasoline. Another way of looking at the amount of CO_2 output by a typical car is to realize that for every gallon of gasoline consumed, a cloud of CO_2 is left behind that is twice the volume of a typical car.

Table 7a.3 Emissions from natural gas and hydrogen engines all measured in grams/kW-h

Emissions of By–products	Natural Gas Engines	Hydrogen Engines
HC	0.19	0.015
CO	0.86	0.0
NO_X	0.42	0.068
CO_2	697	0.0
CH_4	0.19	0.0

The exhaust gas emission can be controlled using catalytic converters. These converters can be used with hydrogen engines to further reduce the NO_x levels. Indeed, the catalytic converter would only be designed to eliminate NO_x, as there is no CO or CO_2 in the exhaust gas. Lean-burning hydrogen engines can operate at EQRs of < 0.45 with NO_x emissions below 10 ppm without a catalytic converter. It is possible to operate at higher EQR_x to obtain higher power and use a catalytic converter to reduce the emissions to acceptable levels. In some systems, such as marine applications, the catalytic converter is difficult to install. Marine engines use water-cooled exhaust manifolds. These manifolds cool the exhaust gas to a point at which catalytic converters do not operate well. In other applications, the additional cost is a problem. Catalytic converters should be considered when designing ICEs for emission sensitivity.

7a.4 Engine Controls

Hydrogen engines require changes in the **control strategy at both starting and stopping**. During the starting cycle, the EQR is increased slightly to make it easier to ignite the fuel-air mixture and to provide a little more power for the engine, until it reaches the operating temperature. Although this increase might be very slight, it is almost always there. During times of increased engine load, such as vehicle

acceleration to pass another vehicle or a sudden increase in load on a generator that is driven by a hydrogen engine, the EQR may increase momentarily to help supply the transient power. In some of today's engines, the engine controller turns off some of the cylinders. HEC do that with their industrial engines and only turn them on, if they are needed. This method of control can be used during the stopping of the engine, but is not used in the starting process, because the starter would need to turn twice as fast for three cylinders to achieve the same firing interval as for a six cylinder engine. Turning off or stopping the engine requires running the engine out of fuel. The controller needs to shut off the fuel a few cycles before the spark is eliminated to make sure that there is not any hydrogen left in the intake manifold and to eliminate as much water from the cylinder as possible.

All HEC hydrogen engines and gensets are equipped with an **electronic control device called *Oxx Boxx*™**. Fig. 7a.2 displays the block diagram of the *Oxx Boxx*. One can see that the engine control monitors water/oil/air temperatures and crank/cam position. It also controls injector opening time, the spark ignition system, and the electronic throttle valve. Fig. 7a.3 displays the closed loop air/fuel ratio. One can see how through the H_2 and O_2 sensors in the exhaust the *Oxx Boxx* can control the air/fuel ratio. The A/F ratio in the combustion chamber is important for the reduction of NO_x to the zero level. As can be seen in Fig. 7a.3, hydrogen below 0.4 stoichiometry in air produces almost no NO_x. Moreover, it is very important to hold the hydrogen stoichiometry level below 0.5 which means about 15% of hydrogen in air. Indeed, above 0.5, the NO_x emission goes up exponentially.

Hydrogen internal combustion is often wrongly criticized as producer of NO_x. Fig. 7a.3 clearly indicates that with a proper control of the air/fuel ratio as the HEC engine does with their Oxx Boxx control, NO_x emission is a thing of the past.

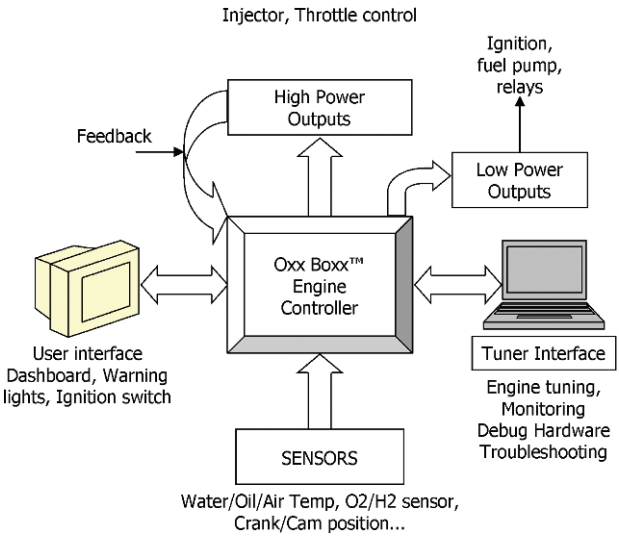

Fig. 7a.2 Block diagram of Oxx Boxx

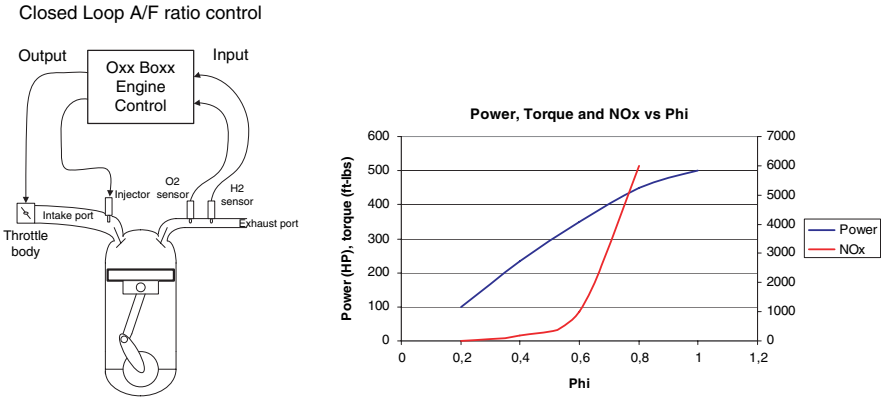

Fig. 7a.3 Schematic diagram of the air/fuel ratio control and graphs of power and NO_x vs. equivalence ratio

Oxx Control [5] is a client software for monitoring, configuring, and performing adjustments on *Oxx Boxx* engine controllers. It works on any Win32 platform. Logical configuration and adjustment parameters can be downloaded to or uploaded from a controller. They can also be loaded from or saved to an external file for later use. Other main purposes of *Oxx Control* are data logging and throttle control, if the engine is equipped with an electrically actuated throttle.

Oxx Control is typically used while a controller is connected to the computer, though it can also be used stand-alone. If a controller is connected, the user can see in real time various operating parameters of the engine. *Oxx Control* can poll continuously the serial communication port for the presence of a controller, thus detecting automatically its connection or disconnection to the computer. The connected state is indicated in a status bar at the bottom of the main screen, which is displayed in Fig. 7a.4.

Other screens in *Oxx Control* allow defining the following parameters:

- Engine configuration, which includes the number of cylinders, the firing order, type of ignition system, type of trigger system,
- injection length map,
- ignition map (timing advance),

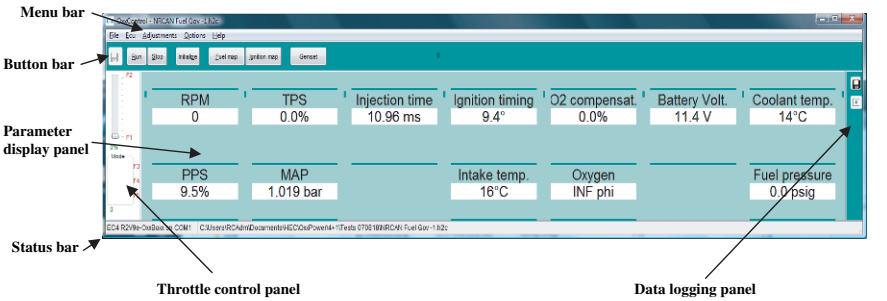

Fig. 7a.4 Oxx Control main screen

– governor settings (if an electrical throttle is present),
– injection temperature compensations,
– O_2 control loop parameters.

7a.5 Delivery Mode of the Fuel (or Fuel Injection)

There are five different ways that hydrogen fuel can be delivered to the engine. The first one is to use a mixer or fumigation system. This is a technique used on natural gas- and propane-fueled engines and should not be used with hydrogen because of the potential for a back fire-caused explosion.

There are three different ways to indirectly inject fuel into an engine:

– Central fuel injection (CFI), which is sometimes called throttle body injection,
– multi-port fuel injection (MFI),
– sequential fuel injection (SFI).

The CFI method was the first to be used. It involved a single large injector that injected fuel into the throttle body and acted a lot like a carburetor. It was an improvement over carburetors and was used during the early 1980. It is phased out in favor of MFI, often referred to as port injection, because MFI offers a much tighter control and can take advantage of the improving electronics that are available for controls. An injector is mounted near the intake valve for each cylinder. The injectors are "bank-switched". That means that all injectors on the left side and on the left bank of the engine will be fired at once and then all the injectors on the right side, right bank, and so on. This is a very effective way of delivering fuel. It has been replaced by SFI, which is the prevalent type of fuel injection in use today. SFI physically looks the same as MFI. The difference is in the controls. An SFI system delivers fuel to one intake at a time and does so in a manner that allows the incoming air to sweep the fuel into the cylinder. This is done by timing the fuel injection to coincide with the cylinder's intake of air. This requires a much better controller. The result is a very efficient fuel delivery system that can be tuned to an individual cylinder.

The final fuel delivery system is direct injection. It is the best way of delivering hydrogen to the cylinder, since the air is already in the cylinder when the fuel is added.

In the following discussion, SFI is selected, since it is the most common type in use today. Once the delivery mode is decided, the choice of fuel injectors needs to be made. Today, there are Quantum and Keihan as recommended suppliers of hydrogen fuel injectors. The Quantum injectors can be used up to 552 kPa, while the Keihan injectors work best at 241 to 310 kPa. The fuel rail or rails must be designed for the pressure and volume of each injector type. HEC has used Quantum injectors at 483 kPa and had good results with hydrogen, propane, natural gas, and the mixture of natural gas and hydrogen.

When running a fuel-injected engine, especially gaseous fuels, it is important to properly filter the gas to eliminate particles that could clog the injector orifice and to have a controller with the proper fuel injector diagnostics software. Unfortunately,

Keihan and Quantum injectors are not directly interchangeable. There are several companies working on new injectors and one can only hope that a standard size and type could be achieved soon.

7a.6 Components in an H2 ICE

7a.6.1 Intake Manifold

The intake manifold does not need to be modified, except to add a larger throttle body to accommodate the larger volume of air that is required for low EQR operation. The area of the throttle body opening needs to be 2.5 times larger for operation at EQRs of 0.4. In the case of larger engines (> 5L), multiple throttle bodies may be needed.

7a.6.2 Cylinder Head

In an internal combustion engine (ICE), the cylinder head sits on top of the cylinder block. The head consists of a platform that contains most of the combustion chamber and determines the location of the intake and exhaust valves as well as the location of the spark plug or plugs.

The cylinder head is a key factor to the performance of the ICE. The size and shape of the intake and exhaust ports and the diameter of the intake and exhaust valves, along with the shape of the combustion chamber, determine a large portion of the volumetric efficiency and compression ratio of the engine. In general, the higher the compression ratio is, the more efficient is the engine.

When running H2-ICE's, the valve seat recession is a concern because of the lack of lubricity of the fuel. Valve recession is the wear of the valve and/or the valve seat, so the valve appears to be recessing into the valve seat. To minimize valve seat wear or failure, hardened valve seat inserts that have a 50–60 Rockwell C hardness are used in the head. The intake and exhaust valves are also stellite-faced to increase wear resistance.

7a.6.3 Exhaust System

The exhaust system does not have the design concerns normally associated with gasoline engines, because the exhaust temperature is approximately one-half of gasoline. Exhaust temperatures of just over 371°C (379.4°C measured on a 4.9L engine) are common compared to 815°C for gasoline. Larger exhaust valves, porting, and polishing will have little effect. Moreover, trying to use the exhaust heat as in a turbo can also be a problem. This point will be discussed in the next section.

The main problem with the exhaust system is the tremendous amount of water generated in the engine. For every one gallon of gas equivalent (gge) consumed, one gallon of water is generated. One gge is about 1 kg of H_2. In a normal vehicle exhaust system, this water would quickly fill the muffler. The exhaust system must be designed to allow this water to pass through and exit out the tail pipe. Care must be taken to prevent the exhaust system components from rusting and the water must not be allowed to "pool" anywhere, as it could freeze in cold climates and cause damage. The exhaust pipes should be designed to descend monotonically from the engine to the point of exit with special care given to the type of muffler chosen and to its installation done so as to prevent water retention. Stainless steel exhaust pipes and mufflers are highly recommended. Flexible iron tail pipes should not be used.

About 2 years ago, our shop truck, a 1988 Ford F150, was modified. This model used an F300, six-cylinder engine and had dual exhausts to run on propane or hydrogen. We had run the engine on hydrogen for quite a few minutes and the idea came that maybe we were filling the mufflers with water. One of our mechanics crawled under the truck and drilled a 0.3 cm hole in the bottom of each muffler near the front. Sure enough, we got about a cup of water out of each muffler.

7a.6.4 Turbo Charger

When using hydrogen as a fuel for spark-ignited (SP) internal combustion engines (ICE), one must pay particular attention to the characteristics or properties of the fuel. Hydrogen (H_2) is available in different states as liquid, low-pressure gas (typically less than 1724 kPa), and high-pressure gas (20,684 kPa and above). Each of these states requires different fuel system components to manage the fuel flow required by the engine. The reason for mentioning the types of hydrogen supplied to the engine is that each has a unique effect on the other engine system components required to achieve the performance and durability targets of the application.

In this section, the discussion is limited to the use of low-pressure gaseous hydrogen. Typically, the hydrogen is stored in a pressure vessel at given supply pressure; it is then delivered to a fuel pressure regulator that steps down the fuel pressure to a predetermined supply pressure for the injectors. The low-pressure regulator typically will require a supply pressure in the range of 862 to 1724 kPa. The output pressure of the fuel regulator will supply the fuel to the injectors at 310 to 620 kPa.

As the fuel used is in a gaseous state (non-liquid), the fuel will displace a large percentage of the inlet air required for combustion. This displacement of available inlet air will cause a reduction in the performance capabilities of the engine. Varying the throttle position will have the largest impact on engine torque. The fueling rate (called 'phi aka EQR') will have the next largest impact on torque and the percentage of inlet air available to the engine for combustion. The ignition timing advance will have the least impact on engine torque, but must not be overlooked. There is a range of acceptable ignition timing advance when utilizing hydrogen as a fuel.

The above background information suggests that utilizing a gaseous fuel displaces a percentage of inlet air required for combustion and will subsequently reduce the performance capabilities of the engine. Another point to understand now is the requirement to match the correct amount of fuel with the incoming inlet air. This is called the air to fuel ratio (A/F). The A/F will vary with the fuel utilized and with the method of calibration. When using gaseous hydrogen in an ICE, the calibration will be typically done with a lean-burn strategy to achieve near-zero emissions in the exhaust gases.

Once the naturally anticipated performance of the engine is fulfilled, one quickly realizes that the engine fueled with gasoline produces almost twice the power compared to the use of lean-burn strategy fueling with gaseous hydrogen. Here is where some method of providing additional inlet air to the engine needs to be addressed to regain performance. Remember, the engine has more capability, if we can just stuff in more inlet air. A super-charger or a turbo charger is a mechanical air pump designed just for this purpose. A turbo charger has been selected because of its lower cost and there is no requirement to redesign the engine's accessory drive system for driving a super-charger.

With a turbo charger installed in the engine's exhaust system, we now have the ability to pump additional inlet air into the engine. The turbo charger is driven by the exhaust gases and heat generated during the combustion process. This energy is wasted without the installation of a turbo charger. The amount of boost or additional air provided by the turbo charger to the engine's inlet is controlled by the waste gate. The waste gate is a vacuum-operated spring-loaded mechanical valve. The waste gate can be locked in one position or be allowed to operate as a variable position valve by utilizing the engine's intake depression (vacuum) to modulate the valve. Electronic variable vane waste gates are also available and used on many of the newer model diesel engines.

Now, with the addition of the turbo charger, one has to determine the maximum amount of boost required to achieve the target performance level. Therefore, the appropriate frame size of the turbo for our engine's displacement has to be determined as well as the boost to meet our performance and, last, estimate the exhaust gas temperature.

Typically, it is safe to boost back to the original gasoline performance of the engine. When fueling with the lean-burn strategy mentioned earlier for hydrogen and with a fueling rate of 0.40 to 0.50 phi (EQR) and a maximum of 1 bar boost (101 kPa), 95% of the performance will be achieved when fueling with gasoline.

With the addition of the turbo charger, it is necessary to compensate for the increased inlet air temperature caused by the turbo charger's boost process. Therefore, a charge air cooler (CAC) (very similar to a radiator) is added to cool the inlet air. The recommended inlet air temperature limit for this application is 60°C. Higher engine inlet air temperatures may cause detonation; therefore, sizing of the CAC is very important. Moreover, the inlet air temperature is monitored and the 60°C limit is used as an engine safety shutdown limit.

The last component which is needed to add to the turbo charger system is an engine oil cooler. As the turbo charger's bearings are lubricated and cooled by the

engine oil, the engine's oil temperature will be increased as a result of the hot oil returning from the turbo charger's bearings. Again, the oil cooler should be properly sized to maintain safe operating engine oil temperatures and validate the cooler size during testing. The easiest way to feed oil to the cooler is by adding a sandwich oil filter adapter to the oil filter boss on the engine block. This adapter will allow unrestricted flow, if sized correctly, and cool the engine oil, because all the oil pump flow is routed through the filter and adapter.

7a.6.4.1 Miller Cycle

Miller cycle engines are more efficient than standard engines, but until recently, they have not been used with small engines. Miller cycle engines are turbo or supercharged and leave the intake valve open for part of the compression stroke. The engine is then compressing against the turbo or super charger. This increases the efficiency by about 15%. The Mazda Millennia uses a 2.3L Miller cycle engine instead of a 3L engine and gets better performance at about 10 to 15% less fuel consumption. Hydrogen-fueled engines could benefit from the Miller cycle. The increased efficiency is very important to hydrogen users, as hydrogen is still higher in cost than gasoline. Industrial engines and gensets should use Miller cycle hydrogen engines.

7a.6.4.2 Engine Oil

The amount of water created in the cylinder causes concern over the engine oil's ability to adhere to the cylinder walls and not been washed away. Hydrogen fuel creates about three times as much water as gasoline. Some requirements are to use the same oil for turbo-charged engines as the one used on naturally aspired engines. Moreover, the hydrocarbon (HC) emissions have to be minimized. Therefore, an oil that has low volatility at high temperatures is necessary. Furthermore, because many of our engines operate outdoors and are used in generator sets, a wide operating temperature for the oil is desirable.

In reviewing the many fine oils available on the market, the Mobil Pegasus one oil has be selected as our oil of choice. This is synthetic oil that was developed for lean-burning engines and turbo-charged engines. It flows down to −54°C. It has a higher viscosity index and provides an excellent oil film at temperatures that are 38°C Celsius higher than conventional oils. It has a flash point of 238°C. Moreover, it is compatible with all the engine seals and extends oil change intervals. It is especially formulated to include 'an additive system that combines high levels of ashless dispersants, medium ash level metallic detergents, and balanced amounts of oxidation and corrosion inhibitors, anti-wear, and anti-scuff agents.' [1] It is designed to reduce oil consumption and, thus, HC emissions and will not harm a catalytic converter, if one is used. Nevertheless, there are other fine oils available on the market and there will be oils formulated especially for hydrogen engines. Such type of oil should be evaluated first and used, if desired.

In conclusion, most of the engine wear occurs during the startup time. It is critical that there be oil retained on the cylinder walls to prevent wear. Any oil used must meet this criterion.

7a.6.4.3 Engine Oil Cooler

The engine oil needs to be cooled for proper engine operation and durability. The engine oil cooler is only necessary for applications that push the engine temperature above normal operating levels and should not be confused with the need for an oil cooler on a turbo-charged engine. Engines in gensets can be operated this way. The oil cooler is a unit that is located external to the engine and is connected to the engine through a pair of hoses. Usually, an oil filter adapter is used to provide the extra connection points. When used in a genset, the oil cooler is usually mounted to the frame of the genset. It requires no maintenance and its only purpose is to reduce the oil temperature. Oil temperature at or approaching 121°C should have an oil cooler added. This is more critical for a hydrogen engine, because hydrogen pre-ignites so easily.

7a.6.4.4 Crankcase Ventilation and Filter System for Hydrogen-Fueled Engines

Using hydrogen as a fuel for spark-ignited internal combustion engines, special attention has to be given to the crankcase venting and filtration system.

The engine's lubricating oil is typically manufactured from crude oil. In an oil refinery, crude oil is separated into various fractions. These become the basis for lubricating oils and fuels. While petroleum refining is an advanced science, small amounts of contaminants, such as sulfur and reactive hydrocarbons, cannot be completely removed from the petroleum and may end up in motor oil-base stocks. All motor oil is made up of base oils and additives. Fully synthetic motor oils contain non-conventional, high-performance fluids. Synthetic blends usually use some non-conventional, high-performance fluids in combination with conventional oil.

Carbon-based deposits from the engine's lubricating oil, in the combustion chamber, on the top of the piston, in the ring grooves, and in the cylinder's squish areas are potential hot spots waiting to happen. Hydrogen will react with these deposits and cause detonation which can be very harmful to the engine's internal components. In an engine fueled with a non-carbon-based fuel, like hydrogen, the only source for carbon-based deposits in the areas stated above will most likely come from the crankcase ventilation system which must be a closed or non-vented system. Moreover, gases escaping past the piston rings will contain oil mist, water, etc. The crankcase air is fed directly into the engine air intake system to be re-burned.

Thus, oil will cause deposits when burned, moisture will cause corrosion and a deterioration of the performance, and eventually damages of the engine's internal

components. That is why two changes are necessary to prevent the ingestion of oil and moisture.

Utilizing synthetic engine oil (non-carbon-based oil) like Mobile Pegasus one and by installing an oil filter separator to trap oil from the crankcase vent system, most of the crankcase emissions can be eliminated. The crankcase gases flow from the engine into the separator underneath a valve diaphragm into the element. The valve regulates the crankcase to a slight negative pressure to reduce engine weeping and prevent damage to seals. The gases then flow through the filter media. Contaminants are trapped by the media and the oil is separated from the air, collected in the housing, and returned to the crankcase. A check valve is installed in the drain line to prevent reverse flow from the crankcase. The filtered gases flow from the media to the inlet air filter and return the gases to the engine's inlet air system for re-burning.

The moisture in the crankcase gases is also a concern which needs to be addressed. During high load and high speed operations, the elevated operating temperatures of all engine systems and the high flow rates keep the majority of the moisture in suspension and it is expelled with the engine exhaust system. However, this is not the case for light load and low speed operation. Moisture can become a severe problem and the addition of a heater to the crankcase vent system is recommended to keep the gas temperature elevated. Keeping the temperature of the crankcase gases from dropping into the dew point range will prevent moisture from collecting in the system and keep the moisture suspended in the air flow. Hydrogen can get past the piston ring and work its way into the oil pan. This can cause a very serious condition. Hydrogen can accumulate in the oil and hydrogenate the oil or, worse yet, cause an explosion. The crankcase ventilation system shown in Fig. 7a.5 eliminates this problem.

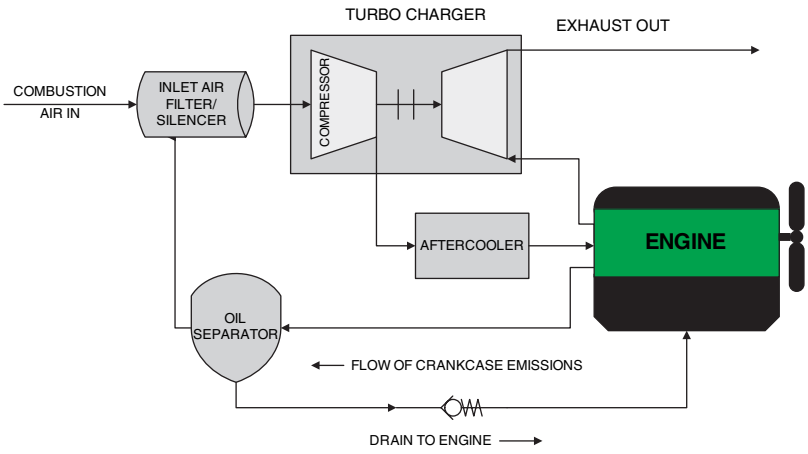

Fig. 7a.5 Crankcase ventilation system

7a.7 What about the Water?

The amount of water that is created in an engine running on hydrogen fuel is very large. For every gallon of gas equivalent that is consumed by the engine, one gallon of water is created. This water must pass through the exhaust system as described earlier. This water could pose a problem, if a hydrogen engine is installed in a fork lift that was going to be used in a warehouse. The extra humidity that would be added to the warehouse air could cause problems for materials stored there.

Automobiles and trucks powered by hydrogen engines would be putting this water and water vapor on the streets and highways or in the air surrounding them. In the winter season, this could cause a serious icing problem. The answer is to capture this water and dispose of it properly or put it to use. For motor-generator sets (gensets), capturing this water offers an opportunity to provide drinking water along with electrical power and heat. Bob Natkin, at Ford Motor Company, demonstrated the viability of this idea by drinking the water out of the tail pipe of hydrogen-powered cars. However, this is not recommended, unless the water has been filtered and the engine's exhaust system has been properly designed so that water cannot become contaminated on the way from the engine cylinder where it was made to the filtration system. The water from a hydrogen engine could be more valuable than the power or heat. Future hydrogen gensets will have this feature. Hydrogen and ammonia (a hydrogen carrier, NH_3) are the only fuels that can create pure water. Remember, it was created at cylinder temperatures well above 38°C.

7a.8 HC and NO_x Emissions

Since one of the objectives in converting an ICE to run on hydrogen is to reduce emissions to a minimum, strict attention is paid to the design details. The NO_x emissions are near a maximum under stoichiometric conditions and decrease, as the engine's equivalence ratio becomes lower (leaner) [6]. There are several concerns which are listed below:

1. Leaner-burning engines need more air. In this case, 2.5 times more air. That means that the gasoline engine's throttle body, intake manifold, and intake valves are not large enough and, as a result, restrict the amount of air that the engine can get into the cylinder. This reduces the amount of power that can be produced. One way of overcoming this problem is to turbo-charge or super-charge the engine as mentioned earlier.
2. Leaner-burning engines are harder to control and need both a good engine control and a good set of sensors, often referred to as the sensor suite. The oxygen sensor is critical, because the only feedback the controller has is from the exhaust gas stream and only the amount of oxygen in that stream is reliable enough for good

control. The amount of oxygen in the exhaust gas increases, as the engine is run leaner.
3. Leaner-burning engines normally run at higher cylinder pressures. Care must be taken to keep the maximum cylinder pressure within specifications.

7a.9 Embrittlement

Whenever one hears of hydrogen, one always thinks about hydrogen embrittlement. 'Hydrogen embrittlement is usually understood as the unwanted delayed brittleness of a material which is caused by the presence of hydrogen, if a sufficient quantity can penetrate into the material' [7]. In general, the factors that facilitate hydrogen embrittlement are:

– Type of alloy,
– hydrogen chemical potential,
– temperature,
– hydrogen diffusion,
– stress.

The alloys that resist embrittlement are:

– Austenite stainless steel,
– copper alloys,
– aluminum alloys.

The alloys that should not be used with hydrogen are:

– Steel alloys of ferrite, martensite, and bainite types,
– titanium and titanium alloys,
– some nickel alloys.

7a.10 Sensors and Venting

Sensor technology is even more important to hydrogen engines, because the control of spark and fuel timing need to be much more precise than in gasoline engines. Hydrogen sensors need to be developed in order to monitor hydrogen in the exhaust stream. This would help in controlling the fuel-spark map more tightly. In addition, sensors are necessary for the space in which hydrogen tanks and/or vehicles reside. As an example, if hydrogen tanks are stored in the trunk of a vehicle, then a sensor is needed to indicate the presence of hydrogen and warn the driver and/or the engine controller. Similarly, the lines leading from the tank to the engine could be sensed.

Hydrogen-sensitive tapes that change color when exposed to hydrogen have been investigated [8]. It is proposed that all fittings be wrapped with this type of tape. Sensors for garages, buildings, etc. need to be made ready as well as those for under

the hood of cars, in the enclosure of hydrogen-fueled gensets, etc. Hydrogen being the lightest of all gases will rise when released, therefore, venting is necessary in all confined areas and should be coupled to a sensor for safety. Ford designed special vents into their hydrogen vehicles. Better mass flow sensors are needed for hydrogen.

Another valuable sensor is a flame detector. Hydrogen burns with a very light blue flame and is almost undetectable in daylight. A flame detector is a specially designed infrared camera that can 'see' the heat from the hydrogen flame (Daycor II – UV detection camera). This is an important piece of safety equipment.

7a.11 Future Applications

Hydrogen engines work well with hybrid electric power trains. In the future, we expect to see hydrogen hybrid electric buses, boats, automobiles, and power generators. The latter will be in the form of variable speed generators. Toyota, Honda, Ford, and GM, to name a few, already have hybrid electric vehicles on the road. ISE corporation in California has had a hybrid electric bus on the road for about 2 years. The use of hybrid electric technology, when combined with hydrogen-fueled engines, will give the most efficient power train available.

The paralleling of engine/generator sets will allow the hydrogen-fueled engine to compete at a higher power level compared to what is possible with a single engine. HEC has a $4+1^{TM}$ hydrogen-fueled genset, displayed in Figure 7a.6, that produces 250 kW of power. This is more than twice the power produced by Ford 6.8L V10 powered hydrogen gensets. 250 kW, $4+1$ gensets can be paralleled to achieve multi-mega-watt power generation capability.

The use of ceramics, composite materials, and plastics will also increase the utilization of carbon fiber usage, as their cost comes down. In addition, there will be

Fig. 7a.6 250 kW hydrogen genset

changes made to increase the engine life, such as ceramic-coated cylinder walls, replaceable wet cylinder sleeves, improved bearing surfaces, and yet harder valves and valve seats.

There is a great potential for hydrogen internal combustion engine vehicles at the airport. Since huge numbers of vehicles, such as shuttle buses, tugs, taxis etc., are all situated in one confined area, the use of hydrogen as a fuel can easily be envisaged, because the installation of one service station for hydrogen will suffice. Normally, the hydrogen infrastructure is the big stumbling block for the emergence of hydrogen economy. This, however, will not be the case at the airport. Therefore, a hydrogen project at the airport makes a lot of sense. Such a project, in fact, will soon be forthcoming at the Montreal airport. Air Liquide will be responsible for the hydrogen infrastructure and HEC will provide the hydrogen internal combustion engine for the tugs. We hope that the Montreal airport project with hydrogen fuel will act as a catalyst for many more similar projects all around the world.

7a.11.1 All Electric Engine

Automotive engineers are designing electric replacements for almost all of the older style mechanical parts for the engine. Air conditioners, water pumps, starter/alternators, oil pumps, and even electrically controlled valves are being added to the list that already contains cooling fans, coil-on-plug ignition systems, and throttle bodies. The new components will allow the engine designer the freedom to operate an engine in ways that would have been never possible before. Oil pumps can be turned on before an engine is started, thereby pre-oiling the engine and reducing wear. Today's designers can eliminate drive belts from the engine in the same way they were able to eliminate the distributor. Hydrogen engines will benefit from these improvements and will be able to increase the engines' efficiency. Efficiencies of 38% are possible today with test engines moving above 40%. These new electric components can be controlled by the engine controller. Because of this, tomorrow's engine controllers will be even more sophisticated and will be able to offer an even wider range of controls. Electrically controlled valves will allow many improvements in the engine fuel system and will increase the engine efficiency in doing so.

7a.11.2 Engine Efficiency

The future will belong to the most efficient. In the world of hydrogen engines, it means using every improvement possible. The difference in an engine running at 30% efficiency and one at 38% efficiency, Table 7a.4, can be seen by comparing the output power from each engine.

One can see that an 8% increase in efficiency for a 120 hp engine gives an additional 32 hp of power and eliminates 32 hp of heat losses. Another way of using this

Table 7a.4 Output power from different engines

Efficiency	Pout	Pheat	Ptotal
30%	120hp	280hp	400hp
38%	152hp	248hp	400hp

efficiency improvement would be to decrease the amount of fuel (Ptotal) from 400 to 316 hp. This is a 21% reduction in fuel consumption. Hydrogen with its higher octane ratings than any of the other alternative fuels except ammonia allows for higher compression ratios and, in turn, higher efficiency. In addition, hydrogen engines can run on a leaner fuel mixture than any other fuel and, again, gain efficiency. Properly designed hydrogen engines should always be higher in efficiency than gasoline engines. It should be noted that running an engine on 1/2 of its cylinders and only using the other 1/2 when the power is needed gives about a 9.9% increase in fuel mileage.

The BMW Group's Research Division is seeking in the long term to achieve an effective degree of efficiency of 50% for its hydrogen engine running at its optimum point. This demanding objective is to be achieved by optimizing the combustion process and capitalizing on the excellent combustion properties of hydrogen (low degree of activation energy, high rate of flame propagation, etc.). [9]

7a.11.3 Air Quality and Efficiency

Cleaner fuels, such as hydrogen, reduce the amount of exhaust gas emissions and promote better air quality. Increasing the efficiency of an engine also reduces the amount of emissions by using less fuel and, thus, providing less exhaust gas. Engines of the future will be designed to only use as much of the fuel, as is required to produce the required amount of power. Cadillac was a pioneer in this area with its 8-4-2 cylinder control. Toyota and Honda presented their versions of six cylinder engines that run on three cylinders at the 2005 Montreal International Auto Show. HEC also presented a six-cylinder engine for industrial use that runs on what they call a 3 + 3 control scheme. The improvement is seen at idle and low-power operations. Engines are most efficient when they are loaded. A hydrogen engine running at full power might get 36% efficiency. At 50% load, it might get 35% efficiency. At 25% load, the efficiency is likely to be 20%. It goes down to 11% efficiency at 10% load. Therefore, dropping 1/2 the cylinders at light loads can improve the efficiency a lot by doubling the effective load.

7a.11.4 Power vs. Speed

The graph of power and torque vs. engine RPM for hydrogen ICE (Fig. 7a.7) looks very similar to a gasoline engine. The maximum power is at 3300 RPM and maximum torque at 2300 RPM.

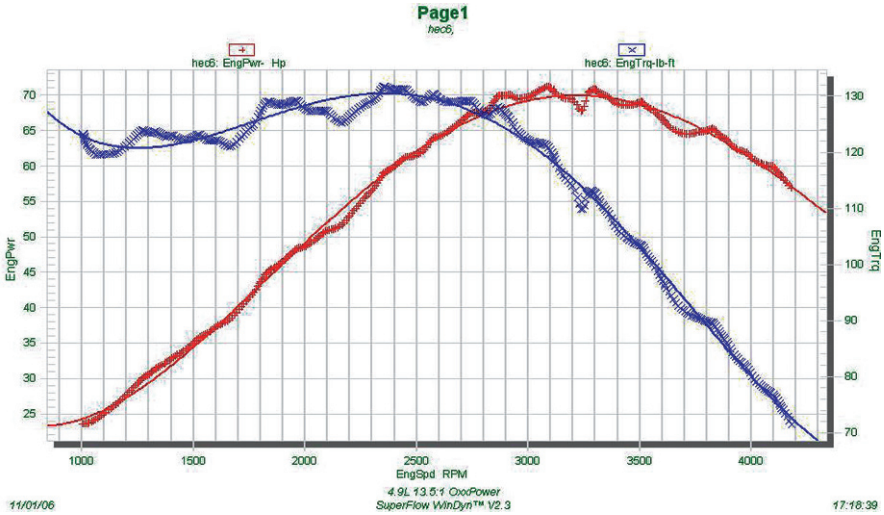

Fig. 7a.7 The graph of power and torque vs. engine RPM for a 4.9 liter HEC six-cylinder hydrogen internal combustion engine with a compression factor of 13.5:1

7a.12 Conclusion

The development in the hydrogen internal combustion engine has attained a level, where market penetration at a competitive price could easily be envisaged. For stationary application, Hydrogen Engine Center (HEC) has developed hydrogen generators varying from 15 up to 250 kW. As discussed in previous sections, HEC hydrogen engines have no emissions. The NO_x emission which is the most likely pollutant from a hydrogen combustion engine has been eliminated by carefully ensuring lean burning of hydrogen with less than 0.4 stoichiometry. In this way, the temperature of combustion is much reduced, eliminating the production of NO_x. The principal application of hydrogen generators is expected to be in the field of renewable energy, such as wind, hydro, and sun. Hydrogen genset has the ability to turn an intermittent source of energy, such as wind and sun, into a constant source. Many isolated areas, not connected to an electrical grid, could operate independently with wind turbines, electrolyzers, and hydrogen generators. The same thing applies to photovoltaic systems. Hydrogen gensets could also replace diesel generators that give off large emissions like CO, particulate matters, and NO_x as well as greenhouse gases, such as CO_2. Hydrogen internal combustion engines developed by HEC will only produce water and no other emissions. In the field of vehicular application, BMW, Ford, Mazda, and Man have developed hydrogen internal combustion engine cars.

In the case of Ford, their Model U is powered by a hydrogen internal combustion engine [10]. The engine is supercharged and inter-cooled for maximum efficiency, power, and range. The emissions from Model U are nearly zero even

for carbon dioxide. The engine is 25% more fuel-efficient than gasoline engines. A hybrid-electric transmission further improves efficiency. The Model U is a 2.3 liter, four-cylinder supercharged, inter-cooled hydrogen internal combustion engine. This car gets about 45 miles per kg of hydrogen.

Whereas the Ford Model [10] U was focused on the fuel economy, the BMW hydrogen internal combustion car sets records for high speed, achieving 300 km/h. BMW sets speed records with a specially designed hydrogen internal combustion vehicle. The BMW single seater H2R hydrogen combustion car uses a 6.0 liter, 12-cylinder power unit producing in excess of 210 kW and reaching a top speed of 302.44 km/h. However, for the commercial purpose, BMW will be launching a dual-mode version of the current seven Series to be able to run on both hydrogen and gasoline [11, 12]. The BMW ICE development is geared towards fuel efficiency and powerful engines. In fact, BMW is a pioneer in hydrogen ICE.

The hydrogen internal combustion vehicle and the hydrogen gensets are both ready for the market. We do not need to wait for the fuel cells to start hydrogen economy. With a fuel efficiency of 36 to 38%, the hydrogen internal combustion engine is competitive with the efficiency of the fuel cell. Of course, the cost of an internal combustion engine for hydrogen is only a fraction of the cost for fuel cells.

The recent Stern [13] report on climate change maintains that the average temperatures of our planet could rise 5°C from pre-industrial levels, if climate change goes unchecked. By the middle of the century, 200 million people may be permanently displaced due to rising sea levels, heavier floods, and drought. The report states that before the industrial revolution, the level of greenhouse gases was 280 ppm CO_2 equivalent, whereas the current level is 430 ppm CO_2 equivalent. The level should be limited to 450–550 ppm CO_2. Anything higher would substantially increase the risk of very harmful impacts. One of the recommended actions of the Stern report stipulates that support for the deployment of low-carbon technologies should be increased by up to five times. The report also states that unabated climate change could cost the world at least 5% of GDP each year, if more dramatic predictions come to pass, the cost could be more than 20% of the GDP. However, the cost of reducing emissions right now could be limited to around 1% of the global GDP. Moreover, each ton of CO_2 emitted causes damages worth at least $85, but emissions can be cut at a cost of less than $25 a ton. It states that shifting the world onto a low-carbon path could eventually benefit the economy by $2.5 trillion a year. By 2050, markets for low-carbon technologies could be worth at least $500 billion. It is clear from the Stern report that moving to the hydrogen economy is the right thing to do. Hydrogen internal combustion engine technology is ready and cost-effective.

Acknowledgements The authors would like to thank Mr. Raymond Courteau for helping us with the Oxx Control section and Mr. Alexandre Palardy for taking the data on the engine power vs. engine speed. We would also like to thank Bob Mendlesky, Joe Lewis, Mike Schiltz, Lucie Bellemare, and Laurie Harms for their writing and editing of this chapter. The contribution of the referees is greatly appreciated.

References

1. Module 3: *Hydrogen Use in Internal Combustion Engines*. College of the Desert, Revision 0, December 2001.
2. Stockhausen, W. F., Robert, J. N., Daniel, M. K., Lowell, R., Xiaoguo, T., Siamaak, H., Steven, J. S., and Vance P. Z. 2002 Ford P2000 *Hydrogen Engine Design and Vehicle Development Program*.
3. Muller, J. and Jonathan F. *Hydrogen Man*. Forbes Magazine, December 27, 2004.
4. Grannell, S. M., Dennis, N. A., Stanislav, V. B., and Donald, E. G. 2006 *The Operating Features of a Stoichiometric Ammonia and Gasoline Dual Fuel Spark Ignition Engine*. ASME International Mechanical Engineering Congress and Exposition. SAE paper 2007–01–0231.
5. Raymond C. *Development of Engine Controllers for Commercial HEC Products*. HEC internal report. September 2005.
6. Natkin, R. J., Xiaoguo, T., Brad, B., Bret, O., and Adam, D. *The Hydrogen Engine Boosting Performance and NO_x Study*. SAE Transactions 112 (2003) 865–875. Society of Automotive Engineers, New York, NY ETATS–UNIS (1927). University of California-Riverside.
7. Jarmila, W. and Rolf, K. *Damage due to hydrogen embrittlement and stress corrosion cracking*. Eng. Failure Analysis 7 (2000) 427–450.
8. TMS 2007 Annual meeting, February 25 – March 1, 2007, Orlando, F. N. Mahajin, A. T. Raissi, G. Bokherman, J. E. Captain, B. Peterson, S. Trigwell, M. and Whitten, A. B. *Effects of PdO distributions over Ti02 particles on its chemochromic behaviours for hydrogen detection*.
9. BMW: Hydrogen and clean energy strategy: http://www.carlist.com/autonews/2004/autonews_36.html.
10. Ford Model U information, specifications, history, and images: http://www.conceptcar2.com/vehicule/Z6655/default.aspx.
11. BMW hydrogen cars: http://www.bmwworld.com/hydrogen/.
12. Gerrit, K., Manfred, K., Christian, B., and Hybert, F., 2006 "The H_2 ICE age has begun", SAE paper 2006–021–0431.
13. Stern report: *The Key Points Hilary Osborne*, Guardian unlimited, October 30, 2006.

Chapter 7b
Hybrid is a Key Technology for Future Automobiles

Ken Tanoue, Hiromichi Yanagihara and Hidetoshi Kusumi

List of Abbreviations

A/F	Air-fuel ratio
ATF	Automatic transmission fluid
BH	B:magnetic flux density, H:magnetic field strength
CNG	Compressed natural gas
CO_2	Carbon dioxide

Ken Tanoue
Toyota Motor Corporation, 1, Toyota-cho, Toyota, Aichi, 471-8571 Japan,
e-mail: k-tanoue@toyota-turbine.co.jp

Hiromichi Yanagihara
Toyota Motor Europe NV/SA, Hoge Wei 33B, Zaventem, 1930 Belgium,
e-mail: hiromichi.yanagihara@toyota-europe.com

Hidetoshi Kusumi
Toyota Motor Corporation, 1, Toyota-cho, Toyota, Aichi, 471-8571 Japan,
e-mail: kusumi@hidetoshi.tec.toyota.co.jp

A. Léon (ed.), *Hydrogen Technology*,

CVT	Continuous variable transmission
DC	Direct current
ECU	Electronic control unit
FC	Fuel cell
FF	Front engine front drive
FR	Front engine rear drive
FWD	Free wheel diode
GM	General Motors
Goe	Gauss-Oersteds
HEV	Hybrid electric vehicle
HV	Hybrid vehicle
IC	Integrated circuit
ICE	Internal combustion engine
IGBT	Insulated gate bipolar transistor
IPM[1]	Internal permanent magnet
IPM[2]	Intelligent power module
LA-4	Los Angels number 4 mode
MG1/2/R	Motor generator 1/2/rear
NMHC	Non-methane hydrocarbon
NMOG	Non-methane organic gas
Nox	Nitrogen oxide
OECD	Organisation for Economic Co-operation and Development
PCU	Power control unit
PM	Permanent magnet
PP	Polypropylene
PVD	Physical vapour deposition
SMR	System main relay
SOC	State of charge
SPM	Surface permanent magnet
SULEV	Super-ultra low-emissions vehicle
SUV	Sport utility vehicle
T	Tesla
THC	Total hydrocarbon
THS	Toyota hybrid system
THS II	Toyota hybrid system type II
THS-C	Toyota hybrid system with CVT
THS-M	Toyota hybrid system mild
TWC	Three-way catalyst
US	United States
USGS	US Geological Survey

7b.1 Introduction

World opinion is increasingly concerned about the security of energy supply, the preservation of the environment, and continuous economic growth. As concerns the first point, a phase-out of petroleum is becoming more and more controversial with recent extreme price rises of oil symbolically shadowing the uncertainty of petroleum as a readily available resource. There are actually lots of arguments related to the future oil production scenario. Fig. 7b.1 displays the prospect of oil supply up to 2100 taking into account the low-, high-, and the expected energy scenario. As can be seen, the phase-out of oil in the three cases will happen with unexpected

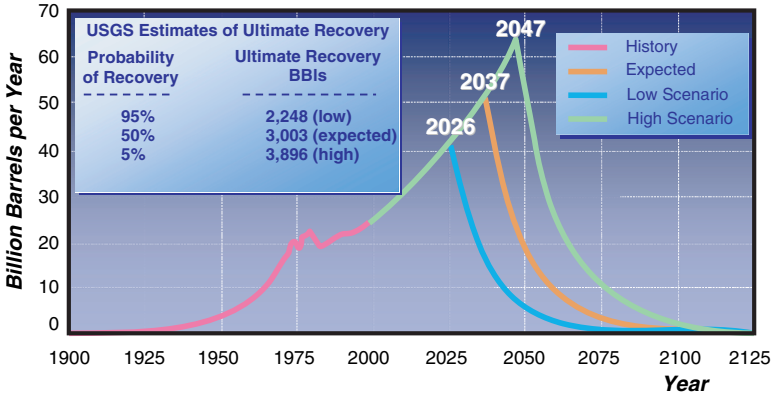

Note: U.S. volumes were added to the USGS foreign volumes to obtain world totals with the assumption that the growth rate of oil demand is 2% per year

Fig. 7b.1 Oil production scenario

speed, because the energy demand is growing, while the sources of hydrocarbon are finite. The second point concerns the very serious climate changes resulting from increasing anthropogenic CO_2 emissions. Indeed, a car that turns twice as much gas adds twice as much CO_2 to the atmosphere. Since this type of pollution is not limited by law, a car has no devices for removing CO_2 from the exhaust.

Today, more than half of hydrocarbon-based energy is consumed by the OECD countries. As can be seen in Fig. 7b.2, the number of vehicles on the road will tremendously increase due to the strong economic growth of many developing countries. Huge quantities of automobiles, closely linked to daily human lives, will have a considerable impact on the environment and issues related to energy supply. However, it is not realistic to expect the developing countries to slow down their growth. Therefore, any solution to this problem must be driven mainly by the developed

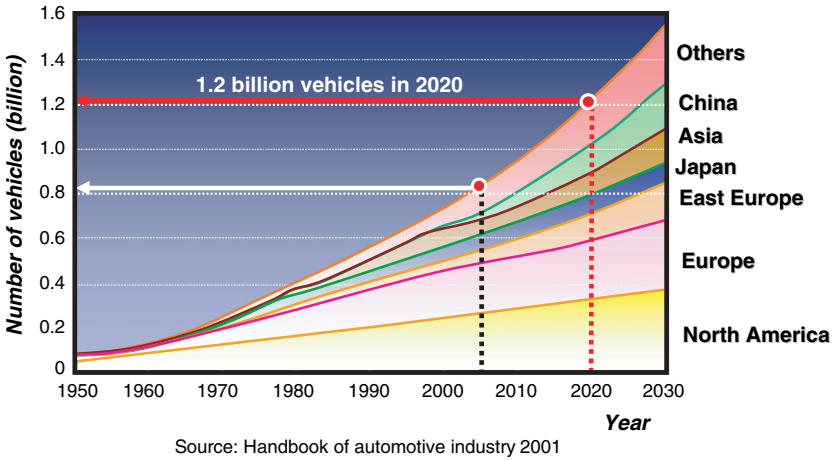

Source: Handbook of automotive industry 2001

Fig. 7b.2 Global vehicles holdings

world. This adds to the sense of urgency in taking action to make our vehicles far less polluting and to seek for cheap energy.

In this context the automobile industry is faced with the challenges to increase fuel economy and meet the emissions legislation. Although the automotive industry is clearly not responsible for supplying energy, it will need to undergo drastic changes in vehicle and engine designs. New technologies and the introduction of alternative energy are suggested by many industries. Apart from their reduced environmental impact and sustainable supply, these "new technologies" should also be considered in terms of production, transportation and cost.

It is extremely difficult to change an energy system within a short period of time. In the short term efficiency is by far the most cost-effective strategy for reducing emissions and fuel use. In this sense increasingly efficient ICE vehicles will probably remain the prevailing propulsion system in the near future, but with parallel research and development focused on alternative systems.

In this challenge of developing more environmentally sustainable vehicles several alternatives have already been proposed. The most widespread ones are the CNG vehicle, flexible fuel vehicle (ethanol vehicle etc.), hydrogen internal combustion engine, pure electric vehicle, hybrid vehicle, and the fuel cell vehicle. Especially fuel cell (FC) vehicle development gained pace towards the late 20th century as the ultimate clean car, but the fundamental problem of establishing sustainable energy source(s) for global use remains. The fact is that hydrogen is the most challenging of all alternative fuels, particularly because of the enormous effort needed to change our existing gasoline infrastructure. Therefore, hydrogen most likely will not be used for refueling of vehicles in the near term. The hybrid vehicle (HV) technology of flexibly combining electrical energy with (any) other power train, including the current ICE, is a promising short-term approach to curb the growth of fossil fuel usage without having to change infrastructure and supply systems. At the same time, new innovative systems have to be pushed depending on their *actual* potential as a viable solution to the global needs.

So, Toyota positions the hybrid technology as a core technology, a platform for various power trains, in order to eventually achieve the ultimate eco-car. Toyota's strategy is to increase worldwide the hybridisation of passenger cars as well as SUV and to quickly introduce them into the market. Although the commitment may vary, Honda, Nissan, GM, and Ford are all actively introducing HV into the US markets. From the European car manufacturers different messages about HV can be found, but in general everyone attempts to develop more environmentally friendly vehicles. At present, it seems that cleaner energy vehicles are being developed according to each maker's strategy.

This chapter shall highlight an example from the automotive industry to demonstrate how a technology innovation can open the gate for a sustainable approach to securing future prosperity and reducing the impact on the environment for our global society. This paper will present an overview of the prototype vehicle and emphasise some of the unique features of this energy-saving clean environment solution. The following sections will focus on several crucial activities that Toyota has been intensively working on in order to tackle the challenges described above.

7b.2 Challenges for HV Development

The gasoline-electric hybrid car is just a cross between a gasoline-powered car and an electric car. The hybrid, is a compromise, as it attempts to significantly increase the mileage and reduce the tailpipe emissions of a gasoline-powered car, while overcoming the shortcomings of an electric car.

The structure of a gasoline-electric hybrid car is composed of a gasoline engine, a fuel tank that is the energy storage device for the gasoline engine, an electric motor, a generator, a set of batteries, which is the energy storage device for the electric motor, and the transmission. By combining two sources of power, a hybrid car increases the efficiency and performance of a vehicle. The two-power source in a hybrid vehicle can be combined traditionally either in a parallel way or in series. In the parallel hybrid the gas engine and the electric motor are connected to the transmission, providing the power for propulsion. In the series hybrid, by contrast, the gas engine turns a generator that can charge the batteries or power the electric motor that drives the transmission. In this case, the gasoline engine never directly powers the vehicle. It should be noted that two other combinations exist, namely, series-parallel hybrid and complex hybrid.

Worldwide HV's in 2006 recorded about one million, which corresponds to about 2% of the total of 50 million conventional vehicles. It is estimated that HV production in 2010 will exceed 2.5 million, which is equivalent to about 4% of the 65 million annual productions of ICE vehicles. However, this is still insufficient to substantially contribute to resolving the global environmental and energy problems.

For real mass-market penetration of HV's, tremendous challenges have to be overcome especially in terms of energy use, cost, and sustainability. First of all, HV's have an increased weight due to an extra installation of an electric motor system, power control unit, and battery compared to conventional vehicles. Moreover, the current cost of the vehicle is too high, as additional units are required. Finally, this additional weight does not allow for a good fuel economy of HV's at high speed due to the worsening of the rolling and wind resistance. Nevertheless, the fuel economy of an HV in urban driving is better due to technologies such as regenerative braking and engine stop-and-go. In the future absolute attention will have to be paid to ensuring downsizing and weight reduction, minimising cost, and enhancing the function of the new generations of hybrid systems.

7b.3 Essence of Hybrid Technology and its Evolution

The tests performed on a hybrid vehicle in urban areas show that the vehicle can reach a higher fuel economy and much lower emissions than a traditional ICE. The key feature of this vehicle is the ability to completely and instantaneously switch off the engine at low speed and low-load operation where efficiency is low, and then be operated by an electric motor. The main focus of the development is to improve and optimise both system and components of a hybrid vehicle. Among the components

of an HV, the ones that require changes compared to the traditional vehicle are the internal combustion engine, the electric motor, the transmission, the inverter, the battery, and the magnet. In the following sections the development work carried out at Toyota on these components will be reviewed.

7b.3.1 The Toyota Prius and its History [1, 2, 3]

The Prius was the first production of an HV with a Toyota hybrid system (THS). This car had an excellent power and energy control system in order to achieve a better environmental performance (fuel economy and emissions), but its driving performance was not as good as that of other conventional vehicles of the same class. Naturally, some customers were not satisfied by this performance. Therefore, an evolved version of the THS was developed, namely, the THS II. Fig. 7b.3 displays a schematic representation of the inner view of the THS II. This new version allowed improving both environmental and driving performances by boosting the voltage of the power source up to 500 V and by increasing the power density of the electric motor by 1.5 times. (For a more detailed description of the system, please visit http://www.toyota.co.jp/en/tech/environment).

The reduction gear unit introduced in this system allowed increasing the revolution speed of the electric motor. As a consequence, the HV of THS II with the reduction gear system reached a higher performance in both fuel economy and fun-to-drive compared to the conventional vehicles of the same class. Moreover, the

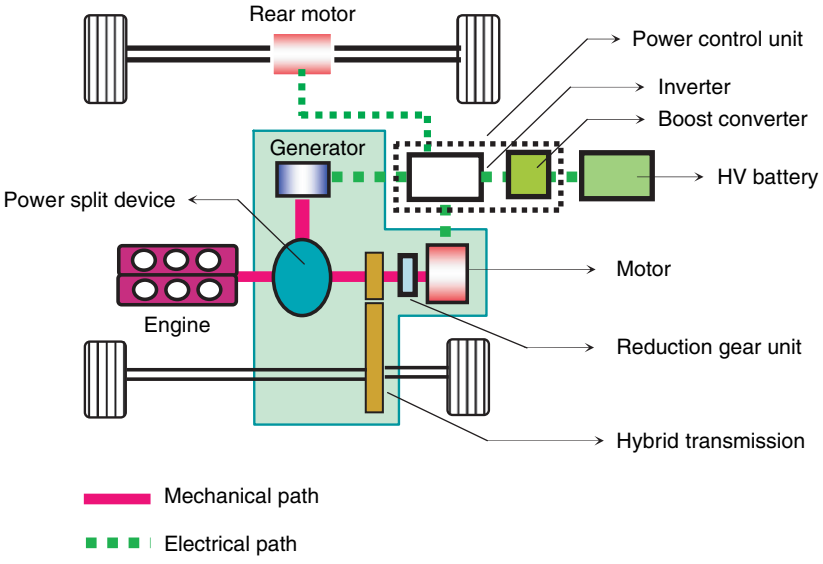

Fig. 7b.3 THS II with motor speed reduction device

compactness of the traction motor allowed installing the motor inside the engine compartment.

The next challenge was to introduce the THS II in the front engine – rear drive (FR) passenger vehicle which requires more power and more compact components compared to the vehicles described. For the FR vehicle with a big engine, fuel economy and driving performance especially at higher speed were the main points of focus in system development. The key solution was the introduction of a two -staged motor speed reduction device combined with the THS II. After huge efforts, the device with low and high gears ensured the appropriate performance of the hybrid system. Fig. 7b.4 displays the schematic representation of the vehicle with this new component. (For more details: http://www.toyota.co.jp/en/tech/environment).

Such an improvement of the THS II allowed hybridising not only FF passenger cars with a small or big engine as well as sports utility vehicles (SUVs), but also FR passenger cars. Furthermore, the variants of THS II have since been developed to meet demands of different types of vehicles, such as

– Series hybrid system for small buses
– THS-C with CVT for mini-van
– THS-M (Mild) with more reasonable and easy installation

However, not only Toyota is pushing for hybrid development. Already several other companies like Honda, Ford, and GM have introduced the IMA, the motor of which assists the engine power, the strong hybrid system with two motors for SUV, and the Mild hybrid for trucks, respectively. So far, each car manufacturer has introduced

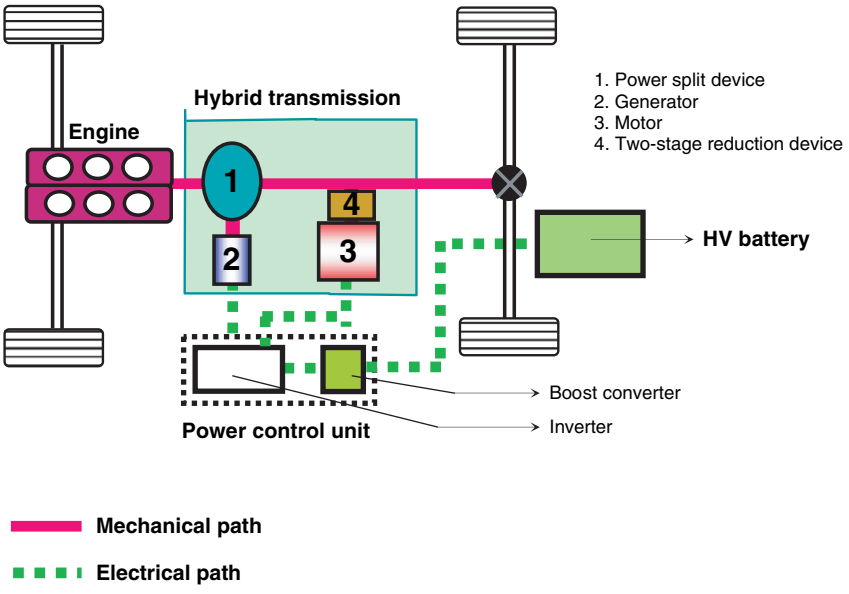

Fig. 7b.4 THS II with two-stage motor speed reduction device

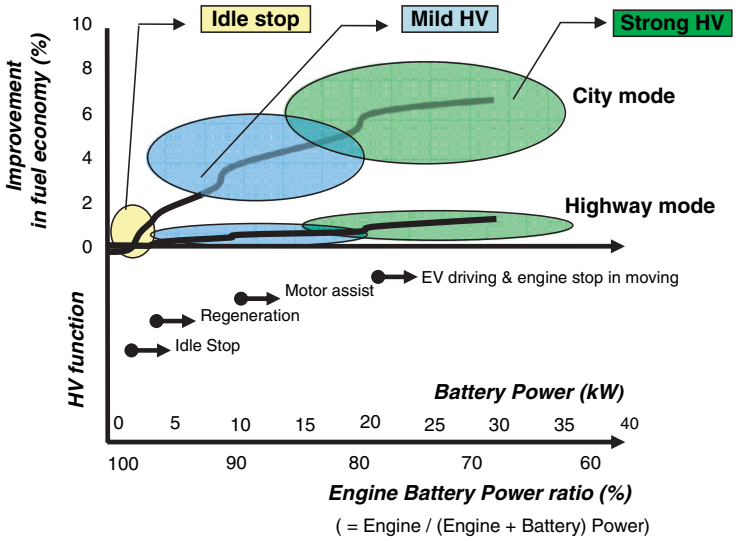

Fig. 7b.5 Engine – Battery power ratio

HV with various systems. Among them, strong hybrid systems are supposed to become mainstream in the future due to their higher potentials in fuel economy, although the challenges in terms of technical and cost reduction requirements in battery development will be very tough (Fig. 7b.5).

The more HV function is applied in a vehicle, the higher powered battery is necessary to maximize the advantage of the sytem

7b.3.2 Internal Combustion Engine for HVs [1, 2]

Figure 7b.6 displays the brake's thermal efficiency versus the engine output for a conventional and a hybrid vehicle. As can be seen, the efficiency of the conventional engine is not good when both speed and load are low. One way to optimise this low-efficiency area is to stop the engine in this zone for a higher fuel economy. The HV achieves this improvement by completely and instantaneously switching off the engine where the efficiency is low and by operating the vehicle via an electric motor. In order to achieve the hybridisation, some modifications of the internal combustion engine hardware as well as the introduction of the exhaust emissions-reducing technology were necessary. The key changes will be described below.

The blue curve represents the improved efficiency by just not using the engine while it is in a bad operation range. Further improvements to the overall engine system rise to much higher efficiency in THS as shown by the red curve.

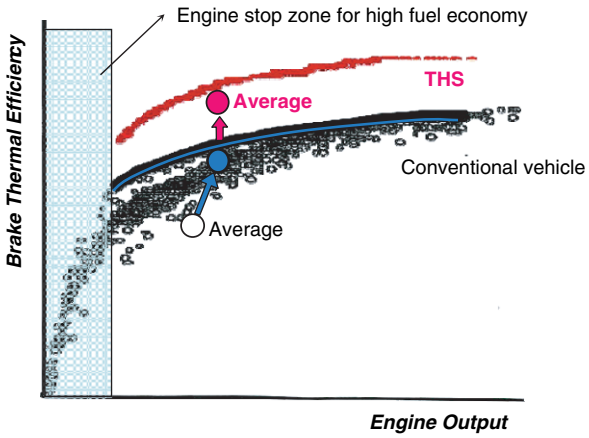

Fig. 7b.6 Optimisation of engine operation range

7b.3.2.1 Modification of Engine Hardware

For hybridisation, the main modification compared to conventional gasoline engine systems concerns the exhaust system, the engine valve system and the wear problem which occurs with an intermittent start/stop engine.

In order to improve the warm-up and exhaust emission performance during cold starting, the base material of the start catalyst as well as of the under-floor catalyst was changed to a thin-walled material with high cell density. The catalyst's cross-section design was also optimised. These modifications of the exhaust system allowed for increasing the exhaust pressure by more than 20% compared to the base engine, with a drop in power performance by approximately 5%.

In order to restrict the vibration generation during intermittent starting of the hybrid vehicle engine, the intake valve closing was retarded by 28° crank angle from the base engine. The valve timing was determined by considering the engine's starting performance at extremely low temperature.

In order to reduce the wear problem due to the intermittent operation of the hybrid vehicle engine, physical vapour deposition (PVD) surface treatment was introduced for the top piston ring. Furthermore, the three-piece oil ring was replaced by a two-piece ring and a plastic coating was added to the crank bearings for cylinders one and four.

7b.3.2.2 Exhaust Emissions-Reducing Technology

This technology consisted in modifying the exhaust system of an ICE and using some special devices for emission reduction. In addition, a better control system of the intake air volume after cold start as well as of the catalyst temperature was implemented to further reduce the emissions from the exhaust system.

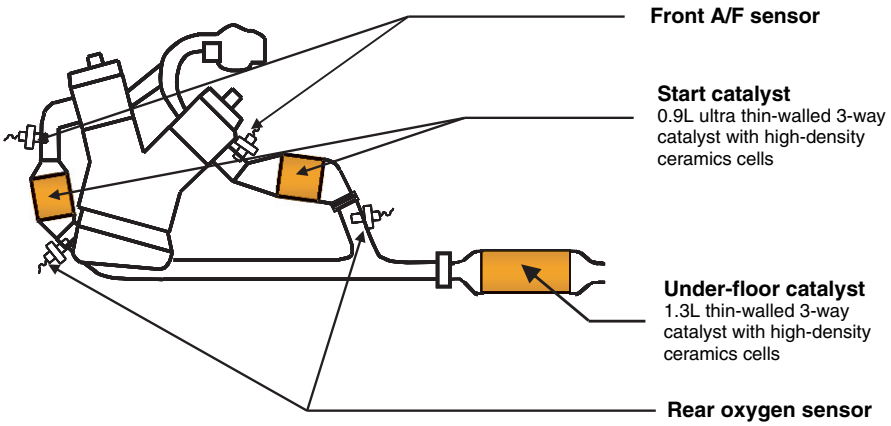

Fig. 7b.7 Exhaust system

Figure 7b.7 displays the exhaust system which was adapted to reduce overall emissions for the hybrid SUV. The start catalyst was changed to a 0.9-litre ultra thin-walled and the under-floor catalyst was changed to a 1.3-litre thin-walled high-cell-density ceramics. These changes allowed to reduce the amount of precious metal inside and to de-install special emission-reducing devices that had been applied to the initial stage of the exhaust system. This newly adapted exhaust system for an HV exhibits a superior efficiency in terms of both environment and cost compared to the original model.

The hydrocarbon emission during cold starting of an ICE had problems to comply with the regulations in each country/region. Figure 7b.8 displays the power management after cold start and how the hydrocarbon emissions were reduced in a THS. In a HV after cold start, the vehicle is driven solely by the battery power until the catalyst is warmed up. During this time, the intake air volume is controlled and maintained constant. By optimising the volume of intake air and retarding the ignition timing during catalyst warm-up, hydrocarbon emissions from the hybrid SUV were reduced to a level even lower than from the conventional model.

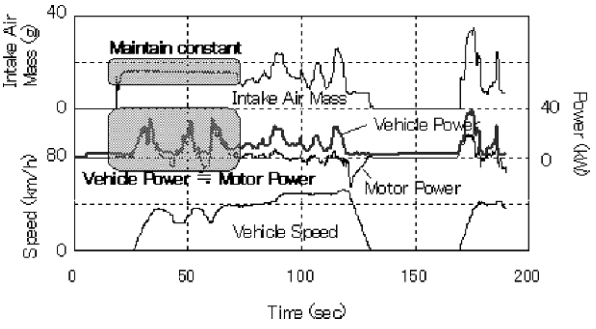

Fig. 7b.8 Power management after cold start

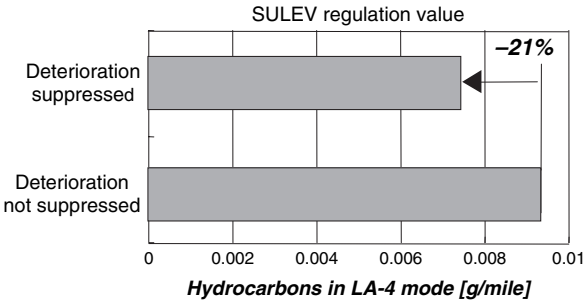

Fig. 7b.9 Effect of suppressing catalyst deterioration in emission

Moreover, it is known that a three-way catalyst deteriorates in the gas at high temperature of the lean air-fuel ratio. As a countermeasure, the control system of the catalyst temperature was linked to the engine power and air-fuel ratio. The temperature of the catalyst was detected by the additional sensor. Figure 7b.9 compares the levels of hydrocarbon emission of HV's in the LA-4 test cycle (LA-4: http://www.dieselnet.com/standards/cycles/ftp72.html) equipped with and without the catalyst anti-deterioration system. As can be seen in Fig. 7b.9 the hydrocarbon emissions dropped by approximately 21% when catalyst deterioration was suppressed.

Finally, the implementation of the new components and controller as well as the optimisation of the overall system enabled the hybrid SUV to meet the most stringent regulations in each country/region. Figure 7b.10 displays the results obtained from an in-house testing using the U.S, European, and Japanese testing cycles.

The red line and the figures indicates the standard of each regulations in each regions. Emission results are in a very good range of the regulation

7b.3.3 Electric Motor & Transmission

Electric motor and transmission units for FF & FR vehicles differ depending on how they are mounted onto the vehicle frame. In case of an FF vehicle, for example, an

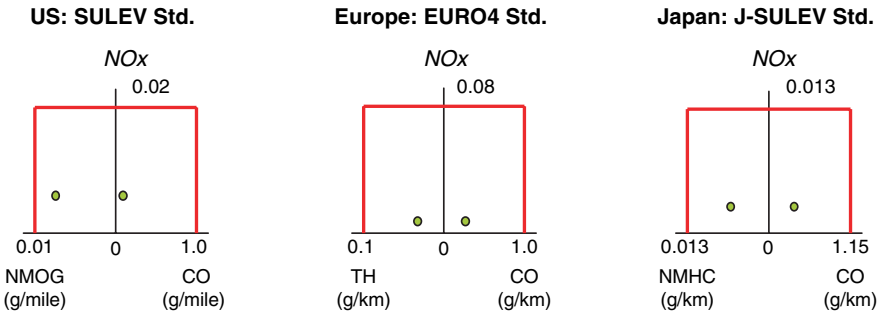

Fig. 7b.10 Emission evaluation results of RX400h

engine with transmission should be installed in the space between side members in the engine compartment. Therefore, only a radial direction of the spatial design of the electric motor and optimising control techniques may be applied to improve the motor output due to the limited space in longitudinal direction (axial direction of the motor). Furthermore, the size of the whole unit basically should be similar to the conventional transmission because the space for mounting is the same as in the conventional vehicle.

7b.3.3.1 High-Power Performance [4, 5, 6, 7]

Basically, a standard electric motor does not satisfy the constant torque characteristic demanded by a vehicle because the motor generates linear torque characteristics according to speed. Therefore, it is necessary to increase the torque by a reduction device. Figure 7b.11 displays the motor speed reduction device that hooks the gasoline engine, generator, and electric motor together (for more details: http://www.toyota.co.jp/en/tech/environment/ths2/).

The reduction ratio is calculated according to [Ring Gear]/ [Sun Gear] via the pinion gear mounted on the fixed planetary carrier.

As the FR passenger car requests both high power and high speed, a two-staged motor speed reduction device has been developed with a high and a low gear. Figure 7b.12 displays this device with the low gear for hill climbing and acceleration and the high gear for high-speed driving. Figure 7b.13 displays the transmission of the GS450h, where all components as well as the positions of the power-split device and the two-staged motor speed reduction unit are visible.

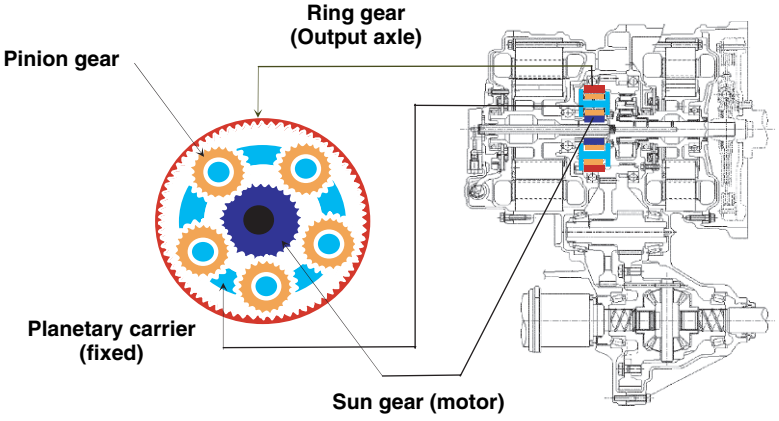

Fig. 7b.11 Motor speed reduction device

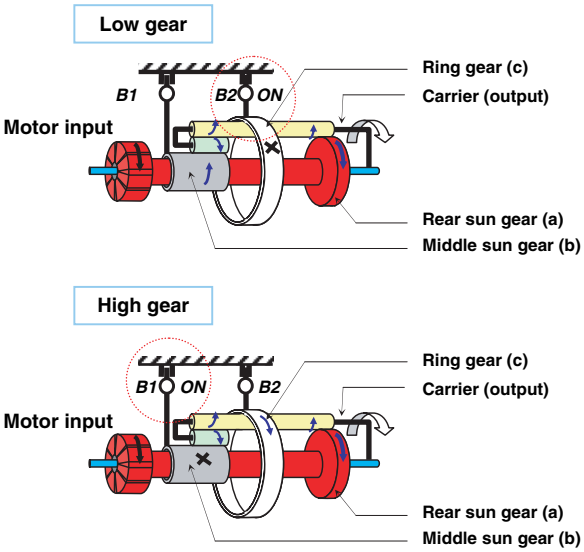

Fig. 7b.12 Two-stage motor speed reduction device

Two different input – output ratios of b/a and c/a will be selected in the low gear mode and in the high gear mode, respectively.

7b.3.3.2 Motor Downsizing [8]

It is well known that the motor size is proportional to the torque performance. The torque demanded by a vehicle requires a certain size of the motor, but it may also be determined by a combination of the reduction device and the low – torque, but high-speed electric motor that is relatively small. Consequently, a new speed reduction device was developed in order to make the overall motor unit compact.

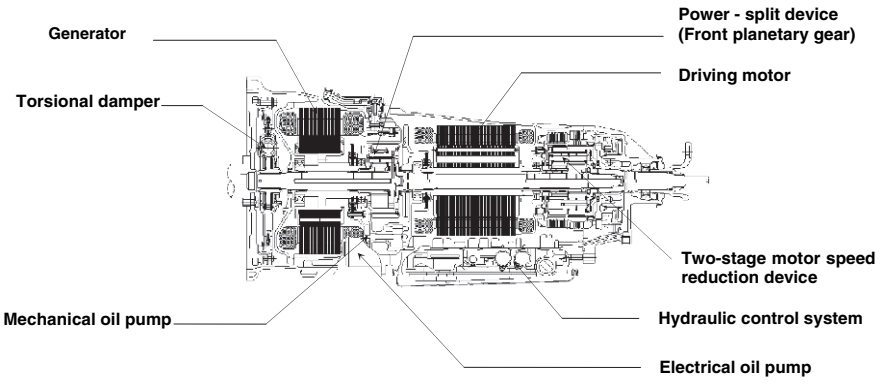

Fig. 7b.13 Transmission for GS450h

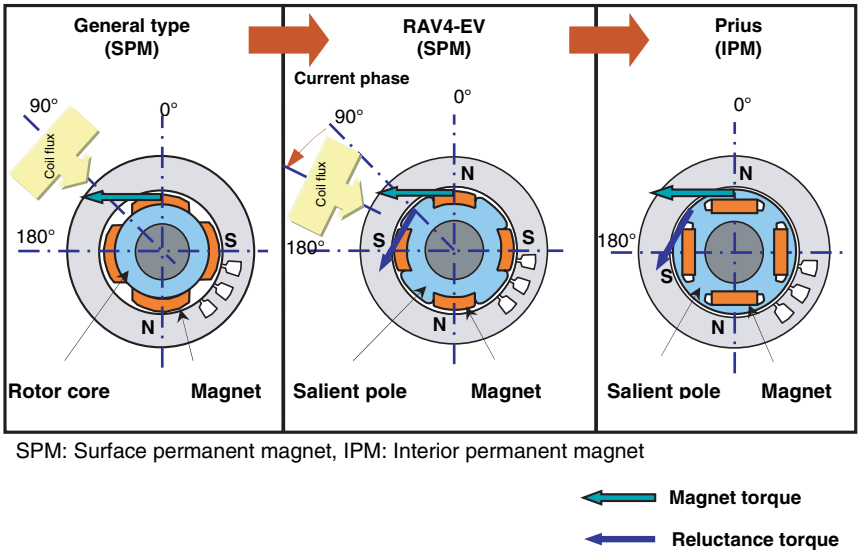

Fig. 7b.14 Rotor configuration

7b.3.3.3 Rotor Design and Current Phase Control [8]

Figure 7b.14 displays the evolution of the rotor configuration from the general type to the Prius. It is obvious that the general type rotor, Fig. 7b.20, left, adopts the SPM system. In this case magnets are attached on the surface of the cylindrical rotor core. Then, an iron salient pole is provided between the magnetic poles in order to achieve a higher torque and higher efficiency. As shown in Fig. 7b.20 (middle), the rotor of RAV4-EV which was introduced in the market back in 1996 was equipped with this reverse salient pole type SPM system. Further improvement in the rotor design was achieved by the use of the reverse salient pole type IPM (interior permanent magnet) system in the Prius. This system consists of electromagnetic steel sheets which are laminated and embedded inside the rotor as can be seen in Fig. 7b.20 (right). The introduction of the reverse salient pole type IPM system allowed eliminating the wire windings on the magnet surface and, in turn, reducing significantly the cost.

The reverse salient pole type rotor reaches a higher torque and higher efficiency by adding a reluctance torque to the magnetic torque. The optimisation of the electromagnetic circuit design based on electromagnetic analysis and simulation work as well as the introduction of the current phase control allowed improving the IPM rotor output torque.

7b.3.3.4 Efficiency of the Motor [4, 5]

The loss occurring in the motor is mainly due to two reasons. The first one is the copper loss due to Joule's heat in the coil and the second one is the iron loss in the motor core. Figure 7b.15 shows which loss is more dominant in the given motor

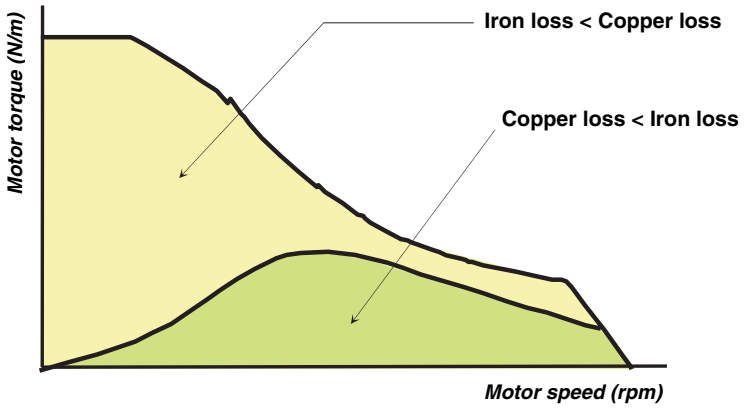

Fig. 7b.15 Motor loss ratios

operation. As can be seen, the iron loss largely affects the overall motor loss during low-load operation in the low torque-high speed range because it is almost proportional to the square of the motor frequency. This indicates that not only the mechanical issues of motor development, such as the improvement of the mechanical strength to withstand centrifugal force, but also reducing the iron loss in the high-speed range for better fuel economy are important. As a consequence, the development work to reduce the iron loss consisted of improving the overall design and modifying specific material.

Figure 7b.16 displays the new design of the rotor permanent magnets that has been created by means of the finite element method (FEM), magnetic field analysis, and mechanical strength analysis. As can be seen in comparison to the conventional motor, the rotor permanent magnets are now arranged in V-shape, which significantly improves the reluctance torque and reduces iron loss during low-load operation. Moreover, mechanical strength of the magnets is improved by introducing the rib between each pair of magnets. These two modifications more than double the motor speed range. In addition, by optimising the open angle θ between each pair of rotor magnets, the harmonic components of the magnetic flux are suppressed. This change makes a major contribution to reducing the iron loss.

Once the design of the rotor permanent magnets had been improved, the material used to produce them was optimised. The material was improved by the development of a new silicon steel plate with a thickness even thinner than the current one of 0.35 mm. Combining this material and a new manufacturing method, such as a layering process for the stator core, the iron loss was reduced compared to the conventional motor.

Figure 7b.17 compares the motor efficiency maps of the single-stage reduction device and the two-stage motor reduction device. In some cases, the motor widened the highly efficient operation range by two times through the two-staged motor speed reduction device, with an improved fuel efficiency.

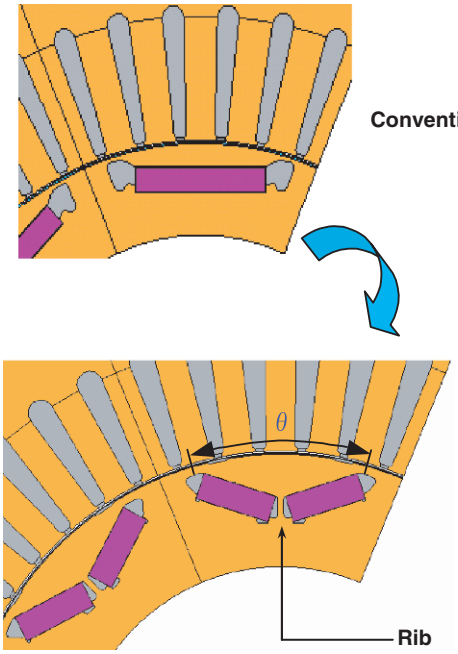

Fig. 7b.16 V – shaped arrangement of rotor permanent magnets

7b.3.3.5 Cooling Performance [6]

A novel cooling technology is the active application of the ATF for the stator and coil ends, together with the conduction of the motor heat to the case through the ATF. The heat generated by the motor flows to the case and is released from there by air cooling as well as water cooling. Fig. 7b.18 displays a schematic representation of oil slinging by the gear. As can be seen, the ATF driven by the gears is collected in an oil catch tank placed on top of the case. From the case, it flows to

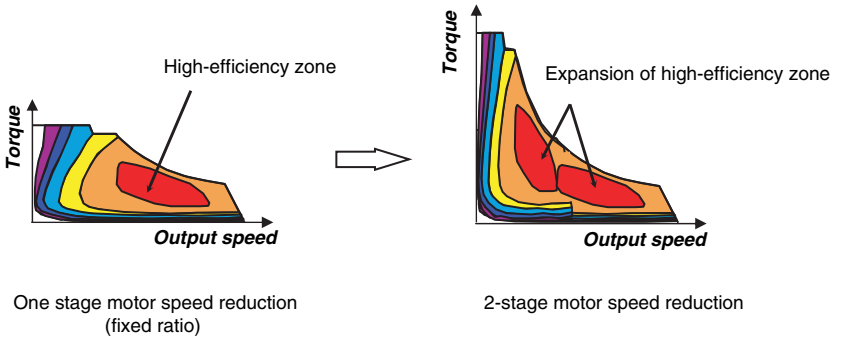

Fig. 7b.17 Comparison of motor efficiency maps

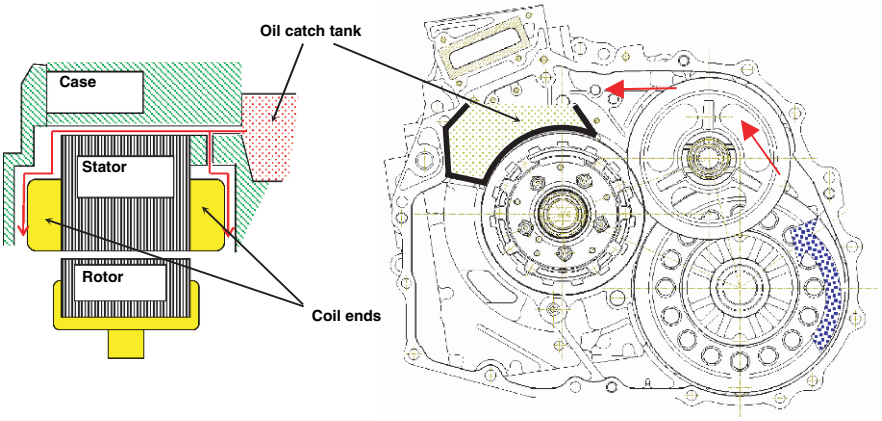

Fig. 7b.18 Oil slinging by the gear

the stator and coil ends. From the stator and coil ends, heat is released by thermal conduction and again by heat transfer to the case using the ATF. The ratio of heat release is in the range from 30 to 50% of the total heat produced during operation by direct contact to the case and from 50 to 70% by the ATF. This allows for a larger heat transfer through the case, resulting in an improved cooling performance. Depending on the vehicle specifications, an oil cooler may also be installed to cool the ATF, by means of which cooling efficiency is further improved.

The overall cooling performance, including the air cooling effect, was improved significantly compared to the transmission case of Prius. Figure 7b.19 displays the evolution of the motor output density. As can be seen, the overall improvements have allowed increasing the output density of the traction motor by more than five times since 1997.

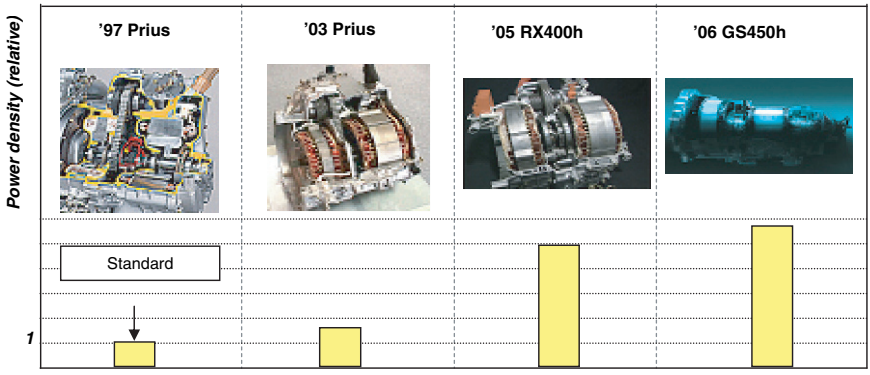

Fig. 7b.19 Development of motor output density

7b.3.3.6 Production Engineering [4]

Two types of motor, one with a distributed winding coil and the other one with a concentrated winding coil, were developed according to the application requirements. In order to ensure the insulation of the motor with a distributed winding coil at high voltage, an automatic assembly of insulating paper and an insulation performance inspection were introduced. During the assembly process of the stator windings using inserter machines, the insulating papers were also placed automatically by the inserter after each three-phase-winding had been inserted. Moreover, the shape of the insulating paper was modified to be inserted easily in order to ensure good insulation quality. Furthermore, reliable insulation required avoiding the generation of partial discharges in the coil. To this end, a certain voltage was applied between or at both ends of the stator windings and it was checked precisely that there was no minute electric current flow.

Furthermore, environmental factors of the assembly, not only temperature and humidity, but also radiation noise from other equipment, which were supposed to affect the testing results, and their influences were investigated carefully. In addition, a quick online inspection program was implemented. Figure 7b.20 displays the production volume versus the voltage. It is evident that the series of production engineering improvements allowed for the production of the electrical traction motor with an operation voltage of DC 500 V at a scale of thousands of units per month. The production volume was definitely the world's largest for this type of electric motor.

Automation of the insulating paper assembly process for the high-voltage electric motor used to be a critical problem in mass production

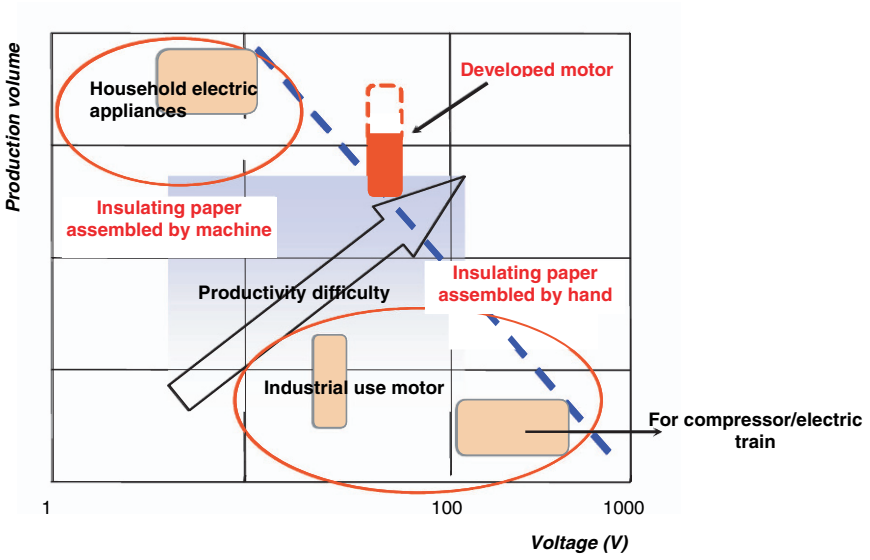

Fig. 7b.20 Motor voltage and production engineering

7b.3.4 Inverter

7b.3.4.1 Early Inverter Development for the Hybrid System [9]

The inverter for the hybrid vehicle had to be designed much differently from the one used for purely electric vehicles. Indeed, the inverter for the HV was designed for direct installation in the engine compartment. This implied the development of a new inverter meeting stricter thermal and vibration requirements compared to the standard one. The main advantage of such an inverter is that it keeps the cabin and the luggage space as wide as possible and minimises the length of the high-power line between the motor/generator. The design concepts and challenges of inverter development for the HV production model will be described below.

Mainly three problems had to be overcome and they concerned the compactness of the inverter, the temperature rise in the engine compartment, and the transistor modules.

(1) In order to design an inverter as compactly as possible, two inverter modules – one for the traction motor and one for the generator – were integrated in one unit. The transistor module that produces three-phase alternating current for each inverter was designed as a 6-arms-in-1 using an insulated gate bipolar transistor (IGBT).
(2) As the inverter was to be placed in the engine compartment, the temperature to which the inverter was exposed was much higher than in purely electric vehicles. Moreover, operation and durability requirements became severer for production models. To tackle these problems, a liquid cooling system was developed and a heat management program was added.
(3) The design of the transistor modules with IGBT was a more serious problem. Indeed, each component of the transistor as well as the material needed to be considered in order to meet the more stringent requirements, especially in terms of thermal performance. However, no components were available that satisfied these criteria, thus implying a complete in-house development.

Figure 7b.21 displays a schematic representation of the new inverter designed for the HV. The main heat source in the inverter is the IGBT devices and they are guaranteed to operate at a certain temperature. The IGBT module is located directly at the bottom of the aluminium case which is the heat sink with the cooling liquid. In order to maximise the heat transfer efficiency, flow resistance is reduced and the flow patterns as well as the dimensions of the fin are optimised.

7b.3.4.2 Evolution of the Electric System [9]

The electric system was modified by increasing the motor output and significant advances in the control system. This allowed achieving a better compatibility between environmental performance and power. The motor output was increased by 1.5 times by boosting the system voltage. Here, it should be pointed out that the

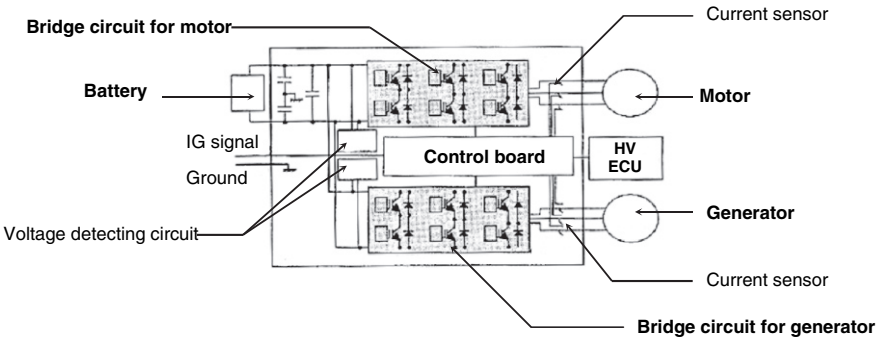

Fig. 7b.21 Construction of inverter

straightforward solution to boost the system voltage by simply installing more batteries actually was not possible due to space constraints. The best approach was to increase the battery voltage by operating the inverter in a higher-power mode thanks to a variable-voltage system. The new Prius introduced by Toyota in September 2003 was equipped with such an electric system.

Figure 7b.22 displays the schematic configuration of the variable-voltage system [10, 11]. The main difference from the battery system is the introduction of a boost converter between the inverter and the battery. The battery voltage drives the motor/generator directly, while the boost converter enables the motor/generator to produce a higher output with the same battery unit. In this way, the approximately 200 V DC battery voltage is increased up to a maximum of 500 V DC when it is supplied to the motor/generator as the operating voltage. In the following sections

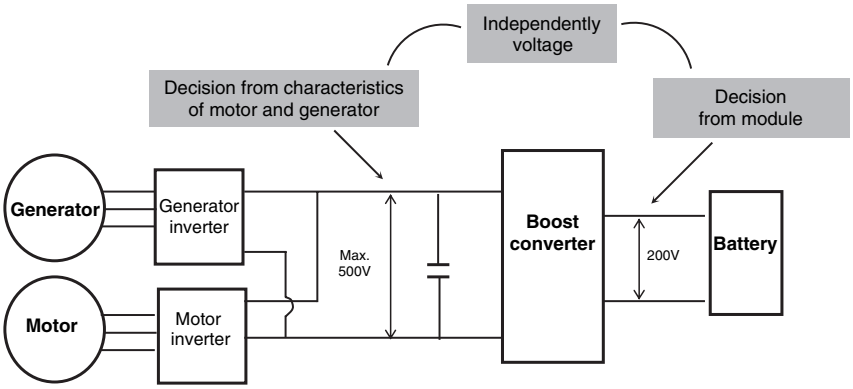

Fig. 7b.22 Design of the variable voltage system

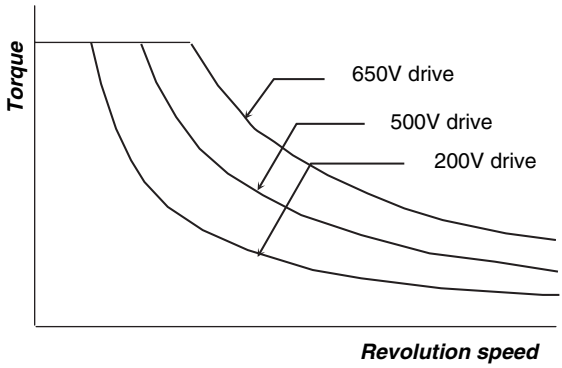

Fig. 7b.23 Motor applied voltage and torque

the output of the motor/generator with the variable-voltage system as well as the optimisation of the boost voltage shall be discussed.

The output of the motor usually is proportional to the drive voltage. Figures 7b.23 and 7b.24 display the relations between the drive voltage and torque as well as between drive voltage and output power, respectively. As can be seen, the 500 V DC voltage increases both torque and output power by approximately 2.5 times compared to the 200 V DC drive voltage, without increasing the motor current. As the current remains unchanged, the overall dimension of the motor/generator stays almost the same.

The new system optimises its output voltage according to the relative relation of the motor and generator states. This optimisation helps to decrease switching losses in the inverter and copper losses of the inductor and boosts the converter by decreasing the ripple current.

The design of the new system can be applied easily to other hybrid vehicles, because the output voltage of the boost converter is independent of the battery voltage. Thus, reducing the number of the battery modules does not influence

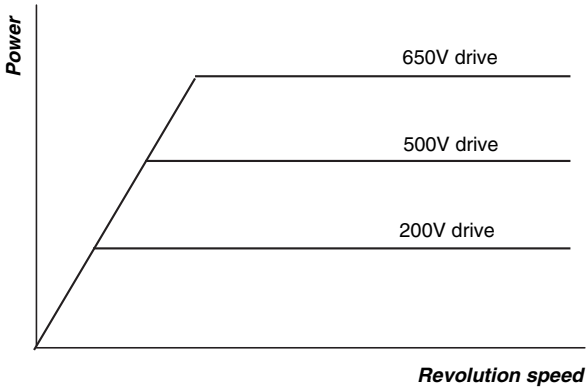

Fig. 7b.24 Motor applied voltage and power

directly the output voltage, as it is designed according to the specifications of the motor/generator.

7b.3.4.3 Power control Unit (PCU) for the Variable-Voltage System [12]

The boost converter is installed in the inverter. Due to the variable-voltage system, the input voltage of the intelligent power module (IPM) described below is high, allowing the system to operate at a higher power and a lower current. Thanks to the lower operating current, it was possible to downsize by 20% the IGBT and to reduce its heat loss.

Figure 7b.25 displays a schematic representation of the structure of the IPM. As can be seen, the IPM consists of two parts. One part is a module which handles high voltage and current, while the other one is a control circuit that controls the module. Moreover, the module is composed of a heat sink, an insulating substrate, the IGBT, and a free-wheel diode (FWD). The heat sink promotes heat dispersion, the insulating substrate ensures insulation, the IGBT power semiconductor turns on and off the current, and the free-wheel diode (FWD) mounted in pairs with each IGBT protects the IGBT from breaking down when a backflow current occurs.

As concerns the modules, the original Prius had two separate, specially designed modules, one for the motor (288 V/600 A) and one for the generator (288 V/200 A). In the second generation of Prius, the THSII booster system increased the voltage to reduce the overall IPM loss, as shown in Fig. 7b.26. The boosted voltage contributed to reducing the operating current that had produced the large conduction loss dominant in the overall IPM operation losses. This design allowed the module to be more compact than the previous model, even though the power performance increased. Finally, the total number of IGBTs decreased from 24 to 18.

The IPM was designed such that each function had it dedicated circuits in order to eliminate unnecessary terminal space. The circuits shared an optimised bus bar, allowing the generator (MG1) and motor (MG2) circuits for the RX400h to be located in a single module. Figure 7b.27 displays the hybrid system diagram of the RX400h. With this newly designed IPM, it was possible to achieve a higher compactness and higher power compared to the original Prius. Indeed, a power increase of 220% was reached using 30% more surface area only.

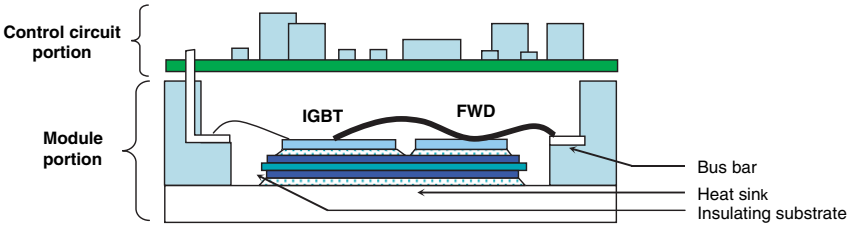

Fig. 7b.25 Structure of the intelligent power module

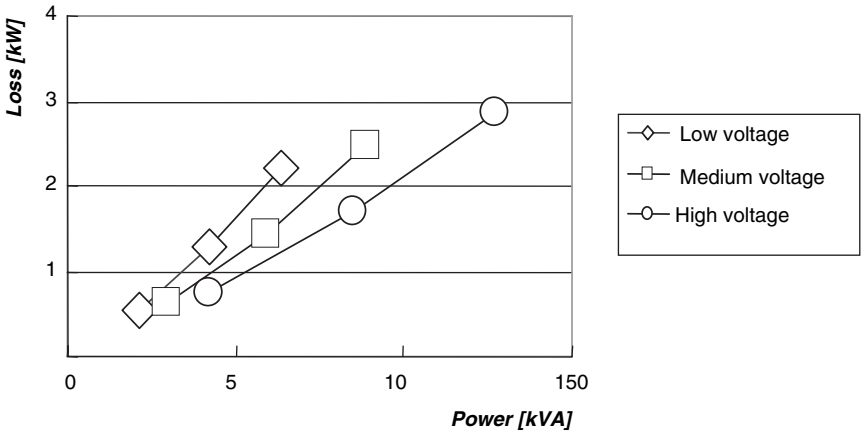

Fig. 7b.26 Power loss characteristics

It should be noted that at high power, it was necessary to revise the heat sink material and the shape of components in order to provide for a better heat dissipation during high-temperature operation. Figure 7b.28 compares the powers of the first and the second generation of HV's. The power density per unit surface area

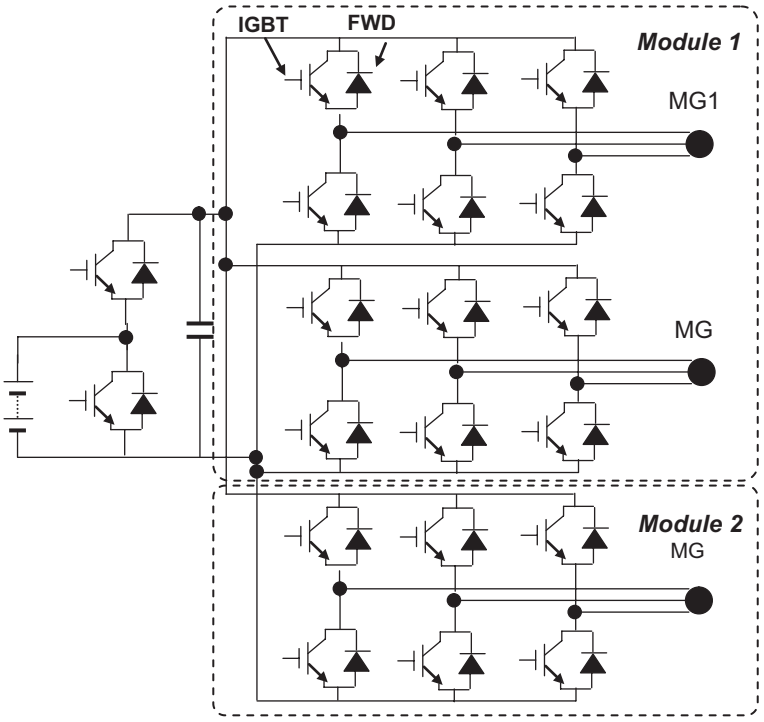

Fig. 7b.27 Hybrid system diagram for RX400h

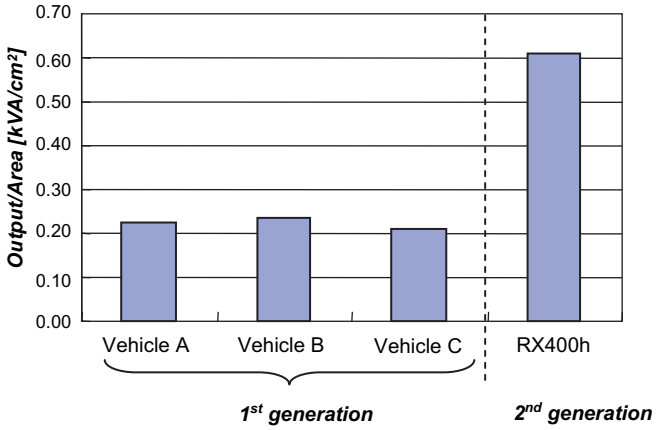

Fig. 7b.28 Power comparison

increased significantly for the RX400h and for the Prius 2003 model compared to the first generation of the inverter system applied in the Prius introduced in 1997.

Usually, the inverter's internal control circuits are divided into three boards, namely:

(1) a power supply board
(2) dead-time generator board to control the IGBT
(3) one IGBT driver board for the motor/generator.

The driver board drives its power semiconductor (a semiconductor device capable of dissipating appreciable power) according to logic signals. It has an IGBT safety circuit for protection against short-circuit current, heating, and other hazards.

For the second generation of hybrid vehicles, the circuit configuration was revised to incorporate a power supply circuit which had not been present in the first-generation IPM. Moreover, a new IC was developed for the power supply and dead-time generator circuits. The IPM layers were added to the board itself to increase the parts' mounting density. Finally, the number of parts was reduced to 75% and the board surface area to 52% compared to the first-generation IPM. Furthermore, combining the motor and generator circuits in a single module allowed keeping enough space for the same functionality being provided in a single control board. In addition, a current sensor was added in the remaining space of the board. These changes of the original system resulted in many benefits: Fewer connectors, a smaller wiring harness, a higher compactness of the IPM, and higher productivity.

Figure 7b.29 displays the IPM used in the RX400h. The development work carried out resulted in a reduced number of connectors and a smaller wiring harness. Moreover, it is more compact and exhibits a higher productivity.

Figure 7b.30 displays an in-house manufactured IGBT and a FWD which make up the power semiconductor. The IGBT plays the role of an IPM switching device generating three-phase current to drive the motor. The role of the FWD is to free-wheel the energy that is accumulated by the motor when the IGBT is switched off.

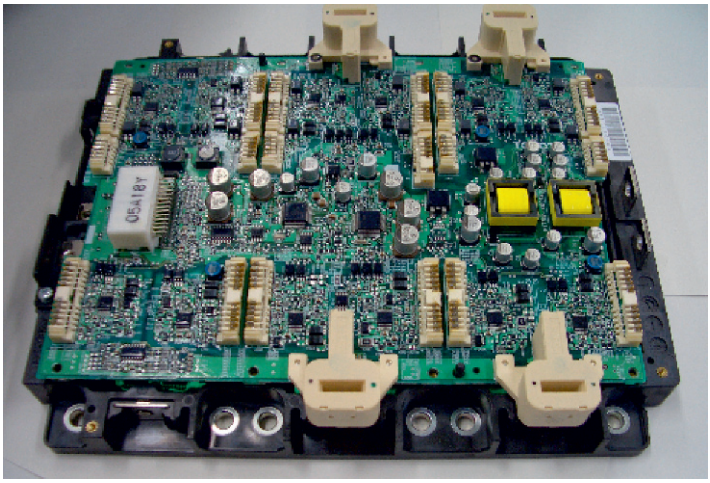

Fig. 7b.29 Intelligent power module for RX400h

Another role is to transfer the surplus energy generated by deceleration and braking into the battery.

For the THSII, the goal was to increase the power supply voltage to 650 V in order to achieve higher power and higher efficiency compared to the original THS. To this end, it was essential to increase the withstand voltage and to decrease the loss in the IGBT, FWD, and other key devices of the IPM. In a power semiconductor, however, the trade-off between withstand voltage and loss is a key issue, which is why the development of the new devices focused on this point. The advanced trench technology and the additional optimisation of the material and processes improved both the withstand voltage and overall losses of the devices.

The boost power module contains semiconductor switching devices to form a chopper circuit at two locations. Just like the inverter power modules, the boost power module has a specially designed and integrated control and drive circuit. The boost power module also contains IGBT power semiconductor devices and four

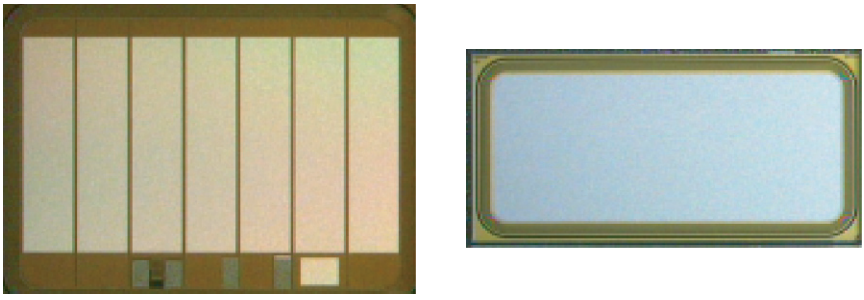

a) IGBT **b) FWD**

Fig. 7b.30 Power semiconductor for RX400h

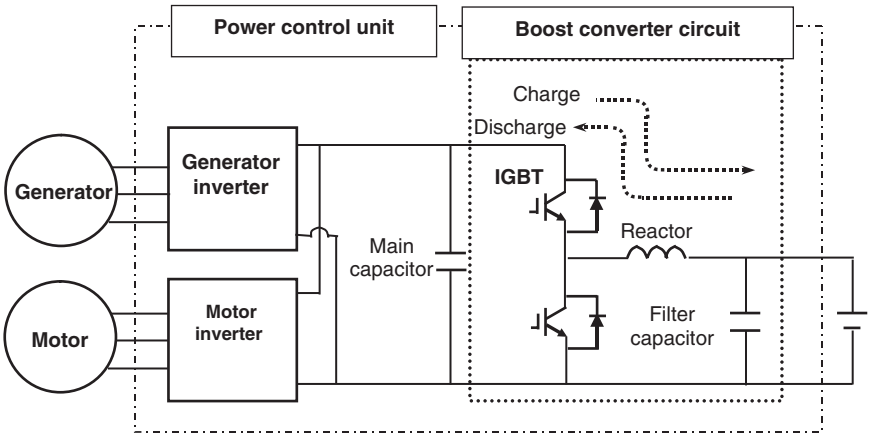

Fig. 7b.31 Variable-voltage system circuit

150 A class IGBT's connected in parallel. Moreover, this module has a protective function against overvoltage, -current, and -heat as well as internal power supply malfunctions. The sensors can detect the battery voltage and the temperature of the power semiconductor devices. Figure 7b.31 displays the system circuit, including the boost power module IGBT. (For more details: http://www.toyota.co.jp/en/tech/environment/tst2/).

The capacitor module contains a specially designed film-type capacitor which is provided with a smoothing capacitor in order to smooth the system voltage. Moreover, it is equipped with a filter capacitor that reduces battery ripple current and noise. The capacitor device has a newly developed, ultra-thin polypropylene (PP) film which allows reducing the size of the capacitor unit. A unique deposition pattern technique was developed to produce optimal patterns to achieve both high ripple support and a self-healing function. Figure 7b.32 displays the power control unit. As a result, the capacitance density of the smoothing capacitor was improved by approximately 20% compared to the 2003 Prius.

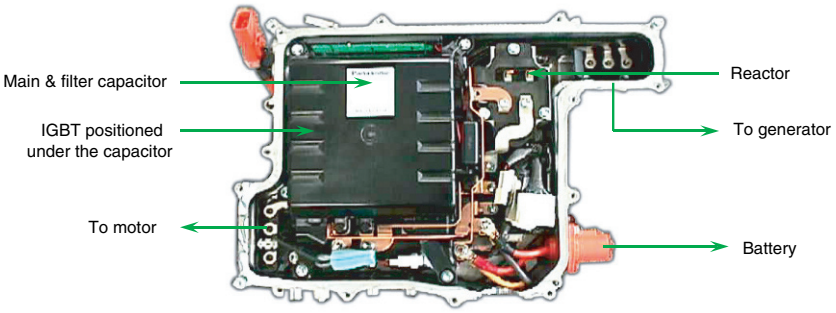

Fig. 7b.32 Power control unit

The early generation of hybrid vehicles, such as Prius and RX400h, had a specially designed vehicle body construction in order to ease the mounting of the PCU in the engine compartment. However, to largely expand hybridisation to conventional vehicles, it is necessary to install the PCU in the original body construction. Hence, a smaller PCU was developed and successfully mounted in the GS450h and Camry HV[13]. Thus, expansion of hybridisation to general passenger cars became reality.

In order to downsize the inverter power module, ultrasonic bonding technology is applied to some of the high-voltage wire connections. This technology allows saving space for wire bonding and reduces the dimension required for the installation of the IGBT. The size of the voltage-smoothing capacitor has also been reduced by integrating each control board. Moreover, the motor control method has been improved and a thinner film capacitor with a thickness of 3.0 µm only has been implemented.

A new water-cooled heat sink with the wavy-shaped fin cooling channels was developed for heat radiation of the power module. The conventional straight fin works as a simple radiation fin, whereas the wavy-shaped fin elegantly works as turbulence generator in the coolant through its refined shape. The improvement in heat removal from the boost power module as well as the inverter power module saved space for the PCU and to increase the power.

The PCU for the GS450h was reduced in size by one third in volume, with the power density being improved by 225% compared to the original design. Following the successive improvements of the PCU and cooling system, power density of the PCU in GS450h is drastically higher compared to the 1997 Prius. Currently, an inverter with the plane-type IGBT is the main direction, but a trench-type device will probably gain popularity due to its compact size. Figure 7b.33 displays these two types of IGBT.

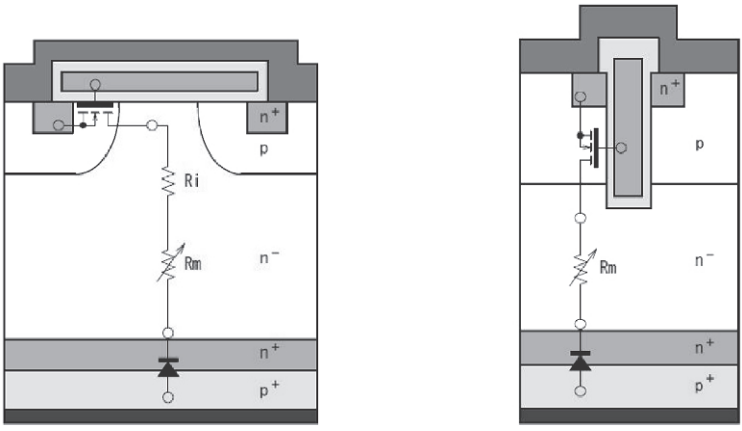

Planar type ***Trench type***

Fig. 7b.33 Type of IGBT

7b.3.5 Battery [14, 15, 16]

7b.3.5.1 Battery Development

The Ni-MH battery was introduced for HV application. Improvement over all the years results from changes in the shape of the battery. Figure 7b.34 displays the development work on the batteries at Toyota from 1997 to 2007. As can be seen, the cylindrical modules were introduced in the 1997 Prius model with six cylindrical cells connected in series. Then, the 2000 model Prius was equipped with a prismatic battery instead of a cylindrical one with six connected cells in series. The cells were incorporated in one unit in order to achieve a significant size reduction. The Toyota Prius in the U.S. and on the European market started with this design. The later model in 2003, the new-generation Prius, also contained a Ni-MH prismatically shaped battery, but with an improved version in terms of power and cost. The same battery module was used in Estima HV and Alphard HV. SUV HV, however, such as RX400h and Highlander HV, required different characteristics. A new metallic casing was developed in order to improve the cooling performance and the compactness in terms of power density. The new battery packs allowed these hybrid SUVs to keep the same versatility in seat arrangement and a comfortable interior space.

Table 7b.1 displays the improvement of the battery module specifications achieved with the development work. As can be seen, the voltage and power density have been increased by using a prismatic metallic case Ni-MH battery instead of the classical cylindrical battery. Moreover, the overall dimension of the battery has been reduced to a certain extent.

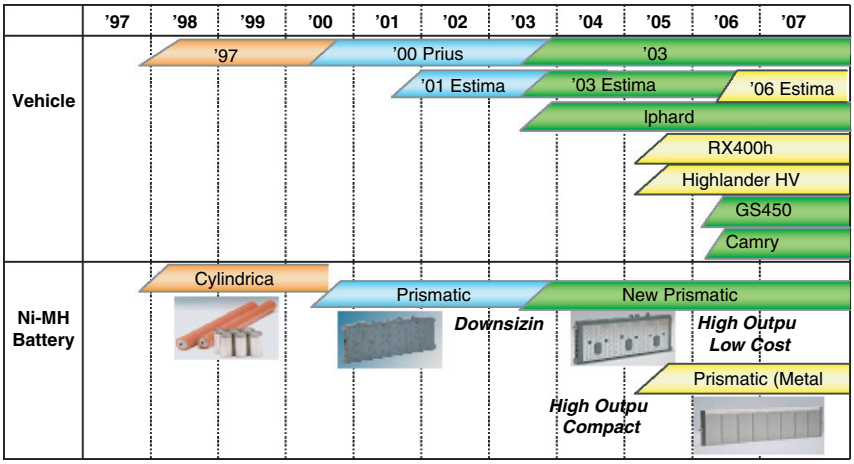

Fig. 7b.34 Development of Toyota HV

Table 7b.1 Battery module specifications

	1997 1st Prius	2000 Prius	2003 Prius	2005 RX400h
Battery shape	Cylindrical	Prismatic	Prismatic	Prismatic (metal case)
Voltage (V)	7.2	7.2	7.2	9.6
Capacity (Ah)	6.5	6.5	6.5	6.5
Power density (W/l)	1.620	1.618	2.041	2.870
Weight (g)	1090	1050	1040	1510
Dimension (mm)	35 (ϕ)	275 (L)	285 (L)	363 (L)
	384 (L)	19.6 (W)	19.6 (W)	15.6 (W)
		106 (H)	114 (H)	96 (H)

7b.3.5.2 Details of the Battery

As stated earlier, the battery designs differed for the Prius and the RX400h applications. The details the of development work carried out with respect to the output power of the battery, its size reduction, and its cooling system will be described below for these two models from Toyota.

Prius Application

Figure 7b.35 shows the battery module used in the 2003 Prius. The output power of the battery has been improved by modifying the electrode material and the collector design. As concerns the electrode material, the additive for the positive electrode was changed and the negative electrode material was optimised to reduce plate resistance. The collector design was changed in a way that the connection points at each cell were doubled from one to two. Moreover, with the reduction of the resistance of the connector and by making the internal current flow homogeneous by

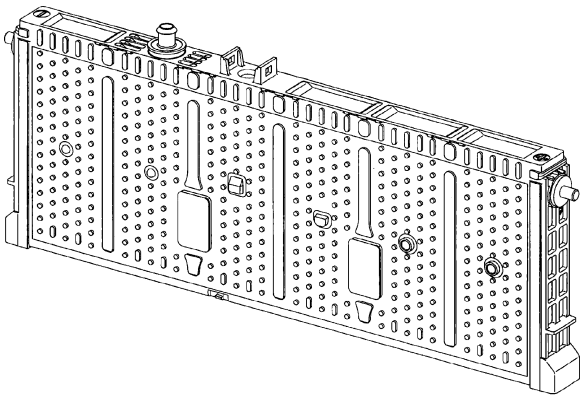

Fig. 7b.35 Battery module for 2003 Prius

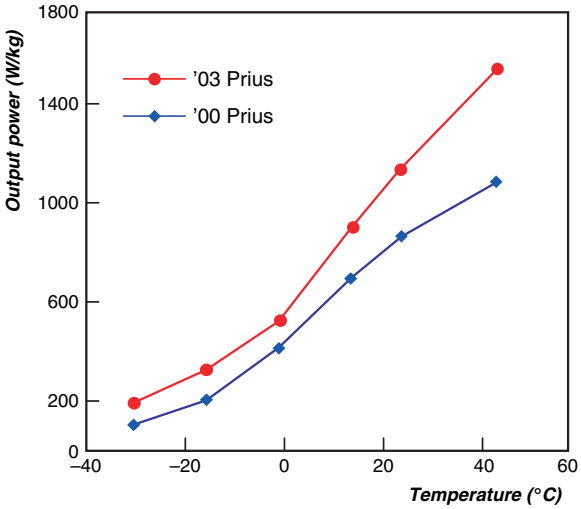

Fig. 7b.36 Specific power

optimising the position of doubled connection points, the temperature distribution of the electrodes was dramatically decreased. Figure 7b.36 displays the output power versus the temperature elevation observed in the battery modules installed in the 2000 and 2003 models of Prius. Obviously, the modifications of the collector design and the electrode materials allowed increasing the power density of the 2003 model, with the operation temperature range being widened. For example, power density at ambient temperature could be increased by 35% compared to the 2000 model. This performance at present is the highest level in the world.

Figure 7b.37 displays the battery pack configuration used in the Prius 2003 model. The 28 modules which compose the battery are stacked in series, closed by end plates on each side, and covered with the restraint rods on the top and the

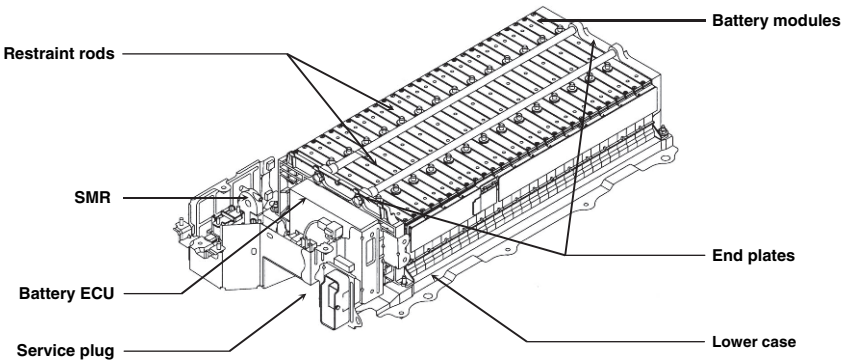

Fig. 7b.37 2003 Prius battery pack configuration

bottom. The battery pack was downsized by changing the shape of the pack from the cylindrical to the prismatic one in the 2003 model. Then, the number of modules could be reduced due to the increase of power density. Moreover, the components of the battery system, such as the ECU, were compacted through integration. All these modifications allowed reducing the battery pack by 65% in mass and 50% in weight compared to the original configuration, the 1997 model. Figure 7b.38 displays the evolution of the volume and weight of the battery pack for the three Prius models. As can be seen, the volume was reduced from around 120 to 25 L/unit in the 1997 and 2003 model, respectively. At the same time, the weight decreased from around 120 to 40 Kg/unit in the 1997 and 2003 model, respectively. The development work performed on the downsizing of the battery contributed to a better marketability of the vehicles as well as to a reduction of the vehicle weight together with an increased luggage space and the introduction of a split back seat.

Figure 7b.39 displays the battery pack cooling system on 2003 Prius. As can be seen, the battery pack was installed behind the rear seat. The battery was cooled by conducting the cabin air on to the battery. The air flowed from a port behind the rear seat through the space between the modules in the battery pack and exits via the air exhaust port. The optimisation of the design of the cooling fan, the intake and exhaust duct, and the modules reduced the temperature difference between each module. This, in turn, allowed eliminating the temperature sensors in the 2003 model.

RX400h Application

The prismatically shaped battery which exhibits a superior heat radiation performance and compactness for installation was introduced in the RX400h. For this

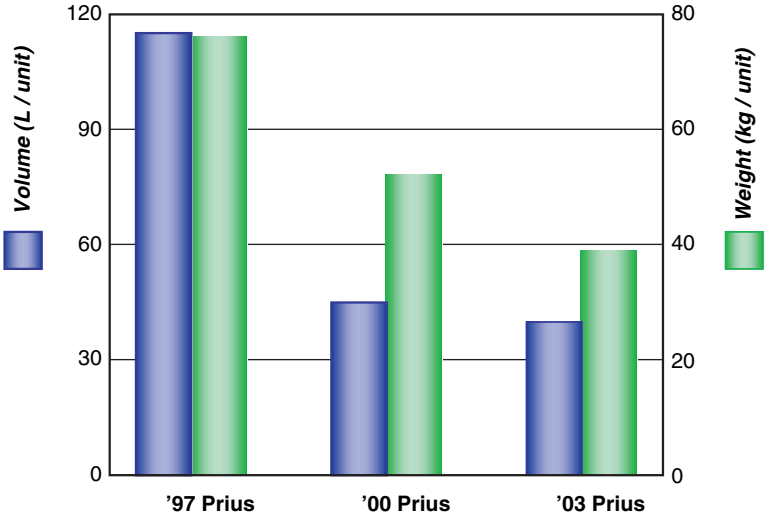

Fig. 7b.38 Volume and weight reduction on Prius

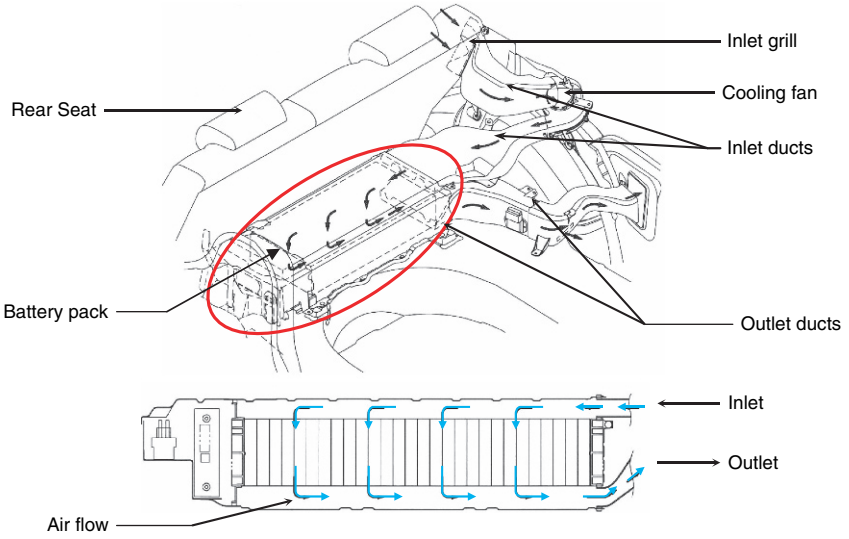

Fig. 7b.39 Battery pack cooling system on 2003 Prius

application, the metal casing technology was adopted for the battery modules. Concerns were the process cost of the reliable sealing technology for metal parts and the price of the case itself. The laser welding process and the deep squeezing technology were dispositive for the case. As a consequence, the module for RX400h became 20 mm shorter in height than the previous one seen in the 2003 Prius. Figure 7b.40 displays the specific power of the battery pack for the three different Prius and for the RX400h. As can be seen, the power density was improved by approximately

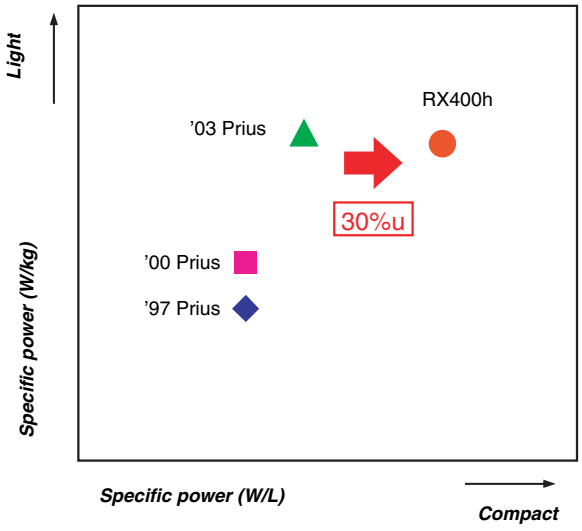

Fig. 7b.40 Specific power

30% compared to the previous module when applying the metal casing technology. This is the highest level in the world at the moment.

For this application, cell connection was designed with two positive electrode terminals in order to reduce the internal resistance. Since each cell was independent of each other, modules with different numbers of cells were implemented. In the RX400h model, for example, one module is composed of eight cells, while another one is made of six (ref. Table 7b.1) cells.

Figure 7b.41 displays the battery pack configuration for the RX400h. The significant difference is that the pack for the RX400h incorporates the high-voltage components to improve space efficiency and a cooling fan. The different features of the new Prius battery, such as the battery module groups, the junction box, and the battery monitoring unit will be reviewed shortly below:

The battery pack is composed of 30 battery modules which are separated into three groups. One group is equipped with six modules and the two others with 12 modules each. The modules are stacked in series and joined with end plates on the side. Moreover, metallic bands are clamped on the top and bottom of each group.

The junction box composed of three system main relays (SMRs), resistor, current sensor, and others in one block contribute to a better installation and an easy assembly during the manufacturing process.

The battery monitoring unit is used solely to detect the battery condition signal and cooling fan voltage as well as to communicate these signals to the HV-ECU. Figure 7b.42 displays the HV battery control system used in the RX400h. The SOC (stage of charge) management, cooling control, and other functions are managed directly by the HV-ECU. By integrating some of the functions in the HV-ECU, the battery monitoring unit was improved in size, weight, and cost.

7b.3.5.3 Improvement of Battery Performance

Figure 7b.43 displays the evolution of the Toyota HV battery performance development from 1995 to 2005. The specific power and power density of the battery pack increased step by step. From around 300 W/Kg and 200 W/L in 1997,

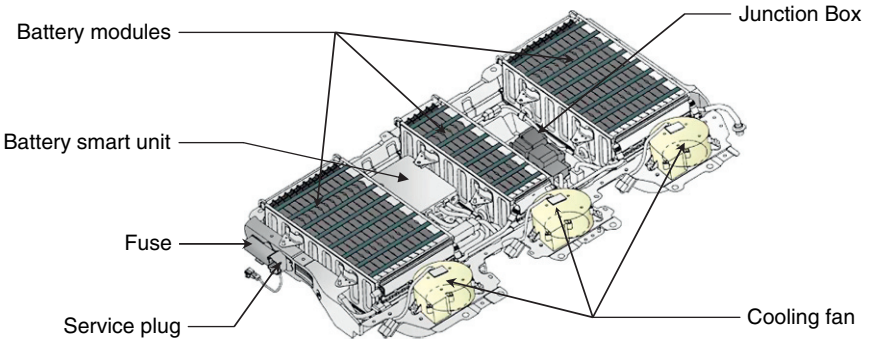

Fig. 7b.41 RX400h battery pack configuration

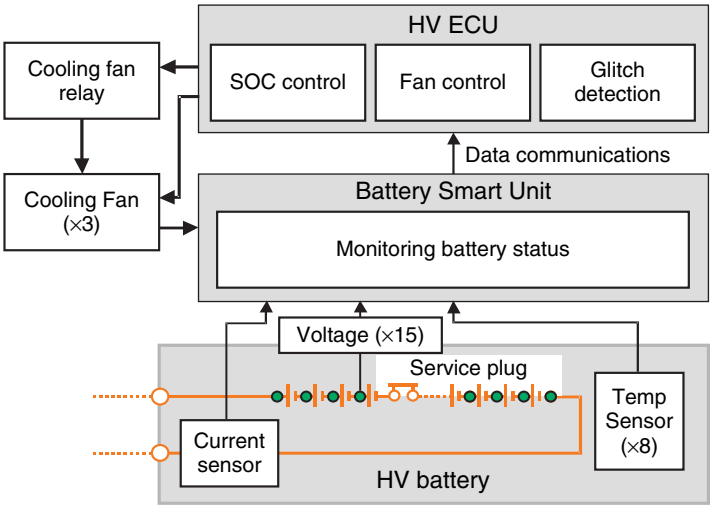

Fig. 7b.42 HV Battery Control System for RX400h

development work resulted in improved battery values of around 550 W/Kg and 600 W/L in 2005. Although this result is remarkable, the development of a high-power battery at low cost and of space-efficient systems will continue in the future.

To sum up, the specific power of the battery module and power density have been improved thanks to the downsizing of battery modules, power improvement, and battery monitoring unit. Moreover, the size reduction and the optimum packaging of system components allowed achieving a more compact and lighter battery pack which, in turn, allows reducing the cost.

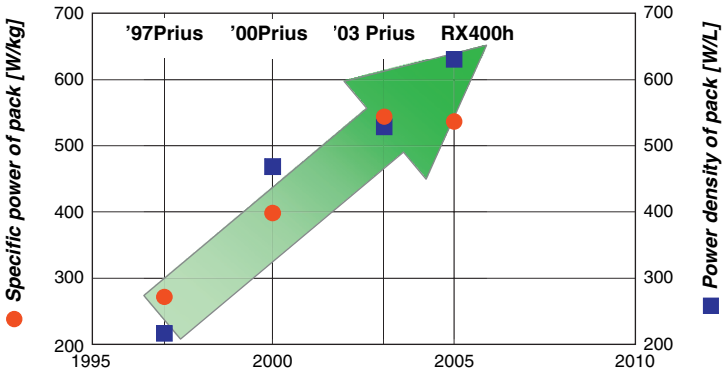

Fig. 7b.43 Toyota HV battery performance transition

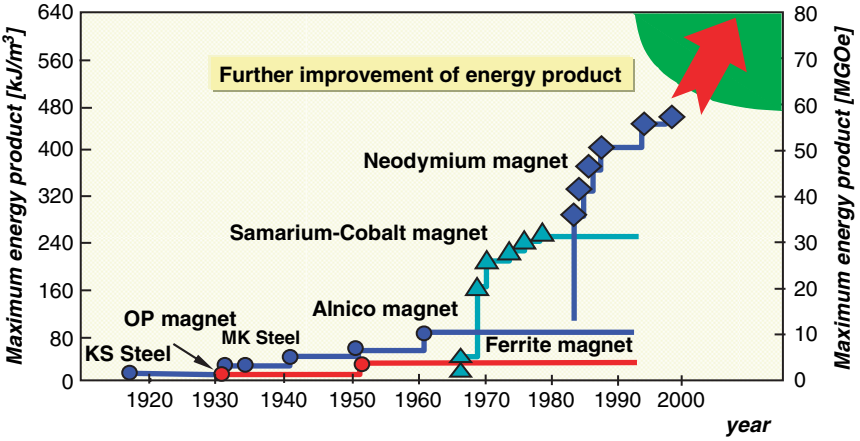

Souce: Y.Kaneko, Powder and Industry, Vol.31, No.6 (1999) p37

Fig. 7b.44 Trend of magnet material

7b.3.6 Magnet Material [17]

Figure 7b.44 displays the evolution of the maximum energy product with the nature of the magnet materials from 1920 to 2005. As obvious, the magnet performance has become better and better since 1983 due to the development of a new type of magnet.

The AlNiCo magnet had been introduced first in the market. However, in spite of the higher residual magnet flux, application of this material has slowed down due to the cost and the low reserved magnet force characteristics which are not suitable for a flat magnet. On the other hand, a ferrite magnet that is composed mainly of ferrite oxide and produced by a powder alloying process is characterised by both a low residual magnetic flux and a low reserved magnet force. Moreover, the shape design flexibility of this magnet as well as the rich supply capacity facilitates wide industrial use at a best cost performance.

The Sm-Co magnet based on rare materials exhibited a drastic advance in performance, but the price was high due to the composition with rare elements. Therefore, a ferrite-based magnet free of Co was investigated and an Nd-Fe-B-based magnet was developed. This magnet showed an extremely superior magnet force compared to the Sm-Co magnet. Its magnet force (BH) exceeded 50MGOe even at mass production level. This type of magnet opened the gate to building a relatively big PM motor and triggered the application of the PM motor in the HV vehicle.

Permanent magnets exceeding 70MGOe BH were developed in 2002, followed by bulk magnet material of more than 3T saturated magnet force in 2003. This means that if the current magnet material was replaced by a new material, size reduction of the electric motor by 30–40% would become reality (Fig. 7b.45). Consequently, introduction of a new material will be a big step forward and bring about huge changes in applications.

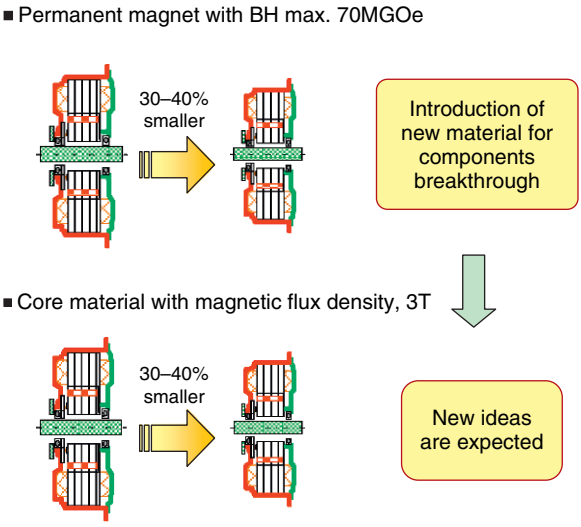

Fig. 7b.45 Effect on traction motor

7b.4 The Presence and Future of HV Mass Market Penetration

7b.4.1 The Prius Development

As mentioned previously, HV currently is one of the most promising technologies to address the concerns regarding global energy issues. Toyota's first hybrid vehicle was the Prius in 1997. Then, the second generation Prius was launched in 2003 with both a better fuel economy and driving performance. Since then, the sales volume of this HV has been increasing rapidly.

7b.4.2 Hybrids Compared to Gasoline and Diesel

Though diesel vehicles have a better fuel economy in high-speed cruise, the emissions are worse compared to the emissions from gasoline engine systems. Also when comparing hybrid vehicles with diesel vehicles (as well as with gasoline engines) by just focusing on a few parameters, judgment may be confused. Besides the maturity of the current ICE technology, concerns of how best to reduce fossil fuel dependence and utilise renewable energies are becoming increasingly important. Of course, both global aspects of economy and local aspects of production, distribution, and patterns of use are taken into account. As we have seen, HV is currently outperforming the traditional ICE in many respects, such as emissions and urban fuel consumption. On the other hand, if the bio fuel potential could be made use of to the complete extent, traditional ICEs with minor modifications could support

even large-scale sustainable transport. However, keeping in mind the principle of the hybrid system as being independent of any type of power train, the true benefits of HV can be understood: HV is a bridging system, a power boosting platform to be applied in conjunction with a power train (including, of course, ICE) depending on which fuel source offers the best potential to reduce the environmental impact.

7b.5 New Potential Energy Sources

Recently, many new possible energy sources emerged. Keeping in mind that automotive fuel in the future can be diverse, including liquid, gas, and electricity, bio fuels, hydrogen, and/or electricity appear most promising.

Some of these alternative fuels are being introduced on the market at the moment. However, the use of these fuels is not expanding at any significant pace, partly because they are not competitive for current demands. Cost, availability, and energy density continue to be the key requirements. While struggling to satisfy these basic requirements, it is difficult to meet new, more complex demands. Still, given the right circumstances, an alternative fuel would potentially grow at drastic pace.

Besides cost, the key issue of bio fuel is the current lack of large-scale supply from non-food-related biomass. As a result, current use is limited to partial replacement of other fuels. Electricity and hydrogen suffer from both lack of competitive, large-scale supply as well as from the lack of significant technical challenges, such as FC technology, for actual vehicle deployment. As a result, both will remain interesting, but candidates in the long term.

7b.6 Conclusion

The long and strenuous road of hybrid technology development as well as some key challenges for the future were outlined in this paper. How hybrid technology and other key developments will continue to grow in today's society is not just up to functionality, but also to how well they will adapt to a new social framework of growing concern for sustainable development.

In this context, hybrid technology is proposed as a broad platform to introduce new power train systems. Moreover, advances in alternative energy supply will make these new systems gradually available for mass market penetration. Through shared visions, such developments will experience significant technological progress across a wide field of science, and Toyota is committed to close collaboration with all interested parties in order to achieve a better future.

References

1. I. Ando, et al., "Development of Engine for New Hybrid SUVs", *Toyota Technical Review* Vol. 54 No. 1, 2005.
2. A. Kimura, et al.,"Development of Hybrid System for SUV", SAE 2005-01-0273.

3. H. Kusumi, et al., “42V Power Control System for Mild Hybrid Vehicle (MHV)”, SAE 2002-01-0519.
4. H. Hata, et al., “Development of a new hybrid transmission for FWD sports utility vehicles”, *Toyota Technical Review* Vol. 54 No. 1, 2005.
5. K. Takizawa et al., “New Hybrid Transmission”, EVS 21 Proc., 2005.
6. H. Hata, et al., “Development of a New Hybrid Transmission for FWD Sports Utility Vehicles”, SAE 2005-01-0272.
7. M. Adachi et al., “Development of a New Hybrid Transmission for RWD car”, SAE 2006-01-1339.
8. K. Shingo, et al., “Development of Electric Motors for the Toyota Hybrid Vehicle ‘PRIUS’ ”, EVS17 Proc., 2000.
9. M. Okamura et al., “Development of Hybrid Electric Drive System Using a Boost Converter”, EVS 20 Proc., 2003.
10. T. Kikuchi et al., “Development of Power Control Unit for SUVs”, EVS 21 Proc., 2005.
11. T. Kikuchi et al., ”Development of High Output Power Control Unit for Hybrid SUVs”, *Toyota Technical Review* Vol. 54 No. 1, 2005.
12. M. Imai et al., “Development of Intelligent Power Module for Hybrid Vehicles”, *Toyota Technical Review* Vol. 54 No. 1, 2005.
13. R. Hironaka et al., “Development of Small Size Power Control Unit”, EVS 22 Proc., 2006.
14. M. Ito et al., “Development of a New Battery System for Hybrid Vehicles”, *Toyota Technical Review* Vol. 54 No. 1, 2005.
15. M. Ito et al., “Development of a New Battery System for Hybrid Vehicles”, EVS 21 Proc., 2005.
16. K. Tojima, “Toyota’s Battery Development for HV Applications”, Advanced Automotive Battery and Ultracapacitor Conference (AABC-7) Proc., 2006.
17. Y. Kaneko, “Manufacturing Technology on Super High-performance Magnets through High Orientated Fine Particles”, *Powder and Industry* Vol. 31 No. 6, p. 37, 1999.

Chapter 7c
Fuel Cell Vehicles: Fundamentals, System Efficiencies, Technology Development, and Demonstration Projects

Rittmar von Helmolt and Ulrich Eberle

List of abbreviations

AC	Alternating urrent
AFC	Alkaline fuel cell
BEV	Battery electric vehicle
CGH_2	Compressed gaseous hydrogen
DC	Direct current
EDC	European driving cycle
FCV	Fuel cell vehicle
GM	General Motors
HEV	Hybrid electric vehicle

Rittmar von Helmolt
GM Fuel Cell Activities, Hydrogen & Fuel Cell Research Strategy (Europe), IPC MK-01, 65423 Rüsselsheim, Germany, e-mail: rittmar.dr.von.helmolt@de.opel.com

Ulrich Eberle
GM Fuel Cell Activities, Hydrogen & Fuel Cell Research Strategy (Europe), IPC MK-01, 65423 Rüsselsheim, Germany, e-mail: ulrich.eberle@de.opel.com

A. Léon (ed.), *Hydrogen Technology*,

ICE or IC engine	Internal combustion engine
Li-Ion	Lithium-ion battery
Ni-MH	Nickel-metal hydride battery
PDU module	Propulsion-Dress-Up module
PEM	Proton exchange membrane
PEMFC	Proton exchange membrane fuel cell
G	Gibbs free energy
H	Enthalpy
S	Entropy
T	Temperature
U_{rev}	Reversible cell voltage
U_{th}	Thermoneutral cell voltage
W_{el}	Electrical work
W_{mech}	Mechanical work
η_{FC}	Fuel cell efficiency
η_{th}	Theoretical efficiency

7c.1 Introduction

Currently, virtually all large car manufacturers in the world are actively pursuing the development of hydrogen fuel cell vehicles (FCV). Fuel cell propulsion systems utilizing hydrogen as fuel are the most attractive long-term option for passenger cars, since such a hydrogen FCV represents a true zero-emission vehicle. Its fuel could be produced from various sources and this vehicle concept provides for a very high average efficiency. The latter is due to the fact that a fuel cell reaches its highest efficiency under the frequently utilized low load operating conditions, in contrast to internal combustion engines. At high load, there is almost no advantage over optimized ICE drive trains anymore.

A large variety of FCV concept cars were presented during the last years. Some manufacturers already have begun to hand these vehicles over to selected customers on a leasing base, although still at very high cost and under close technical supervision. Despite these widespread industrial activities and a large number of scientific articles published on the topic of fuel cells, there are only very few reviews available today, which describe the complete power train, its setup, and its efficiency. The goal of this section is therefore to provide an insight into the interactions of all relevant components of such a fuel cell system and their respective efficiency maps. The third generation of the GM fuel cell system is used as a specific example. Additionally, an outlook on future fuel cell vehicle generations is presented.

7c.2 The PEM Fuel Cell

The fuel cell stack represents the core component of the complete fuel cell power system. There is a wide range of fuel cells available, including mid- and high-temperature fuel cells. However, only low-temperature fuel cells working with

a proton-conducting polymer membrane (proton exchange membrane, PEM) are viable for automotive applications. PEM fuel cells combine a comparatively low operating temperature, typically between 60 and 80°C, with a high power density, the option of conventional air operation, and the potential of being manufactured at low cost. PEM fuel cell-based power systems provide similar performance features as internal combustion engines, with which they are competing.

The fuel cell is, like a battery, a direct converter of chemical into electrical energy. The "fuel", however, is not contained at the electrode, but supplied to the electrode from a separate sub-system. As long as fuel and oxidant are supplied to the fuel cell at sufficient quantities, the generation of electrical energy is ensured. The challenge consists in evenly supplying all single cells of the stack with fuel and also in removing the reaction or waste products properly. In the case of a hydrogen PEM fuel cell, the waste product is just pure water.

7c.2.1 Efficiency of the Fuel Cell

A major advantage of the fuel cell is its inherently high conversion efficiency, as it is apparently independent of a Carnot's cycle efficiency. However, a popular misconception exists (even among the educated public) that culminates in claiming that fuel cells are not bound to the conventional laws of thermodynamics, since there is no combustion process taking place. Thus, the purpose of the following section is to clarify the usage of chemical energy and the efficiency of its conversion into electricity.

The efficiency of an internal combustion engine given by the following equation depends simply on a large temperature difference between two reservoirs.

$$\eta_{\text{th}} = \frac{W_{\text{mech}}}{\Delta H} = \frac{T_2 - T_1}{T_2} \tag{7c.1}$$

where W_{mech} represents the mechanical work, ΔH the enthalpy of the reaction, T_2 the highest temperature, and T_1 the lowest temperature.

This Carnot's cycle efficiency represents the theoretical upper limit of a thermodynamic machine operating between a high temperature, typically achieved by burning fuel in the combustion chamber, and a low temperature which is somewhere between exhaust gas and feed gas temperature. In practice the higher temperature is limited by material properties and heat losses. The lower process temperature usually cannot be decreased below the ambient temperature values (assuming air or water cooling). Consequently, efficiencies greater than about 55% are not possible even in a perfect-world scenario (e.g., implemented in large-scale thermal power plants). For internal combustion engines, the maximum combustion chamber temperatures are in the order of 2900°C and the exhaust gases are shoved out at about 1100°C non-ideal cycle. For real-world applications, the theoretical efficiency is further reduced by other technical losses to values below 40%. These technical losses are attributed to the system's inherent properties, such as heat losses, friction, and

gas exchange losses as well as to losses caused by auxiliary drives, such as oil and water pumps.

In the case of a fuel cell, two gases – hydrogen and oxygen – are converted into water, and the difference in their chemical potentials is transformed into electrical work. Since a fuel cell does not a priori represent a thermal engine, no temperature difference between two reservoirs is needed for energy generation. Relevant are the internal energies of the chemical compounds involved and only the usable free energy is converted into electrical work. Therefore, the theoretical efficiency of a fuel cell system can not be 100%, as it is sometimes falsely assumed, and is defined by the following equation:

$$\eta_{\mathrm{th}} = \frac{W_{\mathrm{el}}}{\Delta H} = \frac{\Delta G}{\Delta H} \tag{7c.2}$$

where W_{el} represents the electrical work, ΔG the Gibbs free energy, and ΔH the enthalpy of the reaction.

The thermodynamic efficiency of fuel cells is thus defined as the ratio of the Gibbs free energy ΔG and the enthalpy ΔH which is equal to $\Delta G + T\Delta S$. These equations give rise to a question relating to the comparability of the respective usable energies of an IC engine and a fuel cell. The answer is that these energies are indeed comparable, the usable energy generated is equivalent. Since the only work of the cell consists in driving the electrons through the external electric circuit, the energy ΔG and the enthalpy ΔH in Eq. (7c.2) can be expressed as cell voltage by using the definition for electrical energy (charge times voltage). Hence, the efficiency of a fuel cell is the ratio of the reversible (i.e., the usable) cell voltage U_{rev} and the thermoneutral voltage value U_{th} according to Eq. (7c.3). The thermoneutral voltage simply expresses how large the cell voltage would be, if the entire chemical energy could be transformed into electricity.

$$\eta_{\mathrm{FC}} = \frac{\Delta G}{\Delta H} = \frac{\Delta G}{\Delta G + T\Delta S} = \frac{U_{\mathrm{rev}}}{U_{\mathrm{th}}} \tag{7c.3}$$

Where U_{rev} represents the reversible cell voltage and U_{th} the thermoneutral voltage.

However, thermodynamic losses are always present due to the entropy release. In the case of hydrogen and oxygen, a certain amount of entropy is released in the form of heat during the formation of water molecules. The water molecule represents a state of higher order, and its entropy is reduced by heat emission. Theoretically, a fuel cell operating under standard conditions (T = 25°C) achieves an ideal efficiency of 83% (considering liquid water to be the waste product of the H_2/O_2 reaction).

In a real-world electrochemical cell the maximum usable cell voltage U_{rev} is equivalent to the difference of the two standard potentials. These potentials are measured and tabulated in electrochemistry text books for different electrode materials.

The chemical reactions and the relevant thermodynamic potentials of the hydrogen/oxygen system are given below:

a) Acidic electrolyte, e.g. in case of a PEMFC:			b) Alkaline electrolyte, e.g. in case of an AFC:	
H_2	$\rightarrow 2H^+ + 2e^-$	anode reaction	$H_2 + 2OH^-$	$\rightarrow 2H_2O + 2e^-$
$2H^+ + 2e^- + 1/2O_2$	$\rightarrow H_2O$	cathode reaction	$1/2O_2 + 2e^- + H_2O$	$\rightarrow 2OH^-$
$H_2 + 1/2O_2$	$\rightarrow H_2O$		$H_2 + 1/2O_2$	$\rightarrow H_2O$

– Reaction enthalpy ("max. heat"): $\Delta H = -286\,\text{kJ/mol}\,H_2$;
$\Delta H/2F = -1.48\,\text{V} = -U_{\text{th}}$
– Gibbs free energy ("max. work"): $\Delta G = -237\,\text{kJ/mol}\,H_2$;
$\Delta G/2F = -1.23\,\text{V} = -U_{\text{rev}}$
(at standard conditions: $T = 25°\text{C}$ and $p = 1$ bar)

The force driving the reaction is the max. usable energy, i.e., the Gibbs free energy ΔG.

Temperature and pressure dependence
– Temperature dependence (deduced from $\Delta G = \Delta H - T\Delta S$): corresponds to about 0.00085 V/K
– Pressure dependence $\Delta G(\text{p}) = \Delta G_0 + \Delta n\ \text{RT}\ \ln(p/p_0)$,
where Δn is the change in the number of gaseous molecules during the reaction.
For an operating pressure of 5 bar instead of 1 bar: (Δn RT ln 5)/2F corresponds to 0.031 V

7c.2.2 The PEM Fuel Cell Under Load Conditions

If a fuel cell stack is to yield useful quantities of electrical energy, a sufficiently large, continuous current has to be ensured. Moreover, this sustainable current must be dynamically adaptive.

Since the fuel cell is just a special type of a generic electrochemical cell, the generation of current depends on the kinetic reactions taking place at the electrodes, on the actual state of the electrolyte, and the structure of the components. Therefore, it is not surprising that by increasing the currents, a drop in voltage can be observed. The voltage drop of the electrode also is called polarization.

Figure 7c.1(a) displays the setup of a typical PEM fuel cell with the bipolar plates, diffusion medium, and membrane electrode assembly. Figure 7c.1(b) displays the voltage/current density diagram characteristic of a fuel cell. The polarization curve depends on the fuel cell's operating conditions, such as pressure, temperature, and air

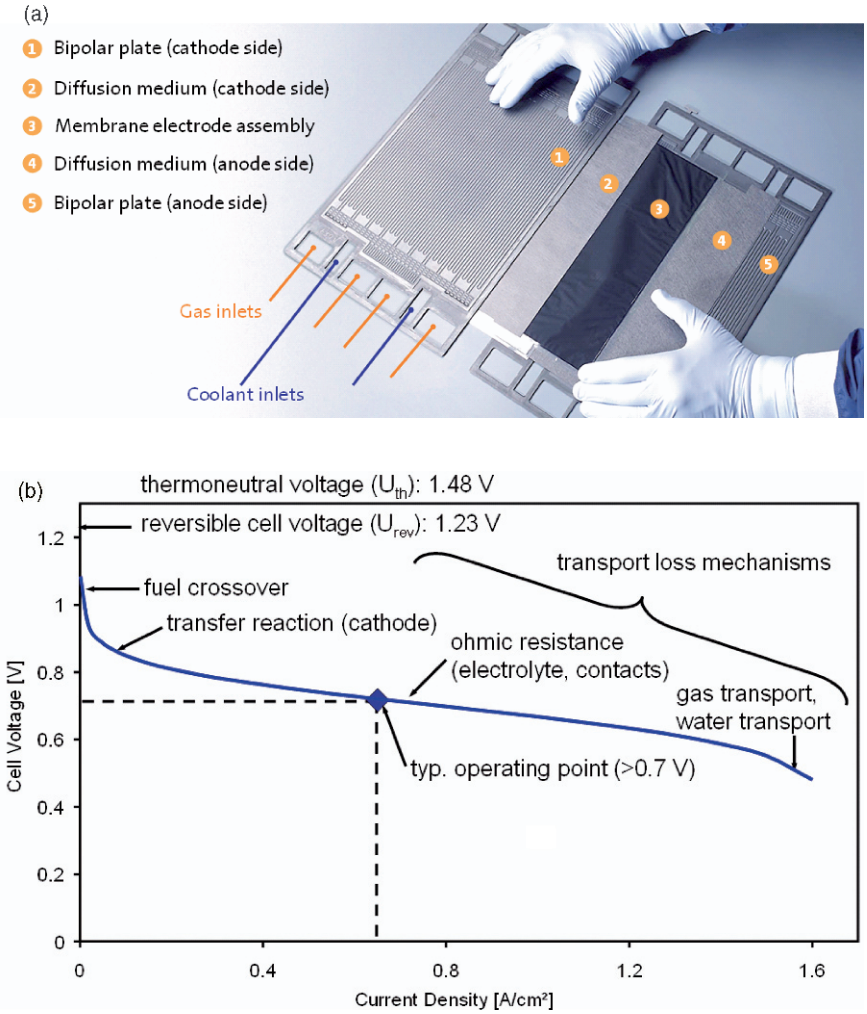

Fig. 7c.1 **(a)** Setup of a PEM fuel cell; **(b)** Schematic representation of the cell voltage versus current density (under idle operating conditions and under load)

humidity. In the H_2/O_2 fuel cell – with an operating temperature of around 70°C – the voltage measured for an open circuit is as low as approximately 0.95 V. Thus, it is already far below the usable voltage, U_{rev}. Within the range of small current densities (up to 0.1 A/cm^2), the voltage significantly drops further, until a nearly proportional behavior with a moderate slope is observed (from 0.1 to 1.4 A/cm^2). For very high current densities, a more or less drastic break-down in voltage takes place.

The characteristic shape of the polarization curve as shown in Fig. 7c.1(b) is essentially caused by the following mechanisms:

- **Hydrogen crossover** – The thin membrane does not completely separate anode and cathode gases. Therefore, there is still a small quantity of hydrogen dissolved

in and, thus, transferred through the membrane. This leads to a direct recombination with air at the cathode and to a reduced ("mixed") potential at the cathode.
- **Activation losses** – A part of the voltage is used for the promotion of the reactions, mainly at the air electrode (cathode activation overpotential).
- **Charge transfer losses** – The reaction at the electrodes results in a concentration gradient which reduces the electrode potential with an increasing rate of reaction (current density). This effect can be described analytically by the *Butler-Vollmer* equation.
- **Ohmic losses** – Occur at the membrane (caused by proton transport processes) and at the respective contacts (caused by electron transport processes).
- **Gas transport losses** – Under high current density conditions, due to the strongly increased consumption of reactants, reactant transport to the electrode or the product water transport to the exhaust channel becomes the limiting process. This results in a reduction of the cell voltage caused by reduced reactant concentration, *starvation*.

The decrease in cell voltage is directly equivalent to a reduction in efficiency. Thus, the efficiency and the voltage vary substantially with the load conditions. For low loads – the most frequently used operating regime of a fuel cell vehicle – efficiencies are around 57% (compared to the gross calorific value) and/or 67% (compared to the net calorific value).

In general, the overall efficiency of a fuel cell propulsion system is lower than that of the stack alone, since obviously further energy conversions are taking place and the auxiliary components must be considered as well. The following chapters will focus on the power demand of these auxiliary components.

7c.3 The Electric Traction System

Downstream transformations of the current generated by the stack depend substantially on the specific down-selection of the electric motor. If a direct current (DC) motor is considered, the generated voltage can be supplied directly to the engine via a DC current controller. For weight and efficiency reasons, however, a three-phase alternating current (AC) asynchronous motor was chosen in the case of the GM HydroGen3.

Hence, a three-phase AC alternating current has to be produced first. For the drive motor to be as small and lightweight as possible, the DC voltage is transformed to higher voltages, such that finally an alternating voltage of 320 V can be supplied to the electric propulsion motor. As DC/DC converter, a throttle controller is applied. Figure 7c.2 displays the efficiency map of this type of converter. It is obvious that an efficiency of approximately 97% is achieved for a broad range of operating conditions. For very low- and very high-load operating conditions, the switching losses of the transistors, i.e. the resistance losses (scaling behavior is proportional to the square current density), lead to a significant reduction of efficiencies. Novel stack generations have more cells and, hence, generate higher voltages (cf. Table 7c.2),

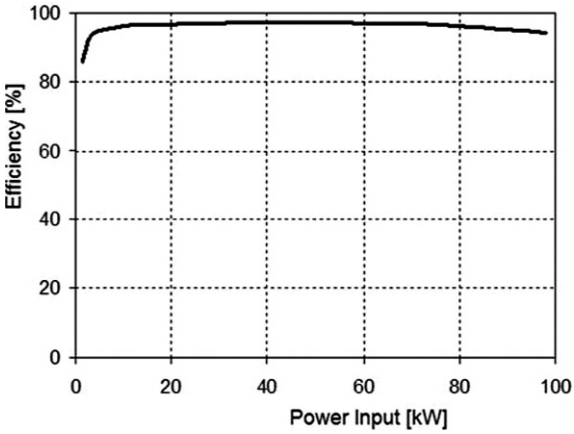

Fig. 7c.2 Efficiency map of the DC/DC converter

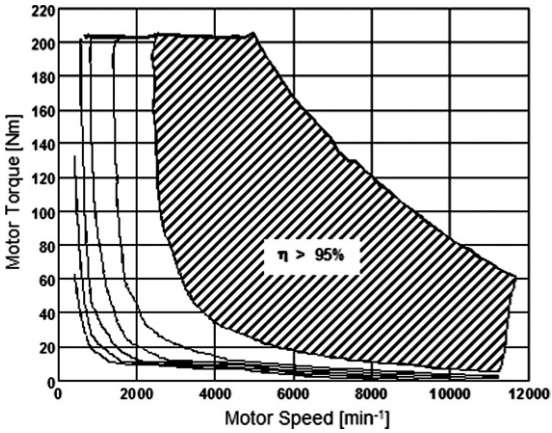

Fig. 7c.3 Efficiency map of the three-phase AC converter

such that the additional DC/DC converter of the HydroGen3 setup (see Fig. 7c.7) may become obsolete. As can be seen in Fig. 7c.3, the downstream three-phase AC power inverter also exhibits an efficiency in excess of 95% over a wide range of operating conditions. Also for this component, however, a drop in efficiency is observed at low-power outputs. Finally, Fig. 7c.4 displays the efficiency map of the three-phase AC asynchronous motor. An efficiency greater than 90% can be reached over a very broad range of operating conditions.

7c.4 Auxiliary Components

For the operation of the fuel cell stack, auxiliary components for media supply and operation control are necessary. They are listed below:

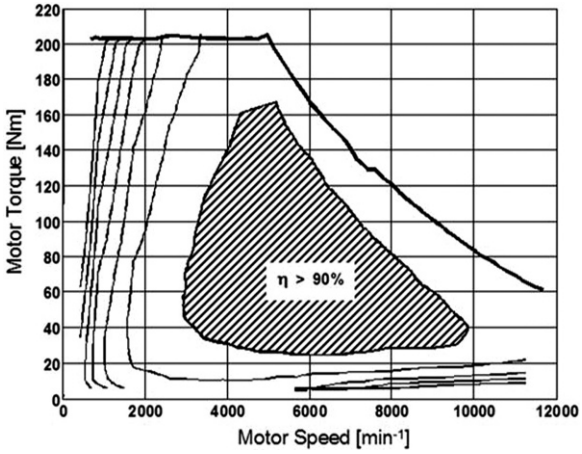

Fig. 7c.4 Efficiency map of the three-phase AC electric motor

- Fuel system
- Air supply
- Coolant cycle
- Controller
- In some cases: Buffer battery and humidification components

It should be noted that the power demand of this *balance-of-plant* is taken from the stack gross power, which subsequently reduces the fuel cell system efficiency.

7c.4.1 Air Supply

In contrast to a four-stroke engine, the fuel cell cannot suck in the air required for reaction during operation. Consequently, this amount of air has to be supplied and exhausted by an auxiliary component. Usually, a compressor is used, since the anticipated current density can only be obtained by utilizing a gas pressure of more than 150 kPa.

Moreover, a pressurized air supply reduces the technical efforts needed for humidification, and an additional external humidification element may even become redundant. In principle, the oxidation of the hydrogen produces a sufficient amount of water needed to moisten the membrane in order to ensure sufficient ion conductivity. However, if the supplied air flow is to dry, humidity is extracted from the membrane at the gas inlets, and this might result in higher membrane resistance and even in an irreversible membrane or electrode damage.

With the HydroGen3, GM succeeded in making external humidification components redundant by compressing the intake air at high temperatures to values of up to 2.7 bar and by raising the relative humidity in such a way that the air flow cannot extract too much of the membrane's humidity. Figure 7c.5 displays the power demand and efficiency over the stack power output for the screw-type compressor used in the

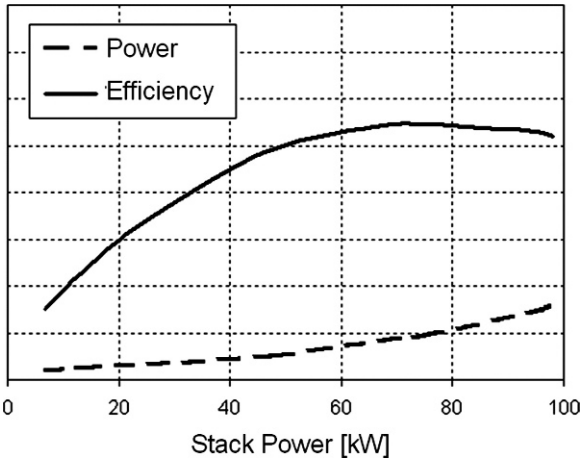

Fig. 7c.5 Normalized compressor power demand and efficiency versus stack power output

HydroGen3 system. Up to a value of 50% of the stack power output, the compressor (including inverters and engine) consumes about 10% of the electricity produced by the stack. This portion rises up to about 15% at maximum stack power outputs.

7c.4.2 Fuel System, Anode Re-circulation Pump

Theoretically, the fuel cell stack could be operated without any complex anode system by just feeding hydrogen to the stack in a "dead-end" mode. This means that the consumed hydrogen only is replaced at the anode. In hydrogen-air systems, however, the resulting low-velocity anode gas stream would first lead to an uneven humidity distribution at the anode and, after a short time, to an inert-gas enrichment. The consequence then would be a significant performance reduction. In the HydroGen3 system, the anode gas at the anode exhaust is therefore taken up and recirculated to the anode inlet port in order to ensure a good humidification of the membrane. The inert gas content can be controlled by bleeding. And a side channel pump is used for the hydrogen recycling loop. Similar pumps, although of much smaller dimensions, are also used as gasoline pumps. Figure 7c.6 displays the power demand and efficiency of this device as a function of the stack power output. The efficiency of the pump, particularly in the low-load region, is disappointingly small, but considering the low power demand of less than a kilowatt, it is still justifiable to implement this concept.

Fuel is supplied to the anode by injectors that are quite similar to those for gasoline fuel injection systems. Theoretically, a single injector would be sufficient. However, three devices are currently used because of the required dosing accuracy and

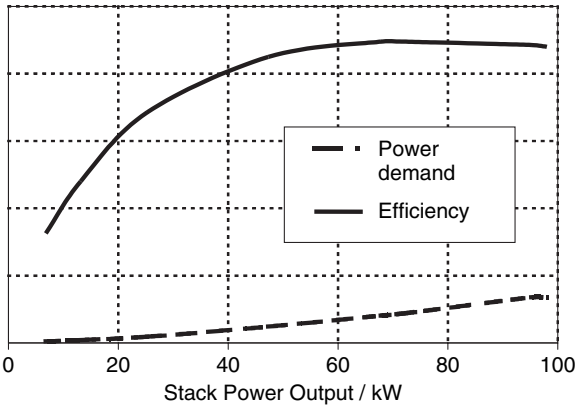

Fig. 7c.6 Normalized power demand and efficiency of the anode recirculation pump

the necessary turndown ratio for different operating conditions. Each injector can be operated individually. The electrical power demand of the injectors is accounted for in the efficiency map of the control system.

7c.4.3 Further Auxiliary Devices

Further auxiliary devices comprise the coolant pump, the radiator fan, and the electronic controller. Their power input amounts to values from approximately 0.6 kW in idle operation up to 3.5 kW for full load. Three-phase alternating-current asynchronous motors with individual inverters power both the compressor and the recirculation pump. The coolant pump and radiator fan are driven by today's conventional DC motors, which are supplied by the vehicle's on-board electrical system. The vehicle electrical system is fed by a DC/DC converter which uses electrical energy from the 320 Volt chain.

Figure 7c.7 displays the complete power flow of the GM HydroGen3 propulsion system. Besides delivering power for the electric propulsion motor, the fuel cell has to drive the auxiliaries described above. Since the fuel cell system provides electrical rather than mechanical power, many of the auxiliaries are actuated electrically. The fuel cell system can be integrated in vehicles similarly to the integration of combustion engines: It has been demonstrated that sufficiently powerful and compact drive trains can be obtained. The fuel cell system and the electric traction system of the GM HydroGen3, Fig. 7c.8, have been packaged in a way (PDU module) that they fit into the same volume as an ICE propulsion module; even the same mounts can be used. This PDU technology allows for a simple and cost-efficient vehicle assembly in existing facilities. Hence, it is a likely scenario for the introduction of mass manufacture on the basis of existing car platforms. However, no technical restriction exists that would forbid a completely different configuration of fuel cell power train components in the vehicle.

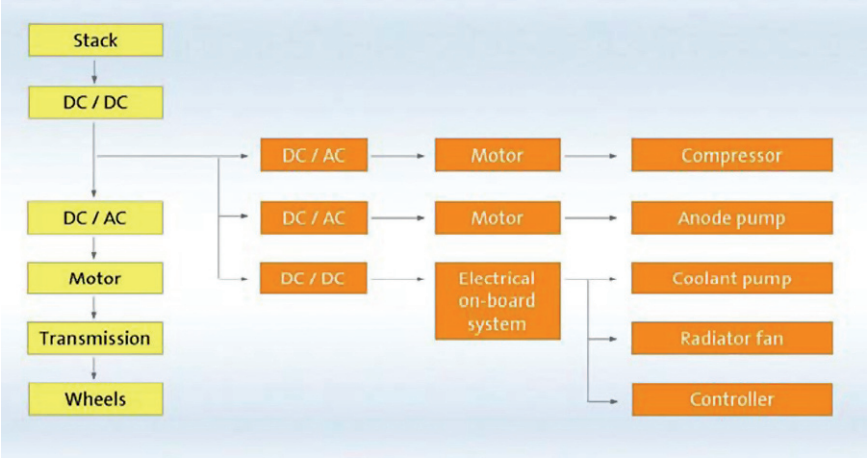

Fig. 7c.7 Power flow of the GM HydroGen3 propulsion system

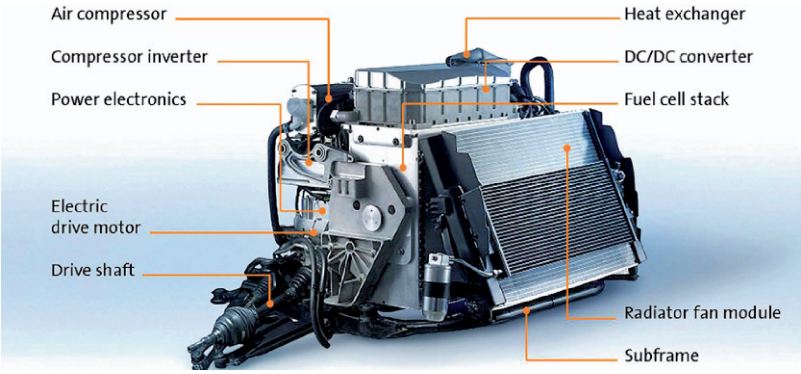

Fig. 7c.8 Physical implementation of the GM HydroGen3 propulsion system (PDU module)

7c.5 Tank-to-wheel Efficiency Map

Figure 7c.9 displays the tank-to-wheel efficiency map. All specific power flows and the respective efficiencies of all sub-components are linked to obtain an overall efficiency map. The lines of equal efficiency are plotted over axle torque and vehicle speed. A fixed transmission ratio of 8.67:1 is used between electric motor and axle. The efficiency map of the propulsion system can now be used directly to determine vehicle propulsion states, since such a single-speed gearbox is used. The shape of the full-load curve is determined by the maximum engine torque of 210 Nm for vehicle speeds up to 60 km/h. At higher velocities, it is determined by the maximum continuous power output of the stack of 100 kW.

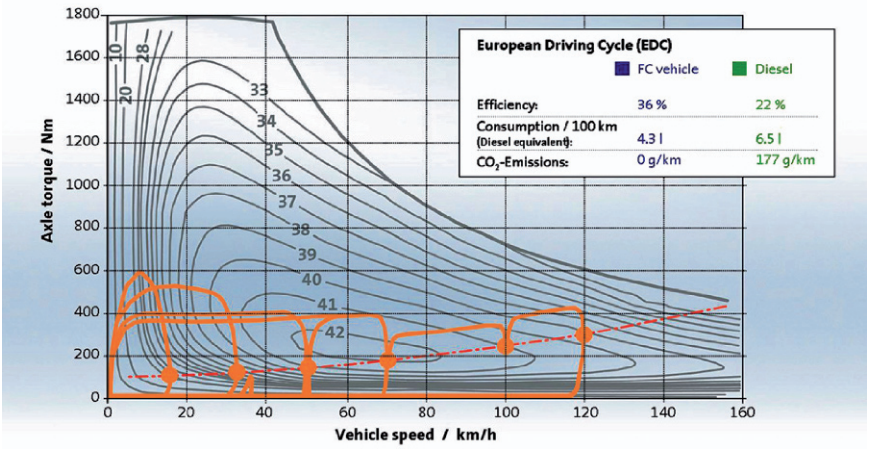

Fig. 7c.9 Tank-to-wheel efficiency map

The orange curve shows the path of the vehicle during a driving cycle, in this case, the European Driving Cycle or EDC. In addition, the road load curve is shown (red dash-dotted line). For periods where the orange curve is below that load curve, the torque value is lower than required for maintaining constant speed, the vehicle is decelerating under these conditions. For values above, the vehicle is accelerating. The GM HydroGen3 needs 16 seconds to accelerate from 0 to 100 km/h, the maximum speed amounts to 160 km/h.

Obviously, also for a fuel cell power train, the overall efficiency decreases with decreasing torque and eventually approaches zero under idle operating conditions. However, the efficiency rises quickly with increasing axle torque, and the region of highest efficiency is reached at quite low torque values already. The depicted EDC (European Driving Cycle) load curve shows that between 50 and 100 km/h the propulsion system operates practically completely within the range of its best efficiencies.

Hence, this efficiency map is nearly perfectly appropriate for urban traffic cycles. The average efficiency for the whole cycle is as high as 36%, compared to 22% for the corresponding Zafira 2.0 DTI diesel vehicle. In total, the EDC fuel consumption of the HydroGen3 amounts to approximately 1.2 kg hydrogen per 100 km, which corresponds to an equivalent diesel fuel consumption of 4.3 l/100 km. Considering a current vehicle weight of still 1765 kg, this value is remarkably low compared to the EDC fuel consumption of the approximately 300 kg lighter Zafira 2.0 DTI, which amounts to 6.3 liters of diesel per 100 km.

Further development of the fuel cell technology is expected to lead to an additional increase in the efficiency (i.a., for the 4th and 5th generation of GM fuel cell power trains). The following potential measures may be taken:

– Stacks with a higher specific cell voltage
– Elimination of the DC/DC converter

– Lower system pressure
– Improved compressor efficiency
– High-efficiency engines and semiconductors
– Weight reduction of the components.

7c.6 Electrical Energy Storage

As mentioned in the previous section, the efficiency map of a fuel cell propulsion system is characterized by the fact that the region of best efficiencies lies in the region of the low-load power output. Therefore, these power trains are particularly suitable for the propulsion of passenger cars operated under urban traffic conditions. Already today, the total tank-to-wheel energy consumption of a state-of-the-art FCV is clearly superior to that of a corresponding vehicle powered by an internal combustion engine. *Hybridization*, i.e. the combination of battery electric and conventional power trains, is a technical solution that yields a significant efficiency improvement over a pure gasoline IC engine-driven vehicle. The addition of an electric drive and a battery, combined with a sophisticated power train management and control system, allows to tailor the gasoline engine in a more appropriate way to continuous load conditions and, on the average, to operate it in a more favorable power range. The effect of hybridization is especially large on gasoline power trains because of their originally poor efficiency values under part load.

In comparison, much less improvements can be achieved by hybridizing a fuel cell drive train. Consequently, a traction battery was not installed in the original HydroGen3 vehicle. However, many of the older fuel cell vehicles, including the HydroGen1, needed hybridization, as their fuel cell systems had not been sufficiently dynamic. It should be noted that hybridization of fuel cell vehicles is simple and cost-efficient compared to ICE vehicles, as major electric components are already on-board. For GM's current fourth generation of fuel cell drive trains, a traction battery (see Table 7c.2) is introduced again, as it is a comparably cost-efficient method to increase peak power for acceleration and to raise the vehicle efficiency through i.a. regenerative braking. Such as power train is installed on the Chevrolet Equinox fuel cell vehicles. The power split between battery and fuel cell system is mainly driven by the performance requirements and the relative costs of battery and fuel cell power. The most favorable energy split will thus be determined by the specific driving profile, but also by the range and cost requirements of the customers. Like *Full Gasoline-Electric Hybrids (HEV)*, also fuel cell vehicles can incorporate a battery that is large enough to propel the vehicle without the need to switch on the fuel cell. Recently, even the option of recharging the vehicle battery from the electric grid was discussed, thus enabling short-range driving on electric energy only (similar to a pure *battery electric vehicle, BEV*), e.g. for commuting purposes in urban areas. However, this puts a heavy burden on the battery, and current battery generations do not have the capability to support such a plug-in mode of operation.

Table 7c.1 Comparison of an electric energy storage with a high-pressure hydrogen storage system. The comparison is based on the assumption that the battery electric propulsion has twice the efficiency than the hydrogen fuel cell electric propulsion. Data are taken from Chalk and Miller [1] and von Helmolt and Eberle [2]. Note that this table may be used for order-of-magnitude considerations only. For a more detailed comparison, the fuel cell system has to be added in the left column, for instance, and also for the automotive battery modules, some additional system components have to be added. Furthermore, a maximum of 70% of the nominal battery capacity only may be used in a charge-discharge cycle

	Hydrogen (70 MPa CGH_2 vessel)	Lead acid battery	Ni-MH battery	Li-ion battery
Gravimetric energy density	1600 Wh/kg	35 Wh/kg	70 Wh/kg	120 Wh/kg
Volumetric energy density	770 Wh/l	70 Wh/l	140 Wh/l	150 Wh/l
Energy required for vehicle ranges of approximately 500 km	6 kg H_2 = 720MJ = 200 kWh		360MJ = 100 kWh	
Weight	125 kg	2860 kg	1430 kg	830 kg
Volume	260 l	1430 l	710 l	670 l
Cost (at volume production)	3600$	15,000$	30,000$	40,000$
Power required for 8 hours overnight charge	–		>12kW	
Power required for 30 min fast charge	–		>200kW	
Power required for 10 min fast charge	–		>600kW	

Generally speaking, although tremendous progress was achieved in battery development in the past years, batteries are still much heavier and bigger than a hydrogen storage system of the same energy content. Furthermore, cost is a major issue for high-capacity batteries. Table 7c.1 gives an overview of battery electric storage in comparison to a high-pressure hydrogen storage system.

On the other hand, further progress is expected to be made with respect to automotive battery development. GM's 5th generation of fuel cell vehicles will be able to make use of these advances, as they are part of the GM E-Flex concept. The E-Flex system is a flexible all-electric production vehicle architecture that can be configured to run on electricity from a number of sources.

7c.7 Summary and Outlook on Future Developments

Since the very beginning, the development of fuel cell technology has been demonstrated by building experimental vehicles. Figure 7c.10 displays two prominent examples from the early days, the 1959 Allis-Chalmers Fuel Cell Tractor and the 1966 GM Electrovan, the world's first fuel cell car.

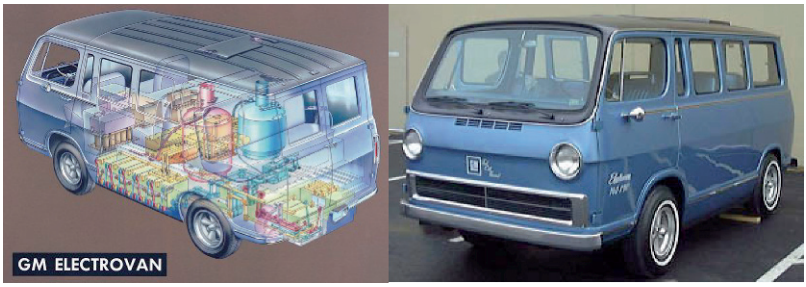

Fig. 7c.10 The 1966 GM Electrovan was powered by alkaline H_2/O_2 fuel cells using cryogenic storage vessels for liquid hydrogen and oxygen

More recent developments focused primarily on performance and drivability properties to become competitive with conventional cars. Meanwhile, this has been demonstrated successfully by different car manufacturers worldwide. The 2002 HydroGen3 was described in detail above. This car proves that the fuel cell system can be designed without external humidification and to be dynamic enough to drive the system without a traction battery or supercaps. Vehicles of this third generation are still on the roads for demonstration purposes; their number, however, is very limited.

The subsequent generation of fuel cell vehicles will show progress in the areas of quality, reliability, and the related manufacturing methods. Furthermore, these 4th generation vehicles will have "real-world capability" for operation by customers in different climate zones around the world. These vehicles will be operated preferably in a few pilot regions only in order to obtain more information about infrastructure installations and "normal" user behavior. In this so-called lighthouse concept, the hydrogen demand for cars is concentrated geographically, which allows for the testing of the impact of higher volumes on the re-fuelling infrastructure. Having started in September 2007, more than 100 Chevrolet Equinox fuel cell vehicles are handed over to customers in demonstration projects in different regions around the globe within the framework of GM's "Project Driveway". However, due to high costs, the further deployment of vehicles will be limited.

The 5th generation of fuel cell vehicles will be ready in between 2010 and 2015. These cars will still be pre-commercial vehicles at high incremental costs, compared to conventional propulsion systems. However, costs projected on the basis of the assumed volume production will have to be in an affordable range, and also performance and reliability will have to be competitive with conventional combustion engines. The number of 5th generation vehicles deployed will be an order of magnitude greater than before, i.e. several 1000s of vehicles. As mentioned, these cars still will be costly, but they are essential for the initial market preparation. A certain hydrogen refueling station infrastructure should be available for customer convenience.

GM's 5th generation fuel cell vehicle will be based on the GM E-Flex electric architecture. The first iteration of the Chevrolet Volt concept vehicle (presented at the 2007 North American International Auto Show in Detroit), for instance, is a battery electric vehicle that can be recharged on the electric grid to a maximum all-electric

Fig. 7c.11 HydroGen3 Liquid, Chevrolet Equinox Fuel Cell, and the Chevrolet Volt Fuel Cell concept – three generations of GM fuel cell vehicles

Table 7c.2 Data sheet for the vehicles shown in Fig. 7c.11

	HydroGen3 (Liquid)	Chevrolet Equinox fuel cell	Chevrolet volt fuel cell (based on the E-Flex concept)
Body style	Compact van	Mid-Size SUV	4–5 passenger sedan, compact
Length	4317 mm	4796 mm	Tbd.
Width	1742 mm	1814 mm	Tbd.
Curb weight	1590 kg (target) (1660 kg target w. optional battery)	2010 kg	1588 kg (target)
Electric traction motor	3-phase asynchronous front motor, 90 kW/215 Nm	3-phase synchronous front motor, 73 kW cont/94 kW max., 320 Nm	Front motor: 70 kW, 250 Nm; rear motors: 2× wheel motor, each 25 kW, 500 Nm
Fuel storage			
Type	Liquid cryogenic	3 Carbon fiber vessels	2 Carbon fiber vessels
Service pressure	4–7 bar	700 bar	700 bar
Hydrogen capacity	4.6 kg	4.2 kg	approx. 4 kg
Fuel cell stack			
Cell count	200	440	> 400
Stack power	94 kW	93 kW	80 kW
Battery			
Type	None/optional NiMH	NiMH	Li-ion
Power	(optional 35 kW)	35 kW	50 kW
Capacity			8 kWh (total)
Operating temp.	–	−25 to +45°C	−25 to +45°C
Operating life	–	2.5 years, 80,000 km	Tbd
Performance			
Acceleration	0–100 km/h in 16 sec. (12.5 sec. with optional battery)	0–100 km/h in 12 sec.	0–60 mph in 8–8.5 sec.
Top speed	160 km	160 km/h	Burst > 190 km/h, cont. 160 km/h
Operating range	400 km	320 km	480 km

range of 65 km. It uses a small gasoline or biofuel engine with a generator to extend its range to more than 1000 km. Another E-flex iteration (announced in April 2007 at the Shanghai Motor Show) uses GM's 5th generation fuel cell propulsion technology and a lithium-ion battery; a range of up to 480 km is achieved. Figure 7c.11 displays three generations of GM fuel cell vehicles. Table 7c.2 provides the characteristics of the vehicles depicted in Fig. 7c.11.

The infrastructure is expected to grow from the existing lighthouse regions. This picture is coherent with other car manufacturers' plans, and it is commonly anticipated that the roll-out of hydrogen vehicles will happen in the phases described here. Commercialization and ramp-up of vehicle production will start after 2015. It is obvious that this phase will only be entered, if real mass production can be achieved within a short term. Manufacturing concepts will have to be fully developed, and necessary production capacities will have to be in place both at the car manufacturers and at the automotive supply industry.

Quantitative targets for a hydrogen-based transportation system in Europe have been defined in strategic documents, i.e. the Deployment Strategy [3] and its Implementation Plan [4] of the European Hydrogen and Fuel Cell Technology Platform. The projection for 2020 assumes an annual vehicle production in the EU of 400,000 to 1,800,000 units, and total sales by 2020 between 1 and 5 million units. The average fuel cell power will be about 80 kW per unit, and the cost will be below 100 €/kW. At that time, in addition to fuel cell electric vehicles, also conventional or hydrogen-based ICE systems [5] will still be on the roads.

References

1. S.G. Chalk and J.F. Miller, Journal of Power Sources 159 (2006) 73–80, resp. Andrew Burke, Presentation at ARB ZEV Technology Symposium, Sacramento, California, September 27. http://www.arb.ca.gov/msprog/zevprog/symposium/presentations/burke1.pdf.
2. R. von Helmolt and U. Eberle, Journal of Power Sources 165 (2007) 833–843.
3. Deployment Strategy of the European Hydrogen and Fuel Cell Technology Platform (HFP), progress report 2005, October 2005. https://www.hfpeurope.org/hfp/keydocs.
4. Implementation Plan – Status 2006, European Hydrogen and Fuel Cell Technology Platform (HFP), April 2007. https://www.hfpeurope.org/hfp/keydocs.
5. SAE TECHNICAL PAPER SERIES 2006-01-0431, Gerrit Kiesgen, Manfred Klüting, Christian Bock and Hubert Fischer, BMW AG.

Chapter 8
Development of Storage Tanks

Chapter 8a
High-pressure Vessels

Neel Sirosh and Alan Niedzwiecki

Neel Sirosh
Quantum Fuel Systems Technologies Worldwide Inc., 17872 Cartwright Road Irvine, California 92614, USA, e-mail: nsirosh@qtww.com

Alan Niedzwiecki
Quantum Fuel Systems Technologies Worldwide Inc., 17872 Cartwright Road, Irvine, California 92614, USA, e-mail: aniedzwiecki@qtww.com

A. Léon (ed.), *Hydrogen Technology*,

List of Abbreviations

AHJ	Authority having jurisdiction
AN	Acrylo nitrile
ANSI	American National Standards Institute
ASME	American Society of Mechanical Engineers
CSA	Canadian Standards Association
DOE	Department of Energy
DOT	Department of Transport
ECE	Economic Commission for Europe
EIHP	European Integrated Hydrogen Project
EV	Electric vehicle
ISO	International Standardization Organization
MLI	Multi-layer insulation
NASA	National Aeronautics and Space Agency
NFPA	National Fire Protection Agency
NGV	Natural gas vehicle
PAI	Polyamide imide
PAN	Polyacrylo nitrile
PE	Polyethylene
PEEK	Poly ether ether ketone
PEI	Polyetherimide
PPS	Polyphenylene sulfide
PRD	Pressure relief device
PSUL	Polysulfone
SAE	Society of Automotive Engineers

8a.1 Introduction

The function of the on-board fuel storage system is to safely accept gas during refueling and store without loss, until needed by the power train. The storage system must deliver hydrogen to the anode gas system of the fuel cell stack or the internal combustion engine, at the required pressure and flow rates and within prescribed temperature limits. The storage system includes the interface to the refueling infrastructure, fuel filters, shut-off devices, safety relief devices, sensors, and pressure and flow management devices, the defueling system, vehicle interface hardware, and associated delivery piping. [1].

Fundamental requirements on the fuel storage system include:

- Fuel availability,
- system safety,
- adequate vehicle range, and
- the ability to meet cost targets.

Fuel availability is one of the first requirements on a fuel storage system from the customer's point view. From the fuel availability perspective, direct compressed hydrogen storage on-board does offer an advantage in the sense that hydrogen is a flexible energy carrier that can be produced from a wide variety of energy

sources. Hydrogen can be produced from fossil fuels or by electrolysis of water using electricity generated from fossil fuels or renewable sources, such as wind, hydroelectric, solar or biomass. Thus, direct hydrogen fuel storage on-board allows various energy sources to be deployed to the vehicle, by decoupling the energy source from the vehicle itself.

Hydrogen fueling infrastructure is likely to evolve in multiple phases, beginning with solutions appropriate for 5–100 vehicles, followed by solutions for thousands of vehicles and hundreds of thousands of vehicles. Substantial infrastructure already exists for hydrogen gas production and distribution to support industrial applications of hydrogen. Compressed industrial gas cylinders are traditionally distributed within 200 km of the hydrogen production facility, if the usage is less than about 250 kg/day. Liquid hydrogen is preferred for distribution over a 1,500 km radius, especially for larger usage rates of the order of 1,000 kg/day.

The hydrogen refueling stations of today use various hydrogen sources, including trucked-in industrial gas (typically 20 MPa), trucked-in liquid coupled with on-site vaporization, and on-site electrolyzers or gas reformers. The simple refueling procedure associated with compressed gas on-board storage is compatible with these different hydrogen sources. As we move towards the next phase involving thousands of hydrogen vehicles, distributed hydrogen production from a variety of energy sources is likely. In the long term, larger central plants (for example, thermo-chemical water splitting at nuclear plants or central steam reformer stations) will economically produce hydrogen for distribution through pipeline networks. Direct compressed storage is compatible with all these scenarios involving hydrogen production and distribution in the gaseous form.

Providing an adequate customer range is a key challenge related to the successful commercialization of hydrogen vehicles. Automobile manufacturers, still scathing from the commercial failure of the early battery-powered electric vehicles (EV), are especially sensitive about the range issue. For most manufacturers the target is 500 km range. On an energy-equivalency basis, one kg of hydrogen is approximately equivalent to 1 US gallon (3.78 l) of gasoline. At the currently reported fuel cell efficiency levels, a fuel cell vehicle is expected to require 5–7 kg of usable hydrogen on-board to meet the 500 km range. It remains a challenge to satisfy this range expectation in view of the fuel storage space parameters of today's gasoline vehicles. However, it has been demonstrated that with creative packaging, the range expectations can be fulfilled by using 70 MPa storage systems without seriously compromising either passenger or cargo space. On-board hydrogen storage at 70 MPa provides up to 1.6:1 advantage over storing at 35 MPa and 2.2:1 advantage over storing at 20 MPa.

Compressed gas tanks appear to be more efficient compared to liquid hydrogen tanks at smaller diameters (~300 mm or 12 inch) due to the penalty associated with the thickness of multi-layer insulation (MLI) required for cryogenic storage. Since smaller-diameter storage tanks enable optimized vehicle packaging solutions, compressed storage will remain the primary solution for passenger cars powered by hydrogen in the foreseeable future.

8a.2 Types of Pressure Vessels

Pressure vessels, ranging from small bottles of a few centimeters in diameter to large storage tanks of several meters in diameter, are in widespread use in several industrial, commercial, aerospace, and automotive applications. Figure 8a.1 displays some typical pressure vessel applications as they evolved over the years. The design, fabrication, usage, and maintenance of pressure vessels are controlled by various national and international codes and standards and they have an excellent safety record. For example, an American Gas Association survey of over 8,000 natural gas fleet vehicles (NGVs) with compressed fuel systems on-board found that the NGV injury rate per vehicle mile (1mile = 1.6km) traveled was 37% less than the rate of gasoline fleet vehicles and 34% less than the entire population of registered gasoline vehicles. In excess of 8 million natural gas vehicles have used high-pressure on-board fuel storage systems globally. Industrial gas companies and gas distributors have close to 1 million hydrogen gas cylinders in service, providing safe and reliable service daily, on a global basis.

The pressure vessels currently utilized in automotive and bus on-board hydrogen storage systems are characterized by 35 or 70 MPa service pressure. It should be mentioned here that 70 MPa is more and more preferred to improve storage density. Figure 8a.2 displays the relationship between compression energy and various pressures. It can be seen that the compression energy does not increase significantly as the pressure increases from 35 to 70 MPa.

The pressure vessels are classified in four types, namely Type I, II, III, and IV. The Type I pressure vessels are most commonly constructed from isometric, metallic materials. These pressure vessels are generally designed with a center cylindrical

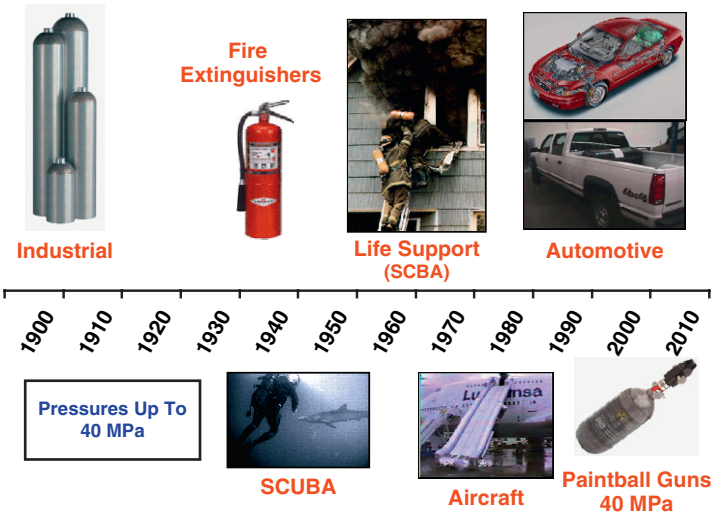

Fig. 8a.1 Pressure vessel applications

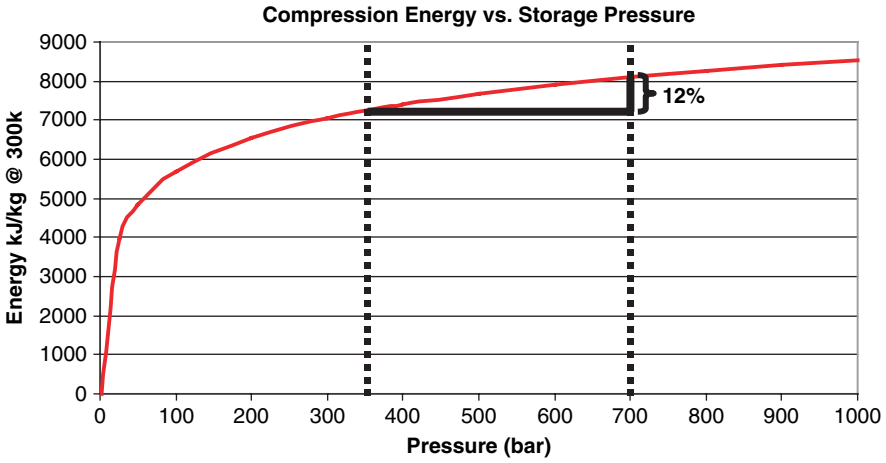

Fig. 8a.2 Relationship between compression energy and service pressure

section, two spherical domes, and polar opening(s). Most industrial and commercial pressure vessels are low-pressure Type I pressure vessels constructed from carbon and low-alloy steels. The working pressures of on-board hydrogen storage vessels are higher compared to those of industrial and commercial pressure vessels. High-pressure vessels require higher-strength materials. However, high-strength steels have limited usage in hydrogen applications due to potential for strength degradation resulting from hydrogen embrittlement.

In the mid 1960s, the need for light-weight pressure vessels for life-support and aerospace applications led to the utilization of high-strength and low-density fiber-reinforced materials. Simply "hoop-wrapping" metallic liners with fiber-reinforced composite materials can lead to a performance advantage in terms of 30–40% reduction in the overall weight, compared to Type I vessels. The pressure vessels with hoop composite reinforcement are called Type II vessels. The hoop reinforcement can also extend the fatigue life of the metallic liner, since a residual compressive stress can be introduced in the liner during the manufacturing process, allowing a reduction in tensile stresses during cylinder pressurization.

The Type III pressure vessel structures are further optimized with a "full wrapping" of high-strength and stiffness orthotropic fiber-reinforced composite materials. These pressure vessels typically have steel or aluminum liners that carry approximately 20% of the pressure load, while the rest of the load is carried by the composite overwrap. The composite wrap may also be used to impose a residual compressive stress in the metallic liner to increase its fatigue life under repeated pressurization-depressurization cycles. Type III vessels were first developed for weight-critical space applications. Presently, such pressure vessels are common in medical, recreational, fire-fighting, aerospace, and commercial applications.

Type IV pressure vessels are similar to the Type III, except that the metallic liner is replaced by a non-load-bearing polymer liner. The "all-composite" construction

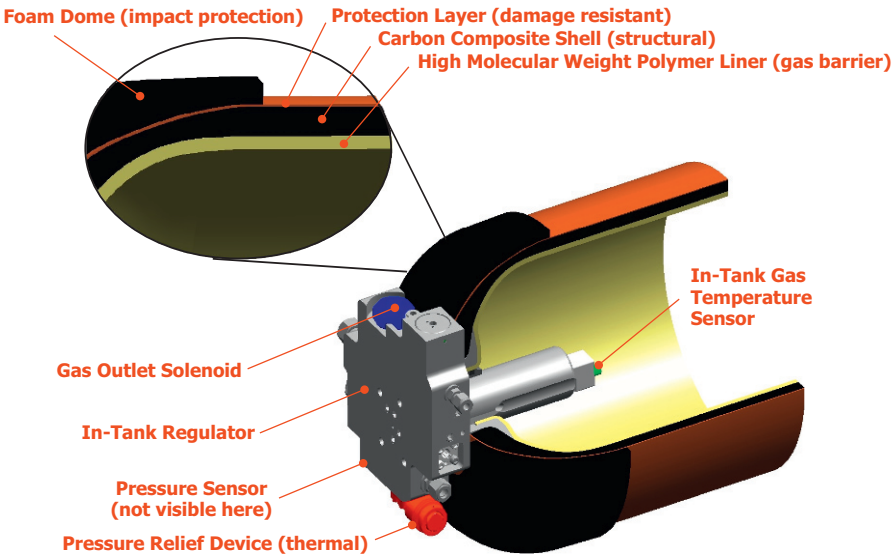

Fig. 8a.3 Construction of a typical Type IV pressure vessel

using polymer liners may offer enhanced cost and performance advantages compared to vessels with metal liners, in certain applications. Figure 8a.3 shows the typical construction of a Type IV pressure vessel [2]. The material and manufacturing costs related to polymer liners could be lower compared to their metallic counter-parts. Polymer liners offer enhanced fatigue life and corrosion resistance and isolate the structural materials from hydrogen "wetting".

Figure 8a.4 compares the hydrogen storage efficiencies (mass of hydrogen stored per unit mass of the vessel) of different types of pressure vessels. Type III and Type IV vessels are common pressure vessels for on-board hydrogen storage. Type I and Type II are less common for on-board hydrogen storage due to their excessive weight. All four types of vessels are useful for ground storage and commercial transportation of hydrogen.

8a.3 Compressed Hydrogen Storage System

Figure 8a.5 displays a typical on-board hydrogen storage system. As can be seen, a compressed hydrogen on-board storage system consists of a single or multiple pressure vessel(s), flow and pressure management components, fittings, sensors, and all fuel lines between the fuel receptacle and the fuel delivery point to the fuel cell system or the hydrogen internal combustion engine. Single tank systems are preferable to multiple-tank systems to maximize volumetric and gravimetric storage efficiencies.

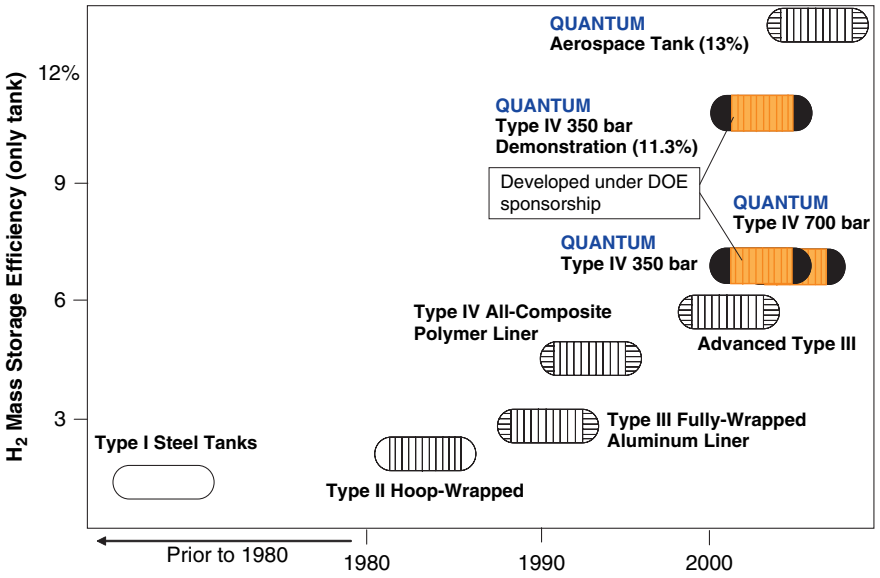

Fig. 8a.4 Comparison of pressure vessel efficiencies [3]

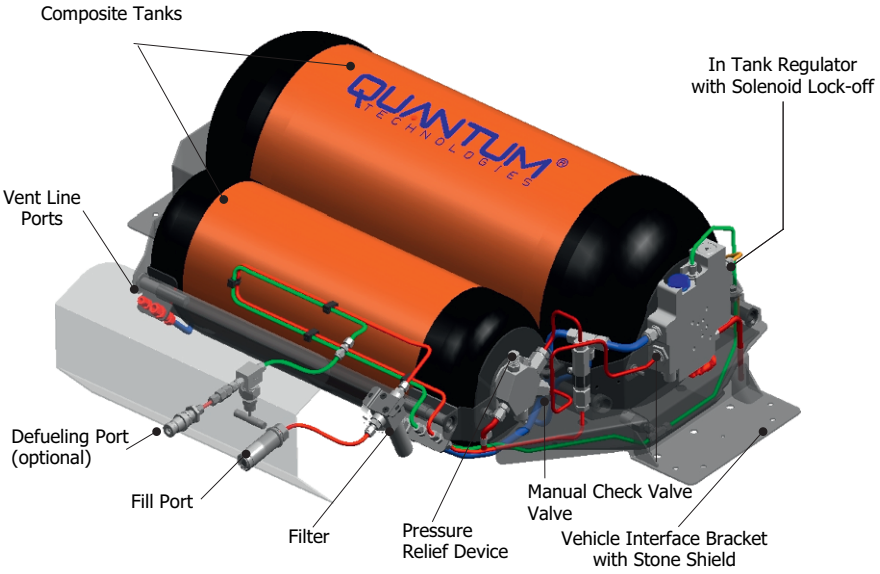

Fig. 8a.5 Typical fuel storage system

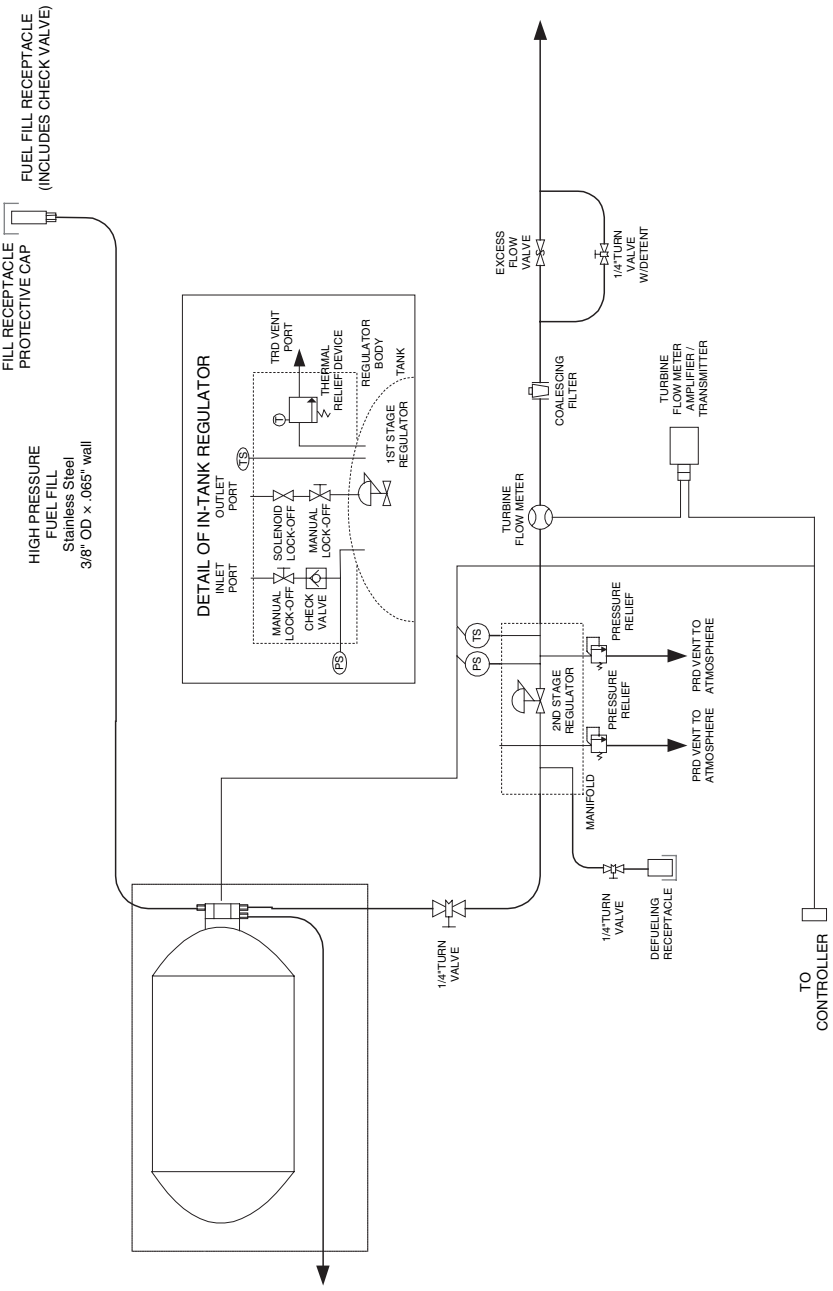

Fig. 8a.6 Generic mechanization of on-board fuel storage system [4]

Generic mechanization of a fuel system is shown in Fig. 8a.6. Hydrogen gas is delivered to the fuel system through the refueling coupler mounted on the side of the vehicle. The gas is routed through a particulate filter and a check valve, into the pressure vessel(s) through a port on the in-tank valve. Depending on the refueling methodology, the gas temperature in the pressure vessel(s) may be monitored during the refueling process and the refueling rate adjusted to keep the fuel temperature inside the tank to less than 85°C.

During vehicle operation, hydrogen needs to be delivered to the power train at a pressure in the 0.35 to 0.50 MPa range. A first-stage regulator reduces the pressure to less than 2.5 MPa and a precision second-stage regulator will reduce the pressure to the required delivery range. Multiple pressure relief valves are strategically placed to protect the system from over-pressurization.

8a.4 Storage System Requirements

The requirements on the on-board hydrogen storage system are simply to accept fuel from the fuel dispensing unit, store, and release fuel on demand. These requirements need to be satisfied during the life of the vehicle under automotive service conditions. Critical design factors include the following parameters [5]:

- Compatibility with hydrogen (including moisture and other potential contaminants),
- prevention of leaks,
- compatibility with temperature extremes (−50 to 85°C),
- compatibility with a variety of pressurization modes (static and cyclic),
- resistance to external corrosion,
- resistance to dynamic and impact loads,
- incorporation of redundant levels of safety.

It is assumed that over-pressure protection is provided at the refueling station side. Figure 8a.7 shows some of the “inside-out” and “outside-in” considerations for on-board hydrogen storage vessels. The inside-out factor primarily is the potential for hydrogen embrittlement, which is largely influenced by the operating temperature, stress levels, and presence of contaminants, such as moisture. Hydrogen embrittlement is the dissolution and diffusion of atomic hydrogen into materials, causing degradation of mechanical properties. The severity of hydrogen embrittlement is affected by gas pressure, since this factor influences the amount of atomic hydrogen that dissolves in the liner material. Pressure cycles from repeating fueling lead to cyclic stress and fatigue crack propagation. The outside-in factors include corrosive agents, such as moisture, ultraviolet rays, road salts, fertilizers, battery acid, acid rain, etc. as well as mechanical loads from vibrations, shocks, and impacts. The fundamental design requirement is that no single-failure mode should lead to a catastrophic event.

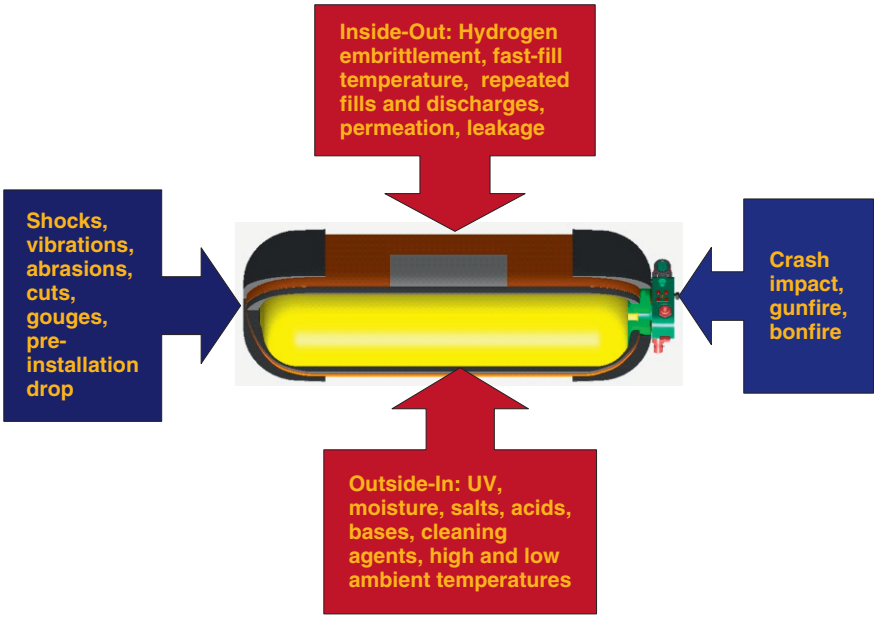

Fig. 8a.7 On-board fuel storage system service environments [6]

8a.5 Construction Materials

Common construction materials for industrial low-pressure hydrogen vessels (< 20 MPa working pressure) are carbon and alloy steels. Design stresses are kept relatively low in these vessels to avoid the onset of hydrogen embrittlement in steel. The walls are still relatively thin, since the working pressure is low. However, on-board storage vessels require higher working pressure (> 35 MPa). Higher-pressure on-board hydrogen storage vessels (> 35 MPa) will require thicker walls to maintain the design stress. Thicker walls lead to practical challenges, including heat treatment of thick steel and weight penalty in automotive applications.

Light-weight polymer composite materials are more common for on-board fuel storage vessels. Polymer composite materials are made of long reinforcing fibers in polymer matrix materials. Reinforcing fibers include carbon fiber, glass fiber, and organic fiber. Matrix materials can be thermoplastic or thermosetting polymers. The fibers provide strength and stiffness, while the matrix material holds the fibers together, enabling load transfer between fibers and between the composite and the supports. The matrix material also protects the fibers from the environment and mechanical abrasion and carries some of the loads, particularly transverse stress and inter-laminar shear stress. Some properties of the composite, such as transverse stiffness and strength and operating temperature limits, are matrix-dominated.

8a.5.1 Thermoset Matrices

A thermoset matrix is formed by an irreversible chemical reaction that transforms a resin system into an amorphous cross-linked polymer matrix. Thermosets are the most commonly used resin systems, primarily due to their desirable mechanical properties, ease of processing, and low cost. The relatively low viscosity of thermoset resins allows for an excellent impregnation of the fiber reinforcement even at high processing speeds.

The most common thermoset resins are polyesters, vinyl ester, epoxy, and phenolics. Epoxy resins are widely used in pressure vessels because of their versatility, high mechanical properties, corrosion and temperature resistance, and low shrinkage. Low shrinkage is an important factor to avoid internal stresses, fiber misalignment, and micro-buckling. Epoxy matrices can be used at service temperatures exceeding 85°C. Thermoset epoxy resins can be toughened using additives, including the addition of thermoplastics.

8a.5.2 Thermoplastic Matrices

Unlike thermosetting resins, thermoplastic resins do not undergo any chemical reaction or irreversible transformation during processing. The thermoplastic polymer is softened from the solid state to impregnate the fibers and subsequently returned to the original solid state once the processing is completed. Thermoplastic materials are attractive due to their high fracture toughness. However, they have yet to gain wide application in the industry due to processing challenges. Examples of thermoplastic matrices are polyethylene (PE), poly ether ether ketone (PEEK), polyphenylene sulfide (PPS), polysulfone (PSUL), polyetherimide (PEI), and polyamide imide (PAI).

8a.5.3 Glass Fibers

Glass fibers have a long history of application in high-performance structures, including pressure vessels. Glass fibers include low-cost general-purpose “E-glass” (low electrical conductivity) or special-purpose fibers, such as “S-glass” (high strength), “ECR-glass” (corrosion resistant) or boron-free E-glass, sold under the trade name “Advantex”, for better chemical resistance compared to the standard E-glass. S-glass or a variant S2-glass have most commonly been used in strength-critical aerospace and pressure vessel applications. However, E-glass has also been used in some applications. Moisture and various chemicals can have a detrimental effect on the strength of glass fibers, leading to the requirement of high design margins when using these materials. High-pressure hydrogen tanks of today do not use glass fibers as the principal load-carrying material. In some cases, glass fibers are combined with carbon fibers to reduce the overall cost and improve the impact toughness of the composite structure.

8a.5.4 Carbon Fibers

Carbon fiber is an ideal engineering material that provides very high strength and modulus, exceptional fatigue life, and resistance to creep and to most chemicals. These fibers are exceptionally suitable for high-pressure vessels due to their mechanical properties and low density. Primary disadvantages of carbon fiber are their brittleness and high cost. The brittleness can be compensated for in the composite design by utilizing tough matrix resins and other strategies.

Commercial-grade carbon fibers are made using polyacrylonitrile (PAN) textile fiber as the raw material. Acrylonitrile (AN) is a product of the chemical industry, using petroleum feedstock. Other raw materials include pitch, lignin, and rayon. The final properties and cost of fiber depend on the choice of the raw material. Pitch-based carbon fibers have lower mechanical properties and are therefore rarely used in critical structural applications. PAN-based carbon fibers include relatively low-strength "large tow" fibers (tensile strength < 480 ksi) and higher-strength fibers (tensile strength > 600 ksi). High-pressure hydrogen cylinders require high-strength fibers because of the weight efficiency requirements.

Costs of carbon fiber are driven by raw material and energy costs, which may be up to 50 and 15% of the total cost. The conversion of raw materials to carbon fibers is normally made in 4 continuous stages as shown in Fig. 8a.8. Processing is energy–intensive, since oxidation involves heating the fibers to around 300°C, while carbonization involves heating up to 3,000°C in an inert atmosphere. Capital investment to produce carbon fiber is about $25 per kg produced.

8a.5.5 Organic Fibers

The most common organic fibers used in structural applications are aramids (for example Kevlar manufactured by DuPont) and poly(p-phenylene-benzobisoxoazole) (example: Zylon, manufactured by Toyobo). Organic fibers have a high tensile

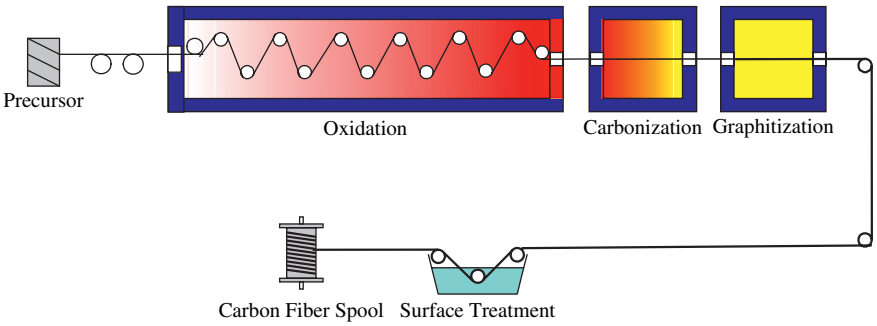

Fig. 8a.8 Manufacture of carbon fibers

strength and high modulus of elasticity at low density. These fibers also provide a high impact strength and damage resistance. Disadvantages include high cost and susceptibility to environmental corrosion and elevated temperatures. Organic fibers are currently not used as primary load-carrying materials in pressure vessels for on-board hydrogen storage.

8a.5.6 Liner Materials

Common liner materials for light-weight on-board hydrogen storage tanks include polymers and aluminum, and in some cases, stainless steel.

8a.6 Design Approach

Pressure vessels for storage of hydrogen are designed to maximize hydrogen storage capacity while staying within the volume envelope, weight budget, and allowable maximum working pressure. Design of composite pressure vessels has evolved over the years, supported by quick calculations using classical load-balancing techniques and advanced finite element analysis techniques that precisely evaluate stresses and strains under various internal and external load conditions.

The first step in the design process is to identify candidate materials that are compatible with hydrogen at the expected exposure level (pressure), mechanical stress levels, temperature extremes, and fatigue loading. Materials that perform well under static load at room temperature may become susceptible to embrittlement and time-dependent crack propagation when exposed to hydrogen. Reaction to moisture-contaminated hydrogen, especially at elevated temperatures needs careful consideration. Design of composite pressure vessels includes the structural design of metallic end pieces, metallic or polymeric liner, the composite wrap, and impact protection systems. Structural design must consider the burst pressure as well as fatigue life requirements. Hydrogen seals are designed to provide reliable performance at temperature extremes, under repeated pressure cycles and dynamic loads.

8a.7 Manufacturing Processes

Manufacturing processes for light-weight polymer composite pressure vessels include processes for the fabrication of the polymeric or metallic liner, filament winding of the composite shell, thermal processing of the resin, pressurization and leak tests, and the subsequent assembly of various components, leading to a complete fuel storage system [7].

Seamless polymer liners are manufactured by a thermoplastic molding process, such as blow molding or rotational molding. Rotational molding is a method of producing stress-free parts, utilizing hollow metal molds that are rotated bi-axially in a heated oven. Incorporation of metallic hardware in the polymer liner requires careful design and process optimization. Another method of liner fabrication is to injection-mold end domes, complete with encapsulated end bosses, and subsequently weld the end domes to a prefabricated pipe that forms the cylindrical portion of the liner. The process parameters for welding require careful selection and optimization to ensure that the welds are void-free and provide equal or better mechanical properties compared to the rest of the liner.

Thin metallic liners are commonly made by flow forming prefabricated tubes to achieve the desired diameter and wall thickness. End domes are formed by spin closing. The liners are then heat-treated to achieve the design strength and threads are cut at both ends. The liner interior needs careful examination, since surface defects can lead to localized stress risers which may promote concentrations of atomic hydrogen, resulting in hydrogen embrittlement. Metallic liners are usually protected with an exterior coating, prior to filament winding, to prevent galvanic corrosion.

The finished liner is used as the mandrel during the next process step of filament winding of the composite shell. The filament winding machine is a numerically controlled multi-axis machine that can be programmed to lay down resin-impregnated fiber reinforcement material in bands of “helical“ and “hoop“ patterns. Helical patterns go longitudinally from one end of the liner to the other, while hoop patterns are applied circumferentially. The fiber reinforcement is either impregnated with liquid resin during the winding process (wet winding) or pre-impregnated and semi-cured prior to the filament winding (tow-preg winding). Tow-preg winding allows for a more precise control of the resin content, higher fiber delivery rates, and therefore, higher throughput. However, wet resin filament winding generally offers lower raw material costs. The resin fraction on the fiber and the tension of the bands while laying down the mandrel need to be controlled to ensure consistency and quality of the composite shell. Once the required numbers of composite layers are applied on the liner by filament winding, the uncured part is removed from the winding machine and subjected to an elevated temperature profile to cure the resin matrix to achieve optimum composite laminate performance. The cured composite shell may be coated with a layer of polyurethane to provide limited abrasion resistance.

Each composite vessel is subjected to a series of acceptance tests to verify the integrity of the liner and the composite shell. Acceptance tests include pressure tests and leak tests and other tests and inspections required to ensure that the product meets internal quality requirements as well as applicable manufacturing standards and regulatory approvals. After the curing process, each composite vessel is subjected to a quality examination and further tested for volumetric expansion when subjected to 150% of the specified working pressure, to verify structural integrity of the composite shell. Acceptable vessels are fitted with hardware, such as a valve or in-tank-pressure regulator, and checked for hydrogen seal integrity. Leak tests are conducted by pressurizing the vessel to service pressure with an air/helium mixture, within a closed chamber.

Random units selected from each production lot are destructively tested to verify burst pressure and fatigue life, to ensure that the manufacturing process stays "in control" and all material data and process parameters corresponding to each vessel are carefully documented for the complete traceability of information. The frequency of batch testing and the production batch size are determined by the manufacturer depending on the quality system and approval requirements.

8a.8 Test and Validation

Composite pressure vessels for aerospace, defense, commercial, and fuel-storage applications have demonstrated a high degree of safety and reliability. Typical development tests of hydrogen storage systems include:

- Ambient cycling: 11,250 (or, 750 × service life in years) pressure cycles < 2MPa to 125% nominal working pressure, without leakage or rupture.
- Burst test: 10-second hold at the minimum prescribed burst pressure (commonly > 2.25 times the nominal working pressure), followed by further pressurization to rupture.
- Accelerated stress rupture test: Pressurized with hydrogen gas to 125% of nominal working pressure and held for 1,000 hours at +65°C.
- Permeation test: Pressurized with hydrogen gas to nominal working pressure and held in an enclosure to establish the steady-state permeation rate (< 2.5 standard CC per hour per liter water capacity of the vessel).
- Penetration test: Storage container is pressurized with hydrogen to the nominal working pressure and penetrated by an armor-piercing bullet or impactor with a diameter of at least 7.6 mm to verify that the vessel does not rupture as a result of complete penetration of the side wall.
- Drop (impact) test: Vessels are dropped horizontally, vertically at both ends, and at 45° onto the end domes, from heights up to 2 m above a rough concrete floor and subsequently subjected to ambient cycling to verify that there is no degradation in fatigue life.
- Flaw tolerance test: 25 mm long, 0.75 mm deep longitudinal flaw and additional surface damages to represent road damage are introduced in the vessel wall and subsequently subjected to ambient cycling to verify that there is no degradation in fatigue life.
- Hydrogen cycling test: Not less than 1,000 fast-fill and defueling cycles are performed at ambient temperature to verify absence of leakage and material degradation.
- Engulfing fire (bonfire) test: Vertical and horizontal tests are performed while filled to 25 and 100% of working pressure to demonstrate that fire protection systems in the hydrogen storage systems prevent rupture of the containment vessel when exposed to fire.
- Localized fire test: The storage system is exposed to localized fires to ensure that the storage system will not rupture from such fire sources.

In addition to testing and validation of the compressed storage vessels, safety-critical functions of components, such as fuel shutoffs, fuel receptacles, pressure management systems, pressure relief devices, etc. should be evaluated to demonstrate their ability to function and prevent unacceptable leakage and other hazardous events.

8a.9 Regulatory Requirements

Codes and standards covering compressed gas fuel systems and fuelling infrastructure are under development at various national and international levels [8]. Examples of nationally or regionally recognized standards, codes or directives include International Standardards Organization (ISO) standards, American Society of Mechanical Engineers (ASME) codes, Society of Automotive Engineers (SAE) standards, American National Standards Institute (ANSI) – approved standards, the European Union Directives, ECE Regulations, Japanese "Betten" regulations, and Global Technical Regulations. In North America, organizations such as CSA America, the Canadian Standards Association, the National Fire Protection Agency (NFPA), and the Society of Automotive Engineers (SAE) are developing codes and standards covering compressed gas vehicle fuel systems [9] and the supporting fueling infrastructure. Examples of draft codes and standards include:

- ANSI/CSA HGV2 Basic Requirements for Hydrogen Storage Vessels for Vehicles [10]
- ISO CD 15869 Gaseous Hydrogen and Hydrogen Blends – Land Vehicle Fuel Tanks [11]
- CSA B51 Boiler, Pressure Vessel, and Pressure Piping Code, Part II for gaseous fuel tanks
- CSA B51 Boiler, Pressure Vessel, and Pressure Piping Code, Part III for ground storage tanks
- National Fire Protection Agency (NFPA) standard for hydrogen transfer, storage, and fueling, including NFPA 52 for vehicular fuel systems and NFPA 55 for gas and cryogenic fluid storage, use, and handling
- ASME's Hydrogen Project Team has begun to draft requirements for hydrogen ground storage, transportation and portable tanks, based on their widely used Section VIII Division 3, as a special "Code Case"
- A Betten 10 draft for hydrogen is being developed in Japan
- ECE Compressed Gaseous Hydrogen Regulations were drafted by a GRPE Informal Group under the European Integrated Hydrogen Project (EIHP)
- SAE is developing various hydrogen interface and vehicle system standards, such as J 2600 refueling connection devices, J 2601 fueling communication devices, J 2578 fuel cell vehicle safety and hydrogen purity specifications.

Regulatory requirements are often different for the compressed storage systems used on-board vehicles, the compressed gas tanks used for ground storage, and those used

for transportation of gas. For example, compressed hydrogen refueling stations incorporate pressure vessels as receivers, buffer tanks, and in cascade banks. These cascade storage vessels must exceed the maximum allowable operating pressure of on-board vehicles (e.g. 70 MPa on-board storage pressure requires up to 100 MPa storage pressure at the station). The requirements for ground storage vessels are typically defined by local authorities having jurisdiction (AHJ). In the United States, the majority of AHJ's prefer ASME (American Society of Mechanical Engineers) vessels which are traditionally designed and constructed for an infinite service life. In some cases, transportable tanks built to the DOT (Department of Transport) specifications are also used for ground storage applications.

8a.10 Compressed Hydrogen Safety

On-board fuel systems must have a service life of 15 years (200,000 km) while exposed to a harsh environment, consisting of extreme ambient temperatures, humidity, ultraviolet radiation, chemicals, such as acids and bases, road salt, flying gravel, stones, and other debris. Other service conditions include torsion loads, vibrations, crash loads, and possible exposure to fire or gunfire.

Hydrogen gas is considered to be an intrinsically safe fuel. Steps to ensure safety during refueling and service include:

- Engineering design and development incorporating FMEA (Failure Modes and Effects Analysis),
- extensive validations,
- testing for compliance with safety codes & standards,
- continuing research and development (R&D).

Gaseous fuels have been used in transportation applications (natural gas vehicles) for over 50 years with an exceptional safety history. Additional safety considerations are required for hydrogen due to an increased risk of leakage, potential for hydrogen embrittlement, higher stresses related to higher service pressure (e.g. 70 MPa vs. 20 MPa for natural gas), and higher temperatures that develop during fast filling. These safety risks are well understood and engineering solutions have been developed and are being deployed successfully. They will be explained in more detail in the following sections.

8a.10.1 Hydrogen Loss

Hydrogen loss in minute amounts may occur during refueling, at the fueling interface, or during service, at the seals between multiple components, or as a result of normal permeation. Fuel systems are usually equipped with hydrogen sensors so that hydrogen flow can be shut off, if leaks are detected. In some cases, the fuel flow

to the fuel cell stack is compared against the usage by the stack to verify if there is a leak in the system.

Safety systems related to hydrogen refueling include industry-standard fueling receptacles, redundant check valves, and filters. On the supply side, industry-standard fueling nozzles, break-away couplings, and redundant pressure relief devices and software controls complete the safety system. Systematic design and validation of interfaces and seal materials ensure leak-free connections under the service conditions involving vibrations, impulse loads, and thermal shocks. Current permeation specifications for 70 MPa systems are designed to provide a margin of safety of 40 to prevent hydrogen accumulation to dangerous levels in a closed garage characterized by statistically worst-case air exchange.

8a.10.2 Hydrogen Embrittlement

Metals are prone to hydrogen embrittlement based on the interactions of the solute hydrogen or hydrogen-based chemical products at the grain boundaries of the molecular lattice. For some metals, the result of embrittlement is a reduction of strength and durability. There has been significant research in this area, especially within NASA, the American Petroleum Institute and ASME, which gives guidance in selecting materials for hydrogen compatibility under high-pressure service. Currently, additional investigations are underway under the sponsorship of the U.S. Department of Energy (DOE).

8a.10.3 Stresses due to Higher Pressures

Current safety codes and standards prescribe "stress ratios" (ratio of stress at burst pressure to that at service pressure) to ensure that higher operating pressures are appropriately accounted for in the pressure vessel designs, regardless of the pressure rating. Thus, a 70 MPa storage system does not impose any additional risk of structural failure, since stresses in the materials of construction are maintained within well-known allowable limits.

8a.10.4 High Temperatures

To maintain operational transparency with gasoline vehicles, fuel cell electric vehicles are expected to be fueled within 3–5 minutes. As gas is compressed rapidly into a storage system, temperature increases. The final gas temperature depends on a number of factors, including temperature of the supply gas, initial temperature of the storage system, initial and final pressure in the tank, density of the gas, specific

heat of the gas, the thermal conductivity of the gas and the storage system, and geometry of the storage tank. Safety implications of high temperatures include the proper functioning of thermally activated pressure relief devices (PRDs) and the endurance limits of various metallic and non-metallic structural and seal materials. Current safety codes and standards do include validation tests to ensure safety of the fuel systems under high-temperature exposure conditions. The safety of both 35 and 70 MPa storage systems under fast-fill conditions has been demonstrated in extensive tests and field trials.

8a.11 Steps to Commercialization

Elements of commercial success include [12]:

- A reliable product,
- consistent process suitable for volume production,
- clear customer value proposition.

While the fitness for purpose of the 35 and 70 MPa hydrogen storage systems has been adequately demonstrated, it is essential to go beyond meeting minimum performance criteria to be ready for mass commercialization. Additional verifications include extensive testing of components and systems to verify the performance and durability limits following well-proven methods used by the automakers and tier-1 suppliers. Standardization of product specifications is the first step towards optimization and fine tuning of processes to ensure production consistency. Composite pressure vessels are currently manufactured in high volumes ($> 500,000$/year) for industrial applications and the lessons learned from these industries are directly applicable to on-board hydrogen storage. Reliability of the supply chain is a critical factor to ensure that quality, consistency, and cost of materials and components are appropriate. Early users have confirmed the value proposition of 70 MPa systems in the context of simplicity and range. Cost reduction efforts currently underway include a combination of material, design, and process optimizations, rationalization of design margins, and evaluation of higher-density gas. It is expected that cost reduction through technology advancements and additional reductions through economies of scale will take us to the cost targets.

References

1. Sirosh, N., “Breakthroughs in Compressed Hydrogen Storage”,Carbon Fiber 2000, San Antonio, Texas, August 2000
2. Sirosh, N., Abele, A., and Niedzwiecki, A., “Hydrogen Composite Tank Program”, DOE FY 2002 Progress Report
3. Niedzwiecki, A., “Advanced Hydrogen Storage to Enable Fuel Cell Vehicles”, 14th World Hydrogen Energy Conference, Montreal, Canada, February 2002

4. Sirosh, N., “Hydrogen Storage Systems”, Materials Science & Technology 2005 Annual Conference, Pittsburgh, PA, September 2005
5. Sirosh, N., “High Pressure Hydrogen Storage: Challenges & Opportunities”, HYFORUM 2004, International Hydrogen Energy Forum, Beijing, May 2004
6. Sirosh, N., “High Pressure Hydrogen Storage: Lessons-Learned and the Path Forward”, H2PS 2003: Hydrogen Production and Storage Forum, DC, December 2003
7. Siroh, N. “High Pressure Storage Applications”, Hydrogen Storage Challenges for Mobility Symposium, Center for Hydrogen Research, Aiken, South Carolina, USA, December 2006
8. Sirosh, N., “International Hydrogen Codes & Standards Development”, H2PS 2004: Hydrogen Production & Storage Forum, Washington DC, December 2004
9. SAE J2579 Draft “SAE Recommended Practise for Fuel System in Fuel Cell and Other Hydrogen Vehicles”
10. CSA HGV2 Draft – Basic Requirements for Hydrogen Storage Vessels for Vehicles
11. ISO 15869 Draft – Gaseous Hydrogen and Hydrogen Blends – Land Vehicle Fuel Tanks
12. Sirosh, N. and Williams, J., “Advanced Hydrogen Storage Systems: Path to Commercialization”, Hydrogen, A Clean Energy Choice, NHA, Los Angeles, April 2004

Chapter 8b
Cryogenic Reservoirs

Friedel Michel

List of Abbreviations

bara	Pressure in bar absolute
LH_2	Liquid hydrogen
EIHP1	European Integrated Hydrogen Project, Phase 1 (1998–2000)
EIHP2	European Integrated Hydrogen Project, Phase 2 (2001–2004)
LHe	Liquid helium

Friedel Michel
Air Liquide Deutschland GmbH, e-mail: friedel.michel@airliquide.com

A. Léon (ed.), *Hydrogen Technology*,

LN_2	Liquid nitrogen
LNG	Liquid natural gas
MAWP	Maximum allowed working pressure
TÜV SUED	International technical service group mainly active in Southern Germany

For a future hydrogen infrastructure, suitability and costs of mobile hydrogen storage systems are important issues. Storage efficiencies and functionalities have to be considered for the supply of vehicle drive train systems for both internal combustion engines and fuel cells [1]. The objectives are the evaluation of appropriate materials and a design and manufacturing technology in order to fulfill the performance targets specified by automotive industry. A challenge related to hydrogen-powered vehicles is the development of light-weight storage systems with conformable tank shapes that can adapt to the space available in various vehicle structures.

So far, highest energy densities have been reached when hydrogen is stored in the liquid phase. However, the development and manufacturing of mobile liquid hydrogen storage systems is very challenging from several points of view. For example, to store the same amount of energy, more volume is required with LH_2 compared to conventional fuels and volume and weight are very limited in today's vehicles [2]. Moreover, the low temperature (−250°C) of liquid hydrogen requires a high-quality vacuum insulation to minimise blow-off losses. In spite of these drawbacks, LH_2 still is of interest for on-board hydrogen storage due to its low working pressure (compared to high-pressure systems), which allows for new concepts with conformable geometries more suited for vehicle design. Furthermore, the use of new materials entails a great potential for weight reduction – with these materials a specific energy storage mass similar to conventional fuel tanks can be achieved.

Herein, an overview of the cryogenic tank development for mobile application will be presented from the requirements to the design. The state of the art as concerns the reference cryogenic LH_2 tank in steel will be described. Then, future developments required to fulfill the targets will be discussed. In particular, the thermal management system, pressure management system, and the weight reduction of the system will be highlighted. This will be followed by a description of the evolution of the cryogenic fuel tank developed for car industries like BMW and GM. Finally, the cost issue for commercialisation will be addressed.

8b.1 Characteristics of Liquid Hydrogen (LH_2)

8b.1.1 Storage Efficiency

Liquid hydrogen under normal pressure has a density of approximately 71 g/l. Moreover, it possesses a higher mass-related energy density than conventional fuels. Indeed, 1 kg of hydrogen contains as much energy as 2.8 kg of gasoline or 2.1 kg of

natural gas. However, the volume-related energy density is not as favourable. It is one quarter and one third compared to gasoline and liquid natural gas, respectively. It should be kept in mind that these data are related only to the fuel. For a correct comparison, the weights and volumes of containment and piping systems have to be taken into account.

Figure 8b.1 displays the energy efficiency of potential hydrogen storage systems for a passenger car [3]. The *X*-axis indicates the gravimetric storage efficiency which is the stored energy divided by the total mass of the system. The *Y*-axis represents the volumetric storage efficiency which is the energy stored divided by the required volume of the system. Areas with continuous lines indicate the existing data, while fields with dotted lines show what could be reached in medium-term future. From this graph, the following statements can be derived as concerns the use of hydrogen in mobile application:

- For the same amount of energy, hydrogen storage tanks will be bigger and heavier compared to conventional fuel tanks for gasoline and diesel.
- Monolithic pressure vessels with less than 5 MJ/kg have insufficient storage properties.
- Metal hydrides can only compete with respect to the volumetric storage efficiency, as they lead to relatively heavy storage systems.
- The storage of hydrogen compressed up to 700 bar in modern and advanced composite systems as described in Chap. 8a is expected to be increased to an interesting range required for mobile use.
- Liquid hydrogen has the highest values with respect to the gravimetric and the volumetric storage efficiencies.

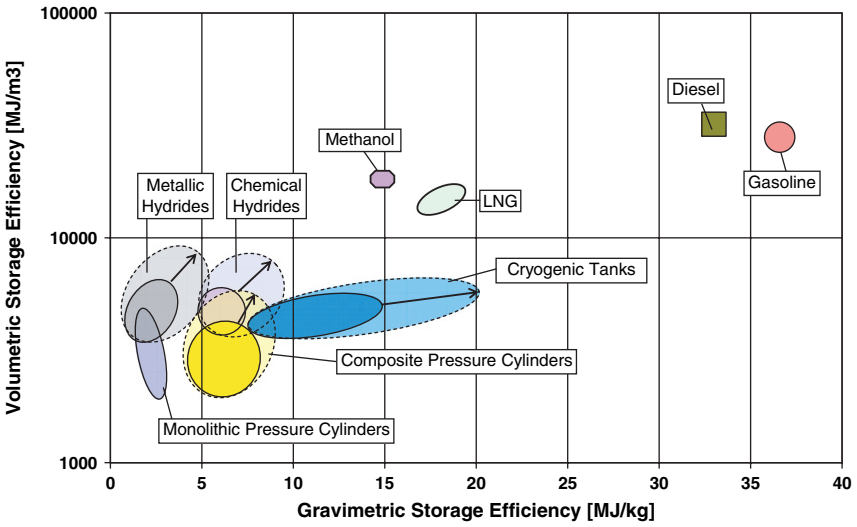

Fig. 8b.1 Energy efficiency of hydrogen storage systems [1, 4, 5]

8b.1.2 General Function of a Liquid Storage

Like for all other fuels, the main function of liquid hydrogen storage is to have a sufficient amount of energy available for the desired driving range and to supply it whenever requested. However, to reach the high energy storage efficiency of LH_2, the fuel has to be liquefied and stored at a temperature of about −253°C [6].

Such a low temperature can only be maintained, if the storage tank has a very good insulation to minimise heat flows from the warm surroundings. The residual heat leak cannot be reduced to zero without consumption of additional energy. That is why the LH_2 storage tank is designed as a pressure tank (usually, for low pressures between 5 and 10 bar). Thus, the unavoidable residual heat flow leads to a slow pressure increase which can be withstood by the tank. During normal operation, no gas is lost, because the pressure decreases again when fuel is consumed. If the fuel is not consumed, for example, when the vehicle is parked for several days, the pressure could reach the maximum operating pressure limit. In this case, a small amount of gas has to be extracted from the tank in order to avoid further pressure increase.

The required fuel flow, e.g. for an engine, is ensured by the pressure difference between the tank and the engine inlet without the use of a pump. For this reason, LH_2 storage systems are equipped with a pressure management system (further details can be found in Sect. 8b.3.4 of this chapter). In addition, a heat exchanger is required for LH_2 evaporation and overheating, if the engine or fuel cell is not adapted to low fuel temperature.

8b.1.3 Advantage of and Challenges Related to LH_2 for Mobile Application

In spite of some differences compared to other fuels or other storage systems, LH_2 is of great interest for a future sustainable fuel scenario [7]. As explained in Chap. 1, LH_2 has reached the highest storage efficiency so far compared to other kinds of hydrogen storage. Its low storage pressure and the double-wall construction are very advantageous with regard to safety. Although gaseous under ambient conditions, it is handled like a liquid during filling and storage. Moreover, the LH_2 is always kept in closed spaces and compared to conventional fuels, no gas can escape to the surroundings even during filling. Actually, the only situation, where gas could escape is when the vehicle is parked for a long time. Therefore, essential design tasks for cryo-engineers are to minimise the residual heat leaks and maximise the time without blow-off (dormancy). Compared to high-pressure storage, LH_2 also offers the chance for tank geometries other than sphere or cylinder, which may facilitate the integration of the storage tank in the vehicle.

8b.2 Requirements on Mobile LH_2 Fuel Tanks

As the properties of liquid hydrogen [8] differ from those of gasoline or diesel, detailed system definitions as well as legal and safety requirements have to be made. Figure 8b.2 displays some of the requirements a liquid hydrogen tank has to fulfill. Obviously, some specific features like the necessity of a vacuum insulation at −250°C to store liquid hydrogen make the design of the LH_2 tank more complex compared to conventional fuel tanks. Besides the costs factor, the main requirements to be met can be divided into the following three groups:

1. "Basic technical requirements".
2. "Vehicle requirements".
3. "Safety/regulations requirements".

Herein, each of these requirements shall be described briefly and discussed.

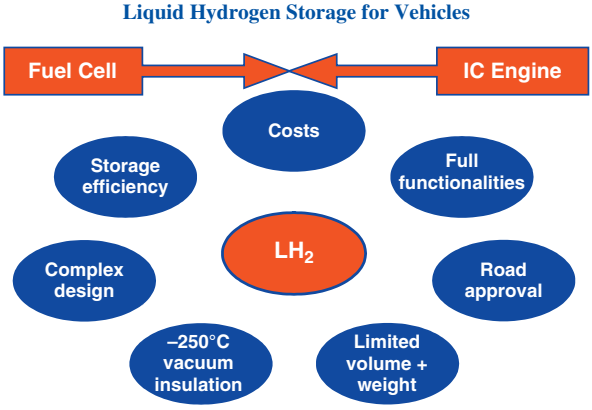

Fig. 8b.2 Requirements on liquid hydrogen storage

8b.2.1 Basic Technical Requirements

Liquid hydrogen tank systems shall be able to store the desired amount of LH_2 without loss as long as possible and supply the required flows for driving the engine or the fuel cell.

In order to keep such a low temperature, the best tank design is the vacuum-insulated double-wall container. The inner tank which contains the liquid hydrogen should withstand a pressure of around 5–10 bar. The outer shell which encloses the inner tank and its insulation system has to withstand a 1 bar pressure difference between the atmospheric pressure and the high vacuum inside.

For refuelling, the system has to be equipped with a filling coupling and for the supply of the engine or the fuel cell typically at approximately ambient temperature,

a heat exchanger is required. Sensors for the pressure and filling level are also parts of the basic technical requirements which are similar to those of standard cryogenic vessels in gas industry.

8b.2.2 Vehicle Requirements

The use of cryogenic reservoirs in mobile applications implies a lot of additional requirements specified by the vehicle manufacturer. Table 8b.1 displays a list of some high-priority (mandatory) requirements from the vehicle side, which have been defined under the European Integrated Hydrogen Project (EIHP2, duration 2001–2004). As can be seen, some of these specifications like the high and fast-changing flows required by far exceed the requirements of an industrial cryogenic reservoir. As a consequence, new designs, new components, and new materials have to considered and developed for LH_2 cryogenic tanks to be integrated in a vehicle.

A main concern is that the design of an on-board LH_2 storage system must be fail-safe, since drivers usually are not experienced with hydrogen. Therefore, the reservoir and its equipment shall reliably withstand the electrical, mechanical, thermal, and chemical operating conditions and it shall remain gas-tight. No uncontrolled release of hydrogen is allowed. Moreover, an efficient recycling process is necessary, a focus lying on the separation of materials and components used in the construction of an LH_2 vessel.

Table 8b.1 Additional requirements defined by vehicle manufacturers

Specifications for LH_2 Storage System EIHP – WP 4.4 (Mandatory Requirements)			
1	conform to EIHP draft	13	instruction manual for vehicle application
2	inner tank evacuable	14	tight system, no liquid fuel losses
3	refuelling time less than 5 minutes	15	gas tight housing vented to the fuel filler cap
4	refuelling possible at 5°C	16	separate pressure relief vent lines
5	refuelling stop automatically	17	accurate cleaning/free of grease
6	dormancy > 3 days	18	refuelling connection on the right side
7	supply temp. −40°C to +80°C	19	basic shape cylindricall
8	mass flow rate 0 to 20 kg per hour	20	service intervals = vehicles service intervals
9	min. to max. flow within 1 second	21	electrical signals accessible
10	total leakage < 5 g H_2 per day	22	power-off when tank runs empty
11	no electromagnetic interferences	23	safety relief valves: design temp. 30 K.. 363 K
12	electrical grounding	24	boil-off valves: design temp. 218 K.. 363 K

8b.2.3 Safety Regulations

Many national and international standards and regulations have to be considered during the construction of a cryogenic reservoir and its safe operation. At present,

a road vehicle in Europe is approved only, if it satisfies some 46 directives. Of the existing criteria, some cannot be fulfilled by a hydrogen vehicle and requirements regarding the safety of on-board hydrogen storage systems are missing. For this reason, new regulations for the use of hydrogen as a fuel were drafted during phase 1 of the EIHP project (1998–2000). The draft for liquid hydrogen was further improved during phase 2 of EIHP and presented in 2003 to WP29 of the Economic Commission for Europe (ECE) [9]. Table 8b.2 shows a short overview as concerns the specifications for hydrogen components.

On the basis of the improved EIHP1 draft, a new LH_2 storage system was designed and manufactured during EIHP2. An approval procedure was defined together with the technical inspectorate (TÜV SUED). It checked more than 100 specific points on the new LH_2 cryo-tank and approved it as safe and viable. Although the EIHP paper still is a draft, it is the guideline for the design and approval of on-board cryogenic storage system at the moment. Therefore, it is recommended to use these standards until a global directive will have been adopted [9].

Besides the EIHP draft, many other investigations concerning the LH_2 fuel tank safety have been performed. As an example, Fig. 8b.3 displays a simulation of a road accident with a drop weight producing an impact velocity corresponding to a rear-end collision accident with 60 km/h [10]. As can be seen, there is no rupture of the tank.

Such tests show that using LH_2 in a double-wall reservoir entails safety advantages. Today, most of the experts are convinced that LH_2 stored on-board of a vehicle is not more (or even less) dangerous than storage of conventional fuels.

Table 8b.2 Example of EIHP specifications regarding hydrogen components

UNIFORM PROVISIONS CONCERNING THE APPROVAL OF:	
I. Specific Components of Motor Vehicles Using Liquid Hydrogen, …	
6	SPECIFICATIONS REGARDING HYDROGEN COMPONENTS
6.1	General provisions (safe function, materials)
6.2	Hydrogen container (type-approval)
6.3	Components (p = 1,5* MAWP, insulation/liquefaction of air)
6.4	Pressure relief devices (Prim.: <110% MAWP, Sec.: <136% MAWP, type-app.)
6.5	Lines incorporating pressure relief devices.
6.6	Hydrogen valves (type-approval)
6.7	Heat exchangers (no direct use of exhaust gases)
6.8	Refuelling connections or receptacles
6.9	Pressure regulators
6.10	Sensors
6.11	Flexible fuel lines
6.12	Electrical components (no electric sparks, ins. resistance >1 kΩ). … .

(MAWP = max. allowable working pressure; Prim. = primary, Sec. = secondary relief device)

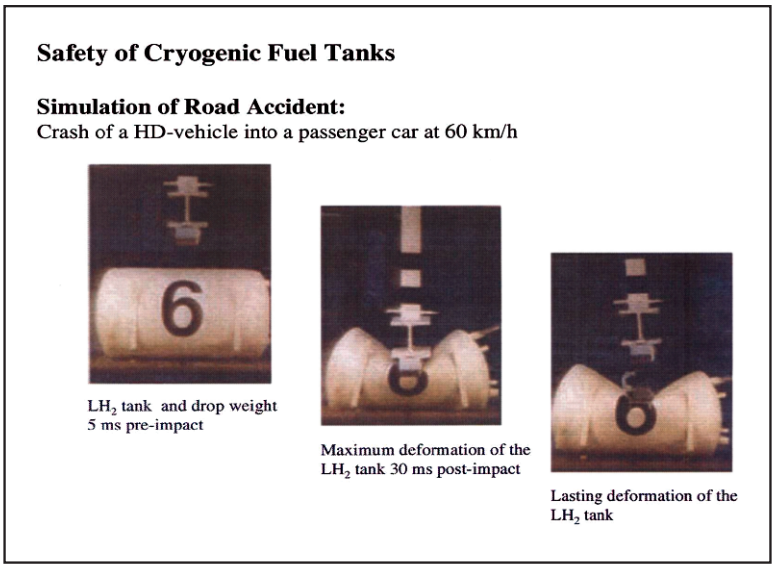

Fig. 8b.3 Simulation of a road accident (source: BMW)

8b.3 State of the Art of the LH_2 Tank

8b.3.1 General Concept of a Liquid Hydrogen Tank

The state of the art of liquid hydrogen storage systems consists in a double-wall cylindrical tank that holds a hydrogen storage mass of about 5–12 kg. Table 8b.3 shows a typical specification of an LH_2 vehicle storage vessel.

Typically, an on-board LH_2 storage system contains the following components:

Table 8b.3 Typical data of a stainless steel LH_2 vehicle storage vessel

Parameter	Unit	Value
Mass of stored hydrogen	kg	11.7
Typical dimensions (diameter × length)	mm × mm	660 × 880
System mass	Kg	126
System volume	l	291
H_2 storage efficiency (mass fraction)	wt%	8.5
Gravimetric energy storage efficiency	MJ/kg	10.2
Volumetric energy storage efficiency	MJ/m^3	4820
Dormancy (system autonomy)	days	>3
Boil-off rate at 1 bara	g/h	16
Refuelling time about	min	5

- An inner tank which is filled with the LH_2 at a temperature of about −253°C. The pressure inside this vessel is between 1 and 10 bar.
- An outer tank which encloses the inner tank. The pressure of the outer tank is atmospheric pressure on one side and high vacuum on the inner tank side. This outer jacket is designed to withstand temperatures between −40 and +85°C.
- The inner tank is kept in position relative to the outer tank by suspensions made of materials with a low thermal conductivity e.g. glass or carbon fibre-reinforced plastics. The space between the inner and the outer tank is used for vacuum super-insulation. Further details as concerns the thermal management of the cryo-tank can be found in the following Sect. 8b.3.3
- The components required in the filling mode are a refuelling connection (e.g. Johnston-Cox coupling) to the filling station, a flexible or rigid fuel line, fittings, cryogenic filling and return valves connected to the inner tank, a fuel level indicator to calculate the fuel level, and a fuel limiter to prevent the tank from overfilling.
- The components required in the operating mode are a cryogenic return valve, heat exchanger, and pressure regulation valve.
- The components required for the safety are the boil-off valve, the safety-relief valves, and possibly a rupture disk.
- A boil-off management system is needed.

Liquid hydrogen flows from the filling station to the inner tank via a filling coupling and a cryogenic filling valve. In order to keep a low pressure inside the tank during filling, the cryogenic return valve is open to evacuate the evaporated gaseous hydrogen back to the filling station (common filling method). Once the level of LH_2 required is reached, both cryogenic valves are closed and the tank is disconnected from the filling station. Normal filling takes about 5 minutes, except for first filling when the inner tank is still warm. It takes about 20 minutes depending on the size of the tank, the pipe diameters, the pressure of the filling station reservoir, etc.

During driving, hydrogen is extracted from the tank by opening the cryogenic return valve only. Liquid hydrogen then leaves the inner tank and enters the heat exchanger, where it is heated up above ambient temperature before it is directed to the pressure regulator. Further details concerning the pressure management can be found in the following Sect. 8b.3.4. It should be noted here that the extraction of hydrogen in the gaseous phase is also possible, e.g. if the pressure exceeds the required operating pressure.

During stand-by or long-term parking, both cryogenic valves are closed. As a result, the pressure inside the tank continuously increases due to unavoidable heat entry. There are three devices which prevent the tank from overpressure. The first one is the boil-off valve which automatically opens once the boil-off pressure is reached. In case of a fault of the boil-off valve, the safety relief valve opens. If the safety relief valve fails, a second safety relief valve opens or a rupture disk placed on the inner tank ruptures.

8b.3.2 Components Design

The specific components like shut-off and safety valves, pressure regulators, heat exchangers, etc., of a cryogenic tank are designed based on the vehicle safety concept. Most of the components of a cryogenic tank described above must have a type approval. For example, components in contact with liquid hydrogen shall withstand temperatures down to −253°C and components in contact with pressurised hydrogen shall withstand a test pressure higher than its maximum allowable working pressure. In addition, the components installed inside the reservoir should be designed maintenance-free for a lifetime of at least 10 years, as they cannot be exchanged easily.

As stated above, the LH_2 system consists of a double-wall reservoir. The preferred shell materials are selected stainless steel alloys, since they are very resistant against low-temperature embrittlement and show negligible hydrogen permeation. In case of stainless steel, the typical wall thickness is about 2 to 4 mm according to regulations for cryogenic vessels. The inner shell is required to sustain the internal pressure. In contrast to this, the outer shell must withstand buckling due to the presence of atmospheric pressure on the outer side and high vacuum on the inner side.

To reach a high gravimetric density, it is essential to reduce the weight of the inner tank and outer jacket shells. Substantial progress has been reached by the use of aluminium due to its low specific weight (see Sect. 8b.3.5). Furthermore, new materials are considered for lightweight LH_2 tanks with regard to properties and performance. One approach is the use of composite materials for the outer and inner jacket. However, the requirements related to jacket materials of a vacuum-insulated cryo-reservoir, e.g. low permeability and flammability, are not easy to meet and development is going on. Further details about weight reduction can be found in the following Sect. 8b.3.5.

Figure 8b.4 displays the possible configuration of a cryo-tank. From the mechanical point of view, the optimum pressure vessel shape is a sphere (Fig. 8b.4, left), because minimum wall thickness and weight can be achieved with this geometry. From the thermal point of view, the optimal cryo-storage tank also is a sphere due to the lowest surface/volume ratio of $3/r$ (r = radius) achievable. For the same volume, all other geometries would have larger surfaces, resulting in higher heat flows per volume unit and implying the necessity of larger insulation areas. However, this spherical shape is not easy to manufacture and mostly it cannot be integrated in a vehicle. For this reason, the LH_2 tank shapes usually are cylindrical and quite often constructed such that the inner tank in the middle is connected to the outer tank by one suspension only, as displayed in Fig. 8b.4 (middle). A special head and special pipings are required to fill and extract hydrogen into/from the inner tank. At present, LH_2tanks of horizontal construction, Fig. 8b.4 (right), are favoured in mobile application due to the higher requirements met and the available space/packaging in vehicles. However, a more sophisticated piping is required for such constructions to avoid thermal disadvantages.

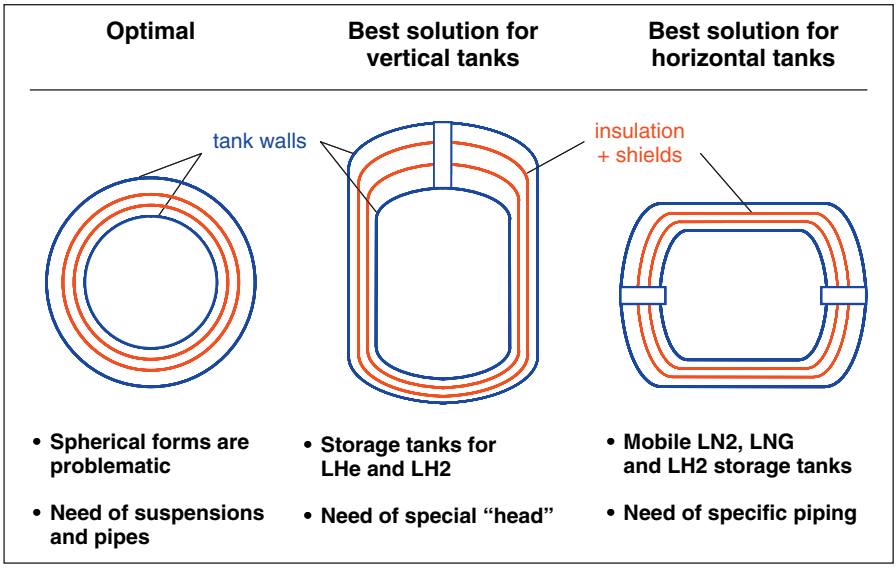

Fig. 8b.4 Cryo-tank configurations

In addition, other shapes (rectangular, mattress-shaped, double-cylinder…) may be considered for LH_2 storage in contrast to compressed gaseous storage, although they lead to a weight and cost increase.

8b.3.3 Thermal Management

To meet the liquid hydrogen storage requirements, a thermal super insulation is necessary. Heat leaks into a high-performance cryogenic tank are generally triggered by thermal conduction, thermal convection, and thermal radiation [4]. Therefore, these three basic mechanisms of heat input have to be considered to minimise the thermal losses of a cryogenic tank.

1. Conduction losses occur when a direct solid connection exists, for example between two components of the tank. Hence, a source of unavoidable loss is the piping. Conduction losses are reduced by making the cross-section for heat flow small and by using materials with low thermal conductivity. For example, to minimise the conductive heat leaks into the inner vessel, this vessel is supported by the outer vessel with low thermal conductivity support.
2. Convection losses are due to heat transport through gases. In a closed space, convective heat flows can be reduced by evacuating the gas. Therefore, the volume between the inner and the outer vessel is evacuated down to 10^{-3} Pa (10^{-5} mbar) by means of a turbomolecular pump. Moreover, outgassing of volatile components can be accelerated using a heater to bake the system before evacuation.

3. Radiation losses take place between surfaces at different temperature, e.g. between a cold inner and a warm outer shell of a cryo-tank. Radiative heat transfer can be reduced by radiation barriers, such as several layers of insulation foils, Fig. 8b.5, to ensure no direct path of electromagnetic radiation from the warm surfaces to the cold surfaces. The radiation barriers usually consist of high-reflecting aluminium foils (about 10 µm thick) or aluminium-metallised polyester foils and spacers of low conductivity between these foils, such as glass fibre layers (about 80 mm thick) or a net of thin plastic threads.

Figure 8b.6 summarises typical heat flow shares from an LH_2 fuel tank. As can be seen, the heat loss through the insulation is by far the most important factor and it ranges between 60 and 80% of the heat flow. The remainder of 20 to 40% is additional heat flow through the pipes, cables, and suspensions. For this reason, the thermal design is an important point within the construction of an LH_2 fuel tank.

Figure 8b.7 displays the design principle of a mobile liquid hydrogen tank with a multi-layer vacuum insulation (left image). Moreover, thermal conductivity is presented as a function of vacuum pressure for different insulations (right graph). The inner cold tank is enclosed by a vacuum space which could be empty or filled with a powder (e.g. perlite) or a multi-layer insulation [10]. The change of total thermal conductivity as a function of the vacuum pressure for the different insulations indicates that the multi-layer insulation under high vacuum is the best alternative for meeting the high thermal requirements related to a cryo-fuel storage tank.

For a cryogenic system, it is of importance to minimise the total heat flux of a cryogenic system, as the evaporation rate and dormancy time which are general performance parameters of cryogenic tanks are directly influenced by the heat input. As a consequence, an increase in the performance of the cryogenic system can be expected.

– Evaporation rate
  The evaporation rate describes the amount of gas that would escape during blow-off within a day. In practice, this value is measured with the tank at constant atmospheric pressure and divided by the maximum possible mass of the 100% filled tank. The evaporation rate is a linear function of the total heat flux. For a 150 litre LH_2 tank, for example, the evaporation rate at 1 bar is 1.8, 3.6, and 7.2% loss per day for 1, 2, and 4 W heat entry, respectively.
  In some automotive applications, the evaporation rate is not measured at atmospheric pressure, but at the respective blow-off pressure of the cryo tank, which results in somewhat higher values. For example, for a 150 litre tank, the evaporation rate for 1 W heat entry would be 2.0%/day at 5 bara and 2.1%/day at 7 bara instead of 1.8%/day at 1 bara.
– Dormancy time
  The dormancy time of a cryogenic tank is the length of time for a pressure rise from the operating pressure up to the blow-off pressure. During this time, no gas gets lost.

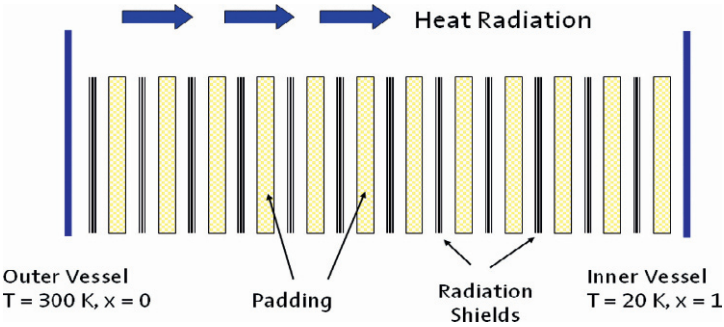

Fig. 8b.5 Multi-layer super insulation

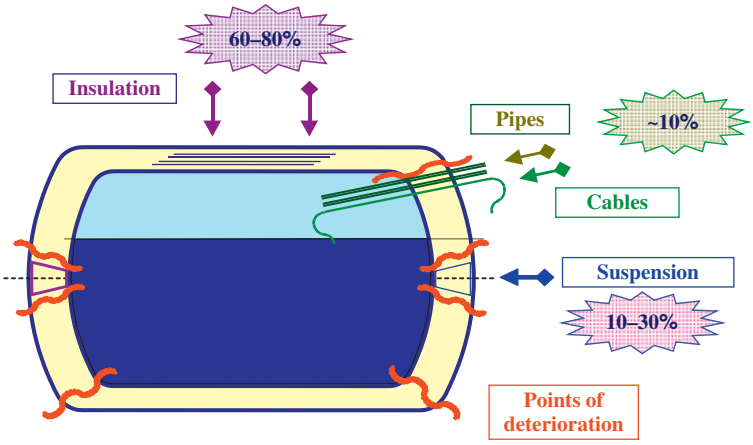

Fig. 8b.6 Heat flow shares of a cryogenic tank

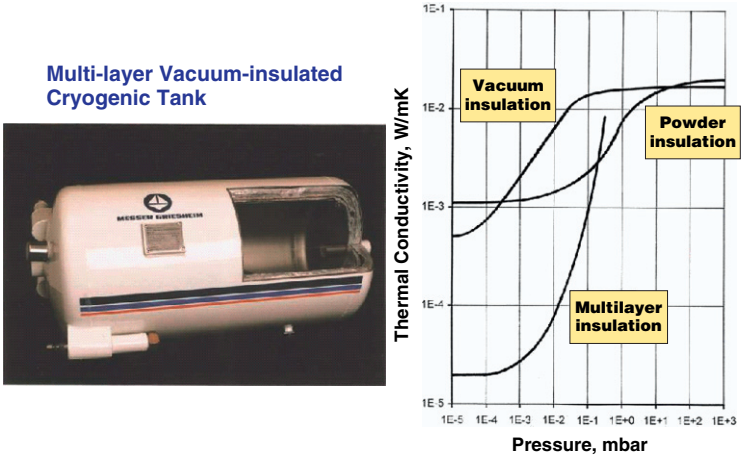

Fig. 8b.7 Multi-layer vacuum-insulated cryogenic tank

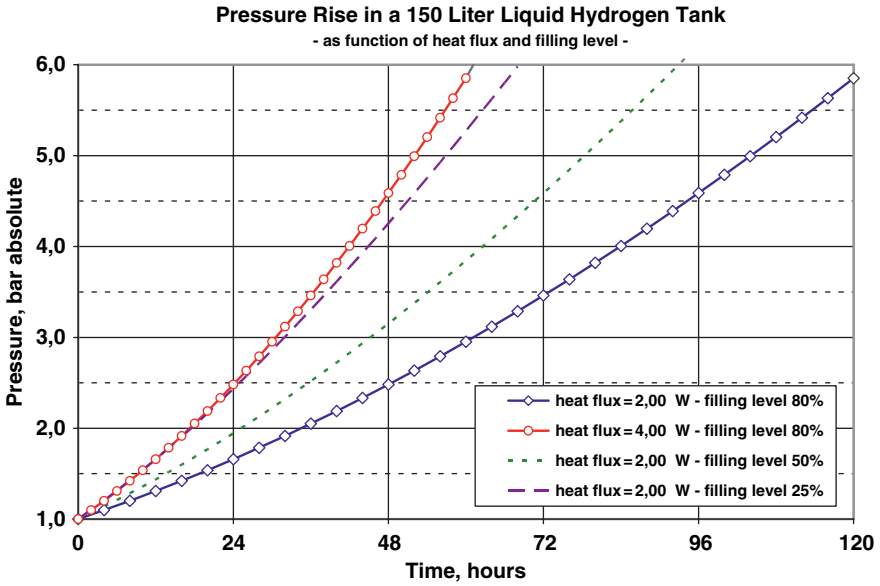

Fig. 8b.8 Pressure rise in a cryogenic tank as a function of time, heat flux, and filling level (filling level of 80% means compared to the completely filled vessel)

The pressure rise in a cryogenic tank with time is not only a function of the heat input, but also of the filling level. Figure 8b.8 displays the dependency of the pressure development on the total heat flux for a 150 litre LH_2 tank. As can be seen for a filling level of 80%, the pressure rises from 1 to 6 bara in 5 days at a heat flux of 2 W. At a heat flux of 4 W, the same pressure is reached in only half of the time (only half dormancy). Moreover, for a heat flux of 2 W, the dormancy time is decreased to less than 4 and 3 days at a filling level of 50 and 25%, respectively. Therefore, the performance of a cryogenic tank is best when the filling level is high.

For other starting and end pressures, the corresponding dormancy time can be read easily from the graphs as the difference of the respective time data.

It should be emphasised here that there no loss of cryo-fuel occurs as long as the cryogenic reservoir operates below the maximum pressure, which is the pressure set for the boil-off valve to open. Moreover, when the gas is extracted from the tank to supply an IC engine or a fuel cell, the pressure of the tank decreases, thus extending the dormancy time. However, if the cryogenic tank does not operate for longer periods, loss occurs. Hence, a high-quality insulation and minimisation of the total heat flux are required.

8b.3.4 Pressure Management

When high hydrogen flows are extracted from an LH_2 cryogenic tank, the pressure of the inner tank may be reduced drastically. For example, when 20 kg/h of liquid

hydrogen are withdrawn from the tank, 150–200 W have to be applied to the tank to maintain the required operating pressure. In case gaseous hydrogen is extracted in the same amount, then around 2500 W are necessary to maintain the pressure inside the inner tank. As a consequence, the cryogenic tank must be equipped with a pressure management system to keep a stable pressure.

Former pressure management systems consisted of electrical heaters placed within the tank. But they are not suitable due to the additional consumption of on-board electrical energy and additional cables between the inner and the outer tank, which will increase the evaporation rate and decrease the dormancy time. Moreover, if any defect of the heater occurs, it would result in very high repair costs.

That is why investigations have been undertaken for new pressure management systems. Figure 8b.9 displays the pressure management system developed for an LH_2 cryogenic tank on-board of a vehicle [11]. It consists of a pressure indicator, two heat exchangers, and a pressure regulator. In principle, the extracted gas for supply is first heated up in the heat exchanger 1. Then, a small portion is directed back to the tank, where it emits the acquired heat and subsequently increases the pressure of the inner tank. The flow leaving the tank is then heated up again by the heat exchanger 2 before it is passed to the pressure regulator. The required amount of return gas with the necessary heating energy is controlled by a special pressure regulator.

This concept has particular advantages, as it works without auxiliary energy. Indeed, it consumes cost-free heating energy from the cooling water. Moreover, it has no parts in the inner tank which may require expensive repairs and it is robust and works reliably. Even the pressure regulator developed together with Samson works without auxiliary energy. The only disadvantage is that this system needs two additional pipes to run through the vacuum space into the inner tank.

Hence, further advanced pressure management systems are under development. Figure 8b.10 displays the schematic diagram of the two possible concepts. The first one (left scheme) consists of an external pump for gaseous hydrogen or, alternatively, a pulsation system controlled by external valves. The pump has the function of returning the flow of warm gas required for the maintenance of the pressure. An advantage is that in case of defects, the pump is easily accessible for repairs.

The second concept is to integrate a pump for liquid hydrogen (right scheme) in the inner tank. With this concept, the dormancy of an LH_2 fuel tank can be improved significantly, because it allows very low operating pressures. But above all, it would provide for a high pressure supply and open a wide field for the optimization

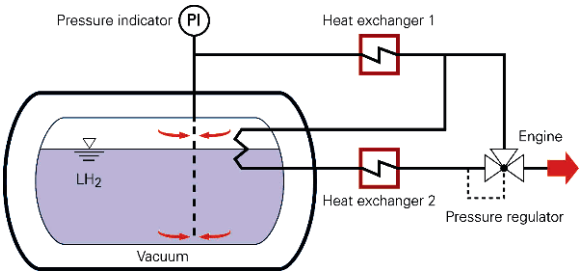

Fig. 8b.9 Pressure management system for liquid hydrogen vehicles

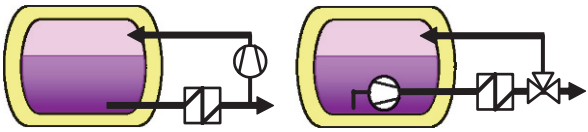

Fig. 8b.10 Possible solutions for new pressure management systems

of hydrogen internal combustion engines (essential improvement of efficiency by higher hydrogen injection pressures). However, there is still development needed concerning the pump itself and its integration in the tank. For thermal reasons, a fully integrated pump would be the best solution. But then, its durability should not be less than the lifetime of a vehicle, because a permeation of the vacuum space and insulation in order to repair the pump would probably not pay off.

8b.3.5 Weight Reduction

The weight of a fuel tank is an important criterion for vehicles. LH_2 storage tanks made of steel are still relatively heavy. That is why different light-weight materials have been investigated for the construction of the cryogenic tank. However, due to extreme requirements on using LH_2 like the low temperatures down to −253°C and the subsequent vacuum tightness and insulation quality necessary, the objective to reduce the weight of an LH_2 storage tank is not a simple task. In addition, durability and reliability for automotive lifetimes as well as costs have to be considered.

In the following section, a development project performed on behalf of BMW to decrease the weight of the tank shall be described in order to illustrate the possibilities. The specifications from BMW as concerns the new cryogenic tank were the same thermal quality, functionalities, capacity of stored hydrogen, and external interfaces than the EIHP tank, but its weight was to be reduced by 40%!

A study was prepared to find out the potential of weight reduction for each single part of the existing systems. The outcome of these calculations was that the weight of the steel reference tank (cf. Table 8b.3) could be reduced by 40% using aluminium in a first step. However, due to the thermal properties of aluminium, this material could not be used for the piping. Therefore, specific aluminium-steel junctions had to be designed and integrated in order to withstand the high loads, e.g. by low temperatures and driving vibration. Two kinds of aluminium-steel junctions have been developed, a friction-welded junction to be used when sufficient space is available and a milled junction from explosive-plated material when space is limited.

Figure 8b.11 displays the new lightweight aluminium design for the storage of LH_2. At first glance, there is no significant difference between the cryo-tanks made of aluminium (new light-weight LH_2 tank) and steel (reference LH_2 tank). However, while keeping the storage mass and the thermal quality of the reference tank, the empty weight of the new tank was reduced down to 66 kg. Thus, a weight reduction of around 50% was achieved. This corresponds to an increase of the hydrogen storage efficiency from about 9 to 15% in one step (for comparison, the DOE's 2015 weight target is 9 wt%).

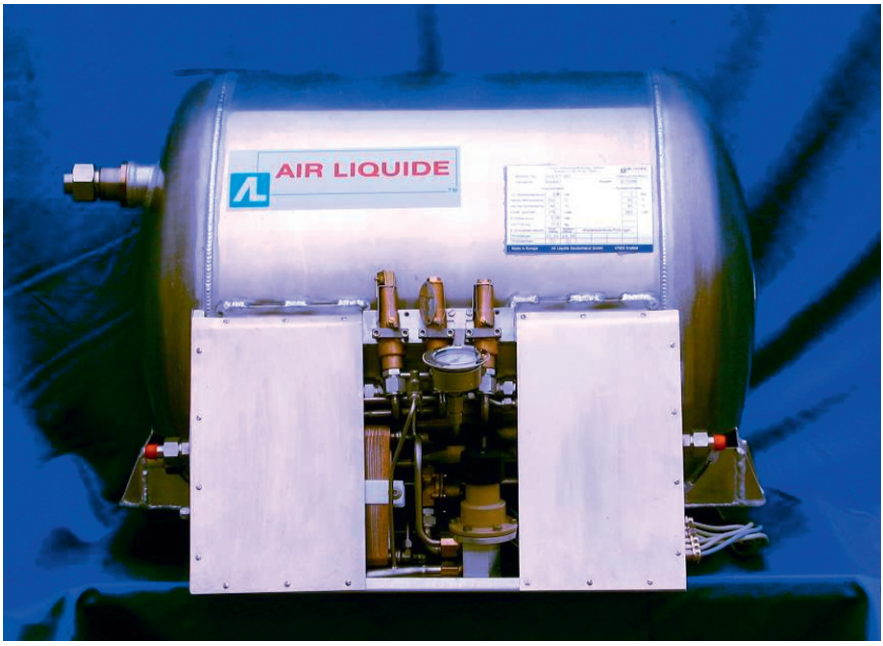

Fig. 8b.11 Light-weight aluminium liquid hydrogen storage system

Figure 8b.12 displays the storage efficiency diagram. The step from 9 to 15% is indicated by the horizontal arrow, while the next step is to reach 18%, indicated by the ascending arrow, without taking into account the valve box. This goal is realistic, as the main components of the valve box presently are far from having their optimum weight.

To further reduce the weight of the tank, investigations are actually going on with respect to the most suitable materials and designs for the inner and the outer vessel.

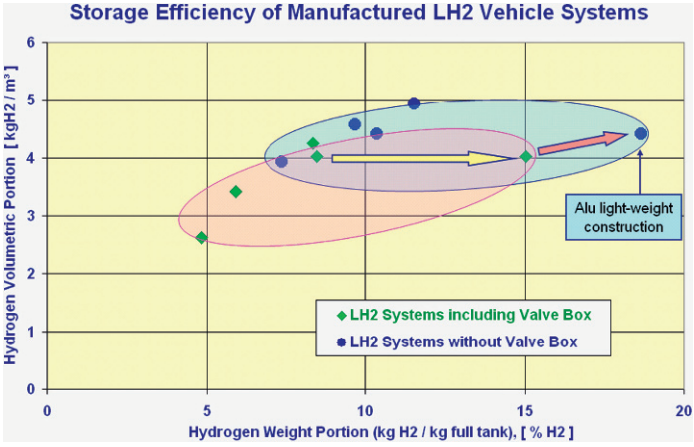

Fig. 8b.12 Light-weight liquid hydrogen storage system

For example, materials of low specific density and high strength like a combination of aluminium and fibre-reinforced plastics are considered. Moreover, a free-form tank, e.g. an envelope geometry other than a cylinder, is analysed for the tanks fit into the available construction space of the vehicle.

8b.4 Types of Cryogenic Tanks

Air Liquide has gained comprehensive experience in the development of LH_2 vehicle tank systems for partners like BMW, GM, Ford, and Honda. Figure 8b.13 illustrates one of the early installations of a cylindrical cryogenic tank in the trunk of a passenger car. The tank was connected by flexible lines to a separate valve box. Thus, the cryogenic storage function and the fuelling and engine supply function were separated, allowing for a better thermal management as well as for an easy exchangeability of repair parts.

Nowadays, all components necessary for storage, piping for fuelling, and extracting the fuel from the tank are integrated in a compact module. Several designs have been implemented. In the following sections, some cylindrical solutions, the flat-shape tank, and the BMW race car tank will be described.

Fig. 8b.13 Early solution of an LH_2 storage tank in a trunk

8b.4.1 Examples of Cylindrical Tanks

To illustrate the performance of a cylindrical tank, the tanks developed for BMW, GM, and within the framework of the European research programmes shall be highlighted below.

One of the liquid hydrogen storage tanks that were designed and constructed for BMW has a storage volume of 143 litres and can be operated at a pressure of up to 5 bar (Fig. 8b.14 left). The tank is able to store 270 kWh of hydrogen energy, which is equivalent to 31 litres of gasoline. In this case, the front housing of the tank module encloses not only the valves and pipes, but also the heat exchanger, safety valves, the control equipment, and all necessary connections for filling and supply. The size and form of the valve box, which is not optimal for a cryo-tank, had been given by the customer to fit between the boot and the rear seats of their hydrogen car. The weight of the complete module is about 100 kg.

Another liquid hydrogen storage system, Fig. 8b.14 right, was developed for "Hydrogen 1", the first fuel cell Zafira by GM. It is also tailoured to the space available below the floor of their vehicle. With a diameter of only 400 mm and a length of 1000 mm, it can store 5.4 kg of hydrogen at a maximum pressure of 5 bar. For easy refuelling, pneumatically operated valves are integrated in the valve box. The weight of the complete module is 85 kg and only 50 kg without the valve box. The system allows for a very rapid changing of the fuel flow, which is required for fast acceleration. Together with the "Hydrogen 1"-Zafira, the system was successfully demonstrated by GM in many places of the world, such as Arizona, China, and even Australia.

Fig. 8b.14 Examples of cylindrical LH_2 tanks for BMW, GM and EQHHPP research program

Under European research programmes, LH_2 storage systems have also been investigated. Within the framework of the Euro-Québec-Hydro-Hydrogen-Pilot-Project (EQHHPP), for example, a special liquid hydrogen storage system for a bus was developed and manufactured (Fig. 8b.14 bottom). The LH_2 storage tank is 5 m long and in spite of the double-wall construction, the outer diameter is only 44 cm. Its storage capacity allows for a driving range of 300 km. The weight of the system is 260 Kg which is only a fourth of a classical pressure storage system for the same range.

Under the European Integrated Hydrogen Project (EIHP2), a cylindrical mobile LH_2 storage tank was developed according to the new draft standard of EIHP. Therefore, it can be called the "First European LH_2 vehicle storage tank" [5], which is displayed in Fig. 8b.15.

Technically speaking, this new cryogenic tank is characterised by an advanced design and excellent performance data. It stores 12 kg LH_2, which is a lot in view of the limited outer dimensions. With an empty weight of only 129 kg, a storage efficiency of 8.5 wt% H_2 is reached. The system reaches a supply flow of 20 kg/h or more without any difficulty. Nevertheless, it has an evaporation rate of less than 3% per day and a dormancy time (1–5.5 bara) of more than 3 days without any evaporation losses. The EIHP LH_2 system meets very well the requirements on internal combustion engines, as is shown by the 7-series hydrogen BMW.

Fig. 8b.15 First European liquid hydrogen vehicle storage tank

8b.4.2 Flat-shape Tank

Frequently, cylindrical tanks do not use the spaces given for fuel tanks in vehicles. Therefore, the need for rectangular hydrogen storage blocks came up in car industry in order to stick as closely as possible to the existing shapes of gasoline tanks and facilitate integration in currently developed vehicles.

For this purpose and with a major car OEM, Air Liquide developed a "flat-shape" liquid hydrogen storage prototype, Fig. 8b.16, for a mobile application [1].

This "flat-shape" LH_2 storage tank does not only fit in a rectangular block, but fulfils the strict thermal specifications and is based on a manufacturing concept suitable for series production for automobile application. Its features are as follows:

- L×W×H: 1080 × 780 × 300 mm
- Total LH2 volume: 102 l
- Total weight, including valve box and heat exchanger: 120 kg
- 10 bar design pressure of inner vessel
- Total heat entry: 1.7 W
- 3 days autonomy
- 5%/day boil-off
- +/−11 g crash resistance
- Manufacturing: prototype deep drawing (steel deep drawing tool)
- Supports, envelopes, and deep drawing validated by finite element calculations
- CODAP 2000, PED, CE labelling by TUV Saarland.

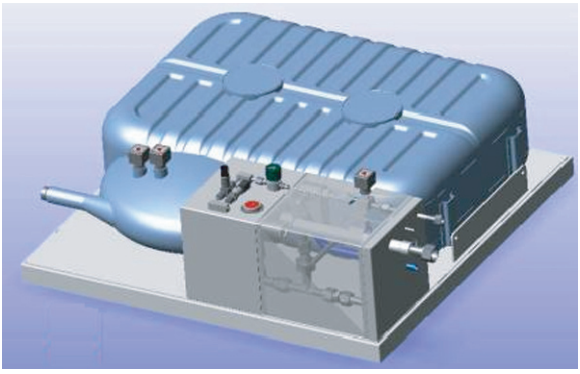

Fig. 8b.16 Flat-shape tank

8b.4.3 BMW Race Car Tank

Air Liquide was asked to construct another LH_2 storage system to fulfil the ambitious requirements defined for the BMW hydrogen race car "H2R" (Fig. 8b.17). Compared to earlier solutions, additional requirements had to be taken into account

Fig. 8b.17 Liquid hydrogen vehicle storage system for the BMW race car

like fast fuelling within 3 minutes and alteration of hydrogen supply from minimum to maximum flow within 1 second [3].

Figure 8b.17 illustrates the cryogenic tank and the integration of the storage tank in the chassis of the race car at the customer's. With this system, BMW reached several world records, e.g. driving faster than 300 km/h with a hydrogen car.

8b.5 Challenges for Commercialisation

Today, LH_2 fuel tank prototypes are of high complexity, entailing high costs for a future series production. One of the reasons is that cryosystems are characterised by completely different manufacturing processes compared to that of a valve for instance. Particularly the necessity of high-quality insulation implies time-consuming steps like leak testing and evacuation. A cryosystem having numerous welding joints increases the potential for leaks. Moreover, increasing numbers of pipes and supports penetrating the insulation layers increase the complexity of the insulation concept and decrease the insulation quality.

For the above reasons, the complete cryosystem should be re-examined with a view to reduce its complexity. The design of a cryosystem should be as simple as possible. As a first step, it would be worthwhile for mobile application to separate more clearly the functions required for the fuel supply from the functions of a storage system for long dormancy. In the future, such a differentiation will give a high potential for improvement and cost reduction in the production of cryo-fuel storage systems.

8b.6 Outlook

Hydrogen storage for mobile use has strict targets and liquid hydrogen storage is one solution which offers great advantages. Promising prototypes have been manufactured and tested successfully. Attractive storage efficiency has been reached without decreasing the quality of the required functions. However, the high costs of today's prototypes are partly due to the integration of automotive functions in a cryosystem. Nevertheless, an optimisation of the current system for future series production provides a high potential for further improvements and cost reduction.

The low working pressure of LH_2 storage systems is advantageous compared to high-pressure systems, as it allows for new concepts with conformable geometries more suited for vehicle design. Furthermore, it is expected that with new lightweight materials a specific energy storage mass similar to conventional fuel tanks can be achieved. As a consequence, specially adapted liquid hydrogen stores could be a good solution for future mobile applications.

References

1. F. Michel, H. Fieseler, and L. Allidieres, "Liquid Hydrogen Technologies for Mobile Use", WHEC 16, June 2006
2. F. Michel, "The Next Step: Driving with Liquid Hydrogen", Focus on Gas, February 2000
3. F. Michel, "Kryotechnische Lösungen für den Kraftstoff Wasserstoff", VDI-Kryoseminar Karlsruhe, March 2006
4. 1x1 der Gase, Physikalische Daten für Wissenschaft und Praxis, AIR LIQUIDE, 2005
5. "Strategic Research Agenda", European Hydrogen & Fuel Cell Technology Platform, July 2005
6. Encyclopédie des Gaz, AIR LIQUIDE, Elsevier, 1976
7. EIHP, Phase 1 and 2: Final Reports
8. M. Kesten, "Die Speicherung von Wasserstoff in der Energietechnik", DKV-Tagung, April 1999
9. H. D. Baehr, "Thermodynamik", Springer-Verlag, Berlin, Heidelberg, New York, 1966
10. F. Michel, "Advanced Solutions for Hydrogen as a Fuel", EIGA – Symposium, February 2004
11. H. Fieseler, "Messer-Entwicklung in BMW-Serienfahrzeugen: Erster nach EIHP- Richtlinien gebauter Flüssigwasserstofftank mit Reichweite bis zu 700 Kilometer", Messenger International, January 2004

Chapter 9
Safety Analysis of Hydrogen Vehicles and Infrastructure

Wolfgang Breitung

List of Abbreviations

CAD	Computer-aided design
CFD	Computational fluid dynamics
FZK	Forschungszentrum Karlsruhe
IRSN	Institute de Radioprotection et de Sûreté Nucléaire

Wolfgang Breitung
Institute for Nuclear and Energy Technologies (IKET), Forschungszentrum Karlsruhe,
P.O. Box 3640, D-76021 Karlsruhe, Germany, e-mail: breitung@iket.fzk.de

A. Léon (ed.), *Hydrogen Technology*,

KI	Kurchatov Institute Moscow
LEL	Lower explosion limit
PRA	Probabilistic risk analysis
S_L	Laminar burning velocity
UEL	Upper explosion limit

9.1 Motivation of Safety Investigations

Although hydrogen has been safely produced, distributed, and used in chemical industry since many decades, the developed safety procedures and technologies provide only limited guidance for mobile hydrogen applications. In the case of hydrogen-powered vehicles, hydrogen will be used within a decentralised infrastructure in relatively small amounts (several kg per user) by a large population without special training in the safety of combustible gases.

The transition in vehicle fuels from liquid hydrocarbons to gaseous hydrogen requires an adaptation of automobile design and safety technology to the special properties of hydrogen. The public will only accept hydrogen transport technology, if a safety level comparable to that of current gasoline vehicles can be obtained. This requires a systematic investigation of the hydrogen behaviour for normal operating conditions, for component mal-functions, for vehicle collisions, and for service/repair conditions. Unacceptable risks should be identified early in time and prevented by design measures before the acceptance of hydrogen technologies is adversely affected.

This chapter aims at giving an idea of how a safety analysis can be performed for hydrogen vehicles and infrastructure. The phenomenology of hydrogen-related incidents will be described first by comparing the safety-relevant properties of hydrogen, methane, propane, and gasoline vapour. It will be obvious that large differences exist between hydrogen and hydrocarbons. Then, the consequences of the specific hydrogen properties will be highlighted by discussing the statistics of hydrogen accidents. As can be supposed, the outcome of H_2-related incidents depends on many parameters and can vary largely, mainly depending on the combustion regime obtained. Therefore, a description of an analysis of hydrogen accidents will follow, which will include the general sequence of events, the analysis procedure, and the mitigation measures. The analysis procedure for hydrogen accidents is based on three-dimensional numerical simulation of hydrogen distribution and different hydrogen combustion modes. This analysis methodology shall then be applied to investigate the release of hydrogen from a car parked in a residential garage. It will be demonstrated that mixtures can develop, which allow for fast turbulent deflagrations or detonations under certain conditions. To understand the potential hazard caused by such mixtures, local explosion experiments were performed in a closed test chamber simulating the garage situation. The measured (and simulated) overpressure data were then compared to known thresholds for structural damage and human injuries. This example will quantify some possible consequences of H_2 release in a confined geometry. Finally, a summary of

safety issues for hydrogen vehicles and infrastructure in general shall be presented. The potential hazards caused by vehicle operation and infrastructure installations will be discussed. The risk connected with postulated accident scenarios can be assessed by probabilistic risk analysis (PRA) and CFD simulations. The latter concentrates on the risk-dominating sequences identified by the PRA studies. As an outlook, some important research topics will be given, which need to be addressed in future work.

There are no indications of fundamental safety issues which might prevent the safe use of hydrogen in mobile applications.

9.1.1 Safety-Relevant Properties of Vehicle Fuels

The safety standards of modern vehicles using hydrocarbons are excellent and the question arises whether the use of hydrogen could have an impact on safety records and statistics. Are there large changes to be expected?

Figure 9.1 compares several important safety-relevant physical and chemical properties of hydrogen and gaseous hydrocarbons like density, buoyancy, etc.... As can be seen, significant differences exist in the properties of hydrogen and hydrocarbons. Hydrogen exhibits a very low density and ignition energy compared to gaseous hydrocarbons, while it has high values for buoyancy, diffusion in air, range of combustible H_2-air mixtures, specific heat of combustion, laminar burning velocity, and detonation sensitivity. Clearly, these properties of hydrogen can influence the initiating event, the development, and the outcome of an accidental hydrogen release.

In the following sections, the expected effects of the specific hydrogen properties will therefore be discussed in a qualitative way.

Figure 9.1b displays the buoyancy of hydrogen in air. The large buoyancy of hydrogen compared to gaseous hydrocarbons suggests that if space is available in vertical direction, a mixing with air will be without any consequence in many cases. Indeed, a free cloud of hydrogen in air experiences an initial vertical acceleration of 13 g, as calculated from Eq. (9.1):

$$\ddot{z} = (\rho_{\mathrm{air}}/\rho_{\mathrm{H2}} - 1)\mathrm{g} \approx 13\,\mathrm{g} \tag{9.1}$$

Thus, the large hydrogen buoyancy will support fast mixing with air.

Figure 9.1c compares the diffusion coefficient of hydrogen and hydrocarbons. The large value of $0.6\,\mathrm{cm}^2/\mathrm{s}$ for hydrogen indicates that hydrogen distribution may noticeably occur also in downward direction. The characteristic diffusion length of hydrogen in stagnant air is given by Eq. (9.2):

$$x = 2\sqrt{Dt} \tag{9.2}$$

where t is the time and $D = 0.6\,\mathrm{cm}^2/\mathrm{s}$. Therefore, distances of a few cm will be affected by H_2 diffusion within 10 s. In the case of hydrogen release into a laminar

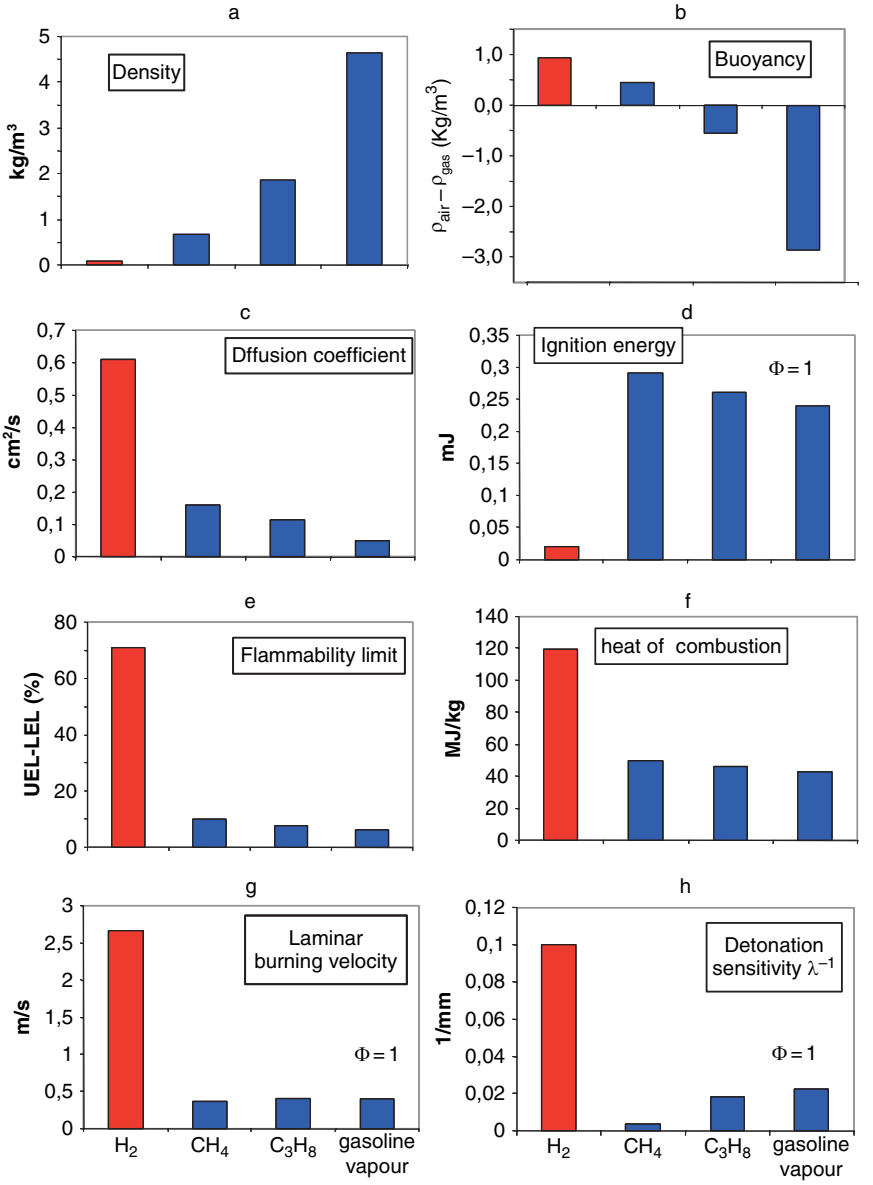

Fig. 9.1 Comparison of safety relevant physical and chemical properties of hydrogen, methane, propane, and gasoline vapour

air flow of constant velocity v_o instead of stagnant air, the total transport distance, x_{total}, increases by the advection length, $v_o t$, as given by Eq. (9.3)

$$x_{total} = 2\sqrt{Dt} + v_o t \tag{9.3}$$

Figure 9.1d shows that the spark ignition energy of hydrogen-air mixtures is exceptionally low, about one order of magnitude lower than most of the hydrocarbons [1]. Weaker sparks or other small energy deposition mechanisms may therefore trigger an ignition in hydrogen rather than in hydrocarbons. On the other hand, it is frequently stated that most sparks from static electricity, switches, relays, and electrical motors have energies well above 1 mJ. For such strong ignition sources the difference in ignition energy does not matter. Other ignition mechanisms, like e.g. gas heating by shock focussing or reflection, are very relevant to hydrogen, but not to hydrocarbons. Altogether, a larger variety of potential ignition mechanisms exists for hydrogen than for hydrocarbons.

Figure 9.1e displays the concentration range of flammable compositions in air for the different gases, depicted as the difference between the upper explosion limit (UEL) and the lower explosion limit (LEL). Under ambient conditions, the combustible H_2-air mixtures range from about 4–75 vol.% of H_2. This large range of combustible H_2-air compositions is of high relevance to safety investigations. This means that if a hydrogen leak occurs, a much larger part of the H_2-air cloud can burn out compared to the hydrocarbons case. It should be noted that hydrogen-rich regions of the cloud (> 29.5 vol.% H_2) cannot react completely due to the local oxygen deficiency. However, the partial hydrogen burning generally creates sufficient overpressure and expansion flow to mix the residual hot mixture of H_2, steam, and N_2 with fresh air. Hence, the remaining hydrogen is consumed in a secondary burning.

The heat of combustion of hydrogen on a mass basis (120 MJ/kg) is significantly higher than that of hydrocarbons due to the small molar weight (Fig. 9.1f). Burning of 1 kg of hydrogen in an accident correspondingly causes more energy to be released into the environment, which may result in higher temperature or pressure loads depending on details of the accident scenario.

Figure 9.1g shows that the laminar burning velocity (S_L) of hydrogen-air mixtures is significantly larger compared to hydrocarbon-air mixtures. S_L characterises the general reaction kinetics of the combustion process and it is a fundamental property of a combustible mixture. The high chemical reactivity of H_2-air mixtures in comparison to hydrocarbon-air mixtures could also be observed in turbulent combustion experiments with a partial confinement of the burnable mixture [2]. This is illustrated in Fig. 9.2 which summarises the maximum flame speeds measured for stoichiometric hydrogen-, methane-, and propane-air mixtures in an obstructed test tube. In the cylindrical tube surface variable openings exist. Burned and unburned gas could vent radially through these openings. The given vent angle α divided by 90° is the fraction of open tube surface available for venting. As can be seen, for methane and propane, small vent angles of only 5–10° are sufficient to suppress flame acceleration completely. This corresponds to 5.5–11% of the total tube

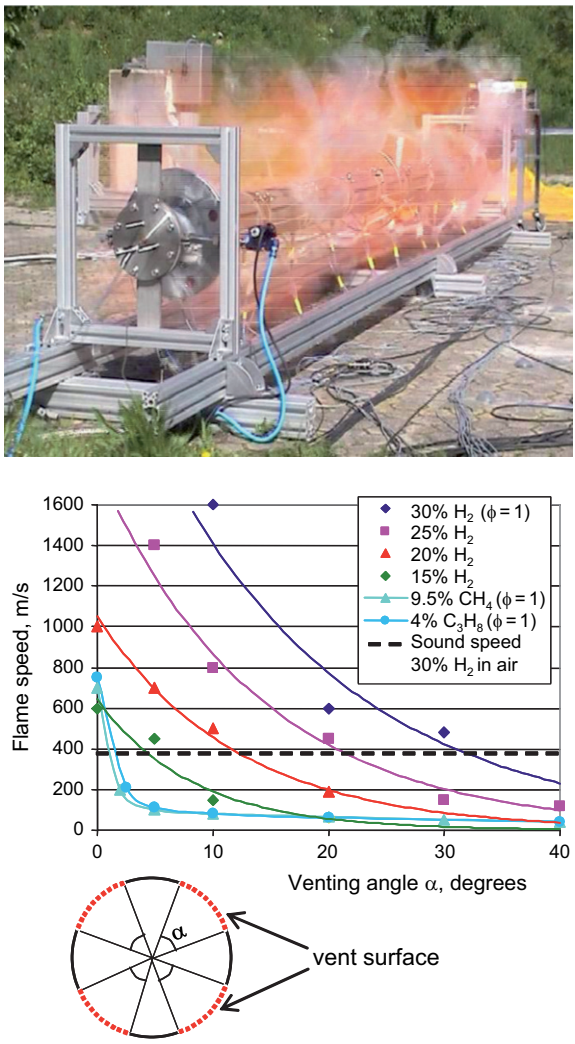

Fig. 9.2 Measured maximum flame speeds in an obstructed tube with vent openings. Hydrogen shows a much more pronounced tendency for flame acceleration than hydrocarbons

surface. In contrast to this, hydrogen-air mixtures show supersonic flame speeds up to 30° of venting. Moreover, even lean hydrogen-air mixtures with only 15% of hydrogen can burn faster than stoichiometric hydrocarbon-air mixtures.

Detonations are supersonic combustion waves in which the unburned gas is ignited by rapid adiabatic compression to a temperature which is higher than the self-ignition temperature. Detonation waves are three-dimensional phenomena which show a cellular structure created by superposition of different shock wave fronts. This so-called detonation cell size λ decreases with increasing chemical reactivity of the mixture, so that λ^{-1} can serve as a measure of detonation sensitivity.

Figure 9.1h displays the detonation sensitivity λ^{-1} of the different gases. The higher reactivity of the H_2-O_2 system results in a higher tendency to undergo spontaneous transitions from a deflagration to a detonation compared to hydrocarbons. Deflagrations are combustion waves in which the reaction is controlled by diffusion of heat and radicals from the burned gas to the unburned gas. In this paper deflagrations with flame speeds smaller than or equal to the sound velocity in the unburned mixture will be called "slow deflagrations", those with higher flame speeds will be referred to as "fast deflagrations".

9.1.2 Statistics of Hydrogen Incidents

Before going into a deeper analysis of hydrogen safety issues, it is informative to review what happened in the past. What were the causes and the consequences of accidents involving hydrogen? Can general trends be identified? How different are the risks from gaseous hydrogen (GH_2) compared to liquid hydrogen (LH_2)?

A comprehensive and recent collection of hydrogen-related incidents can be found in [3]. In this review, 287 accidents with gaseous and liquid hydrogen were analysed and classified in a systematic manner. An older review of hydrogen fire and explosion incidents can be found elsewhere [4]. It should be kept in mind that hydrogen accidents are not only a topic of the past, but also of the present. An accident with a compressed hydrogen gas trailer occurred in Germany in June 2005 for example. Figure 9.3 displays the photo of the accident. As can be seen, the hydrogen bottles fortunately remained intact and the hydrogen could be vented safely.

From the data collected in [3], the following conclusions can be drawn with respect to the causes, ignition sources, combustion regimes, effect of confinement as well as the consequences in a hydrogen-related accident.

Fig. 9.3 Accident with a compressed-hydrogen-gas tanker in Germany, 2005. The hydrogen bottles remained intact and the hydrogen could be vented safely

– For about one third of the accidents with GH_2 and LH_2, no single cause could be identified. Important causes which have been determined were human error, construction deficits, and malfunction of components, both for GH_2 and LH_2.
– The most important ignition sources identified were open fire, spontaneous self-ignition, electrostatic discharge, and hot surfaces. For GH_2, each of these four ignition sources contributed by $10 \pm 2\%$ to the total events, whereas for LH_2, these percentages amount to about half of the given values. The ignition source remained unidentified in about 40% of the cases with GH_2. By contrast, almost 60% of LH_2 accidents resulted in no ignition.
– Figure 9.4 displays the combustion regimes observed in accidents involving GH_2 and LH_2, respectively. In more than 90%, accidents with GH_2 lead to an ignition and in around 60%, to a fast deflagration. With LH_2, almost 60% of the events show no ignition, which subsequently reduces the generation of slow or fast deflagrations significantly. It is evident that the formation of a combustible mixture or the ignition of the resulting cold H_2-air mixture is more difficult to reach with LH_2than with gaseous hydrogen release. The full spectrum of flame speeds from slow deflagrations to detonations was observed in hydrogen-related accidents. If the maximum overpressure p_{max} from combustion is considered,

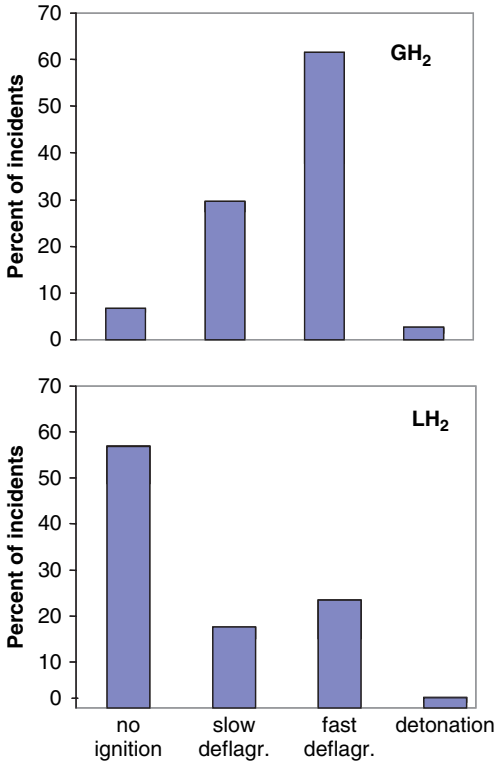

Fig. 9.4 Combustion regimes observed in accidents with GH_2 and LH_2. With GH_2 most cases lead to ignition and fast deflagration. With LH_2 ignition is much less likely [3]. All combustion regimes of hydrogen ranging from slow deflagrations to detonations are observed in accidents

$(p_{max} - p_o)/p_o \approx 0.02$ typically results for a slow deflagration of 10 m/s flame speed, and $(p_{max} - p_o)/p_o \approx 20$ for a detonation with 2000 m/s flame speed.

– The possibility of fast deflagrations and detonations clearly increases with the degree of confinement. Confinement prevents venting of burned and unburned gases and supports flame acceleration. Furthermore, turbulence-generating flow obstacles are more likely to occur in rooms than in open space.
– Important consequences of hydrogen-related accidents are injuries and mortality. Figure 9.5 displays the typical rates from different classes of hydrogen accidents which occurred with GH_2 and LH_2. As can be seen, events with GH_2 lead to significantly more injuries than with LH_2. The total number of fatalities per incident is comparable for GH_2 and LH_2. According to this database, the hydrogen risk is dominated by the release of gaseous hydrogen into the environment or into rooms accessible for persons.

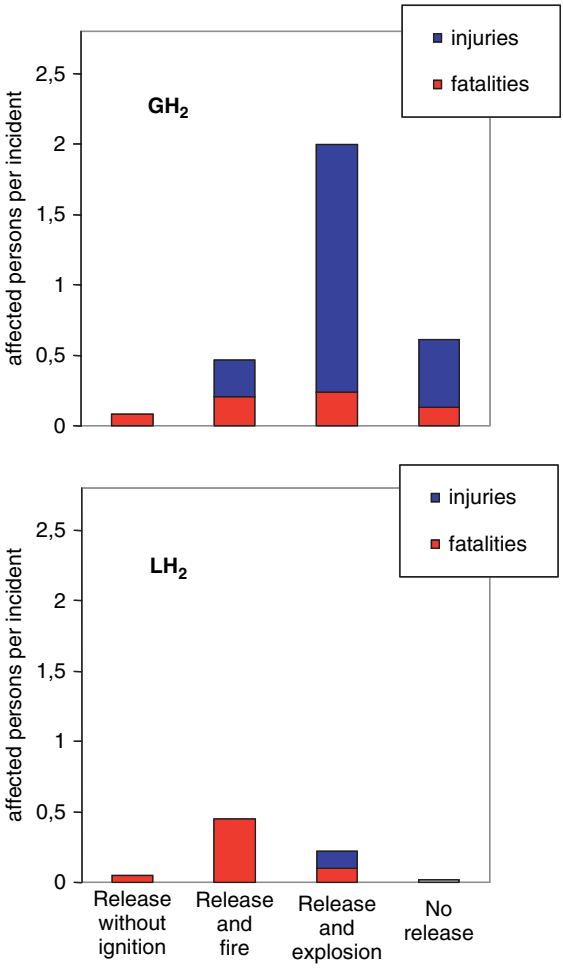

Fig. 9.5 Injury and mortality rates from different classes of hydrogen accidents. Risk is dominated by GH_2 release and explosion [3]. The term "explosion" summarizes fast turbulent deflagrations and detonations

The above discussion of safety-relevant properties of hydrogen and the review of past hydrogen accidents shows that the development and the outcome of an accident scenario depends on many different parameters. Due to the complex combustion physics of hydrogen-air mixtures, the damage potential may vary by orders of magnitude. Since the whole spectrum of flame speeds is observed in accidents, a comprehensive modelling of hydrogen distribution and combustion phenomena is necessary for predictive accident analyses.

9.2 Analysis of Hydrogen Accidents

In this chapter, the general sequence of events during a hydrogen accident shall be described.

Let us consider as an example a vehicle collision in a tunnel involving a car fuelled with liquid hydrogen. If the vacuum of the thermal tank insulation is lost by mechanical damage of the outer tank structure, the LH_2 tank inventory will be released in gaseous form into the environment within 10–15 minutes [5]. Figure 9.6 displays the numerical simulation of the accident. Herein, it is assumed that the release point is below the trunk.

The first event once hydrogen is released is the mixing of the cold gaseous hydrogen (20 K) with air (300 K). This will result in gas mixtures which are buoyant, rise upwards, and spread along the tunnel ceiling. The hydrogen distribution phase continues until an ignition occurs.

Potential ignition sources are e.g. open fire, mechanical sparks, electrical sparks, hot surfaces, and electrostatic discharges. For an ignition to occur, a burnable mixture must exist at the ignition location (4–75 vol.% H_2). In case of a successful ignition, a slow quasi-laminar deflagration will initially propagate from the ignition location to the surrounding mixture with flame speeds in the order of several m/s. The expansion flow of the hot burned gases pushes unburned gas away from the ignition point. In the presence of obstacles, the flow may become turbulent. Depending on the obstacle density, hydrogen concentration, and geometrical confinement, the slow deflagration will or will not accelerate and transform into a fast turbulent deflagration with typically several 100 m/s flame speed.

As can be seen in Fig. 9.6, high hydrogen concentrations were only present near the release point (> 10 vol.% H_2), but no flow obstacles were located in the upper tunnel region. As a consequence, only a slow deflagration with less than 10 m/s flame speed was predicted in this case. However, if disadvantageous conditions exist involving high H_2 concentrations, high obstacle density, correspondingly high turbulence levels, a large degree of confinement, and/or large geometrical dimensions of the burnable cloud, the fast deflagration may turn into a detonation. In this case, flame speeds up to 2000 m/s can be reached.

Table 9.1 gives a summary of the general accident phases and the corresponding important parameters. In a complete and mechanistic model calculation the effect of all these parameters on the development and outcome of the accident must be predicted.

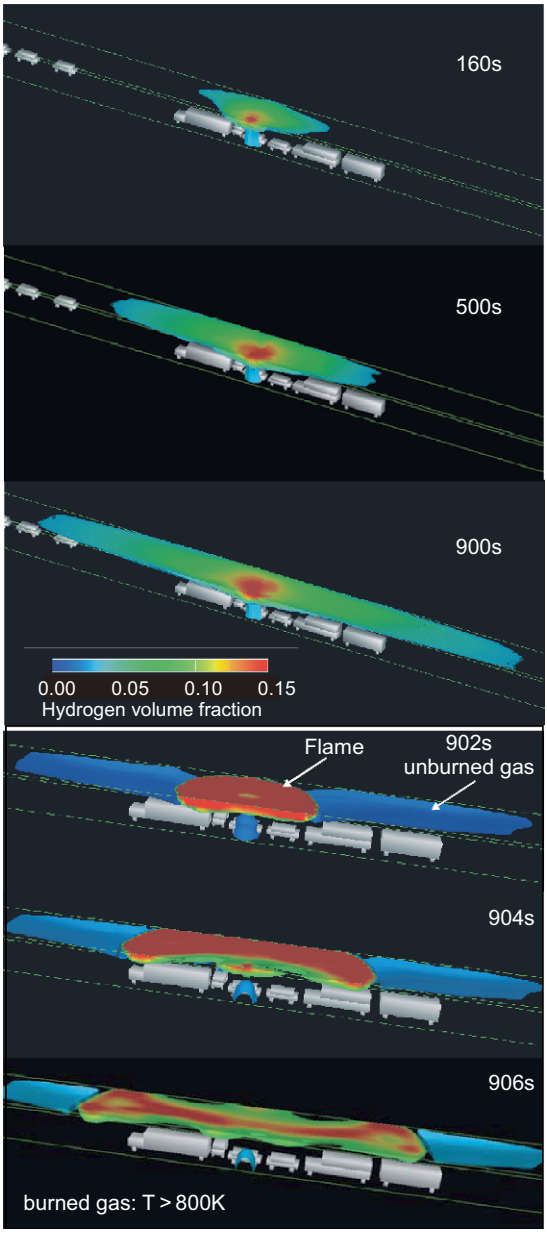

Fig. 9.6 Numerical simulation of a tunnel accident involving release of hydrogen from a LH_2 tank, mixing with air, and late ignition of the burnable H_2-air cloud [5]

Table 9.1 General sequence of events in hydrogen accidents and potentially important parameters which may have an impact on the accident development and outcome

Accident phase	Potentially important parameters
- Hydrogen release	- Leak location, H_2 release rate (g/s), H_2 velocity and direction (plume or jet), total H_2 mass released
- Mixing with air	- Flow regime (plume or jet), confinement, flow obstacles, geometrical scale, time since beginning of release
- Ignition	- Location and time of first ignition (early or late relative to total release period)
- Laminar deflagration	- H_2 concentration, confinement and flow obstacles near ignition point
- Fast turbulent deflagration	- H_2 concentration, degree of confinement, flow obstacles away from ignition point, geometrical scale available for flame acceleration
- Detonation	- H_2 concentration, scale of combustible cloud, confinement, reflecting and focussing walls

9.3 Analysis Procedure

The hydrogen safety-related research activities at FZK concentrated on the development of an analysis procedure allowing for a complete and deterministic modelling of the hydrogen behaviour in accidents. In the following sections, the individual steps of this methodology will be described briefly with special emphasis being placed on the input data required and the resulting output. The methodology is based on three-dimensional numerical simulation tools.

Figure 9.7 displays the four phases of the analysis procedure, the generation of a combustible mixture, the criteria for the hazard potential, the combustion simu-

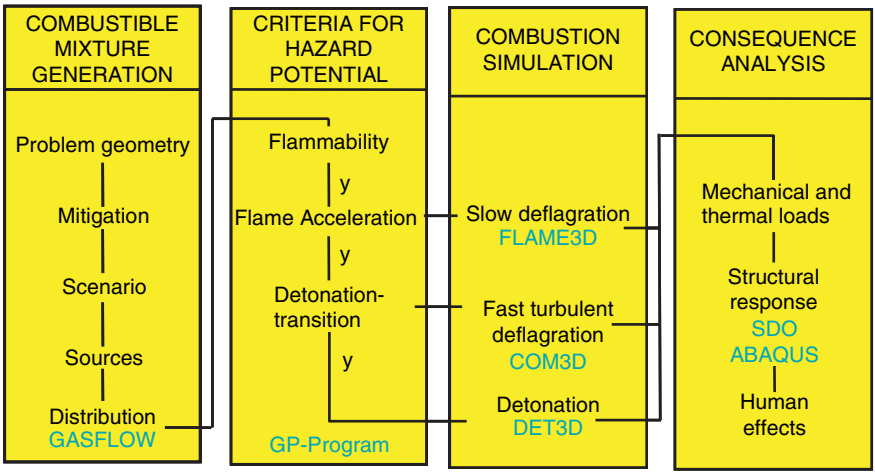

Fig. 9.7 FZK procedure for mechanistic analysis of hydrogen behaviour in accidents [7]

lation, and the consequence analysis. Each of these phases will be described and discussed in the following sections.

9.3.1 First Phase: Combustible Mixture Generation

The first phase of the analysis addresses the formation of a combustible mixture in a given installation and accident scenario. The important parameters in this phase are the geometry model of the installation, followed by the presence or absence of mitigation devices. Then comes the accident scenario. This step in the analysis is of importance, since it will strongly affect the remainder of the analysis. Finally, the hydrogen source and the mode of hydrogen distribution will be taken into account in this first phase.

9.3.1.1 Problem Geometry

At the beginning of every simulation, a geometry model of the installation must be made on the basis of 2D cuts or 3D-CAD files. From a mathematical point of view, the problem geometry defines the boundary conditions for the solution of the three-dimensional equations of flow mechanics. The construction of a 3D computational grid for a complex installation can be a demanding and time-consuming task. Often, a compromise between the desirable level of detail in the geometry representation and the computational possibilities has to be found. It should be noted that neglected or not adequately modelled flow paths may have a significant influence on the calculated flow solution and the resulting H_2 distribution.

9.3.1.2 Mitigation

In the modelling of a given installation, it has to be decided whether measures for hydrogen control should be included in the numerical simulation or not. To integrate such mitigation devices in the analysis, verified CFD models have to be available in order to obtain a reliable prediction of their effectiveness concerning the reduction of the hydrogen inventory and the subsequent effects on other relevant parameters during the accident. As a consequence, numerical models for potential H_2 reduction systems like spark igniters, glow plug igniters, catalytic recombiners were developed, verified in different test series, and implemented in the 3D distribution program GASFLOW. (Catalytic recombiners are devices with catalytic surfaces on which hydrogen can recombine with oxygen from the air without creating an open flame. They have been installed in most German nuclear power plants as mitigation measures against hydrogen release in severe accidents.) It should be noted that if further analysis of the hydrogen behaviour should lead to unacceptable consequences for persons or equipment, then the hydrogen mitigation approach has to be improved.

9.3.1.3 Accident Scenario

For a given installation with a defined geometry and H_2 mitigation system, the next step of the analysis is to decide on the possible type of accident and the sequences which are the most representative cases. This step requires a very good understanding of the investigated system, although some aspects like common mode failure, description of human behaviour, and completeness of the constructed event tree are often difficult to assess. However, it is neither possible nor necessary to examine all sequences with respect to their hydrogen risk. The analysis should cover a small set of boundary (or worst-case) scenarios which in their entity cover all other possible accidents with respect to the potential accident consequences.

9.3.1.4 Hydrogen Sources

Experience has shown that an adequate definition of the hydrogen source is very important, since it has a strong influence on all the following phases of the accident. For a consistent CFD calculation, mass, momentum, and energy of the released hydrogen are required for the complete duration of the accident. Furthermore, position and direction of the source jet have to be defined.

9.3.1.5 Hydrogen Distribution

The knowledge of the time-resolved mass, energy, and momentum fluxes of the hydrogen source in the next step allows to calculate the transport and mixing of hydrogen with the air in the installation. The result of this simulation will be the time- and space-dependent temperature as well as the composition of the H_2/air mixture and temperature.

A large number of interacting physical processes and thermodynamic states have to be simulated with a high spatial resolution to determine gas compositions within a small enough uncertainty band which allows for a meaningful hydrogen combustion simulation. Appropriate goals for this task are the prediction of absolute hydrogen concentrations with an accuracy of a few percent (e.g. $12 \pm 2\%$ H_2).

The CFD code GASFLOW has been developed [6] for the modelling of the 3D hydrogen distribution in complex installations. This code has been tested and verified extensively at FZK [7]. The modelling of hydrogen distribution in general requires the description of:

- 3D fluid flow in a complex 3d domain
- Convective heat transfer between gas and walls
- Radiative heat transfer
- Heat conduction into structures
- Turbulence modelling, and
- Mitigative measures, e.g. recombiners and igniters

The distribution calculation will provide time- and space-resolved hydrogen and air concentrations in the installation.

The next question which arises concerns the hazard potential of this mixture. Is it flammable? If yes, when and where does the ignition occur? After ignition, will the flame be able to accelerate under the given conditions or even undergo a transition to a detonation? These questions are addressed in the second phase of the analysis, which will be presented in the following section.

9.3.2 Second Phase: Criteria for Hazard Potential

9.3.2.1 Ignition

The distribution analysis may result in burnable mixtures for given time and space domains. To initiate the combustion process, an ignition event is necessary. At this stage of the analysis, the location and time of the ignition leading to the first stable flame propagation have to be determined.

Ignition sources can be divided into random and intentional events (e.g. igniters). When igniters are taken into account in the analysis, the location and time of the first ignition are well-defined by the development and expansion of the H_2/air cloud in the installation. As soon as an ignitable mixture ($\geq 4\%$ H_2) reaches the first active igniter, the ignition will be initiated. With correctly designed ignition systems, the ignition of the mixture will occur in the vicinity of the source shortly after the beginning of hydrogen discharge into the installation, which will contain only small amounts of hydrogen at this time. Without this intentional ignition, location and time of the first ignition cannot be predicted mechanistically. A large number of potential ignition sources can be identified during an accident. In this case, the consequences of a random ignition have to be examined. Often, the worst-case ignition which cannot be excluded on mechanistic grounds has to be addressed.

The determination of location and time of the first ignition is important, since it represents the end of the non-reactive phase of the accident and defines the initial conditions of the now starting reactive phase.

9.3.2.2 Flame Acceleration

After ignition, the combustion starts as a slow, quasi-laminar, premixed H_2/air deflagration. It will propagate preferably into the direction with the highest flame speed. This means generally towards richer mixtures and into regions of high turbulence. This effect and also the self-induced turbulence which is generated due to the expansion of the burned gas behind the flame front may cause the transition from a slow laminar to a fast turbulent deflagration.

In order to derive general scaling laws for flame acceleration, FZK and the Kurchatov Institute Moscow (KI) performed joint test series in obstructed tubes.

The tubes were geometrically similar with different diameters of 80, 174, 350, and 520 mm. Experiments in a large facility near Moscow provided data for a channel diameter of around 2250 mm. Optimum conditions for flame acceleration were created in these experiments (strong turbulence, repeated obstacles, no venting) to derive conservative criteria. H_2-air mixtures with additions of mono-, bi-, and triatomic inert gases were investigated (He, Ar, N_2, CO_2) [8]. The systematic analysis of the measured data showed that the expansion ratio σ (= ratio of specific volumes [m^3/kg] of burned to unburned gas at constant pressure) is the most important mixture parameter, as it determines the flame propagation regime. The expansion ratio σ also represents the ratio of chemical energy in the unburned mixture to the initial thermal energy (Q/c_pT_0).

Figure 9.8 displays the criterion for flame acceleration in H_2-air mixtures. The outcome of these experiments is that a borderline exists between tests with accelerating and with non-accelerating mixtures. The border correlates with $\sigma \approx 3.75$ independently of the geometrical scale. This critical expansion ratio is valid for lean and rich hydrogen-air diluent mixtures under ambient conditions. In H_2-air mixtures at NTP, this limit corresponds to 10.5% H_2 on the lean side and 74% H_2 on the rich side. For rich mixtures, the flammability and flame acceleration limits coincide.

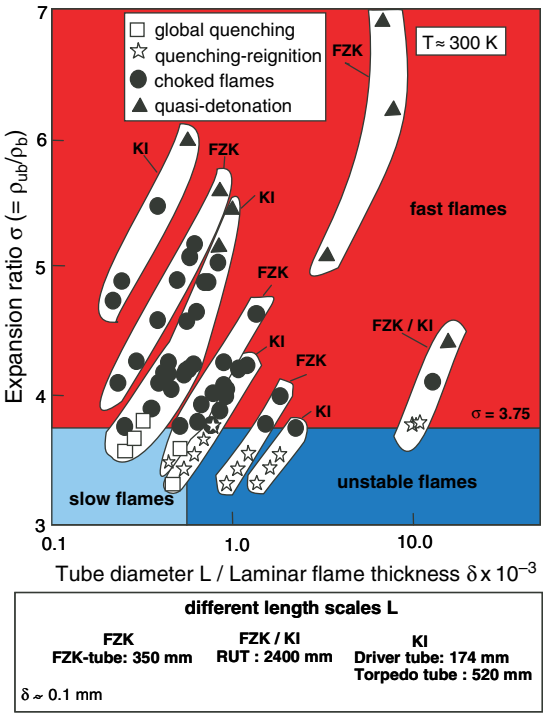

Fig. 9.8 Criterion for flame acceleration in H_2-air mixtures. Fast combustion regimes are only observed for mixtures with an expansion ratio above 3.75 (at an initial temperature T_0 of about 300 K)

If this criterion is not fulfilled, a slow laminar combustion has to be expected, which may be modelled with a suitable code. In the case of the σ criterion showing the possibility of flame acceleration, the question is then whether the mixture predicted in the distribution calculation may even be capable of a transition to detonation.

9.3.2.3 Deflagration-to-Detonation Transition (DDT)

To predict whether such a transition may occur, the λ-criterion is applied as a decision tool in the FZK analysis methodology. The idea of DDT requiring some minimum size of the reactive mixture was first proposed by researchers of the Kurchatov Institute (KI) and substantiated by a 1D numerical simulation [9]. A large number of joint KI-FZK experiments were subsequently performed in various facilities, partly with the participation of the French Nuclear Safety Authority (IRSN), to test this hypothesis. In addition, literature data on detonation onset conditions were collected and evaluated. Detailed analysis of these test data showed that – in agreement with the numerical simulations – a correlation exists between the occurrence of DDT and the geometrical size of the reacting gas mixture. Furthermore, it could be demonstrated with tests in scaled-down facilities that the detonation cell size of the mixture allows to consistently scale DDT in different mixtures and facilities.

The final result of the analysis is that a minimum volume is required for the onset of DDT, which can be expressed by $D \geq 7\lambda$, where D is the characteristic size of the reactive gas cloud and λ is the average detonation cell size of the (generally non-uniform) gas mixture (Fig. 9.9). DDT is only possible, if this criterion is met.

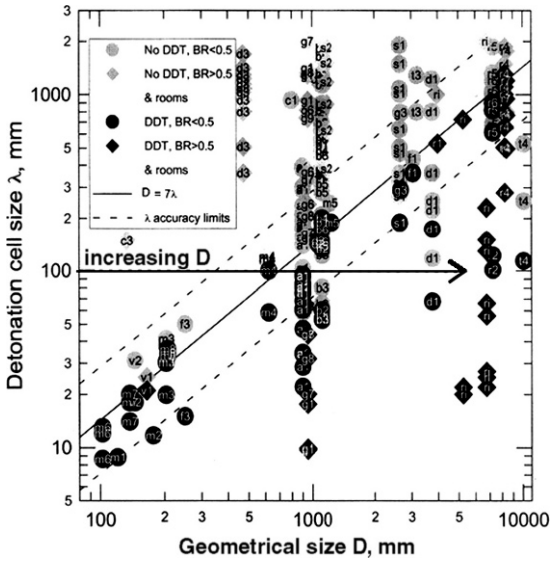

Fig. 9.9 Criterion for detonation onset in H_2-air mixtures. D is the characteristic size of the combustible cloud (= $V^{1/3}$), λ is the average detonation cell size of the mixture. For a given mixture, here one choosen with λ = 100 mm, the increase of the geometrical size D of the reacting cloud will cause a transition from the deflagration regime to the detonation regime; in this example the critical size is near D = 700 mm

Further details can be found elsewhere [10]. It is important to note that contrary to earlier literature data, DDT limits are scale-dependent. The larger the reactive cloud, the leaner mixtures can undergo a detonation transition. If the characteristic size is not sufficient for DDT, a fast turbulent combustion has to be modelled, for which the COM3D code is used at FZK. Otherwise, the simulation of a detonation is necessary, e.g. with the code DET3D.

The three transition criteria of

1. Flammability (inert to burnable mixture composition)
2. Flame acceleration (slow to fast deflagration, σ-criterion)
3. Detonation onset (deflagration to detonation, λ-criterion)

are used to determine the appropriate combustion mode and select the corresponding numerical simulation tool for subsequent combustion modelling. Such transition criteria are necessary for the analysis of the hydrogen behaviour, since a direct numerical simulation of the transition process currently is not feasible. Much smaller time and length scales need to be resolved for such calculations, compared to the distribution and combustion simulation on a large scale. The mechanistic modelling of an ignition event, for instance, requires the resolution of the initial ignition kernel, including detailed chemistry, turbulence, and radiation losses. In the flame acceleration process the transition from laminar to turbulent combustion must be modelled. During the initiation of a detonation, the formation of a "hot spot" with strong ignition and its amplification in the surrounding mixture have to be resolved numerically. Direct simulation of these processes is currently hindered by a limited understanding of physical details and by insufficient computational resources.

It is important to note that the determination of the three empirical transition criteria used here only requires information about concentrations and geometrical dimensions of the burnable mixture formed during the accident. This information is available from the 3D distribution calculation. Therefore, the three criteria can be evaluated "online" during the distribution analysis to identify time and space domains with sufficiently extended and reactive mixtures (implemented in GASFLOW).

The criteria can give early hints with respect to maximum possible combustion velocities and mechanical loads on the investigated structure without a full reactive combustion simulation. They are an easy way to check and optimise the effectiveness of the mitigation measures introduced at the beginning of the analysis. If, for instance, local detonations shall be excluded, it has to be shown that the λ-criterion is not fulfilled.

The criteria described were implemented in an interactive program called GP-code which stands for "Gas Properties" [11, 12]. Figure 9.10 displays an example of the limits calculated for the different combustion regimes in H_2-air-steam mixtures at 400 K. The example relates to a characteristic size of the combustible cloud of $D = 1$ and 5 m, where $D = (\text{Volume})^{1/3}$. As can be seen, the DDT limit is scale-dependent. Indeed, a wider range of mixtures can undergo a detonation transition with increasing size of the system.

In summary, the criteria described have two important functions in the analysis of the hydrogen behaviour. At first, an early judgement as to the fastest possible

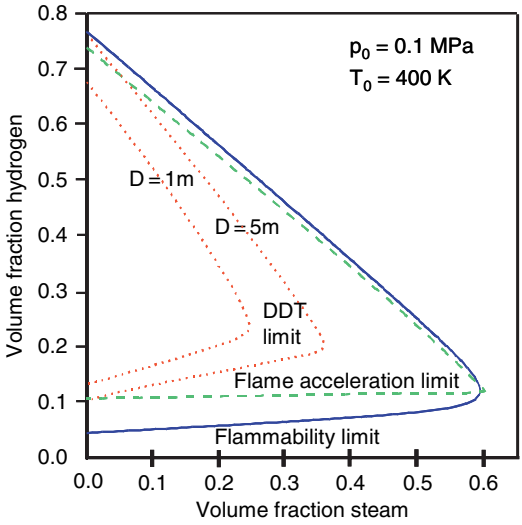

Fig. 9.10 Calculated limits for flammability, flame acceleration and detonation transition (DDT) in H_2-steam-air mixtures at 400 K. Output of GP-code [12]. The DDT limit is scale dependent, a wider range of mixtures can detonate in a larger system

combustion regime and the related pressure loads can be made without a detailed combustion analysis. Secondly, this knowledge allows for the selection of the appropriate numerical combustion program for further 3D analysis.

9.3.3 Third Phase: Combustion Simulation

The following 3D codes have been developed at the Hydrogen Safety Centre of the Forschungszentrum Karlsruhe to simulate the different hydrogen combustion regimes. They are used as follows:

- The FLAME3D and V3D codes for slow deflagration (slow premixed deflagration and non-premixed diffusion flame)
- The COM3D code for fast premixed turbulent deflagration
- The DET3D code for stable detonations in homogeneous H_2/air mixtures.

In V3D a semi-implicit and in COM3D an explicit numerical scheme is used for the solution of the reactive Navier-Stokes equations. FLAME3D and DET3D use an explicit solver for the reactive Euler equations. Most of the combustion energy is transformed into heat, kinetic energy of the gas phase, and finally into pressure waves. Therefore, fast turbulent deflagrations (modelled with COM3D) and stable detonations (modelled with DET3D) mainly lead to pressure and impulse loads, since the high combustion rates do not provide sufficient time for significant heat transfer to structures.

All codes can model arbitrary geometrical boundary conditions and internal flow obstacles by using a structured mesh with cubic computational cells. A graphical user interface allows for an easy representation of complex 3D geometries with

the aid of geometry elements (plates, cubes, spheres, etc.). An intensive validation process was performed for all physical models and numerical methods with the use of suitable experimental data on different geometry scales. This validation work was described and published recently [7].

9.3.4 Fourth Phase: Consequence Analysis

9.3.4.1 Mechanical and Thermal Loads

The thermal and mechanical loads of the 3D combustion simulation, particularly the temperature and pressure histories at different positions in the installation, are recorded in the calculation. The time of the first ignition determines which of these two load forms dominates. In both cases, the same combustion energy is released, but on very different time scales resulting in different heat release rates. In most cases, early ignition leads to low pressures, but high thermal loads due to stably standing diffusion flames. On the contrary, late ignition of a hydrogen accumulation in an installation causes high pressure loads, but the temperature increase is negligible in large structures.

9.3.4.2 Structural Behaviour and Human Injury

The calculated thermal and pressure loads represent the input for the last step of the analysis, which is the investigation of the structural behaviour and human injuries.

Thermal loads due to stable diffusion flames should not lead to structural failures caused by the degradation of sensitive components.

Mechanical loads due to fast flames include pressure waves, impulses, and possibly the impact of debris generated by combustion pressure waves. If fast combustion processes cannot be ruled out with mitigation methods, further investigation of the structural behaviour is required to exclude structural failures. First-order estimates of the structural behaviour of building components under gas dynamic loads can be made with a single degree oscillator model. A numerical model was developed for this purpose [7] and an example of the application of this oscillator model can be found elsewhere [13]. If the single degree oscillator model indicates hazardous situations, more detailed 3D finite-element calculations should be applied to obtain more precise statements about the structural behaviour of the investigated installation.

9.3.5 Mitigation Measures

The primary goal of a safety analysis is to determine the risk which could arise from a given accident scenario. In case the risks are unacceptable, it is necessary to

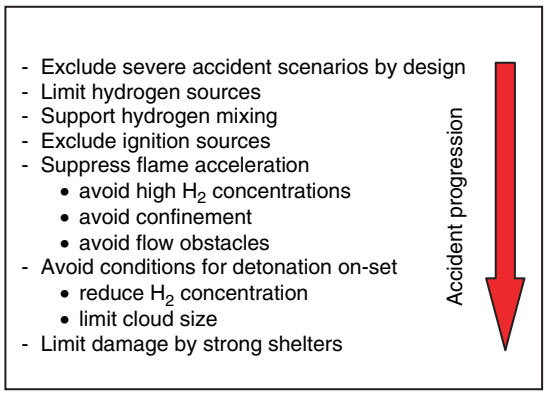

Fig. 9.11 Possibilities for mitigation of accident consequences. The combination of such physically independent countermeasures can provide a robust "defence- in- depth" approach for a safe design

derive effective mitigation measures to reduce the hazard below a certain limit. The analysis methodology described above provides a good guideline on how accident consequences could be mitigated, as it covers the complete accident progression.

Figure 9.11 displays a summary of the possibilities to interrupt or mitigate the progression of a hydrogen-related accident. The list of mitigation measures provided here follows the general sequence of events in an accident. The first objective is to eliminate accidents with very high risks by changing the design of the installation. Once the design has reached the maximum possible degree of safety, the next line of defence is to limit the sources releasing hydrogen into the environment. The remaining hydrogen release must then be dealt with by the analysis. The next step to limit consequences is to exclude ignition sources as far as possible. If this cannot be achieved completely, the likelihood of fast flames should be decreased by reducing confinement or by avoiding heavily obstructed geometries. In addition, favourable conditions for detonation onset should be avoided to the largest possible extent. Finally, as a last resort, a sufficiently strong shelter may be used to protect against severe accident consequences.

A countermeasure generally is most efficient when it influences accident progression in an early stage. The principle of "defence-in-depth" has proven to be very successful in other areas of energy technology. It tries to include in the design a series of safety barriers which are completely independent and rely on different physical principles. The combination of several of the measures described above can provide a robust "defence-in-depth" approach to a safe hydrogen-powered system.

9.4 Application in the Case of H_2 Release in a Garage

Knowledge of the risks which may develop due to the release of hydrogen into confined spaces is of importance, especially in mobile applications. In the following sections, the analysis procedure described above shall therefore be applied to investigate the consequences of hydrogen release from a car parked in a residential garage.

The scenario investigates the release at different rates of cold boil-off gas from a liquid hydrogen tank into initially stagnant air at ambient temperature in a simple rectangular garage [14]. It is assumed that the cryogenic LH_2 tank leads to 170 g of hydrogen boil-off gas per day and that this amount is released in 5 venting intervals of 34 g each. The first scenario considers this amount to be released in 10 s, while the release duration in the second scenario is 100 s. Table 9.2 summarises the different parameters for the investigated garage geometry and hydrogen release scenario. It should be noted here that the case of hydrogen penetration into confined compartments of the car is not addressed.

9.4.1 Mixture Generation

If the amount of 34 g H_2 would be homogeneously distributed in the garage volume, then the resulting H_2 concentration would be only 0.6 vol.%. This value is far below the ignition limit of 4 vol.% of H_2. Does such a hydrogen release represent any risk? The GASFLOW program [6] has been applied to simulate hydrogen release and subsequent mixing with air in the garage in the two scenarios above.

Figure 9.12 displays the computed hydrogen distribution in the garage in the case of 34 g of hydrogen being released in 10 s. As can be seen, two separate plumes rise along two sides of the trunk within 7 s. Once the flow reaches the ceiling, a mushroom-shaped cloud forms. About 20 s after the beginning of hydrogen release, the cloud reaches its largest extension. The velocities in the rising plume are around 1 m/s. The momentum in the flow is redirected at the ceiling, causing an initially circular expansion of the burnable cloud and then reflections at the nearby walls. These reflections lead to a preferential flow along the ceiling towards the front of the car. Air is entrained by these convective gas motions, leading to a decrease of the combustible volume. Finally, the calculation predicts a stable stratification with most of the released hydrogen in a shallow layer underneath the ceiling.

Figure 9.13 displays the computed H_2 concentration in case of the slow release (0.34 g H_2/s). As can be seen, the calculation predicts a completely different distribution process. Here, only one thin, tube-like H_2-air plume extends from the source below the trunk to the ceiling. The plume is quasi-stationary with a slight pulsa-

Table 9.2 Garage geometry and hydrogen release scenarios investigated

Case	Geometry		Hydrogen source				
	Volume (m^3)	Vent Openings	Tot. Mass (g)	Duration (s)	H_2 Rate (g/s)	Temper. (K)	Release Location
1	70.2	Two times $10 \times 20\,cm^2$	34	10	3.40	22.3	Underneath the trunk
2	70.2		34	100	0.34	22.3	

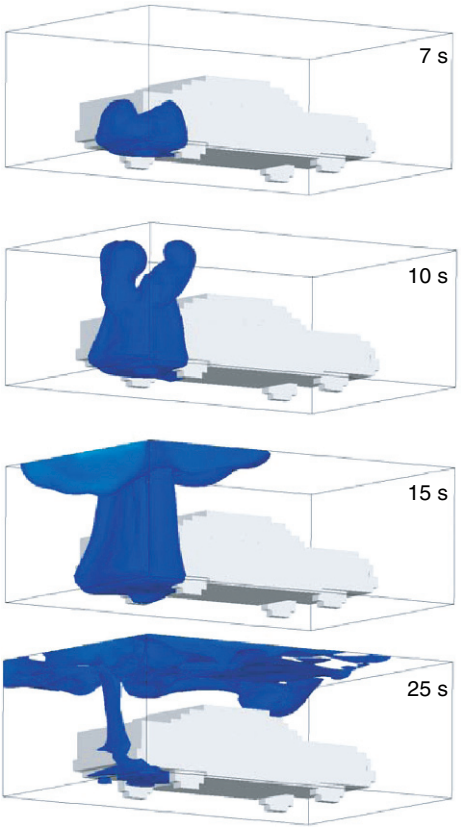

Fig. 9.12 Computed H_2-concentration field in the garage for Case 1 in which 3.4 g H_2/s were released for 10 s. The shown isosurface depicts the region with burnable H_2-air mixtures (> 4% H_2)

tion in the flow rate and diameter. Similarly to the first scenario, a stably stratified hydrogen distribution develops in the garage, but with less gas motion along the ceiling. Shortly after the release of the total amount of gas (around 100 s), the combustible regions which are shown in red have nearly disappeared. This indicates that naturally mixing mechanisms exist, which can dilute this weak hydrogen source to unburnable mixtures. This example demonstrates the necessity of CFD modelling for reliable hydrogen safety investigations. A lumped parameter calculation of these two cases, treating the garage as one single volume would have resulted in a completely different result (0.6 vol.% H_2) and an incorrect risk estimate.

9.4.2 Hazard Potential

For a risk assessment, it is necessary to know the hazard potential associated with the calculated hydrogen distributions in the garage. The criteria for the hazard potential described in Sect. 9.3.2 were evaluated from the computed time-dependent H_2-air distributions. Figure 9.14 displays the results for the three hazard levels, namely,

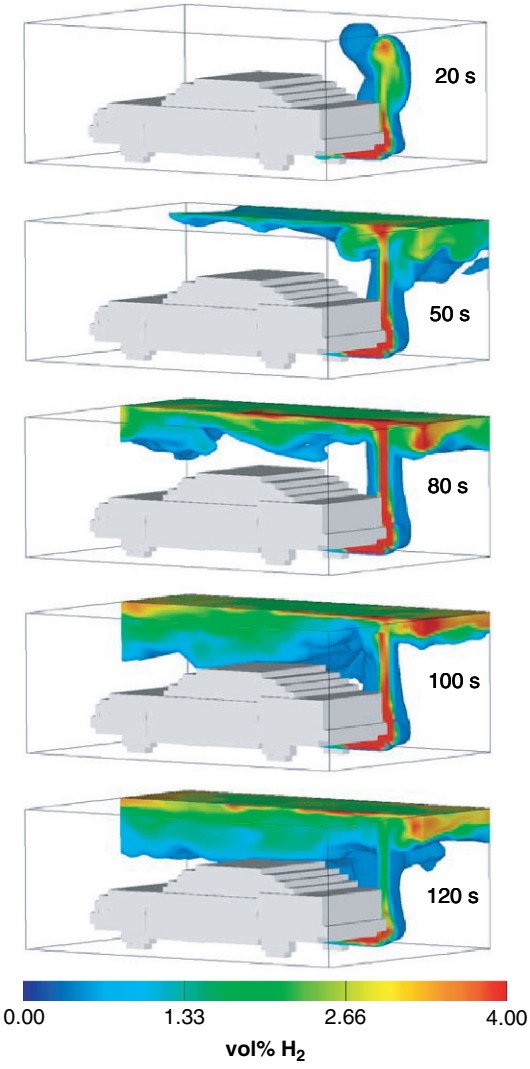

Fig. 9.13 Vertical cut through the computed H_2-concentration field in the garage for Case 2, in which 0.34 g H_2/s were released for 100 s. The burnable region corresponds to the red volume (> 4% H_2)

flammability, flame acceleration, and detonation transition. The results computed for a hydrogen release rate of 3.4 g H_2/s and 0.34 g H_2/s are given on the left and right hand side of Fig. 9.14, respectively.

In the first scenario, the high release rate of 3.4 g H_2/s leads to a maximum characteristic size d_{cc} of the combustible cloud of around 1.6 m, which is equivalent to 4.1 m^3 (d_{cc} = Volume$^{1/3}$). After the end of the release (10 s), the combustible cloud continues to grow due to the dilution of its enriched kernel by further entrainment of air. The maximum value for d_{cc} is reached within 20 s. Once the maximum is reached, the cloud size decreases due to convective mixing by the

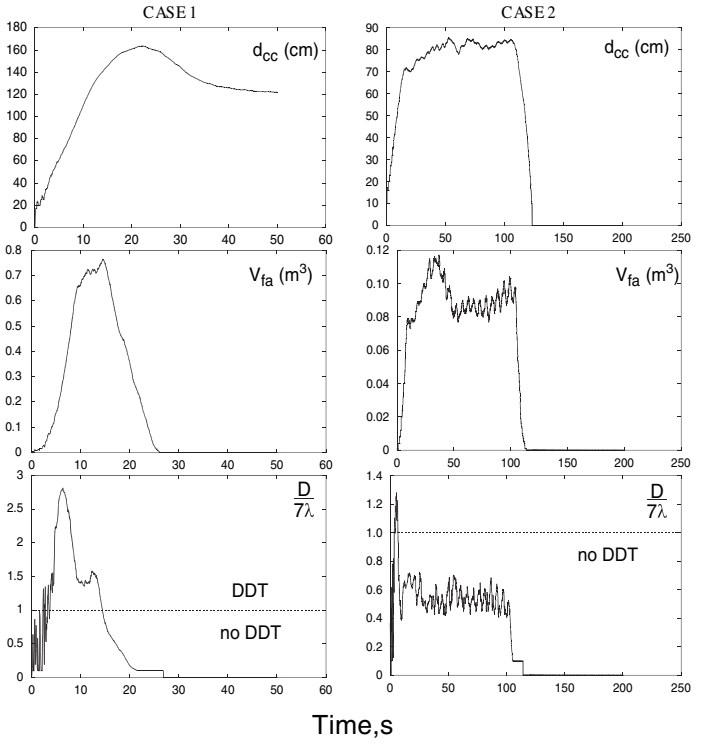

Fig. 9.14 Computed hazard parameters for a hydrogen release of 3.4 g H_2/s for 10 seconds (*left*) and a release of 0.34 g H_2/s for 100 s (*right*). Top: Characteristic dimension of the combustible cloud (4…75 vol% H_2). Middle: Volume of cloud which could support spontaneous flame acceleration (10.5…75 vol% H_2). Bottom: DDT index $D/7\lambda$ of cloud with H_2- concentrations between 10.5 and 75 vol%

momentum-induced gas flows. Finally, the volume of the combustible mixture approaches a constant value.

The cloud which could support flame acceleration (middle left figure) grows directly with the start of hydrogen release and reaches a maximum volume around 0.7 m^3 shortly after the termination of the release. The corresponding H_2 inventory is 20 g. Thereafter, the cloud disappears in about 10 s. This growing and shrinking of the sensitive cloud result from the balance between the hydrogen source strength and the mixing processes. In the first phase (< 10 s), the release dominates and in the second phase (> 10 s), the mixing dominates. Comparison of the time scales shows that the decay of the sensitive cloud (≥ 10.5%) feeds the growth of the combustible cloud (≥ 4%).

The evaluation of the DDT potential shows even higher dynamics. The cloud reaches a detonable composition and size around 2 s after the hydrogen release starts. The most sensitive situation exists a few seconds later, during which hydrogen accumulates underneath the car. DDT possibility is predicted for a total duration

of about 10 s ($D/7\lambda > 1$). In analogy, the decay of the detonable cloud at > 8 s corresponds to the simultaneous growth of the cloud which is able to support flame acceleration (increase of V_{fa} in the figure above the DDT plot).

In the second scenario with the slow release rate, different hazard parameters evolve. As can be seen, a much smaller combustible cloud is formed in this case ($d_{cc} \leq 0.8$ m, $V_{cc} \leq 0.5\,m^3$). Moreover, about 20 s after beginning of the H_2 release, a quasi-equilibrium is established between the source and the mixing processes, leading to a nearly constant cloud volume. After the termination of the release, the combustible cloud dissolves within 20 s, because the plume is cut off and regions with 4% of H_2 or more cannot be sustained below the ceiling during the long release period.

The cloud capable of supporting flame acceleration also is much smaller in this case compared to the first scenario (about $0.1\,m^3$ vs. $0.7\,m^3$). Again a quasi-equilibrium exists between sources and sinks. The cloud disappears within 10 s after the termination of hydrogen release. The maximum hydrogen inventory of the flame acceleration cloud was 2.7 g only.

The evaluation of the DDT criterion $D/7\lambda$ shows that the size and hydrogen concentration of the enriched cloud are insufficient in practice for a transition to detonation for the entire duration of the hydrogen release.

Table 9.3 summarises the computed hazard parameters for the two scenarios investigated. From the computed results, it can be concluded that a strong dependence exists between the hydrogen release rate and the hazard parameters.

In the case of a low hydrogen release rate, only a relatively small flammable cloud develops ($< 0.5\,m^3$). A combustible mixture is present in the rising plume only during the release period. Once the release stops, no combustible mixtures are left in the garage and no combustion hazard remains.

At the large release rate, around $4\,m^3$ of combustible mixture develop in the garage. As long as the source is active, an inner kernel of enriched mixture exists (up to $0.7\,m^3$), which has the potential for sustaining supersonic combustion modes. However, these enriched regions dilute rapidly to more insensitive mixtures after the source is cut off. This process, on the other hand, supports the persistence of the deflagration cloud ($\geq 4\%$ H_2). At the end of the calculation, it shows a stably stratified distribution near the ceiling of the garage. This indicates that accidental ignition of such a mixture would lead to a substantial damage of the car and the garage. Therefore, active or passive countermeasures seem necessary in this case to control H_2

Table 9.3 Summary of computed hazard parameters for hydrogen release in a garage [14]

Case	Flammable Cloud		Flame Acceleration Cloud			Detonable Cloud		
	s (m^3)	t (s)	s (m^3)	m (g H_2)	t (s)	s (m^3)	m (g H_2)	t (s)
3.4 g H_2/s	4.1	CAT = (50)	0.7	20	RT + 15s = 25	0.7	20	10
0.34 g H_2/s	0.5	RT + 15s = 115	0.1	2.7	RT + 15s = 115	–	–	–

s = maximum size; m = maximum mass; t = time of existence; CAT = complete analysis time; RT = release time

release rates in the range of few 0.1 grams per second. Such countermeasures need careful design calculations to prove the required efficiency.

9.4.3 Combustion

The hazard parameters computed for the high hydrogen release rate of 3.4 g/s show that spontaneous flame acceleration and detonation onset could be possible. The GASFLOW calculations predict that almost 20 g of hydrogen can be involved in such a fast combustion event. The next step is then to analyse the consequences of such a local explosion in a residential garage.

The corresponding experiments were performed at FZK in a closed test chamber representing the garage. Since the fraction of hydrogen burning in a fast mode can depend on many parameters, differently sized combustion units were developed, which contained 2, 4, 8 or 16 g of hydrogen in a homogeneous stoichiometric H_2-air mixture. These cubic combustion units contained layers of mesh wire to promote flame acceleration. They were ignited by a centrally located weak electric spark. Figure 9.15 displays the flame velocities measured inside the combustion unit for 8 and 16 g of hydrogen. Flame speeds typical of quasi-detonations were observed at the outer edge of the combustion unit. With this arrangement, local explosions with conservative overpressures were produced inside the test chamber. Figure 9.16 shows a photograph of the fast deflagration obtained with the 8 g H_2 combustion unit shortly after complete combustion of the H_2-air mixture. The pressure wave generated by the local explosion propagates into the surrounding air volume.

The experiments were afterwards simulated with the COM3D code using the measured flame speeds inside the combustion unit as input data. The grid resolu-

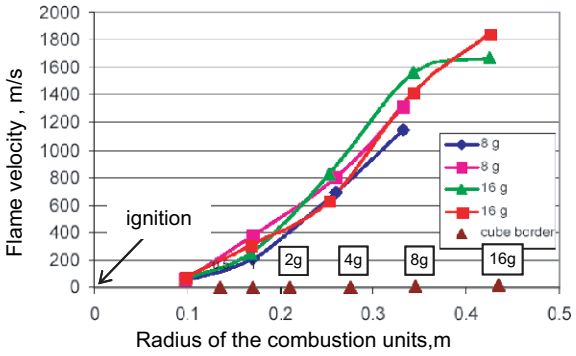

Fig. 9.15 Measured flame speeds in the combustion unit for 8 and 16 g of hydrogen. The combustion unit was a cube filled with stoichiometric H_2-air mixture, ignited by a weak electric spark in the middle (r=0). The flame speed reached quasi-detonation velocities at the outer edge of the cubes for 8 and 16 g of hydrogen inventory. The generated pressure waves have limiting, upper bound overpressures and impulses for the given hydrogen mass

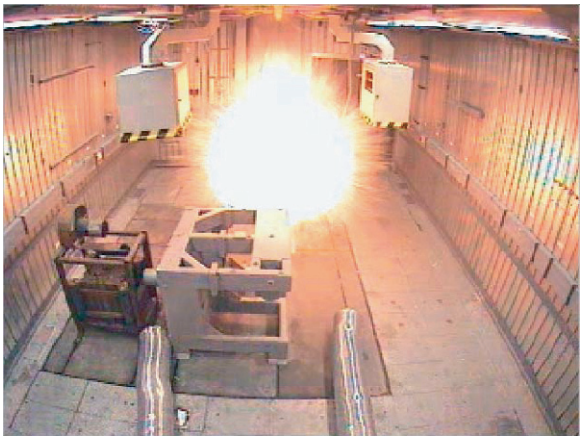

Fig. 9.16 Local explosion of 8 g of hydrogen in the FZK test chamber, simulating an accident scenario in a residential garage

tion used in the COM3D calculation was 3 cm. Figure 9.17 displays a vertical cut through the 3D pressure field in the garage 7.7 ms after ignition of the 8 g H_2 combustion unit located in the centre of the spherical pressure wave. At this time, the pressure wave emitted from the combustion unit into the surrounding air reaches the walls of the garage. A reflected wave returns from the bottom of the test chamber. Figure 9.18 compares the measured and the computed overpressures for a position on the floor of the test chamber. As can be seen, the agreement is good between the experiment and the model at the beginning of the event. The differences observed between experiment and simulation later are mainly due to the wall properties of the test chamber. They moved in the experiment, but were assumed rigid in the simulation.

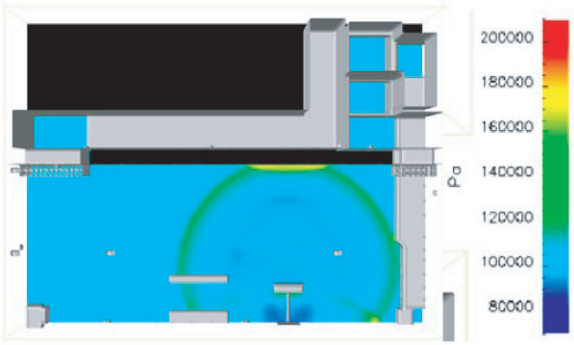

Fig. 9.17 COM3D calculation of the fast deflagration of 8 g of hydrogen in the test chamber. Shown is a vertical cut through the 3d pressure field, 7.7 ms after ignition of the combustion unit which was located in the center of the spherical pressure wave

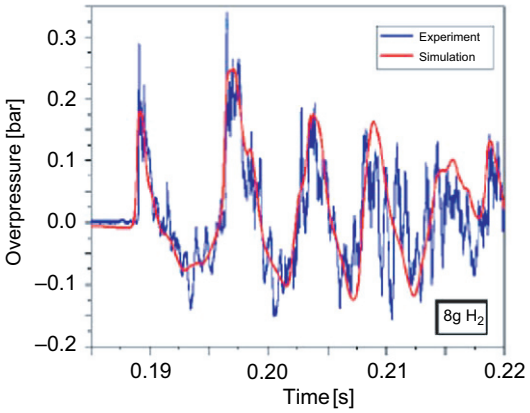

Fig. 9.18 Comparison of measured and calculated overpressure for a position on the floor of the test chamber

It can be concluded that local pressure loads in complex confined geometries can be well predicted, if the flame velocity is correctly modelled.

9.4.4 Consequence Analysis

The output of the 3D combustion analysis allows to estimate the consequences of a local hydrogen explosion in a garage. Thermal and mechanical loads on structures and humans are of interest. The following discussion shall be limited to the effects of the pressure loads generated by a confined local explosion of 2 and 16 g of hydrogen, respectively.

9.4.4.1 Structural Response

Figure 9.19 displays a comparison of the measured peak overpressures Δp^+ and durations T^+ of the first incident positive overpressure waves from confined local H_2 explosions with damage thresholds of civilian buildings. The damage thresholds expressed in the form of $\Delta p^+ - I^+$ relations were taken from Baker et al. [15]. The positive impulse I^+ was converted into positive pressure duration T^+ by using the following equation:

$$T^+ = 2I^+/\Delta p^+ \tag{9.4}$$

Glass breakage depends on a number of parameters like glass thickness, glass area, and aspect ratio of the glass pane. In Fig. 9.19, two examples covering the typical overpressure range for glass breakage are plotted [15].

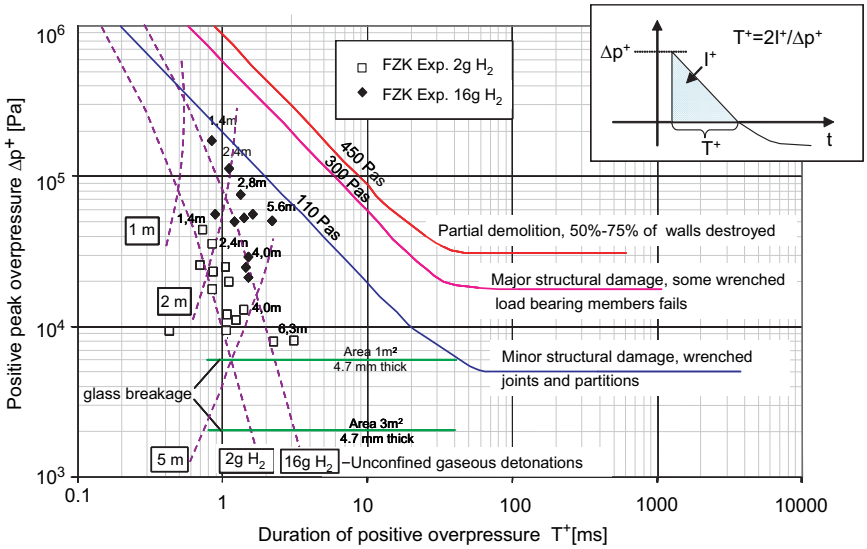

Fig. 9.19 Comparison of measured blast wave parameters Δp^+ and T^+ from confined local H_2 explosions to damage thresholds for civilian buildings

Three different degrees of damage to civilian masonry buildings are presented, ranging from minor structural damage to a significant demolition of walls [15]. These lines represent the limit values for Δp^+ and T^+ that have to be reached in order to cause the indicated degree of damage. Therefore, a pressure wave with parameters above these lines will even cause a higher degree of damage. A given damage may be caused either by a certain peak overpressure or by a certain overpressure impulse. In Fig. 9.19 the lines with a slope of -1 correspond to a constant impulse. The limiting impulse is given for each of the three levels of building damage (110, 300, and 450 Pas, resp.).

The data points given in Fig. 9.19 indicate the Δp^+ and T^+ values measured in the experiments with 2 g and 16 g of hydrogen. The distance from the ignition location of the stoichiometric H_2-air mixture to the pressure sensor location varies between 1.4 and 6.3 m. The peak overpressure decreases in general with increasing distance from the combustion unit. The spread in the measured $\Delta p^+/T^+$ points reflects the effects of the confinement and obstacles present in the test chamber (see Fig. 9.16). Indeed, obstacles can shadow pressure sensors (giving small Δp^+ values). Furthermore, confining walls can lead to oblique or normal reflection and focussing of pressure waves in 2D edges or 3D corners (giving high Δp^+ values).

Figure 9.19 also compares the data points measured under these confined and partially obstructed conditions with published correlations for unconfined gaseous detonations. In [16] $\Delta p^+/I^+$ correlations were derived for unconfined gaseous detonations of hydrogen-air mixtures. Here, these correlations are converted into a $\Delta p^+/T^+$ format. Results for 2 and 16 g of hydrogen are shown in Fig. 9.19. The

lines marked 1m, 2m, and 5m, resp., are lines for constant distance from the centre of the explosion. The peak overpressure increases with decreasing distance from the explosion origin and with increasing hydrogen mass. There is a quite good agreement in the general trends of the unconfined load parameters with the data measured in the confined experiments. The deviations of the measured data points from the shown lines indicate the effect of the confinement and obstructions on the blast wave parameters Δp^+ and T^+.

9.4.4.2 Human Injury

The human organs which are most sensible to pressure waves are ear drums and lungs [17, 18]. Figure 9.20 displays a comparison of the blast wave parameters Δp^+ and T^+ measured during the confined local H_2 explosions described with the literature data for human injury thresholds of these organs. As can be seen, pressure waves with higher blast wave parameters Δp^+ and T^+ cause increasing grades of injuries. In case of waves with a positive phase duration above 10 ms and a peak overpressure above 0.8 bar, for example, lung damage must be expected. Shorter waves need higher overpressures.

The injury thresholds for ear drums were reviewed extensively by Richmond et al. [17]. Their statistical treatment of the experimental data resulted in the two bands shown in Fig. 9.20 for 1 and 50% probability of ear drum rupture. The width of the bands represents the scattering due to parameters like age or gender. With

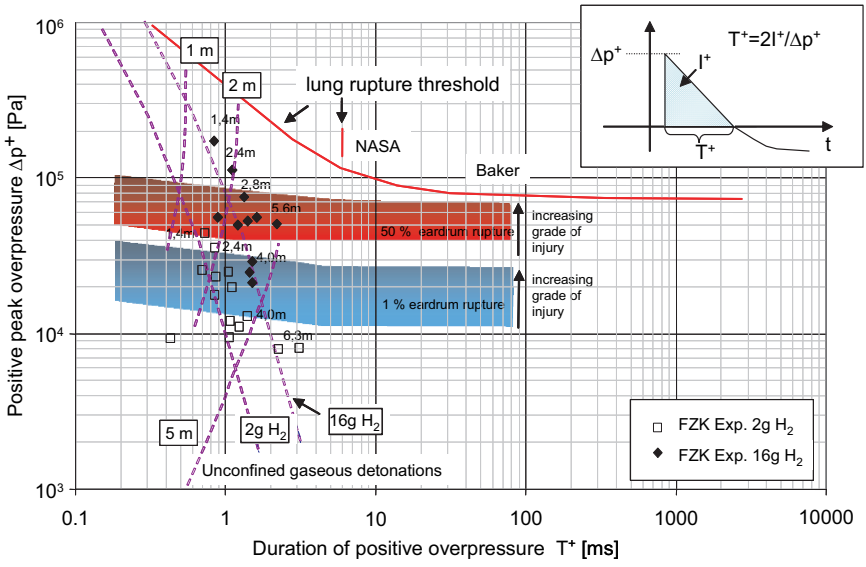

Fig. 9.20 Comparison of measured blast wave parameters Δp^+ and T^+ from confined local H_2 - explosions to human injury thresholds

increasing Δp^+, the event of an ear drum rupture leads to increasing grades of ear injury, affecting also inner ear bones.

The ear response is also dependent on the orientation of the incoming wave front with respect to the ear canal. The worst case is a normal incidence of the wave, which causes a higher reflected overpressure. The same effect occurs, if the ear canal is oriented towards and located near a reflecting surface. The Δp^+ and T^+ values given in Fig. 9.20 correspond to the incident wave, assuming a nearby normal reflecting surface. These data are conservative and appropriate for confined local explosions in small rooms like a garage.

The data points given in Fig. 9.20 represent the Δp^+ and T^+ values measured in the experiments with 2 and 16g of hydrogen. They indicate that local fast deflagrations or detonations of 2–16 g of hydrogen can easily cause ear membrane rupture, but not lung damage. Significantly larger amounts of hydrogen are needed for lung damage. The scaling laws for unconfined detonations predict a doubling of T^+ for a 8-fold increase in the reacting hydrogen mass, which is due to the doubling of the (spherical) cloud radius. Therefore, if the hydrogen mass is increased to 128 g, the line for 16g H_2 ($8 \cdot 16 = 128$ g) is shifted by a factor of two to a higher T^+ value. Thus, the threshold for lung damage can be reached by an explosion of 128 g H_2 at a distance of about 2 m.

9.4.5 Summary of Results of Garage Investigations

The transient release of hydrogen into a private garage was investigated, assuming that 34 g H_2 were released with a mass flow rate of 0.34 and 3.4 g/s, respectively. The homogeneous distribution of this hydrogen mass would result in an inert mixture far below the flammability limit (0.6 vol.% of H_2). In reality, complete mixing occurs after many hours only. The objectives were to analyse the risk and the possible consequences of such a release of hydrogen into a confined space.

The 3D distribution calculations with GASFLOW identified the size, shape, composition, and time evolution of the reactive H_2-air clouds developing during and after the H_2 release period (see Figs. 9.12 and 9.13).

The knowledge of the hydrogen concentration distribution obtained from GASFLOW then allowed for a quantification of several risk parameters like size, hydrogen mass, and time of existence of burnable mixtures. These parameters are of importance, as the mixture could sustain a slow deflagration, a fast turbulent deflagration or even a detonation under inadvertent conditions (see Fig. 9.14).

The dynamics of the reactive cloud evolution are governed by the balance between the H_2 source strength and the physical mixing mechanism. The latter tends to dilute the pure hydrogen released from the source location. If the release rate is high, then the source dominates the mixing processes for the whole release period (10 s), leading to a large and continuously growing combustible cloud. In contrast, if the release rate is low, then the mixing dominates, leading to a small and practically constant cloud size during the whole release period (100 s).

The slow release rate (and total mass) creates only a low risk in terms of flammable cloud size, time of existence, and hydrogen mass involved (Table 9.3), whereas with the high release rate, a long-term potential for slow deflagration is possible. Indeed, much of the injected hydrogen mass exists in the form of a stably stratified layer below the ceiling in the high-release scenario. As a consequence, fast turbulent deflagration and detonation are possible during the release period itself (10 s) and around 15 s after the end of the H_2 injection. A hydrogen mass of up to 20 g could generate fast combustion events.

To evaluate the consequences of such local explosions in a garage, fast combustion experiments were performed in a closed test chamber at FZK using stoichiometric H_2-air mixtures containing 2, 4, 8 or 16 g of hydrogen. The used combustion units contained layers of mesh wire to promote flame acceleration and to create boundary (worst-case) pressure loads. The measured pressure histories were analysed with respect to peak overpressure and duration of the first positive pressure wave (Δp^+, T^+) and then compared with known thresholds for structural damage and human injuries.

Fast combustion of 2–16 g of hydrogen could have the following consequences for the garage structure:

- window panes and other light garage components like e.g. the usual metal sheet door would break
- damage to a masonry wall would occur only, if the H_2 explosion would take place near the wall (Fig. 9.19, local explosion with 16 g of H_2 at 1 m distance)
- wooden framework constructions as often used in the USA for residential garages would be destroyed.

A local explosion of 2–16 g in a garage would have the following impact on persons present in the garage:

- high probability of ear drum rupture
- no lung damage.

It is clear from these results that H_2 release rates of several g/s into a garage should be either prevented by adequate vehicle safety technology or mitigated by active or passive countermeasures installed in the garage. Such mitigation systems need careful design calculations to prove the required efficiency. Mitigation measures are necessary also in case of the small leak rate investigated here (0.34 g/s), if the duration (and total H_2 mass released) is more than 5–10 times larger.

9.5 Safety Issues for Hydrogen Vehicles and Infrastructure

In the previous chapter the example of hydrogen release from a car parked in a residential garage was investigated to demonstrate the course of a complete mechanistic safety analysis. The garage situation is only one accident scenario among many others. In a future hydrogen economy the spectrum of safety issues connected with the widespread use of hydrogen-powered cars will be significant.

Herein, an overview will be given as concerns the safety issues for hydrogen vehicles and infrastructure. The potential accident scenarios are divided into two classes, hazards resulting from vehicle operation and hazards connected with infrastructure (filling/repair/service stations).

9.5.1 Hazards Resulting from Vehicle Operation

A hydrogen risk develops only, if hydrogen is released from vehicle components containing hydrogen in liquid or gaseous form. By mixing with air, combustible H_2-air clouds can be created and then pose a threat in case of ignition. The consequences of such a loss of hydrogen confinement depend on many design details of the car.

Figure 9.21 displays a simplified layout of a hydrogen car equipped with compressed gaseous hydrogen and a fuel cell. The hydrogen system can generally be divided into a high-pressure part and a low-pressure part. Both parts are separated by the pressure regulation valve (PRV). All the components of such a system are carefully selected and tested for their performance and compatibility with hydrogen. The test objectives vary from non-destructive to destructive, from single to endurance tests at the level of single components, sub-systems or the entire system. Generally recommended design guidelines for hydrogen cars are listed below [19]:

- Hydrogen leak prevention by the selection of appropriate materials and by minimising the number of flanges and threaded connections
- Hydrogen leak detection
- Ignition prevention by minimising the sources for ignition.

These guidelines provide for a reliable defence-in-depth concept for avoiding hydrogen-related incidents. Other good overviews of safety issues for hydrogen vehicles can be found in [20] and [21].

Nevertheless, the consequences of component failures, both in normal operation and during a collision, must be systematically evaluated to identify potentially unacceptable hazards and to prevent such scenarios by design countermeasures. In the following sections the different failure modes which can occur with a hydrogen/PEM fuel cell vehicle shall be considered [19]. They may be generated by

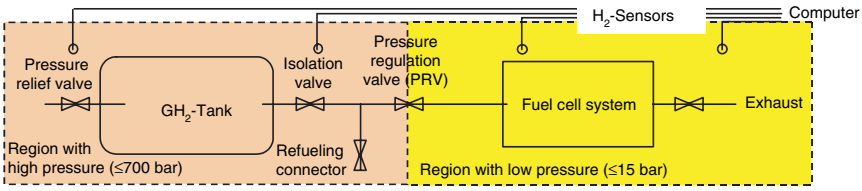

Fig. 9.21 Simplified layout of the hydrogen containing components of a car using compressed gaseous hydrogen and a fuel cell

failures in the compressed hydrogen storage system, in the hydrogen delivery system, and/or in the fuel cell system.

1. *Failure of the compressed hydrogen storage system*

   a) Under normal operation

      – Catastrophic rupture due to a manufacturing defect in the tank, defect caused by abusive handling of the tank, local destruction of epoxy resin in an area of the tank and stress rupture.
      – Large hydrogen release due to faulty pressure relief valve tripping without cause, fault in tank wall.
      – Slow hydrogen leak due to a defect in the tank, stress cracks in the tank liner from pressure cycling, faulty pressure relief device, and faulty coupling from tank to feed line.

   b) During a collision, potential failure modes for the storage cylinders are:

      – Catastrophic rupture due to collision impact, puncture by a sharp object, external fire with failure of pressure relief device to open.
      – Large hydrogen release due to puncture by a sharp object, fire-created hole in the tank, opening of pressure relief valve in a fire (which is the purpose of the device).
      – Slow hydrogen leak due to fire-induced openings in the fuel line connection and impact-induced opening in the fuel line connection.

2. *Failure of hydrogen delivery systems*

   a) In normal operation:

      – Large hydrogen release due to failure of fatigued connection in the high-pressure line, simultaneous failure of check valve and quick disconnect shut-off.
      – Slow hydrogen leak due to connection loosened by vibration, temperature, and/or pressure cycling, faulty solenoid or shut-off valve, faulty pressure regulator, or fatigue crack in the fuel line.

   b) Additional failure modes may arise due to collisions:

      – Large hydrogen release due to shearing of the high-pressure fuel line, fire-induced melting of solenoid valve, and rupture of pressure regulator valve.

3. *Failure modes in the fuel cell system*

The fuel cell system consists of the fuel cell stack and additional auxiliary components, such as air compressors, gas humidification equipment, heat exchangers, and others. During normal operation, a hydrogen leak may develop and lead to combustible mixtures in distribution manifolds, humidification system, heat exchanger, hydrogen recirculation compressor, car compartments or the exhaust system. Also purging the fuel cell may lead to hydrogen and to combustible H_2-air mixtures release into the environment. In case of a collision, no additional risk is expected from

the fuel cell, since the solenoid valves will have shut off the hydrogen flow before it can reach the fuel cell [19]. The fuel cell system, however, should be designed to minimise the risk of hydrogen ignition.

Over the past decade, car manufacturers carefully addressed these issues by appropriate testing and research. An example is the activities carried out by BMW. They started in the 1990s on the component level [22] and meanwhile have produced convincing safety results for the complete car system [23]. The consequences of the failure modes described above will depend strongly on the degree of confinement of the released hydrogen gas. Scenarios with a high degree of confinement of the produced H_2-air cloud have a much higher potential for fast combustion modes than those with H_2 release into an open environment. In mobile applications all accident situations with restricted possibilities of hydrogen dispersion therefore are of special concern:

- Parking in a residential or public garage
- Collision-induced H_2 release in a tunnel
- Hydrogen leak from a car in a ferry
- Accidents underneath bridges or in narrow street canyons

Other topics which may require special safety investigations in the future are vandalism and neglect/misuse of hydrogen vehicles and equipment.

9.5.2 Safety Issues for Refuelling Stations

The most recent and comprehensive European effort to analyse the safety of hydrogen refuelling stations was undertaken within the EU-funded HyApproval project [24]. This project combined expertise from petrochemical industry, suppliers of hydrogen filling station equipment, research organisations, and licensing authorities. In the following sections, a summary shall be given as concerns the main open questions and issues connected with the installation of hydrogen refuelling stations in urban areas. The final results of the HyApproval project will be published in early 2008.

9.5.2.1 Accident Scenarios

Figure 9.22 displays a schematic diagram of the main components of a hydrogen filling station with supplies of compressed gaseous hydrogen (CGH_2) and liquid hydrogen (LH_2). In this design a reformer and an electrolyser are included for on-site production of gaseous hydrogen. The cost scaling and the technical complexity of LH_2 production favour a centralised large LH_2 plant and the delivery of LH_2 by trailers to the filling station.

For each sub-system of the filling station, potential accident scenarios were identified at the beginning of the project. Possible leak sizes were classified into very small, small, medium, and large size, which corresponds to leakage from the gland

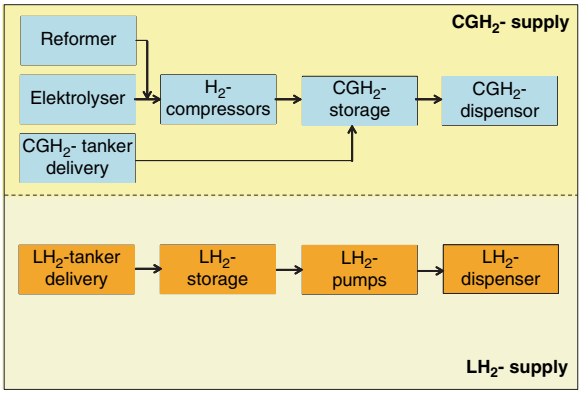

Fig. 9.22 Main components of a hydrogen filling station with supply lines for compressed gaseous hydrogen (CGH_2) and liquid hydrogen (LH_2)

packing of valves, crack or pinhole, partial opening of a valve, and rupture of a storage vessel [25, 26]. Hazards and accident scenarios were identified for each of the filling station components. Some examples are given below concerning the line delivering compressed gaseous hydrogen.

1. *Reformer inside closed container*:

   – leakage or rupture of the natural gas feed line,
   – rupture of the reforming tube,
   – pipe rupture due to hydrogen-induced embrittlement,
   – rupture of a hydrogen pipe,
   – leakage or burst of the H_2 line to the compressor.

The main safety barriers which can be used to protect structures and personnel are

   – ventilation inside the container,
   – detectors for natural gas and hydrogen combined with an isolation system,
   – venting surfaces on the container,
   – restricted access to the container,
   – regular inspection of the reformer installation.

2. *Electrolyser inside closed container*:
   Accident scenarios are related to the hazardous substances of lye and hydrogen.

   – Lye leak through cells due to overpressure or gasket failure, leading to explosion or jet flame inside the container,
   – lye leakage from pipes,
   – oxygen leak inside the container, leading to fire enhancement,
   – hydrogen leak inside the container, leading to explosion or jet fire,
   – large H_2 ingress into container by backflow of H_2 from the storage vessel.

The main safety barriers in this case are

- preventing a mixture of H_2 and O_2 inside the electrolyser,
- H_2 and O_2 detectors with an isolation system for up- and down-stream direction,
- venting surfaces on the container,
- restricted access to the container,
- regular inspection of installation.

3. *Compressor inside container*:
   Hydrogen is pressurised by a compressor from about 10 to several 100 bar. Since the compressor is connected to high-pressure buffer tanks, leakage and back-flow from the buffer tanks are important scenarios. Further unwanted events are excessive pressure at the compressor outlet, compressed air ingress into the hydrogen line, leakage of hydrogen due to vibrations.

   As possible safety barriers, pressure control, vibration control, hydrogen detection, and forced ventilation were identified.
4. *Buffer storage in open air*:
   The buffer storage contains the major hydrogen inventory handled in the refuelling station. The main hazardous phenomena are hydrogen leaks with subsequent explosion or jet fire and bursting of hydrogen pressure vessels due to mechanical or thermal loads. Due to the high pressures and volumes of H_2 bottles, a burst would also create a large mechanical energy release. No sufficient data are currently available to predict whether bursting of one bottle would trigger the failure of others bottles in the bundle. The simulation of hydrogen release from a high-pressure storage system can be found elsewhere [27].

   The main safety barriers against such scenarios are the ability to limit hydrogen leak rates, to isolate a leaky storage bottle, and to discharge the hydrogen inventory in a safe way. Moreover, the bottles must be safely vented in case of fire.
5. *Dispenser in open air*:
   The dispenser consists of the refuelling unit and the dispenser hose. The dispenser is generally covered by a weather protection shield. The use of a flexible hose and the connection/disconnection actions with the car significantly increase the probabilities of a hydrogen leak or a line rupture. One scenario of many others is the leakage at the filling nozzle due to the deterioration of the isolation valve [25]. Other unwanted events are hose rupture during/after refuelling and backflow from the vehicle tank. The dispenser scenarios are critical for the whole safety evaluation of the filling station, because customers are involved and located close to the release location. This scenario was investigated experimentally by Tanaka et al. [28] and Takeno et al. [29]. Results from tests with premixed H_2-air clouds and H_2 jet releases can be found in [30].

   Possible precautious and safety barriers are hydrogen leak detection before connection, good nozzle and hose maintenance. Furthermore, an automatic filling procedure can be envisaged, where the customer is not involved and where an emergency shutdown procedure is implemented with well-defined actuation criteria.

6. *CGH_2 tanker delivery in open air*:
   Instead of on-site production, CGH_2 could also be delivered to the filling station by a CGH_2 cylinder truck. This operation involves the transfer of large quantities of hydrogen at high pressures. For a 700 bar filling station, the delivery pressure must be well above 1000 bar to obtain a reasonable discharge time and discharge fraction. Important accident scenarios are the leakage of hydrogen from the trailer hose, hose failure during refilling, or leakage after decoupling from the station side.

   Important safety barriers in this case are hydrogen leak detection before, during, and after tanker connection, loading of the storage tanks in a separately protected area, and emergency shut-down procedures.

9.5.2.2 Risk Assessment

After identification of possible initiating events and accident scenarios, the next task is to quantify the risk connected with each event and to identify the dominating risk contributors. The EU project HyApproval uses two methodologies which are probabilistic risk assessment and computational fluid dynamics (CFD) calculations. These methods complement each other by providing information on different levels of detail.

The first stage of the standard risk assessment approach is hazard identification. Its objective is to identify the major hazards that could contribute significantly to the risk caused by the refuelling installation. Then, the frequencies and consequences of the hazards are calculated. These are combined (often by a multiplication) to derive a measure of the risk of each hazard. Next, the obtained risk is compared with an acceptance criterion to decide whether this risk is acceptable or not. If not, risk-reducing countermeasures by both technical and operational improvements must be investigated.

For the leading risk contributors, it is necessary to obtain more detailed information on fire and explosion hazards which may affect station personnel or customers mainly by heat radiation and pressure waves. In the EU project HyApproval credible accident scenarios were selected for CFD simulations, which are based on experience gained by gas industry [31]. These include CGH_2 dispenser failures at 35 and 70 MPa, CGH_2 tanker discharge hose failure at 25 MPa, and LH_2 dispenser failure at 3–8 bar. A complete list of the selected accident scenarios can be found in [31]. It should be noted that some of the scenarios given in the Chap. 19.1 are considered to be too improbable like the catastrophic failure of a CGH_2 buffer storage vessel. Therefore, no CFD simulation will be made for such a case.

9.6 Outlook

Additional research activities will be needed in order to improve the knowledge and, in turn, mitigate the above potential hazards from the use of hydrogen in vehicle operation and in infrastructure installations. General issues which are largely

independent of the specific vehicle design will be addressed. It would be very convincing, if these topics could be resolved by the automobile community in a joint effort to generate internationally accepted and harmonised hydrogen safety standards and procedures.

Issues related to the development of safe fuel cell cars can be found in [32]. With respect to vehicle safety, the following research topics will deserve closer attention in the future:

- safe venting of compressed hydrogen gas cylinders (350 and 700 bar),
- optimum arrangement of H_2 storage vessels in the vehicle,
- fire safety of hydrogen-powered vehicles with the primary goal to prevent bursting of the high-pressure hydrogen system,
- guidelines for fire fighters in case of fire or accident,
- optimum number and location of hydrogen detectors,
- safety concept in case of a hydrogen leak detection in a running car,
- tolerable H_2 leak rates in the vehicle for different operating conditions, including a parked car,
- optimum position and activation criteria for pressure relief devices on the H_2 tank,
- procedures to prevent penetration of hydrogen into the passenger compartment,
- effectiveness of forced ventilation for reducing local H_2 concentrations in sensitive car areas,
- maximum possible reduction of ignition sources,
- development of standardised safety test procedures for new solid storage materials, such as nanocrystalline powders.

Safety investigations for hydrogen infrastructure installations like maintenance, service, repair, and filling stations should address the following research topics:

- determination of tolerable H_2 releases during vehicle repair, which pose no risk to the personnel,
- design of effective and low-cost ventilation systems,
- CFD analysis of leaking hydrogen scenarios, including complex surroundings near the vehicle, extension of the investigations described in [33],
- control of ignition sources,
- in case of filling stations, the issues of protecting walls and safety distances need to be investigated.

More basic research is also needed to further improve the current knowledge of hydrogen properties:

- measurement of ignitable space regions, given a certain leak size, shape, and mass flow rate, an extension of the work described in [34],
- systematic investigation of active and passive safety systems, e.g. ventilators, catalytic recombiners, or flame arrestors,
- modelling of ignition processes under realistic boundary conditions,
- investigation of diffusion flame stability after ignition (limits for lift-off and extinction),

– criteria for flame acceleration and detonation onset in H_2-air mixtures with concentration gradients and partial confinement (Note: the criteria described in Sect. 9.3.2 are valid for homogeneous and fully confined mixtures; they are, hence, very conservative with respect to practical accident conditions in mobile applications and should be extended to more prototypic conditions).

References

1. M. Hattwig, H. Steen (Eds.), Handbook of Explosion Prevention and Protection, Wiley-VCH Verlag Weinheim, 2004, ISBN 3-527-30718-4.
2. A. Veser, J. Grune, G. Stern, W. Breitung, S. Dorofeev, Flame acceleration in a vented explosion tube, 19th Int. Coll. On the Dynamics of Explosions and Reactive Systems (ICDERS), Hakone, July 27–August 1, 2003, Paper 183, Proc. on ROM.
3. A.M. Kreiser, G. Fröhlich, M. Eichert, A. Schatz, Analyse von Störfällen mit Wasserstoff in bisherigen Anwendungsbereichen mit besonderer Berücksichtigung von LH2, Report IKE 2-116, Universität Stuttgart (April 1994).
4. R.G. Zalosh, Comparative Analysis of Hydrogen Fire and Explosion Incidents, Report COO-4442-1, Factory Mutual Research Corporation, Norwood, Massachusetts, USA (December 1977).
5. W. Breitung, U. Bielert, G. Necker, A. Veser, F.-J. Wetzel, K. Pehr, Numerical Simulation and Safety Evaluation of Tunnel Accidents with a Hydrogen Powered Vehicle, Proc. of the 13th World Hydrogen Energy Conference, June 12–15, 2000, Beijing, China, Vol. 2, pp. 1175–1181.
6. J.R. Travis, P. Royl, R. Redlinger, G. Necker, J.W. Spore, L.L. Lam, T.L. Wilson, B.D. Nichols, C. Müller, "GASFLOW-II: A Three-Dimensional Finite-Volume Fluid Dynamics Code for Calculating the Transport, Mixing, and Combustion of Flammable Gases and Aerosols in Geometrically Complex Domains", Vol. 1, Theory and Comp. Manual, Vol. 2, Users Manual, Reports FZKA-5994, LA-13357-MS (1998).
7. W. Breitung, W. Baumann, U. Bielert, B. Burgeth, S. Dorofeev, B. Kaup, A. Kotchourko, G. Necker, R. Redlinger, P. Royl, J. Starflinger, G. Stern, J.R. Travis, A. Veser, Z. Xu, Innovative Methoden zur Analyse und Kontrolle des Wasserstoffverhaltens bei Kernschmelzunfällen, Report FZKA 7085, Forschungszentrum Karlsruhe Germany (February 2005), available in full text under www.fzk.de/hbm (free search).
8. S.B. Dorofeev, M. Kuznetsov, V. Alekseev, A. Efimenko, W. Breitung, Evaluation of limits for effective flame acceleration in hydrogen mixtures, Journal of Loss Prevention in the Process Industries 14, 2001, pp. 583–589.
9. S.B. Dorofeev, A. Kotchourko, S.B. Chaivanov, Detonation Onset Conditions in Spatially Non-Uniform Combustible Mixtures, Proc. of the 6th Int. Symposium on Loss Prevention and Safety Promotion in the Process Industries, 1989, Oslo, Vol. 4, pp. 22–21.
10. S.B. Dorofeev, V.P. Sidorov, M.S. Kuznetsov, I.D. Matsukov, V.I. Alekseev, Effect of scale on the onset of detonations, Shock Waves 10, 2000, pp. 137–149.
11. A. Gavrikov, A. Lelyakin, W. Breitung, S. Dorofeev, Calculation of Detonation Cell Sizes for Hydrogen-Air-Steam Mixtures at ITER Typical Pressures, Forschungszentrum Karlsruhe, Germany, Report FZKA 6812 (2003).
12. M. Kuznetsov, A. Lelyakin, S. Dorofeev, Flammability Limits for Nuclear Safety Applications, Report of Kurchatov Institute, prepared for FZK-IKET (1999), and A. Lelyakin, A. Gavrikov, S. Dorofeev. A Computer Code Package to Calculate Explosion Properties of Hydrogen Combustibles, Report of Kurchatov Institute, prepared for FZK-IKET, Moscow (2001).

13. W. Breitung, Analysis Methodology for Hydrogen Behaviour in Accident Scenarios, Proc. Int. Conf. on Hydrogen Safety, September 8–10, 2006, Pisa, Italy.
14. W. Breitung, G. Necker, B. Kaup, A. Veser, Numerical Simulation of Hydrogen Release in a Private Garage, Proc. of the 4th Int. Symposium on Hydrogen Power – HYPOTHESIS IV, September 9–14, 2001, Stralsund, Germany, Vol. 2, p. 368.
15. W.E. Baker, P.A. Cox, P.S. Westine, J.J. Kalesz, R.A. Strehlow, Explosion Hazards and Evaluation, Elsevier Publ. Co., Amsterdam, 1983, p. 596.
16. S.B. Dorofeev, Blast Effects of Confined and Unconfined Explosions, Proc. 20th Symposium (Int.) on Shock Waves, July 1995, Pasadena, California, USA, pp. 77–86.
17. D.R. Richmond, E.R. Fletcher, J.T. Yelverton, Y.Y. Phillips, Physical correlates of ear drum rupture, Annals of Otology, Rhinology & Laryngology 98, 1989, pp. 35–41.
18. NASA Office of Safety and Mission Assurance, Safety Standard for Hydrogen and Hydrogen Systems, Report NSS 1740.16 (1997).
19. C.E. Thomas, Direct-Hydrogen-Fueled Proton-Exchange-Membrane Fuel Cell System for Transport Applications, Report by Ford Motor Comp. Dearborn, MI, USA, for US-DOE, Report DOE/CE/50389-502 (May 1997).
20. J.T. Ringland, Safety Issues for Hydrogen-Powered Vehicles, Report SAND94-8226, Sandia Natl. Laboratories Livermore Cal., USA (March 1994).
21. L.C. Cadwallader, J.S. Herring, Safety Issues With Hydrogen as a Vehicle Fuel, Report INEEL/EXT-99-00522 (September 1999).
22. K. Pehr, Experimental Examinations on the Worst Case Behaviour of LH2/LNG Tanks for Passenger Cars, Proc. 11th World Hydrogen Energy Conference, June 23–28, 1996, Stuttgart, Germany, Vol. 3, p. 2169.
23. J.-M. Vernier, C. Müller, S. Fürst, Safety Measures for Hydrogen Vehicles with Liquid Storage, Proc. of 16th World Hydrogen Energy Conf., June 13–16, 2006, Lyon, France.
24. HyApproval internet page: www.hyapproval.org.
25. S. Lim, L. Perrette, Risk Assessments and Accident Simulations as per Matrix Table, Report by INERIS, HyApproval Deliverable WP4, ST3 (October 2006), www.hyapproval.org.
26. L. Perrette, S. Lim, Proposed List of Scenarios for the Modelling Task, Report INERIS HyApproval Deliverable WP4, 4.X (June 2006), www.hyapproval.org.
27. B. Angers, P. Bènard, A. Hourri, P. Tessier, J. Perrin, Simulations of Hydrogen Releases from High Pressure Storage Systems, Proc. of 16th World Hydrogen Energy Conf., June 13–16, 2006, Lyon, France.
28. T. Tanaka, T. Azuma, J.A. Evans, P.M. Cronin, D.M. Johnson, P. Cleaver, Experimental Study of Hydrogen Explosions in a Full-Scale Hydrogen Filling Station, Proc. Int. Conf. on Hydrogen Safety, September 8–10, 2005, Pisa, Italy.
29. K. Takeno, K. Okabayashi, A. Kouchi, T. Nonaka, K. Hashiguchi, K. Chitose, Phenomena of Dispersion and Explosion of Highly Pressurized Hydrogen, Proc. Int. Conf. on Hydrogen Safety, September 8–10, 2005, Pisa, Italy.
30. L.C. Shirvill, P. Roberts, C.J. Butler, T.A. Roberts, M. Royle, Characterization of the Hazards from Jet Releases of Hydrogen, Proc. Int. Conf. on Hydrogen Safety, September 8–10, 2005, Pisa, Italy.
31. Report by Shell Hydrogen, Establishment of Best Practices for Safety; HyApproval Deliverable 4.2 (November 2006), www.hyapproval.org.
32. L. Perrette, H. Paillère, G. Joncquet, Presentation of the French National Project DRIVE, Proc. of 16th World Hydrogen Energy Conference, June13–16, 2006, Lyon, France.
33. Technical report for California Fuel Cell Partnership (CaFCP), Support Facilities for Hydrogen-fueled Vehicles. Conceptual Design and Cost Analysis Study (July 2004), info@cafcp.org.
34. M. Swain, Codes and Standards Analysis DE-FC36-00GO 10606, A007, Final Technical Report 04/15/03–04/14/04, Univ. of Miami, Coral Gables, Florida, USA.

General recommendation for further literature: Extensive literature on all aspects of hydrogen safety can be found in the US-DOE database: www.hydrogen.energy.gov/biblio_database.html.

Part III
State of the Art Portable Applications

Chapter 10
Introduction

Aline Léon

Portable fuel cells have the potential to increase the energy density by a factor of 3–10 compared to presently used lithium ion batteries. Moreover, recharging is not needed and the requirements of 'green electronics' are met. However, the 'classical' fuel cell approach known for large-power automotive and stationary applications is not suitable for portable applications. Therefore, a new approach to micro fuel cell development is necessary. A major challenge in this new technology is to miniaturize the different parts of a portable fuel cell as well as the water management. It comprises the fuel cell stack which is the core of the system, the fuel tank which is related to the runtime of the device, and the balance of plant which includes all peripheral components that support the power generation process.

Part III of this book will outline the state of the art of portable applications. After a review of existing technologies for portable applications (batteries, photovoltaic portable modules, and portable fuel cell), the performances of the Li ion battery and portable fuel cell will be compared. Then, the development of the direct liquid fuel cell and PEM fuel cells will be considered. Finally, the industry point of view will be outlined by analyzing the direct methanol fuel cell.

Aline Léon
Institut für Nanotechnologie, Forschungszentrum Karlsruhe, P.O. Box 3640, D – 76021 Karlsruhe, Germany, e-mail: aline.leon@int.fzk.de

A. Léon (ed.), *Hydrogen Technology*,

Chapter 11
Status of Existing Technologies

Robert Hahn

List of Abbreviations

C-rate	Charge/discharge rate of secondary batteries, 1C = 1 h full charge/discharge
PVDF	Polyvinylidene fluoride
hv	Photon energy, h-Planck constant, v frequency
E_{gap}	Band gap energy of a semiconductor
I_{ph}	Photo current
PCB	Printed-circuit board
FR4	Flame-resistant 4, substrate material for PCB
BOP	Balance of plant
MEA	Membrane electrode assembly
GDL	Gas diffusion layer
DMFC	Direct methanol fuel cell
PEM	Polymer electrolyte membrane

Robert Hahn
Fraunhofer-Institut Zuverlaessigkeit und Mikrointegration (IZM), Gustav-Meyer-Allee 25,
D-13355 Berlin, Germany, e-mail: robert.hahn@izm.fraunhofer.de

A. Léon (ed.), *Hydrogen Technology*,

11.1 Batteries

Primary and secondary batteries are well-established power supply technologies for portable applications. For many decades, only two or three chemical systems have dominated the market and by now, a diversification with new applications specified and novel chemical systems is emerging. Still, there is a lot of on-going development and improvement in battery industry, although the energy density increases by some percent per annum only and not by orders of magnitude. In general, battery industry has adapted smaller devices with a high power and energy demand to the market requirements within the limits of chemical storage capabilities. A significant research effort is the increase of power density of primary and secondary systems.

11.1.1 Existing Power and Energy Density

Nowadays, alkaline primary cells have the biggest market volume of 40 billion $ compared to 400 million $ of secondary batteries. However, alternatives to alkaline cells are emerging on the market, such as Ni-MH and other systems like the Energizer primary $LiFeS_2$ system, which allow for a higher current drain. Another example is Duracell that introduced a Ni/Zn primary system in 2006, which has the same characteristics than the alkaline battery.

The lithium-ion batteries are currently one of the most popular types of battery for portable electronics with one of the best energy-to-weight ratios, no memory effect, and a slow loss of charge when not in use. The cellular phone market with a required capacity of around 850 and 1100 mAh was one of the biggest markets for this type of battery in 2006 with about 800 million handsets. Despite the success of Li-ion batteries, the Ni-MH secondary batteries are still prevailing, as their energy density increases every year by 5–10% with a special trend to using nano-scale materials.

For most of the chemical systems, there are several versions on the market, which are currently being optimised for high energy or for higher power. Table 11.1 shows some average values of energy and power density of the most prominent battery systems.

The nickel-cadmium (NiCd) system is a mature and well-understood battery. Its energy density is lower compared to NiMH and Li-ion batteries. So far, it has been the battery type with the highest possible discharge rate. However, due to the high material fraction of Cd, the usage of this battery is restricted to special applications. Unlike other rechargeable batteries, the NiCd battery prefers fast charge (up to 10C) to slow charge (0.1C) and pulse charge to continuous charge. Because of the ‘memory’ effect, the NiCd battery has to be fully discharged from time to time.

The nickel-metal hydride battery (NiMH) has a higher energy density compared to NiCd at the expense of a reduced cycle life. In contrast to the NiCd battery, NiMH

Table 11.1 State of the art of primary and secondary batteries for portable electronics. Energy density as function of power density

	High energy		High power	
	(Wh/l)	(W/l)	(Wh/l)	(W/l)
Primary batteries (not rechargeable)				
Zn/carbon	140	20	80	100
Alkaline	470	50	160	180
Li-ion	**500**	**200**	**250**	**900**
NiOOH	400	150	200	350
$LiFeS_2$	**500**	**200**	**400**	**420**
Secondary batteries (rechargeable)				
HE Li-ion	550	200	300	900
HP Li-ion	350	600	250	>1000
Ni/MH	350	400	300	800
Ni/Cd	–	–	200	>1000

does not contain any toxic metals. On the other hand, utilization of high quantities of Ni is not unproblematic from an environmental point of view. A possible disadvantage of NiMH and NiCd batteries regarding several applications is the low cell voltage of 1.2 V. Therefore, at least two cells are required in most applications.

The lithium-ion battery (Li-ion) is increasingly used in portable electronics applications, since it has the highest energy density. The Li-ion batteries must follow strict guidelines to ensure safety when charging. The voltage typically is 3.6–4 V (open circuit voltage). Special Li battery chemistries were developed for high-current applications like power tools. The energy density of Li-polymer batteries is comparable with that of the Li-ion. Li-polymer batteries allow for a very slim design (up to 1 mm). They are packaged in a so-called pouch or coffee bag package, which is important to the overall mass. High-current Li-polymer batteries are available.

In general, the difference in energy density of the mentioned battery systems is lower at high power levels than at low power drain.

The low-current drain system of most used batteries is of a coin type. In a coin-type battery the active masses of anode and cathode are filled into a metal cup and a metal cover, respectively, in the form of powder or pastes in order to provide the two electrical contacts to the outside. Both parts are separated by a separator and joined by means of a polymer sealing ring. Table 11.2 shows the characteristics of several coin-type batteries. As can be seen, Zn air batteries have the highest energy density, but the life time is very short. Hence, small Zn air batteries are only used for hearing aids.

In general, the energy density of small coin-type cells of the same chemical system is much lower compared to cylindrical or prismatic cells, due to the volume fraction of the metallic casing.

In the sections below the focus will be on the lithium-based rechargeable batteries, as they provide one of the best energy/ weight ratios of rechargeable batteries at present.

Table 11.2 Examples of primary and secondary coin-type cells

Type	System	Dimension (dm × h) [mm]	Voltage [V]	Capacity [mAh]	Energy density [mWh/cm^3]
Primary coin cells					
P675	Zn air	11.6 × 5.4	1.4	570	1400 [a]
CR1220	Li	12.5 × 2.0	3	35	430 [b]
CR1216	Li	12.5 × 1.6	3	27	410 [b]
V 12GA	Alkaline	11.6 × 2.1	1.5	25	170 [c]
Secondary coin cells					
ML1220	Li	12.5 × 2	3	16	200 [d]
MC 621	Li	6.8 × 2.15	3	3	115 [e]
V 6HR	Ni/MH	6.8 × 2.15	1.2	6.2	95 [f]
V 40H	Ni/MH	11.5 × 5.35	1.2	43	90 [g]
MC 614	Li	6.8 × 1.4	3	1.5	90 [h]

Source: data sheets of Panasonic, Sanyo, Varta.

11.1.2 Lithium-based Rechargeable Battery

Lithium-based rechargeable batteries are used in very high volumes in applications, such as mobile phones, laptops, cameras, and other consumer electronics products. They have many attractive performance advantages which make them ideal for higher-power applications, e.g. automotive and standby power. At the moment, there is a strong trend for Li-ion batteries to enter the power tool market.

11.1.2.1 Description

Two kinds of lithium-based secondary batteries are available on the market. **LITHIUM-ION batteries** are widely used in the portable equipment market. Such a battery consists of lithium metallic oxide ($LixCoO_2$, $LiNiO_2$, $LiMnO_4$) in its positive electrode (cathode) and carbon material ($LiXC_6$) in its negative electrode (anode), with an electrolyte like $LiPF_6$, $LiAsF_6$ etc, ... The principle shown in Fig. 11.1 is that lithium ions inside the battery move between the positive electrode and the negative electrode during charge or discharge, i.e. rocking chair batteries (RCB). A polymer separator made of polyalkene, such as polypropylene or polyethylene, prevents an electronic short circuit.

LITHIUM-ION POLYMER rechargeable batteries are similar to the lithium-ion batteries, but with a solid polymer as electrolyte. Some gelled ionically conductive material is added to promote conductivity. Lithium-ion polymer batteries use liquid lithium-ion electrochemistry in a matrix of conductive polymers that eliminate the free electrolyte from the cell. The polymer matrix is based on modified PVDF (polyvinylidene fluoride) homopolymer or copolymer. For operating effectively over a broad range of temperatures and conditions, lithium-ion polymer batteries do not contain any metallic lithium anodes.

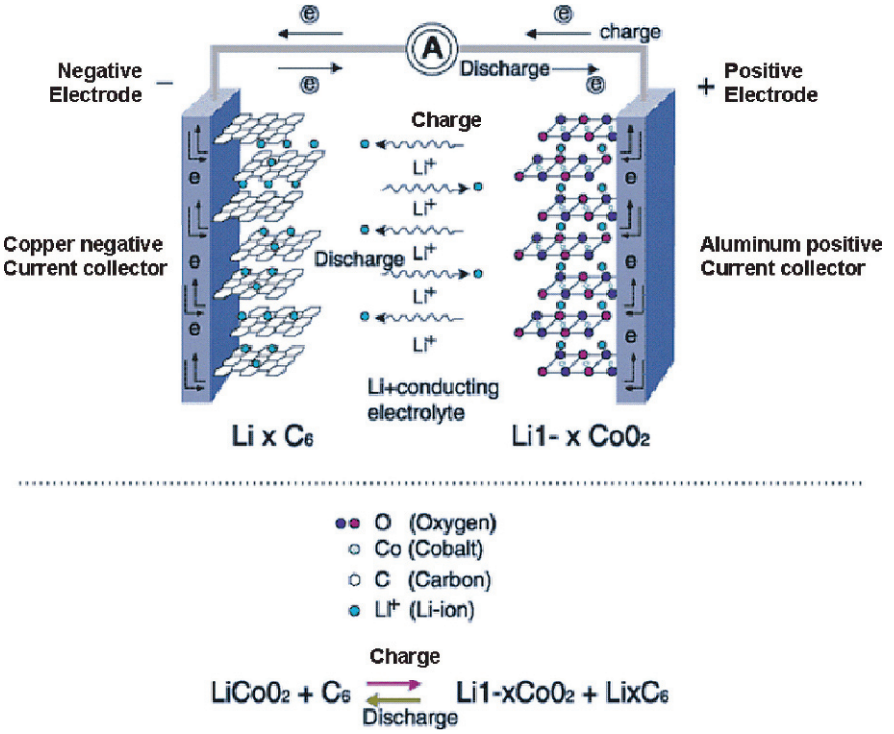

Fig. 11.1 Principle of a Lithium-ion battery

The charge/discharge duration of secondary lithium batteries is determined mainly by the internal resistance of the cell. High-power batteries for special applications are available. A fast charge step can be done in 10…15 min. High-power optimised batteries have a lower overall energy density because of the higher amount of current collector materials to yield a low internal resistance.

Lithium-ion batteries can reach a life time (80% of the initial capacity remaining) of about 500 full charge/discharge cycles with conventional anodes. By using special anode material (lithium titanate instead of graphite), more than 1200 cycles can be reached. The self-discharge is in the range of 3 … 5% per month. The life cycle, self–discharge, and cell degradation depend strongly on the ambient temperature and the current profile.

Safety is a very important issue for Li-ion and Li-polymer batteries. Electronics can be used to keep the batteries within a certain range, where they can be used safely. For the system to operate within a safe voltage and current range only, safety electronics is used. This electronics opens the circuit in the following case:

- overvoltage (e.g. >4.30 V)
- undervoltage (e.g. <2.50 V)
- overcurrent (e.g. >3 A)

Basic circuits include a safety IC, a double mosfet, and some few resistors and capacitors. The most important task of an Li-ion and Li-polymer cell is to avoid an overcharge situation. Above around 4.8 V, the cell runs into an unstable situation, where the cell temperature may get out of control, which may result in fire and explosion.

Lithium-ion batteries have a nominal open-circuit voltage of 3.6 V and a typical charging voltage of 4.2 V. Due to the high cell voltage and the high volumetric energy density, intercalation materials, such as lithium carbon and lithium cobalt oxide, are commonly used for the anode and the cathode, respectively. However, the capacity density of the cathode electrode is much lower compared to the anode electrode. Hence, alternative cathode materials with a higher capacity density like lithium manganese oxide, lithium cobalt oxide, lithium nickel cobalt oxide or lithium phosphate-oxy-nitride are used. The direct consequence is an increase of the energy density. As an example, Fig. 11.2 displays the evolution of the energy density of the Panasonic 18650 Li-ion cylindrical cell during the last years. As can be seen, the energy density doubled in a ten-years period.

Nevertheless, there still is a great demand for alternative materials. Research is under way to introduce new materials for anode and cathode, non-flammable electrolytes, and nanomaterials. High-power designs are developed continuously as well as new charging profiles and charging technologies.

Safety remains a challenge for both high-power and high-energy designs and there is an ongoing research to develop alternative Li-ion chemistries that would be safe. An alternative is the lithium polymer technology [2, 3] which uses the safe salt $LiPF_6$ instead of $LiClO_4$ for shut-down separators and electrolytes. Thus, a high safety level is reached for high-energy batteries.

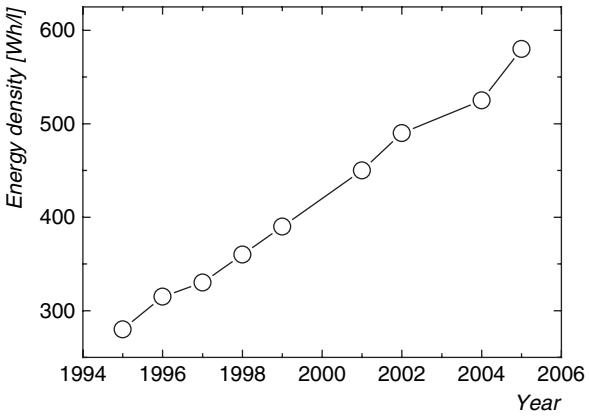

Fig. 11.2 Volumetric energy density of the Panasonic 18650 Li-ion cylindrical cell over ten years [1]

11.1.2.2 Why Lithium?

Lithium is the third lightest element, giving a substantial saving in weight compared to batteries using much heavier metals. The strength of Li-ion chemistry is the high open-circuit voltage in comparison to aqueous batteries (such as lead acid, nickel metal hydride, and nickel cadmium). Due to the very high energy density (in practice 3.4 Ah/g is reachable), lithium also is the material of choice for high-energy cells. Table 11.3 lists the most frequently used battery materials and their theoretically reachable energy density. However, it is not possible to use pure Li as cell anode in a practical rechargeable battery. The reason is that the deposition of metallic Li during charging is possible for very thin layers only. Instead, graphite is used as intercalation anode with an atomic ratio between Li and C of 1:6, the energy density being reduced by a factor of about ten. On the other hand, the overall energy density is much more determined by the cathode than by the anode, as shown in Table 11.3. Concerning the cathode side, LiCoO2 has the highest energy density. Moreover, thermal stability and, hence, the safety of $LiMn_2O_4$ is much higher, but only at a lower capacity. Safety and energy density were optimised by mixing several cathode alloys [1]. It should be emphasised that the values which are given in Table 11.3 are the theoretical maximum values for these materials. For further improvement new materials which use a lower molecule mass (for example, less C at the anode) have to be discovered. The practical energy density will always be lower than the given values, since the polymer binder, separator, electrolyte, current collectors, and packaging add to the weight and volume.

Of the materials developed for the cathode electrode, Ni-Mn-based material and nanomaterials with olivine structure are most promising. They are summarized in Table 11.4 and will be described briefly below:

11.1.2.2.1 Mn- or Ni-based New Cathode Material

Recently, Panasonic developed the “PSS“ system (Panasonic Solid Solution) [1] which is characterised by a high stability (for safety and reliability) with a decomposition temperature similar to $LiMn_2O_4$ (325°C). This battery will be used especially in applications, where high operation temperatures and safety are major concerns, like in medical devices.

A novel $LiNiO_2$ (F-type) system was developed for high capacity demands. Indeed, the capacity of cylindrical cells was increased to nearly 600 W/l with a similar safety level than $LiCoO_2$.

11.1.2.2.2 Fe Olivine Structures

Nanomaterials are currently being investigated in order to further increase the current density. It has been found that cathode materials with an olivine structure are

Table 11.3 Electrode materials of Li-ion secondary batteries: theoretically reachable energy densities

	Molar mass [g/mol]	No. of intercalated Li atoms	Level of intercallation	Single electrode capacity density		Capacity density [mAh/g]	Energy density [mWh/g]
				[As/g]	[mAh/g]		
Anode Li (metal)	6.9410	1	100%	13900.78	3861.33		
Anode $Li_{(0...1)}C_6$	12.0107	6	100%	1338.88	371.91		
Cathode $Li_{(0.4...1)}CoO_2$	97.8730	1	60%	591.49	164.30	114.0	410.3
Anode $Li_{(0...1)}C_6$	12.0107	6	100%	1338.88	371.91		
Cathode $Li_{(0.5...1)}Ni_{0.8}Co_{0.2}O_2$	97.6812	1	50%	493.88	137.19	100.2	360.8
Anode $Li_{(0...1)}C_6$	12.0107	6	100%	1338.88	371.91		
Cathode $Li_{(0.4...1)}Mn_2O_4$	180.8147	1	60%	320.17	88.94	71.8	208.1

Source: Values were calculated according to the atomic mass and the Faraday's law. A mean discharge voltage of 3.7 V was assumed for energy density, source Fraunhofer IZM.

Table 11.4 Comparison of Li secondary battery cathode materials

Materials	Safety	Capacity density
$LiMn_2O_4$	high	low
$LiCoO_2$	medium	medium
$LiNiO_2$	medium	high
$LiNiMnCoO_2$ (PSS)	high	medium

Source: Matsushita

suitable for a better lithium intercalation [4]. $LiFePO_4$ with olivine structure belongs to the family of NASICON-type compounds (NASICON – sodium super-ionic conductor) that are known to be fast ionic conductors and used as solid electrolytes in electrochemical cells. In $LiFePO_4$ the hexagonal close-packed lattice of oxygen has a two-dimensional channel network that may act as fast diffusion paths for lithium ions. In addition, $LiFePO_4$ has the highest theoretical capacity of all known cathode materials (170 mAh/g) and the highest thermal stability, which guarantees safe use and stable capacity after numerous work cycles.

Indeed, with a crystallite size in the range of $\sim 10^{-9}$ m, high-current/high-power batteries can be achieved. Thus, the diffusion length within the bulk material is dramatically reduced due to the high surface area of the active material. As a result, power density is increased.

At the moment, lithium titanate ($Li_4Ti_5O_{12}$) is a promising alternative material for the negative electrode. This material has a better cycle stability than conventional mixed graphite anodes. Optimised active materials, such as nanoparticles of $Li_4Ti_5O_{12}$ with olivine structures as cathode intercalation matrix, can be used to reduce the bulk diffusion and, hence, increase the ability to operate at high current peaks.

11.1.2.3 Fast Charge Method

The traditional charging procedure is one of constant current with voltage limiting. This means charging with constant current until a voltage of 4.2 V is reached by the cell and continuing with a constant voltage until the current drops close to zero (typically, the charge is terminated at 7% of the initial charge current).

In contrast to the conventional constant current – constant voltage charge systems with an optimal charge time of about two hours, Sanyo has developed a novel quick charge technique [5] for lithium-ion batteries, which is based on a pulse charge system. This shortens the charge time to less than 90 min. The system accomplishes this quick charge operation by constantly monitoring the battery voltage and fine controlling the charge profile, such that 4.2 V/4.1 V (charge voltage with battery) is not exceeded. Based on the fact that the voltage drop within a battery pack increases with a greater charge current, an optimal compensation value is determined in accordance with the specific type of battery, charge current level, and circuit configuration of the charger.

11.1.3 Wafer-level Batteries

Another development relates to very thin micro batteries [6, 7, 8, 9] which are even smaller than coin-type cells. Several companies are working on thin-film batteries using many of the same techniques to create integrated circuits, such as sputtering and reactive vapour deposition. Most of these systems are based on Li chemistry. They may be used in smart cards, active smart lables, medical implants, and others. An example is the thin-film battery of Bates et al. [7], which is a true solid-state battery with unique temperature characteristics and quick charge.

However, there are several concerns with thin-film batteries. First, the deposition processes for these products are very expensive and the performance improvements may justify the higher prices. Second, the capacity is rather low, because very thin layers of active material only can be deposited due to mechanical integrity. As an alternative, Fraunhofer IZM developed the so-called wafer-level battery [9], where battery laminates are assembled on a silicon wafer and then encapsulated with the help of thin-film processing. Battery laminates from Li-polymer mass production can be used for this technology. Thus, costs are relatively low. Figure 11.3 displays the arrangement of 12 small batteries of $9 \times 9 \times 0.16\,\mathrm{mm}^3$ in size on a test wafer. The charge/discharge characteristics of this type of battery have been found to be similar to those of the prismatic or cylindrical Li-ion cells as can be seen in Fig. 11.4.

Finally, no battery design is perfect for every application. Choosing a design requires a compromise regarding the performance parameters of the battery. In Table 11.5 properties of small battery types are listed for comparison and to illustrate the different advantages and disadvantages.

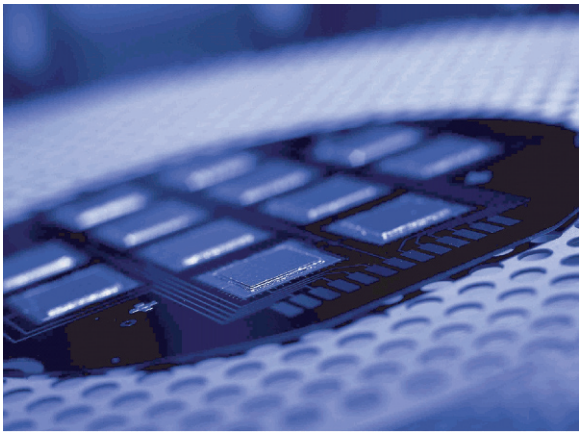

Fig. 11.3 Wafer-level batteries, *Source*: Fraunhofer IZM

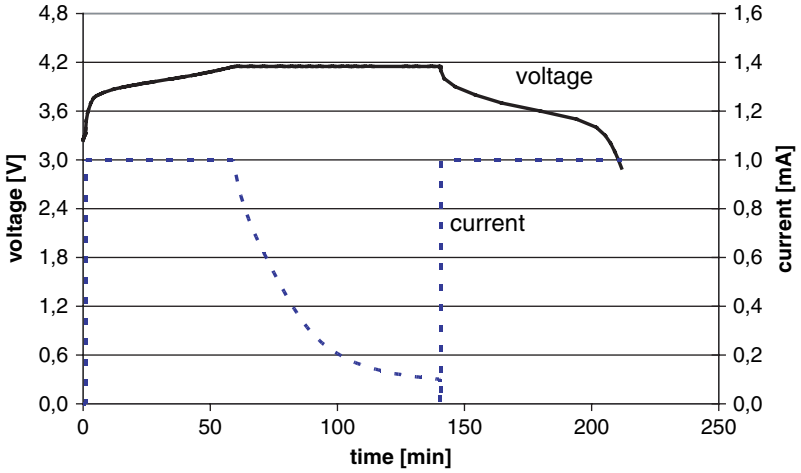

Fig. 11.4 Charge/discharge curve of an LiC/$LiCoO_2$ wafer-level battery, size $9 \times 9\,mm_2$, 160 µm thick

Table 11.5 Advantages and disadvantages of some small battery types

Type	Advantages	Disadvantages
Thin prismatic lithium polymer batteries pcCoin-type cell	■ high energy density ■ high power density ■ low-cost production	■ high fraction of battery package ■ temperature range : < 80°C ■ low power density ■ medium energy density
Wafer-level battery	■ high energy density ■ flexible battery chemistry ■ integrable	■ temperature range : < 80°C
Solid-state battery	■ high temperature performance ■ very thin ■ integrable	■ low energy ■ manufacturing complexity

11.2 Photovoltaic Portable Modules

Photovoltaic modules have been developed primarily as an alternative "green" source of electrical energy. Important is the efficiency or power density of a certain module, but also its fabrication technology and the amount of energy required to manufacture it. For large photovoltaic power plants, for example, the return of investment or establishing a positive energy balance as soon as possible is of primary interest. For portable electronics, the efficiency of solar modules is of importance, since the usable area is restricted. Up to now, however, solar cells have been able to establish themselves only in niche applications, such as pocket calculators and watches.

11.2.1 Description

A solar cell basically is a semiconductor diode. The semiconductor material absorbs the incoming photons and converts them into electron-hole pairs. In this photo generation step, the decisive parameter is the band gap energy E_{gap} of the semiconductor. In an ideal case, no photons with an energy $hv < E_{gap}$ will contribute to photo generation, whereas all photons with an energy $hv > E_{gap}$ will generate an electron-hole pair and the excess energy (hv-E_{gap}) is lost because of the thermalisation process.

The maximum electric photo current I_{ph} is given by the flux of photons with an energy $hv > E_{gap}$. Since I_{ph} decreases with increasing E_{gap}, but the energy transferred to the electron-hole pairs increases with E_{gap}, an optimum for E_{gap} (approx. 1.1 eV) exists, where a maximum of the sunlight energy can be converted into the energy of the photo-generated electron-hole pairs. At this band gap, roughly half of the incident solar energy is transferred.

The efficiency of solar cells is determined by several loss mechanisms: about half of the average absorbed photon energy goes into heating. Some photons are reflected by the exposed surface of the crystal. The U-I curve which is the outcome of the charge separation process, where the electrons diffuse to the electrodes results in a maximum power point with significantly lower current than short-circuit current and a lower voltage than the open-circuit voltage. There is also some internal resistance in the crystal that inhibits the flow of electrons. This internal resistance increases as the crystal is heated. The efficiency is strongly temperature-dependent. Thus, typical solar cells have only half the efficiency at operation temperature compared to 0°C. For a material like silicon, the operating efficiency of a photovolatic array therefore will probably never be higher than 20% and most likely be in the range of 15%.

The practical output power is the product of incoming power density, area, and efficiency. Table 11.6 displays the maximum power which can be achieved with several small-sized modules under standard conditions of 1000 W/m^2 and 14% efficiency. As expected, a smaller surface area leads to the decrease of the maximum electrical power reachable. As can be seen in Table 11.7, the efficiency is determined by the type of solar cell. For niche applications, amorphous silicon or thin-film solar cells are commonly used, because serial interconnection of a number of cells at low

Table 11.6 Maximum energy obtained from solar modules as a function of their size

Area	cm^2	Example	Maximum electrical power
DIN A0	10000	Roof element	120 W
DIN A3	1250	Case	15 W
DIN A4	625	Sheet of paper	7 W
DIN A6	156	PDA	2 W
DIN A8	39	Smart card	500 mW
DIN A11	4.8	Surface of mignon cell	60 mW

Table 11.7 Efficiency and application area of photovoltaic technologies

Type of solar cell	Efficiency	Use
Mono Si (high eta)	15–22	space, high performance
Mono Si (standard)	9–17	outdoor/indoor (window)
Poly Si	8–15	outdoor/indoor (window)
Amorphous Si	4–7	(outdoor)/indoor
CuInGaSe2 (CIGS)	6–10	outdoor/indoor
CdTe (1)	3–6	outdoor/indoor (window)
CdTe (2)	6–9	outdoor/indoor (window)

Source: High-eta modules are based on high-grade silicon and advanced technologies, which results in higher prices compared to standard silicon.

cost during the fabrication process is feasible with these technologies. However, these technologies exhibit a lower efficiency compared to single and poly-crystal silicon cells.

The reason of the limited market share of photovoltaic modules for portable electronics mainly lies in the fact that portable electronic products are used primarily indoors, where the light intensity smaller than standard conditions by several orders of magnitude. Moreover, they are kept in cases or enclosures with no light at all most of the time. As a consequence, portable solar charger modules appeared on the market during the last years. They are capable of charging secondary batteries of a variety of chemistries or they are directly connected to the portable device as an external charger. By way of example, Fig. 11.5 displays the microprocessor-controlled universal battery charger e.Go by Solarc GmbH [10]. Portables, such as mobile phones, digital cameras, MP3 players, and others, can be operated directly from this device or recharged by the system. Loading can be done via ordinary electrical outlets (110–240 V) or car port (12 V). The maximum power is 4 watts. The DC output is between 4 and 14 V. The system is water-resistant for outdoor use, has a volume of $160 \times 85 \times 33\,\text{mm}^3$, and a weight around 300 g. There are several versions available, ranging from 1.1 –2.6 W nominal solar power, which translates into charging times between two and fife hours for two AA batteries or one Li-ion

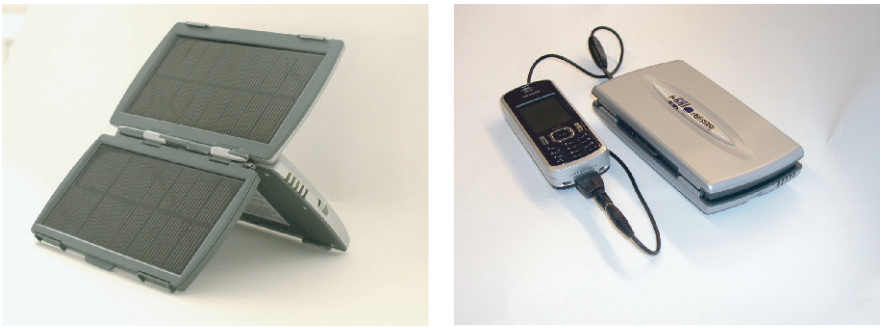

Fig. 11.5 Universal battery charger e.Go, Solarc [10]

mobile phone pack. Under non-optimal lighting conditions, the internal secondary batteries can be charged for a longer period and then be used to charge the mobile device rather quickly at 1.3 or 4 watts. The retail prices are between 100 and 200 Euros depending on the version.

11.2.2 Flexible Photovoltaic Modules

Portable products are characterised by curved or sometimes mechanically flexible surface areas. It is important to use these areas available for photovoltaic cells. The best way is to use mechanically flexible solar cells which have already been demonstrated for wearable computing applications. So far, amorphous solar cells and thin-film solar cells deposited on flexible substrates have exhibited a low efficiency between 2 and 6%. Consequently, a packaging technology was developed, which allows for a cost-effective assembly of semi-flexible solar micromodules [11]. This technology is based on rigid high-efficiency silicon cells which can be designed in a mechanically flexible manner and mounted on curved surfaces.

Silicon solar cells which are used in larger modules are usually interconnected by soldering of ribbons or by means of single technology. But this is not appropriate for small portable modules mainly because of the lack of automation and the poor reliability. Hence, a modified module technology was developed by adapting the printed-circuit board technology from electronics industry. Silicon solar chips are bonded on printed-circuit boards using a silver-filled adhesive (back-side contact) and connected with wire bonds on the front side as displayed in Fig. 11.6.

Figures 11.7 and 11.8 display both types of bendable solar modules. The first one uses a polyimide-based flexible substrate which is reinforced rigidly below the solar cell. The second low-cost type uses thicker glass-reinforced epoxy (FR4) substrates with meandering slots. The modules are finished by laminating the transparent encapsulation foil. The technology has two advantages. Due to the automatic assembly

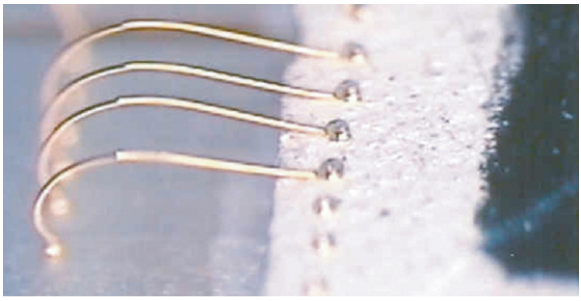

Fig. 11.6 Typical front-side wire bond contacts on an Si solar cell

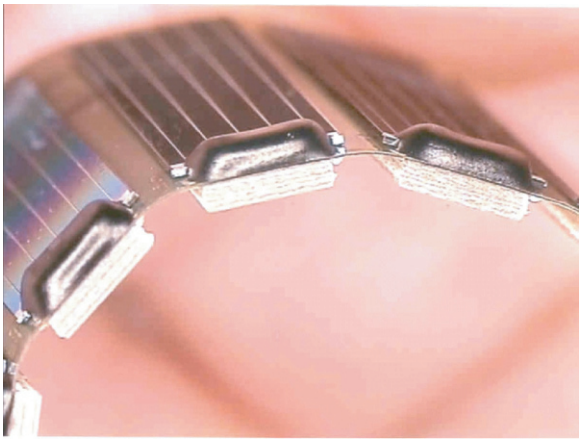

Fig. 11.7 Bendable solar module based on star-flex substrate and wire bond technology

with chip-on-board technologies on printed-circuit boards, an efficient high-speed production even of small and medium quantities is ensured. Due to the established partial substrate flexibility, mechanically flexible or bendable modules can be fabricated. To test the ductility and reliability for wearable electronics applications, the modules were qualified for 10,000 bendings with a bending radius down to 3 cm with the help of a bending test machine.

Flexible photovoltaic modules were tested in several prototypes like a medical wrist strap demonstrator, a GPS distance meter, and a helmet application. Figure 11.9 displays the power output of a helmet with integrated solar modules of 20 cm^2 in size as a function of the incident angle and the radiation power. Although the modules are applied in the front-side region of the visor of the helmet only, a sufficient electrical power is reached even in case of sun incidence from the back.

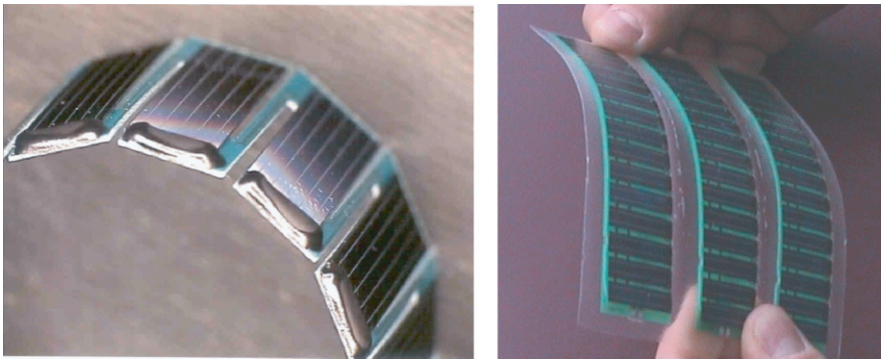

Fig. 11.8 Bendable solar module based on meandering FR4 substrate

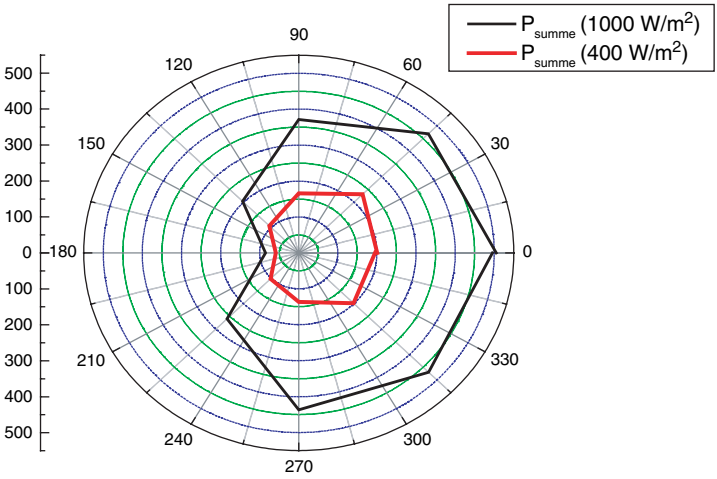

Fig. 11.9 Power output [mW] of helmet-integrated solar modules of 20 cm^2 in size as a function of the incident angle

11.3 Status of Portable Fuel Cells

In recent years, work on small portable fuel cell systems advanced significantly. The main goal is to increase the runtime and the availability of portable electronic devices far beyond those of battery-powered systems. The complete portable fuel cell consists of three major parts in analogy to the fuel cell systems for automotive and stationary applications:

- the fuel cell stack which determines the power output,
- the fuel tank which determines the total amount of available energy, and
- the balance of plant (BOP) which includes all of the peripheral systems like reformer, valves, pumps, and control circuits that support the overall function of the systems.

For smaller systems, however, it was not simple to scale down components and system architectures of the existing fuel cell. Consequently, many of the components were redesigned taking into account the requirements of portable systems and the knowledge available on traditional fuel cell systems. Many components, such as micropumps, valves, and sensors, presently do not have the long-term stability which is required in portable power supplies. It is therefore focused on reducing the peripheral components and building the so-called "passive systems". Thus, costs and volume can be reduced and reliability increased. This fuel cell type will be described below in Sect. 11.3.1.

Currently, several advanced prototype fuel cell units are commercially available in the power range up to 100 W.

The most developed fuel cell system is the PEM fuel cell which uses hydrogen gas as fuel stored in a high-pressure tank or in a reversible hydrogen storage material. The portable PEM fuel cell now is available on the market. PEM fuel cell stack

performance was drastically improved in recent years and reaches a power density above 1000 W/kg. However, the higher energy density compared to batteries and the low-cost mass production promised have not been achieved. Moreover, hydrogen storage capacity of reversible metal hydride is not sufficient to compete with lithium-ion batteries. At present, a lot of prototypes, demonstrators, and first niche applications like military fuel cells can be found.

A second option which has emerged is the direct methanol fuel cell (DMFC).

11.3.1 Air-breathing Portable PEM Fuel Cell

The passive air-breathing design simply requires hydrogen and no other active cooling or humidification components. It runs continuously on hydrogen and ambient air. The system operates under ambient conditions without the "balance-of-plant" (BOP), such as pumps and fans typically required by conventional fuel cell systems. Hydrogen combines with oxygen that diffuses into the stack from the surrounding air. The only products are electrical power and water which serves to maintain the moisture necessary for the unit's performance.

Diffusion and free convection are the primary transport mechanisms for delivering oxygen to the cathode of air-breathing fuel cells. They are attractive for portable-power applications because of the simplicity of free-convection oxidant delivery which outweigh the costs, limited lifetime, reliability, complexity, noise, volume, weight, and parasitic power consumption of an auxiliary fan or compressor. However, the performance of air-breathing fuel cells is highly dependent on the ambient conditions. Balancing water in free-convection cells is challenging due the lack of control of ambient air stream conditions (flow stoichiometry, temperature, and humidity).

Air-breathing cells are typically characterised by low output power densities compared to forced-convection fuel cells. Cylindrical and planar geometries are feasible. Air-breathing stacks have already been used in flashlights, remote-controlled cars, and laptop computers.

11.3.1.1 Planar Fuel Cell

Figure 11.10 displays an example of a fully passive, air-breathing planar fuel cell which was fabricated based on printed-circuit board technology [12, 13]. Herein, BOP is only required for the control of the hydrogen flow. The contact pressure between MEA (membrane electrode assembly) ,GDL (cathode gas diffusion layers) and current collectors is achieved due to the stiffness of the glass-reinforced epoxy compound materials. Three single cells are serially interconnected to achieve a power of 2 watts at a voltage of 1.5 V as can be seen in Fig. 11.11. The serial interconnection is obtained with the help of patterned opposing printed-circuit board plates. Overlapping copper structures are interconnected by soldering to connect

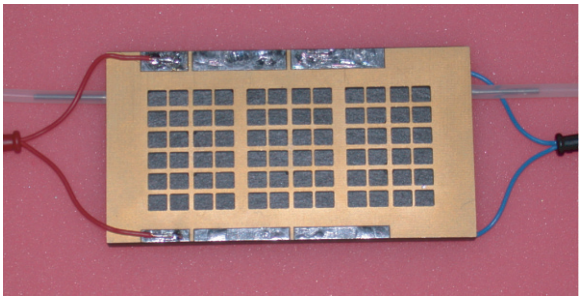

Fig. 11.10 Planar PEM fuel cell based on printed-circuit board technology

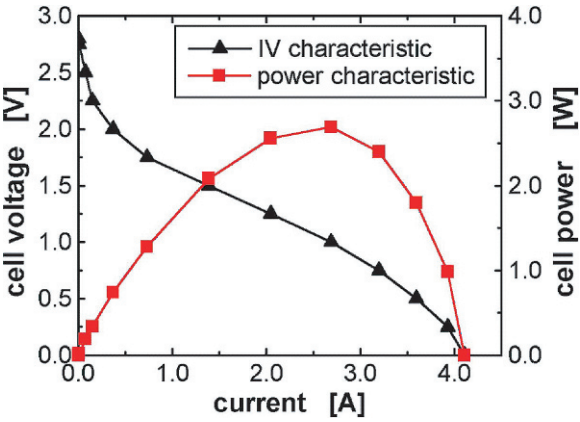

Fig. 11.11 Current/voltage and power characteristics of a planar fuel cell with three serially interconnected cells

neighbouring anodes and cathodes outside the active area of the fuel cell. A single membrane electrode assembly (MEA) is used for all three cells. An insulation of the electrodes between the cells is patterned by laser ablation. A serpentine structure is machined mechanically into the bottom plate to act as an anode-follow field, while the top plate has large openings for oxygen supply. Additional frames are laminated to the boards to achieve the compartments required for the gas diffusion layers. The maximum power density achieved is 150 mW/cm^2 at room temperature, 50% relative humidity, and dry hydrogen supply under closed-end anode conditions. For stable long-term operation, however, the planar stack must be operated at lower power density and higher potentials. Otherwise, instabilities will occur due to self-heating of the lightweight system. The advantage of this technology is that a proven mass production process for printed-circuit boards can be used with a straightforward adaptation of designs to individual applications.

11.3.1.2 300 W Air-cooled PEM Fuel Cell

For a higher-power PEM fuel cell, a 300 W air-cooled stack by MES-DEA S.A. [14], which is displayed in Fig. 11.12, has been tested and integrated into a traction application. The fuel cell stack is equipped with microprocessor-controlled

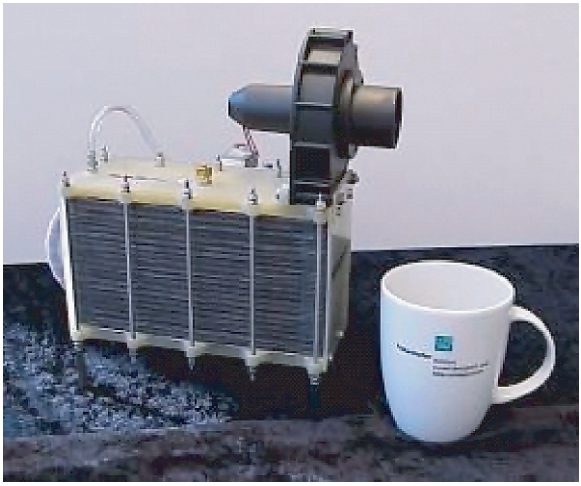

Fig. 11.12 PEM fuel cell stack 300 W, MES-DEA

electronics, blowers, and valves. The fuel cells are separated by corrugated metal sheets for air cooling with two blowers. Another blower is installed for cathode air supply. All components, including the hydrogen purge valve, are controlled by the electronics. The specifications are obvious from Table 11.8. Figure 11.13

Table 11.8 Specification of the air-cooled PEM fuel cell. Source: MESDEA

Size [mm^3]	110*180*70
Rated power [W]	300
Weight [g]	2.2
Operation voltage [V]	14.4/20
Gravimetric power density [W/kg]	136
Volumetric power density [W/l]	216

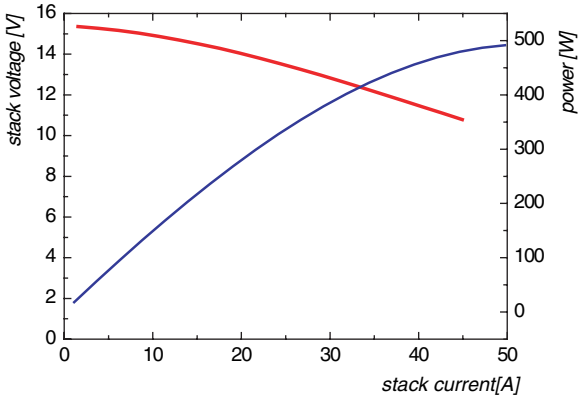

Fig. 11.13 Current/voltage and power characteristics of the air-cooled PEM fuel cell stack

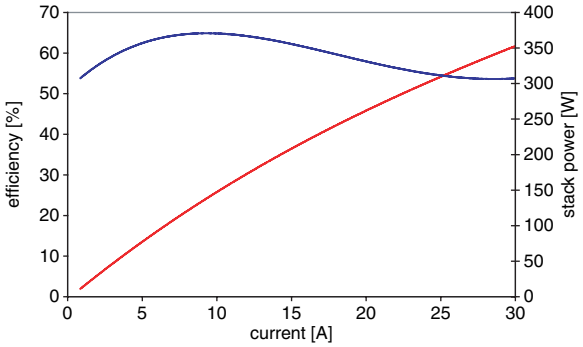

Fig. 11.14 Efficiency of fuel cell stack shown in Fig. 11.12

shows the electrical characteristics and efficiency of the stack. Figure 11.14 illustrates the measured fuel cell stack hydrogen-to-electrical energy efficiency with output load. The highest efficiency is around 65%. Together with the peripherals and control electronics, the maximum system efficiency drops to 55% at a power of 125 W.

11.3.2 Portable PEM Fuel Cells Available

In the following sections examples of PEM fuel cell units with different types of hydrogen supply will be discussed in order to highlight the technical advancements in this field.

The benchmark system is a direct methanol fuel cell (DMFC) system. The characteristics of the DMFC can be summarised as follows: diluted and heated methanol is circulated at the anode, where it is directly converted into water, CO_2, and electricity. Pure methanol is pumped into the anode cycle, based on measurements of the concentration or filling level. The cathode air flow goes into a heat exchanger after leaving the fuel cell stack, where part of the water and methanol that has passed the membrane are condensed and recycled to the anode side.

The smart fuel cell C20-MP DMFC 20 W system designed for a soldier power system is taken here as a reference [15]. The system is optimised for military usage for soldier power. In contrast to most of the other systems described below, the DMFC was tested extensively and data about lifetime and fuel efficiency are available. Two versions exist, depending on the value of the ambient temperature. Fuel cartridges with high-purity methanol are used in the temperature range between 1 and 35°C, while the high-temperature system between 1 and 50°C uses a water-methanol mixture. The fuel efficiency at 20 W constant load is between 19 and 20%.

11.3.2.1 Angstrom Power 1 W PEM Fuel Cell System for Flashlight

The system was designed for a 1 W constant power flashlight of cylindrical dimension with a diameter of 2.6 and 15 cm length. So far, this has been the smallest system demonstrated [16]. The used fuel cell technology allows for the packaging of a large amount of surface area into a small volume using microstructured topology. The fuel cell operates under ambient conditions with convective air transport at the cathode. The fuel storage technology used is based on metal hydride. At Angstrom power, the fuel tanks have demonstrated a performance in small packages of 700 Whr/l and 170 Whr/kg. The system can be "recharged" (re-fuelled) in minutes without the need for electric power by means of a refuelling station. Refuelling may be accomplished using cartridges. The stationary or semi-portable refueling solution is based on regular compressed hydrogen or an existing on-site hydrogen source.

11.3.2.2 Fraunhofer Camcorder 10 W PEM Fuel Cell Demonstrator

The system was designed for a camcorder and has been available since 2002 [17]. The power of 10 W at 8 V is achieved with a stack of 15 microstructured bipolar plates which are glued to each other. Hydrogen is supplied from a metal hydride cartridge which is thermally connected to the stack. The hydrogen pressure is controlled by means of a piezo-actuated MEMS valve*. Simple ventilation with ambient air using two miniature fans is sufficient for oxygen supply.

11.3.2.3 FLEXIVA 15 W Portable Charging Set

This system was developed for maintenance-free automatic charging of 12V/24V lead accumulators. The dimensions are 315 mm × 213 mm × 156 mm and the weight is 3.3 kg without the hydrogen tank. Two systems are available with a maximum charging current of 1 and 2 amperes. The working temperature range is specified to be between −15 and +30°C with a restart temperature above 0°C. The system uses a PEM fuel cell with an external source of hydrogen [18]. This is the simplest solution, but appears not to be efficient for a miniature fuel cell in terms of energy density.

11.3.2.4 Protonex/Millennium Cell 30 W Sodium Borohydride PEM as Soldier Power System

Another system for military applications was developed by Protonex in cooperation with Millennium Cell [19]. Hydrogen for the PEM fuel cell is generated in a cartridge from a 20–25% sodium borohydride, 3% sodium hydroxide, 72–77% de-ionised H_2O solution. The system has two parts. First, hydrogen is filled into a replaceable cartridge and then introduced into the fuel cell. Both parts have

approximately the same size. The cartridge comprises the tanks for fuel and reaction products as well as the catalyst reactor with the thermal interface, water, hydrogen, and electrical interface. The energy density is rather promising and can be increased, if dry cartridges are carried and filled with water during usage.

11.3.2.5 VOLLER Automatic Battery Charger ABC, 70 W PEM Unit

The ABC is a 100 W portable fuel cell system which is available at two different AC voltages, either 110 V or 230 V. Both versions have a 12 VDC output and a USB charging port [20]. These systems can be used to power small portable devices, such as mobile phones, or to simply recharge any battery. This PEM system allows for a peak power of 200 W and is fuelled with a reversible hydrogen storage alloy. The tank is integrated in the housing for efficient heat exchange with the fuel cell. The system has a frost sensor which enables usage under freezing conditions. The minimum temperature of the system is +2°C. If the ambient temperature is lower, then the system automatically switches from stand-by to the on-mode.

11.3.2.6 MES-DEA 200 W Portable PEM Fuel Cell for Electrical Bicycles

At TU-Berlin, a demonstration system was tested based on a MES-DEA PEM fuel cell stack [21] with reversible hydrogen storage, a DC-DC converter, and super capacitors (c.f. Fig. 11.11). This system was compared with new types of Li-polymer batteries. It was shown that the weight of the fuel cell system with the reversible hydrogen storage tank was equal to that of Li-ion secondary batteries. Only if a better or bigger hydrogen storage could be used, can a weight improvement be achieved.

11.3.2.7 100 W Water-cooled PEM Fuel Cell System for Long-endurance Unmanned Aerial Vehicles

A PEM fuel cell system based on a water-cooled stack and compressed hydrogen from a small 200 bar pressure tank was investigated at the US Naval Research Laboratory for micro air vehicles [22]. For this application, both weight and power density are of great importance. The system was designed for a three-hour flight. The data shown in Table 11.10 represent the first-generation vehicle demonstrated in 2005.

11.3.2.8 10 mW Micro PEM Fuel Cell with Coin-cell Hydrogen Generator

Since the storage of gaseous hydrogen is not reasonable in very small-sized applications (1 cm3) and microsystems, an “on-demand” hydrogen generation established with the help of the electrocatalytic Zn-H_2O reaction was investigated by the Fraunhofer IZM [23]. This system will be described in detail in Chap. 12. A demonstrator of 4 cm^3 volume and a weight of 10 g yields an energy of 2.1 Wh at

a current of 10 mA. The system voltage is the sum of the voltage of the galvanic Zn cell which produces the hydrogen and the fuel cell voltage. Electrical energy is generated in both parts of the system.

It should be noted that at present, only the systems designed by FLEXIVA, Smart Fuel Cell, MES-DEA, and VOLLER are available on the market.

11.4 Comparison of Li-ion Batteries and Portable Fuel Cells

The only parameters of interest when comparing portable fuel cells and batteries are the energy and power density of fuel cell systems. Table 11.9 and Fig. 11.15 summarise the specifications of the systems described in Sect. 11.3.1. The DMFC system as benchmark (the system using pure methanol is considered herein) is compared with the Li-ion battery. In addition to energy and power density, all other aspects like safety, durability, reliability, and costs are of importance. Table 11.10 displays some typical battery test specifications with pertinent remarks concerning portable fuel cells.

As can be seen in Table 11.9, the use of reversible hydrogen storage alloys and small compressed hydrogen tanks (200 bar) does not improve the energy density compared to batteries. Nevertheless, these systems can be useful, if quick recharging is necessary or for applications out of the range of the electricity grid.

DMFC and $NaBH_4$ systems outperform Li batteries in terms of gravimetric energy density. If several fuel cartridges are considered, gravimetric as well as volumetric energy density can be improved by a factor of two or more compared to Li secondary batteries. At present, this is achieved only with systems of above about 2 l or 2 kg in size. An exception is the micro fuel cell with a Zn-water hydrogen generator. In this case, it is possible to reach higher energy densities compared to Li-polymer batteries, because it is a complete passive system, where the hydrogen is generated proportionally to the current flow. Peripherals like valves or pressure

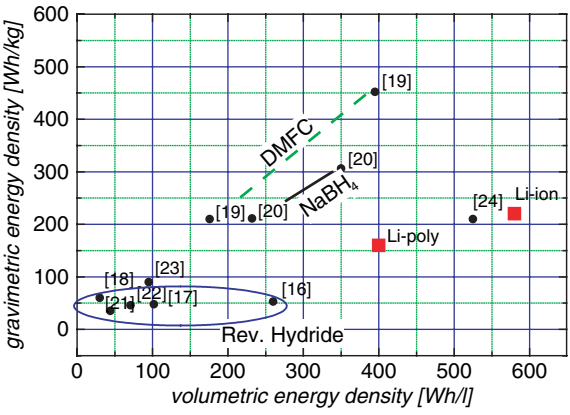

Fig. 11.15 Energy densities of fuel cell systems and Li-ion cylindrical and Li-polymer prismatic cells

Table 11.9 Impact of portable battery test conditions on micro fuel cells

Test	Battery specification	Remarks concerning portable fuel cells
Cycling performance	80% of capacity after 200 cycles 100% discharge at room temperature	So far, rechargeable fuel cells have not been developed for portable products. Nevertheless, it would be a big advantage for the user to recharge the fuel by plugging the system into the mains instead of buying new fuel cartridges. At the moment, this parameter can be used as a lifetime indicator. After two to four years, the performance should not fall below 80% of the initial value
Performance at different discharge temperatures	−10°C, 40°C 20% of initial capacity after 200 cycles	Fuel cell restart at temperatures below zero has only been demonstrated for stationary systems with the help of elaborate thermal management systems. For small fuel cells, this still is an issue. A solution is the hybrid system, where a Li battery powers the system at temperatures below zero degrees. Long-term operation at +40°C could lead to membrane dry-out. DMFCs with concentrated methanol supply also may have problems with water loss. Nevertheless, these issues will be solved
Capacity at different currents	Capacity comparison between 50 and 5 hours discharge: less than 20%	The working point of the fuel cell has to be designed properly. In contrast to batteries, the efficiency does not only drop at high currents, but also at low currents
Voltage drop at high currents	Capacity comparison between 5 and 0.5 hours discharge: less than 20%	The power density of fuel cells is much lower compared to Li batteries. Consequently, intermediate energy stores like capacitors or secondary batteries should be introduced for high power peaks
Short-time storage characteristics	Capacity drop at 50°C, 25% RH after 7 days below 30%	Capacity will be unaffected, but start of the fuel cell may be difficult due to membrane dry-out
Long-term storage	Capacity recovery after one year at −20…+35°C above 60%	See above. Hydrogen leakage through packages and valves may be of concern.
Mechanical tests	Drop test: survive drop from 1.5 metres height onto a concrete base	Since fuel cells have a lot of mechanical components, this may be a crucial point. A low weight and stable design of the stack and components are very important.
Safety tests	No fire in case of short circuit, overcharge or overheating	For fuel cells, new safety tests have to be created [24]

Table 11.10 Power and energy density comparison of portable fuel cell systems

	Fraunhofer IZM	Angstrom power	Fraunhofer	Flexiva	Smart Fuel Cell	Protonex	Voller^{++}	MES-DEA, TU-Berlin	NRL, Protonex
Power, type	10 mW PEM	1 W PEM	8 W PEM	15 W PEM	20 W DMFC	30 W PEM	70 W PEM max. 200 W	200 W	100 W
Ref.	[23]	[16]	[17]	[18]	[15]	[19]	[20]	[14, 21]	[22]
Fuel	Zn-H_2O hydrogen cell	Reversible hydride	Reversible hydride	Reversible hydride*	Methanol cartridges	NaBH4 cartridges	Reversible hydride	Reversible hydride	CGH_2 200 bar
Volume ** [l]	0,004	0,092	0,177	9	3	2	9	5,3	ca. 2
Weight ** [kg]	0,01	0,45	0,38	5,5	2,5	2,2	9	8	2.1
Energy density^{+} [Wh/kg]	210	53	48	60	210/452	211/306	35	46/68	90
Energy density^{+} [Wh/l]	525	260	102	30	176 / 395	232/350	44	71/124	ca. 95
Power density [W/kg]	1	2	21	3	8	13	22	25	30
Power density [W/l]	2,5	11	35	1,7	6,7	15	22	37	-

* Since no data for hydrogen storage were available, a reversible hydrogen storage tank was considered.
** One fuel cartridge included.
+ One fuel cartridge / three fuel cartridges.
++ Hydrogen to electricity efficiency of 65% has been considered.

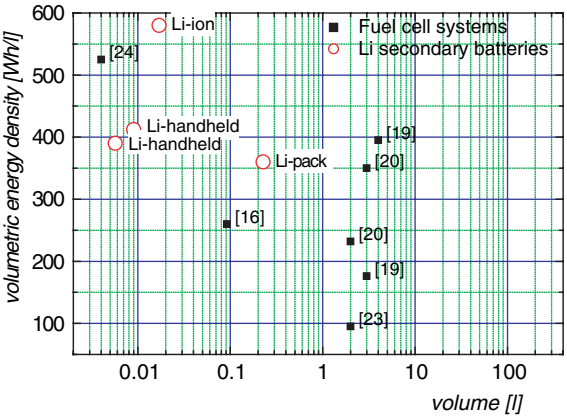

Fig. 11.16 Size comparison of portable fuel cells and Li-ion batteries

controllers are not required. On the other hand, only a relatively low current drain can be delivered at a constant rate.

Figure 11.16 compares the sizes of the fuel cell systems described in Sect. 11.3.1 and Li secondary batteries. Obviously, only the passively working PEM systems [23] and [16] fit into the range of handheld devices or notebook computers. All the other systems are at least one order of magnitude bigger. This dramatically demonstrates the issue of fuel cell miniaturisation. The size range achieved may hardly compete with secondary batteries. The key challenge is how to reach the desired power performance, while simplifying the design of the BOP in order to miniaturise the whole system.

The power density of all fuel cell systems is much lower compared to secondary batteries. The hydrogen PEM fuel cells are better than the DMFC systems by a factor of two only, which is remarkable, since the MEA or stack power density of DMFCs is about 4–10 times lower compared to hydrogen PEMs. The highest power density of 30 W/kg was reached for the micro air vehicle system and corresponds to a three-hour discharge.

Another issue of fuel cell integration is the efficiency and additional thermal load. Li secondary batteries have a very high charging and discharging efficiency above 90%. Since fuel cells have a system efficiency in the range between 20 and 65%, much more heat is produced, which has to be removed from the portable device. Table 11.11 demonstrates the increase in heat load when fuel cells are integrated in an electronic device.

Table 11.11 Heat dissipation of integrated fuel cells compared to batteries

Power source	Li secondary battery	PEM fuel cell	DMFC
Electrical power requirement	10 W	10 W	10 W
Power source efficiency	90%	50%	20%
Waste heat of power source	1 W	10 W	50 W
Total heat to be removed from the device	11 W	20 W	60 W
Increase of heat load, Li benchmark	100%	182%	545%

Another principal difference between batteries and portable fuel cells is that fuel cells are open systems with access to ambient air, whereas batteries are closed systems, which can be encapsulated and packaged easily. Several aspects have to be considered, as ambient conditions like temperature and humidity may influence the fuel cell performance. Moreover, atmospheric pollution may degrade the fuel cell and, finally, air access must be allowed during operation time. This limits usability under wet ambient conditions and in harsh environments. For example, it is not possible to use fuel cells, which rely on air supply, under water.

11.5 Outlook

In general, lithium-ion batteries will remain the dominant power source for portable electronics for the next years. They are required to handle the peak power demands. Fuel cells can be added to power the devices during non-peak times as continuous charger of the internal battery or as a means of recharging the battery when power outlets are not available. Perhaps, fuel cells will be integrated as a hybrid, where a lithium battery supports the current spikes, in a later stage.

Another significant research effort is to miniaturise the fuel cells. Special improvement is required for the balance of plant by using miniaturised and high-reliability components and more passively working fuel cell technologies. Especially, water management is a crucial part of any fuel cell system and is particularly challenging to miniaturise. For small, portable, and handheld units, MEMS pumps and valves probably will have to be developed. While the first components appear on the market, a huge effort is still needed to increase the reliability, reduce their own energy consumption, and the costs. For piezo-actuated pumps and valves, in particular, a high-voltage converter is required with a much higher efficiency or low-voltage actuators have to be developed.

References

The following pages referred to in Table 11.2 were available on the internet on 2/1/2007:

[a] http://www.powerone-batteries.de/en/assortments/hearing-aid/zinc-air/zinc-air.php

[b] http://www.powerone-batteries.de/en/assortments/electronic/lithium-button-cells/lithium-button cells.php

[c] http://www.varta-microbattery.com/en/mb_data/documents/material_data_sheets/MDSMNO2.pdf

[d] http://www.**varta-microbattery**.com/en/mb_data/documents/data_sheets/DS65013.pdf

[e] http://www.varta-microbattery.com/en/MB_DATA/DOCUMENTS/DATA_SHEETS/DS60621.PDF

[f] http://www.varta-microbattery.com/en/MB_DATA/DOCUMENTS/DATA_SHEETS/DS55996.PDF

[g] http://www.varta-microbattery.com/en/MB_DATA/DOCUMENTS/DATA_SHEETS/DS55604.PDF
[h] http://www.varta-microbattery.com/en/MB_DATA/DOCUMENTS/DATA_SHEETS/DS60614.pdf

1. O. Sonnemann, New technology for Li-Ion batteries, Panasonic, Batterieforum Karlstein, February 23, 2006.
2. A. S. Gozdz, J.-M. Tarascon, O. S. Gebizlioglu, C. N. Schmutz, P. C. Warren, and F. K. Shokoohi, Eds., A new hybrid polymer electrolyte for lithium-ion rechargeable batteries, no. 94–28. Proc. Electrochem. Soc. (Rechargeable Lithium-Ion Batteries), 1995.
3. A. S. Gozdz, J.-M. Tarascon, C. N. Schmutz, P. C. Warren, O. S. Gebizlioglu, and F. K. Shokoohi, Eds., Polymer Considerations in rechargeable lithium ion plastic batteries. The Tenth Annual Battery Conference on Advances and Applications, 1, 1995.
4. Molenda, "Lithium-ion batteries – state of art of novel phospho-olivine cathode materials", Materials Science-Poland, Vol. 24, No. 1, 2006, Faculty of Materials Science and Ceramics, AGH University of Science and Technology, al. Mickiewicza 30, 30-059 Cracow, Poland.
5. Sanyo, Technical Paper SEB 0-17, http://www.sanyo.com/batteries/pdfs/pack_E.pdf. page 4, October 10, 2002.
6. http://www.seag.de/start_frameset.shtml?/deutsch/technologie_d/technologietrends/02seagpowerboard.shtml.
7. J. B. Bates, N. J. Dudney, B. Neudecker, A. Ueda, and C. D. Evans, "Thin-film lithium and lithium-ion batteries," Solid State Ionics, Vol. 135, pp. 33–45, 2000.
8. M. Nathan, D. Golodnitsky, V. Yufit, E. Strauss, T. Ripenbein, I. Shechtman, S. Menkin, and E. Peled, "Three dimensional (3d) thin film microbatteries," DTIP of MEMS u. MOEMS, 2005.
9. K. Marquardt et al., Assembly and hermetic encapsulation of wafer level secondary batteries. In 19th IEEE International Conference on Micro Electro Mechanical Systems (IEEE, Istanbul, Turkey, 2006), 954957. Jan. 22–26, 2006.
10. www.solar-lader.de
11. R. Hahn, Autonomous energy supply for electronic grains and wireless sensors, Wafer-Level-Battery, Frequenz 3–4/2004, 87–91.
12. A. Schmitz, R. Hahn, C. Hebling, et al. "Planar self breathing fuel cells', Journal of Power Sources, Vol. 118, pp. 162–171 (2003).
13. A. Schmitz, R. Hahn, S. Wagner, and C. Hebling, Stability of planar PEMFC in printed circuit board technology, Journal of Power Sources, Vol. 127, pp. 197–205 (2004).
14. MES-DEA, Fuel cell technical datasheet, http://www.cebi.de.
15. J. M. Cristiani and N. X. Sifer, test and evaluation of the smart fuel cell C20-Mp direct methanol hybrid fuel cell system as a soldier power source, The 2005 Annual Meeting (Cincinnati, OH) 31 October 2005.
16. http://www.angstrompower.com/.
17. www.ise.fhg.de/english/ publications / brochures_productinfos/gf5/pdf/02e_fh_initiative_flyer_mikro-fc.pdf.
18. http://www.flexiva.de/.
19. S. A. Shah, Chemical Hydride Based PEM Fuel Cells for Portable Power Applications, Tactical Power Sources Summit 2005, http://proceedings.ndia.org/.
20. www.voller-energy.com/.
21. http://www.extraenergy.org/files/Diplomarbeit_Severin_Neubauer_2006_BZ_Akku_bike.pdf.
22. J. C. Kellogg, L. Monforton, D. White, and M. Vick, Fuel cells for micro air vehicles, Joint Service Power Expo, Tampa FL 5 May 2005.
23. R. Hahn "Miniaturization of fuel cells – low-cost manufacture of micro fuel cells with the help of microelectronics", F-cell 2005, Stuttgart, Germany, Sept. 26–28, 2005.
24. Small Fuel Cell Conference 2006 Test von BZ.

Chapter 12
Development of Portable Systems

Robert Hahn

List of Abbreviations

BOP	Balance of plant
CNT	Carbon nanotube
DEFC	Direct ethanol fuel cell
DFAFC	Direct formic acid fuel cell
DMFC	Direct methanol fuel cell
GDL	Gas diffusion layer
LTCC	Low-temperature co-fired ceramic
MEA	Membrane electrode assembly
MEMS	Micro electro mechanical system
PCB	Printed-circuit board
PEM	Polymer electrolyte membrane
SEM	Scanning electron microscope
UN	United Nations

Robert Hahn
Fraunhofer-Institut Zuverlaessigkeit und Mikrointegration (IZM), Gustav-Meyer-Allee 25, D-13355 Berlin, Germany, e-mail: Robert.Hahn@izm.fraunhofer.de

A. Léon (ed.), *Hydrogen Technology*,

12.1 Introduction

During the last 5 years, the development effort related to small, portable fuel cells increased significantly. The main motivation of the development of micro fuel cells is the possibility to achieve higher energy densities compared to batteries. This development benefits greatly from the existing knowledge and attempts to improve larger fuel cells for automotive, residential, and stationary applications. For the commercialisation of both big and small fuel cell systems, however, improvements still are required in several areas. For DMFCs, for example, it has been recognised that the success of this fuel cell technology depends largely on developing better membranes with lower methanol cross-over and improving the electro-catalysts which can overcome the slow anode kinetics. A comprehensive overview of catalyst development for DMFCs, including carbon nanotube (CNT) catalyst support, can be found elsewhere [1]. Research is required with respect to the electrolyte membrane with lower cross-over flow at higher ion conductivity, the durability and enhanced catalysts with high activity as well as regarding the selectivity for the desired reaction and stability.

When developing smaller fuel cells, it is impossible to simply use scaled-down systems architectures and components applied in their larger counterparts. Therefore, only the developments specific for small fuel cells and microsystems shall be reviewed in this chapter. A complete portable fuel cell system consists of three major parts:

1) The fuel cell stack which is the core of the system. Its size is related to the power output.
2) The fuel tank. Its size is related to the amount of stored energy and, hence, to the runtime of the device.
3) The balance of plant (BOP) which includes all the peripheral components that support the power generation process. In most cases, this is the hydrogen-generating system for PEM fuel cells.

Since compressed gas or liquid hydrogen cannot be used for portable or small fuel cells, the research focuses on three kinds of fuel cell. The first are the ***direct liquid fuel cells*** using methanol (DMFC), ethanol (DEFC) or formic acid (DFAFC). Then, the ***PEM fuel cells with hydrogen*** are considered, where the hydrogen is generated from reformed methanol, reversible storage alloys or chemical hydrides and water-reactive alloys. The last type of interest, but still in the state of basic research is the ***biofuel cell***. In this case, organic materials like alcohols, organic acids or glucose are used as a fuel and biocatalysts convert chemical into electrical energy. So far, the existing prototypes have shown a very low power density and short lifetime. Therefore, they will not be examined here.

Many attempts have been made to date to reduce the balance of plant of portable fuel cells in order to increase reliability and reduce costs. The related studies revealed that for portable fuel cells sophisticated peripheral components have to be developed to allow for a higher power density and operation under varying loads and ambient conditions. The key challenge in this field is how to achieve the desired

power performance, while simplifying the design of the BOP in order to miniaturise the whole system. With miniaturisation, application-specific components like valves and pumps based on micro systems technology have to be developed.

12.2 The Fuel Cell Core – Micro Fabrication Technologies

Typically, large fuel cells are mechanically compressed sandwiches of a graphite composite or metal electrodes and membrane assemblies. As stated in the introduction, a miniature fuel cell for portable devices that delivers power in the range of up to 20 W cannot be obtained by simply scaling down the larger system design. Each component of the fuel cell has to be re-designed based on well-established technology platforms for miniature components in order to achieve a cost-effective miniaturisation. Therefore, most researchers use available manufacturing techniques like:

- Silicon and MEMS technologies
- Foil processing of polymer and metal foils, polymer substrates
- Printed-circuit board technology
- Planar ceramic technology like low-temperature co-fired ceramics (LTCC).

Silicon fabrication of micro fuel cells often comprises the electrochemical etching of Si to form a porous layer, followed by electro polishing the wafer underneath to form fluidic channels. To act as electrode layer, the porous layer is then covered with platinum by sputtering or electroplating.

The micro porous layer can be used as a support of the ionic conductor as well. In this case, it is filled with Nafion or made conducting for ions with the help of other procedures to act as an electrolyte membrane with high dimensional stability.

The advantage of printed-circuit board technology as a basis of flow field and current collector fabrication above all is the low-cost mature technology. Furthermore, light-weight and stiff composite materials are used and design flexibility is ensured, as complex conductor/insulator patterns are applied either as a mono- or multi-layer design. However, the standard material like the copper/glass epoxy composite of printed-circuit boards cannot be used for long-term stable fuel cells without modification. Indeed, copper would degrade in the corrosive fuel cell environment. This, in turn, will increase not only the contact resistance between electrode and current collector, but also introduce metal ions that may enter the membrane and significantly decrease the membrane conductivity.

Water and methanol may dissolve ingredients of the glass epoxy composite, which may poison the catalysts subsequently. That is why appropriate material modifications or surface coatings have to be established in order to use printed-circuit board technology in portable fuel cell applications [2].

The advantages of using ceramic technology for micro fuel cell development are the inertness and mechanical stiffness of the material. Fluidic channels as well as gold or silver current conductors can be integrated in a complex layered set-up using

LTCC technology [3]. However, the heavy weight and high costs prevent ceramic technology from being used for low-temperature fuel cells in portable electronics.

The use of micro technologies is aimed at reaching two objectives:

1) The specific fuel cell performance may be significantly improved when micro scaling processes are used. Fuel cells built to investigate micro-scale phenomena are smaller, use the volume more efficiently, and improve heat and mass transfer. Therefore, problems critical in conventional stack technology may be solved by the micro technological design of the three-phase boundary, the development of ultra-thin ion-conducting membranes, the fabrication of transport-optimised flow channels on the micro scale, the introduction of nanomaterials, and others. Most of these aspects are interdependent and have to be investigated and designed simultaneously. For example, ultra-thin electrolytes require the presence of narrow support structures in the micrometre range that may impede the flow of reactants.
2) The majority of research activities related to micro-scale fuel cells is also aimed at micro-power applications. There are many new miniaturised applications which can only be implemented, if a higher-energy-density power source is available compared to button cells and other small batteries. Miniaturisation of the conventional fuel cell stack technology is not possible down to these dimensions.

In the following sections, some examples of micro fuel cell fabrication and characterisation will be presented to illustrate the development of this technology.

12.2.1 Hydrogen PEM Micro Fuel Cells

Several approaches to fabricating micro fuel cells are pursued:

a) The most prominent approach takes advantage of highly optimised MEAs and GDLs of larger systems. Only the flow field plates are miniaturised by means of micro patterning technologies. This may be hot embossing of lithographically structured flow field plates of Si, polymers or metals as well as laser machining of mechanically patterned multi-layer ceramics or etched and milled printed-circuit boards. Flow field optimisations were made for each of these technologies. The advantage over conventional bipolar plates is that stacks can be made smaller. In-plane interconnection of cells in planar stacks is more straightforward.
b) If the flow field structures have sufficiently small features or they are integrated in a micro porous substrate, then the fuel cell construction can be modified in a way that only the standard MEA and the micro flow field plates are employed. Extra GDLs are not required. Silicon micro patterning and polymer or metal foil substrates are the prominent candidates for this technology.
c) If the micro flow field is combined with a micro porous surface as described in b), it can be additionally coated with a catalyst to act as a fuel cell electrode. Hence, only an ion-conducting membrane is required to complete the fuel

cell. Here, the ion-conducting connection between electrode and ion conductor is of greatest importance. It is mostly accomplished with the help of a nafion solution.

d) If the ion-conducting membrane is fabricated with the help of micro and deposition technologies, the complete fuel cell can be fabricated without standard components. Since the sequential deposition and patterning of all fuel cell layers is far from being straightforward, the anode and cathode sides are fabricated separately in most cases and at least one assembly step is necessary. It is also possible to fabricate only the ion conductor with the help of micro technologies and then sandwich the ion conductor between standard electrodes fabricated separately. Here again, the ion-conducting connection between electrode and ion conductor is of greatest importance. The use of micro porous silicon with ion-conducting fillings as well as plasma polymerisation has been reported for the fabrication of ion conductors in micro fuel cells. Table 12.1 gives an overview of the described approaches.

12.2.1.1 Design of Micro-Patterned Flow Fields and Planar Air-Breathing Fuel Cells

A study of the influence of the flow field design in combination with the operational parameters of lithographically fabricated flow structures in SU-8 of 5 cm^2 size showed that an inter-digitated flow field at high pressure has a higher maximum power density than mesh and serpentine flow fields [4]. However, the difference was not very pronounced, which is not very surprising, since a GDL was used, which is much thicker than the flow channels. Thus, the GDL will dominate the transport properties.

Another study with gold-coated spiral flow fields laser-ablated into PMMA at a size of 3 cm^2 revealed relatively similar results in terms of power density [5]. With the help of parallel flow channels fabricated in SU-8, it was shown that a channel dimension of 100 µm yields the highest power density [6]. It was assumed that the performance of smaller channels degrades due to flooding.

Table 12.1 Overview of approaches to miniaturising micro fuel cells (s = standard components, m = micro patterning and deposition technologies)

Micro fuel cell structure	Ion conductor/ MEA	GDL	Flow field	Material basis	Ref.
a)	s	s	m	PCB	[2, 9, 10, 11]
a)	s	s	m	polymer	[4, 5, 6]
b)	s	–	m	polymer, metal	[7, 8]
c)	s	m	–	Si	[13, 14]
d)	m	m	m	Si	[15]
d)	m	m	m/s	polymer	[18]
d)	m	s	s	Si	[16, 17]

The influence of the thickness of GDL layers as well as of the size of air slots on the performance of passive air-breathing fuel cells was investigated using cells fabricated by the printed-circuit board technology [7].

Gas diffusion layer thicknesses in the range from 0.27 to 1.75 mm (Toray) were tested. It was shown that the use of diffusion layers with increasing thickness improves the contact resistance. Moreover, thicker diffusion layers are able to better compensate possible gaps between the backing and current collector and ensure a homogeneous contact. The best result was achieved with 1.05 mm thick backing layers on the cathode side. A stationary behaviour of cell potentials evolving between the Voc and short circuit was demonstrated by diffusion layers thicker than 0.35 mm. Air slots of 1.5, 2, and 4 mm width were investigated at the cathode. It was found that increasing the opening of the air slots leads to a significant increase in current for potentials lower than 500 mV. Under an optimised design, a maximum power density of 110 mW/cm^2 was achieved. Figure 12.1 displays a comparison of the measured and the simulated polarisation curves at room temperature. In general, the optimum cathode opening for self-breathing cathodes is a trade-off between unrestricted air circulation and low contact resistance. A relatively large opening can be reached, if the mechanical stiffness of the cathode plate and the GDL is sufficiently high.

The use of printed-circuit board technology for planar fuel cells was further elaborated with a forced air, the so-called "micro stitch", design [9]. The effects of the cathode structure on the performance of air-breathing PEM fuel cells were studied extensively in order to optimise the cathode design [10]. The results were related to the water transport phenomena in air-breathing fuel cells. With increasing cathode catalyst loading from 0.3 to 1.6 $mgcm^2$, the cell performance improved significantly up to a Pt loading of 0.6 mg/cm^2 and then increased only slightly. With increasing GDL thickness, water evaporation could be reduced, while the mass transport limitation increased. An intermediate thickness of 280 µm exhibited the best performance

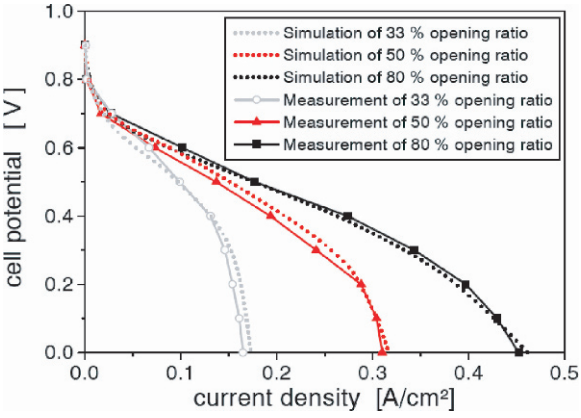

Fig. 12.1 A comparison of polarisation curves of planar self-breathing PEM fuel cells at room temperature for three different cathode openings [8]

in the range from 100 to 370 µm. A GDL with 5 … 10% PTFE was found to be the best for air-breathing fuel cells. At higher concentrations, performance degraded at high current densities due to a smaller porosity. In contrast to this, a GDL without PTFE did not appear to adequately remove water from the cathode.

While these micro fuel cells differ from larger ones in the fabrication of the flow field only and use the same MEAs and GDLs and forced air flow at the cathode, a next step towards micro engineering is made by a fuel cell concept which uses a conventional MEA without a GDL and a passive air-breathing cathode. This concept shall be described in detail in the section below.

12.2.1.2 Micro Porous Flow Fields and Polymer Laminate Technology

This foil-type approach is based on a number of technologies adapted from wafer level packaging and thin film technology, such as sandwich laminates of polymer – stainless steel foils, lithography and patterning of free-standing grid microstructures, and micro patterning of gas flow fields. A commercially available MEA is used. MEA electrodes are subtractively patterned to define individual cells. Sealing and electrical interconnection are achieved by adhesive technology [11]. All cells of a planar stack use the same membrane. Due to the lack of GDLs, the fuel cell consists of only three foils regardless of the number of single cells. This, in turn, facilitates an efficient, low-cost reel-to-reel manufacturing. During fabrication, a foil substrate tape (with the anode structure) spools into a machine that sequentially deposits a sealing material, places the MEA accurately into a pre-formed gasket, and mounts the cathode foil. A curing process completes the cycle and, finally, the finished fuel cells are punched out of the tape.

Figure 12.2 displays an example of a micro fuel cell based on metal/polymer foil technology. Figure 12.3 shows the anodic flow fields of a single-cell fuel cell and of a planar stack with three serially interconnected cells. The active area in both cases is 0.54 cm^2.

Characteristics of Foil-Type Micro Fuel Cells

Figure 12.4 displays the typical V/I curve measured at 2°C, 50% RH, with passive air and dry hydrogen supply at 150 mbar. These measurements indicate that variations in the automatic assembly process result in minor changes of the electrical performance only [12]. Moreover, the open-circuit voltage of the three-cell stack has a lower value compared to the value expected from three single cells. Such a decrease is probably due to small leakage currents in the membrane between the cells.

By using the thinnest available MEA, the fuel cell works at 200 mW/cm^2 under standard conditions. At present, 4000 hours lifetime can be achieved for such a system and the low-cost mass production technology is well developed. This air-breathing fuel cell has cathode structures that are open to air. Consequently, the

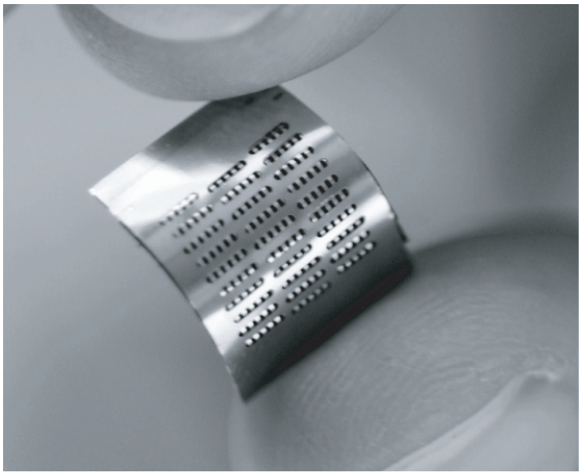

Fig. 12.2 Micro fuel cell based on metal/polymer foil technology [11]

performance is strongly affected by the atmospheric conditions, including relative humidity and temperature. For an efficient operation, the membrane electrolyte must be properly hydrated to maintain a high ionic conductivity. However, external water supply is avoided for air-breathing portable fuel cells in order to reduce the system complexity. In such a case, the product water generated at the cathode by the electrochemical reaction only can be used to hydrate the system. This is accomplished by the back diffusion process which is induced by the difference in water concentration between the anode and the cathode.

Figure 12.5 compares the *steady-state current densities at a voltage of 0.4 volts of two planar self-breathing fuel cells, a foil-type micro fuel cell without gas diffusion layer (GDL) and a standard configuration with GDL*, but equipped with the same MEA as in [13]. As can be seen, current density is reduced in both cases for hot and dry as well as for cold and wet ambient conditions. This is mainly attributed to a dried

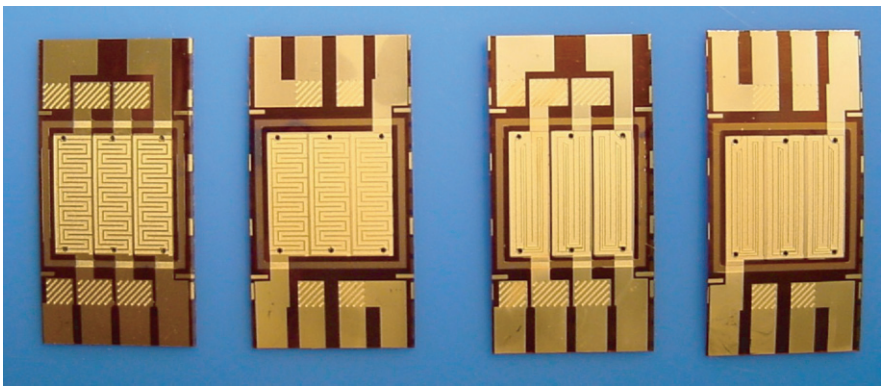

Fig. 12.3 Anodic flow fields of a foil-type micro fuel cell corresponding to the one of Figure 12.2. Active area: 0.54 cm^2

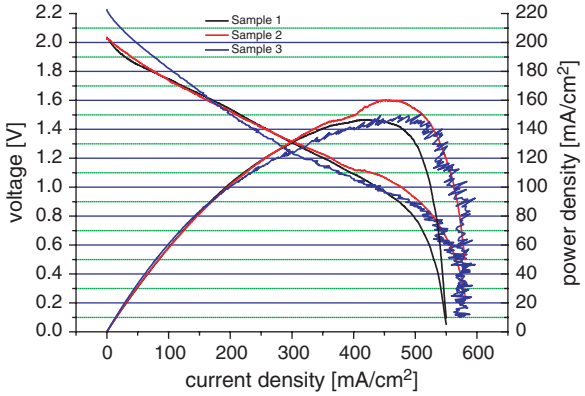

Fig. 12.4 Voltage/current curve and power density of foil-type micro fuel cells fabricated with modifications in the assembly process, planar stack of three cells with 0.18 cm^2 active area each

membrane and an electrode flooding, respectively. The performance of the foil-type micro fuel cell is only slightly more reduced than that of the reference fuel cell.

12.2.1.3 Micro Patterned Electrodes

Further down-sizing of micro fuel cells was investigated with the help of Si technologies. Silicon substrates are used to fabricate micro patterned electrodes [13, 14]. Here, the micro structured substrate is coated with an electrically conducting layer and with the catalyst. It acts as diffusion and catalyst layer at the same time. Subsequently, a Nafion membrane is pressed between two of such substrates to form a micro fuel cell. It was shown that the electroplated catalyst works better on the

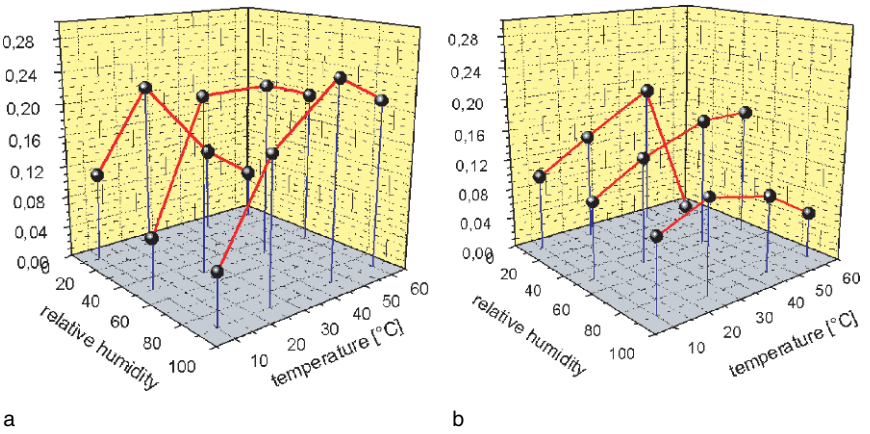

Fig. 12.5 Steady-state current densities at a voltage of 0.4 volts of planar self-breathing fuel cells: foil-type micro fuel cell (no GDL) (a) and standard configuration with GDL (b)

silicon electrode when a graphite support layer was deposited first [13] instead of a direct electro deposition of Pt black on the substrate [14]. The highest power density of 300 mW/cm^2 was reported for porous silicon coated with a catalyst [15].

12.2.1.4 Micro Fabricated ion Conductors

The micro porous substrate can be used as a support for the proton exchange material. Nano porous substrates were filled with Nafion to create a proton conductor. Alternatively, a process was developed for grafting the pores' internal surfaces with silane molecules bearing the ion-conducting acid functions [16]. This is an important step towards a monolithic integration of all fabrication steps of the micro fuel cell technology, because Nafion is not really compatible with silicon processing due to its restricted temperature stability and swelling. First experiments with the micro porous membranes and standard electrodes showed a power density of 17 mW/cm^2. A critical issue of the grafted pore membrane is the large hydrogen cross-over.

A modified concept is that of using liquid electrolyte confined inside a micro channel network [17]. Moreover, a novel proton membrane technology for micro fuel cells was developed by the use of plasma polymerisation [18]. This technology allows for the deposition of very thin proton-conducting membranes in the µm range onto micro porous substrates. Especially DMFCs may benefit from tailour-made plasma-polymerised membrane properties. A critical requirement of this technology is the availability of defect-free, micro porous electrode substrates as a basis of membrane deposition. Figure 12.6 shows an SEM picture of a plasma polymerised membrane on a porous substrate.

For further reading, a comprehensive review of micro fuel cell technology from 2002 to 2005 can be found elsewhere [19].

Table 12.2 compares the basic parameters of the reviewed planar hydrogen fuel cells. All fuel cells were tested at room temperature except for [6]. In most of the cases, the fuel cells operate with passive air breathing on the cathode side [5, 12, 13, 16], forced air supply [4, 6]. One system is supplied with oxygen [14]. In this stage, the fuel cells with commercial MEAs [6, 12] still outperform the systems

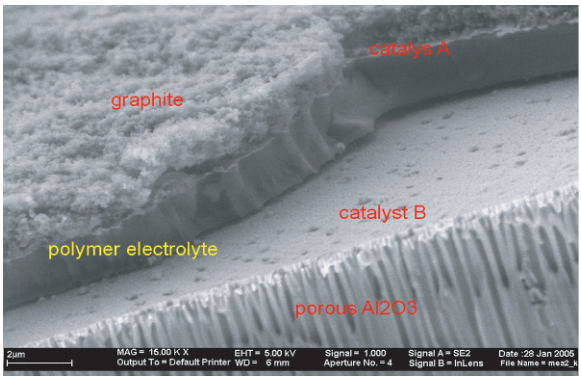

Fig. 12.6 SEM of a thin-film micro fuel cell using sputtered catalysts and a plasma-polymerised ion conductor on a micro porous ceramic support
(Source: TU Hamburg-Harburg) [40]

Table 12.2 Overview of planar PEM micro fuel cells

Substrate technology	MEA/GDL	Flow field dimensions, channel width/depth µm Active area cm^2	Maximum power density [mW/cm^2] at current density [mA/cm^2]	Conditions	Ref.
Silver-sputtered SU-8 flow field on Cu foil	Nafion 112 Pt 1 mg/cm^2, Lynntech, 290µm GDL	200…2000/– 5	60/120	dry H_2 25 sccm, 152 kPa, air 25 sccm, 25°C	[4]
Au-sputtered PMMA flow field	Nafion 1135 + Toray TGPH-090, 260µm, Pt 1 mg/cm^2	200/200 3	82/220	dry H_2 dead end 10 psi air 50 sccm, RT	[5]
Sputter-metallised SU-8	Nafion 115, GDL, BCS, Pt 1 mg/cm^2	100/100 2	160/–	H_2, 20 sccm air 80 sccm, both fully saturated at 50°C	[6]
Electroplated composite foil	GORE MEA, no GDL 0.3 mg/cm^2	80/40 0.54	160/550	Dry H_2 dead end passive air supply 25°C	[12]
Printed-circuit board technology	GORE MEA, Toray GDL 0.3 mg/cm^2	1000–4000 10	110/260	Dry H_2 constant flow passive air supply 25°C	[8]
Printed-circuit board technology	BCS MEA, Nafion 112 Pt 2 mg/cm^2 carbon cloth	500/500 2	140 / 400	H_2 30 sccm air 60 sccm 25°C	[9]
Graphite plate, Au-plated copper grid	PFSA membrane Toray carbon paper, E-Tec Pt 0.7mg/cm^2	1000/2000 25	145/350	Dry H_2 passive air supply 35°C, 60% RH	[10]
Micro porous silicon	Pt electroplated on spray-coated graphite support	30/40 0.49	125/260	Dry H_2 passive air supply	[13]
Micro porous silicon	Electroplated Pt black 2.5 mg/cm^2	150/50	35/75	Saturated H_2, saturated O_2, 25°C	[14]
E-tek electrodes	Micro porous Si Pt	–/– 7 mm^2	17/60	Wet H_2 ambient air	[16]

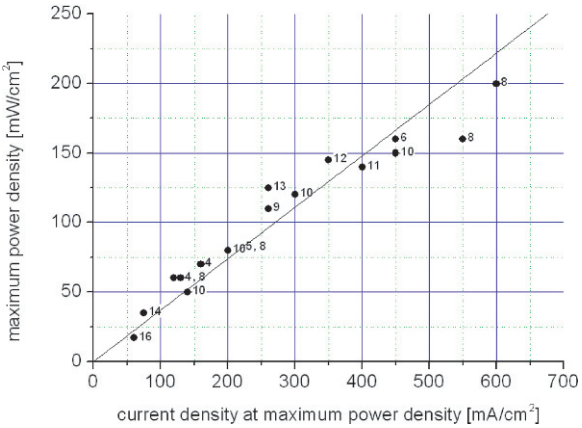

Fig. 12.7 Maximum power density versus current density of planar PEM micro fuel cells according to *Table 12.2. With the exception of [14], where oxygen is supplied, all fuel cells use ambient air*

with deposited micro porous proton exchange and catalyst layers. However, this may change soon, as the micro system deposition technologies will mature and further concepts will emerge in the next development stage utilising the micro scale effects. The linear fit in Fig. 12.7 yields a value of 0.37. This means that the mean voltage at maximum power is 0.37 volts. Higher voltages are achieved in the cases, where a tailour-made optimised catalyst is used [13]. Further improvements in power density are necessary. From the view point of OEM which wants to use micro fuel cells as a battery replacement, power densities between 0.3 and $1\,W/cm^2$ must be achieved to obtain systems small enough for integration in mobile phones or other handheld devices.

12.2.2 Direct Methanol Micro Fuel Cells

A micro DMFC has much more design diversity compared to hydrogen PEM fuel cells due to a number of different operational concepts and operational difficulties. The main differences and difficulties of these two systems can be summarised as follows:

- Instead of gaseous fuel, a liquid as to be fed into the anode flow field.
- According to the reaction equation, CO_2 evolves at the anode. Therefore, a two-phase flow has to be dealt with.
- Due to the slow anodic reaction kinetics, operation at elevated temperatures is preferred to increase the power density.
- Due to the large methanol cross-over, only diluted methanol can be filled into the anode.
- Due to the methanol cross-over and water drag to the cathode side, performance can be greatly improved by enhanced air convection on the cathode side.
- To achieve a high energy density, reaction water from the cathode has to be recycled and fed back to the anode.

Despite numerous efforts during the last years to develop miniature DMFCs, no truly commercial system is currently available for consumer electronic devices, which is mainly due to the issues associated with the micro DMFC design. In the following sections, major approaches to micro DMFC development shall be discussed.

The most conventional design of a DMFC is an active system equipped with a fuel cell stack, methanol sensor or methanol volume sensor, CO_2 separator, methanol feed pump, circulation pump, pump drivers, and electronic control [3]. Apart from the complexity and costs of the system, reliable micro components like micro pumps of the required size and low-power design, including the electronic drivers, are not available. The system components consume considerable electricity from the fuel cell and reduce the net power output.

The DMFC design can be simplified to a great extent, if the methanol cross-over can be reduced significantly. Samsung reported the development of a membrane with 30% methanol cross-over and a proton conductivity corresponding to that of Nafion when 5M or higher methanol concentrations were used [20]. An even further reduction of the methanol cross-over was reported for the use of polymerised membranes. Figure 12.8 compares the DMFC maximum power densities (normalised) of a Nafion 117 and plasma-polymerised membrane (3P-PEM) as a function of the methanol concentration. This figure suggests that the cross-over is reduced to a great extent and higher methanol concentrations can be applied directly to the anode.

As it is intended to miniaturise active DMFC systems, several investigations focus on passive designs. Such a system has a great impact on the design of the fuel cell components like the diffusion layers and current collectors.

A fully passive planar DMFC was developed using a laminated multi-layer construction [21]. MEA, GDLs, and metal mesh current collectors were laminated together to reduce the contact resistance and allow for a light-weight design. Only a thin fixing frame made of glass epoxy composite material with large openings was

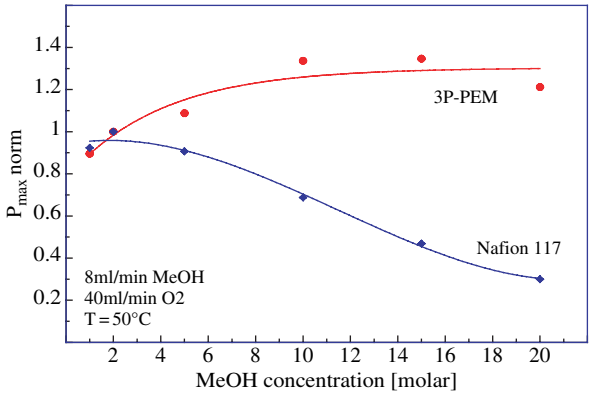

Fig. 12.8 Comparison of the DMFC maximum power densities (normalised) of Nafion 117 and a plasma-polymerised membrane (3P-PEM) as a function of the methanol concentration (Source: TU Hamburg-Harburg) [40]

sufficient to provide for an even distribution of compressive force for cells with a large active area. Anode and cathode were both fabricated with large openings in order to allow passive air-breathing operation at the cathode. The anode was immersed into a methanol reservoir. No information was supplied about the reservoir and CO_2 degassing. All experiments were carried out at room temperature, allowing for the self-heating of the cells.

A maximum power density of 30 mW/cm^2 was achieved with methanol concentrations between 2 and 3 M. Using 5 g methanol solution, the power density was relatively constant at 12–14 mW/cm^2 for a period of 80 minutes and then degraded due to methanol depletion. At 2 M methanol concentration, an overall efficiency of 15% was achieved. This is a remarkable value when taking into account that fully controlled active systems currently reach a maximum efficiency of 20%. It is also a significant improvement compared to the self-breathing operation of a planar DMFC [22]. In this experiment the power density of self-breathing operation was compared to an active air-blown mode at a variety of operation parameters. Stable operation at 22 mW/cm^2 was achieved at room temperature only under air-blown conditions at the cathode, while the performance in the self-breathing mode dropped down to 10 mW/cm^2 during 40 minutes and then remained constant.

This result is also comparable to the standard flow channel design, where the micro DMFC construction is based on Au-plated stainless steel bipolar plates with 750 µm channel and rib width and an active area of 1.625 cm^2 [23]. At room temperature, a maximum power density of 34 mW/cm^2 was achieved, but additional power was needed to pump the fluids into the flow fields. Furthermore, it was pointed out that the large mass transport capability of a GDL cathode was necessary to allow for cell operation at a low air stoichiometry and to reach a high performance.

Figure 12.9 displays the maximum power densities of several DMFCs as a function of current density at room temperature. All systems were tested in the passive operation mode except for the system described in [14, 23]. The linear fit yields a mean voltage at maximum power density of 0.23 volts.

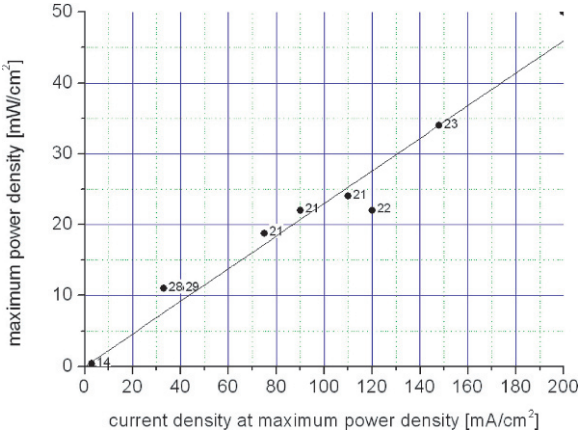

Fig. 12.9 Maximum power densities of passive DMFCs and micro DMFCs at room temperature

In general, the important parameters of passive DMFC construction can be summarised as follows:

– light-weight frame materials of sufficient stiffness and large openings
– corrosion-stable metallic current collectors with a high opening ratio
– special hydrophilic anode backing layers
– special hydrophobic cathode backing layers

The modifications and pre-treatments of MEAs or catalyst layers, backing layers (GDL), and current collectors to optimise the passive operation performance are presented elsewhere [21, 24].

12.3 System Concepts for Small Fuel Cells

12.3.1 DMFC

As stated earlier, two approaches are being developed to solving the problems associated with small DMFCs: "active" and "passive". The active system requires moving parts, such as fans and pumps to feed fuel and oxygen into the fuel cells. In this case, the focus is on miniaturising the external components, reducing the costs, and increasing reliability. The performance of the cell can be increased by integrating the components very closely to the fuel cell stack. The different aspects of active DMFC systems will be described in Chap. 13 "Challenges for the industry" of this chapter. Here, it will be restricted to passive or partly passive systems.

The simplest passive DMFC is equipped with a reservoir containing the methanol/water mixture at the anode [25]. It should be noted that the use of dilute methanol solution significantly reduces the energy density.

The outflow of CO_2 can be used to drive methanol and water in the fuel cell system with on-board pure methanol and water recycling. This operation is controlled by a number of valves and a CO_2 driving pump [26].

In another concept for low-power applications methanol diffuses through the walls of the fuel ampoule and condenses at the anode surface, where it combines with water to form the water/methanol solution [27].

In order to circumvent the problems associated with anode two-phase flow, methanol and water can be supplied to the anode in the vapour state. A fuel cell system was described, where methanol is delivered through a wick structure into the fuel cell. The fuel is vaporised and supplied to the anode. A dedicated thermal management is required for this fuel cell [28]. A fully passive system that can be filled with pure methanol and takes advantage of self-heating was developed with the help of a "thermal fluids management system" [29].

A fully passive water management was developed based on micro porous hydrophilic and hydrophobic layers as shown in Figure 12.10. The cathode side comprises the combination of a laminated micro porous sub-layer, the hydrophobic GDL, and a deep filter layer. These stacked layers result in an enhanced diffusion of

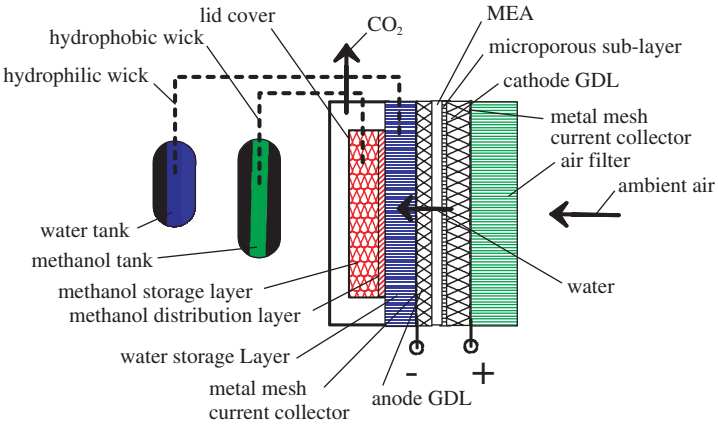

Fig. 12.10 Schematic representation of a passive miniature DMFC with a thermal fluids management system

reaction water back to the anode side, a prevention of water evaporation at the air interface, and improved thermal insulation. On the anode side, pure methanol diffuses from the tank through a wick into a micro porous distribution layer. The combination of the hydrophobic methanol distribution and hydrophilic water storage layer allows for the diffusion of methanol into the water-rich anode compartment to establish there a methanol concentration suitable for the DMFC operation. However, water cannot diffuse into the methanol layers due to their hydrophobic nature. Thus, a significant methanol concentration gradient is established in this layer stack. During initial tests, the system allowed cells to be run for 36 hours at an average power density of 11 $mWcm^2$ under a constant load of 40 $mAcm^2$. An overall system efficiency of 6% was achieved. From the point of view of system design, many challenges remain, such as self-sustainable operation, low costs, sustained performance over a wide range of exterior humidity, pressure, and temperature, endurance and reliability as well as packaging.

Figure 12.11 displays the more conventional solution of water management in a silicon-based DMFC [30]. Here, the water is accumulated at the bottom of the air compartment and returned to the anode chamber by means of a micro pump. This system may be considered a semi-passive approach, since the ambient air is conducted passively to the cathode side. Currently, micro valves and micro pumps as well as hydrophobic-hydrophilic patterned porous silicon substrates are being developed for water management. The advantage compared to the fully passive approach is that the system can actively respond to variations of ambient conditions and start-up after long storage is enhanced. A constant methanol concentration of about 3% in the methanol chamber is achieved with the help of a methanol sensor and micro valves. Furthermore, the passive system is gravity-independent. This is a critical factor in portable applications. The system shown in Fig. 12.11 uses gravity for water accumulation at the bottom of the air chamber, for air convection in the air

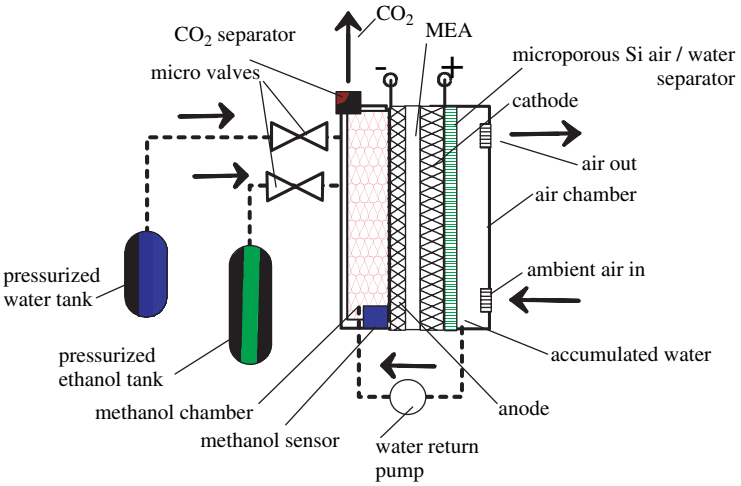

Fig. 12.11 Schematic representation of a silicon-based DMFC

chamber, and for CO_2 removal from the methanol chamber. The stack efficiency of the controlled system must be higher compared to passive system, since additional energy is required for the BOP. It was estimated that a cubic inch-sized system generates 25 mW. 10 mW of this power will be usable for the application, while 15 mW are required for the active MEMS system. Energy is saved by the use of pressurised tanks. Hence, only valves have to be controlled and only one pump is required for water recycling.

The silicon-based approach has a significant advantage in terms of miniaturisation. MEMS components like mesh membrane micro pumps and valves and passive liquid-gas separators are all fabricated with a common set of micro manufacturing processes on the same pair of silicon wafers.

12.3.2 PEM Fuel Cells with Chemical Hydrides

Storage of hydrogen in chemical hydrides has the potential of a high gravimetric and volumetric storage density (see Table 12.3). In addition, power density of PEM fuel cells is higher than of DMFCs. A hydrogen supply system based on chemical hydrides may therefore be small, light, and, in contrast to compressed or liquefied gas, easy to handle in a micro fuel cell or a portable system. The principle of such storage systems is to produce a substance containing a high percentage of hydrogen via chemical reactions and to release the hydrogen gas when it is needed.

Figure 12.12 displays a schematic diagram of the production and hydrogen release via catalytic reactions using chemical hydrides. The challenge with chemical hydrides as storage materials is to find materials which can be produced easily at low energy costs. Moreover, the chemical hydrides and/or their by-products should

Table 12.3 Comparison of hydrogen storage densities of different materials

Material	Gravimetric storage density [wt% H_2]	Volumetric storage density [kg H_2/m^3]
Ammonia	17.7	0.14
Methanol	12.6	100
MTH	6.2	48
$NaBH_4$(s)	10.5	105
$NaBH_4$ (aq, 30 wt%)	6.3	63

not harm man or the environment. Another critical issue is to re-load the resulting reaction products with hydrogen. Indeed, substances that release hydrogen easily are usually hard to re-load with hydrogen. However, such a refuelling process would be advantageous especially for portable applications.

Regarding the supply of fuel cell systems with hydrogen generated from chemical hydrides, a main issue is the control of the evolving gas. In the ideal case, hydrogen is produced exactly according to the demand of the cell. There are different ways of constructing such on-demand hydrogen generation reactors for the supply of PEM fuel cells.

In the following sections, several state-of-the-art principles will be introduced with sodium borohydride ($NaBH_4$) fuel being used as an example. US-based Millennium Cell has developed a patented chemical process that safely stores and delivers hydrogen energy to power portable devices. The borohydride-based technology can be scaled to fit any application requiring high energy density for a long run-time in a compact space.

Sodium borohydride fuel solutions usually consist of about 20 wt% of $NaBH_4$ and 5 to 10 wt% of sodium hydroxide dissolved in water. In contact with a catalyst or under acid conditions, the dissolved $NaBH_4$ will undergo hydrolysis and hydrogen gas will be generated. Sodium hydroxide is added to prevent self-hydrolysis of the sodium borohydride in order to increase the shelf life of the fuel solution. A complete hydrolysis of 20 wt% $NaBH_4$ solution delivers some 470 standard milli-

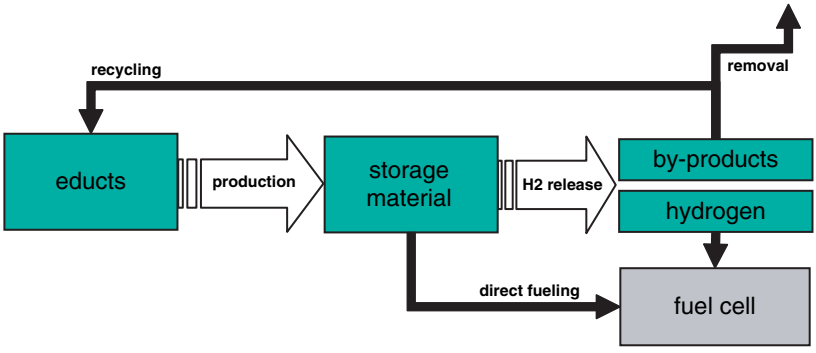

Fig. 12.12 Use of chemical hydrides for fuel cell applications – schematic diagram

litres of hydrogen per millilitre of solution at a reaction rate of more than 1500 sccm per gram of catalyst material [31]. The reaction rate depends on several factors, such as catalyst material, distribution of catalyst (active area), proportion of NaOH in the fuel solution, and concentration of sodium borohydride [32].The production of more hydrogen than needed may cause heat and mass flow losses as well as an increase to higher pressure. That is why it is necessary to control hydrogen evolution according to the demand of the respective application by monitoring either the flow rate or the pressure.

12.3.2.1 Control by Flow Rate

The sodium borohydride fuel solution stored in a fuel tank is first pumped through a catalyst chamber, where it reacts to form hydrogen gas and sodium metaborate ($NaBO_2$). Hydrogen production is controlled by controlling the contact between the fuel solution and the catalyst, i.e. the flow rate of the $NaBH_4$ solution.

Figure 12.13 displays a schematic diagram of the on-demand hydrogen generation process. Once the reaction has occurred, hydrogen gas and the liquid metaborate by-product are separated from each other in a gas/liquid separator. During this separation phase, some liquid water is converted into vapour by the heat of reaction. Hence, the resulting hydrogen stream is fully humidified. This mixed stream of hydrogen gas and water vapour is then sent to feed the fuel cell directly or to a heat exchanger in order to adjust the amount of moisture to a fixed level. The by-product of the reaction, metaborate, can be collected in a discharged fuel container which is removed from the system and subsequently disposed of or recycled. As described in Chap. 11, prototypes of systems working with this technology are already available.

An improvement will be to link the hydrogen reactor and the fuel cell directly via a gas/liquid separator membrane in order to increase the efficiency of the used space [33]. In such a case, the humidified hydrogen resulting from the oxidation of sodium borohydride is fed directly into the fuel cell's anode compartment. Depending on the flow rate, the fuel solution is more or less discharged after passing the catalyst zone. The construction of hydrogen reactors usually aims at a high level of depletion of sodium borohydride. This is achieved by selecting a high-performance

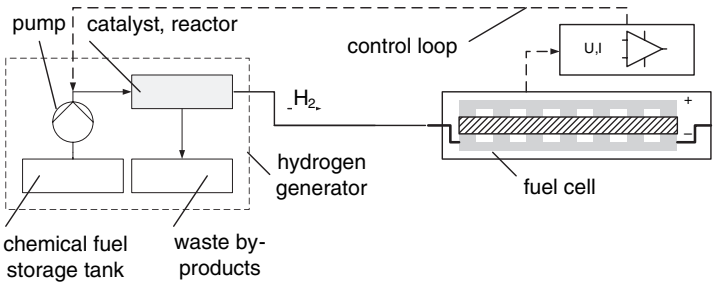

Fig. 12.13 Schematic diagram of on-demand hydrogen generation for portable fuel cells

catalyst for the oxidation of sodium borohydride, such as ruthenium, but also the less expensive nickel [34] and cobalt [31]. A major impediment in increasing the energy density is the clogging of the catalyst with precipitations of metaborate, if the concentration of the fuel solution is too high. Improvements can be achieved, if the reaction water of the fuel cell cathode and water condensed in the anode hydrogen flow are recycled and added to the fuel solution. A higher fuel concentration can be used, if the pressure in the catalyst chamber can be increased.

12.3.2.2 Control by Gas Pressure (Kipp's Principle)

Another way to control the reaction rate is to use the Kipp's principle to control the pressure. If the pressure resulting from hydrogen gas evolution exceeds a certain level, the fuel solution will be pressed out of the reaction zone by suppressing the contact between fuel and catalyst material and subsequently stopping further formation of new hydrogen gas. The remaining hydrogen will then be consumed by the fuel cell until the gas pressure again falls below the level necessary to separate the fuel solution from the catalyst zone. Then, the oxidation of sodium borohydride can re-start. It is also possible to combine principles of active control with pumps and flow controllers and the utilisation of the generated gas pressure to save energy of the BOP.

12.3.2.3 Safety and Transport of Chemical Hydrides

New regulations for the commercial transport of sodium borohydride-based fuel cartridges for fuel cells were approved by the United Nations Subcommittee of Experts on the Transport of Dangerous Goods at the meeting in Geneva in September 2006. Formal ratification by the full UN Committee of Experts is expected in 2007. The UN regulations will be used world-wide to establish shipping requirements for fuel cartridges containing sodium borohydride. The UN shipping name, number, and packaging instructions will also assist international air transport authorities in developing regulations to allow passengers to carry and use these cartridges on-board an aircraft.

Nevertheless, it should be kept in mind that $NaBH_4$ solutions have a very high pH value, are highly caustic, and corrosive. A leakage of the system has to be prevented under any circumstances.

12.3.3 Galvanic Cells

Galvanic cells are another option to achieve a high volumetric energy density. Hydrogen is produced by the reaction of zinc and water according to Eq. (12.1)

Fig. 12.14 Button cell hydrogen generator, size 3.5 cm^3

$$Zn + H_2O \rightarrow ZnO + H_2 \tag{12.1}$$

Since the hydrogen flow is proportional to the cell current according to Faraday's law, the rate control is straightforward. If the fuel cell and the galvanic cell are electrically connected in series, the galvanic cell produces precisely the amount of hydrogen the fuel cell consumes. Only minor leakages have to be compensated. Thus, a very low component overhead compared to other known hydrogen-generating systems can be achieved [35], since pressure tanks and pressure or flow controllers are not required.

Currently, hydrogen-evolving cells are commercially available only in the form of a button cell of different size, as shown in Figs. 12.14 and 12.15 [36].

A zinc cell is composed of the Zn electrode and KOH electrolyte very similarly to a classic primary zinc-air cell and has an equivalent configuration.

The cell consists of a gas-generating electrode, a counter electrode with the active mass and filled with an aqueous electrolyte. The gas electrode and the counter electrode are electrically connected to the metal cup and metal cover, respectively, to provide for the electrical contact to the outside.

The main difference from primary batteries is that the system has an opening for hydrogen release. In the past, these systems were developed for lubricant dispensers, drug delivery or hydrogen reference electrodes. The user will replace the hydrogen

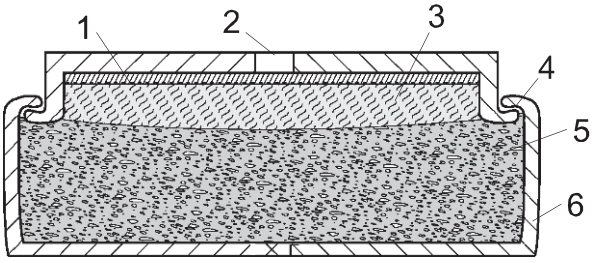

Fig. 12.15 Cross-sectional view of a hydrogen-generating button cell: 1- gas diffusion electrode with catalyst, separator; 2- opening; 3- water/electrolyte; 4- plastic seal; 5- Zn electrode; 6- metal cover

cell like a primary battery. The costs are anticipated to be similar to those of button-sized cells or alkaline batteries.

Besides the Zn electrode and the water/electrolyte reservoir, the most important component is the gas-generating electrode. It is supplied with a non-noble catalyst, a hydrophobic layer (to prevent water or electrolyte leakage of the system), and a hydrogen permeable-membrane in the form of the so-called "double porous layer". The zinc can be used in the form of sheet zinc metal, as a pressed zinc powder, or as a zinc gel electrode, like in primary battery applications.

As stated above, additional components, such as pressure regulators and valves, are not required. This reduces costs and complexity. Moreover, system efficiency and miniaturisation can be improved dramatically.

Since the hydrogen flow is proportional to the cell current according to Faraday's law, the most straightforward electrical circuit is a serial interconnection. Figure 12.16 displays an electrical circuit of a hydrogen generation cell and a fuel cell system. The Schottky diode acts as a current by-pass during the start phase when a load current would result in a reverse fuel cell polarity. Once enough hydrogen is produced to establish a fuel cell potential, the diode is blocked. It should be noted that not only the fuel cell, but also the galvanic hydrogen cell adds to the system voltage. Depending on the current, the hydrogen-evolving cell yields a voltage between 0 and 0.4 volts. The by-pass resistor Rby, in parallel to the gas-evolving cell, is designed to compensate hydrogen losses or any deviation from a current efficiency equal to one. Instead of the resistor Rby, a controllable electronic load can be used to improve hydrogen generation at load steps.

A major disadvantage of small fuel cells with galvanic hydrogen generation cells is the low hydrogen rate and the resultant low power density of the system. In comparison to alkaline batteries, the energy density in terms of the generated hydrogen volume is reduced significantly at higher currents. As an example, a prototype system of 4 cm^3 in size for a power output between 5 and 20 mW was presented in Chap. 11 (Figs. 12.14 and 12.15, Ref. 24). It was shown that the galvanic cells reach the highest volumetric energy density and improvement compared to Li-ion batteries, but the power density is currently limited to approx. 5 W/l. For the Zn system, a 4 cm^3 demonstrator (total volume) yielded 2.1 Wh at a current of 10 mA [37]. This is approximately twice the energy capacity of primary batteries. Currently, the combination of the micro fuel cell with the hydrogen generator works well at constant load. However, there is still a lot of work to be done to improve the behaviour under varying load conditions.

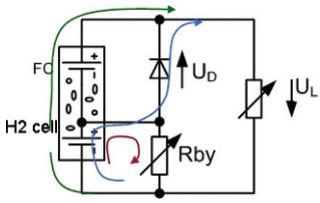

Fig. 12.16 Electrical circuit of a fuel cell system with hydrogen generation cell: a continous by-pass current flows through Rby, a start current flows through the diode, normal working current through H2 cell and FC

Compared to the power density limitation of the Zn/H_2O system, the chemical hydride $NaBH_4$ systems described above show a much better dynamics of hydrogen generation and allow for a far higher rate of production – giving the potential for power densities up to 500 W/l. In contrast to the Zn galvanic cell, though, storage and release of hydrogen using $NaBH_4$ require a complex micro reactor.

Developments of improved catalysts and cell architectures are underway to improve the power density. A scaling-up to the size of about 20 cm^3 in the form of cylindrical cells is under development as well [37].

12.4 System Integration and Thermal Management

To discuss the system aspects of small fuel cells, Table 12.4 gives a summary of the available energy and power densities of the Zn/H2O, **$NaBH_4/H_2O$**, methanol systems. For comparison, the values for the Li ion battery are presented. Only the fuel and the system efficiency of the fuel cell are considered. Therefore, the fuel cell stack, BOP, and packaging are excluded. This implies that in reality the energy densities given in Table 12.4 will be achieved only, if the system has a big fuel storage tank and a very small fuel cell (e.g. low-power applications). Under this assumption, the energy density can be increased by **three to four times** compared to batteries. If higher power is required, the fuel cell can occupy a significant volume of the system. If half of the volume is occupied by the fuel cell, then only half of the given energy densities can be achieved. This suggests that the advantage of these systems over batteries will be only 1.5 to 2-fold at high power levels. In contrast to the table, where a 24 wt% solution of $NaBH_4$ in $H_2O/NaOH$ was assumed, a better energy density of the chemical hydrides could be achieved, if the dry material and the water recycled from the fuel cell were used. However, solutions for such a system in the required small format have not been found so far. If the efficiency of small DMFCs can be increased to over 30%, then the highest energy density will be reachable with this system.

For applications with low power demand like sensors or other applications, where primary batteries are currently used, the power density of the prototypes developed so far may be sufficient, although the most interesting market of consumer electronics requires higher power levels. At present, the power density of PEM fuel cells even is too low for a direct integration of micro fuel cells in mobile phones and other devices. DMFCs will probably only be used as parts of hybrid systems in combination with high-power secondary batteries. If the DMFC operates at a much lower power level than the electronic device, it will be possible to remove the waste heat from the system. Otherwise, the efficiency of the fuel cell systems has to be increased up to about 65% to allow for a direct system integration in portable electronic products[38].

The concept of the fuel cell system will depend greatly on the load cycle of the device. Figure 12.17 displays a vision of a MEMS-based PEM-NaBH4 system. Special features of the system are a MEMS-based flexible hydrogen buffer (6) to store hydrogen for load peaks and a check valve (9) at the fuel cell anode exit. The

Table 12.4 Comparison of energy and power densities of various fuel cell systems and Li ion batteries based on the energy density of the fuel and the efficiency of the fuel cell (fuel cell, BOP, and packaging not considered). The power density of PEM fuel cells is estimated based on hydrogen generation rates obtainable in small systems, for DMFCs it is estimated according to the power density of prototypes of the DMFC

	Zn/H_2O	24 wt% $NaBH_4/H_2O$ solid catalyst	24 wt% $NaBH_4/H_2O$ + 38%H_2SO_4 acid catalysis	Methanol 100%	Methanol 100%	Comparison: Li ion battery
Fuel cell syst. efficiency [%]	PEM, 50	PEM, 50	PEM, 50	DMFC, 15	DMFC, 30	–
Volumetric energy density [Wh/l]	1500	1100	590	825	1650	400
Gravimetric energy density [Wh/kg]	480	860	470	825	1650	200
Estimated power density [W/l]	5	10 … 300	500	5 … 20	5 … 20	100 … 600

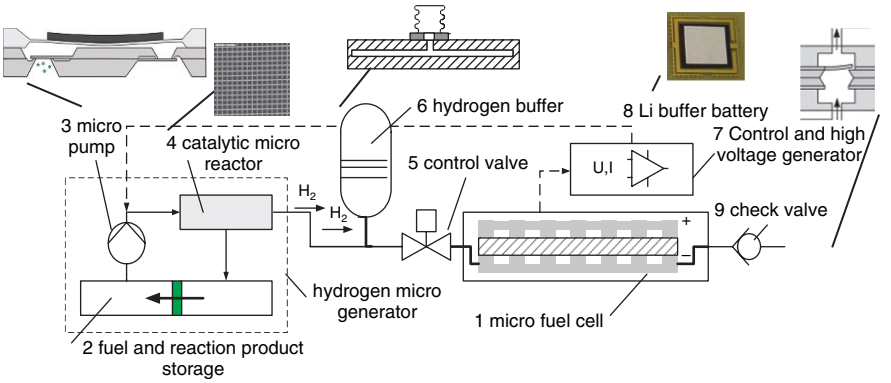

Fig. 12.17 Concept of a MEMS-based PEM $NaBH_4$ fuel cell system
Source: Fraunhofer IZM

anode flow field will be purged by controlled pressure pulses. Only one normally closed piezo valve (5) is required for pressure control. During long periods of idle or sleeping modes, fuel leakage and permeation of hydrogen into the surroundings have to be considered.

Table 12.5 shows the system configuration as a function of the load cycle. Naturally, the simplest system can be used at a constant load.

Future miniaturisation and further development of MEMS peripheral components will allow for the fabrication of a system as small as $1\,cm^3$. Figure 12.18 displays a schematic representation of such a system. Two planar PEM micro fuel cells are incorporated in the side walls. Table 12.6 presents a size estimation of the components involved in the MEMS-based PEM NaBH4 fuel cell system corresponding to the one of Fig. 12.17. Nevertheless, the system is so small that 80% of the volume in this case is used for fuel storage.

From the point of view of system design, many challenges remain to be solved by future development, such as assembly and fluidic interconnection of the compo-

Table 12.5 System configuration (required elements) of the fuel cell system shown in Fig. 12.17 as a function of load modes. The load modes are labelled A, B, C, D, and E, where A = continuous constant load, B = continuous load + constant period constant pulses, C = medium power variation, max. duty cycle about 1/100, D = high load variations and long stand-by times, E = same as D, improved fuel utilisation

Components	Ref. to Fig. 17	A	B	C	D	E
micro pump	**3**			**x**	**x**	**x**
micro reactor	**4**	**x**	**x**	**x**	**x**	**x**
hydrogen valve	**5**				**x**	**x**
hydrogen buffer	**6**			**x**	**x**	**x**
electronic and high-voltage generator	**7**			**x**	**x**	**x**
Li buffer battery	**8**		**x**	**x**	**x**	**x**
purge valve	**9**					**x**

Source: Fraunhofer IZM

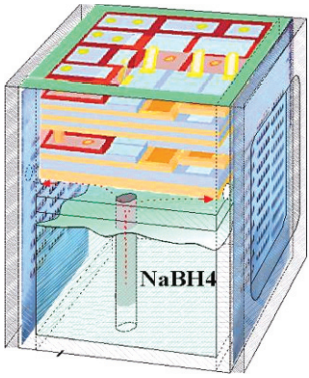

Fig. 12.18 Schematic representation of a cubic micro fuel cell system of 1 cm^3 in size

Table 12.6 Size estimation of the components corresponding to those of Fig. 12.7

Number	Components	Thickness (mm)	Width (mm)	Length (mm)	Volume (mm^3)
1	fuel cell	0.4	9	8	28.8
2	$NaBH_4$-H_2O storage	8	10	10	800
3	micro pump	0.5	6	6	18
4	micro reactor	0.5	4	4	8
5	hydrogen valve	0.5	6	6	18
6	hydrogen buffer	0.5	4	4	8
7	electronic, high-voltage generator	1.2	9	9	97.2
8	Li buffer battery	0.2	9	9	16.2
9	purge valve	0.5	4	4	8
	total				1002.2

Source: Fraunhofer IZM

nents in such a small value, low-power DC supply of the MEMS actuators, and cost reduction.

12.5 Standardisation

For a successful market launch of fuel cell systems, world-wide uniform fundamental requirements have to be defined for the certification of fuel cells. The standardisation of the interface and the cartridges for micro fuel cells will enable the manufacturer to independently introduce the systems on the market. Due to the toxicity and combustibility of methanol, its use will have to be restricted.

The main force driving the standardisation of fuel cell technologies is automotive industry. Figure 12.19 gives an overview of international regulations and standards relating to the fuel cell.

The committees responsible for small fuel cells are working in IEC TC 105 on fuel cells and methanol and in the ISO TC 197 on fuel cartridges. The focus of

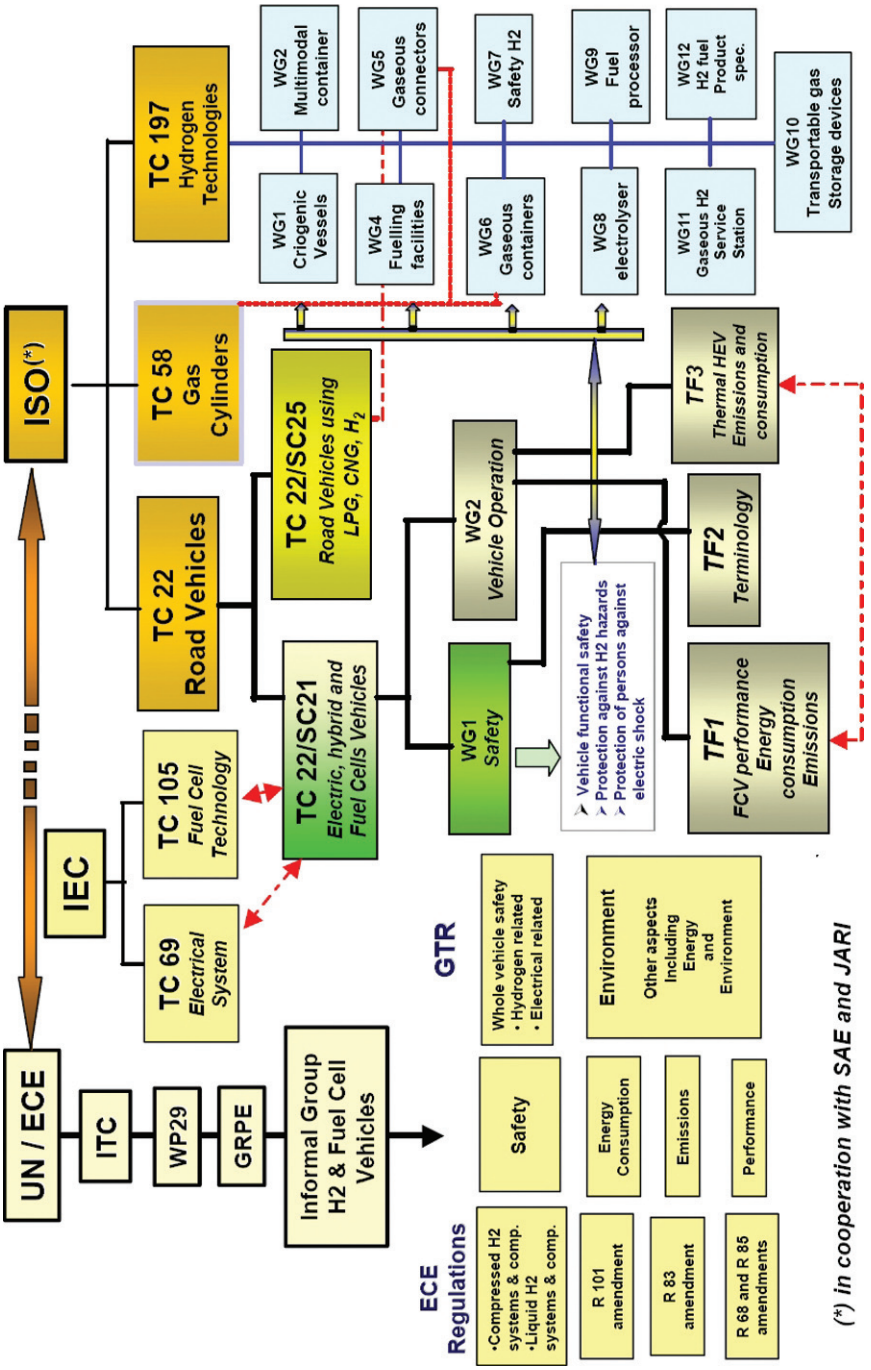

Fig. 12.19 Fuel cell standardisation and regulation authorities [39]

the Technical Committee 105 is on terminology, the fuel cell module as well as on stationary, mobile, portable, and micro fuel cells.

The focus of Technical Committee 197 is on the fuel. International standards and draft standards include:

Published standards:
ISO 13984 Liquid hydrogen – Land vehicle fuelling system interface
ISO 14687 Hydrogen fuel – Product specification

Draft international standards:
ISO/DIS 13985 Liquid hydrogen – Land vehicle fuel tanks
ISO/DIS 15869 Gaseous hydrogen and hydrogen blends – Land vehicle fuel tanks –
Part 1: General requirements
Part 2: Particular requirements for metal tanks
Part 3: Particular requirements for hoop wrapped composite tanks with metal liner
Part 4: Particular requirements for fully wrapped composite tanks with metal liner
Part 5: Particular requirements for fully wrapped composite tanks with non-metallic liner
ISO/DIS 17268 Gaseous hydrogen – Land vehicle filling connectors (based on SAE J2600)
ISO/ DIS 21009- 1 Liquid hydrogen storage

Working drafts:
ISO/WD 22734 Hydrogen generators using water electrolysis process
ISO WD 13986 Tank containers for multimodal transportation of liquid hydrogen

Committee drafts:
ISO/CD PAS 15594 Airport hydrogen fuelling facility
ISO/ CD 22734 Electrolyser
ISO/CD 24490 Cryogenics pump

Draft publicly available specifications:
ISO/PRF TR 15916 Basic considerations for safety of hydrogen systems

Proposed new work items:
ISO/AWI 16110 Hydrogen generators using fuel processing technologies
ISO/AWI 16111 Transportable gas storage devices – Hydrogen absorbed in reversible metal hydride
ISO/TC 197 NWIP N 253 Dispensing unit
ISO/NP 20012 Gaseous hydrogen and hydrogen blends — Fuelling stations (draft technical specification)

References

1. H. Liu, C. Song, et al. “A review of anode catalysis in the direct methanol fuel cell” Journal of Power Sources 155 (2006) 95–110.

2. A. Schmitz, R. Hahn, S. Wagner, and C. Hebling. “Stability of planar PEMFC in printed circuit board technology” Journal of Power Sources 127 (2004) 197–205.
3. [l] Bostaph, J., et al. ”Microfluidic Fuel Delivery System for 100 mw DMFC”. Direct Methanol Fuel Cell Proceedings of the 19 gh Electrochemical Society Meeting, March 25–29, 2001 pp. 274–285.
4. S.-S. Hsieh, et al. “Study of operational parameters on the performance of micro PEMFCs with different flow fields” Energy Conversion and Management 47 (2006) 1868–1878.
5. S. H. Chan, et al. “Development of a polymeric micro fuel cell containing laser-micro machined flow channels” Journal of Micromechanics and Microengineering 15 (2005) 231–236.
6. S. W. Cha, et al. “The influence of size scale on the performance of fuel cells” Solid State Ionics 175 (2004) 789–795.
7. A. Schmitz, et al. “Planar self breathing fuel cells”, Journal of Power Sources, 118 (2003) 162–171.
8. T. A. Schmitz, “System Development of Planar Self-breathing PEM Fuel Cells: Simulation, Characterization, Construction”, Thesis Technical University Berlin 2006.
9. R. O’Hayre, et al. “Development of portable fuel cell arrays with printed-circuit technology”, Journal of Power Sources 124 (2003) 459–472.
10. S. Uk. Jeong, et al. “A study on cathode structure and water transport in air-breathing PEM fuel cells” Journal of Power Sources 159 (2006) 1089–1094.
11. R. Hahn, S. Wagner, A. Schmitz, and H. Reichl, “Development of a planar micro fuel cell with thin film and micro patterning technologies”, Journal of Power Sources 131 (2004) 73–78.
12. R. Hahn “Miniaturization of Fuel Cells – low-cost manufacture of micro fuel cells with the help of microelectronics” f-cell 2005, Stuttgart, Germany, September 26–28, 2005.
13. S. C. Kelley, et al. “Miniature fuel cells fabricated on silicon substrates” AIChE Journal May 48 No. 5 (2002) 1071.
14. J. Yeom, et al. “Microfabrication and characterization of a silicon based millimeter scale PEM fuel cell operating with hydrogen, methanol and formic acid. Sensors and Actuators B, 107(2) (29 June 2005) 882–891.
15. D. Marsacq, “Les micropiles à combustible, une nouvelle génération de microgénérateurs électrochimiques”, Clefs CEA 50–51, 2004–2005.
16. T. Pichonat and B. Gauthier-Manuel, “Development of porous silicon-based miniature fuel cells”, Journal of Micromechanics and Microengineering 15 (2005) 179–184.
17. S. M. Mitrovski, and L.C. Elliott, Microfluidic devices for energy conversion: Planar integration and performance of a passive, fully immersed H_2–O_2 fuel cell, Langmuir 20 (17) (2004) 6974–6976.
18. L. Mex, M. Sussiek, and J. Müller, Plasma polymerized electrolyte membranes and electrodes for miniaturized fuel cells, Chemical Engineering Bulletin, 190(9)(2003) 1085–1095.
19. N.-T. Nguyen and S.H. Chan, “Micromachined polymer electrolyte membrane and direct methanol fuel cells – a review”, J. Micromechanics and Microengineering 16 (2006) R1–R12.
20. H. Chang, “DMFC pack of 3.6 V–2000 mW and its application in mobile electronics” Small Fuel Cells 2002, Washington, USA, April 21–23, 2002.
21. Z. Guo and A. Faghri, “Development of planar air breathing direct methanol fuel cell stacks” Journal of Power Sources 160 (2) (2006) 1183–1194.
22. C.Y. Chen and P. Yang, “Performance of an air-breathing direct methanol fuel cell”, Journal of Power Sources 123 (2003) 37–42.
23. G.Q. Lu and C.Y. Wang, “Development of micro direct methanol fuel cells for high power applications” Journal of Power Sources 144 (2005) 141–145.
24. B.-K. Kho et al., “The effect of pretreatment methods on the performance of passive DMFCs” Electrochimica Acta 50 (2004) 781–785.
25. T. Shimizu et al., “Design and fabrication of pumpless small direct methanol fuel cells for portable applications”. Journal of Power Sources 137 (2004) 277–283.
26. S. Gottesfeld, “Methods and apparatuses for a pressure driven fuel cell system”, US Patent No. 6, 686,081 B2 (2004).

27. R.G. Hockaday, “Small diffusion driven fuel cells”, in: The Knowledge Foundation’s 5th Annual International Symposium – Small Fuel Cells for Portable Power Applications, Hyatt Regency, New Orleans, LA, USA, May 7–9, 2003.
28. M. Yonetsu, M. Takashita, and H. Sumino, “Liquid fuel-housing tank for fuel cell and fuel cell”, US Patent No. 6, 506, 513 (2003).
29. Z. Guo and A. Faghri, “Miniature DMFCs with passive thermal-fluids management system” Journal of Power Sources, 160(2) (6 October 2006) 1142–1155.
30. S.-C. Yao et al., “Micro-electro-mechanical systems (MEMS)-based micro-scale direct methanol fuel cell development”, Energy 31 (2006) 636–649.
31. S.U. Jeong et al., “A study on hydrogen generation from $NaBH_4$ solution using the high-performance Co-B catalyst”, Journal of Power Sources 144, (2005) pp. 129–134.
32. S.C. Amendola et al., “A safe, portable, hydrogen gas generator using aqueous borohydride solution and Ru catalyst”, International Journal of Hydrogen Energy 25, (2000) 969–975.
33. D. Gervasio, S. Tasic, F. Zenhausern, “Room temperature micro-hydrogen-generator”, Presentation for IMAPS Advanced Technology Workshop on Fuel Cell Electronics Packaging, 2006.
34. A.M.F.R. Pinto et al., “Hydrogen generation and storage from hydrolysis of sodium borohydride in batch reactors”, International Journal of Hydrogen Energy 31, (2006) 1341–1347.
35. J. Wills, “Small fuel cells”, Fuel Cell Review, (April 2006), 12–14 http://www.iop.org/IOP Publishing Ltd 2004–2006.
36. http://www.varta.com
37. R. Hahn, S. Wagner, T. Stolle, S. Krumbholz, and H. Reichl, “Button cell sized micro fuel cell system”, International Symposium PowerMEMS Tokyo, November 28–30, 2005.
38. R. Hahn, M. Krumm, and S. Wagner, “Thermal Management of Portable Fuel Cell Stacks”, Fuel Cells Science and Technology 2002, Scientific Advances in Fuel Cell Systems, Amsterdam, September 25–26, 2002.
39. CRF-Vehicle – “Fuel Cell Systems” – Feb. 2005.
40. L. Mex, “Brennstoffzellenkomponenten in dünnfilmtechnologie”, www.hiat.de/pdf/Vortrag 17_3P.pdf.

Chapter 13
Challenges for the Industry

Matthias Bronold

List of abbreviations

DMFC	Direct Methanol Fuel Cell
PEMFC	Proton Electrolyte Membrane Fuel Cell
PFSA	Perfluorosulphonic Acid
MEA	Membrane Electrode Assembly
FMEA	Failure Modes and Effects Analysis
IEC	International Electrotechnical Commission
ICAO	International Civil Aviation Organization

The limitations of the operation time of mobile electronics equipment due to a non-satisfying performance of batteries have been discussed for a long time. Even though the battery capacity increased considerably – and will continue to increase for some years at least – there are applications like TV viewing from hand-held devices, where battery runtime presently is a distinct barrier to a widespread use. As a consequence, a strong market pull for new power supply technologies like fuel cells is

Matthias Bronold
Samsung SDI Germany GmbH, European Research Center, Ostendstr. 1–14, 12459 Berlin, Germany, e-mail: Matthias.bronold@samsung.com

A. Léon (ed.), *Hydrogen Technology*,

observed. The expectation is to offer superior device runtimes and the independence of the electric grid for powering mobile electronic devices like mobile phones, hand-held computers, MP3 players, and notebook computers. For this purpose, different types of fuel cells are under development and each of them presents benefits and disadvantages with respect to the applications envisaged.

Of the applications mentioned above, the notebook computer fuel cell system will be the largest one in terms of power output, energy content, and size. It was demonstrated [1] that a notebook computer can be powered by scaling down "conventional" types of fuel cell systems, i.e. the devices are assembled from a fuel cell stack, pumps, process-related system components, etc. The notebook computer application (see Fig. 13.1) appears to be the most feasible entry product for fuel cells in mobile electronic devices, because it relies on previous experience in the fuel cell industry. The advantages and disadvantages of different types of fuel cell systems for the present status of technology are compared in Table 13.1. The compilation shows that the direct methanol fuel cell (DMFC) has the best advantage/disadvantage profile for a notebook computer application. As a consequence, the majority of electronics companies have been concentrating on this technology so far. Different notebook and battery manufacturers presented a number of DMFC-based power supplies as prototypes. In contrast to this, powering of smaller systems in hand-held devices will require completely new technology platforms based on microsystems technologies in order to yield compact and cost-effective solutions.

In the following sections the basics of the DMFC system will be described (more details can be found in Chapter 4 of this book by Jens Oluf Jensen) and the main challenges as concerns the membrane, the water management, and the control parameters will be highlighted. In recent years several manufacturers presented prototype DMFC systems for mobile electronics applications and also estimated dates for market introduction. However, a thorough analysis of the present status of technology compared to the market requirements will show that issues like performance,

Fig. 13.1 Notebook PC with a fuel cell docking station attached for power supply

Table 13.1 Comparison of advantages (+) and disadvantages (−) of different types of fuel cell/fuel combinations for powering notebook computers (neutral: o). The question mark for $NaBH_4$ refers to safety issues which are not fully evaluated

Fuel cell type	DMFC	PEMFC Reformer	PEMFC	PEMFC
Storage	100% Methanol	50% Methanol	$NaBH_4$ Fuel	Metal Hydride
Energy density of fuel	+	o	+	−
Fuel/cartridge costs	+	+	−	−
Ignition hazard of fuel	o	+	?	−
Toxicity of fuel	−	−	+	+
Proof of concept in real customer application	+	−	−	−

reliability, durability, and infrastructure remain to be solved with mobile DMFC. Herein, each of these basic challenges will be described and discussed.

13.1 Basics of DMFC System Technology

The basic principle – i.e. the cell set-up and cell reaction – of a direct methanol fuel cell is similar to a hydrogen-supplied PEM-type fuel cell. The main difference of today's DMFC concepts versus the PEMFC is that the fuel is supplied as a liquid, a diluted solution of methanol in water.

The core component is the membrane-electrode assembly (MEA), where the membrane is sandwiched by anode and cathode active layers (also named three-layer arrangement). In the so-called five-layer arrangements also diffusion media for the anode and cathode fluids are laminated onto the structure which by itself may contain gradients in porosity, hydrophobic/hydrophilic nature, and other properties. The optimisation of these complex layer structures is a major focus of DMFC (as well as of PEMFC) development [2]

The cell reactions of a DMFC are (assuming a water drag coefficient of three as shown below):

$$\text{Anode}: \quad CH_3OH + 19H_2O \rightarrow CO_2 + 6H^+(3H_2O) + 6e^-$$

$$\text{Cathode}: \quad 3/2\ O_2 + 6H^+(3H_2O) + 6e^- \rightarrow 21H_2O$$

$$\text{Overall}: \quad CH_3OH + 3/2\ O_2 \rightarrow CO_2 + 2\ H_2O$$

At the anode, methanol is oxidised in a reaction with water to yield carbon dioxide, releasing electrons to the outer circuit. The resulting protons – six per methanol molecule – migrate through the membrane towards the cathode, where they react with oxygen from the air, yielding the product water. Due to the transport properties of the perfluorosulphonic acid (PFSA) electrolyte, the protons have to be surrounded by a

number of water molecules in order to be mobile within the membrane (hydration shell). The number of water molecules in this hydration shell depends on material properties, temperature, and the dwelling state of the membrane. In a DMFC (nafion 117 membrane at 70°C), for example, it amounts to about $3H_2O$ per proton [3] under typical application conditions. At the cathode, oxygen from air is reduced by the electrons from the external circuit. Upon uptake of protons, three water molecules are formed at the cathode per methanol molecule consumed at the anode.

In total, about 21 molecules of water are released on the cathode side. 19 of them have to be fed back to the anode side in order to cover water consumption. This has principal implications on system design. Since a supply of considerable amounts of water within the fuel cartridge would reduce the energy density to a non-acceptable level, an efficient feedback of water from the cathode off-stream of the stack is essential to obtain a functional system.

An additional impact on the water feedback function is imposed by the so-called methanol crossover [4]. Due to intrinsic properties of conventional types of membranes, a certain amount of methanol diffuses through the membrane and reacts directly with the oxygen in a catalytic thermal reaction, also yielding water and CO_2 while generating heat. Thus, a complex water balance has to be achieved within the system, depending on the concrete system design and operation parameters. In order to keep the methanol crossover at a reasonable level, the methanol concentration is adjusted to about 1–3%.

Figure 13.2 displays a general set-up of a DMFC system with the anode cycle marked in medium grey and the cathode side with air supply and water recycling in light grey. At the outlet of the anode side of the stack, a two-phase mixture is present with the depleted fuel and CO_2 in the reactant stream. At first, the CO_2 is separated from the liquid by using a CO_2 separation device and vented into the ambient air. Then, the depleted fuel free of CO_2 is mixed with concentrated fuel from the fuel cartridge. The reactant stream leaving the cathode side of the stack consists of a mixture of depleted air and water. The major part of this water is extracted by condensation using a water recycling device (essentially a heat exchanger) and directed into the anode loop. Then, the mixture of depleted fuel, concentrated fuel, and water flows to the inlet of the anode side of the stack.

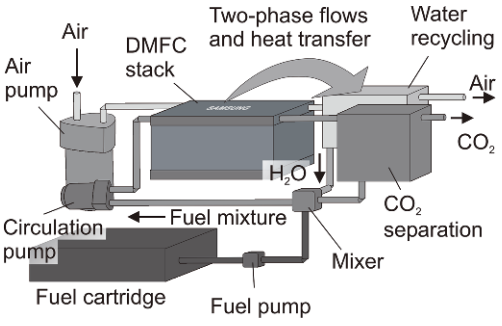

Fig. 13.2 Typical set-up of a DMFC system showing the most important system components and media streams. The anode cycle is marked medium grey, the cathode side with air supply and water recycling light grey. The part containing concentrated methanol is displayed in dark grey

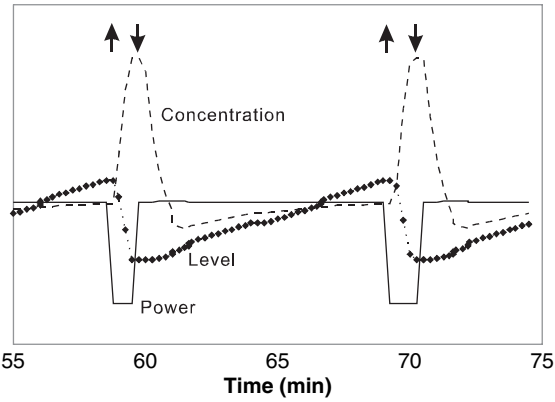

Fig. 13.3 Results of a transient system simulation showing the impact of a simple control strategy (see text) on stack power, liquid level, and methanol concentration in the anode loop [5]. Quantities are given in relative values for comparison. Arrow up: level high, fan switched off. Arrow down: level low, fan switched on

In operation, the reactant streams from the electrodes form two interconnected loops. Material and heat transfer occurs between the devices from each stream, leading to highly non-linear interrelations of the system design and operation parameters. This will be demonstrated below by a transient system simulation result summarised in Fig. 13.3 [5]. The graph displays the stack power, the liquid level, and the methanol concentration within the anode cycle. In order to compare the relative effects, all operation parameters are displayed in arbitrary units. A simple control algorithm is applied to illustrate the dependence among the parameters. When the liquid level in the CO_2 separation device (or the mixer) exceeds a pre-determined level, the cooling fan of the heat exchanger is switched off. As a consequence, the parasitic system power is reduced (by the fan power) and the stack power is reduced accordingly, leading to the reduction of water condensation and, subsequently, of the liquid level. At the same time, if the flow of concentrated fuel from the cartridge is constant, the fuel concentration in the anode loop increases instantly, leading to non-optimised operation conditions. These perturbations have to be levelled out by properly adjusting the control parameters.

The more compact the DMFC system is, the smaller will be the liquid amount inside the anode cycle. Hence, the system will be more sensitive to these perturbations. It will become more challenging to keep the system within the pre-determined range of operation parameters.

13.2 Basic Challenges

In general, the basic challenges are similar to other fuel cell systems and the most important issues can be summarised as follows:

- Performance
- Reliability
- Durability
- Infrastructure

13.2.1 Performance

The principal competitors of mobile fuel cells are secondary batteries of nickel-metal hydride and lithium-ion type. The customer will prefer fuel cells to batteries when the performance of the fuel cell becomes superior, the advantage compensating a possibly higher sales price. In a first instance, this means to supply more energy for a given volume or a given weight [6, 7] while fulfilling the other specifications of the application like the power output.

The most widespread lithium-ion battery in notebook PC applications is the cylindrical 18650 cell (18 mm in diameter and 65 mm in length) with 3.6 V and 2–2.4 Ah. Typical cell chemistry is lithium/graphite for the anode and cobalt oxide for the cathode. For battery packs based on this type of cells, there is a relatively small variation in the weight for a given notebook runtime (see Fig. 13.4 (a)).

The volume of the battery packs additionally is determined by the size of the control electronics and the packaging technology, which are considerably different among different suppliers. Hence, there is a larger spread in the volumes per runtime of available notebook PC power packs (see Fig. 13.4 (b)).

In Fig. 13.4 specific energies (energy per weight) and energy densities (energy per volume) of different types of notebook and military power supplies are compared. For being more instructive, the energy is expressed in terms of projected runtime assuming a continuous load of 20 W, i.e. one hour runtime corresponds to 20 Wh of energy. The weight of a DMFC system results from adding the core weight (the system without the fuel cartridge) and the weight of the fuel cartridge to achieve a certain runtime. The same principle applies to the volume.

The weight needed for a certain runtime of notebook power supplies is displayed in Fig. 13.4 (a). It is obvious that a DMFC with a core weight of 0.8 kg (line A) and about 0.15 kg of fuel added (i.e. total weight 0.95 kg) achieves a runtime of about 8 hours which is comparable to that of a battery pack with the same weight. For higher runtimes, the DMFC is superior to the battery. When reducing the core weight to 0.6 (line B) and 0.4 kg (line C), the fuel cell is superior starting with about 6 and 4 hours, respectively.

In the case of military batteries, a state-of-the-art DMFC prototype (line D) is superior to standard military batteries after about 30 hours of runtime. When the core weight would be reduced by about 50% (line E), the “break-even” of the fuel cell is at about 20 hours.

Since battery systems contain at least partly heavy elements, there is a clear value added of fuel cells against batteries in terms of weight. This is especially true for military applications, where very long runtimes (projected 72 hours) are required and a reduced weight gives advantages in logistics and transport.

However, it is obvious from the customer behaviour in mobile electronics that the volume of a power supply, i.e. energy density, is an issue of at least the same importance as that of specific energy. Figure 13.4 (b) compares the energy density (runtime vs. volume) of DMFC’s and notebook batteries. It is evident that for each of the selected core volumes, the total volume of the fuel cell is larger than the

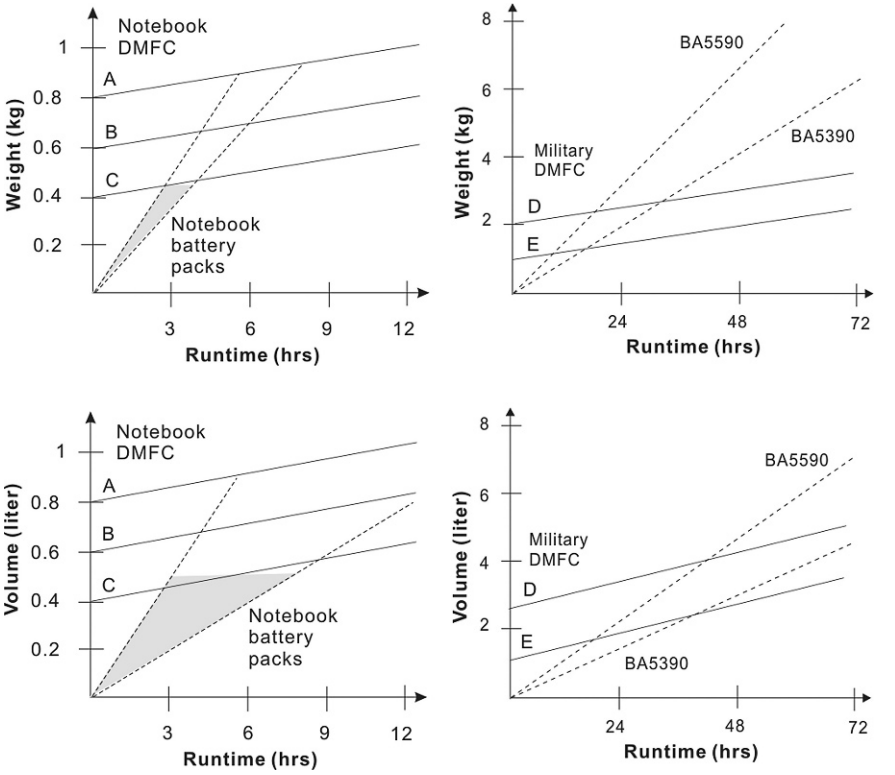

Fig. 13.4 Weight and volume comparison of DMFC and battery power supplies assuming a continuous power output of 20 W. **a**) (top left) and **b**) (bottom left) for notebook power supplies; **c**) (top right) and **d**) (bottom right) for military applications. Notebook battery pack data and US Army BA5390 and BA5590 standard battery data based on supplier information, extrapolated to larger runtime (multiple battery packs). Notebook DMFC, lines A – C: Weight and volume for potential notebook DMFC systems with different core weights/volumes (system without fuel cartridge, represented by the intercept with the y-axis). Lines D: Military DMFC: taken from US CERDEC [10]. Lines E: Military DMFC, core weight/volume reduced by 50% compared to lines D

batteries for a one-day operation. Only for multiple-day use is the necessary volume of the fuel cell system smaller.

Also for military applications (Fig. 13.4 (d)), the advantage of fuel cells in terms of volume is only small. The state-of-the-art military DMFC (line D) is inferior to the BA5390 battery in the whole range discussed. By reducing the core volume of the fuel cell system by about 50% (line E), a small volume advantage is given for 72 hours of runtime.

Since the weight of the system is highly important for military applications, the performance level of fuel cell systems is reaching a competitive level. However, other issues, such as reliability and durability [8], have to be solved before a market introduction will be possible.

For standard notebook applications, the volume of the power supply has to be further reduced considerably in order to compete with the higher-performing batteries. To date, it is still difficult to exactly anticipate at which level a possible decrease in volume is accepted by the customer when a higher specific energy and the independence from the grid are ensured.

Measures to further increase the energy density of DMFC systems are:

- Development of improved membranes/MEAs with higher power density and/or higher voltage
- Reduction of methanol crossover and water drag
- Development of volume-optimised system components like heat exchangers and phase separators
- Development of "dedicated" pumps with low volume, low power consumption, and low noise.

The former two issues are the most important ones, since the properties of the MEA mainly determine the system properties. Promising approaches to solving these material-related problems are the development of hydrocarbon-based membranes with improved methanol and water permeation properties, which were presented recently [8, 9].

13.2.2 Reliability

Early field tests with residential fuel cells indicated that a major source of technical problems was the failure of system components. As far as the DMFC is concerned, the complexity is much lower than that of a reformer type fuel cell system for example. However, the components used in a DMFC have been developed for other applications and consequently, they might not fully comply with the requirements of fuel cell systems. Taking into account the high cost pressure on system design, it is crucial to properly understand the factors determining reliability in order to achieve a reliability level comparable to batteries.

A common method to determine and improve system reliability is the failure mode and effects analysis (FMEA). In this method the possible failure modes are ranked according to their severity, the probability of the occurrence, and the detection of a failure (more details can be found elsewhere [11]). Even though it is difficult in a development stage to give precise estimations of the occurrence and detection ratings, the FMEA is a helpful tool for developing systems which are inherently reliable.

Table 13.2 displays a small part of a system FMEA with some failure modes like the leaking of liquid or a too low flow rate of the fuel supplying the stack anode. The potential failure effects are ranked on a scale from one to ten giving the severity of the failure (SEV), where ten accounts for the worst severity (injury of a person) and one for an unperceptable effect. A medium ranking of e.g. six accounts for a partial perturbation of the function. Then, the occurrence of potential causes of

Table 13.2 Part of a system FMEA in order to rank possible failure modes of a DMFC system. SEV accounts for the severity of the failure mode on a scale from 1 to 10. The occurrence (OCC) and detection (DET) ratings are given on a more tentative level in order to demonstrate the usage of the Risk Priority Number RPN. The RPN ranking shows that a possible degradation of system components is an important reliability issue to be aware of

Potential failure mode	Potential failure effects	SEV	Potential causes of failure	OCC	CSC	DET	RPN
Leaking of fuel mixture/water	System shutdown due to low level	6	Aging of sealings	5		7	210
	Electrical short circuit	8	Disconnection of tube, partial loss of liquid inventory	4		5	160
	Damaging of system surrounding (computer, table, documents etc.)	9	Disconnection of tube, complete loss of liquid inventory	3		4	108
Too low anode flow rate	System shutdown due to low stack voltage	6	Circulation pump degradation	5		8	240
		6	Circulation pump clogging	4		3	72
	Stack degradation	5	Circulation pump degradation	5		8	200

failure (OCC) and the detectability with current system control methods (DET) are estimated with ten accounting for very frequent occurrence and non-detectability of the failure mode, respectively. Finally, the Risk Priority Number (RPN) is calculated as the product of the three ratings.

The different RPNs of the DMFC indicate that of the listed failure modes, the degradation of materials and components is most critical, because it is relatively difficult to detect. Thus, these issues have to be addressed thoroughly during system component development.

13.2.3 Durability

The durability (operational lifetime) of a fuel cell system is determined by the lifetime of the system components and the stack.

As discussed in the preceding section, stability and lifetime of system components have an influence on the stack performance. Failures in this respect may lead to unwanted shutdowns or a degradation of the system performance. These problems have to be treated by developing appropriate system components.

In addition, the durability is determined by the stack lifetime on a principal level, i.e. the stack as the core component determines the maximum possible lifetime. Degradation modes of the DMFC stack as discussed in literature are listed below:

- Dissolution of ruthenium from the anode catalyst and crossover to the cathode, which leads to a decreasing oxygen reduction reactivity of the cathode [12]
- Decrease in the catalyst's active surface area [13]
- Attack of the membrane by reactive reaction intermediates, which leads to a weakening of the membrane structure [14]
- Change in the hydrophobic structure of the cathode gas diffusion medium, leading to (partial) cathode flooding [15]

Due to the higher potential costs of a DMFC power supply – at least in the initial stage -, it is aimed at offering a power supply with a lifetime comparable to that of the notebook PC. Depending on the utilisation scheme, this leads to a lifetime specification well above 1000 hours. It has been demonstrated with portable DMFC systems that operational lives of this order of magnitude are feasible. However, to reach the target specifications of volume and weight as discussed in Chap. 13.2.1 Chap. 13., there is only a very small "margin" for oversizing components to compensate for degradation effects. The required durability can only be achieved by a proper understanding of the conditions leading to degradation. On this basis, the system control strategies especially during load changing situations, start-up, and shut-down have to be thoroughly adjusted to avoid excessive degradation effects.

13.2.4 Infrastructure

Establishing an infrastructure for the fuel is one of the major hurdles for a broad market introduction of fuel cells in mobile electronics. In order to make fuel cells a real consumer product, the fuel cartridges have to be available without limitation on the every-day routes of the customers, e.g. in supermarkets, hardware stores or filling stations. The high investments needed for such an infrastructure system require the collaboration of several players in the fuel cell industry, probably also with partners, who have direct access to a retail system.

Fig. 13.5 Concept design for a so-called "satellite" cartridge and fuel connector for refilling a docking station-type DMFC system. When designing a connector, it is crucial to ensure an easy and safe connection/disconnection also for non-trained users. (Image courtesy of Statoil ASA)

In recent years, considerable efforts were undertaken to define standards for fuel cartridges. In the Technical Committee TC105 of the International Electrotechnical Commission (IEC) a standard draft has been worked out in order to give design and test standards for fuel cartridges. Among others, fuel cartridges have to withstand [16]

- pressure and vibration
- high temperature and temperature cycling
- dropping
- long-term storage

Since business travellers are one of the most interesting target groups for mobile fuel cell applications, the safety aspects related to taking the fuel cartridge on board of an aircraft are of special importance. In 2005, it was proposed to the International Civil Aviation Organization (ICAO) to approve micro fuel cell systems and cartridges for carriage onboard of commercial aircrafts. Methanol was among those fuels which were included in this proposal. A decision of the ICAO is expected to be taken in the near future.

After fixing and approving the standards for fuel cartridges, the implementation process for the infrastructure can be shifted more into the focus than in the past. However, since many different partners have to be involved, finalising a concept for the fuel cartridges (one example shown in Fig. 13.5) and setting up an infrastructure system may still need some time.

13.3 Outlook

Direct methanol fuel cells have proven to be one of the most promising fuel cell types for mobile electronics. Nevertheless, parallel work on other types of fuel cells show that this position is not unchallenged.

Recent incidents with lithium batteries showed that there are inherent safety issues related to this technology, which are less pronounced with DMFCs. On the other hand, the increasing concern about potential terrorist attacks on airplanes may prevent the permission to use fuels onboard of an aircraft. Presently, it is not clear whether these issues will lead to a stronger or a weaker market pull for fuel cells.

For developing consumer products with fuel cells, considerable research and development work has to be performed to reach the required performance, reliability, and lifetime level, while keeping costs at an acceptable level. More likely, DMFCs and other fuel cells will penetrate additional niche markets first, giving the technology the opportunity to demonstrate superior performance over existing technologies.

References

1. Y. Goto, 7th Small Fuel Cell Conference, Washington D.C., April 2005, Knowledge Press.
2. H. Martin, “Prospects of the Direct Methanol Fuel Cell”, in G. Hoogers (Ed.), Fuel Cell Technology Handbook, CRC Press, Boca Raton, 2003.

3. X. Ren, and S. Gottesfeld, J. Electrochem. Soc. “Electro-osmotic Orag of Wakes in Poly (perfluorosulfonic acid) Membranes” 148, A87–A93 (2001).
4. J. T. Mueller, “Reality checks to Commonly Heard Direct Methanol Fuel Cells Myths” from www.fuelcelltoday.com, 2005.
5. D. Larrain, 3rd Fuel Cell Research Symposium, EPMA, Duebendorf, (Switzerland), March 2006.
6. A. Heinzel, in K. Ledjeff-Hey, F. Mahlendorf, J. Roes (Eds.), Brennstoffzellen, 2nd edition, C.F. Mueller, Heidelberg, 2001.
7. M. Bronold, OTTI Technology Workshop, Ulm (Germany), 2002.
8. H. Boehnke, Fuel Cell Seminar 2006, Hawaii, from www.fuelcellseminar.com.
9. P. Cox, 8th Small Fuel Cell Conference, Washington D.C., April 2006, Knowledge Press.
10. J. Christiani, and N. Sifer, US Army CERDEC, from http://stinet.dtic.mil, 2005.
11. Guidelines for Failure Mode and Effects Analysis (FMEA), for Automotive, Aerospace, and General Manufacturing Industry, Dyadem Press, Richmond Hill, 2003. D. H. Mueller, T. Tietjen, FMEA-Praxis, Carl Hauser, Munich, 2000.
12. P. Piela, C. Eickes, E. Brosha, F. Garzon, and P. Zelenay, J. Electrochem. Soc. 151, A2053–59 (2004).
13. P. Zelenay and Y.S. Kim, Fuel Cells Durability Conference, Washington, 2005, Knowledge Press.
14. D. Y. Seung, G. Park, Y. Chung, C. Pak, and H. Chang, 10. Ulm Electrochemical Talks, Ulm, 2006. Center for Solar Energy and Hydrogen Research.
15. S.R. Narayanan and T.I. Valdez, Fuel Cells Durability Conference, Washington, 2005, Knowledge Press.
16. Draft specification PAS 62282-6-1 of the TC105 of the IEC International Electrotechnical Commission.

Part IV
Advanced Tools for the Development of new Materials

Chapter 14
Introduction

Aline Léon

Hydrogen storage is a key technology required for the development of a hydrogen-based economy. However, as shown in Chap. 3, however, the storage capabilities of current materials are far from meeting the requirements of viable on-board automotive storage. Therefore, fundamental research will be required to design novel materials and reveal the principles underlying the control of hydrogen uptake and release.

Part IV of this book will give an overview of the techniques currently used to develop storage materials from their synthesis to their characterization.

The first section will be dedicated to the synthesis of nanoscale hydrogen storage materials. It will be shown that new reaction pathways can be developed by theoretical calculation. Then, the Schlenk technique will be described and applied as an example for the chemical synthesis of $Mg(AlH_4)_2$ and $Ca(AlH_4)_2$. Finally, the mostly used technique to date, namely, ball milling shall be outlined. The parameters that are of importance in a mechanical synthesis will be listed. A description of the synthesis by different types of reaction, such as reactive ball milling, metathesis reaction, and destabilization reaction, will follow.

The second section will present the methods used to characterize the kinetic and thermodynamic properties of a material. At first, the theoretical background of the thermodynamics and kinetics of metal hydrides will be outlined briefly. Then, volumetric and gravimetric methods used for the determination of the hydrogen storage capacity and sorption kinetics will be highlighted. Volumetric measurement will be presented in particular detail, with a description of the apparatus, accessories, and measurement process. Then, the practical problems encountered in carrying out accurate and reproducible measurements will be highlighted with particular attention being paid to the safety issues related to the use of such an apparatus in a laboratory environment. Finally, the direct determination of the thermal and thermodynamic properties of a material by means of differential scanning calorimetry (DSC)

Aline Léon
Institut für Nanotechnologie, Forschungszentrum Karlsruhe, P.O. Box 3640, D – 76021 Karlsruhe, Germany, e-mail: aline.leon@int.fzk.de

A. Léon (ed.), *Hydrogen Technology*,

will be described from the measurement principles to the measurement setup and applications to $Mg(BH_4)_2$, MgH_2, and $LiAlH_4$.

The third section will give an overview of the tools presently used to investigate the atomic arrangement, phase composition, morphology and texture, surface, and bulk composition of a material. It will start with X-ray diffraction and powder neutron diffraction (XRD-PND) that reveal the atomic structure of solid materials. Then, scanning electron microscopy (SEM) and scanning transmission electron microscopy (STEM) will be described with a special focus on analytical techniques like energy dispersive spectroscopy (EDS) or electron energy loss spectroscopy (EELS) which can be combined in the imaging tool. This will be followed by a description of X-ray photoelectron spectroscopy (XPS) which is a surface-sensitive technique used to identify elements and chemical bonding in the outermost atomic layers. Finally, a local structural probe, namely, X-ray absorption fine structure (XAFS), will be presented, which allows for the investigation of the chemical state and local atomic environment of an element in the material.

For each of these techniques, the principle of the method, including the experimental aspects, will be first outlined. A general overview of the experimental method, theory, and data analysis will be given. Then, application of these techniques to selected hydrogen storage materials will be presented in order to illustrate which information can be extracted by each of them.

Chapter 15
Synthesis of Nanoscale Hydrogen Storage Materials

Michael Felderhoff

List of Abbreviations

Eq	Equation
PEM	Proton exchange membrane
THF	Tetrahydrofuran
wt.-%	Weight-%

15.1 Introduction

The synthesis of nanoscale hydrogen storage materials needs different tools for the preparation of such systems. Due to the reactivity of nanoscale metal hydrides to moisture and oxygen, most of the reactions must be carried out in an inert gas atmosphere. The Schlenk technique is the method of choice for wet chemical preparation methods and mostly used for solution synthesis. Unlike the wet chemical synthesis,

Michael Felderhoff
Max-Planck Institut für Kohlenforschung, 45470 Mülheim an der Ruhr, Germany,
e-mail: felderhoff@mpi-muelheim.mpg.de

A. Léon (ed.), *Hydrogen Technology*,

materials preparation without any kind of solvent has found a wide range of applications over the last 10 years. High-energy ball milling methods are now widely used for the preparation of nanoscale materials. Both methods shall be described in the following section.

The particle size, surface area, number of defects in a crystal material, and grain boundaries influence the reactivity and the kinetics of a solid-state material. In contrast to the bulk material, nanoscale systems have a grain size not larger than 100 nm, with a more typical range between 5 and 50 nm. The size of the whole particles normally is much larger with diameters in the μm range. However, these grains inside the particles make the materials inhomogeneous due to reaction pathways along the grain sizes or high reactivity at surface defects. This high reactivity of nanoscale materials depends on the numbers of atoms in and near the grains. In particles with a diameter of 10 nm, 30% of all atoms are within the grain sizes. In particles with a diameter of only 5 nm, this value is increased to 50–60% of all atoms.

For the development of new materials or the tuning of known materials to a special application, two methods exist. One is the kinetics of a reaction, which is affected by the amount and the type of a catalyst and does not change the thermodynamics of the reaction. Only the rate of decomposition and refilling of the material can be tuned by the addition of a catalyst. Since every chemical reaction has its own thermodynamics, the thermodynamics of a system cannot be changed in principle. However, the addition of a second or a third component to a hydrogen storage system may open up new reaction pathways with different thermodynamics. Theoretical calculations may help to find such new reaction pathways for the development of other types of hydrogen storage systems.

15.2 New Reaction Pathways Using Theoretical Calculations

Besides the practical approaches to developing new (nanoscale) metal hydride and complex metal hydride systems, theoretical calculations may focus on alternative or new solutions. First principle quantum mechanics calculations are not only a tool for providing a fundamental understanding of electronic properties of metal hydride systems [1]. These calculations could serve as guidance in the search for new materials. For a first assessment of possible reaction pathways of potential metal hydride systems, the enthalpy of the decomposition (or hydrogenation) is a useful parameter and can be determined with quantum mechanics calculations.

The reaction enthalpy ΔH for the decomposition reaction of a mixture of $LiBH_4$ and MgH_2 was calculated to be 65–67 kJ/mole H_2 [2]. For a reversible hydrogen storage material that is ready for technical PEM fuel cell applications, the ΔH value must be in the range of 40 kJ/mole H_2 at 20°C and 1 bar pressure [3]. The calculated value for the $LiBH_4/MgH_2$ mixture is approximately 20 kJ/mole H_2 too high for practical application. These theoretical findings, however, fit very well with the experimental results of this decomposition reaction (Eq. 15.1).

$$2\,LiBH_4 + MgH_2 \rightleftarrows 2\,LiH + MgB_2 + 4\,H_2 \quad (15.1)$$

Another interesting example is the combination of $LiNH_2$ and MgH_2 at a molar ratio of 1:1, in contrast to the experimental results presented for a 2:1 $LiNH_2$: MgH_2 ratio. The decomposition reaction is calculated by (Eq. 15.2).

$$LiNH_2 + MgH_2 \rightleftarrows LiMgN + 2\,H_2 \quad (15.2)$$

With a calculated energy of 30 kJ/mole H_2, this reaction is too unstable and cannot be used as a room-temperature metal hydride system. Still, it is an interesting challenge to prepare this hydrogen storage mixture at a 1:1 molar ratio and compare the experimental findings with those of the 2:1 $LiNH_2$:MgH_2 system.

Quantum mechanics calculations may disclose new interesting starting points for the development of metal hydride systems. But the last evidence as to whether a description of a calculated reaction pathway is correct or not will depend on the experimental results.

15.3 Chemical Synthesis (Schlenk Technique)

15.3.1 Description

Most of the metal hydrides are very sensitive to the reaction of water and oxygen. It is therefore necessary to handle these materials in a protecting inert gas atmosphere. A widely used and convenient experimental method for handling such air- and water-sensitive materials is the Schlenk technique. To facilitate handling under inert gas conditions and remove air and moisture from the glassware, a manifold attached to an inert gas source and a vacuum pump is used, as displayed in Fig. 15.1. One manifold is connected to a source of inert gas, while the other is connected to a high-vacuum pump. A Schlenk line has several ports with two-way stopcocks to provide for a fast switching between inert gas and vacuum and can be used to purge different Schlenk tubes and flasks at once. When working with highly moisture-sensitive materials, like hydrides, it is often important to use special drying processes for the glassware. The glassware can be baked out in a drying oven at 130°C for several hours and flushed with the dry inert gas during cooling. Alternatively, it can be evacuated during heating with a heat gun and flushed with inert gas during cooling. Dry solvents are required in metal hydride chemistry. Standard procedures for the drying of these solvents exist.

The Schlenk technique was used for the recrystallisation and doping of sodium aluminium hydride $NaAlH_4$, demonstrating that Ti-doped $NaAlH_4$ can be used as a reversible hydrogen storage material [5]. Figure 15.2 displays a scanning electron microscopy (SEM) of $NaAlH_4$ crystals precipitated from a tetrahydrofuran solution with diethyl ether using the Schlenk technique. The crystal size is in the range of 50 μm.

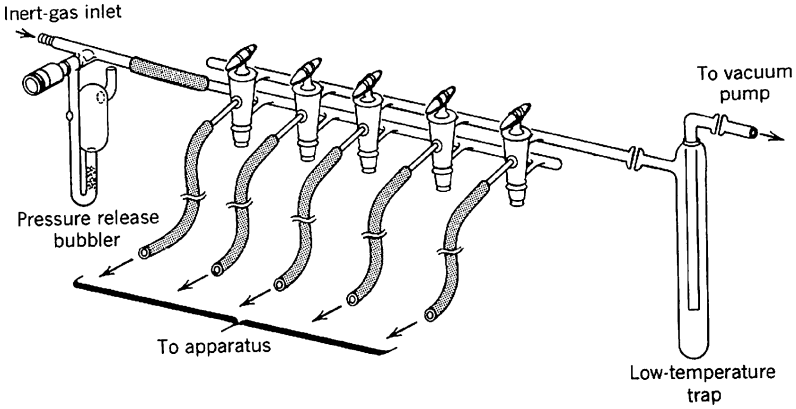

Fig. 15.1 Manifold for the handling of chemicals under inert gas conditions (Schlenk line) [4]

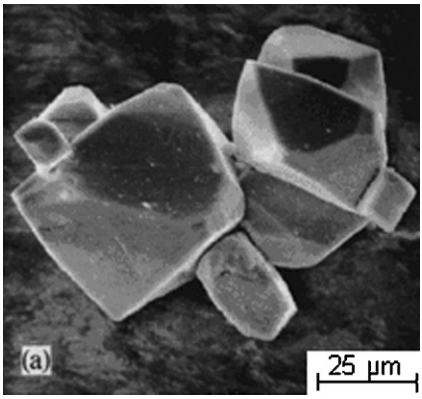

Fig. 15.2 $NaAlH_4$ crystals from THF solutions precipitated with diethyl ether

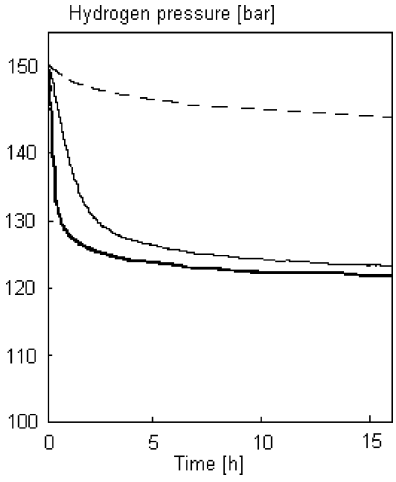

Fig. 15.3 Progression of the rehydrogenation of decomposed Ti-doped $NaAlH_4$ (NaH + Al) at 170°C/152 bar. ▬ $Ti(OBu)_4$, — $TiCl_3$, ---- undoped $NaAlH_4$

With different Ti-doped materials, a reversible storage capacity in the range of 4 wt.-% at 170°C and pressures around 152 bars can be achieved (Fig. 15.3). The hydrogenation rate is slow (in the range of hours), but using this material, reversibility of a complex metal hydride was demonstrated for the first time.

15.3.2 Synthesis of $Mg(AlH_4)_2$ and $Ca(AlH_4)_2$

The alkaline earth alanates $Mg(AlH_4)_2$ (7.0 wt.-% H_2) and $Ca(AlH_4)_2$ (5.9 wt.-% H_2) are interesting hydride materials because of their high hydrogen content. Under inert gas conditions, the ether adduct of $Mg(AlH_4)_2$ was prepared with the Schlenk technique according to (Eq. 15.3).

$$\begin{aligned} MgCl_2 + 2\,NaAlH_4 &\xrightarrow{Et_2O} Mg(AlH_4)_2 \cdot Et_2O + 2\,NaCl \\ Mg(AiH_4)_2 \cdot Et_2O &\xrightarrow[\text{vacuum}]{90^\circ C} Mg(AlH_4)_2 + Et_2O \uparrow \end{aligned} \tag{15.3}$$

Magnesium alanate precipitated as a solvent adduct together with sodium chloride. It was separated from the salt by Soxhlet extraction with diethyl ether. After removal of the solvent and drying at 90°C in vacuum to decompose the adduct, a white nanocrystalline powder of $Mg(AlH_4)_2$ was obtained [6, 7].

The same metathesis reaction with $CaCl_2$ instead of $MgCl_2$ was carried out for the preparation of $Ca(AlH_4)_2$ using the Schlenk tube technique in THF solution in a glass mill reactor. Without milling, no products could be observed. It seems that milling is necessary to create fresh particle surfaces. The solvent-free product was obtained after evaporation in vacuum at temperatures up to 90°C [8].

15.4 Mechanical Synthesis (Ball Milling and Reactive Ball Milling) [9]

15.4.1 Description of the Ball Milling Process

High-energy ball milling is a powerful grinding technique for the synthesis of different kinds of nanoscale metal hydride materials. The synthesised materials often have grain boundaries in the nm range. With this method, solid-state chemical reactions can be induced at room temperature. During the mechano-chemical process, powder mixtures or other materials are trapped between colliding balls or between a ball and the vial. The outcome of this collision is a plastic deformation and an increase of the temperature in the particles. The particles are fractured and welded, which gives rise to an exchange of matter between the particles and, hence, increases the chemical reaction rate between the solid-state compounds [10]. Depending on the type of mill (planetary ball mill,

vibration mill, etc.), the material (steel, hardened steel, tungsten carbide, etc.) used for the vial and the balls, the size and number of balls, the vibration frequencies of the mill, and the milling time, nanoscale powders with dimensions from 1 to 100 nm can be produced. Since highly reactive powders with large surface areas are prepared during the process, ball milling is often performed in an inert gas atmosphere. For the direct preparation of nanoscale metal hydride systems, reactive milling can be used. Starting from a metal powder, ball milling in a hydrogen atmosphere at normal or higher hydrogen pressure directly produces the nanoscale metal hydride. Ball milling can be accomplished on the g scale in the laboratory or on the kg or higher scale in technical plants. In the case of commercialisation of the production of nanoscale hydrogen storage materials by high-energy ball milling, cost-effective production processes will have to be developed. Running the mill in a continuous mode, short milling times, and low energy consumption of the process are essential requirements. The transfer of the laboratory results to a technical scale will pose a challenge for chemists and engineers [11].

Different types of ball mills have been established for laboratory experiments. Planetary ball mills (www.fritsch.com, www.retsch.com), where the vials with material and balls rotate around their own axis on a counter-rotating supporting disc, are often used for the preparation of nanoscale hydrogen storage materials, as displayed in Fig. 15.4.

Other frequently used mills are shaker mills (www.spex.com). The milling vial swings in a complex motion, combining backward and forward with lateral movements of approximately 1000 cycles per minute. Figure 15.5 displays a third type of mixer mill, where the grinding jars perform radial oscillations in a horizontal position.

In all these mills, the vials are in movement, which results in some difficulties to measure the conditions inside the vial and to change or manipulate the atmosphere inside the vials. To overcome these problems, telemetric systems for measuring the conditions inside the vials and during the ball milling process are developed. The pressure and temperature values measured are transmitted via a radio signal to a

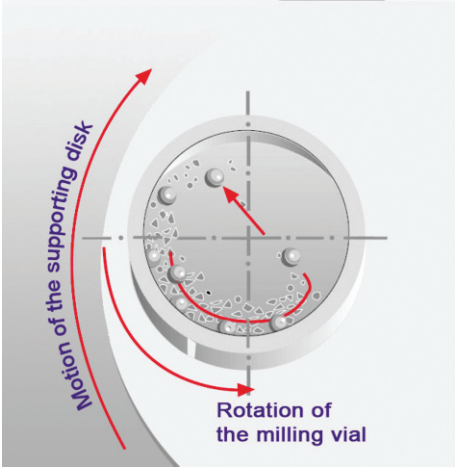

Fig. 15.4 Motion of the milling vial in the planetary mill

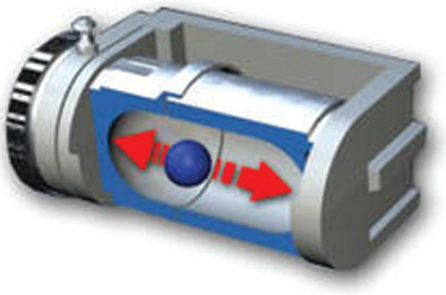

Fig. 15.5 Motion of milling balls in a vibrating mill

receiver outside the mill [12]. Fixed vials are used in magnetic mills, where only the balls are in motion. This ball movement is driven by an external magnet. In such a system, the milling environment is completely controllable. Milling can be performed at higher temperature or under pressure. To account for aspects of structure and composition and to minimise the degradation during ball milling, the process may be carried out at liquid nitrogen temperatures (cryo-milling). With vibrating mills, materials preparation on the kg scale is possible (www.siebtechnik-gmbh.de). Combination of several vibrating mills allows for material production on a technical scale. Ball milling on a technical scale can be done in vacuum, under higher pressure, or in an inert gas atmosphere.

15.4.2 Parameters of Importance (Milling Time, Addition of Catalyst, etc. . .)

The examples given below shall illustrate how ball milling can influence the properties of different metal hydride systems and how this technique can be used for the development of new nanoscale materials.

15.4.2.1 Magnesium Hydride

For more than 30 years, magnesium hydride has been of particular interest as hydrogen storage material because of his high content of hydrogen (theoretically, 7.7 wt.-% H_2) and the low costs of the magnesium metal. Unfortunately, magnesium hydride is a typical high-temperature metal hydride with a decomposition temperature of 300°C. This high temperature depends on the heat of formation of 76 kJ/mole for MgH_2. Consequently, MgH_2 is not used as a hydrogen storage material in combination with PEM fuel cells. On the other hand, the high energy content, exergetic quality, and constant temperature make MgH_2 a favourable material for energy storage in solar (e.g. solar thermal power plants) and thermal applications [13].

Figure 15.6 shows the grain size effect on ball-milled and bulk Mg metal as a function of the size of the particles [14]. Pure Mg powders were ball-milled in an argon atmosphere using a commercial Spex ball mill with modified hardened steel vials and steel balls. The smallest particle size in the range of 30 nm was obtained after more than 20 h of milling. The bulk material (ball-milled for only 5 min to exclude surface effects) with a particle size in the range of 50 µm did not absorb any significant amounts of hydrogen at 300°C in 120 min. The difference to the nanoscale Mg metal is obvious. The Mg particles with an average size of 50 nm absorb 6 wt.-% of hydrogen in 120 min. The hydrogenation of the smaller particles with a size in the range of 30 nm is much faster and the Mg particles absorb approximately 90% of the whole hydrogen amount in only 60 min.

15.4.2.2 Complex Aluminium Hydrides

Having observed that sodium alanate can be reversibly de- and rehydrogenated under moderate conditions in the presence of a catalyst [5, 15], the complex aluminium hydrides are promising hydrogen storage materials due to their high hydrogen capacity (5.6 wt.-% H_2 for $NaAlH_4$). Most of the complex aluminium hydrides decompose in a two-step mechanism, changing from a tetrahedral AlH_4^-unit to the octahedral AlH_6^{3-}unit (Eq. 15.4). Sometimes, e.g. during the decomposition of magnesium alanate [16] the intermediate product cannot be observed. In other cases, the AlH_6^{3-}units are no separated ions, they are connected to each other, producing long chains [17, 18]

$$3\ NaAlH_4 \rightleftarrows Na_3AlH_6 + 2\ Al + 3\ H_2 \rightleftarrows 3\ NaH + Al + 1.5\ H_2 \qquad (15.4)$$

Unlike most other complex aluminium hydrides, sodium alanate has favourable thermodynamics and can be used as a reversible hydrogen storage material.

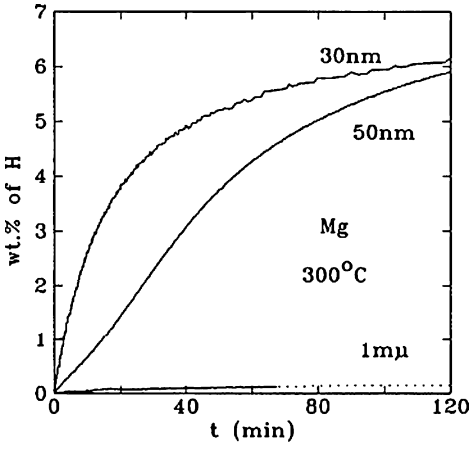

Fig. 15.6 Effect of grain size on hydrogen absorption of ball-milled magnesium powder without activation, first cycle (with permission of Springer-Verlag 2001)

For an enhanced kinetics, doping of the sodium aluminium hydrides with a catalyst precursor is necessary. As typical precursors, $TiCl_3$ or other transition metal halides are used. The active catalyst species is produced during ball milling of the $NaAlH_4$ catalyst precursor mixture according to the following reaction (Eq. 15.5).

$$3\ NaAlH_4 + TiCl_3 \longrightarrow 3\ NaCl + Ti + 3\ Al + 6\ H_2 \qquad (15.5)$$

The real structure of the catalyst is not yet clear and extensive discussions and investigations are going on.

After doping with Ti compounds and 3 h ball milling of the material, the particle size is reduced to the nm scale. Figure 15.7 displays a transmission electron microscopy (TEM) of decomposed material (NaH + Al). It should be noted here that typically the high energy of the TEM electron beam causes the hydrogenated material to decompose. However, under special beam conditions it is possible to visualize the hydrogenated state without any decomposition as it is described within this book in the Sect. 17b of this Part IV. In contrast to the $NaAlH_4$ crystals, the lack of crystallinity is apparent. The boundaries between the dark and weak contrast areas are diffuse, which reflects the highly dispersed nature of the material.

Hydrogenation curves of ball-milled $NaAlH_4$ with different amounts of $TiCl_3$ as dopant are presented in Fig. 15.8. The amount of hydrogen absorbed during the hydrogenation reaction is shown. The dopant quantity was varied from 0.9% up to 9% of $TiCl_3$ [19]. Hydrogenation conditions were 125°C and approximately 80 bars of H_2. With increasing doping level, a faster hydrogenation is observed. On the 2% doping level, the reaction is finished after 1 h and reaches 4.5 wt.-% of hydrogen storage capacity. Compared to the wet chemical doping procedure with $Ti(Obutyl)_4$, the reaction is much faster by about an order of magnitude and the reaction conditions are smoother.

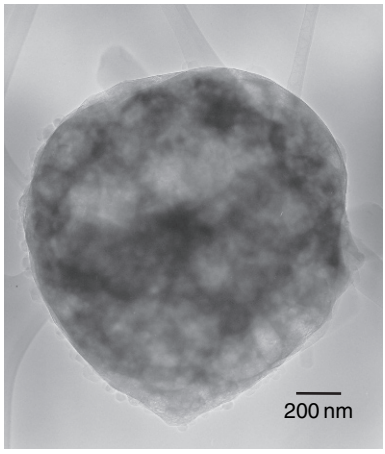

Fig. 15.7 TEM of decomposed Ti-doped $NaAlH_4$ (NaH + Al) prepared with the ball milling method

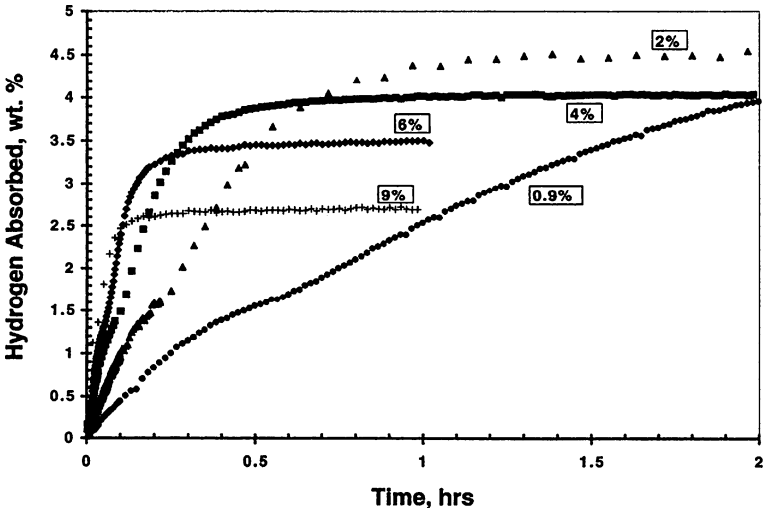

Fig. 15.8 Hydrogenation rates of ball-milled $TiCl_3$-doped $NaAlH_4$ as a function of the concentration of the dopant ($T = 125°C$, $p = 80$ bar)

15.4.3 Synthesis of Potential Hydrogen Storage Materials

15.4.3.1 Mixed Hydrides

The reaction of two or sometimes three different hydrides during ball milling may produce new types of complex hydrides or other simple metal hydride systems. An example is the synthesis of the complex aluminium hydride system Na_3AlH_6, the decomposition intermediate of $NaAlH_4$. Starting from $NaAlH_4$ and two moles of NaH, the complex hydride Na_3AlH_6 can be prepared easily by the ball milling method (Eq. 15.6) [20].

$$NaAlH_4 + 2\,NaH \longrightarrow Na_3AlH_6 \tag{15.6}$$

By ball milling of NaH, LiH and $NaAlH_4$ at the molar ratio of 1:1:1, the complex hydride Na_2LiAlH_6 can be synthesised. An alternative reaction for the preparation of this alanate is the ball milling of $LiAlH_4$ and 2 NaH at a 1:2 molar ratio. The same reaction routes are used for the preparation of K_2LiAlH_6 and K_2NaAlH_6 [21].

Ternary hydrides like $NaMgH_3$ can be synthesised by ball milling from the hydrides NaH and MgH_2 (Eq. 15.7) [22]. A lot of similar materials, like $KMgH_3$, $KCaH_3$, $RbMgH_3$, $RbCaH_3$, $CsCaH_3$, $CaLiH_3$, $SrLiH_3$, $BaLiH_3$, and $BaNaH_3$, are described in literature.

$$MgH_2 + NaH \longrightarrow NaMgH_3 \tag{15.7}$$

Most of these ternary hydrides are synthesised by classical solid-state hydrogenations. Temperatures are much higher and reaction times much longer compared to the ball milling method.

15.4.3.2 Destabilisation Reactions

The main problem in the field of hydrogen storage materials is the lack of reversible systems under possible technical conditions. Sometimes, high hydrogen-containing systems are too unstable, e.g. $Mg(AlH_4)_2$ with 7.0 wt.-% H_2 storage capacity, or they are much too stable, e.g. $LiBH_4$ with more than 18 wt.-% of hydrogen. In these cases, thermodynamic tailouring represents a possibility to stabilise or destabilise a decomposition reaction. In thermodynamic tailouring, the addition of a second or sometimes a third component to the hydrogen storage material opens up new reaction pathways with different thermodynamic properties. Again, ball milling often is the method of choice for the preparation of these mixtures, because small particles with a high amount of defects in the crystal structure are always needed for satisfying reaction kinetics in these solid-state reactions.

$LiBH_4/MgH_2$ System

In principle, complex boron hydrides are attractive materials for hydrogen storage because of their high hydrogen content (up to 18 wt.-% for $LiBH_4$). These materials, however, have high decomposition temperatures and they are not reversible under acceptable technical conditions. Recently, it was shown that a ball-milled mixture of $LiBH_4$ and MgH_2 can be de- and rehydrogenated reversibly according to (Eq. 15.8) [23]. The thermodynamics of the reaction is changed by the addition of a second component and by extended ball milling for 1 h. During the decomposition of the ball-milled mixture, LiH and MgB_2 (instead of LiH and B metal for the pure $LiBH_4$) are produced and the right side of the reaction is stabilised, which means that $LiBH_4$ is destabilised, the decomposition temperature is reduced, and the material becomes reversible.

$$2\,LiBH_4 + MgH_2 \rightleftarrows 2\,LiH + MgB_2 + 4\,H_2 \qquad (15.8)$$

In the presence of 2–4 mole-% of $TiCl_3$ as a catalyst, the $LiBH_4/MgH_2$ mixture stores 8–10 wt.-% of hydrogen. Figure 15.9 shows the Van't Hoff plots of pure $LiBH_4$, MgH_2, and the mixture of both substances. The dehydrogenation enthalpy calculated from these measurements for the $LiBH_4/MgH_2$ system was 25 kJ/mole H_2 smaller than that of the pure $LiBH_4$ system. The result is an equilibrium pressure increasing from 1 to 12 bar at 400°C. The decomposition temperature still is too high for a practical fuel cell application, but these findings reveal how the thermodynamics of hydrogen storage systems are affected by thermodynamic tailoring. Similar results of destabilisation and alloying of hydrogen materials with other metals were obtained for the combinations of ball-milled LiH/Si and MgH_2/Si [24].

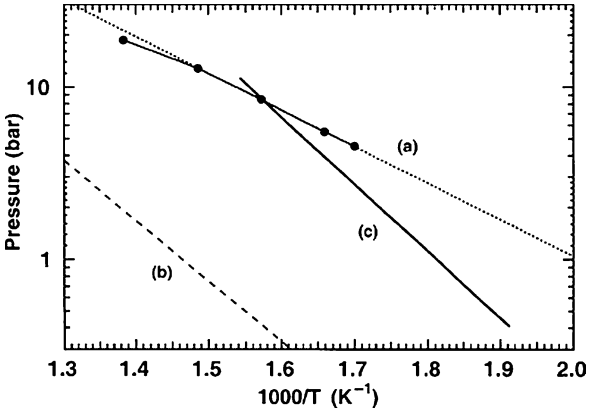

Fig. 15.9 Van't Hoff plots of destabilised 2 $LiBH_4 + MgH_2$ (curve a), pure MgH_2 (curve c), and $LiBH_4$ (curve b). Addition of MgH_2 increases the equilibrium pressure by approximately 10 times, while the enthalpy is reduced by 25 kJ (per mol H_2) compared to pure $LiBH_4$

Amide/Imide System

For some years, light element amides and imides have been potentially interesting candidates for hydrogen storage materials [25]. Starting from lithium nitride, the substances in principle can absorb two moles of hydrogen with a theoretical storage capacity of more than 10 wt.-%. The final hydrogenation product is a mixture of lithium amide and lithium hydride (Eq. 15.9).

$$Li_3N + 2\,H_2 \rightleftarrows Li_2NH + LiH + H_2 \rightleftarrows LiNH_2 + 2\,LiH \tag{15.9}$$

The decomposition temperature of pure $LiNH_2$ with the release of ammonia is around 380°C. For LiH, this temperature amounts to about 500°C, with hydrogen being released. Hydrogen release from the nanoscale ball-milled mixture is observed at much lower temperatures around 200°C. Only minor amounts of ammonia are detected under these conditions [26, 27]. After the addition of small amounts of $TiCl_3$ catalyst to a 1:1 LiH: $LiNH_2$ mixture and ball milling, no ammonia is observed within experimental accuracy.

New amide/imide storage materials are obtained by the partial substitution of Li by other elements. An example is the destabilisation of $LiNH_2$ with magnesium hydride [28, 29].

$$2\,LiNH_2 + MgH_2 \rightleftarrows Li_2Mg(NH)_2 + 2\,H_2 \tag{15.10}$$

According to (Eq. 15.10), a ball-milled sample of a 2:1 $LiNH_2$-MgH_2 mixture may theoretically release 5.4 wt.-% of hydrogen. The mixture can reversibly de- and absorb hydrogen at a pressure of 32 bar and 200°C.

Research related to amide/imide hydrogen storage systems has grown extensively over the last few years. Typical examples of investigated amide/imide systems are $Mg(NH_2)_2$/NaH, [30] $Mg(NH_2)_2$/LiH, [31] $Mg(NH_2)_2/MgH_2$[32] or the more

complex system $Mg(NH_2)_2/Ca(NH_2)_2/LiH$ [33]. Again, ball milling is used for the preparation of these mixtures. An unsolved problem of all amide/imide systems is the release of ammonia during decomposition. For fuel cell applications, the release of this toxic gas will have to be reduced completely.

15.4.3.3 Metathesis Reactions

A metathesis reaction is a simple ionic reaction in which cations and anions exchange their partners. By application of the ball milling technique, new complex aluminium hydrides can be prepared via this simple reaction pathway. The driving force of the reaction is the formation of sodium or lithium chloride with its high heat of formation when sodium or lithium alanate is used in combination with metal chlorides. Earth alkaline complex hydrides are obtained from the ball milling of the corresponding metal chloride and a complex metal hydride ($NaAlH_4$, $LiAlH_4$) according to (Eq. 15.3). Following this reaction pathway, $Mg(AlH_4)_2$ and $Ca(AlH_4)_2$ are synthesised in quantitative yields after 3 h of ball milling. Under inert conditions, $Ca(AlH_4)_2$ was prepared in a vibration mill at a frequency of 30 Hz for 3 h. The synthesis was performed in a 25 ml steel vial with two steel balls and a ball to powder ratio of approx. 15:1 [34]. The produced salts are inert substances and have no influence on the properties of the prepared hydrides in principle. For a first screening of the properties and preparation of new hydrides, a separation from these alkaline chlorides is not always necessary. In contrast to the wet chemical preparation of these alanates, where different types of ether solvents are used, no solvents are necessary in the ball milling methods.

$$CaCl_2 + 2\ NaAlH_4 \longrightarrow Ca(AlH_4)_2 + 2\ NaCl \tag{15.11}$$

In principle, the Ca^{2+} ion in (Eq. 15.11) can be substituted by any other metal ion. Depending on the stability of the produced alanate, the hydride may decompose during the milling process and only simple metal hydrides or alloys are the final products. Cryo-milling at very low temperatures could be a way out for the preparation of these unstable complex metal hydrides.

More complex systems may be prepared by the same metathesis reaction. During the ball milling of $MgCl_2$ with three equivalents of $LiAlH_4$, a mixed Li-Mg alanate system is formed (Eq. 15.12) [31].

$$MgCl_2 + 3\ LiAlH_4 \longrightarrow LiMg(AlH_4)_3 + 2\ LiCl \tag{15.12}$$

15.4.3.4 Reactive Ball Milling

An attractive approach to synthesising nanoscale metal hydride systems is reactive ball milling under hydrogen pressure, starting from a metal powder or an alloy. The preparation of finely dispersed metallic (Mg, Ti, Zr) [35, 36, 37, 38] and

intermetallic (TiFe, 2 Mg + Fe) [39, 40, 41, 42] hydrides was demonstrated by several authors. The complex hydride Mg_2FeH_6 as the only reaction product was produced according to (Eq. 15.13) by ball milling at 5 bar of hydrogen and room temperature for 40 h.

$$2\,Mg + Fe + 3\,H_2 \xrightarrow[\text{ball milling}]{H_2\ \text{pressure}} Mg_2FeH_6 \qquad (15.13)$$

Mg_2FeH_6 is a typical high-temperature metal hydride with an equilibrium pressure of 1 bar in the range of 300°C. This means that this hydride cannot be hydrogenated at room temperature and under low hydrogen pressure. The preparation of this metal hydride with the ball milling method again illustrates the great potential of mechanochemical synthesis reactions for the development of new hydride materials.

Starting from the mixture 2 MgH_2 + Co, the ternary hydride Mg_2CoH_5 was synthesised by reactive ball milling in a similar manner [43]. All these materials prepared by the reactive milling method exhibit the characteristics of nanoscale materials with improved kinetics of re- and deloading processes and a line broadening in X-ray diffraction patterns of these substances.

Complex aluminium metal hydrides can also be prepared by ball milling under hydrogen pressure. A highly reactive Ti-doped $NaAlH_4$ can be synthesised from NaH and Al with $TiCl_3$ as catalyst in a one-step reaction at 80 bar hydrogen pressure (direct synthesis). In Fig. 15.10, the hydrogenation rates of a ball-milled Ti-doped $NaAlH_4$ and a Ti-doped material prepared by direct synthesis are compared. The decomposed $NaAlH_4$ needs approximately 60 min for a complete rehydrogenation

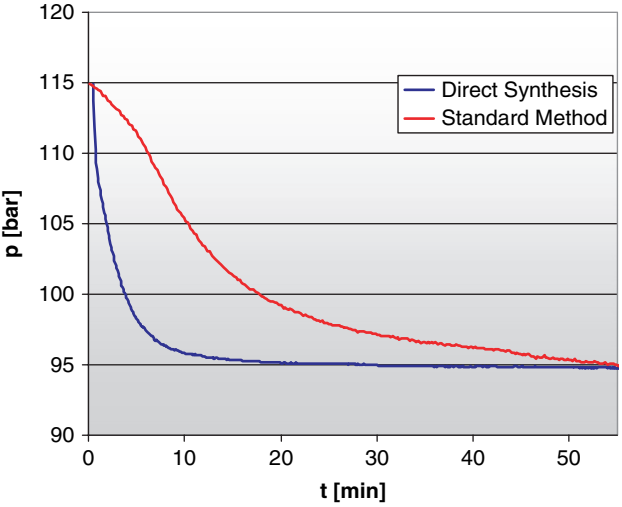

Fig. 15.10 Comparison of the hydrogenation rates of a decomposed Ti-doped $NaAlH_4$ prepared by ball milling and by direct synthesis (hydrogenation conditions: 115 bars H_2 pressure, 100°C)

at 115 bar and 100°C. The material prepared by the direct synthesis process, by contrast, is fully rehydrogenated after 15 min only.

A recently published study demonstrated that doped $NaAlH_4$ can be prepared by ball milling under a H_2 pressure slightly higher than the equilibrium pressure of the alanate. Prolonged milling times are necessary to obtain fully hydrogenated products [44].

15.5 Conclusion

The preparation of new nanoscale and other hydride systems for technical applications is a great challenge for chemists and material scientists. The different tools of mechano-chemical reactions and quantum mechanics calculations can help in the search for new hydride systems. For all the different possible applications of fuel cell systems, different types of solid-state hydrogen storage materials are necessary. It is therefore important that research on hydride systems is not reduced to a limited number of hydrogen storage systems.

References

1. M. Gupta, *Ann. Chim. Sci. Mat*. **2005**, *30*, 455.
2. S.V. Alapati, J.K. Johnson, D.S. Sholl, *J. Phys. Chem*. **2006**, *110*, 8769.
3. L. Schlapbach, A. Züttel, *Nature* **2001**, *414*, 353.
4. D.F. Shriver, M.A. Drezdzon, *The manipulation of air-sensitive compounds*, John Wiley & Sons, Inc. **1986**.
5. B. Bogdanović, M. Schwickardi, *J. Alloys Compd*. **1997**, *253–254*, 1.
6. M. Fichtner, O. Fuhr, *J. Alloys Compd*. **2002**, *345*, 286.
7. M. Fichtner, O. Fuhr, O. Kircher, *J. Alloys Compd*. **2003**, *356–357*, 418.
8. M. Fichtner, C. Frommen, O. Fuhr, *Inorg. Chem*. **2005**, *44*, 3479.
9. C. Suryanarayana, *Prog. Mat. Sci*. **2001**, *46*, 1.
10. E. Gaffet, F. Bernard, J.-C. Niepce, F. Charlot, C. Gras, G. Le Caër, J.-L Guichard, P. Delcroix, A. Mollecin, O. Tillement, *J. Mater. Chem*. **1999**, *9*, 305.
11. M. Dornheim, N. Eigen, G. Barkhordarian, T. Klassen, R. Bormann, *Adv. Eng. Mat.* **2006**, *6*, 377.
12. J.M. Bellosta von Colbe, M. Felderhoff, B. Bogdanović, F. Schüth, C. Weidenthaler, *Chem. Commun*. **2005**, 4732.
13. B. Bogdanović, A. Ritter, B. Spliethoff, *Angew. Chem. Int. Ed*. **1990**, *29*, 223.
14. A. Zaluska, L. Zaluski, J.O. Ström-Olsen, *Appl. Phys. A* **2001**, *72*, 157.
15. B. Bogdanović, R.A. Brand, A. Marjanovi, M. Schwickardi, J. Tölle, *J. Alloys Compd*. **2000**, *302*, 36.
16. M. Fichtner, O. Fuhr, O. Kircher, *J. Alloys Compd*. **2003**, *356–357*, 418.
17. Q.A. Zhang, Y. Nakamura, K. Oikawa, T. Kamiyama, E. Akiba, *Inorg. Chem*. **2002**, *41*, 6941.
18. C. Weidenthaler, T.J. Frankcombe, M. Felderhoff, *Inorg. Chem*. **2006**, *45*, 3849.
19. G. Sandrock, K. Gross, G. Thomas, *J. Alloys Comp*. **2002**, *339*, 299.
20. J. Huot, S. Boily, V. Günther, R. Schulz, *J. Alloys Comp*. **1999**, *283*, 304.
21. J. Graetz, Y. Lee, J. J. Reilly, S. Park, T. Vogt, *Phys. Rev. B* **2005**, *71*, 184115.

22. S. Ikeda, Y. Nakamori, S. Orimo, *Acta Mater.* **2005**, *53*, 3453.
23. J.J. Vajo, S.L. Skeith, F. Mertens, *J. Phys. Chem. B* **2005**, *109*, 3719.
24. J.J. Vajo, F. Mertens, C.C. Ahn, R.C. Bowman, Jr., B. Fultz, *Phys. Chem. B* **2004**, *108*, 13977.
25. P. Chen, Z. Xiong, J. Luo, J. Lin, K. L. Tan, *Nature* **2002**, *420*, 302.
26. P. Chen, Z. Xiong, J. Luo, J. Lin, K. L. Tan, *J. Phys. Chem. B* **2003**, *107*, 10967.
27. T. Ichikawa, S. Isobe, N. Hanada, H. Fujii, *J. Alloys Compd*. **2004**, *365*, 271.
28. W. Luo, *J. Alloys Compd*. **2004**, *381*, 284.
29. Y. Nakamori, S. Orimo, *J. Alloys Compd*. **2004**, *370*, 271.
30. Z. Xiong, J. Hu, G. Wu, P. Chen, *J. Alloys Compd*. **2005**, *395*, 209.
31. Z. Xiong, J. Hu, G. Wu, P. Chen, W. Luo, K. Gross, J. Wang, *J. Alloys. Compd*. **2005**, *398*, 253.
32. J. Hu, G. Wu, Y. Liu, Z. Xiong, P. Chen, K. Murata, K. Sakata, G. Wolf, *J. Phys. Chem. B* **2006**, *110*, 14688.
33. Y. Liu, Z. Xiong, J. Hu, G. Wu, P. Chen, K. Murata, K. Sakata, *J. Power Sources* **2006**, *159*, 135.
34. M. Mamatha, B. Bogdanović, M. Felderhoff, A. Pommerin, W. Schmidt, F. Schüth, C. Weidenthaler, *J. Alloys Comp*. **2006**, *407*, 78.
35. Y. Chen, J.S. Williams, *J. Alloys Compd*. **1995**, *217*, 181.
36. J.-L. Bobet, C. Even, Y. Nakamura, E. Akiba, B. Darriet, *J. Alloys Compd*. **2000**, *298*, 279.
37. J.-L. Bobet, C. Even, J.-M. Quenisset, *J. Alloys Compd*. **2003**, *348*, 247.
38. Z.-H. Cheng, G.R. MacKay, D.A. Small, R.A. Dunlap, *J. Phys. D: Appl. Phys*. **1999**. *32*, 1934.
39. I.G. Konstanchuk, E. Yu. Ivanov, V.V. Boldyrev, *Russ. Chem. Rev*. **1998**, *67*, 69.
40. C.-H. Chiang, Z.-H. Chin, T.-P. Perng, *J. Alloys Compd*. **2000**, *307*, 259.
41. F.C. Gennari, F.J. Castro, J.J. Andrade Gamboa, *J. Alloys Compd*. **2002**, *339*, 261.
42. M. Herrick, N. Ismail, J. Lyubina, A. Handstein, A. Pratt, O. Gutfleisch, *Mater. Sci. Eng. B* **2004**, *108*, 28.
43. J. Chen, H. T. Takeshita, D. Chartouni, N. Kuriyama, T. Sakai, *J. Mater. Sci*. **2001**, *36*, 5829.
44. N. Eigen, M. Kunowsky, T. Klassen, R. Bormann, *J. Alloys Compd*. **2007**, *430*, 350.

Chapter 16
Kinetics and Thermodynamics

Chapter 16a
Measurement of H_2 Sorption Properties

Jacques Huot

List of Abbreviations

CV	Contracting Volume
DPG	Differential Pressure Gauge
JMA	Johnson-Mehl-Avrami
PIS	Pneumatochemical Impedance Spectroscopy
PCI	Pressure Composition Isotherm
PCT	Pressure Composition Temperature

Jacques Huot
Institut de Recherche sur l'Hydrogène, Université du Québec à Trois-Rivières, 3351 des Forges, PO Box 500, Trois-Rivières (Qc) G9A 5H7, Canada, e-mail: Jacques.Huot@uqtr.ca

A. Léon (ed.), *Hydrogen Technology*,

PDSC	Pressure Differential Scanning Calorimetry
TEOM	Tapered Element Oscillating Membrane
TCD	Thermal Controlled Desorption
TDS	Thermal Desorption Spectroscopy
TG	Thermogravimetry
TIG	Tungsten Inert Gas
VCR	Vacuum Coupling Radius Seal

16a.1 Introduction

Researches on metal hydrides for hydrogen storage applications have been active for almost 40 years and the literature is abundant [1–11]. Despite this intensive research, a metal hydride fulfilling all the prerequisites listed in the Chap. 3 has yet to be found. Therefore, the development of new hydrogen storage material is still an active research field. As each practical application has its own requirement in terms of the hydrogen storage capacity, sorption kinetics, and thermodynamics, these parameters have to be determined precisely.

Hydrogen storage capacity is usually reported in terms of weight of hydrogen over weight of the hydride expressed in percentage (wt% of H_2). A more fundamental unit is the number of hydrogen atoms over the number of metallic atoms in the alloy (H/M). The advantage of this unit is to easily visualize the stoichiometry of the hydride. It should be noted that the volumetric capacity measured as the ratio of the weight of hydrogen stored in a unit volume of hydride (kg H_2/L) which is usually not reported is also of importance, because it reflects the compactness of the material.

A key factor to determine whether a metal hydride could be used in practical applications is the absorption/desorption kinetics of hydrogen. Identification of the rate-limiting step and the enthalpy of the reaction [12] are important to the effect of heat and mass transfer and the determination of the intrinsic properties of the hydride. It is therefore vital to have a precise and accurate measurement of hydrogen sorption kinetics of a material as well as of its thermodynamics properties.

In early works, researchers had to build their own instruments for measuring hydrogen storage capacity and sorption kinetics. This led to the development of a wide variety of techniques for the measurement of hydrogen sorption properties. In the last decade, the progress in electronics and user-friendly computer programs allowed designing more sophisticated instruments. Today, a number of systems that provide efficient measurements in a wide range of temperature and pressure are commercially available (see Appendix A).

For hydrogen storage materials, the interaction between hydrogen and the metal could be divided into two types: Physical adsorption (or physisorption) and chemisorption. In physisorption the hydrogen molecules are weakly attracted to the surface of the materials by Van der Waals forces. The energy released on adsorption (heat of adsorption) typically is in the range of -5 to $-40\,\mathrm{kJmol^{-1}}$. Due to this low heat of adsorption, physisorption is present at low temperature (typically 77 K). In the case of chemisorption, the hydrogen is incorporated in the metal through a strong

chemical bond. The heat of chemisorption is in the range of −20 to −100 kJmol^{-1} and the operating temperatures are between 250 and 650 K. Usually, sorption kinetics is not an issue in physisorption, but is a main concern for chemisorption. As we will see below, chemisorption involves many steps. Depending on the conditions, each of these steps could limit the speed of the reaction. It is therefore important to precisely determine the sorption kinetics in order to identify the rate-limiting steps. Once the rate-limiting step is identified, proper actions could be taken to speed up the reaction, such as addition of a catalyst, modification of working conditions (temperature and pressure), improvement of heat and mass transfer, etc.

In this chapter, the focus is on the characterization of materials storing hydrogen by chemisorption. It begins with a short presentation of the theoretical background of the thermodynamics and kinetics of metal hydrides. This is followed by an overview of the principal techniques used for the determination of hydrogen storage capacity and sorption kinetics. Special attention is given to the volumetric measurement (usually done with experimental equipment named Sieverts' apparatus). The practical problems encountered for accurate and reproducible measurements are highlighted. Finally, the safety issue is considered for using such an apparatus in a laboratory environment.

16a.2 Thermodynamics and Kinetics of Hydrogenation

16a.2.1 Thermodynamics

This section will present the phenomenology of the direct interaction of a metal with gaseous hydrogen to form metal hydrides. Figure 16a.1 displays a schematic view of metal-hydrogen interaction. As can be seen, the hydrogenation mechanism can be divided into the following steps [13]:

1. Adsorption of molecular hydrogen gas on the surface and dissociation to atomic hydrogen at the metal surface.
2. Diffusion of the hydrogen atom into the bulk of the metal. Hydrogen is dissolved at interstitial sites of the host metal and forms a solid solution.

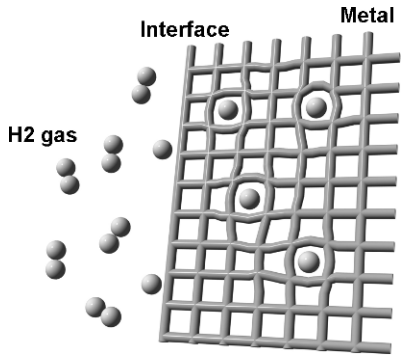

Fig. 16a.1 Schematic representation of hydrogen dissociation at the interface and solution of atomic hydrogen in the bulk

3. When the local hydrogen exceeds a certain limit (which depends on the metal host), a hydride phase starts to precipitate.
4. Diffusion of hydrogen through the hydride layer to react with underlying metal.

This sequence of events is true for the ideal case where the metal surfaces are bare. In general, however, the surfaces of metals are covered with oxides of various thicknesses depending on the formation process of each particular metal. This oxide layer acts as a hydrogen barrier and must be broken for the gaseous hydrogen to get access to the bare metal. Therefore, the first hydrogenation usually is performed (for conventional alloys) at high temperature and hydrogen pressure in order to 'force' the hydrogen through the oxide layer. Upon hydrogenation, the lattice volume increases significantly, while dehydrogenation makes the lattice revert to its original size. This expansion–contraction breaks the metal particles, exposing the fresh metal surface and reducing particle size [14]. This so-called activation process should be performed on the alloy in order to obtain the true thermodynamic characteristics of the hydride. Usually, a few absorption/desorption cycles are performed before attempting to measure the "true" thermodynamics and kinetics of the sample. The exact number of cycles that have to be performed depends on each system, but the experimentalist has to make sure that the activation process is finished. It should be mentioned here that the characterization of the activation process (pressure, temperature, time to reach full capacity) could be important to industry. Further details concerning the activation process can be found elsewhere [15].

Once the alloy is fully activated, its thermodynamic characteristics can be measured. The reaction of a fully activated alloy (M) with hydrogen is represented by:

$$M + \frac{x}{2} H_2 \Leftrightarrow MH_x \tag{16a.1}$$

The formation of the hydride is a chemical process and therefore the knowledge of the heat of reaction associated with this process is of interest. The thermodynamics of this reaction is usually described by the pressure-composition isotherms (PCI), sometimes also called pressure-composition temperature (PCT) curves, displayed in Fig. 16a.2. The shape of the isotherm reflects the phenomenology of the reaction. This isotherm can be divided into three regions. The first region (I in Fig. 16a.2) is related to the low hydrogen concentration ($x << 1$) regime where hydrogen dissolves in the metal lattice and forms a solid solution phase (α phase). The crystal structure of the α phase is the same as the metal. As the hydrogen pressure increases, the concentration follows the Sieverts' law which simply is the Henry's law for a dissociating solute [16]:

$$c \approx K_s^{-1}\, p^{1/2} \tag{16a.2}$$

where K_S is a constant that could be expressed as:

$$\ln K_S = \frac{1}{RT} [\Delta H_s - T \Delta S_s] \tag{16a.3}$$

where ΔH_s and ΔS_s are the solution enthalpy and solution entropy of the reaction, respectively. In this region, the Sieverts' law is valid, because gaseous hydrogen can

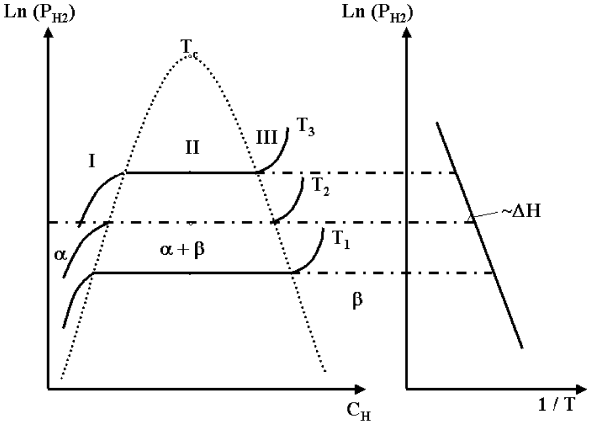

Fig. 16a.2 Schematic view of a pressure–composition isotherm. α is the solid solution of hydrogen and β is the hydride phase. A Van't Hoff plot giving the enthalpy of hydride formation ΔH is shown on the right-hand side

be considered an ideal gas and H_2 molecules are dissociated into atoms (protium) before getting dissolved in metals [17].

The hydrogen concentration increases with hydrogen pressure until the attractive H–H interactions become important [18]. This attraction is explained by the fact that the host metal lattice is expanded by hydrogenation, thus reducing the elastic energy for hydrogen introduction [19]. When hydrogen concentration reaches this level, nucleation of a higher concentration phase (β phase) occurs. The system has now three phases (α, β, and hydrogen gas) and two components (metal and hydrogen). The Gibbs phase rule gives the degree of freedom (f) as:

$$f = C - P + 2 \tag{16a.4}$$

where C is the number of components and P is the number of phases. Therefore, at a given temperature, the hydrogen pressure is constant in the two-phase region (region II of Fig. 16a.2). The equilibrium pressure P_{eq} at the $\alpha \rightarrow \beta$ phase transformation is then given by the Van't Hoff law.

$$\ln P_{eq} = \frac{-\Delta H}{RT} + \frac{\Delta S}{R} \tag{16a.5}$$

where ΔH and ΔS are the enthalpy and entropy of the $\alpha \rightarrow \beta$ transition, respectively. In most cases, the entropy change is mainly given by the loss of standard entropy of the hydrogen gas as it enters the metal lattice. Therefore, the entropy term does not depend significantly on the nature of the metal and the ΔS term could be considered constant to a first approximation [14]. The enthalpy term depends on the H–H interactions and could be represented by elastic and electronic contributions that are comparable in magnitude [17]. Experimentally, the transition enthalpy and entropy are obtained by the Van't Hoff plot of plateau pressure against reciprocal

temperature (Fig. 16a.2). Once the pure β phase is reached, hydrogen in solid solution enters the β phase and the hydrogen pressure again rises with concentration (region III of Fig. 16a.2). In-depth treatment of the thermodynamics of the metal-hydrogen system can be found in literature [14, 17, 18, 20–22]

The PCT curve drawn in Fig. 16a.2 displays the behavior of an ideal hydride. In most metal hydrides, plateau slope and hysteresis will occur as shown schematically in Fig. 16a.3.

Hysteresis is a complex phenomenon which means that the absorption plateau is at a higher pressure than the desorption plateau. There are thus two sets of "thermodynamic" parameters which correspond to each plateau [21]. Quantitatively, hysteresis is represented by the free energy difference:

$$\Delta G_{H_2}(\text{hyst}) = RT \ln(P_A/P_D) \tag{16a.6}$$

where P_A is the absorption pressure and P_D is the desorption pressure. There are some views that P_D represents the "true" equilibrium plateau pressure, but Flanagan and Oates provided evidence that the equilibrium pressure lies somewhere between P_A and P_D [21]. Sandrock et al. pointed out that hysteresis is not a unique materials property and depends on the sample's history and on the test procedure used [23]. For practical applications, hysteresis is an important feature, because it has an important impact on the service pressure of the storage tank. In fact, it could translate to a loss in the efficiency of the material due to irreversible deformation during absorption and desorption of hydrogen. In most applications, hysteresis should be as small as possible. This can be achieved by element substitution and heat treatment. Further details on hysteresis can be found in review papers [24–28].

Another important characteristic of a "real" PCT curve is the plateau slope which is usually represented by the relation [23]:

$$\text{slope} = \frac{d(\ln P)}{d(H/M)} \tag{16a.7}$$

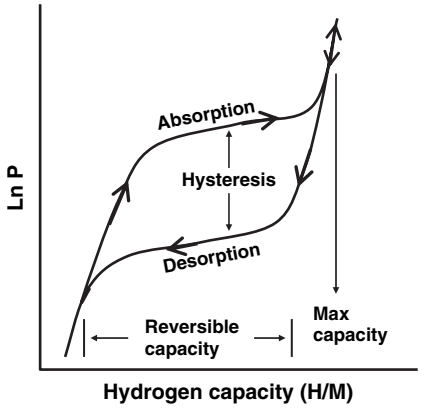

Fig. 16a.3 Representative pressure–composition isotherm with illustration of plateau slope, hysteresis, and reversible capacity

The plateau slope is not necessarily constant all along the plateau. The major cause of sloping plateaus can be attributed to compositional inhomogeneities [29–31]. For arc melt alloys, heat treatment could reduce plateau's slope. Usually, the pressure in the middle of the plateau is used for the characterization of the alloy. As with hysteresis, sloping plateaus have important technological impacts on some applications and reduction of the plateau's slope is usually advisable.

An important concept for practical applications is the reversible capacity $\Delta(H/M)_r$ which is defined as the plateau width. Reversible capacity can be considerably less than the maximum capacity $(H/M)_{max}$ [11]. Hydrogen capacity can be reported either in terms of the atomic ratio (H/M) or in weight percent (wt.%). The atomic ratio is the number of hydrogen atoms stored with respect to the number of metallic atoms. Weight percent is the weight of hydrogen stored over the weight of the hydride phase. Another way to report hydrogen capacity that is not often quoted, but has an important technological impact is the volumetric capacity expressed by the number of hydrogen atoms per unit volume. Usually, the reversible capacity (ΔN_H) and crystal volume are used to calculate this number. This definition does not include the void volume in the crystal (always present to some extent) and, thus, should be seen as an upper boundary.

16a.2.2 Kinetics of Hydride Formation

Hydrogenation is a complex process in which a molecule in the gas phase is split into individual atoms which are then bonded in the crystal lattice of the metal hydride. The overall kinetics is limited by the slowest step, the so-called rate-limiting step. In material development, it must be ensured that heat and mass transport are minimal during measurements and therefore do not constitute the rate-limiting step [12]. This means that great care should be given to the design of the sample holder in order to ensure maximum heat conduction and minimal hydrogen flow resistance.

The main challenge is the heat management. As an example, let us consider the hydrogenation of magnesium. Currently, the fastest kinetics are achieved by ball-milled MgH_2 composites doped with 1 mol% Nb_2O_5 which, at 150 and 250°C, can absorb more than 5.0 wt.% within 30 seconds [32]. This translates to a power of 2 kW per mole of hydrogen that has to be removed from the sample holder in order to keep it at constant temperature. This is a large amount of heat that has to be transferred out of the sample holder.

Various reactors which enable rapid heat transfer have been used. In an early version, Akiba et al. used a container in which the sample layer was only 1 mm [33]. This design kept the temperature within 5 K of the set temperature during reaction of Mg-Ni alloys. Good conductivity is also obtained when the powder sample is distributed in the annulus between a coaxial filter tube and a stainless tube [34–38]. In order to maintain uniform sample distribution, Wang and Suda chose to fill only the lower part of the annulus which helps to maintain temperature deviation within ±0.1 K except for the beginning of the reaction where the temperature variation is of

the order of a few degrees [39]. Another way to reduce the temperature gradient is to increase the heat capacity of the sample by mixing the metal hydride with an inert metallic ballast [40, 41]. However, to achieve adequate isothermal conditions, the ballast fraction has to be very high; 97.5 wt.% [42]. This could cause an important restriction of the gas flow. Particle size of the ballast also is an important parameter: When the particles are too small, the good thermal conductivity is counterbalanced by bad hydrogen flow [41].

Experimentally, the kinetics curve for a given reaction is the transformed fraction versus time. The dependence of this curve on pressure and temperature should be investigated in order to deduce the rate-limiting steps of the reaction. In the case of hydrogen/metal reaction, the situation is particularly complex because of the heat of reaction, relatively fast reaction rates, poor thermal conductivity of the hydride phase, and embrittlement of the products [12]. Sample size, particle size, surface properties, and the purity of solid and gas phases are also factors that could have an important impact on the kinetics of a given sample. Moreover, Mintz and Bloch [43] argued that the determination of the intrinsic rate-limiting step could only be performed on massive samples and not on powders. All these facts make the comparison of different experiments a difficult task that should be done with great care.

The detailed theory of hydrogen sorption by metal and alloys has been treated by various authors [40, 42, 44–53] In the following sections, some general characteristics of kinetic curves will be presented together with the discussion of Gerard and Ono [12]. A kinetic curve of the reacted fraction as a function of time gives two types of information: Qualitative information from the shape and quantitative from the slope. As an example, consider the curve shown in Fig. 16a.4. The sigmoidal shape indicates that the nucleation process is a slow reaction. The maximum rate of transformation is the slope at the inflexion point, and the intersection of the tangent at this point and the abscissa give the incubation time (t_i) [54]. Curves of this type are typical of first hydrogenation (activation).

Figure 16a.5 displays the second type of curves where the slope decreases with time. In this case, the reaction proceeds over the entire surface and the initial slope is

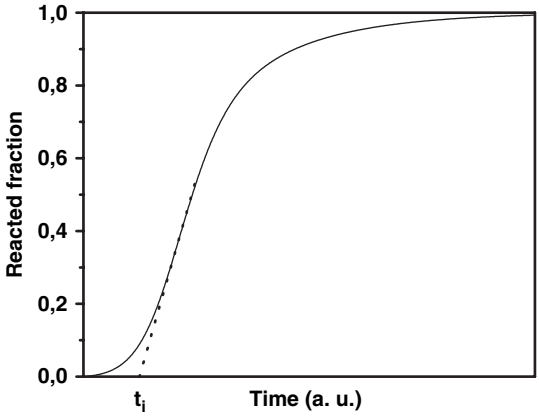

Fig. 16a.4 Representative kinetic curve of a reaction involving nucleation and growth of nuclei

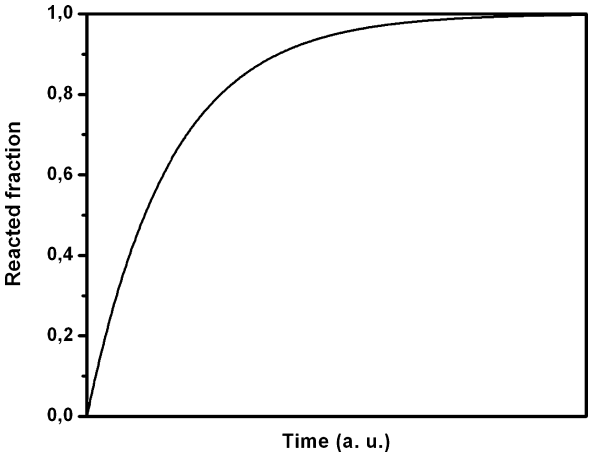

Fig. 16a.5 Representative kinetic curve of a reaction proceeding evenly over the entire surface

the product of the rate constant at the interface with the initial surface area. From the characteristic form of the curve, the rate-limiting step can be determined. As pointed out by Barkhordarian et al. [55], three models describe the different kinetic steps of the sorption reaction: (1) Surface reaction, (2) Johnson-Mehl-Avrami (JMA), and (3) contracting volume (CV). It should be noted here that JMA and CV describe the same kinetics step, namely nucleation and growth. Each of these reactions has a particular relation between reacted fraction and time. In surface reaction, the slowest step is chemisorption and the reacted fraction depends linearly on time

$$\alpha = kt \tag{16a.8}$$

In the JMA model, nucleation and growth start randomly in the bulk and surface and the dependence of the reacted fraction with time is given by:

$$[-\ln(1-\alpha)]^{1/n} = kt \tag{16a.9}$$

where the parameter n depends on the dimensionality of the growth. For the CV model, nucleation starts at the surface of a particle. If the growth occurs with constant interface velocity, then the reaction is given by:

$$1-(1-\alpha)^{1/n} = kt \tag{16a.10}$$

A complete description of the different models and dimensionalities can be found in the classic text of Christian [56] and in review papers of Mintz et al. [43, 57]. It is pointed out here that in order to distinguish between the different models and to accurately determine the dimensionality of the reaction, great care should be taken in the measurement process. Temperature, pressure, sample preparation, and history should be well controlled and the kinetics stability should be confirmed for many cycles.

16a.2.3 Other Important Properties

Other fundamental properties of metal hydrides, which should be considered in addition to thermodynamics and kinetics characteristics, are the activation and decrepitation processes.

Activation was discussed in the previous section, but it should be stressed again that before measuring the thermodynamics and kinetics properties of a metal hydride, the experimentalist should make sure that the sample to be measured is fully activated. Sometimes, activation could take a very long time (up to a few days) and a quick observation may lead to the conclusion that a certain alloy does not absorb hydrogen, while in reality the activation process was not performed. As an example, the activation curve at 623 K under 1.3 MPa of hydrogen of ball-milled Mg+2.5at.%Pd is presented in Fig. 16a.6 [58]. The curve has the general shape of Fig. 16a.4 with an incubation time of 750 minutes. Even after 2000 minutes, the full hydrogen capacity is still not reached. Once the sample is fully activated, the hydrogen sorption kinetics is much faster as shown in Fig. 16a.7. The shape is similar to the one shown in Fig. 16a.5 with no incubation time.

Decrepitation is the self-pulverization of alloy particles into smaller-size powder because of volume change upon hydrogenation and the brittle nature of hydriding alloys [11]. This could change the packing of material which in turn will change the heat transfer and gas flow of the sample holder. This effect is amplified by the fact that the intrinsic heat conductivity is usually different for the hydrided and dehydrided state.

16a.3 Experimental Methods and Devices

A variety of methods and apparatuses are available for the determination of hydrogen storage properties of materials. Each of them has advantages and disadvantages, thus, selection of a particular method/apparatus depends on a number of criteria, such as:

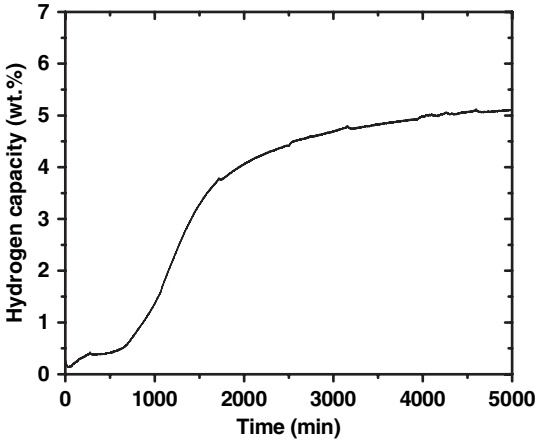

Fig. 16a.6 Activation curve of ball-milled Mg-Pd 2.5 at.%. Activation temperature 623 K, pressure 1.3 MPa

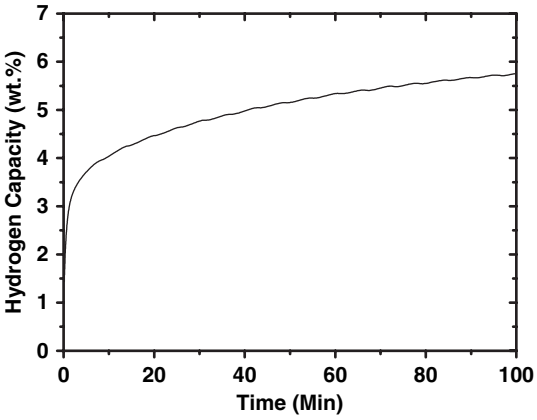

Fig. 16a.7 Hydrogen absorption at 623 K of fully activated ball-milled Mg-Pd 2.5 at.%. Absorption pressure 1.0 MPa

- Nature of material to be analyzed (metal hydrides, carbon nanotubes, metal organic framework, etc.).
- Pressure and temperature range to be covered.
- Mass of material available for measurement.
- Type of measurement to be performed (PCT, measurement of enthalpy change, and/or kinetic).

There is not a single technique/apparatus that could provide an accurate measurement of all properties. For a complete investigation, complementary methods should be used. In the selection of the right method, special care should be taken in order to ensure that the apparatus will not disturb the sample response (transient period as small as possible) and that the dead time in the beginning of recording is as short as possible. In the following section, some of the most common methods and apparatuses for hydrogen storage characterization will be reviewed with special emphasis on the ones used for metal hydrides.

Essentially, all existing methods can be divided into three classes:

1. Volumetric.
2. Gravimetric.
3. Other methods.

The volumetric method is based on the change of pressure in a calibrated volume, while in the gravimetric method it is the mass variation of the sample that is registered. Over the years, variations of each method have been implemented in order to meet specific requirements. Here, the general principles of each method will be discussed and a few modifications mentioned.

16a.3.1 Volumetric Methods

Volumetric methods are commonly used to determine the storage capacity and the absorption/desorption kinetics. Storage capacity is given in terms of applied

hydrogen pressure (P vs. H/M), while the kinetics are expressed as the capacity as a function of time (H/M vs. t).

16a.3.1.1 Constant Volume Systems (Sieverts' Apparatus)

Volumetric devices are widely used for determining hydrogen sorption properties of metal hydrides. In literature, volumetric instruments are also called Sieverts' apparatuses, but in the following section the former expression will be used. Volumetric instruments are conceptually simple and can be used for a wide range of sample sizes, temperatures, and pressures. In this type of instrument, the change of pressure due to hydrogen sorption is registered and the hydrogen capacity is deduced from the calibrated volume of the apparatus. A good proportion of research laboratories are using *in-house* instruments. The advantages of building own apparatuses are a better knowledge and control of all intricacies of the system and cost reduction. However, the time and manpower needed to build and test the system have to be taken into account. There are now a few commercial instruments that can handle practically all the measuring conditions of most researchers. A list of manufacturers is given in Appendix A.

A detailed description of the volumetric measurement is given in Sect. 16a.4. But before discussing the details of the conventional volumetric apparatuses, some variations of the basic volumetric apparatus shall be presented.

16a.3.1.2 Constant Pressure Systems

In principle, kinetic measurements should be made at constant pressure. In order to achieve this condition, Gerard et al. coupled a bellow to the reaction vessel [59]. The bellow's volume is controlled by a differential pressure transducer between the reaction vessel and the reference pressure. The evolved hydrogen is given by the change of the bellow's volume. This system was developed for a sample mass not exceeding a few milligrams and designed for pressures up to 1.5 MPa and a temperature range of 0–100°C.

A mass flow meter could be coupled to a volumetric apparatus [36, 60]. In this way, the reaction occurs at constant pressure, while the evolved hydrogen is deduced from the flow meter. In this type of measurement, the plateau pressure and hysteresis are strongly dependent on the mass flow rates. High flow rates give unrealistic plateau shapes and large hysteresis. Nevertheless, this type of experiment is probably more representative of practical conditions. Goodell et al. [44] also built an apparatus that can perform constant pressure or constant flow experiments.

Poirier et al. [61] designed a volumetric apparatus with a mass flow meter to measure the amount of gas adsorbed with an uncertainty of 20 µg for a sample mass of the order of 20 mg. In their procedure, a helium flow is sent to the sorbing system under the same flow, pressure, and temperature conditions as when using hydrogen. By subtracting from the amount of hydrogen the amount of helium, the sorbed mass of hydrogen is deduced.

In the design of Checchetto et al. [62], the pressure of the sample chamber is constantly controlled by dosing from a reservoir. Although this is not a true constant pressure apparatus, the sample pressure could be kept within a small range, thus effectively conducting a constant pressure experiment.

16a.3.1.3 Burette

The burette system was developed by Bogdanovic and Spliethoff [63] and used in the development of alanates for hydrogen storage [64, 65]. In this method, the sample is held in an autoclave which is connected, through high-pressure valves, either to a pressure transducer for recording pressure change or to a gas burette to measure the hydrogen evolved. The gas burette volume is allowed to change by the displacement of a mercury-sealed piston. The piston is connected to a distance-tension transformer to accurately register the piston's position. This apparatus is relatively simple to build and operate and has proven its usefulness in the development of alanates.

16a.3.1.4 Temperature Controlled Desorption (TCD)

In temperature controlled desorption (TCD), the sample is heated at a constant rate and the hydrogen release is monitored either by pressure increase in a calibrated volume or by measuring the hydrogen flow (flow meter). The advantages of this technique are that it is relatively easy to build both in terms of software and hardware. Commercial temperature controllers easily do the ramping of temperature. The disadvantages are that thermodynamics parameters (plateau pressure) are practically impossible to determine accurately and the kinetics cannot be determined analytically. A variation of this technique is the thermal desorption spectroscopy (TDS) where the hydrogen desorbed in high vacuum is analyzed by mass spectroscopy. This method is highly selective and very small samples could be measured (below 1 mg) [66, 67]. In their apparatus, Castro and Meyer [68] used a mass flow meter to measure the flux of gas desorbed. A complete description of this method, both from an experimental and theoretical point of view, is given by Mintz et al. [69].

16a.3.2 Gravimetric Methods

16a.3.2.1 Thermogravimetry (TG)

In gravimetric methods, the weight change of the sample due to hydrogen sorption is measured. The gravimetric method provides a direct and sensitive measurement of gas release or uptake through the use of a microbalance and is more adaptable to

high vacuums [61]. This last feature is important, because some materials (such as nanotubes) need degassing before the actual measurement. This is problematic for most volumetric systems, because the vacuum level at the sample location usually is quite high due to the use of small-diameter high-pressure tubes which impose important flow restrictions. This method has been used for determining the hydrogen storage capacities of various materials like carbon materials [70–76] and metal hydrides [77–80].

In a standard gravimetric system, a conventional microbalance head is mounted in a vacuum-pressure vessel. Temperature and pressure inside the vessel are transmitted to a microcomputer which collects and processes data. The major sources of errors are related to buoyancy, thermal, and mechanical disturbances [61]. The buoyancy effect arises from the force exerted by the volume of fluid displaced by the sample. This causes a systematic error which can be corrected by tarring the other arm of the balance with an equal mass of non-sorbing material. This material should have a density similar to that of the sample to be measured and be inert in hydrogen atmosphere.

The temperature gradient in the gas phase produces convection currents that cause noisy mass reading. Using a long stabilization time to let the system reach the thermal equilibrium minimizes this effect. Leveling the apparatus and fixing it firmly on anti-vibration cushions reduce mechanical disturbances.

In a recent paper, Poirier et al. [61] compared the volumetric and gravimetric methods for the measurement of small sorbent samples. Both systems are described in detail and uncertainties associated with each method are discussed.

16a.3.2.2 Magnetic Suspension

An interesting variation of the gravimetric system is a “contactless” apparatus where the sample cell is linked to the balance through a magnetic suspension system [73]. It is claimed that this configuration eliminates almost all restrictions inherent to conventional gravimetric measurements.

16a.3.2.3 Tapered Element Oscillating Microbalance (TEOM)

Another variation of the gravimetric method is the tapered element oscillating microbalance (TEOM). In a TEOM apparatus, the sample is inserted into a vibrating tube. As the sample mass changes, the natural vibration frequency of the tube changes. A feedback system maintains the oscillation of the tapered tube. In principle, the measurements are not influenced by effects associated with flow patterns and buoyancy [81]. This technique was recently used to measure the hydrogenation dynamics of catalyzed nanocrystalline magnesium [81]. A detailed description of this apparatus can be found in Chen et al. [82].

16a.3.3 Other Methods

16a.3.3.1 Pressure Differential Scanning Calorimeter (PDSC)

A detailed description of this technique is given in Chap. 15.5 of this book. This method is becoming increasingly popular when coupling thermal analysis and gas analysis (mass spectrometer). In this arrangement, structural transformation can be distinguished easily from gas evolution and the nature of the evolved gas can be determined. This method was demonstrated for different metal hydride materials by Fernandez et al. [83].

16a.3.3.2 Pneumatochemical Impedance Spectroscopy (PIS)

Pneumatochemical impedance spectroscopy is the indirect transposition of electrochemical impedance spectroscopy to solid-gas reactions [84]. The goal is to perform Fourier analysis of the hydrogen sorption kinetics. Gray [85] used monochromatic pressure modulations generated by thermal heating, but this technique has a limited frequency domain. Millet [84] used a needle valve to restrict hydrogen flow. In the equivalent electrical circuit, the needle valve is represented by a resistance and the volumetric chambers act as capacitors. The main problem in the analysis is the fact that particle size and slope of the isotherm should be determined accurately in order to have a reliable value of the hydrogen diffusion constant. Nonetheless, it is claimed that PIS could be used to determine the reaction's rate-limiting steps.

16a.4 Details of the Volumetric Measurement

16a.4.1 Description of the Apparatus

Figure 16a.8 displays a schematic view of the volumetric apparatus used in our laboratory. Some of its features are unique, but it still represents a typical volumetric instrument [59, 86–90]. It will be used to discuss the main features of this type of device and point out a few distinctive characteristics. With this apparatus, kinetics and thermodynamics properties of samples between 100 mg and 1 g are measured at temperatures from 20 to 500°C and pressures up to 60 MPa.

Because of the high pressure, all tubings (seamless) and fittings are made of stainless steel (316L) with an external diameter of 6 mm and a wall thickness of 1.2 mm. All fittings are of the VCR (Vacuum Coupling Radius Seal) type. The advantage of this type of fitting is a zero clearance assembly which makes the construction and repair much easier. All weldings are of the TIG (Tungsten Inert Gas) type to ensure better mechanical and temperature resistance. The valves are all high-pressure (working pressure 240 bar) and air-actuated (normally close) valves. Most

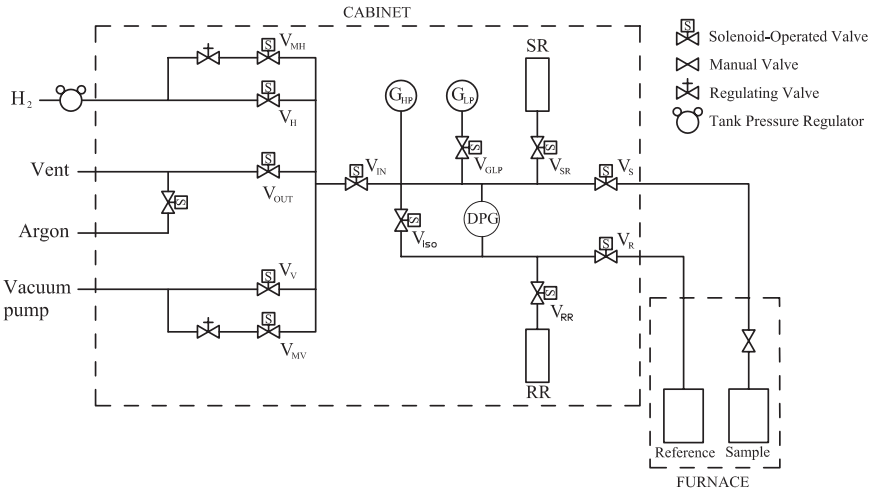

Fig. 16a.8 Schematic view of a volumetric apparatus. The dashed boxes represent constant temperature enclosures (heating cabinet and sample furnace)

of the components are enclosed in the insulated cabinet which is kept at constant temperature (30.00 ± 0.05°C). An explosion-proof fan evenly distributes the heat in the cabinet. The tubing going from cabinet A to the furnace is insulated to reduce heat transfer with the room. Such a thermally insulated and temperature-controlled environment is necessary due to the fact that at high pressures, minor variations in room temperature can cause significant errors in both plateau pressures and capacity measurements.

The hydrogen supply is divided into two parts, each controlled by a solenoid valve. One entrance (valve V_H) allows for a high hydrogen flow to ensure rapid filling of the apparatus. The other solenoid valve (V_{MH}) has a metering valve upstream to reduce the flow in order to precisely achieve the desired pressure at the start of the experiment. In the same way, the vacuum line is divided into two. At the beginning of pumping, when the system pressure is near one bar, the pumping is made through a solenoid valve equipped with a metering valve. This protects the vacuum pump from an overpressure or too large flow for the pumping speed of the pump. When the vacuum reaches an acceptable value (around 25 kPa), the valve V_V opens to increase the pumping speed.

The venting system is used to decrease the system pressure down to atmospheric pressure before pumping. For safety reasons, the purge line is first purged with an inert gas (argon or nitrogen) before opening V_{OUT} for venting hydrogen. It should be pointed out that the purge line should be directed outside the laboratory in a safe place out of reach of human activities and protected from possible fire or lightning.

The valve V_{IN} isolates the system from the purge, hydrogen inlet, and pumping system. In principle, this valve could be omitted. In this case, however, there are five possible leaks (V_{MH}, V_H, V_{OUT}, V_V, V_{MV}) instead of one (V_{IN}). As the inlet valves

endure many cycles and may develop small leaks over times, it is a safe procedure to isolate them from the measuring system.

In the simplest version of the volumetric apparatus, the reaction progress is recorded by the variation of the absolute pressure of the calibrated reservoir [91–93]. However, better resolution is achieved when the differential pressure between sections with and without the sample is measured [88, 94, 95]. The apparatus shown in Fig. 16a.6 is of the differential type. The system is divided into two parts separated by the differential pressure gauge (DPG). The valve V_{ISO} serves to isolate the reference side from the sample side. Two absolute pressure gauges are installed on the sample side. The high-pressure gauge (G_{HP}) (rated to 6×10^4 kPa) is constantly monitored, while the low-pressure gauge (G_{LP}) (rated to 1.7×10^3 kPa) is used for low-pressure measurement. During high-pressure measurements, the low-pressure gauge is protected by closing the valve V_{GLP}. Each side has a one liter volume that is used to adjust the internal volume such that an optimum pressure change is achieved according to the evolved hydrogen. Both reservoirs are open or closed simultaneously with the valves V_{SR} and V_{RR}. Other researchers have equipped their volumetric apparatus with several calibrated gas reservoirs of different volumes to give a bigger range of working conditions [36, 88].

The main particularity of the present apparatus is the presence of a reference port inside the furnace, thus making it a true differential system [86]. In a conventional configuration, the differential pressure is measured between the pressures of a tank inside the cabinet and the sample side of the system. The limitation is that when the hydrogen is introduced in the sample, there is a heat effect due to the change of temperature of the gas itself, which is not balanced in the reference port. In our system, a reference cell having the same volume as the sample cell has been added. In this way, hydrogen flow is identical on both sides of the reference gauge and only the contribution of the sample itself is registered. The effect of the reference port is easier to visualize when a kinetic measurement with an empty sample cell is made with and without the reference. Figure 16a.9 displays a kinetic measurement at 623 K, where a pressure of 1400 kPa was suddenly applied and the differential pressure was registered at $t = 0$. Without the reference port, the differential pressure rises to 5.4 kPa in 8 seconds, while with the reference port the system is stable after 5 seconds and the differential pressure is only 3.4 kPa. It is obvious that the reference reduces the equilibrium time by almost half. For perfectly matched volumes, this should be zero. The non-zero value of differential pressure measured here is due to the slight difference in volume between the reference and sample sides.

All the valves, hydrogen and inert gas source, vacuum pump, gas release and heating system are controlled automatically on a real time scale via a LabView®-based software. As a consequence, sequential acquisition of several isotherms or dynamic cycles can be programmed.

Commercial and in-house built volumetric instruments are widely used for the characterization of materials for hydrogen storage. This type of apparatus is robust, easy to calibrate and to maintain. It allows for the measurement of a broad range of sample types. Probably, the main drawback of this method is that reactions could never be truly isobaric. A number of modifications have been made to circumvent

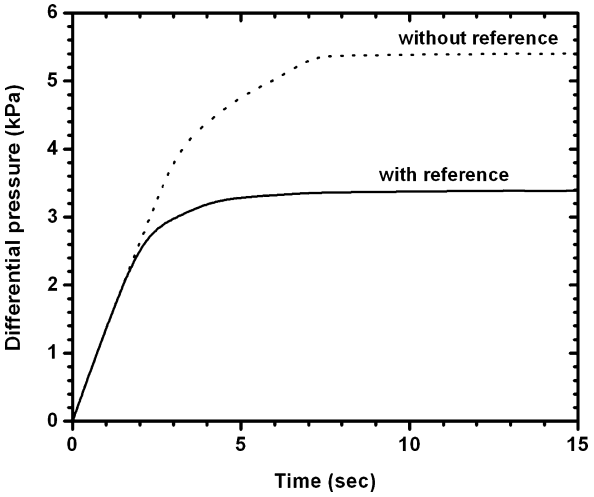

Fig. 16a.9 Differential pressure between reference and sample ports for empty sample cell measurements with and without reference port. At $t = 0$, a pressure of 1400 kPa was established. Sample holder temperature: 623 K, cabinet temperature: 303 K

this difficulty (as described in the previous section), but this problem could never be totally eliminated. During dehydrogenation in particular, the sample releases hydrogen and the pressure inside the apparatus rises quite rapidly to a value close to the dehydrogenation plateau pressure. If the system's pressure reaches or is close to the plateau pressure, then the reaction stops. To prevent this situation, the experimenter should estimate the pressure build-up during dehydrogenation and select the right mass of sample.

16a.4.2 Accessories

In this section, some general aspects of measurement and apparatus that could have an important impact on the quality of the measurements shall be discussed.

16a.4.2.1 Sample Holder

As hydrogenation/dehydrogenation strongly depends on temperature and the reaction itself involves a large amount of heat (up to 75 kJ mol^{-1} for some hydrides), it is essential that good thermal conductivity is ensured in the sample holder. Many designs have been used and a few were mentioned in Sect.16a.2.2. The problem of heat flux was thoroughly investigated theoretically and experimentally by Dantzer et al. [96–99]. It is emphasized again that the sample holder design has an important impact on the ultimate performance of the system. Material, shape, and even sample mass should be considered [100–102].

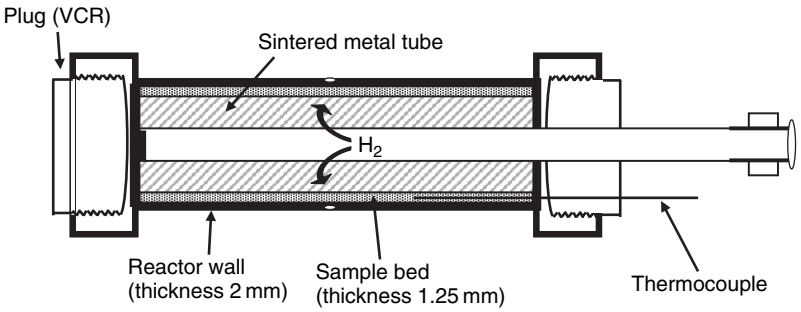

Fig. 16a.10 Schematic view of reactor (source: Institute of Nanotechnology, FZK Karlsruhe)

As an example, Fig. 16a.10 displays the schematic view of a reactor designed for a sample amount ranging from 1 to 2 grams. The reactor made of stainless steel can be heated up to 400°C and all fittings are of the VCR type. The sample powder is located in a cylindrical slit with a width of only 1.25 mm underneath the steel wall of the reactor to provide for a good heat exchange between the heat reservoir and the whole sample. A fast reacting thermocouple of 0.5 mm in diameter is in direct contact with the sample powder, thus giving the direct measurement of the sample temperature. Gas exchange with the Sieverts' apparatus is possible via the porous metal filter inner tube (particle size of 3 µm). This tube is ended with a manual valve which allows the reactor to be filled with an inert atmosphere for samples that are sensitive to air. The reactor is then connected via a VCR-type fitting from the manual valve to the volumetric apparatus.

16a.4.2.2 Heating System

To control the temperature of the sample, the reactor can be immersed into an oil bath (running with silicon oil M100, temperature range ~20 to 200°C) or surrounded by a specially designed heater jacket (temperature range 20 to 450°C) or placed inside an oven (temperature range 20 to 500°C). Temperature is recorded with a type-K thermocouple.

16a.4.2.3 Hydrogen Gas

The choice of hydrogen purity has a major impact on the experimental results, especially for cycling experiments where tens, hundreds, and even thousands of absorption/desorption cycles are carried out [103–106]. The highest purity is, of course, recommended, but inclusion of a filter or some other purification system is a good procedure, as was shown for carbon nanotubes measurements [107].

16a.4.2.4 Vacuum Pump

The majority of volumetric devices are made to go to a relatively high pressure and the tubing is usually made of small caliber (typically 6 mm outside diameter) stainless steel tubing. Such high-pressure tubing is too restrictive for vacuum service and makes it practically impossible to achieve high vacuum on the sample. For volumetric units, the most important features of the vacuum system are the hydrogen compatibility, the absence of oil vapor (mechanical pumps are not recommended, except if provided with a good oil filter), the pumping speed, and the capability to accept a slight overpressure (in the case of mishandling). For this last feature, a large buffer volume is sometimes added between the vacuum pump and the volumetric device to serve as a safeguard.

16a.4.3 State Equation of the Gas

Hydrogen could be considered an ideal gas for relatively high pressures (up to 100 bar). However, it is a good procedure to always use viral coefficients of hydrogen gas or its compressibility factor to compute the number of moles evolved. When using the compressibility factor, the hydrogen density is given by Eq. (16a.11).

$$\rho_{H_2} = \frac{p}{z \cdot R \cdot T} \tag{16a.11}$$

where p is the pressure, R is the gas constant, T is the temperature, and z is the compressibility factor which is a function of pressure and temperature. The expression for the compressibility factor can be found in the standardized equation for hydrogen gas established by Lemmon et al. [108]. The densities computed by their equation agree with the current standard within 0.01% from 220 to 400 K with pressures up to 45 MPa. A commercial package for accurate hydrogen density calculation is available from NIST Standard Reference Database 12 [109].

16a.4.4 Measurement Process

First, the sample holder is filled in the glove box with the material to be tested and then transferred to the apparatus with the manual valve closed. Then, the control program evacuates and purges the different parts of the system as well as the sample holder. Before starting the measurement cycle, stability of the sample temperature is checked. In hydrogenation kinetic measurement, a hydrogen pressure is applied to the sample once the temperature is stabilized to the required value and the pressure drop is monitored as a function of time. At each instant, the amount of hydrogen is calculated from Eq. (12).

$$n_{H_2}(\text{absorbed/desorbed}) = [\rho(t) - \rho(t=0))]\,V \qquad (16a.12)$$

where V is the calibrated volume. In fact, Eq. (16a.12) should be computed twice. Once for the gas inside the sample holder volume which is at the set point temperature and another time for the gas that is inside the calibrated volume of the cabinet, the temperature of which usually differs from that of the sample. The total amount of hydrogen is the sum of these two contributions. When the pressure drop is smaller than a predetermined value during a certain time interval, equilibrium is considered to be reached. The experiment is then stopped or turned to the dehydrogenation mode. The dehydrogenation mode is essentially the same process as hydrogenation, except that vacuum (or a pressure below the plateau pressure of the material at this temperature) is established in the sample and calibrated volumes instead of hydrogen pressure.

For isotherm measurement, the measuring procedure is almost the same as for the kinetic process. The main difference is that here the pressure is increased stepwise, each step having a measuring sequence identical to the kinetic method. In this way, a complete isotherm (hydrogenation and dehydrogenation) can be plotted. More detailed explanation of the measuring sequence can be found in Brinks et al. [87].

The main problem encountered with volumetric systems probably is the presence of leaks. Small leaks that develop over the time may be hard to identify. A leak could be interpreted incorrectly as hydrogenation or dehydrogenation. Temperature instability in the sample cell or cabinet may give rise to a large experimental error. Therefore, both the sample holder and cabinet temperatures should be well controlled and registered during the whole experiment.

16a.4.5 Effect of Aliquot Size

Under dynamic conditions (kinetic measurements), the sample is continuously subjected to hydrogen gas. In static isotherms (PCT measurements), the pressure is increased by steps. After each step, a certain time is needed to reach equilibrium. Usually, the equilibrium criterion is that the pressure should not vary by more than a pre-determined value over a specified time period. Park and Flanagan reported that bigger pressure steps (large aliquot) markedly reduce the hysteresis between absorption and desorption curves [110, 111]. Several microscopic mechanisms were proposed to explain this behavior. Park and Flanagan explained this effect by the interface velocity in the metal atom local equilibrium at the interface [112]. Shilov and Kuznetsov argued that for a large aliquot, the plastic deformation is performed at the expense of external work, whereas for a small aliquot, it is the free energy of the system [113]. For their part, Qian and Northwood suggested that for a large aliquot, the plateau pressure is controlled by the energy barrier for growth of the hydride phase, while for a small aliquot, it is the nucleation energy barrier that determines

the plateau pressure [114]. Gray et al. pointed out a pressure-drive effect instead of aliquot size and they suggested that a decreased hysteresis resulted from extra defects caused by the passage of the α-β interface at high velocity for large aliquots [115]. Gray et al. [116, 117] used the thermal model described by Pons and Dantzer [98] to explain the aliquot artefact by a temperature gradient. For Friedlmeier et al. [36], the large aliquot pressure artefact results from plateau slope. A critical review of all these explanations was made by Gray et al. [116]. Their general conclusions are: (1) Most of the large aliquot effect reported could be explained by the artefact room temperature gradient, (2) a large pressure drive could result in a false pressure plateau in the case of a sloping plateau, (3) the microstructure models are still untested, (4) for a certain number of experiments, a large aliquot effect seems to exist, resulting in a reduction of hydrogen capacity, (5) isobaric techniques appear to be the most satisfactory for avoiding pressure artefacts. As could be seen, this phenomenon is still not well understood. Therefore, caution has to be exerted in the design and interpretation of measurements.

16a.5 Safety

Before closing this chapter, safety aspects of hydrogen measurement should be examined. The safety aspects of hydrogen itself are well documented. For up-to-date information about safety and handling of hydrogen, the following sources can be consulted:

- Material Safety Data Sheet (MSDS) of hydrogen gas.
- *Source book for hydrogen applications* available at: www.tisec.com.
- Compressed Gas Association (CGA) [www.cganet.com].
- European Industrial Gases Association (EIGA) [www.eiga.org].
- Japanese Industrial Gases Association (JIGA) [www.jiga.gr.jp/english].
- American Chemistry Council [www.americanchemistry.com].

Concerning the inherent safety aspects of hydrogen gas, the problem of handling metal hydride has to be considered. Depending on alloy composition, state, and history, the metal hydride can:

- Be pyrophoric.
- React violently with water or moisture.
- Be toxic.
- Release a high amount of heat (on hydrogenation).

The association metal hydride/hydrogen means that the problems associated with each of them is added to the problem of the other and may lead to an acceleration of a dangerous reaction. Consequently, safety considerations should come first in all handlings and measurements. The first step is to know the characteristics of the materials handled, but the nature of scientific investigation means that this is not always the case. Then, unknown (or partially known) materials should be handled

in a "worst case" scenario. It is a good procedure to limit the quantity of material as much as possible and ideally to perform all manipulations under a protective atmosphere. Personnel should have the appropriate training in the safety aspects of laboratory work. Finally, the disposals of samples and all material should be done with respect of the environment. A specific procedure for the disposal of all used material should be planned and explained to all personnel.

Safety in the measurement process should also be considered. For measurements performed with commercial apparatuses, the manufacturer's recommendations should be followed. The manufacturer should have included all safety features of the apparatus itself and give to the customer the requirements for the apparatus and supporting systems needed (exhaust line, remote emergency shut-down, etc.). A more complicated issue is the safety of in-house built apparatuses. Due to the lack of experience, there is the risk of missing some essential safety features. Having a hydrogen detector in the laboratory is essential. Usually, the detector is set for a first alarm when the hydrogen level reaches 10% of the lower flammable limit of hydrogen in air. A second alarm with an automatic shut-off of operation is set at 20% of the lower flammable limit. Valves should be operated pneumatically and a separated enclosure should be provided for electronics and gas systems. Moreover, it is preferable to have the electronic enclosure below the gas system in order to prevent leaking hydrogen from contacting electrical parts. Periodic leak inspections should be performed. It is advisable to take as much information as possible from the open literature and by seeking advices from other users. Validation of the drawings by a knowledgeable person before starting the construction will save time and money. The point to remember is that safety should always come first especially when dealing with the combination hydrogen/metal.

16a.6 Conclusion

Measurement of hydrogen sorption properties is in the center of development of new hydrogen storage materials. From the PCT curves, the hydrogen storage capacities are measured as well as plateau pressure, hysteresis, and reversible capacities. From the Van't Hoff plot, the hydride heat of formation is deduced, while kinetic measurements give the rate-limiting step of the reaction. Thus, measurements of hydrogen sorption properties give valuable information for the practical aspects, such as tank design as well as fundamental knowledge on hydrogen/metal interactions.

Now, various methods and types of apparatuses are available either from commercial suppliers or to be built. The choice of a particular type depends on the sample's nature, amount, and type of information searched for. It was shown that there are many apparatuses available, either commercials or built by the experimentalists for their specific needs. Most of them use one of the two main methods: Volumetric or gravimetric. The principle of each method was presented and critically assessed.

References

1. Joubert, J.-M., et al., *Differentes méthodes de stockage de l'hydrogène*. Annales de Chimie-Science des Materiaux Chim. Sci. Mat., 2005. **30**(5): pp. 441–454.
2. Bowman, R.C. and B. Fultz, *Metallic hydrides I: Hydrogen storage and other gas-phase applications*. MRS Bulletin, 2002. **27**(9): pp. 688–693.
3. Dantzer, P., *Properties of intermetallic compounds suitable for hydrogen storage applications*. Materials Science and Engineering A, 2002. **329–331**: pp. 313–320.
4. Suda, S. and G. Sandrock, *Three decades of intermetallic hydrides – What happened to the applications?* Zeitschrift fuer Physikalische Chemie, 1994. **183**: pp. 149–156.
5. Chandra, D., J.J. Reilly, and R. Chellappa, *Metal hydrides for vehicular applications: The state of the art*. JOM, 2006. **56**(2): pp. 26–32.
6. Schlapbach, L., *Hydrogen as a fuel and its storage for mobility and transport*. MRS Bulletin, 2002. **27**(9): pp. 675–676.
7. Schlapbach, L. and A. Züttel, *Hydrogen-storage materials for mobile applications*. Nature, 2001. **414**: pp. 353–358.
8. Schlapbach, L., et al., *Hydrogen for novel materials and devices*. Applied Physics A, 2001. **72**(2): pp. 245–253.
9. Züttel, A., *Materials for hydrogen storage*. Materials Today, 2003. **6**(9): pp. 24–33.
10. Züttel, A., *Hydrogen storage methods*. Naturwissenschaften, 2004. **91**: pp. 157–172.
11. Sandrock, G., *A panoramic overview of hydrogen storage alloys from a gas reaction point of view*. Journal of Alloys and Compounds, 1999. **293–295**: pp. 877–888.
12. Gerard, N. and S. Ono, *Hydride formation and decomposition kinetics*, in *Hydrogen in Intermetallic Compounds II*, L. Schlapbach, Editor. 1992, Springer-Verlag: Berlin. Chapter 4.
13. Libowitz, G.G., *The Solid-state Chemistry of Binary Metal Hydrides*. 1965, New-York: W.A. Benjamin. p. 139.
14. Yamaguchi, M. and E. Akiba, *Ternary hydrides*, in *Electronic and Magnetic Properties of Metals and Ceramics Part II*, K.H.J. Buschow, Editor. 1994, VCH: Weinheim. pp. 333–398.
15. Schlapbach, L., *Surface properties and activation*, in *Hydrogen in Intermetallic Compounds II*, L. Schlapbach, Editor. 1992, Springer-Verlag: Berlin. pp. 15–95.
16. Wiswall, R., *Hydrogen storage in metals*, in *Hydrogen in Metals II*, G. Alefeld and J. Völkl, Editors. 1978, Springer-Verlag: Berlin. p. 201.
17. Fukai, Y., *The metal-hydrogen system*, in *Springer Series in Materials Science*, U. Gonser, Editor. 1993, Springer-Verlag: Berlin. p. 248.
18. Schlapbach, L., I. Anderson, and J.P. Burger, *Hydrogen in metals*, in *Electronic and Magnetic Properties of Metals and Ceramics Part II*, K.H.J. Buschow, Editor. 1994, VCH: Weinheim. pp. 271–331.
19. Tanaka, K. and O. Yoshinari, *Hydrogen-metal systems: Basic properties (1)*, in *Encyclopedia of Materials: Science and Technology*, K.H.J. Buschow, et al., Editors. 2001, Elsevier: Amsterdam.
20. Schlapbach, L., *Thermodynamics of metal, alloy and intermetallic/hydrogen systems*. in *Hydrides for Energy Storage*. 1977, Pergamon: Geilo, Norway.
21. Flanagan, T.B. and W.A. Oates, *Thermodynamics of intermetallic compound-hydrogen systems*, in *Hydrogen in Intermetallic Compounds I*, L. Schlapbach, Editor. 1988, Springer-Verlag: Berlin. pp. 49–85.
22. Griessen, R. and T. Riesterer, *Heat of formation models*, in *Hydrogen in Intermetallic Compounds I*, L. Schlapbach, Editor. 1988, Springer-Verlag: Berlin. pp. 219–284.
23. Sandrock, G., S. Suda, and L. Schlapbach, *Applications*, in *Hydrogen in Intermetallic Compounds II*, L. Schlapbach, Editor. 1992, Springer-Verlag: Berlin. pp. 197–258.
24. Balasubramaniam, R., *Hysteresis in metal-hydrogen systems*. Journal of Alloys and Compounds, 1997. **253–254**: pp. 203–206.

25. Flanagan, T.B., *The thermodynamics of hydrogen solution in 'perfect' and defective metals alloys*, in *Progress in Hydrogen Treatment of Materials*, V.A. Goltsov, Editor. 2001, Donetsk State Technical University: Donetsk. pp. 37–63.
26. Flanagan, T.B. and J.D. Clewley, *Hysteresis in metal hydrides*. Journal of the Less-Common Metals, 1982. **83**: pp. 127–141.
27. Flanagan, T.B., C.N. Park, and D.H. Everett, *Hysteresis in metal hydrides: An illustration of entropy production*. Journal of Chemical Education, 1987. **64**(11): pp. 944–946.
28. Flanagan, T.B., C.N. Park, and W.A. Oates, *Hysteresis in solid state reactions*. Progress in Solid State Chemistry, 1995. **23**: pp. 291–363.
29. Lototsky, M.V., et al., *Modelling of phase equilibria in metal-hydrogen systems*. Journal of Alloys and Compounds, 2003. **356–357**: pp. 27–31.
30. Park, C.N., S. Luo, and T.B. Flanagan, *Analysis of sloping plateaux in alloys and intermetallic hydrides. I. Diagnostic features*. Journal of Alloys and Compounds, 2004. **384**: pp. 203–207.
31. Luo, S., C.N. Park, and T.B. Flanagan, *Analysis of sloping plateaux in alloys and intermetallic hydrides. II. Real systems*. Journal of Alloys and Compounds, 2004. **384**: pp. 208–216.
32. Hanada, N., et al., *Remarkable improvement of hydrogen sorption kinetics in magnesium catalyzed with Nb_2O_5*. Journal of Alloys and Compounds, 2006. **420**: pp. 46–49.
33. Akiba, E., et al., *Kinetics of the reaction between Mg-Ni alloys and H_2*. International Journal of Hydrogen Energy, 1982. **7**(10): pp. 787–791.
34. Miyamoto, M., K. Yamaji, and Y. Nakata, *Reaction kinetics of $LaNi_5$*. Journal of the Less-Common Metals, 1983. **89**: pp. 111–116.
35. Friedlmeier, G. and M. Groll, *Experimental analysis and modelling of the hydriding kinetics of Ni-doped and pure Mg*. Journal of Alloys and Compounds, 1997. **253–254**: pp. 550–555.
36. Friedlmeier, G., M. Schaaf, and M. Groll, *How to measure pressure-concentration-isotherms representative for technical applications*. Zeitschrift fur Physikalische Chemie, 1994. **183**: pp. 185–195.
37. Nahm, K.S., W.B. Jung, and W.Y. Lee, *The reaction kinetics of hydrogen storage in $CaNi_5$*. International Journal of Hydrogen Energy, 1990. **15**(9): pp. 635–641.
38. Kircher, O. and M. Fichtner, *Hydrogen exchange kinetics in $NaAlH_4$ catalyzed in different decomposition states*. Journal of Applied Physics, 2004. **95**(12): pp. 7748–7753.
39. Wang, X. and S. Suda, *Hydriding-dehydriding reactions of $LaNi_{4.7}Al_{0.3}$-H system under quasi-isothermal conditions*. Journal of Alloys and Compounds, 1993. **194**: pp. 173–177.
40. Goodell, P.D. and P.S. Rudman, *Hydriding and dehydriding rates of the $LaNi_5$-H system*. Journal of the Less-Common Metals, 1983. **89**: pp. 117–125.
41. Hammioui, M.E., L. Belkbir, and N. Gerard, *Study of a hydride forming system by thermogravimetry. Hydriding characteristics of $LaNi_5$ mixed with nickel*. Thermochimica Acta, 1994. **231**: pp. 225–230.
42. Rudman, P.S., *Hydriding and dehydriding kinetics*. Journal of the Less-Common Metals, 1983. **89**: pp. 93–110.
43. Mintz, M.H. and J. Bloch, *Evaluation of the kinetics and mechanisms of hydriding reactions*. Prog. Solid State Chem., 1985. **16**: pp. 163–194.
44. Goodell, P.D., G.D. Sandrock, and E.L. Huston, *Kinetic and dynamic aspects of rechargeable metal hydrides*. Journal of the Less-Common Metals, 1980. **73**: pp. 135–142.
45. Jung, W.B., K.S. Nahm, and W.Y. Lee, *The reaction kinetics of hydrogen storage in Mg_2Ni*. International Journal of Hydrogen Energy, 1990. **15**(9): pp. 641–648.
46. Martin, M., et al., *Absorption and desorption kinetics of hydrogen storage alloys*. Journal of Alloys and Compounds, 1996. **238**: pp. 193–201.
47. Hjort, P., A. Krozer, and B. Kasemo, *Hydrogen sorption kinetics in partly oxidized Mg films*. Journal of Alloys and Compounds, 1996. **237**: pp. 74–80.
48. Bloch, J. and M.H. Mintz, *Kinetics and mechanisms of metal hydrides formation – A review*. Journal of Alloys and Compounds, 1997. **253–254**: pp. 529–541.

49. Schweppe, F., M. Martin, and E. Fromm, *Model on hydride formation describing surface control, diffusion control and transition regions*. Journal of Alloys and Compounds, 1997. **261**: pp. 254–258.
50. Inomata, A., H. Aoki, and T. Miura, *Measurement and modelling of hydriding and dehydriding kinetics*. Journal of Alloys and Compounds, 1998. **278**: pp. 103–109.
51. Bloch, J., *The kinetics of a moving metal hydride layer*. Journal of Alloys and Compounds, 2000. **312**: pp. 135–153.
52. Chou, K.-C., et al., *Kinetics of absorption and desorption of hydrogen in alloy powder*. International Journal of Hydrogen Energy, 2005. **30**: pp. 301–309.
53. Gabis, I.E., et al., *Kinetics of hydrogen desorption from the powders of metal hydrides*. Journal of Alloys and Compounds, 2005. **404–406**: pp. 312–316.
54. Delmon, B., *Introduction à la cinétique hétérogène*. 1969, Technip: Paris.
55. Barkhordarian, G., T. Klassen, and R. Bormann, *Kinetic investigation of the effect of milling time on the hydrogen sorption reaction of magnesium catalyzed with different Nb_2O_5 contents*. Journal of Alloys and Compounds, 2006. **407**: pp. 249–255.
56. Christian, J.W., *The Theory of Transformations in Metals and Alloys. Part 1*. 2002,Pergamon: Oxford.
57. Mintz, M.H. and Y. Zeiri, *Hydriding kinetics of powders*. Journal of Alloys and Compounds, 1994. **216**: pp. 159–175.
58. Dufour, J. and J. Huot, *Rapid activation, enhanced hydrogen sorption kinetics and air resistance in laminated Mg-Pd2.5at.%* Journal of Alloys and Compounds. 2007. **439**: pp. L5–L7.
59. Gerard, N., L. Belkbir, and E. Joly, *High-accuracy volumetric device for hydrogen sorption kinetic studies*. J. Phys. E: Sci. Instrum., 1979. **12**: pp. 476–477.
60. Hirata, T., *Hydrogen absorption and desorption properties of $FeTi_{1.14}O_{0.03}$ in impure hydrogen containing CO, CO_2 and oxygen*. Journal of the Less-Common Metals, 1985. **107**: pp. 23–33.
61. Poirier, E., et al., *Gravimetric and volumetric approaches adapted for hydrogen sorption measurements with in-situ conditioning on small sorbent samples*. Review of Scientific Instruments, 2005. **76**(5): p. 055101.
62. Checchetto, R., G. Trettel, and A. Miotello, *Sievert-type apparatus for the study of hydrogen storage in solids*. Measurement Science and Technology, 2004. **15**: pp. 127–130.
63. Bogdanovic, B. and B. Spliethoff, *Untersuchung von Reaktionen unter Gasentwicklung oder Gasverbrauch bei Normaldruck mit Hilfe einer automatisch registrierenden Gasburette*. Chemie Ingenievr Technik, 1983. **55**(2): p. 156.
64. Bogdanovic, B. and M. Schwickardi, *Ti-doped alkali metal aluminium hydrides as potential novel reversible hydrogen storage materials*. Journal of Alloys and Compounds, 1997. **253–254**: pp. 1–9.
65. Bogdanovic, B., et al., *Metal-doped sodium aluminium hydrides as potential new hydrogen storage materials*. Journal of Alloys and Compounds, 2000. **302**: pp. 36–58.
66. Dillon, A.C., et al., *Storage of hydrogen in single-walled carbon nanotubes*. Nature, 1997. **386**(27 March): pp. 377–379.
67. Mommer, N., et al., *Influence of the microstructure on the desorption kinetics of single and multiphase LaNiFe alloys*. Journal of Alloys and Compounds, 1998. **266**: pp. 255–259.
68. Castro, F.J. and G. Meyer, *A novel thermal desorption spectroscopy apparatus*. Review of Scientific Instruments, 2000. **71**(5): pp. 2131–2133.
69. Mintz, M.H., I. Jacob, and D. Shaltiel, *Experimental techniques II: Adaptation of new techniques to study surface and bulk properties of H-metal systems*, in *Hydrogen in Intermetallic Compounds II*, L. Schlapbach, Editor. 1992, Springer: Berlin. p. 304.
70. Poirier, E., et al., *Storage of hydrogen on single-walled carbon nanotubes and other carbon structures*. Applied Physics A, 2004. **78**: pp. 961–967.
71. Pinkerton, F.E., et al., *Thermogravimetric measurement of hydrogen absorption in alkali-modified carbon materials*. Journal of Physical Chemistry B, 2000. **104**: pp. 9460–9467.

72. Ströbel, R., et al., *Hydrogen adsorption on carbon materials*. Journal of Power Sources, 1999. **84**: pp. 221–224.
73. Lan, A. and A. Mukasyan, *Hydrogen storage capacity characterization of carbon nanotubes by a microgravimetrical approach*. Journal of Physical Chemistry B, 2005. **109**: pp. 16011–16016.
74. Henneberg, E., B. Bernhardt, and K. Bohmhammel, *Thermoanalytical investigations of hydrogen adsorption on carbon materials*. Thermochimica Acta, 2004. **415**: pp. 43–45.
75. Li, X., et al., *Measuring hydrogen storage capacity of carbon nanotubes by tangent-mass method*. International Journal of Hydrogen Energy, 2003. **28**: pp. 1251–1253.
76. Hirscher, M., et al., *Hydrogen storage in carbon nanostructures*. Journal of Alloys and Compounds, 2002. **330–332**: pp. 654–658.
77. Benham, M.J. and D.K. Ross, *Experimental determination of absorption-desorption isotherms by computer-controlled gravimetric analysis*. Zeitschrift fuer Physikalische Chemie Neue Folge, 1989. **163**: pp. 25–32.
78. Ryden, J., et al., *Unusual kinetics of hydride formation in Mg-Pd sandwiches, studied by hydrogen profiling and quartz crystal microbalance measurements*. Journal of the Less-common Metals, 1989. **152**: pp. 295–309.
79. Feenstra, R., et al., *Gravimetrical determination of pressure-composition isotherms of thin PdH_c films*. Journal of Physics F: Metal Physics, 1986. **16**: pp. 1953–1963.
80. Feenstra, R., R. Griessen, and D.G.d. Groot, *Hydrogen induced lattice expansion and effective H-H interaction in single phase PdH_c*. Journal of Physics F: Metal Physics, 1986. **16**: pp. 1933–1952.
81. Xu, X. and C. Song, *Improving hydrogen storage/release properties of magnesium with nano-sized metal catalysts as measured by tapered element oscillating microbalance*. Applied Catalysis A: General, 2006. **300**: pp. 130–138.
82. Chen, D., et al., *Catalyst deactivation studied by conventional and oscillating microbalance reactors*. Applied Catalysis A: General, 1996. **137**: pp. L1–L8.
83. Fernandez, J.F., F. Cuervas, and C. Sanchez, *Simultaneous differential scanning calorimetry and thermal desorption spectroscopy measurements for the study of the decomposition of metal hydrides*. Journal of Alloys and Compounds, 2000. **298**: pp. 244–253.
84. Millet, P., *Pneumatochemical impedance spectroscopy: 2. Dynamics of hydrogen sorption in metals.*y Journal of Physics Chemistry B, 2005. **109**: pp. 24025–24030.
85. Gray, E.M.A., *Frequency-domain hydriding and dehydriding kinetics of $LaNi_5H_x$*. Journal of Alloys and Compounds, 1992. **190**: pp. 49–56.
86. Schulz, R., S. Boily, and J. Huot, *Apparatus for Titration and Circulation of Gases and Circulation of an Absorbent or Adsorbent*. 2003, Hydro-Quebec: US. #6582663.
87. Brinks, H.W., et al., *Pressure-composition isotherms of $TbNiAlH_x$*. Journal of Alloys and Compounds, 2006. **417**: pp. 92–95.
88. Fichtner, M., et al., *Small Ti clusters for catalysis of hydrogen exchange in $NaAlH_4$*. Nanotechnology, 2003. **14**: pp. 778–785.
89. Blackman, J.M., J.W. Patrick, and C.E. Snape, *An accurate volumetric differential pressure method for the determination of high storage capacity at high pressures in carbon materials.*y Carbon, 2006. **44**: pp. 918–927.
90. Tibbetts, G.G., G.P. Meisner, and C.H. Olk, *Hydrogen storage capacity of carbon nanotubes, filaments, and vapor-grown fibers.*y Carbon, 2001. **39**: pp. 2291–2301.
91. Boser, O., *Hydrogen sorption in $LaNi_5$*. Journal of the Less-Common Metals, 1976. **46**: pp. 91–99.
92. Ryan, D.H. and J.M.D. Coey, *Thermopiezic analysis: Gas absorption and desorption studies on milligram samples.*y Journal of Physics E: Science Instruments, 1986. **19**: pp. 693–694.
93. Karty, A., J. Grunzweig-Genossar, and P.S. Rudman, *Hydriding and dehydriding kinetics of Mg in a Mg/Mg_2Cu eutectic alloy: Pressure sweep method.*y Journal of Applied Physics, 1979. **50**(11): p. 7200.
94. Batalla, E., et al., *Hydrogen in amorphous Ni-Zr: Pressure concentration isotherms, site occupation, and binding energy.*y Journal of Materials Research, 1986. **1**(6): p. 765.

95. Tessier, P., *Hydrogen storage in metastable Fe-Ti*, in *Department of Physics*. 1995, McGill: Montreal, Canada. p. 143.
96. Dantzer, P. and P. Millet, *Advances in hydride phase growth: Automatic high precision calorimeter-volumetric devices, for thermodynamic and kinetic analyses*. Review of Scientific Instruments, 2000. **71**(1): pp. 142–153.
97. Dantzer, P. and P. Millet, *On the accuracy of heat flux calorimetry in stable intermetallic-$H_{2(g)}$ systems*. Journal of Alloys and Compounds, 2002. **330–332**: pp. 34–40.
98. Pons, M. and P. Dantzer, *Heat transfer in hydride packed beds. II. A new experimental technique and results on $LaNi_5$ powder*. Zeitschrift Für Physikalische Chemie, 1994. **183**: pp. 213–223.
99. Pons, M., P. Dantzer, and J.J. Guilleminot, *A measurement technique and a new model for the wall heat transfer coefficient of a packed bed of (reactive) powder without gas flow*. International Journal of Heat and Mass Transfer, 1993. **36**(10): pp. 2635–2646.
100. Bayane, C., E. Sciora, and N. Gerard, *Influence of the material and the shape of the container on $LaNi_5$ hydride formation*. Journal of Materials Science Letters, 1993. **12**: pp. 1821–1822.
101. Gerard, N., C. Bayane, and M.E. Hammioui, *Study of hydride forming system by thermogravimetry. Role of the sample mass in exothermic kinetics*. Thermochimica Acta, 1984. **82**: pp. 171–177.
102. Bayane, C., et al., *$LaNi_5$ hydride formation. The effects of the thermal conductivity of the holder on the kinetics*. Thermochimica Acta, 1993. **224**: pp. 193–202.
103. Dehouche, Z., et al., *Influence of cycling on the thermodynamic and structure properties of nanocrystalline magnesium based hydride*. Journal of Alloys and Compounds, 2000. **305**: pp. 264–271.
104. Dehouche, Z., et al., *Moisture effect on hydrogen storage properties of nanostructured MgH_2-V-Ti composite*. International Journal of Hydrogen Energy, 2003. **28**: pp. 983–988.
105. Sun, D., et al., *Rehydrogenation and cycling studies of dehydrogenated $NaAlH_4$*. Journal of Alloys and Compounds, 2004. **373**: pp. 265–269.
106. Srivastava, S.S., et al., *Long term cycling behavior of titanium doped $NaAlH_4$ prepared through solvent mediated milling of NaH and Al with titanium dopant precursors*. Journal of Alloys and Compounds, 2004. **377**: pp. 283–289.
107. Yang, R.T., *Hydrogen storage by alkali-doped carbon nanotubes-revisited*. Carbon, 2000. **38**: pp. 623–641.
108. Lemmon, E.W., et al., *Standardized Equation for Hydrogen Gas Densities for Fuel Consumption Applications*, in *SAE 2006 World Congress & Exhibition*. 2006. Detroit SEA International.
109. Lemmon, E.W., et al., *NIST Thermodynamic and Transport Properties of Pure Fluids Database: Version 5.0*. 2000, National Institute of Standards and Technology: Boulder, Colorado.
110. Park, C.N. and T.B. Flanagan, *The effect of hydrogen aliquot size on the plateau pressures of $LaNi_5 - H$*. Journal of the Less-Common Metals, 1983. **94**: pp. L1–L4.
111. Park, C.N. and T.B. Flanagan, *Experimental observations on the effect of the rate of hydride formation and decomposition on the plateau pressure of intermetallic compounds hydrides*. Ber. Bunsenges. Phys. Chem., 1985. **89**: pp. 1300–1304.
112. Park, C.N. and T.B. Flanagan, *The effect of interface velocity on the plateau pressure of intermetallic compounds hydrides. Theoretical interpretation of hydrogen aliquot size on the plateau pressures of $LaNi_5 - H$*. Berichte der Bunsen-Gesellschaft Physical Chemical Physics, 1985. **89**: pp. 1305–1311.
113. Shilov, A.L. and N.T. Kuznetsov, *The peculiarities of the behavior of hydride systems related to mechanisms of phase transitions*. Journal of the Less-Common Metals, 1989. **152**: pp. 275–285.
114. Qian, S. and D.O. Northwood, *Effect of hydrogen aliquot size on the plateau pressures and pressure hysteresis in intermetallic compounds-hydrogen systems*. International Journal of Hydrogen Energy, 1992. **17**(8): pp. 631–634.
115. Gray, E.M.A., C.E. Buckley, and E.H. Kisi, *New experiments on pressure hysteresis in $LaNi_5 - H_x$*. Zeitschrift fuer Physikalische Chemie, 1993. **179**(1–2): pp. 85–91.

116. Gray, E.M.A., C.E. Buckley, and E.H. Kisi, *Stability of the hydrogenabsorption and desorption plateaux in LaNi$_5$-H. Part 2: Effects of the absorbing and desorbing large aliquots of hydrogen*. Journal of Alloys and Compounds, 1994. **215**: pp. 201–211.
117. Kisi, E.H. and E.M.A. Gray, *Stability of the hydrogen absorption and desorption plateaux in LaNi$_5$-H. Part 3: Experimental observations of compositional inhomogeneities due to temperature gradients*. Journal of Alloys and Compounds, 1995. **217**: pp. 112–117.

Appendix A

List of manufacturers of hydrogen storage measurement systems.

Advanced Materials Corporation (AMC)
850 Poplar Street
Pittsburgh, PA 15220 USA
Phone : +1 (412) 921-9600 Fax : +1 (412) 921-1790
E-mail: sales@advanced-material.com
http://www.advanced-material.com/

Hiden Isochema Ltd
231 Europa Boulevard, Warrington, WA5 7TN, UK
Phone: + 44 (0) 1925 244678 Fax: +44 (0) 1925 244664
E-mail: info@HidenIsochema.com
http://www.isochema.com/index.html

Hy-Energy, LLC
8440 Central Ave, Suite 2B
Newark, CA 94560
Telephone: (510) 793-3345
E-mail: info@hy-energy.com or info@hyenergy.com
http://www.hy-energy.com/index.html

Japan Metals & Chemicals Co., Ltd.
Higashi Kayaba-cho Bldg. 3rd Floor
17-25, Shinkawa 1-chome, Chuo-ku,
Tokyo, 104-8257, Japan
http://www.jmc.co.jp/jmc.nsf/doc/english_index

(in Japanese only)
Lesca Corporation
http://www.lesca.co.jp/H2menu.html

Suzuki Shokan Co.,Ltd.
1-12-11 FUNADO, ITABASHIKU
TOKYO 174-8567, JAPAN
PHONE 81-3-5970-5569
FAX 81-3-5970-1510
http://www.suzukishokan.co.jp/english/index.html

Chapter 16b
High-pressure DSC

Ekkehard Füglein and Aline Léon

List of abbreviations

ASTM	American Society for Testing and Materials
°C	Degrees celsius
c_p	Specific heat capacity
DIN	Deutsches Institut für Normung (German Standardisation Institute)
DSC	Differential scanning calorimetry
DTA	Differential thermal analysis
EN	Europäische Norm (European standard)
FTIR	Fourier transform-infrared spectroscopy
g	Gram

Ekkehard Füglein
NETZSCH-Gerätebau GmbH, Wittelsbacherstraße 42, 95100 Selb, GERMANY,
e-mail: ekkehard.fueglein@netzsch.com

Aline Léon
Institut für Nanotechnologie, Forschungszentrum Karlsruhe, P.O. Box 3640, D – 76021 Karlsruhe, Germany, e-mail: aline.leon@int.fzk.de

A. Léon (ed.), *Hydrogen Technology*,

H	Enthalpy
HP-DSC	High-pressure DSC
ICTAC	International Confederation for Thermal Analysis and Calorimetry
ISO	International Organization for Standardization
J	Joule
K	Kelvin
K	Calibration factor
l	Litre
m	Milli
M	Mega
min	Minute
MS	Mass spectrometry
µ	Micro
Pa	Pascal
s	Second
S	Sensitivity Calibration factor
STA	Simultaneous thermal analysis, combination of DSC and TG
t	Time
T	Temperature
TA	Thermal analysis
TG	Thermogravimetry
V	Volt
W	Watt
R1	Reaction 1

16b.1 Introduction and Definitions

Knowledge of the enthalpy of formation and decomposition is of importance when determining the suitability of a material for hydrogen storage application. Indeed, the enthalpy indicates the energetic exchange related to chemical reactions, structural transitions, melting or thermal stability of a material. This information is relevant to the design of the reactor where the reaction takes place, the heat exchanger, and so on. The enthalpy of formation (decomposition) of a hydrogen storage material represents the heat released (consumed) when one mole of hydrogen is absorbed (desorbed) by the material. The change of enthalpy (ΔH) can be measured experimentally by the combination of a pressure composition isotherm (also known as pcT diagram) and a Van't Hoff plot as presented in Chap. 16a, or directly by differential scanning calorimetry (DSC). The latter allows for determining the thermal and thermodynamic properties of a material. In addition, the specific heat capacity c_p of the material as well as the Van't Hoff plot and the activation energies of phase transformations can be determined. Moreover, it is a quick method (a few hours) compared to the pCT isotherm method (depending on the material, several days or weeks are required). The handling of a DSC is easy and only very small sample sizes (typically between 5–10 mg) are required. That is why this technique is very useful in the first characterisation of a potential hydrogen storage material. The principle of this thermal analysis method is based on the measurement of temperature

and heat flow associated with transitions in materials as a function of temperature and time.

The International Confederation for Thermal Analysis and Calorimetry (ICTAC) and national institutes of standardisation (DIN) have defined common terms of thermal analysis. These definitions of thermoanalytical equipment, methods, and data evaluation are published in several national and international standards, such as ASTM, ISO, EN, DIN. Thermal analysis is defined as follows "Thermal Analysis (TA) is a group of techniques in which a physical property of a substance is measured as a function of temperature or time while the substance is subjected to a controlled-temperature program" (ICTAC 1999) [1, 2]. DSC is a special thermoanalytical technique and defined as follows "Differential Scanning Calorimetry (DSC) is a technique in which the heat flow difference into a substance and a reference material is measured as a function of temperature while the substance and reference material are subjected to a controlled-temperature program" (ICTAC 1999) [1, 2]. Another definition is given by Höhne et al. [3] "Differential Scanning Calorimetry (DSC) means the measurement of the change of the difference in the heat flow rate to the sample and to the reference sample while they are subjected to a controlled temperature program". As an example, the ISO 11357 standard (parts 1 to 7) describes the application of DSC to the characterisation of plastics. It covers the general principles [4], determination and evaluation of glass transition temperature [5], temperature and enthalpy of melting and crystallisation [6], specific heat capacity [7], oxidation induction time [8], and crystallisation kinetics [9]. Other standards describe purity determination during melting of crystalline materials [10], oxidation onset temperatures for hydrocarbons [11], determination of the amount of bound water sorbed by polymers [12] or transition temperatures of petroleum waxes [13]. Hence, the DSC technique is applied in a wide variety of fields. It can also be combined with thermogravimetry (TG) in a simultaneous thermal analysis (STA) and with spectroscopic methods, such as MS or FTIR, for identification of the released gases. High-pressure DSC (HP-DSC) is a special modification of a DSC instrument for pressure-dependent sample investigation. It allows for studying the reaction under conditions of use of hydrogen storage materials. In addition to the thermodynamic properties, the kinetics of hydrogen absorption and desorption as well as the decomposition reaction under a defined gas pressure can be investigated.

The present chapter is aimed at introducing this thermoanalytical method for material characterisation. Theoretical reviews of thermoanalytical methods and DSC in particular can be found elsewhere [3, 14, 15]. Here, interest will focus on the experimental side with the measurement principles of DTA and DSC and the constitution of the measured signal. It shall be understood why a calibration of the instrument is necessary for the evaluation of the data. Hence, the calibration procedure shall be discussed. Finally, some examples of investigations of the thermal decomposition and the kinetic behaviour of hydrogen storage materials using the DSC technique will be presented.

16b.2 Measurement Principles of DTA and DSC

DSC is an enhanced development based on the technique of differential thermal analysis (DTA). "Differential Thermal Analysis (DTA) is a technique in which the temperature difference between the substance and a reference material is measured as a function of temperature while the substance and reference material are subjected to a controlled-temperature program" [1, 2]. This definition suggests that the major difference between the DTA and DSC methods is the measured signal. With a DTA, temperature differences are detected, whereas a DSC determines the change of the difference in the heat flow rate. The difference between the two methods results from the construction principle of the sensors used in these instruments. The DTA sensors for determining the temperatures of the sample and reference are the tips of the thermocouples located underneath the crucibles as displayed in Fig. 16b.1(a). In contrast to the point contact DTA sensors, the DSC consists of area sensors for sample and reference as presented in Fig. 16b.1(b). The crucibles are cylindrically shaped with a flat bottom in order to cover the complete sensor area. If a sample can be prepared in a way that it covers the whole bottom of the crucible, the sample to crucible and crucible to sensor contacts are further improved in comparison to DTA. As a consequence, the signal to noise ratio is significantly higher and the repeatability of the signal over the entire temperature range is much better for DSC.

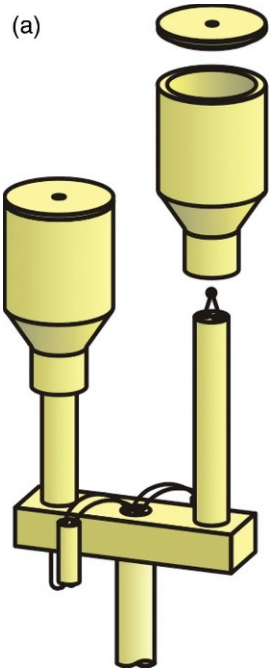

Fig. 16b.1 Comparison of a DTA **(a)** and DSC **(b)** sample carrier

Therefore, the DSC data have a higher reliability and signal quality compared to DTA data. This allows the heat flow signal to be quantified by means of peak area integration. The peak area is proportional to the converted heat, and the enthalpy of the transition can be calculated from the peak area with the so-called sensitivity calibration (cf. Sect. 16b.3.4) (sensitivity calibration). The questions that can be answered by each technique are summarised in Table 16b.1.

There are two possible DSC construction principles, the heat flux DSC and the power-compensated DSC displayed in Fig. 16b.2. The heat flux DSC, see Fig. 16b.2(a), has a common furnace that symmetrically surrounds the sample and the reference sensor positions, while the power-compensated DSC, Fig. 16b.2(b), has one furnace for each sensor position (two independent furnaces). In the latter, the signal measured is the difference in power required for the two sensor positions (furnaces) in order to ensure a linear temperature increase. Due to its construction principle, the power-compensated DSC has a faster response (smaller time constant) which may be an advantage in terms of fast or superposing effects. On the other hand, all influences that cause an unsymmetrical arrangement, such as different furnace masses, the distances of the furnace to the sample or reference position, and performance changes of the furnace over time (caused by reaction with the gases released by the sample) have to be taken into account in order to separate the true sample signal from equipment-based influences. The single furnace arrangement of a heat flux DSC can be protected better from disturbing influences and, hence, is the more robust and widely used system. However, as long as each instrument is properly calibrated, the same caloric transformation investigated by heat flux or power-compensated DSC should give the same enthalpies and transition temperatures for the studied material.

The "standard DSC" actually is a heat flux DSC composed of a disc-shaped sensor. The schematic design of a typical heat flux DSC is displayed in Fig. 16b.3. The furnace block located in the centre of the measurement unit is heated electrically and connected to a cooling device. The minimum sample temperature is approximately −85°C, if equipped with a circulating cooling unit based on a Joule-Thomson principle, or −185°C when using liquid nitrogen. In most of the commercial instruments the temperature range is limited to 700°C to allow for the use of thermocou-

Table 16b.1 Comparison of the information obtained from DTA and DSC

DTA	DSC
• Does any transformation occur within the investigated temperature range?	• Does any transformation occur within the investigated temperature range?
• If yes, at what temperatures are these effects detected?	• If yes, at what temperatures are these effects detected?
• If yes, do these effects consume heat or release heat (endothermic or exothermic effects)?	• If yes, do these effects consume heat or release heat (endothermic or exothermic effects)?
–	• What is the enthalpy of the transformation?
–	• What is the specific heat capacity of the sample?

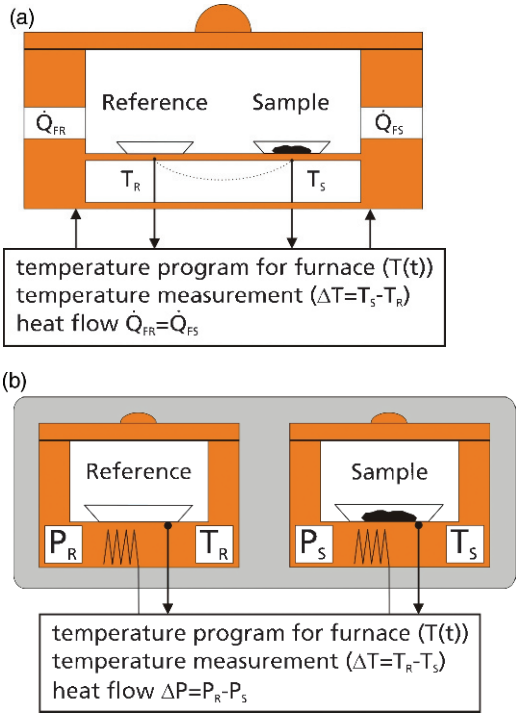

Fig. 16b.2 Comparison of a heat flux DSC **(a)** and a power-compensated DSC **(b)**

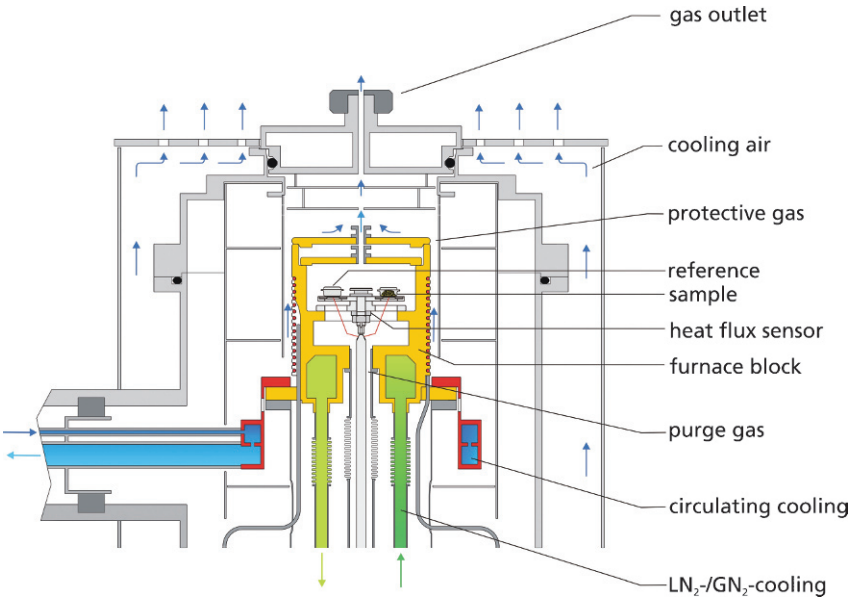

Fig. 16b.3 Cross-section of the heat flux DSC, NETZSCH DSC 204 ***F1 Phoenix***® with different cooling supports

ple materials of high sensitivity. However, special DSC equipment may go up to 1600°C [16]. To guarantee a stable and reproducible DSC signal performance, the DSC unit is well insulated in order to protect the measurement cell from uncontrolled temperature influences that might be caused by temperature changes of the laboratory or air conditioning systems.

Both temperature sensors (reference and sample) are integrated in the sensor disc and arranged symmetrically to the centre and to the cylindrical furnace block. Therefore, the same amount of heat is transferred to both positions when the furnace block is heated. Both temperature sensors are completely covered by the crucibles which are used as sample containers in order to avoid a direct contact between the sample and the sensor. The whole area underneath each of the crucibles acts as a temperature sensor. The reference crucible remains either empty or filled with a chemically inert material. The sample crucible contains the sample to be investigated. The two temperature sensors underneath the sample and reference crucibles inside the measurement instrument as depicted in Fig. 16b.3 provide the relevant data about a possible sample transformation (see Sect. 16b.3.3) (signal constitution). A third temperature sensor close to the electrical heater (furnace thermocouple) only serves for the temperature control of the furnace block.

16b.3 High-pressure DSC

16b.3.1 Description

Besides the variety of DSC applications discussed above, the possibility of applying pressure further improves the capabilities of this analytical technique. In principle, pressure DSC measurements can be conducted using either an inert gas or a reactive gas. If an inert gas is used, the pressure dependency can be studied when sample transformation does not only show a caloric effect, but also is accompanied by a considerable volume change. As a consequence, dehydration and decomposition reactions with a gas release are often studied by means of pressure DSC. If a reactive gas is used, the gas is one of the reactants and the pressure therefore is a measure of its concentration. With the latter method, accelerated ageing tests can be carried out for organics, such as oil, fat, wax, grease, and polymers. Several pressure DSC standards suggest to use an oxygen pressure of 3.5 MPa for the investigation of oxidation stability [11, 17, 18]. Melting usually is slightly pressure-dependent within the accessible pressure range. Therefore, metal standards that are usually employed as calibration materials can also be used for temperature and sensitivity calibration of a pressure DSC.

In contrast to the setup of a standard DSC, the measurement unit of a high-pressure DSC (HP-DSC) is surrounded by an autoclave that is supported by pressure and flow control systems as displayed in Fig. 16b.4. Pressure and purge gas flow adjustment is accomplished via a separate control board. It is equipped with a pressure controller that allows to pressurise the whole autoclave up to a certain pressure (max.

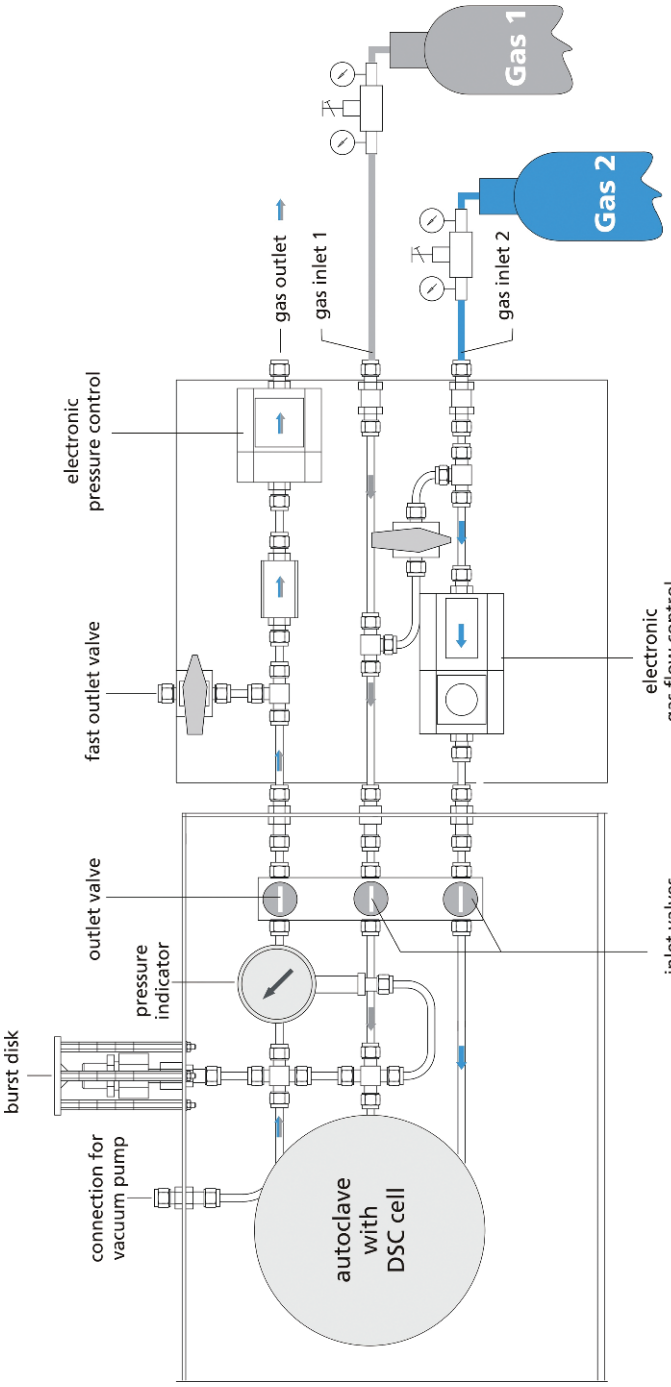

Fig. 16b.4 Setup of the NETZSCH HP-DSC 204 *Phoenix*® with pressure and flow control system for two gases

15 MPa) and to work at constant pressure. In this so-called static mode the pressure controller has to compensate for the increasing pressure inside the autoclave during heating segments of the temperature program. The above-mentioned control board additionally supports a mass flow controller that allows for the purging of the unit at a constant pressure level with a purge gas flow of up to 500 ml/min. Commercially available systems are designed for a maximum pressure of 15 MPa. Self-made constructions also exist for pressures up to 500 MPa [19]. If reactive gases, such as hydrogen, are used, special thermocouples (without Pt or Pt alloys) are connected. Moreover, the control board supports a second gas inlet for an inert gas, e.g. helium. The second gas is needed to allow for a complete gas exchange before and after opening and closing the instrument. A vacuum pump can also be connected for exchanging the sample atmosphere via evacuation and refilling cycles with dry inert gas. The main objective is to prevent amounts of oxygen from remaining inside the unit before changing the sample atmosphere to hydrogen. To remove the sample, an analogous procedure is chosen to exchange the reactive gas by inert gas in order to prevent amounts of hydrogen from remaining before the unit is opened.

16b.3.2 Sample Preparation

Often, oxygen- and humidity-sensitive samples are investigated. If the pressure DSC is operated inside the glove box, the sample transfer is easy, but one glove box is more or less needed exclusively for the use of the pressure DSC. When operating the pressure DSC in a laboratory (equipped with the necessary safety installation for the use of reactive gas), the samples have to be transferred to the analytical system without any contamination. In this case sample preparation is carried out in a glove box and the crucible is transferred to the DSC cell by means of an air-tight container which is opened inside the pressure DSC purged with dry inert gas.

Aluminium pans (sealed with pierced lids or open) are often used in both standard and pressure DSC. All metals, even if they are extremely pure, are coated with a thin metal oxide surface layer, if they are exposed to air. This oxide layer usually prevents the residual metal from further oxidation. In principle, this is true for both crucible materials and metal calibration standards. However, if reducing atmosphere like hydrogen is used, the metal oxide surface layer is reduced to metal. Hence, aluminium crucibles and the usual metal standards like indium, tin, lead, bismuth or zinc cannot be used for calibration purposes because of alloy formation. On the other hand, ceramic crucibles are chemically inert, but they reduce the caloric signal yield. It has been found that stainless steel crucibles are not suitable under hydrogen atmosphere. Experience has shown that the best arrangement for hydrogen application is a two-in-one crucible sandwich as displayed in Fig. 16b.5. It consists of an outer aluminium crucible (1) that improves the heat flow and a thin aluminium oxide liner (2) that prevents the metal sample from directly contacting the metallic crucible. The thickness of the wall of the aluminium oxide liner is less than half of that of a standard aluminium oxide crucible. Consequently, the signal

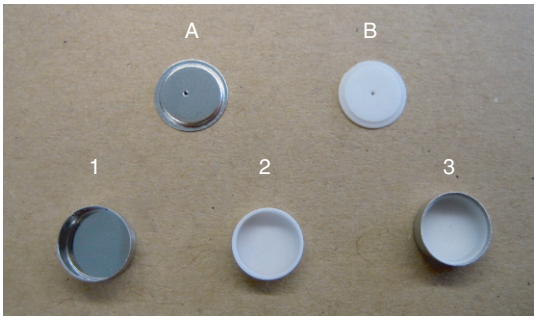

Fig. 16b.5 Aluminium crucible (1), aluminium oxide liner (2), two-in-one crucible sandwich (3), pierced aluminium lid (A), aluminium oxide lid (B)

yield is roughly more than two times better for the crucible sandwich and contact reactions are avoided. This is a great advantage not only for the calibration of the DSC unit, but also for all reactions that form pure metal phases.

16b.3.3 Signal Constitution

Figure 16b.6 displays the signal constitution for a sample undergoing melting. During a programme of linear temperature increase (10 K/min, for example), both sensors detect a constant increase in temperature versus time as long as no enthalpy change of the sample occurs as shown in Fig. 16b.6(a). If, for instance, the melting temperature of the sample investigated is reached at t_1, the heat provided to the sample position is consumed in order to melt the sample (endothermic effect). The sample temperature remains constant until the whole sample is completely molten (from t_1 to t_2), while the temperature of the reference side increases linearly as programmed. Once melting is finished, the difference between sample and reference temperature is compensated, because the amount of heat transferred to the sample position is no longer consumed for melting, but leads to a temperature increase again. From this point (t_3), both positions linearly follow the programmed temperature increase. By scaling the difference between reference and sample temperature ($\Delta T = T_R - T_S$) rather than the individual temperature signals, the diagram displayed in Fig. 16b.6(b) is obtained. It represents a simplified DSC result for a melting process. ΔT, the measured signal, is almost constant (not equal to zero) as long as no caloric transition of the sample occurs. Actually, a slight positive slope is observed with increasing temperature due to the fact that the difference signal still contains the information on the temperature-dependent change of the specific heat capacity of the sample, although no phase transformations occur. The extrapolated onset of the melting peak represents the melting temperature, whereas the peak maximum represents the temperature at which the sample is completely molten. The peak area is proportional to the amount of heat converted. The signal measured by the DSC equipment is then given by the following equation:

$$\Phi_\mathrm{r} = \mathrm{d}q_\mathrm{r}/\mathrm{d}t = K(T)\,(T_R - T_S) \qquad (16\mathrm{b}.1)$$

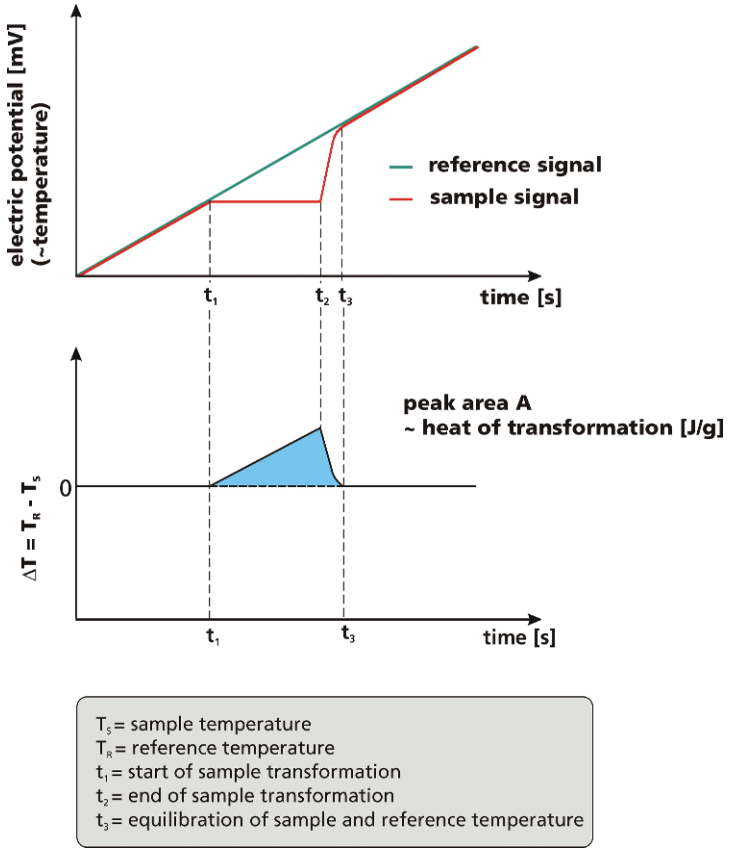

Fig. 16b.6 **(a)** Simplified time-dependent illustration of the temperature signals detected at the sample sensor position (T_S) and reference sensor position (T_R) for an endothermic effect (melting); **(b)** simplified DSC signal (temperature difference ΔT) for the same endothermic effect

where Φ_r represents the heat flux, q_r the heat, and A the peak area (measured signal, including baseline correction). All equipment-based influences are considered by a calibration factor $K(T)$.

A precise description of a melting peak evaluation according to ISO 11357-1 [4] is depicted in Fig. 16b.7. The beginning of the melting effect is defined as extrapolated onset (T_{eim}). Therefore, this value is used for temperature calibration of the system (see Sect. 16b.3.4.1). The ISO and DIN [20] standards suggest the scaling up of endothermic signals ($T_{reference} - T_{sample}$); whereas the ASTM standards [21] suggest to scale up exothermic signals ($T_{sample} - T_{reference}$). Modern thermoanalytical software usually allows for both types of scaling. The caloric sensitivity of the complete sensor arrangement has to be determined by a calibration procedure. In further measurements it is considered by means of a sensitivity calibration factor S given in $\mu V/mW$ (see Sect. 16b.3.4.2).

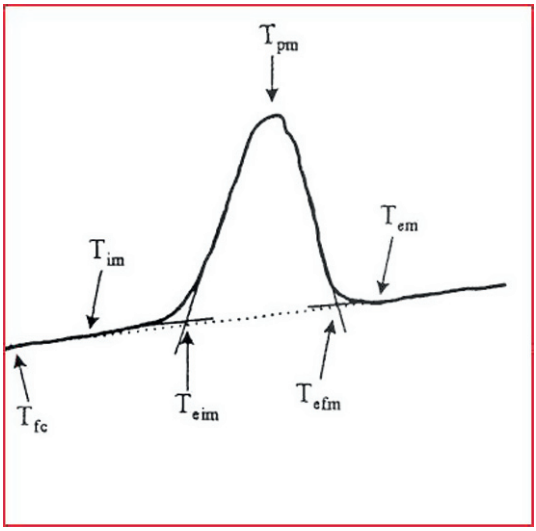

Fig. 16b.7 Peak evaluation according to ISO 11357-1; T_{im}: first detectable deviation of the DSC curve from extrapolated start baseline; T_{eim}: intersection of extrapolated start baseline and tangent at point of inflection; T_{pm}: greatest difference of DSC curve and virtual baseline; T_{efm}: intersection of extrapolated end baseline and tangent at point of inflection; T_{em}: last detectable deviation of the DSC curve from extrapolated end baseline

16b.3.4 Calibration (Temperature and Sensitivity)

Experimental variables, such as sample mass, crucible type, heating rate or atmosphere, have an influence on the measurement results. Indeed, the crucible type influences both the transfer time and quantity of the heat flow signal due to the different heat conductivities of the crucible materials. Moreover, heat conductivity of the purge gas affects the strength of the signal detected at the sensor. The caloric sensitivity of indium is reduced from 3.1 µVs/mg to approximately 1.2 µVs/mg, if hydrogen is used instead of nitrogen, while identical measurement conditions are maintained for all the other parameters. That is why the calibration of the temperature and sensitivity has to be carried out under the conditions defined for the material to be analysed.

16b.3.4.1 Temperature Calibration

The temperature sensors used in differential scanning calorimeters are thermocouples. The measured signal of a thermocouple is a voltage (Seebeck coefficient). The temperature dependency of this coefficient is used for temperature determination. It is different for each type of thermocouple (e.g. type S, B, E, K) and taken into account by the software. However, the temperature indicated is not the "true" sample temperature due to the fact that the temperature-detecting thermocouple is not located inside the sample, but connected underneath the sensor plate. Therefore, a certain distance exists between the sample filled into a crucible and the temperature sensor. This has to be taken into account to obtain the "real" temperature of the sample. The calibration procedure consists of the measurement of at least five standard

substances covering the desired temperature range. The melting temperature of each material (extrapolated onset) is used for temperature calibration. Then, a correlation between the evaluated temperature and the literature value for each standard yields a temperature-dependent calibration polynomial which gives the temperature calibration coefficient. This correction factor is taken into account for every temperature value during measurement. Consequently, the indicated temperature values are converted online into the true sample temperature.

16b.3.4.2 Sensitivity Calibration

In addition to the extrapolated onset, the peak area also can be evaluated during the measurement carried out with standard material for temperature calibration. The time-based integration of the peak area A yields values in µVs/mg. The literature values for the melting enthalpy of the measured standard materials are well-known (J/g). Comparison of the experimental values for the melting standard investigated with its literature data yields sensitivity calibration factors for each standard material as given by the following equation:

$$S = \frac{1}{K(T)_S} = A/H_{\text{fus}} \qquad \text{(16b.2)}$$

given in µV/mW

where H_{fus} is the heat of fusion of the reference material and A represents the peak area in µVs/mg.

With these calibration factors, a polynomial is calculated that represents the change of the caloric sensitivity of the DSC over the entire temperature range as displayed in Fig. 16b.8. This correction factor is taken into account online by the software during the measurement. Hence, the peak area values evaluated represent the ”true” transition enthalpy, if the measurements are carried out under the same measurement conditions (crucibles, atmosphere, heating rates, sample’s weight) as the calibration procedure.

Certified standard materials for the calibration of differential scanning calorimeters are available from institutions, such as the Physikalisch-Technische Bundesanstalt (PTB) in Braunschweig, Germany [22].

16b.4 Applications

Physical processes and chemical reactions involving hydrogen storage materials are influenced by pressure. It is therefore necessary to conduct a pressure-dependent DSC measurement under hydrogen. Generally, three measurements are necessary to obtain accurate thermal analysis results of a material. The first one, the baseline run, is a measurement with empty crucibles. The second one, the calibration

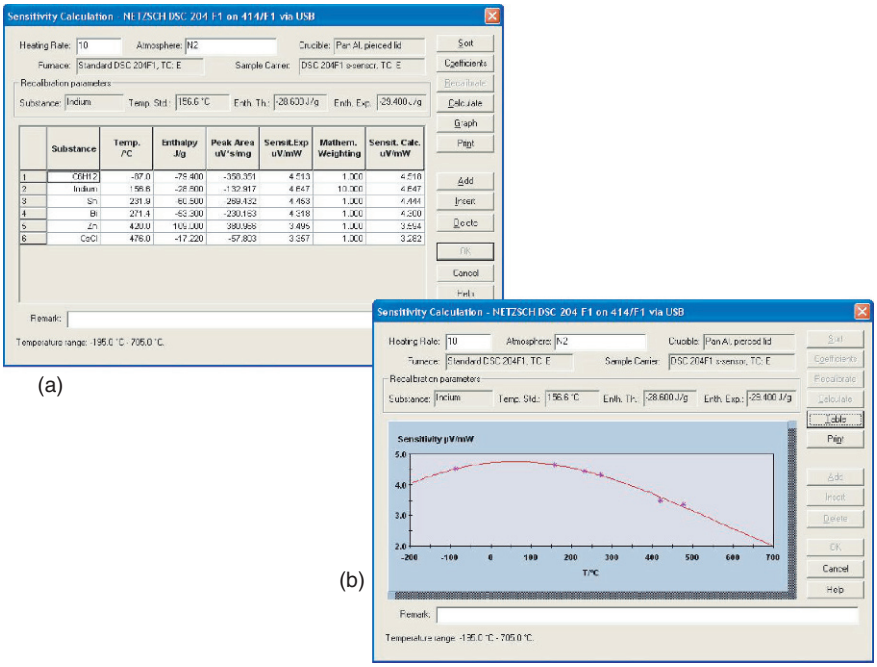

Fig. 16b.8 Results of a sensitivity calibration procedure, **(a)** table, **(b)** polynomials taken for online correction of enthalpy evaluation

run, is a measurement under the same conditions using a standard material in the sample crucible (this run serves for a calibration check in order to prove that the calibration function is reliable for the current measurement conditions). The third one, the measurement run, is done with the sample to be analysed in the sample crucible. Typical amounts of the sample range between 5 to 10 mg. Standard software (Proteus-Software SW/DSC/670.01) supplied along with the DSC instrument was used to obtain the reported calorimetric results from the DSC curves. From the calibration and testing results of the calorimeter in hydrogen, it was found that the uncertainties of temperature measurement and enthalpy measurement are ±0.5°C and ±3 J/g, respectively.

The routine application of an HP-DSC is to determine the thermal behaviour of a material as well as the associated transition enthalpy. This will be illustrated below for the characterisation of magnesium boronate [23]. In addition, the HP-DSC can be used to construct the Van't Hoff plot (the example for MgH_2 is shown in the Sect. 16b.4.2) and the Kissinger plot for a given material [24] (the example for $LiAlH_4$ is shown in the Sect. 16b.4.3 [25]) to determine its thermodynamic and kinetic properties, respectively. HP-DSC measurements are also useful for preparing samples for structural characterisation in different stages of the reaction. Indeed, the measurement run can be stopped at different temperatures and X-ray patterns of the quenched samples display the crystal structure at this particular point of the reaction. This has already been

done for a magnesium-based system, for instance [26, 27]. In addition, coupling of thermal analysis and gas analysis (mass spectrometer) is becoming more popular. In this setup, structural transformation is distinguished from gas evolution and the nature of the formed gas is determined. This method was applied to different metal hydride materials by Fernandez et al. [28].

16b.4.1 Thermal Behaviour of $Mg(BH_4)_2$ [23]

$Mg(BH_4)_2$ is one of the few complex hydrides which have the potential to meet the requirements made on hydrogen storage materials, because it contains 14.9 mass% hydrogen and has suitable thermodynamic properties. α-$Mg(BH_4)_2$ from direct wet chemical synthesis is used in order to study the decomposition behaviour of the material. TG-MS, TG-DSC, and HP-DSC experiments are performed to examine the temperatures of the various transformation steps, the transformation enthalpies, and to identify the decomposition products.

The TG-DSC measurements are performed under a helium flow at ambient pressure. In order to obtain quantitative information about the transitions, the experiments are repeated in an HP-DSC instrument under a 5 bar static hydrogen atmosphere, with the same heating rate. Figure 16b.9 shows the results of a TG-DSC and an HP-DSC experiment.

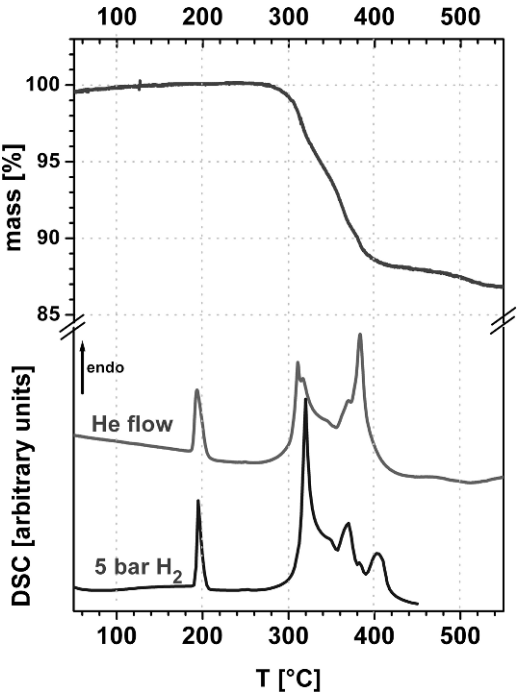

Fig. 16b.9 Data of a TG-DSC experiment with α-$Mg(BH_4)_2$ under a helium flow of 50 ml/min and a HP-DSC experiment under 5 bar H_2 at 10 K/min

As can be seen, the major effects of the transformations are all endothermic. The first peak at 193°C (He flow) and 195°C (5 bar H_2) is identified to be a polymorphic transition from the alpha to the beta phase. It is not associated with a mass loss of the sample, as indicated by the TG curve in the upper part of the diagram. Moreover, the polymorphic transition is not reversible, as shown by an HP-DSC experiment, where the sample is heated up to 240°C and then cooled down to 100°C at different cooling rates. This indicates that the alpha phase is metastable and irreversibly transforms into the beta phase when heated.

A considerable mass loss is detected together with the following endothermic events. A mass spectrometric analysis of the gas phase above the sample shows that the gas released consists almost exclusively of hydrogen, with a trace of B_2H_6. The weight loss detected between 290 and 500°C is 13 wt.%, which is close to the total hydrogen content of the material. Most of the weight is lost between 300 and 400°C.

The HP-DSC data provide a picture which differs slightly from the one obtained in the experiments under helium flow. The first decomposition peak is detected at 320°C (5 bar H_2) compared to around 310°C under helium atmosphere. It should be noted that a shoulder at around 310°C appears in the HP-DSC trace. Moreover, the DSC data under helium flow reveal a minor contribution at 320°C. The second major caloric effect is determined in both experiments at the same temperature (367°C). The third caloric effect is detected at 383°C (He flow) or 403°C (5 bar H_2). It is likely that the peak shifts to higher temperatures, which is due to the hydrogen pressure in the HP-DSC experiments. Such an effect suggests decomposition reactions which occur in equilibrium with hydrogen. The second and the third endothermic effects are assigned to the first decomposition step of $Mg(BH_4)_2$ into MgH_2 and to the decomposition of MgH_2 in the second step, respectively. The DSC data exhibit that the transformation of $Mg(BH_4)_2$ is a rather complex process where decomposition occurs in 4–5 subsequent transformation steps at least.

16b.4.2 Van't Hoff Plot of MgH_2

Experimental investigations of the thermodynamic properties of a metal-hydrogen system are mostly based on the measurement of equilibrium pressures as a function of temperature and the construction of the so-called pressure-composition isotherms. Thermodynamic evaluation of these experimental results usually is based on the Van't Hoff equation

$$\ln P_{H_2} = \frac{\Delta H}{RT} - \frac{\Delta S}{R} \tag{16b.3}$$

where R is the molar gas constant.

This model allows for the calculation of the enthalpy of formation ΔH and entropy of formation ΔS, which are related to absolute temperature T and hydrogen gas pressure P_{H_2}. Knowledge of ΔH and ΔS enables the calculation of ΔG.

Van't Hoff plots can also be determined with the HP-DSC, which is associated with the advantage of requiring a small amount of samples and reducing the measurement time. The method applied in this case is a dynamic one where the sample

is heated (or cooled) at a constant rate, while the hydrogen pressure is kept approximately constant. This means that the reaction kinetics has to be assumed to be very fast compared to the heating (cooling) rate in order to use the peak temperature as the equilibrium value under the prevailing pressure. This is rarely the case, but the equilibrium can be approached by using sufficiently low heating (cooling) rates.

Figure 16b.10 displays the Van't Hoff plot of MgH_2 obtained from the calorimetric measurement with an HP-DSC. For comparison literature data are plotted as well. The measurement is conducted at a heating rate of 1 K/min under various pressures ranging from 1 to 80 bar. As can be seen, a significant deviation from the linear function is observed at a pressure below 10 bar. In addition, the discrepancy between the HP-DSC and the literature data increases as the pressure decreases. An explanation is that the kinetics may play a more pronounced role at low pressure than at high pressure. Figure 16b.11 depicts the DSC signal of the decomposition of MgH_2 for different heating rates under 1 and 50 bar of hydrogen. At low pressure, a difference of around 70 K is observed between a heating rate of 10 K/min and 1 K/min, whereas a difference of only 15 K is measured at high pressure for the same heating rates. These results suggest that at low pressure, the experiment should be conducted at a heating rate below 0.1 K/min for the reaction rate being fast compared to the heating rate. Furthermore, at a heating rate of 10 K/min the pressure increase to 50 bar significantly shifts the decomposition reaction to higher temperature ($\sim 50\,K$).

Taking into account the experimental data obtained at 80, 50, 30, 15, and 8 bar, an enthalpy of $-73\,kJ/mol$ can be evaluated, while an enthalpy of $-76\,kJ/mol$ is determined using the literature values at 15, 6, 2.5, and 1 bar.

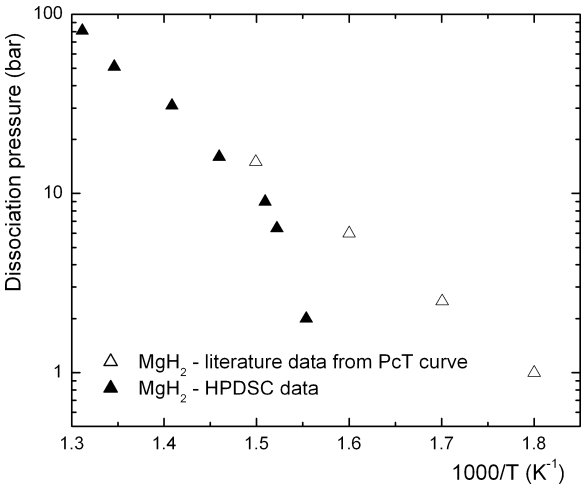

Fig. 16b.10 Van't Hoff diagram of MgH_2 from HP-DSC data. Values of the isothermal measurement are plotted for comparison

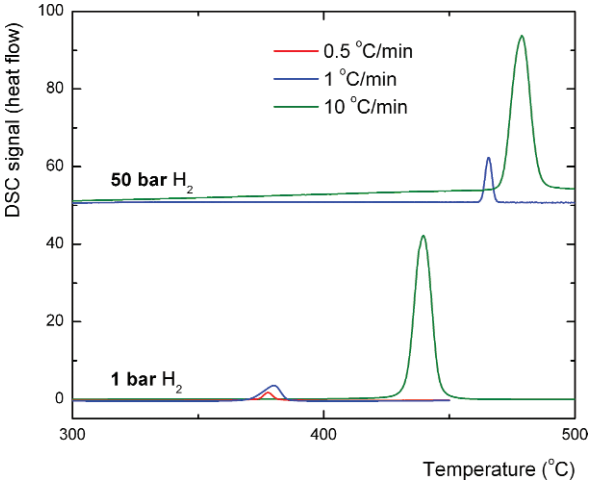

Fig. 16b.11 Effect of pressure and heating rate on the decomposition behaviour of M_gH_2

16b.4.3 Activation Energies of $LiAlH_4$ [25]

When a reaction occurs, the change of heat content and thermal properties of the sample is indicated by a deflection or peak in differential thermal analysis. If the reaction proceeds at a rate varying with temperature, i.e. in case of a kinetic process, the position of the peak varies with the heating rate, while all other experimental parameters are maintained. This variation of peak temperature can be used to determine in first approximation the energy of activation for reactions of any order. Hence, by varying the heating rates at a given hydrogen pressure, kinetic data can be obtained for the material. For experiments that are non-isothermal, but with a constant heating rate, a range of methods to determine the activation energy has been developed. They are based on the measurement of the temperature at which the new phase has been formed (isoconversion methods). One of these methods is the generalised Kissinger or Kissinger-Akahira-Sunrose (KAS) approximation, which allows to determine the activation energies of the processes controlling the rate of solid-state transformations. This method involves the measurement of the temperature T_m corresponding to the maximum rate of reaction during heating from an initial temperature T_o at a constant heating rate β. The temperature T_m can be equated with the maximum of a DSC peak, if the specimen is in good thermal contact with the sensor of the thermal analysis system. The apparent activation energy, E_A, can be obtained from the following equation:

$$\frac{\mathrm{d}\ln\left(\frac{\beta}{T_m^2}\right)}{\mathrm{d}\left(\frac{1}{T_m}\right)} = -\frac{E_A}{R} \tag{16b.4}$$

Thus, the slope of the plot $\ln\left(\frac{\beta}{T_m^2}\right)$ versus $\frac{1}{T_m}$ gives the activation energy E_A.

This method is illustrated below for the decomposition reaction of $LiAlH_4$. Hydrogen is released from $LiAlH_4$ in a three-step decomposition according to the following equations:

$$LiAlH_4 \rightarrow 1/3Li_3AlH_6 + 2/3Al + H_2 \qquad (R1 : 5.3\,wt.\%\ H_2)$$
$$1/3Li_3AlH_6 \rightarrow LiH + 1/3Al + {}^1/_2H_2 \qquad (R2 : 2.6\,wt.\%\ H_2)$$
$$LiH + A \rightarrow LiAl + {}^1/_2\,H_2 \qquad (R3 : 2.6\,wt.\%\ H_2)$$

Figure 16b.12 displays the DSC results obtained at four different heating rates. The samples are heated from room temperature to 300°C under an argon atmosphere with a flow of approximately 85 ml/min. The DSC signal exhibits an exothermic peak at 150°C, an endothermic peak around 170°C, an exothermic peak at 178–198°C, and an endothermic peak around 227–247°C. The first exothermic effect is assigned to the interaction of $LiAlH_4$ with surface hydroxyl impurities and the first endothermic peak to the melting of $LiAlH_4$. Melting is then followed by the second exothermic effect corresponding to the formation of Li_3AlH_6 (R1). The second endothermic peak is related to the decomposition of Li_3AlH_6 (R2). Figure 16b.13 displays the Kissinger plot for the dehydrogenation of as-received $LiAlH_4$ to the exotherm (R1) and the endotherm (R2) in particular. The apparent activation energy for (R1) and (R2) is found to be 81 ± 4 kJ/mol and 108 ± 8 kJ/mol, respectively. This is in good agreement with the reported values of 102 and 100 kJ/mol for the decomposition of $LiAlH_4$ into Li_3AlH_6, Al, and H_2 (R1) and for the decomposition of Li_3AlH_6 into LiH, Al, and H_2 (R2) [29]. $LiAlH_4$ then exhibits a lower activation energy compared to the one of undoped-$NaAlH_4$, which is around 120 kJ/mol [30].

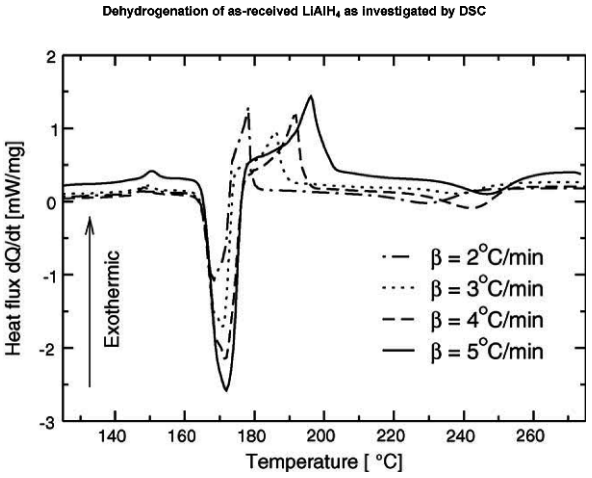

Fig. 16b.12 Dehydrogenation of as-received $LiAlH_4$ as investigated by DSC [25]

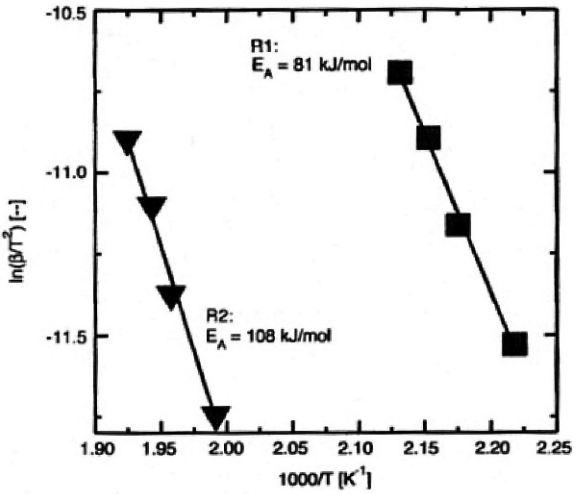

Fig. 16b.13 Kissinger plot for the dehydrogenation of as-received $LiAlH_4$ [25]

16b.5 Conclusion

It was demonstrated for hydrogen applications in particular that DSC and especially HP-DSC are fast and precise analytical methods to obtain information about caloric changes of the investigated sample. Influences, such as sample preparation or measurement conditions, might affect the results and, hence, have been taken into account. Signal constitution as well as calibration procedures regarding temperature and caloric sensitivity have been discussed. From the results, information is obtained as to whether and at which temperature sample transformation occurs. Furthermore, endothermic and exothermic sample effects can be distinguished and quantified. This information allows to determine the specific heat capacity and to calculate the activation energy and the Van't Hoff plot. Differential scanning calorimetry is a very useful technique for the characterisation of potential hydrogen storage materials.

References

1. ASTM E 473-00, "Standard Definition of Terms Relating to Thermal Analysis", 2000.
2. Deutsches Institut für Normung, DIN 51005, "Thermische Analyse (TA) Begriffe".
3. G.W.H. Höhne, W.F. Hemminger, and H.-J. Flammersheim, "Differential Scanning Calorimetry", Springer Verlag, Berlin Heidelberg, 2003.
4. ISO 11357 – 1, "Plastics – Differential Scanning Calorimetry – Part 1: General principles", 1998.
5. ISO 11357 – 2, "Plastics – Differential Scanning Calorimetry – Part 2: Determination of glass transition temperature", 1999.

6. ISO 11357 – 3, “Plastics – Differential Scanning Calorimetry – Part 3: Determination of temperature and enthalpy of melting and chrystallization”, 1999.
7. ISO 11357 – 4, “Plastics – Differential Scanning Calorimetry – Part 4: Determination of specific heat capacity”, 2005.
8. ISO 11357 – 6, “Plastics – Differential Scanning Calorimetry – Part 6: Determination of oxidation induction time”, 2002.
9. ISO 11357 – 7, “Plastics – Differential Scanning Calorimetry – Part 7: Determination of crystallization kinetics”, 2002.
10. ASTM E 928-85, “Standard Test Method for Mol Percent Impurity by Differential Scanning Calorimetry”, 1985 (reapproved 1989).
11. ASTM E 2009-99, “Standard Test Method for Oxidation Onset Temperature of Hydrocarbons by Differential Scanning Calorimetry”, 1999.
12. ISO 11357 – 8, “Plastics – Differential Scanning Calorimetry – Part 8: Determination of the amount of bound water sorbed by polymers”, 1997.
13. ASTM D 4419-90, “Standard Test Method for Measurements of Transition Temperatures of Petroleum Waxes by Differential Scanning Calorimetry (DSC)”, 1990.
14. G.W. Ehrenstein, G. Riedel, and P. Trawiel, “Thermal Analysis of Plastics, Theory and Practice”, Carl Hanser Verlag, München, 2004.
15. W.F. Hemminger and H.K. Cammenga, “Methoden der Thermischen Analyse”, Springer-Verlag Berlin Heidelberg, 1989.
16. NETZSCH-Gerätebau GmbH, product information for DSC 404 C *Pegasus*®, 2006.
17. ASTM E 1858, “Standard Test Method for Determining Oxidation Induction Time of Hydrocarbons by Differential Scanning Calorimetry”, 1997.
18. ASTM E 537-86, “Standard Test Method for Assessing the Thermal Stability of Chemicals by Methods of Differential Thermal Analysis”, 1986.
19. G.W.H. Höhne and K. Blankenhorn, Thermochimica Acta, 238 (1994) 351.
20. Deutsches Institut für Normung, DIN 53765 1994, “Dynamische Differenzkalorimetrie (DDK)”.
21. ASTM E 793, “Standard Test Method for Enthalpies of Fusion and Crystallization by Differential Scanning Calorimetry”, 1995.
22. Hans-Walter Krupke, Arbeitsgruppe 3.31, Physikalisch-Technische Bundesanstalt, Bundesallee 100, 38116 Braunschweig.
23. K. Chłopek, C. Frommen, A. Léon, O. Zabara, and M. Fichtner, Journal of Materials Chemistry, 2007, DOI:10.1039/B702723K.
24. H. Kissinger, Analytical Chemistry, 29(11) (1957) 1702.
25. A. Andreasen, Journal of alloys and compounds, 419 (2006) 40.
26. R.A. Varin, T. Czujko, and Z. Wronski, Nanotechnology, 17 (2006) 3856.
27. F.C. Gennari, F.J. Castro, and G. Urretavizcaya, Journal of alloys and compounds, 321 (2001) 46.
28. J.F. Fernandez, F. Cuevas, and C. Sanchez, Journal of alloys and compounds, 298 (2000) 244.
29. D. Blanchard, H.W. Brinks, B.C. Hauback, P. Norby, and J. Muller, Journal of alloys and compounds, 404–406 (2005) 743.
30. G. Sandrock, K.J. Gross, and G. Thomas, Journal of alloys and compounds, 339 (2002) 299.

Chapter 17
Status on Existing Technologies

Chapter 17a
Powder Diffraction

Magnus H. Sørby

List of Abbreviations

ESRF	European Synchrotron Radiation Facility
FoM	Figure of Merit
FWHM	Full Width at Half Maximum
PND	Powder Neutron Diffraction
PSD	Position Sensitive Detector
PXD	Powder X-ray Diffraction
SR-PXD	Synchrotron Radiation Powder X-ray Diffraction
TOF	Time Of Flight

Diffraction is the most important tool to investigate the atomic structure of solid materials. Diffraction measurement on powdered samples is becoming increasingly

Magnus H. Sørby
Department of Physics, Institute for Energy Technology, P.O. Box 40, N-2027 Kjeller, Norway, e-mail: magnuss@ife.no

A. Léon (ed.), *Hydrogen Technology*,

important with the development of powerful techniques for data analysis. Powder diffraction does not only yield information about the atomic arrangement, but also about phase composition, morphology, defects, and strain. Measurements can be performed *in-situ* to investigate chemical reactions and phase transitions.

17a.1 Principles of Diffraction

A wave of electromagnetic radiation or particles that passes through a material will be scattered by the atoms in the material. If the wavelength is comparable to the inter-atomic distances, the total scattered wave will have features resulting from the interference of the waves from the individual atoms. Naturally, these features depend on the atomic arrangement in the scattering material. This phenomenon is known as *diffraction*. X-rays have wavelengths in the region of 1 Å (10^{-10} m) and are thus suitable for diffraction experiments.

The description and interpretation of the diffracted wave is greatly simplified when the scattering material is *crystalline*. A crystalline material has a long-range periodicity in its atomic arrangement. Thus, it can be represented by a *unit cell* which is the smallest building block that can be repeated in 3 dimensions to build up the entire atomic structure. Such materials scatter strongly in certain directions which are the directions where all the unit cells scatter in phase and thereby give constructive interference. In all other directions, there will be very little scattering due to the almost perfect destructive interference from the many unit cells that scatter out of phase with each other.

The condition for constructive interference is elegantly formulated in *Bragg's law*. Scattering is regarded as specular reflection from families of equally spaced lattice planes that intersect the edges of each unit cell an integer number of times. A family of lattice planes is denoted by a *Miller index*, which is three integers, *hkl*, that indicate how many times the planes cut the a-, b- and c-axis, respectively. If the scattered beams from two neighbouring planes are to be in phase, the path difference (A-B-C in Fig. 17a.1) must be an integer number of wavelengths. Simple geometry gives the condition for this:

$$n\lambda = 2d_{hkl}\sin\theta_{hkl} \tag{17a.1}$$

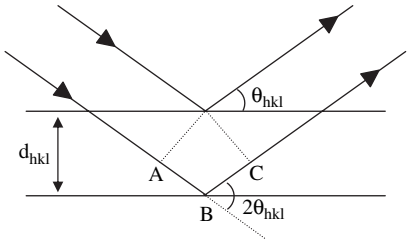

Fig. 17a.1 Diffraction from a crystal regarded as specular reflection from lattice planes. The difference in path travelled by the two beams is the distance A-B-C

where n is an integer, λ is the wavelength, d_{hkl} is the spacing between the lattice planes, and θ_{hkl} is half the scattering angle. Usually, the integer n is omitted, since a higher-order reflection ($n > 1$) from the planes hkl with interplanar spacing d_{hkl} is indistinguishable from the first-order reflection from the planes $(nh)(nk)(nl)$ with interplanar spacing d_{hkl}/n.

The intensity of a Bragg reflection is determined by the atomic arrangement in the unit cell. More specifically, the measured intensity of the reflection I_{hkl}, is proportional to the square modulus of the *structure factor*, F_{hkl}, which is a complex number that describes the amplitude and the phase of the scattered wave in the reflection hkl:

$$I_{hkl} \propto |F_{hkl}|^2 = \left| \sum_{j=1}^{N} f_j \exp\left(2\pi i(hx_j + ky_j + lz_j\right) \right|^2 \qquad (17a.2)$$

where the summation is over all N atoms in the unit cell. $x_j y_j z_j$ are the fractional coordinates of the j'th atom in the unit cell and f_j is its *atomic scattering factor* which is a measure of how strongly the atom scatters the beam. i is the imaginary unit $\sqrt{-1}$.

Diffraction experiments on crystalline matter are performed on either *single crystals* or *polycrystalline materials*. In a single crystal, the periodicity in the atomic arrangement is continuous throughout the material. When a single crystal is oriented in such a way that Bragg's law is fulfilled for a family of lattice planes, those planes will scatter in one well-defined direction in space, thus yielding 3-dimensional data (Fig. 17a.2a). A polycrystalline material, on the other hand, contains many, differently oriented crystals. They are often investigated in the form of a *powder*, where the particle size is in the μm range. If a powder contains a large number of crystals and all crystal orientations are equally represented, it is referred to as an *ideal powder*. The Bragg reflections from each lattice plane hkl will fall on a cone with the

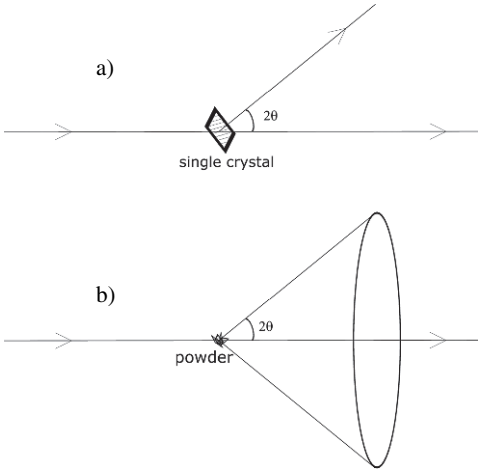

Fig. 17a.2 (**a**) Bragg scattering from a family of lattice planes in a single crystal occurs in one direction. The scattered beam makes an angle of 2θ with the incident beam and is in the plane defined by the incident beam and the normal to the lattice planes. (**b**) Bragg scattering from a family of lattice planes in a powder falls on a cone with an angle of 2θ with the primary beam

angle $2\theta_{hkl}$ to the direct beam (Fig. 17a.2b). Thus, a powder diffraction measurement aims at measuring the scattering intensity as a function of the scattering angle, yielding 1-dimensional data. Information is clearly lost as compared to the 3-dimensional data obtained from a single crystal diffraction experiment. This complicates the data analysis which will be discussed in Sect. 17a.3. Still, powder diffraction has some advantages over single crystal diffraction. First of all, it allows to investigate materials that are not available as single crystals. Phase transitions that would destroy a single crystal can also be investigated readily (see Sect. 17a.4). Furthermore, the measurement is simple and fast, since Bragg scattering occurs from all possible lattice planes without any need to reorient the sample.

17a.2 Diffraction of X-Rays and Neutrons

X-rays are by far the most commonly used radiation for diffraction experiments. An important reason is the good availability of experimental facilities, since X-rays of quite high intensity are readily generated in the laboratory. The X-ray beam, due to its high intensity, can be well collimated and monochromised to yield diffraction data of high resolution in a relatively short time. Experimental facilities will be discussed further below.

X-rays are scattered by the electron cloud of the atom. This has two important implications:

1) The atomic scattering factor, (f in Eq. 2), increases linearly with the atomic number, Z.
2) The volume from which the scattering occurs is significant compared to the wavelength of the X-rays. Scattering intensity therefore decreases with the scattering angle due to destructive interference between X-rays scattered by different parts of the electron cloud.

Both points are illustrated in Fig. 17a.2 which shows the atomic X-ray scattering factor as a function of the atomic number Z for the scattering angles zero and $(\sin\theta)/\lambda = 0.5\ \text{Å}^{-1}$.

The first point may be a serious drawback in investigations of hydrogen-containing materials. Hydrogen, with its single electron, scatters X-rays an order of magnitude weaker than even light metal atoms like aluminium and magnesium. In compounds with heavier elements, e.g. transition metals or rare earths, scattering from hydrogen is practically negligible compared to that from the metals. Thus, it is often impossible to extract reliable information about the position of hydrogen atoms in crystal structures from powder X-ray diffraction data. This problem may be overcome by using neutrons instead of X-rays. According to the *de Broglie* relation, a particle with linear momentum p has a wavelength λ given by $\lambda = h/p$, where h is the Planck constant. The neutron is an uncharged particle found in all atomic nuclei except for the ^{1}H nucleus. Beams of neutrons with wavelengths suitable for diffraction experiments can be created in processes, where the neutrons are liberated

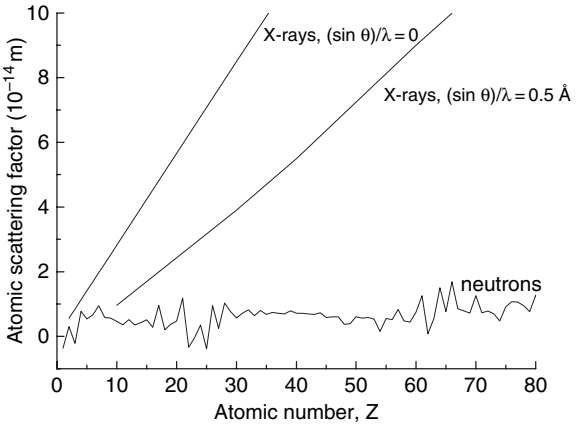

Fig. 17a.3 Atomic scattering factor for X-rays and neutrons as a function of the atomic number. Note that the atomic scattering factor is dependent on the scattering angle for X-rays

from the atomic nuclei (see 17a.2.1). Neutrons are scattered by the atomic nuclei. As opposed to X-rays, there is no correlation between the atomic number and the atomic scattering factor for neutrons. Instead, the atomic scattering factor which is often called the *scattering length* in the neutron case varies chaotically from element to element (and actually from isotope to isotope) as shown in Fig. 17a.3. This has two advantages. Firstly, neighbouring elements in the periodic table, which are difficult to distinguish with X-rays, may have rather different neutron scattering factors and, thus, be easy to differentiate. Secondly, and more important for hydrogen-containing compounds, light and heavy elements often have comparable atomic neutron scattering powers. For instance, scattering from hydrogen is stronger than from most metals. Hence, information about hydrogen positions are readily available from neutron diffraction data. A third advantage is that the atomic nuclei practically are point scatterers, since they are very small compared to the wavelength of the neutrons. The atomic neutron scattering factor is therefore independent of the scattering angle, which makes it possible to collect useful data over a wider angular range than with X-rays.

Neutrons interact much weaker with matter than X-rays do. This is a disadvantage in the sense that much larger samples and longer counting times are needed for neutron diffraction. On the other hand, it facilitates measurements of samples under non-ambient conditions, since the neutron beam can easily penetrate furnaces, cryostats, pressure cells (cf. Fig. 17a.4), etc. Samples for neutron diffraction experiments are usually prepared with the ^{2}H isotope (deuterium, D) instead of natural hydrogen. The ^{1}H isotope which comprises 99.99% of natural hydrogen is a very strong incoherent scatterer, which means that it mainly gives featureless "background" scattering. Deuterium, on the other hand, scatters mainly coherently, which gives featured scattering with structural information (i.e. Bragg scattering in the case of crystalline samples). The concepts of coherent and incoherent scattering are explained e.g. in Ref. [1].

Fig. 17a.4 A sample cell for PND made of the Inconel superalloy. The walls are 3.5 mm thick, allowing for the introduction of gas with a pressure up to 3000 bar at temperatures up to 600°C. The cell is penetrable for neutrons, but not for X-rays

17a.2.1 Sources of Radiation for Diffraction Experiments

X-rays are generated in the laboratory by bombarding a metal target in an X-ray tube with electrons that are accelerated over a potential of several kV. Core electrons in the metal target are knocked out by the energetic electrons, and X-rays are emitted when electrons from a higher shell fall into the vacancy in the core shell. The X-rays have well-defined wavelengths that correspond to the energy difference between the two shells. These energy differences are characteristic for the material in the metal target, and these X-rays are therefore called *characteristic X-rays*. The retardation of the energetic electrons when they hit the target generates a continuous spectrum of X-rays, called *white radiation* or *bremsstrahlung*. The characteristic X-rays are far more intense than the white radiation and, hence, used for diffraction experiments. A characteristic wavelength is singled out by a filter that is highly absorbing for other characteristic wavelengths or by a *crystal monochromator* which is a single crystal of e.g. Si, Cu or graphite. The monochromator is oriented such that the Bragg condition is met for the characteristic wavelength desired, which is reflected onto the sample.

Alternatively, X-rays of extreme intensity can be produced in large facilities, called *synchrotrons*. Electrons are accelerated to relativistic speeds in a *booster* and injected into a *storage ring*. The storage ring consists of several straight tubes that are connected to form a closed semi-circular path with a circumference of up to more

than a thousand metres. Between the straight sections, *bending magnets* are installed that force the electrons to follow the storage ring. The sudden change in direction causes the electrons to give of a burst of very intense radiation in the X-ray regime (IR, visible light, UV, and soft gamma radiation may also be produced, but are of no interest for diffraction). The same is achieved, with even higher resulting intensity, by magnetic devices, called *wigglers* and *undulators* that make the electron path oscillate in the straight sections of the storage ring. At each bending magnet, wriggler, and undulator, there is a beamline, where the synchrotron radiation is used for experiments, for instance, powder diffraction. Synchrotron radiation does not only have a high flux, it is also very well defined. The beam divergence is considerable in the horizontal plane, but very small in the vertical plane. Synchrotron sources are usually characterised by their *brilliance* (or spectral brightness) which is a quantity that takes the divergence of the beam into account. The brilliance is defined as the number of photons within an energy bandwidth of 0.1% emitted into a unit solid angle every second, divided by the area of the source. Modern synchrotrons can have a brilliance of up to 10 orders of magnitude larger than an X-ray tube. Among the around 20 synchrotrons that serve as X-ray sources worldwide, some of the best-known are the European Synchrotron Radiation Facility (ESRF) (Grenoble, France), the Super Photon ring (SPring-8) (Hyogo, Japan), and the Advanced Proton Source (APS) (Argonne, USA). Their properties are summarised in Table 17a.1.

Neutron beams are most often produced in nuclear reactors. Rods of uranium are brought together in the core of the reactor. The uranium is radioactive, so some atoms will spontaneously undergo fission, i.e. they break up into lighter elements and free neutrons. The neutrons are very energetic, but are moderated (slowed down) by a medium, usually water or heavy water, surrounding the rods. The moderated neutrons may be absorbed by another uranium atom which will immediately undergo fission itself and release three more free neutrons. Thus, a chain reaction starts. The conditions in the nuclear reactor are adjusted such that a steady state is achieved, where each fission triggers exactly one other fission. Beams of neutrons for various experiments, e.g. neutron powder diffraction, are obtained from the reactor core through channels in the surrounding shielding material. There are about 30 nuclear reactors that serve as neutron sources around the world. Some of the best-known are ILL (Grenoble, France), HFIR (Oak Ridge, USA), and JRR-3M (Tokai, Japan). Their properties are summarised in Table 17a.2.

A more efficient, but also much more expensive way to obtain neutron beams is by *spallation.* Highly energetic charged particles, for instance protons, are shot

Table 17a.1 Properties of some synchrotron X-ray sources

Synchrotron	Electron energy [GeV]	Circumference of storage ring [m]	Number of beamlines
ESRF	6.0	844	56
SPring-8	8.0	1436	62
APS	7.0	1104	68

Table 17a.2 Properties of some neutron reactor sources

Reactor	Power [MW]	Flux [neutrons s^{-1} cm^{-2}]	Beamlines
ILL	58	$1.5 * 10^{15}$	~ 50
HFIR	85	$2.0 * 10^{15}$	17
JRR-3M	20	$2.0 * 10^{14}$	21

at a target of a heavy material like lead, tungsten or mercury. The particles practically smash atoms in the target, breaking them up into lighter elements and cascades of neutrons. Up to 30 neutrons may be released from a single target atom and very high neutron fluxes can be obtained. The neutrons are moderated to obtain the desired wavelength distribution, guided out through channels in the shielding material surrounding the target, and used for experiments. There are only a few spallation sources worldwide: ISIS (Didcot, UK), SNS (Oak Ridge, USA), IPNS (Argonne, US), LANCE (Los Alamos, US), SINQ (Switzerland), KENS (Tsukuba, Japan). More are under construction or planning, e.g. in J-PARC in Tokai, Japan which will be finalised in 2008.

17a.2.2 Instruments for Powder Diffraction

The two crucial parameters of a powder diffractometer are *resolution* and *intensity*. Resolution determines how well fine features in the data are resolved. Bragg reflections that occur closely together in scattering angle may still be discernable as separate Bragg reflections, if the resolution is high enough. With lower resolution, they will merge together and look like one ill-defined reflection. High resolution is very important to determine new, complicated crystal structures, as will be clear in Sect. 17a.3 of this chapter.

The intensity determines how fast data are collected. Using a high-intensity diffractometer, data can be collected in shorter time than in a low-intensity instrument or, alternatively, data with better counting statistics can be collected in the same amount of time.

All diffractometer designs are trade-offs between resolution and intensity. To achieve high resolution, the beam should be well monochromised and there should be a set of slits and collimators that make the beam as well-defined as possible. This will, however, result in a lower flux on the sample. Monochromators on reactor-based PND diffractometers serve as good examples. A perfect crystal monochromator picks out a very narrow distribution of wavelengths. Since the total neutron flux from reactors is low, extremely few neutrons would be left in a “perfectly” monochromised beam. PND crystal monochromators are therefore made imperfect on purpose, so that they pick out a broader wavelength distribution. This greatly enhances the neutron flux on the sample, but reduces the resolution, since a distribution

of wavelengths will give a distribution of scattering angles for each set of lattice planes (cf. Eq. 2).

The detector system is the heart of a powder diffractometer. A coarse distinction can be made between point detectors and position-sensitive detectors (PSD). A point detector simply registers that it is hit by an X-ray photon or a neutron, while a PSD also registers *where* on the detector it is hit. The resolution of a point detector can be made arbitrarily high, since slits can be used to make an arbitrarily small angular range visible for the detector. This, of course, goes at expense of the intensity, and factors other than the detector resolution (collimation, sample size, accuracy in the detector movement, etc.) will eventually dominate the overall resolution. On the other hand, a PSD has an intrinsic resolution limit given by how well two close-lying points on the detector can be separated. The reduction in resolution is compensated by an enormous increase in intensity or reduction in measurement time. Fig. 17a.5 shows the difference between data of $LiAlH_4$ recorded by two different instruments at the Swiss-Norwegian Beam Line at the ESRF in Grenoble, France. The data coloured blue in Fig. 17a.5 were measured by an instrument that is optimised for high resolution. It features 6 point detectors that are mounted on a common arm with 1.1° separation. The arm moves in the vertical plane to benefit from the inherent vertical collimation of the synchrotron beam. In front of each detector, an *analyzer crystal* is located. The analyzer crystals' orientations are changed synchronously with the movement of the detector. Their purpose is to filter away all scattered radiation that leaves the sample with 2θ angles that are slightly different from those the detectors are set to measure. This eliminates loss of resolution due to the finite size of the sample and imperfect sample alignment. The resulting resolution is superb. The data in Fig. 17a.5 were collected in steps of 0.003° with a

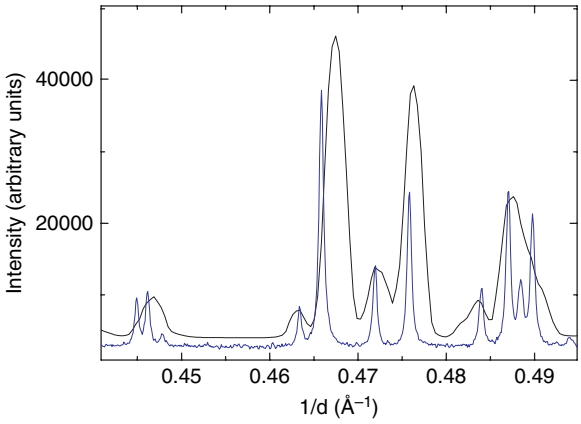

Fig. 17a.5 Part of the powder diffraction diagram for $LiAlH(D)_4$ measured by a high-resolution instrument (blue line) and image plate-based instrument (black line). The peak positions do not match completely, since the high-resolution measurement takes place on a deuterated sample with slightly different unit cell parameters. Note the superior resolution, but inferior noise level in the high-resolution data

counting time of 1 s per step. Hence, the data collection time over the 2θ range from 4–30° is about 2.5 hours. The black data in Fig. 17a.5 were measured by an instrument designed for quick measurements to follow reactions in situ. The detector is a two-dimensional image plate that covers a 2θ range from 0–41° with a sample-detector distance of 200 mm. The image plate was exposed for 30 seconds and another 90 seconds were used to read out the data and erase the image plate, resulting in a total data collection time of 2 minutes. The two-dimensional data are integrated to yield a 1-dimensional data set with excellent statistics. On the other hand, resolution is relatively poor due to the limitations of the image plate and the lack of an analyzer crystal.

Neutron diffractometers at pulsed spallation sources are usually designed completely differently than other reactor-based diffractometers to benefit from the pulsed nature of the neutron beam. Instead of measuring the scattering intensity as a function of the scattering angle at constant wavelength, the intensity is measured as a function of wavelength at a constant scattering angle. The wavelengths of the neutrons are inversely proportional to the their speed and therefore measured by the time it takes to fly from the source to the detector via the sample. A certain time of flight corresponds to a certain wavelength and, hence, to a certain *d*-value according to Bragg's law. The neutron beam obviously needs to be pulsed so that the flight time can be measured from the instance the pulse leaves the source. Such *time-of-flight* (*TOF*) measurements can yield data with extreme resolution when the flight path is long. The instrument HRPD at ISIS has a flight path of almost 100 m and a resolution that is comparable to or better than that of high-resolution synchrotron diffractometers.

17a.3 Extracting Information from Powder Diffraction Data

17a.3.1 The Fingerprint Method for Phase Identification

Powder diffraction data can be analysed by different techniques and on different levels, depending on the purpose of the experiment. Sometimes, a powder diffraction measurement is performed simply to find out which phase or phases is/are present in a sample. The positions and relative intensities of the Bragg reflections from a crystalline phase are determined by fundamental structural properties of that phase, *i.e.* the unit cell dimensions and the atomic arrangement within the unit cell, respectively. Thus, the powder diffraction pattern can be regarded as a "fingerprint" from a phase. Phase identification can therefore be performed simply by comparing the measured fingerprint with the fingerprints of known phases. The searching process is done very effectively with computers. The digital database *PDF-4* contains a list of d-values (which are used instead of the scattering angle, because they are independent of the wavelength) and relative intensities for the Bragg peaks of 271813 phases (in the 2005 version; more entries are added every year). These lists are the

"fingerprints" that are matched with the observed data. Searches can be done on the entire database or on a subset defined by *e.g.* chemical composition.

In most cases, the fingerprint method is only successful, if the phases in the sample have already been described in literature and, hence, included in the PDF-4 database. Nevertheless, there is a slight chance of success even with a new, undescribed phase present, if another phase with a similar crystal structure, but different composition can be found in the database.

The PDF-4 database is limited to X-ray diffraction data, but this is not an important drawback. Samples are almost always characterised by PXD prior to PND measurements to avoid spending precious PND beam time on a poor sample. Thus, PND is seldom used on samples with unknown phase composition.

17a.3.2 The Rietveld Method

The Rietveld method has revolutionised the treatment of powder diffraction data. It was developed in the late 1960s as a method for *structure refinement* with PND data [2, 3]. Structure refinement is a process, where an approximate structure model is refined to be in best possible agreement with the experimental data so that accurate structural details (like interatomic distances and angles) can be extracted. With single crystal data, this is done by measuring $|F_{hkl}|(=\sqrt{I_{hkl}})$ for a large number of Bragg reflections and then refining the atomic coordinates in the model with a least-square algorithm to obtain a set of calculated structure factors that are in best possible agreement with the observed ones. This strategy was previously used on powder diffraction data as well, but with less accuracy, because the compression of the data into one dimension makes most reflections overlap with other reflections. Thus, few structure factor moduli can be extracted accurately.

Hugo M. Rietveld noticed that the well-resolved Bragg peaks measured by the powder neutron diffractometer at the reactor in Petten (The Netherlands) had an almost perfect Gaussian shape. A diffraction profile consisting of several overlapping peaks could simply be described by a sum of Gaussian peaks. Thus, structure refinement can be performed by fitting a calculated diffraction profile to the entire measured data set, including clusters of overlapping reflections, instead of fitting individual intensities. This is the essence of the Rietveld method. The diffraction profile is calculated from the structure model in discrete steps that match the steps of the measured data. The calculated intensity in the *i*th step is given by

$$y_i^{\mathrm{calc}} = K_i s \sum_{hkl} M_{hkl} |F_{hkl}|^2 \varphi(2\theta_{hkl} - 2\theta_i - zero) A_i P_i + bg_i \qquad (17a.3)$$

where K is an instrument-dependent correction factor and s the scale factor. M_{hkl} is the multiplicity of the hkl reflection, *e.g.* the number of different reflections that are compressed into one reflection in one dimension (for instance, M_{100} is 6 for a cubic unit cell, since the 100, 010, 001, $\bar{1}00$, $0\bar{1}0$, and $00\bar{1}$ reflections will occur

at the same scattering angle and have the same structure factor moduli). F_{hkl} is the structure factor (Eq. 2). φ is a *profile function* that distributes the intensity from the reflection *hkl* around the ideal Bragg angle $2\theta_{hkl}$ according to instrumental and sample broadening (a Gaussian function in Rietveld's original work). $2\theta_i$ is the scattering angle corresponding to point *i*, *zero* is the instrumental zero-point offset, *A* is an absorption correction, *P* is a correction for a preferred orientation, which is necessary, if some orientations of the crystallites are over- or under-represented. *bg* is the background (*i.e.* everything that is not Bragg scattering) which is described by a polynomial or by interpolation between selected points. The sum is over all the reflections *hkl* that contribute to the Bragg scattering in point *i*. If more than one phase is present, there must be an additional sum over all phases with Bragg contribution to point *i*. Both structural and non-structural parameters can be refined in a least-square refinement to minimise the disagreement, R_{wp}, between the observed and calculated profile:

$$R_{wp} = \frac{\sum_i w_i (y_i^{\text{obs}} - y_i^{\text{calc}})^2}{\sum_i w_i \left(y_i^{\text{obs}}\right)^2} \tag{17a.4}$$

where w_i is the statistical weight of the observed intensity, y_i^{obs}, in point *i*, which is usually taken as the inverse of the squared standard deviation of y_i^{obs}, $1/\sigma(y_i^{\text{obs}})^2$.

The Rietveld method is by no means an automatic process, and the refinement requires continuous surveillance and input from the user. If too many parameters are refined simultaneously and/or the values of the parameters are too far away from their correct values, the refinement will frequently diverge or fall into a local minimum of R_{wp}. On the other hand, if a good starting model is used and the sequence of parameters to refine is carefully chosen, very large and complex structure models can be refined successfully. The most extreme example is the work of von Dreele *et al*. who solved and refined the crystal structure of a protein with 1630 atoms in the unit cell based on high-resolution synchrotron radiation powder diffraction [4].

A powder with large, perfect crystallites measured on a (hypothetical) diffractometer with infinite resolution would give infinitely sharp Bragg peaks exactly at the Bragg angle. Bragg reflections in real life are broadened by the instrument and often by imperfections in the crystallinity as well. The resulting profile shape is the convolution of instrumental and sample broadening. The Gaussian profile function worked well on old powder neutron diffractometers, where the overall peak shape was largely determined by the (Gaussian) distribution of wavelengths provided by the monochromator. PXD profiles have a more Lorentzian character and were first treated by the Rietveld method in 1977 [5, 6], some 10 years after its introduction. Today, the *pseudo-Voigt* function which is a linear combination of a Gaussian and a Lorentzian function is the most commonly used profile function.

Instrumental broadening of Bragg reflections measured by the "full-width-at-half-maximum" (FWHM) has an angle dependence that follows the so-called *Cagliotti expression*:

$$FWHM = \sqrt{U\tan^2\theta + V\tan\theta + W} \tag{17a.5}$$

The instrumental values U, V, and W for a diffractometer can be determined from a Rietveld refinement using data from a reference material with negligible sample broadening (e.g. LaB_6). Any deviations from the instrumental profile shape yield information about the *microstructure* of the sample. Sample broadening may be due to *strain*. Strain broadening increases with the scattering angle as $\tan\theta$ and usually is Gaussian, thus leading to an increased value of U in Eq. 5. Small *particle size* (say, below 100 nm) which leads to an imperfect destructive interference at scattering angles close to the ideal Bragg angle is the other important source of sample broadening. Size broadening is predominantly Lorentzian and increases with the scattering angle by $1/\cos\theta$. The Lorentzian FWHM is therefore described as

$$FWHM_{Lorentzian} = \frac{Y}{\cos\theta} + X\tan\theta \qquad (17a.6)$$

where the first term describes Lorentzian size broadening and the second term accounts for the strain contribution to Lorentzian broadening. The Gaussian FWHM is described by the Cagliotti expression (Eq. 5), sometimes with an additional $Z/\cos\theta$ term to account for Gaussian size broadening.

A careful extraction and examination of sample broadening by the Rietveld method may yield detailed quantitative information about the sample particle size and strain. Insight in the mechanisms of hydrogen capacity loss for $LaNi_5$ on cycling was obtained from examination of strain broadening (e.g. [7]).

Quantitative phase analysis which is aimed at determining the relative amount of different phases present in the sample is another important application of the Rietveld method. The crystal structures of the phases need to be known, so that a multi-phase Rietveld fit can be performed. The scale factor of a phase is proportional to the number of unit cells in the beam for that phase. Molar, weight, and volume fractions of the different phases can be calculated from the ratio of scale factors, the weight of the content in the unit cells, and the unit cell volumes. A major obstacle in quantitative phase analysis is *microabsorption*, i.e. absorption of X-rays or neutrons within the individual particles. If a phase has more absorbing particles than the average of the sample due to larger particles and/or a higher absorption coefficient, its phase fraction will be underestimated. Some Rietveld programs compensate this by the so-called Brindley correction [8], but it requires a good estimate of the particle sizes for the different phases and only works well in cases of moderate to low microabsorption differences.

17a.3.3 Crystal Structure Determination

Determination of a new crystal structure from scratch based on powder diffraction data is often a long and difficult process. It usually proceeds in 4 steps:

1) Indexing, *i.e.* determining the size and shape of the unit cell.
2) Space group determination, *i.e.* determining the symmetry of the atomic arrangement.

3) Structure solution, *i.e.* creating a rough model of the atomic arrangement within the unit cell.
4) Structure refinement, *i.e.* making the structure model as accurate as possible with the Rietveld method described above.

The *indexing* step consists in assigning the correct Miller indices to a number of reflections in order to determine the six parameters *a, b, c*, α, β, *and* γ that define the length of the unit cell axes and the angles between them. The task seems manageable compared to the structure solution step, where several hundred structure parameters must be determined in complicated cases. In reality, indexing often is the most difficult step in a powder diffraction-based crystal structure determination. There is no deductive approach to solving the problem. Consequently, it has to be tackled by trial-and-error; obviously with the help of computers. Several programs with different search algorithms are available. They all take a list of d-values as input (or equivalently a list of 2θ values and the wavelength). The algorithms are very sensitive to systematic errors. Hence, only well-resolved reflections should be used. This typically limits the number of usable reflections to 20–30; sometimes less. Different programs have different strengths and weaknesses when it comes to speed and tolerance of impurity reflections (*i.e.* accidental inclusion of reflections from an impurity phase), missing reflections, and systematic errors (*e.g.* zero shift). Some work best for high-symmetry unit cells, while others are optimised for low-symmetry cases. The best strategy is to use several programs and compare the results. The computer program Crysfire [9] provides a common user interface for 9 different powder indexing programs and writes the results into a common summary file for easy comparison. The suggested unit cells are ranked by a figure of merit (FoM) which takes into account the average absolute discrepancy between the calculated and observed peak positions and also the number of reflections that *could* be observed in the considered 2θ range. The latter is necessary to avoid favouring large unit cells with a high density of possible reflections (an infinitely large unit cell has an infinite density of possible Bragg reflections and can therefore account perfectly for any set of observed reflections). The unit cell suggestion with the best FoM usually is the correct one, although there is no guarantee; especially if there are several unit cell suggestions with rather similar FoM. Thus, it is up to the user to decide what unit cell he or she believes in. The summary file from Crysfire can be imported into the program ChekCel for a graphical evaluation of the different suggestions.

Once a viable unit cell is found, the next step is to examine the possible *space group symmetry* of the material. A space group is a set of symmetry elements, such as mirror planes and rotation axes that describe the symmetry of the atomic arrangement. There are 230 space groups that are compatible with the long-range periodicity of a crystal. The choice of space group is restricted considerably by the shape of the unit cell, since all except two space groups put constraints on the possible combinations of unit cell parameters. For instance, presence of a 4-fold rotation axis requires that two of the unit cell axes have the same length and that all of the interaxial angles are 90° (tetragonal symmetry). The possible choices can be narrowed down further, if *systematic absence* is observed. Systematic absence means that certain

rules must be fulfilled for the Miller indices of the Bragg peaks having non-zero intensity. For instance, a crystal structure that can be described in a body-centered space group, meaning that the origin and the centre of the unit cell are equivalent by symmetry, will only have intensity in Bragg reflections, where $h + k + l$ equals an even number. The combination of the unit cell shape and systematic absence (if any) may point towards one specific space group or a set of space groups that have to be considered in the next step.

The next step is the actual structure solution, i.e. to make a model of the atomic arrangement in the unit cell. If it was possible to measure both the amplitudes and the phases of the scattered wave in the Bragg peaks, it would be possible to derive the atomic coordinates from the expression for the structure factor. Unfortunately, all information about the phases is lost in the measurement, since only the square modulus of the structure factor, and not the structure factor itself, is measurable. Without the phase information it is impossible to analytically derive the atomic coordinates. This is called *the phase problem* in crystallography.

There are several ways to cope with the missing phase information. Two classical techniques are the so-called *direct methods* and the *Patterson method*. They both require a large number of measured structure factor amplitudes and, thus, are best suited for the analysis of single crystal data. The direct methods treat the phase problem statistically, making use of the fact that there is a statistical relation between the phases of reflection triplets hkl, $h'k'l'$ and $h\text{-}h'\,k\text{-}k'\,l\text{-}l'$. The *Patterson method* considers a density map constructed by Fourier transformation of the square moduli of the structure factors. The peaks in the density map correspond to vectors between atoms, and the amplitude of a peak corresponds to the product of the atomic scattering powers of the two atoms connected by the vector. Thus, the Patterson method is an effective way to locate strongly scattering atoms, i.e. heavy atoms in the case of X-ray diffraction. These two techniques are very powerful with single crystal data, where structure solution is almost automatic in many cases. In order to use them with powder diffraction data, structure factor amplitudes must be extracted by a *pattern decomposition technique*. The technique is very similar to Rietveld refinement, with the important difference that each Bragg reflection intensity is treated as a *free variable*. Thus, only parameters needed to define the position of the Bragg reflections (unit cell parameters, zero shift, space group, and wavelength) and the profile shape are given (and refined), while parameters that determine the intensities (atomic coordinates and temperature factors) are not given. The Bragg reflection intensities can be refined using the least-square algorithm, which is referred to as a *Pawley refinement* [10]. Alternatively, they can be refined iteratively by a separate and less computing-intensive algorithm in a *Le Bail refinement* [11]. Both Pawley and Le Bail refinements produce a list of individual Bragg peak intensities. These can then be treated as single crystal data with direct methods or the Patterson method. However, the treatment usually is less straightforward than with real single crystal data, due to the higher uncertainty resulting from the peak overlap in the powder data.

Dedicated powder diffraction methods for structure solution, *global optimisation techniques*, are gaining popularity as computer power increases. The concept is to minimise the disagreement (measured e.g. by R_{wp}) between the observed data and

a diffraction profile calculated from a structure model. The similarity with the Rietveld method is obvious, but the minimisation cannot be done with a least-square algorithm, since the starting model will generally be far away from the "correct" model. Thus, more robust, but also far more computing-intensive techniques must be employed. *Monte Carlo* simulations are most commonly used. Random changes are made on the structure model and the resulting change in the disagreement, ΔR_{wp}, between the model and the data is calculated. If disagreement decreases, the change is accepted. If the disagreement increases, the change is accepted with the probability P:

$$P = \exp\left(\frac{-\Delta R_{wp}}{T}\right) \tag{17a.7}$$

The process is repeated millions of times until there is no further reduction in R_{wp}. T is a parameter used to control the chances of accepting "bad" moves. It is often referred to as the "temperature" of the simulation, due to the similarity between Eq. 6 and the probability $\exp(-\Delta E/kT)$ of overcoming the activation energy ΔE at temperature T. At high "temperature", there are high chances for "bad" moves to be accepted, and the optimisation may never settle in the desired state that gives the global minimum of R_{wp} At low "temperature", there are small chances for "bad" moves to be accepted, and the optimisation can get trapped easily in a local minimum of R_{wp}. Thus, the optimisation is never run at just one value of T. T can be gradually decreased from a high to a low value during the optimisation, such that the entire solution space is accessible in the beginning, while the finer details of the solution space around the (hopefully) global minimum in R_{wp} are explored towards the end. This is called *simulated annealing* due to the similarities to a physical annealing process. The success of simulated annealing depends on a proper choice of the cooling scheme. Alternatively, the optimisation may be run at several temperatures in parallel. Regularly, the models at two different temperatures are compared. If the high-temperature model has a lower R_{wp} than the low-temperature model, they swap temperatures such that the best model can be further optimised and the poorest model can get out of a possible local minimum trap. This is called *parallel tempering* and has the advantage that no cooling scheme or runtime must be chosen prior to the optimisation.

17a.4 Powder Diffraction Investigations of Hydrogen Storage Materials

This chapter gives some examples of investigations of hydrogen storage materials using powder diffraction as the key technique. It is not meant to be a comprehensive review, but aims at giving an idea of the practical possibilities offered by powder diffraction.

17a.4.1 Crystal Structure Determination

Crystal structure determination of metal hydrides has always relied heavily on powder diffraction techniques. Solid pieces of metals and alloys shatter to powders under hydrogen absorption due to the strain introduced during the formation of the hydride phase. Thus, single-crystal diffraction has not been an option for metallic metal hydrides. Single crystals of complex hydrides can be produced (e.g. [12]). Still, powder diffraction usually is the method of choice for crystal structure determination of complex hydrides due to the simplicity of the experiment and the easier synthesis and handling of powdered samples compared to single crystals.

Since the discovery of reversible hydrogen storage in Ti-doped $NaAlH_4$ in 1997 [13], there has been an intense research activity on $NaAlH_4$ and other alanates. Meanwhile, 12 alanate phases have been structurally characterised by PND. Their crystal structures are widely different, with symmetries ranging from cubic (i.e. $a = b = c$, $\alpha = \gamma = \beta = 90°$) to monoclinic (i.e. $a \neq b \neq c$, $\alpha = \gamma = 90° \neq \beta$), but they have some features in common. Obviously, they contain one of the two "alanate" anions, AlH_4^- ("tetrahydride") or AlH_6^{3-} ("hexahydride"), and some charge-balancing cation(s). The tetrahydride and hexahydride anions assume the shape of regular or somewhat distorted tetrahedra and octahedra, respectively. The average Al-H(D) distances in reported tetrahydride structures are in the narrow range between 1.62 Å and 1.64 Å, but internal variations of up to 7% are reported in $KAlD_4$(Al-D =1.55–1.67 Å) [14] and $Mg(AlH_4)_2$ (Al-H = 1.56–1.67 Å) [15]. The average Al-H(D) distance in AlH_6^{3-} units falls in the wider range between 1.74 Å and 1.80 Å, and variations of up to 9% and 11% are reported for $BaAlD_5$ (1.69–1.85 Å) [16] and Ba_2AlD_7 (1.67–1.85 Å) [17], respectivly. The alanate anions appear as isolated units, except in $BaAlD_5$, where all AlD_6^{3-} octahedra share two corners with two other octahedra, thus forming chains [16]. Phases with a mixture of hexahydride anions and hydride anions (H^-), Sr_2AlH_7 and Ba_2AlH_7, are also known [18, 17].

The crystal structure determination of Li_3AlD_6 will be studied in some more detail as an example. The material was first prepared by Ehrlich *et al.* in 1966 [19]. The PXD pattern was indexed according to a rhombohedral unit cell ($a = b = 8.11$ Å, $c = 9.57$, $\alpha = \beta = 90°$, $\gamma = 120°$), but the crystal structure was not determined. Several subsequent investigations claimed that a monoclinic unit cell ($a = 5.67$ Å, $b = 8.12$ Å, $c = 7.92$ Å, $\beta = 92.17°$) describes the observed PXD reflections better [20, 21]. Balema *et al.* compared the proposed monoclinic and rhombohedral unit cell with their own PXD data [22]. They noted that three weak peaks that were inconsistent with the rhombohedral unit cell were accounted for by the monoclinic one. They were, however, unable to solve the crystal structure. The full crystal structure determination was not performed until 2003 [23].

The work was based on high-resolution SR-PXD and PND data. Even with the superb resolution offered by SR-PXD, it was hard to discriminate between the proposed rhombohedral and monoclinic unit cell, since both account very well for the observed reflection positions. However, the rhombohedral unit cell has very few possible peaks that are not observed, while the monoclinic suggestions have very many

possible, undetected peaks. Moreover, the weak peaks observed by Balema *et al.* were not seen in the SR-PXD data. Thus, the rhombohedral unit cell was the first choice. The structure solution was done in two steps. The atomic X-ray scattering factor for Al is more than four times larger than that for Li and more than an order of magnitude higher than that for H. Even though Al only constitutes 10% of the atoms in Li_3AlD_6, it contributes almost 50% of the electrons. Thus, it was expected that the Al sub-structure alone would be able to explain the SR-PXD data relatively well. The Al sub-lattice is described with 10 times less parameters than the full crystal structure and, hence, is a much simpler problem to solve. The approximate Al atom positions were found by a Monte Carlo global optimisation with the SR-PXD data. From spectroscopic measurements [24] and experience, the D atoms were expected to coordinate the Al atoms in a (slightly distorted) octahedral configuration at a distance of around 1.75 Å. Hence, the remaining structure solution consisted in finding the orientation of the AlD_6^{3-} units and locating the Li atoms. This was done by parallel tempering in the computer program Fox [25], where the AlD_6^{3-} were defined as semi-rigid octahedra, whose position (defined by Al) was fixed, but the orientation was optimised. The optimisation was done to PND and SR-PXD data simultaneously. The obtained structure model was refined by the Rietveld method with the program FULLPROF [26] without any geometrical constraints. The obtained fits of the experimental data were very good, as shown in Fig. 17a.6.

The refined structure model is shown in Fig. 17a.7. The hexahydride units are very close to regular with Al-D distances between 1.734 Å and 1.754 Å. The D-Al-D angles are between 87.36° and 93.02° (ideal is 90°). The Li^+ ions are coordinated by 6 D-atoms in a distorted octahedral configuration.

17a.4.2 In Situ Investigations

"In situ" powder diffraction refers to investigations, where the sample is manipulated during measurement. For hydrogen storage materials, manipulation usually consists of either hydrogenating or dehydrogenating the sample. In situ powder diffraction can thus provide information about reaction pathways, metastable intermediate phases, and reaction kinetics. Gross *et al*. conducted a series of in situ desorption PXD measurements on $NaAlH_4$ with and without transition-metal additives [27]. The sample was sealed under argon inside an airtight steel and aluminium cell with a beryllium window that is highly transparent to X-rays. The sample was squeezed against the window by a spring, thus providing a well-defined flat sample geometry. The cell could be heated to a maximum of 400°C, and it allowed extraction (or introduction) of gas from (or to) the sample. The measurements were done on a laboratory X-ray diffractometer with a point detector. To achieve an appreciable time resolution, only a small angular region ($2\theta = 28.5 - 40°$) that contains Bragg peaks for all expected phases was measured. A new scan could then be performed about every 7 minutes.

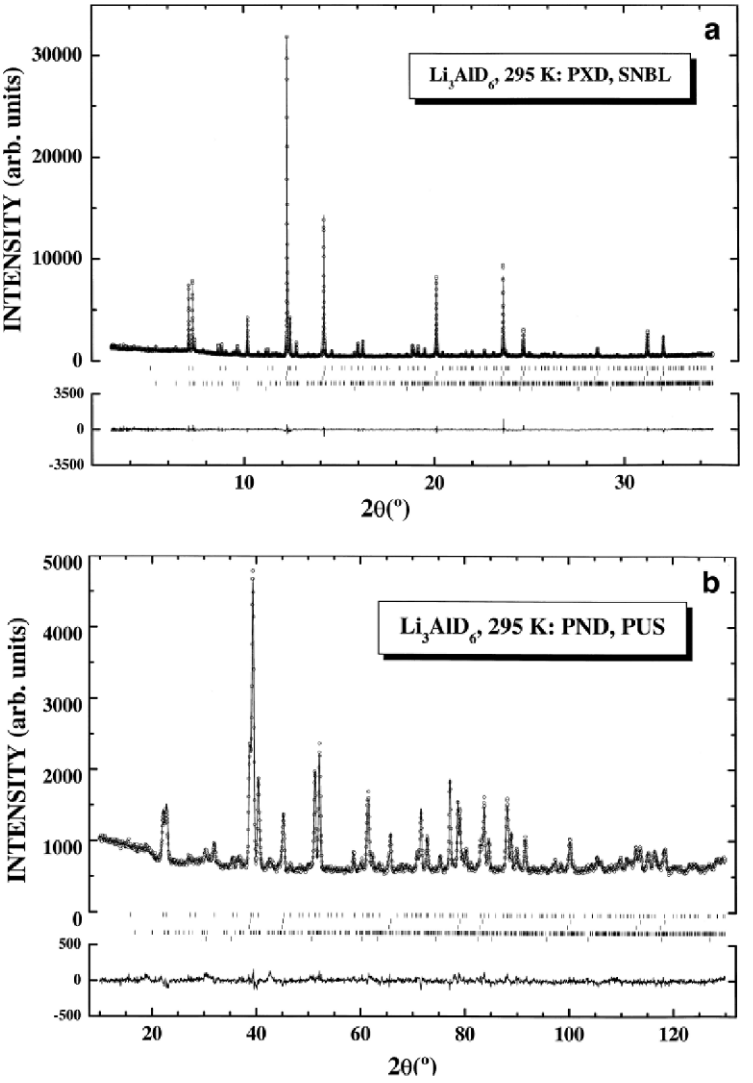

Fig. 17a.6 Rietveld refinement of Li_3AlD_6 with: (**a**) SR-PXD data (R_{wp} = 5.33%) and (**b**) PND data (R_{wp} = 3.93%). The open symbols are observed data, the solid line is calculated from the refined structure model, and the bottom line is the difference between the two. The vertical ticks mark the Bragg peaks for (from the top) Li_3AlD, Al, LiD, $LiAlD_4$, and LiD

The first measurement was carried out on undoped $NaAlH_4$ that was heated up and kept at 150°C for about four hours under a dynamic vacuum (Fig. 17a.8). Except for a slight change in the reflection positions due to thermal expansion, no changes occurred. Only peaks from $NaAlH_4$ (and from trace amounts of Al that was present from the start) were detected. Thus, no decomposition took place in the course of the four hours at 150°C. The temperature was then quickly raised

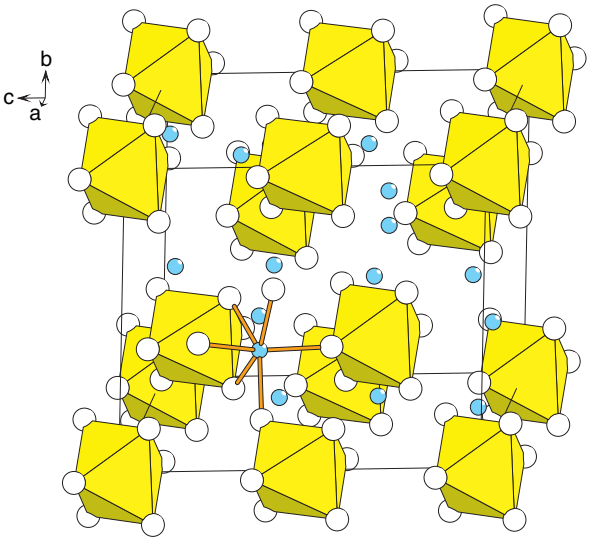

Fig. 17a.7 The crystal structure of Li_3AlD_6 as refined from PND and SR-PXD. The yellow octahedra are AlD_6^{3-} (Al in the centres are not shown; D are white spheres; blue spheres are Li). The 6-coordination of D around Li is outlined

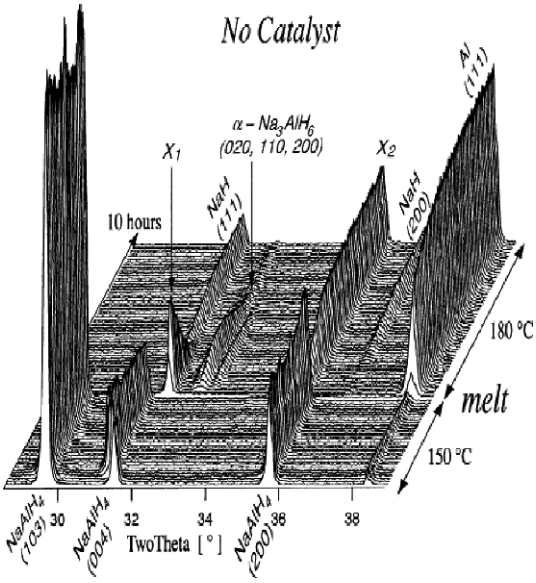

Fig. 17a.8 In situ PXD measurement of undoped $NaAlH_4$. See text for discussion. The peak marked X_2 is probably due to reaction between the sample and the Be window. Reprinted from Ref. [27] with permission from Elsevier

to 180°C, which is just above the melting point of $NaAlH_4$. The reflections from $NaAlH_4$ naturally disappear on melting, and the molten $NaAlH_4$ promptly starts to decompose as seen by the rapid growth of the reflection for free aluminium. Surprisingly, α-Na_3AlH_6 was not formed initially together with Al. Instead, a peak from an unknown phase, marked X_1 in Fig. 17a.8 appeared. The intensity of the X_1 peaks reached its maximum almost immediately and then decreased rapidly, while peaks from α-Na_3AlH_6 appeared. Thus, the X_1 phase is thought to be a metastable modification of Na_3AlH_6, although this has not been verified. The peaks from α-Na_3AlH_6 reached a maximum after about 1 hour at 180°C and then started to decrease, as the hexahydride decomposed into NaH and Al. Interestingly, the hexahydride did not appear to decompose before all the (molten) tetrahydride was decomposed, since Bragg peaks from NaH were not observed before the hexahydride peaks started to decrease. Thus, the two decomposition reactions appear to be highly correlated.

The decomposition proceeded very differently for a sample with 2 mole% of Ti butoxide and Zr propoxide. Whereas the uncatalysed sample was stable at 150°C, the catalysed sample decomposed readily to α-Na_3AlH_6 and Al at 100°C (Fig. 17a.9). The growth rate of the hexahydride was comparable to the rate at which the tetrahydride decreased, indicating a direct transformation. The X_1 phase was not observed as an intermediate. The reaction became sluggish, before the first decomposition step was finished, and the temperature was therefore raised to 150°C. Most of the remaining $NaAlH_4$ decomposed quickly at 150°C except for a small portion which remained stable at 150°C throughout the experiment; probably undoped pow-

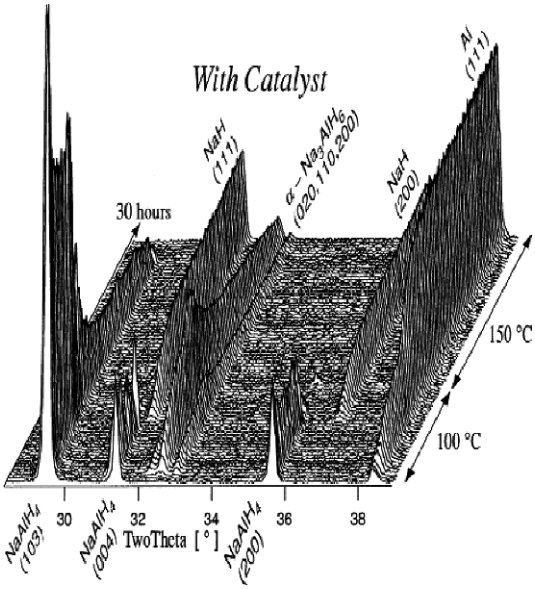

Fig. 17a.9 In situ PXD measurement of doped $NaAlH_4$. The sample decomposes readily at 100°C. See text for discussion. Reprinted from Ref. [27] with permission from Elsevier

der grains due to non-uniform distribution of the dopant. The hexahydride phase did not start to decompose until almost all the (catalysed) tetrahydride had disappeared, again indicating some correlation between the reaction steps. α-Na_3AlH_6 decomposes directly to NaH and Al. Thus, no intermediate phases were observed in the decomposition of doped $NaAlH_4$.

$Mg(AlH_4)_2$ is another alanate that has attracted attention as a possible hydrogen storage material due to its high hydrogen capacity of 9.3 wt.%. A first decomposition step into MgH_2, Al, and 6.9 wt.% H_2 was suggested by several groups, whereas a reaction through an intermediate phase, $MgAlH_5$, was suggested Dynmova *et al.* [28]. They did not observe the intermediate phase directly, but some thermal investigations (e.g. [29]) support a multi-step mechanism.

Fossdal *et al*. performed an in situ SR-PXD investigation to study the decomposition pathway of $Mg(AlH_4)_2$ [30]. The work was performed at the Swiss-Norwegian Beamline of the ESRF, Grenoble, France. The sample was kept under dynamic vacuum in a 0.5 mm boron-silicate capillary which was heated at constant heating rates with a hot air gun. The sample contained 96% $Mg(AlH_4)_2$, 4% NaCl, and trace amounts of Al. Diffraction patterns were recorded with a two-dimensional detector (image plate), which covered the angular range from 0 to 35°. The wavelength was 0.71 Å. Thus, the measured range corresponded to $2\theta = 0 - 80°$ with a Cu X-ray tube. The exposure time was 30 seconds and read-out and erasing of the image plate took another 90 seconds, thus giving a time resolution of 2 minutes. Data measured at 2 K/min, 5 K/min, and 10 K/min showed the same characteristics, except for an increase in the onset temperature for decomposition with increasing heating rate (from 150 to 170°C). There was no indication of an $MgAlH_5$ phase at any point (cf. Fig. 17a.10).

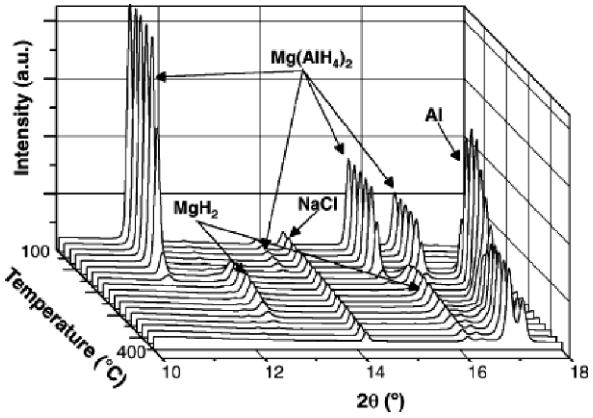

Fig. 17a.10 In situ SR-PXD measurement of the decomposition of $Mg(AlH_4)_2$ during heating at 10 K/min. Only a section of the measured angular range is shown for clarity. The peak marked as Al actually is a solid solution of Mg in Al. See text for discussion. Reprinted from Ref. [30] with permission from Elsevier

However, it turned out that pure Al was not one of the decomposition products. The peaks from the Al impurities which were present from the beginning shifted to lower angles on heating in accordance with the expected thermal expansion. The expansion of the Al unit cell increased abruptly on the onset of decomposition. This clearly indicates that a solid solution of Mg in Al, rather than pure Al, is a decomposition product. The first decomposition step of $Mg(AlH_4)_2$ therefore is

$$(1-x)\,Mg(AlH_4)_2 \rightarrow (1-3x)\,MgH_2 + 2Al_{1-x}Mg_x + (3+x)\,H_2$$

where x ≈ 0.02 at 150°C and may increase to a maximum of 0.19 at 400°C according to the Mg-Al phase diagram. Quantitative phase analysis showed that the ratio of $Al_{1-x}Mg_x$: MgH_2 always was in agreement with the stated reaction, thus excluding the presence of amorphous reaction products. The first decomposition step of $Mg(AlH_4)_2$ therefore does not proceed via an intermediate product like $MgAlH_5$.

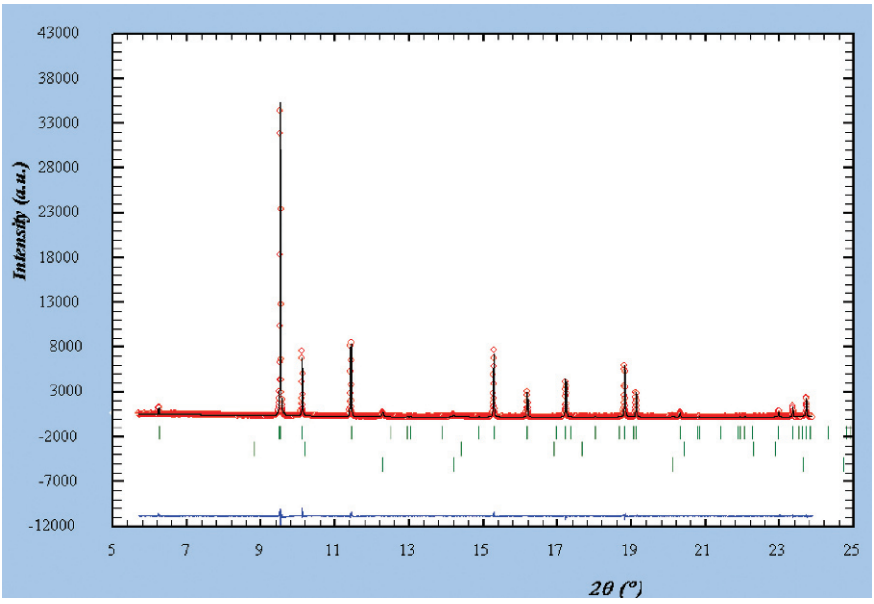

Fig. 17a.11 Rietveld fit to SR-PXD data of $NaAlH_4$ hand-ground with 6 mol.% $TiCl_3$. The vertical ticks mark the position of Bragg peaks from $NaAlH_4$ (top), NaCl (middle), and Al (bottom). Two crystalline Ti-containing phases are observed

17a.4.3 The Solid Solubility of Ti in $NaAlH_4$

The positive effect of Ti- (and other transition metal)-based additives on alanate decomposition and recombination has been investigated for nearly a decade. The enhancement of the kinetics is very well documented, but still poorly understood. It is not even clear *where* the transition metal is after it has been added. From a powder diffraction point of view, the Ti simply disappears on mixing with alanate. This is well illustrated in Fig. 17a.11 which shows the Rietveld fit to SR-PXD data of $NaAlH_4$ that is grinded manually with 6 mol% $TiCl_3$. The data have a superb resolution and counting statistics. Still, the data can be fitted perfectly by three phases, $NaAlH_4$, Al, and NaCl, of which none contains Ti. A crystalline Ti phase would be detected very easily. The signal would be many orders of magnitude stronger than the noise level in the data. Thus, it can be concluded that the Ti does not form any new crystalline phase. Still, the data give some clue about the fate of the Ti. Free Al and NaCl were not present in the starting materials and must be products of a reaction between the sodium alanate and the additive. Consequently, at least part of the trivalent Ti is reduced to a lower valency state. But in what state is it? It is now generally agreed that the transition metal is in a zero-valent metallic state, as demonstrated by various XANES measurements (see 17d). It also seems likely that it forms an amorphous or nano-crystalline phase with Al [31, 32]. However, the possibility of Ti forming a bulk solid solution with the alanate remained open for a long time. Density functional theory calculations show that such a solid solution would significantly change the unit cell parameters of the $NaAlH_4$ phase [33]. Very accurate unit cell parameters can be obtained with high-resolution SR-PXD. Therefore, the technique is well suited to settle the solid solution question. Brinks *et al*. prepared a set of $NaAlH_4$ samples doped with $TiCl_3$, $TiCl_4$, and TiF_3 under different conditions [34]. The samples were measured by the high-resolution instrument at the Swiss-Norwegian Beamline of ESRF and the unit cell parameters were compared to those of pure $NaAlH_4$.

The unit cell parameters obtained for the $NaAlH_4$ phases are shown in Table 17a.3 There is practically no variation in the a-axes. The c-axes vary slightly (11.3482–11.3498 Å). The variations are large compared to the standard deviations (about 15 times larger), but it should be noted that any systematic error in the data or the model (which will practically always be present to some degree) leads to an underestimation of the standard deviations. Moreover, there is no systematic variation in the c-axes with the Ti content. Thus, the SR-PXD data indicate that no appreciable bulk solid dissolution of Ti in $NaAlH_4$ takes place.

References

1. G. E. Bacon (1975). *Neutron Diffraction*. Oxford, Oxford University Press.
2. H. M. Rietveld, Acta Cryst. 22 (1967) 151–152.
3. H. M. Rietveld, J. Appl. Cryst. 2 (1969) 65.

Table 17a.3 The unit cell parameters of doped and undoped $NaAlH_4$ as obtained by the Rietveld method from SR-PXD data

Sample	a (Å)	c(Å)
$NaAlH_4$	5.0232(1)	11.3483(1)
$NaAlH_4 + 6\%$ $TiCl_3$ (hand-ground)	5.0231(1)	11.3482(2)
$NaAlH_4 + 6\%$ $TiCl_4$ (hand-ground)	5.0235(1)	11.3495(1)
$NaAlH_4 + 6\%$ TiF_3 (ball-milled)	5.0230(2)	11.3497(1)
$NaAlH_4 + 2\%$ $Ti(OBu)_4$, cycled 7 times	5.0233(1)	11.3498(1)

4. R. B. von Dreele, P. W. Stephens, G. D. Smith, R. H. Blessing, Acta Cryst. D 56 (2000) 1549–1553.
5. R. A. Young, P. E. MacKie, R. B. von Dreele, J. Appl. Cryst. 10 (1977) 262–269.
6. G. Malmros, J. O. Thomas, J. Appl. Cryst. 10 (1977) 7–11.
7. Y. Nakamura, J. Sato, S. Fujitani, K. Nishio, K. Oguro, I. Uehara, J. Alloys Comp. 267 (1998) 205–210.
8. G. W. Brindley, Phil. Mag. 7(36) (1945) 347.
9. R. Shirley (1999). *The CRYSFIRE System for Automatic Powder Indexing: User's Manual*, The Lattice Press, 41 Guildford Park Avenue, Guildford, Surrey GU2 5NL, England.
10. J. S. Pawley, J. Appl. Cryst. 14 (1981) 359–361.
11. A. Le Bail, H. Duroy, J. L. Fourquet, Mat. Res. Bull. 23 (1988) 447–452.
12. J. W. Lauher, Acta Cryst. B35 (1979) 1454–1456.
13. B. Bogdanovic, M. Schwickardi, J. Alloys Comp. 253–254 (1997) 1–9.
14. B. C. Hauback, H. W. Brinks, R. H. Heyn, R. Blom, H. Fjellvåg, J. Alloys Comp. 394 (2005) 35–38.
15. A. Fossdal, H. W. Brinks, M. Fitchner, H. B.C., J. Alloys Comp. 387 (2005) 47–51.
16. Q. A. Zhang, Y. Nakamura, K. I. Oikawa, T. Kamiyama, E. Akiba, Inorg. Chem. 41(26) (2002) 6941–6943.
17. Q. A. Zhang, Y. Nakamura, K. I. Oikawa, T. Kamiyama, E. Akiba, J. Alloys Comp. 631 (2003) 180–186.
18. Q. A. Zhang, Y. Nakamura, K. I. Oikawa, T. Kamiyama, E. Akiba, Inorg. Chem. 41(25) (2002) 6547–6549.
19. R. Ehrlich, A. R. Young, G. Rice, J. Dvorak, P. Shapiro, H. F. Smith, J. Am. Chem. Soc. 88 (1966) 858–860.
20. P. Chini, A. Baradel, C. Vacca, Chim. Ind. 48(6) (1966) 596.
21. J. Mayet, S. Kovacevic, J. Tranchet, Bull. Soc. Chim, Fr. 2 (1973) 503–506.
22. V. P. Balema, V. K. Pecharsky, K. W. Dennis, J. Alloys Comp. 313 (2000) 69–74.
23. H. W. Brinks, B. C. Hauback , J. Alloys Comp. 354 (2003) 143–147.
24. J. C. Bureau, Z. Amri, J. M. Claudy, J. M. Letoffe, Mat. Res. Bull. 24 (1989) 23.
25. V. Favre-Nicolin, R. Cerny, J. Appl. Cryst. 35 (2002) 734–743.
26. J. Rodríguez-Carvajal, Physica B 192 (1993) 55.
27. K. J. Gross, S. Guthrie, S. Takara, G. Thomas, J. Alloys Comp. 297 (2000) 270–281.
28. T. N. Dynmova, N. N. Mal'tseva, V. N. Konoplev, A. I. Golovanova, D. P. Aleksandrov, Russian J. Coord. Chem. 29(6) (2003) 385–389.
29. M. Fichtner, J. Engel, O. Fuhr, O. Kircher, O. Rubner, Mat. Sci. Eng. B 108 (2004) 42–47.
30. A. Fossdal, H. W. Brinks, M. Fichtner, B. C. Hauback, J. Alloys Comp. 404–406 (2005) 752–756.
31. J. Graetz, J. J. Reilly, J. Johnson, A. Y. Ignatov, T. A. Tyson, Appl. Phys. Lett. 85(3) (2004) 500–502.
32. B. Bogdanovic, R. A. Brand, A. Marjanovic, M. Schwickardi, J. Tölle, J. Alloys Comp. 302(1–2) (2000) 36–58.

33. O. M. Løvik, S. M. Opalka, Phys. Rev. B 71 (2005) 054103.
34. H. W. Brinks, C. M. Jensen, S. S. Srinivasan, B. C. Hauback, D. Blanchard, K. Murphy, J. Alloys Comp. 376 (2004) 215–221.

Further Reading

Baruchel, J., Hodeau, J. L., Lehmann, M. S., Regnard, J. R., Schlenker, C. (eds.) (1993). *Theory, Instruments and Methods*. Neutron and Synchrotron Radiation for Condensed Matter Studies. Berlin, Springer-Verlag.
Coppens, P. (1992). *Synchrotron Radiation Crystallography*. London, Academic Press Limited.
Giacovazzo, C., Monaco, H. L., Viterbo, D., Scordari, F., Gilli, G., Zanotti, G., Catti, M. (1992). *Fundamentals of Crystallography*. Oxford, Oxford University Press.
Pecharsky, V. K., Zavalij, P. Y. (2003). *Fundamentals of Powder Diffraction and Structural Characterization of Materials*. Boston, Kluwer Academic Publishers.

Chapter 17b
SEM/(S)TEM

Eric Leroy and Brigitte Décamps

List of Abbreviations

B	Boron
Be	Beryllium
BF	Bright field
DF	Dark field
EDS	Energy-dispersive spectroscopy
EELS	Electron energy loss spectroscopy
EFTEM	Energy-filtered transmission electron microscopy
H	Hydrogen

Eric Leroy
Institut de Chimie des Matériaux Paris-Est, UMR 7182, CNRS, Paris 12, 94320 Thiais, France, e-mail: eric.leroy@icmpe.cnrs.fr

Brigitte Décamps
Institut de Chimie des Matériaux Paris-Est, UMR 7182, CNRS, Paris 12, 94320 Thiais, France, e-mail: brigitte.decamps@csnsm.in2p3.fr

A. Léon (ed.), *Hydrogen Technology*,

He	Helium
HRTEM	High-resolution transmission electron microscopy
Li	Lithium
Na	Sodium
PEELS	Parallel electron energy loss spectroscopy
SAED	Selected-area electron diffraction
SE	Secondary electron
SEM	Scanning electron microscopy
STEM	Scanning transmission electron microscopy
TEM	Transmission electron microscopy
XAFS	X-ray absorption fine structure
Z	Atomic number

17b.1 Introduction

Scanning electron microscopy (SEM), transmission electron microscopy (TEM), and scanning transmission electron microscopy (STEM), combined with energy-dispersive spectroscopy (EDS), are techniques perfectly adapted to imaging micro-structural features, to studying the morphology of the particles, to evaluating their form, dimension, and texture as well as to obtaining information on the chemical composition and crystallographic structure. These techniques allow for the qualitative and quantitative elemental analysis of micro-structural features. SEM provides access to the microstructure and chemistry of the material down to a tenth of the nanometer scale. TEM (conventional and high-resolution (HRTEM)) supplies information on the morphology and crystallography down to the atomic scale. In TEM/STEM, EDS can be combined with electron energy loss spectroscopy (EELS) that provides more detailed information on the chemical state of the elements present in the material.

This chapter will focus on the characterisation of hydrogen storage materials, especially in $NaAlH_4$ which has become a very promising compound for hydrogen storage since the year 1997 when Bogdanovic et al. showed that Na alanates could be made reversible by the addition of catalysts [1]. Complex metal hydrides, in particular sodium alanate ($NaAlH_4$) doped with Ti-based materials, reversible at moderate temperature (Eqs. (17b.1 and (17b.2)) satisfy several of the prerequisites for fuel cell applications [2].

$$3NaAlH_4 \leftrightarrows Na_3AlH_6 + 2Al + 3H_2 \quad (3.7\,\text{wt.\% of } H_2) \tag{17b.1}$$

$$Na_3AlH_6 \leftrightarrows 3NaH + Al + \frac{3}{2}H_2 \quad (1.9\,\text{wt.\% of } H_2) \tag{17b.2}$$

However, mechanisms involved in hydrogen absorption/desorption and the role of the titanium dopants are still not well understood. In order to optimise the process, an analysis down to the nanometer scale of the species present in the samples in different stages of the reactions has to be performed. The evolution of the microstructure and the local chemistry (species present, spatial distribution, and chemical states of the elements) during the cycles is of importance to understand the mechanisms by

which bulk deformation and reformation of the compound can occur in the presence of a catalyst.

A brief description of the different techniques mentioned above will be given below. Conventional TEM, HRTEM, and STEM are classical techniques that are widely described in several text books [3, 4, 5, 6, 7]. Therefore, they will not be treated here and the focus will be on the analytical techniques, such as EDS which may be combined with SEM or (S)TEM and EELS that is linked with (S)TEM. Moreover, problems encountered with these highly sensitive materials in air and under the electron beam as well as in performing quantitative analysis with these materials will be highlighted. Sodium alanate will be taken as an example.

17b.2 Principle of EDS and EELS Spectroscopy

The interactions of an electron beam with a thin specimen (case of the TEM) give rise to many signals. Figure 17b.1 displays the signals generated by the interactions between the electron beam and the specimen.

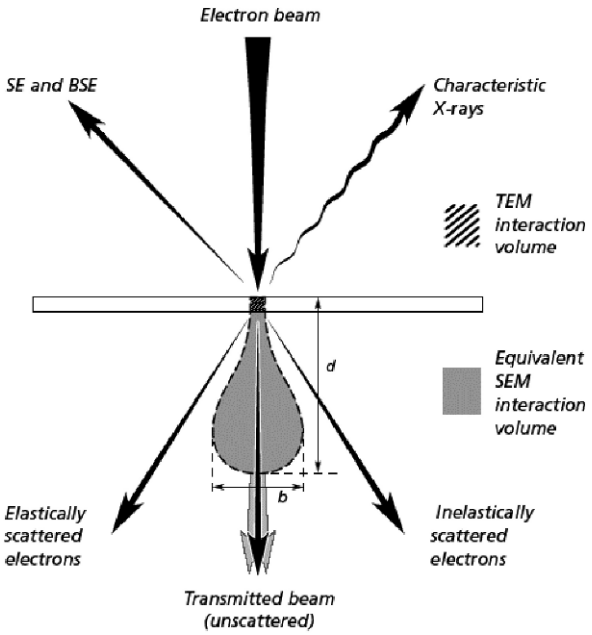

Fig. 17b.1 TEM beam-specimen interactions and signals [7]

17b.2.1 The EDS Technique

The EDS technique is based on the detection of the characteristic X-rays coming out of the sample. These X-rays are detected by a semiconductor device and the principle of detection is the generation of electron-hole pairs in a reverse-biased p-i-n diode. These characteristic X-rays are due to the inner-shell excitation by the incident electron beam. For the *K* lines, an electron is ejected from the inner *K* shell level, leading to the creation of a hole that will be filled with an electron of another outer shell; the excess energy is relaxed by the emission of characteristic X-ray photons. According to the extinction rule, all transitions are not allowed. Figure 17b.2 displays the possible transitions detectable by EDS and the corresponding notation. As an example, when the hole is in the *K* shell and is filled by an electron coming from the *L* shell, characteristic K_α X-ray emission occurs.

Figure 17b.3 displays the schematic representation of a typical EDS detector. This figure shows the locations of the different components of the detector. In particular, a separating window is located between the detector and the TEM. Figure 17b.4 represents the geometry of X-ray detection in the TEM. When the photons arrive in the diode, they excite or ionise the diode atoms according to Mosley's law which states that the energy of the characteristic X-rays is proportional to Z^2 (where Z is the atomic number). The number of electrons $\mathbf{f}(\chi_A) = \frac{1}{\chi_A \rho \mathbf{t}}[1 - \exp(-\chi_A \rho \mathbf{t})]$ or holes (N) created then is directly proportional to the energy of the incoming X-ray (E_0). This results in the simple relation $N = E_0/\varepsilon$, where ε is the energy of creation of the pairs ($\varepsilon = 3.6$ eV for silicon and 2.9 eV for Ge).

Most elements of the periodic table may be identified, except for the very light elements like H, He, Li, and Be. For the elements between B and Na, the nature of the separating window is crucial. Indeed, using a Be window, the first detectable element is Na. Using polymer ultra-thin windows, however, elements down to B can be detected. It should be noted here that the X-ray energy of light elements is very small and as a consequence, the quantity of charges created is small, which makes the detection of the photons difficult. That is why EDS is not very precise in the detection and quantification of light elements. The local composition of the sample can be calculated from the measurement of the area of the different characteristic

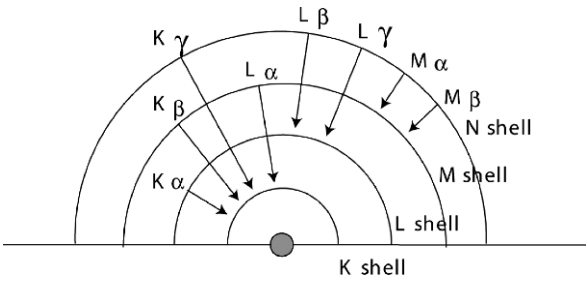

Fig. 17b.2 Possible electron transitions that give rise to *K*, *L*, and *M* characteristic X-rays detectable by EDS

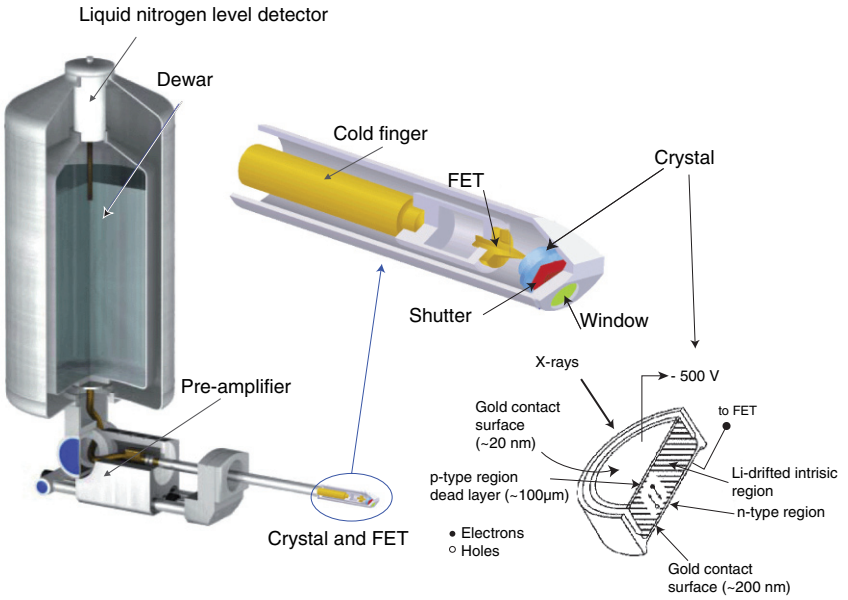

Fig. 17b.3 Schematic diagram of an EDS detector [8]

peaks present in the spectrum. In the STEM mode, where the beam is scanned over the specimen, it is possible to record elemental maps or line profiles.

The detected intensity is given by Eq. (17b.3):

$$I_A = C^{te} \frac{C_A}{A_A} Q_A \cdot \omega_A \cdot z_A \cdot t \cdot I \cdot t_c \cdot \varepsilon_A \cdot f(\chi) \tag{17b.3}$$

where C_A is the weight concentration of element A, A_A the atomic weight of element A, Q_A the ionisation cross-section of the K level of element A, ω_A the fluorescence yield of the K level of element A, z_A the weight of the $K\alpha$ line in the total intensity

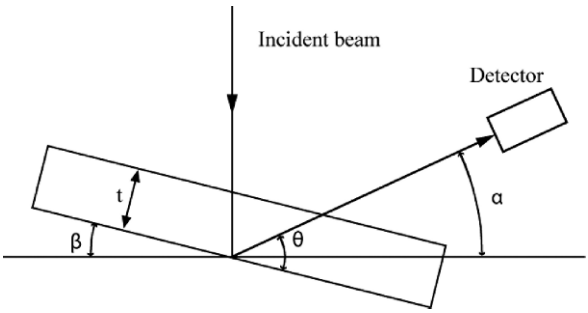

Fig. 17b.4 Geometry of X-ray detection in the TEM. α is the elevation angle of the detector, β the specimen tilt angle, and θ the effective detector take-off angle

of K lines, ε_A the detection efficiency for the $K\alpha$ line of element A, t the thickness of the analysed zone, t_c the counting time, and I the intensity of the electronic beam.

The function $f(\chi)$ is defined as follows:

with $\chi_A = \mathrm{cosec}\,(\theta) \cdot (\mu)^A_{\mathrm{ech}}$, where θ is the effective detector take-off angle.

In the case of thin specimens, quantification is usually performed according to the Cliff-Lorimer method [9]. Then, Eq. (17b.3) yields a proportional relation between the concentration of the elements and the peak areas:

$$\frac{C_A}{C_B} = k_{AB} \frac{(\mu)^A_{ech} \cdot \{1 - \exp[-(\mu)^B_{ech} \cdot \rho t \cdot \mathrm{cosec}(\theta)]\} I_A}{(\mu)^B_{ech} \cdot \{1 - \exp[-(\mu)^A_{ech} \cdot \rho t \cdot \mathrm{cosec}(\theta)]\} I_B} \tag{17b.4}$$

with $k_{AB} \cdot \dfrac{A_A \cdot \omega_B \cdot z_B \cdot Q_B \cdot \varepsilon_B}{A_B \cdot \omega_A \cdot z_A \cdot Q_A \cdot \varepsilon_A}$

N elements present in the spectrum lead to N–1 relations, see Eq. (17b.4). In order to solve the system, it is therefore necessary to add a supplementary relation according to the nature of the sample. Very frequently, the relation used is $\sum \mathrm{C_i} = 1$. The k-factor k_{AB} is specific for each diode, since it takes the detector efficiency into account. The k-factors are usually provided with the analytical system, but if more accuracy is needed, they can be calculated or determined experimentally. Different techniques were developed during the last years to determine experimental k-factors [10, 11, 12, 13, 14]. These equations assume that the sample is homogeneous in the analysed zone. For complex geometries, the Cliff-Lorimer technique is no longer valid and more complicated treatments, such as Monte-Carlo simulations, are required.

17b.2.2 The EELS Technique

Electron energy loss spectrometry (EELS) is the analysis of the energy distribution of the electrons that have interacted inelastically with the specimen [7, 15, 16]. EELS is the spectroscopy of the unoccupied states of an atom, a molecule, or a solid. It reveals the nature of the atoms, their bonding and nearest-neighbour distributions, and their dielectric response. Two types of EELS spectrometers are presently on the market. These are the post-column filter (Gatan Image Filter (GIF) or PEELS) and the in-column filter (Zeiss and JEOL). Figure 17b.5 displays a schematic diagram and a comparison of energy-filtered TEM systems. In both cases, the dispersive system consists of a magnetic prism. The range of energy loss covered by this spectroscopy is 0–3 keV.

Figure 17b.6 displays a typical EELS spectrum. Three regions may be distinguished in the spectrum. The zero loss peak (0–2 eV) that represents about 90% of the total intensity, the low-energy loss region (2–50 eV) that contains the plasmons, and the high-energy loss region (above 50 eV) that contains information on the inelastic interaction of the inner electrons that leave the atom. Additionally, solid-state chemistry results in a fine structure of these core loss features, which alters the

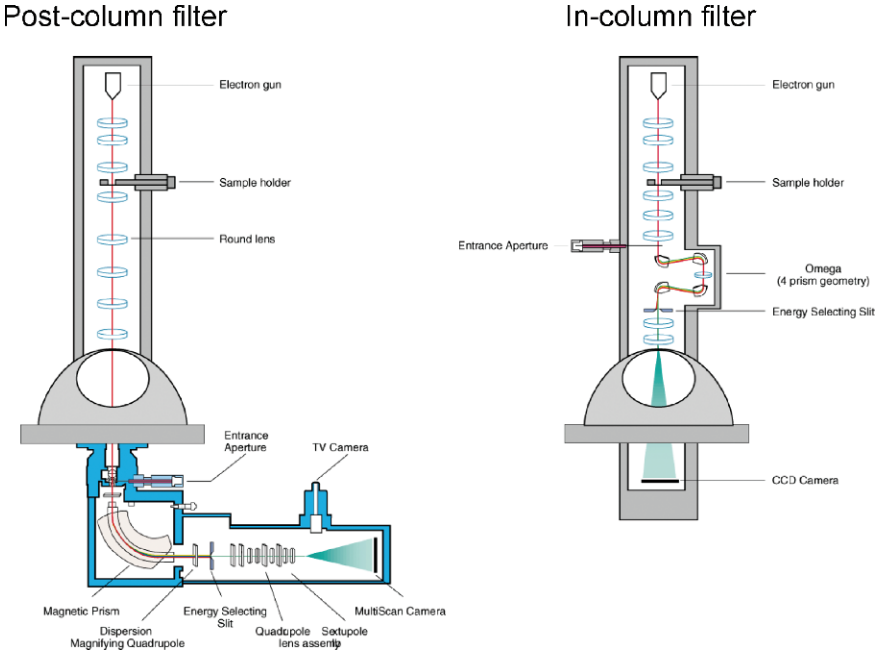

Fig. 17b.5 Comparison of energy-filtered TEM (EFTEM) systems [17]

energies and the shape of the core edge excitation onset. Figure 17b.7 displays the nomenclature of the EELS ionisation edges.

EELS is well adapted to the analysis of light elements, but requires very thin specimens due to the occurrence of plasmons and the decrease of the signal/background ratio. In the TEM mode, two types of EELS analysis can be performed: a spectrum of the illuminated zone can be recorded and with the use of a GIF or an

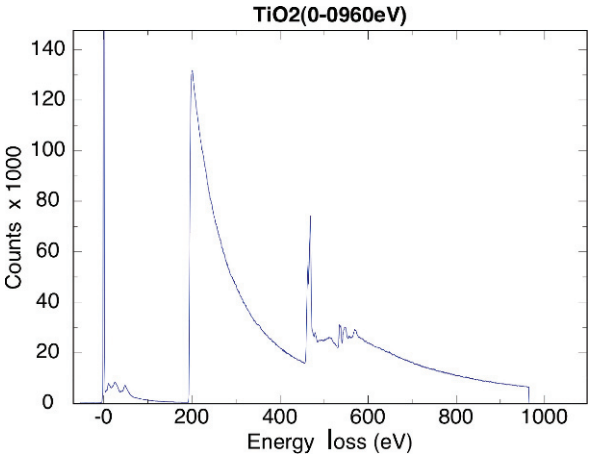

Fig. 17b.6 EELS spectrum of TiO_2 from the EELS atlas [18]

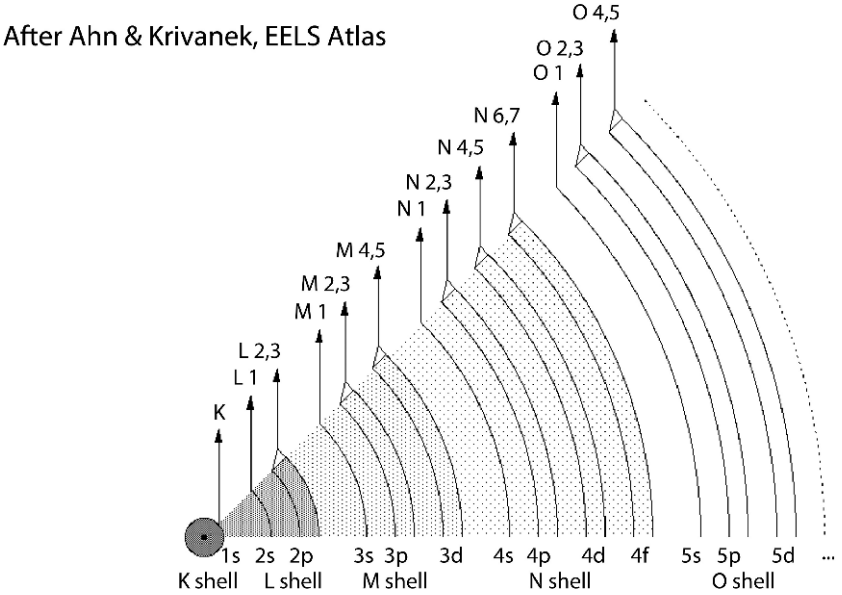

Fig. 17b.7 Nomenclature of EELS ionisation edges [18]

in-column filter, an energy-filtered image is obtained at a specific energy corresponding to a specific feature of the spectrum (edge, plasmon peak, etc.)

The coupling of the STEM technique with EDS and/or EELS analysis allows for the collection of a set of 3D data (*XY* positions and energy) that is called data cube and shown in Fig. 17b.8. This data cube can be filled in two different directions: one energy spectrum at each *XY* position or one image at each energy. In the first case, the energy resolution is privileged; this technique is called STEM spectrum

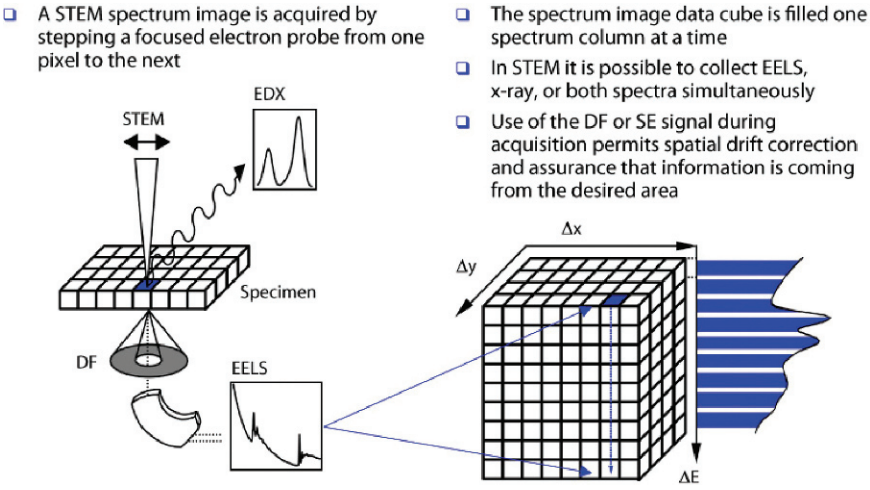

Fig. 17b.8 Simultaneous EELS/EDS data capture [17]

imaging. In the second case, spatial resolution is favoured. This mode is called EFTEM spectrum imaging.

Quantitative micro analysis may be performed to obtain the concentration of the elements. For a full description of the data treatment, it is referred to the work of Egerton [16]. However, EELS gives more information about the local chemistry of the sample based on the edge position and shape. For this purpose, either the fingerprint technique (comparison with reference spectra) or calculation (modelling of the electronic structure) is used.

17b.2.3 Sample Preparation Technique for Air-Sensitive Samples

The possibility of simultaneously obtaining the microstructure and the chemical composition is a major advantage of the TEM technique. That is why it is of interest to apply it to study the mechanisms involved in the absorption and desorption reaction of hydrogen in the light metal alanates. However, several problems are encountered when performing TEM studies of alanates:

- Reactivity of alanates when exposed to air and water
- Extreme beam sensitivity of these materials, with a decomposition of the $NaAlH_4$ compound under the beam (the melting point of $NaAlH_4$ is 183°C [19])

These problems can be circumvented by an appropriate preparation technique and under special beam conditions with certain limitations.

Due to the reactivity of Na alanates with air and water, all material processing has to be performed in a dry Ar glove box. This requirement precludes the use of any powder specimen preparation techniques, such as ultra-microtomy for TEM or resin embedding for SEM and techniques using solvents containing water. In most cases, samples are finely crushed using an agate pestle and mortar, then dispersed (or not) in an inert organic solvent like dry xylene, ether, or benzene. The most simple and common technique for TEM is the dispersion of the powder on a coated grid (formvar, carbon, holey carbon…) and the deposition of the powder onto a SEM stub. However, it is impossible to slice the grains and only the as-cast powder can be studied.

Then, to transfer the specimen to the SEM or the (S)TEM, it is necessary to maintain an Ar overpressure between the glove box and the microscope to prevent moisture contamination. This is achieved by using a dedicated transfer device. The effect of a brief air exposure was shown by Thomas et al. [20] in SEM experiments and mentioned by Andrei et al. [21] in TEM experiments.

17b.2.4 Special Conditions of the Preparation of Beam-Sensitive Samples

From the morphological point of view, beam sensitivity can be demonstrated easily, as shown in Figures 17b.9 and 17b.10, which reveal the degradation of $NaAlH_4$ under the beam. This effect was reported by several authors [2, 19, 20, 22, 23]. To

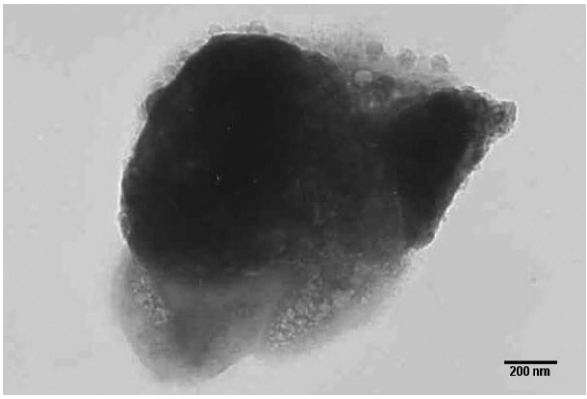

Fig. 17b.9 $NaAlH_4$ doped with 5 mol.% of $TiCl_3$ quenched once with 2.3 wt.% of hydrogen absorbed. TEM bright-field micrograph taken at the beginning of the observation

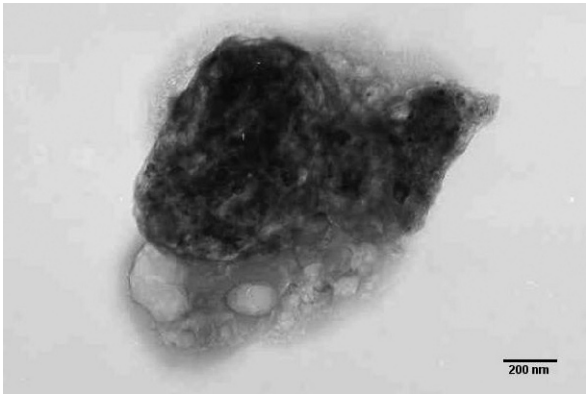

Fig. 17b.10 Same particle after exposure to the electron beam

prevent the decomposition of Ti-doped materials by electron irradiation, Felderhoff et al. [2] worked on dehydrogenated Ti-doped $NaAlH_4$. However, it was shown that it is possible to work on sodium alanate in different stages of the hydrogenation/dehydrogenation reaction [23].

The effect of the electron beam on these beam-sensitive metal hydrides was studied specifically by Jones et al. [24] and Herley and Jones [25]. They followed the course of the decomposition process under the beam by TEM and demonstrated that following a prolonged electron irradiation of sodium aluminium hydride single crystals and subsequent hydrogen evolution, phase separation occurs with a growth of single crystals of sodium metal.

Another very common effect of beam irradiation is evaporation of Na during EDS analysis, as can be seen in Fig. 17b.11. Here, EDS analyses were performed on

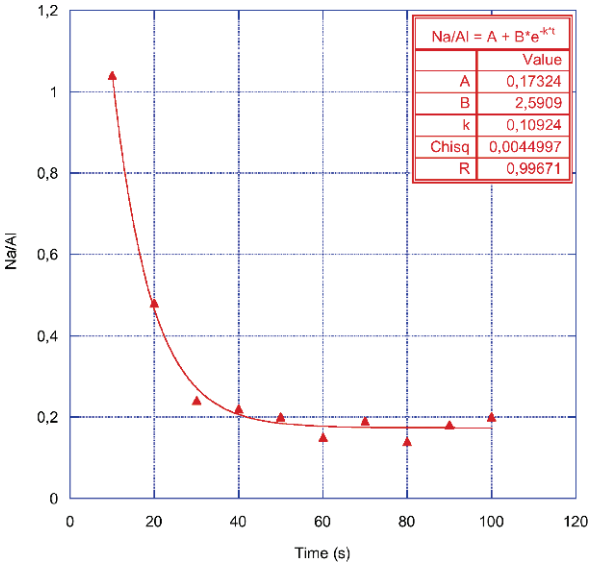

Fig. 17b.11 Evolution of the sodium-aluminium ratio during EDS spectrum acquisitions and curve fitting according to Eq. (17b.5)

$TiCl_3$-doped $NaAlH_4$. Before map acquisition, several point analyses were recorded. In order to study the possible evolution of the sodium content during irradiation, ten spectra were acquired with an acquisition time of ten seconds. A full quantitative analysis of each spectrum was made and Fig. 17b.11 displays the evolution of the Na-Al ratio. The rapid decrease of the Na content is clearly visible, indicating the evaporation of sodium under the beam. The decrease curve can be fitted with a simple exponential decay law expressed by formula 5 which has been derived from the paper of Vesely and Finch [26]. In the case displayed in Fig. 17b.11, $A = 0.17$, $B = 2.59$, and $k = 0.11$.

$$Na/Al = A + B * \mathrm{e}^{-kt} \tag{17b.5}$$

This can also be seen in Fig. 17b.12, the X-ray maps of which were recorded after this experiment. Al $K\alpha$, Ti $K\alpha$, and Na $K\alpha$ maps and bright-field (BF) as well as secondary electron (SE) images were acquired. The electron images give information about the morphology of the sample. The SE image shows the specimen topography, while the BF image is very sensitive to the density, the specimen thickness, and the crystallographic orientation. On the Na map, dark points are clearly visible. These points are not present in the Al map. Moreover, the Ti map reveals that Ti is not uniformly distributed within the sample.

This effect was obtained during the acquisition of EDS data in a SEM experiment by Thomas et al. [20]. They used catalysed $NaAlH_4$, where Na was lost from the surface or near-surface region of the particles during beam exposure. The decomposition of NaH and the evaporation of Na were shown by Felderhoff et al. [2] by EDS

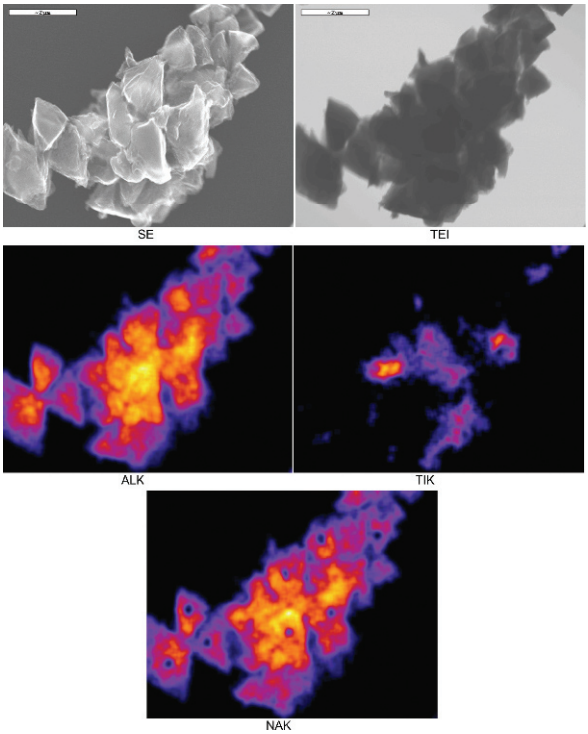

Fig. 17b.12 X-ray map of $TiCl_3$-doped $NaAlH_4$ recorded after point quantitative analysis

measurements in TEM. Such degradation could be reduced by EDS measurement using a low-energy density beam [2].

In order to prevent the decomposition of samples in the hydrogenated state under the beam, special observation conditions involving STEM with fast mapping were applied [27]. Fast mapping involves the recording of images with a resolution of 512×532 pixels and a dwell time of 0.12 ms/pixel. Under these conditions, the morphology of the particles observed was found to be unchanged after mapping. This observation underlines the importance of avoiding keeping the probe for a long time in the same area. For example, ten analyses of one second are not equivalent to one analysis of ten seconds in terms of degradation. These results indicate that the integral dose received by the material is not the only parameter to be considered. The variation of the received dose with time also has to be taken into account. That is why fast mapping with multiple accumulations can be accomplished without degradation during tenths of minutes, whereas a simple ten seconds spectrum acquisition leads to Na evaporation.

Despite the beam sensitivity of the material, however, no charging problems were encountered under the beam [23].

17b.3 SEM/(S)TEM Investigation of $NaAlH_4$ Doped with Different Precursors

Since the discovery of the reversible hydrogen absorption/desorption capabilities [1], very few electron microscopy studies have been made.

SEM and TEM investigations were performed on pure sodium alanate as well as on sodium alanates doped with different dopants, such as carbon nanotubes (CNT) [28], titanium fluoride TiF_3 [22], titanium tetrabutylate $Ti(OBu^n)_4$ [2, 29]; titanium tetrabutylate in combination with zirconium tetrapropylate $Ti(OBu)_4/Zr(OPr)_4$ [20, 30], titanium chloride $TiCl_3$ [2, 23], and Ti cluster (Ti_{13}.6THF) which consists of a core of 13 Ti atoms coordinated by O atoms from tetrahydrofuran (THF) [2, 23]. These studies reveal that the nature of the dopant and the doping method have a great influence on the microstructure and the local chemistry of the material.

Electron microscopy studies can be divided into two categories:

1) Simple morphological characterisation without chemical and/or structural analysis
2) A complete study providing information about the reaction processes

In the following section, the reaction processes of Na-alanate will be presented with respect to the precursor used.

17b.3.1 TiF_3 Precursor

A combination of TEM (bright field, dark field, selected-area electron diffraction (SAED), and HRTEM), STEM, SEM, and EDS was used to study the microstructure of $NaAlH_4$ doped with TiF_3 (2 mol.% TiF_3 by ball milling 30 min, 350 rpm in a Fletcher 7 planetary mill) [22] after the initial ball-milling process and after 15 cycles. EDS maps reveal that there is a low degree of mixing between the TiF_3 and the alanate phase just after the ball-milling process. The inverse process is observed after 15 cycles. Indeed, TiF_3 decomposes and Ti-riched particles are distributed over the alanate phase with a correlation between Al and Ti as indicated by STEM EDS mapping. Additionally, bright-field and dark-field images, together with SAED patterns, provide information about the grain size and potential clustering of particles. It was shown that mechanical ball milling does not break up particles, but rather produces some agglomeration to larger clusters of particles [20].

17b.3.2 $Ti(OBu^n)_4$ Precursor

TEM, SEM, and EDS analysis were performed on dehydrogenated $Ti(OBu^n)_4$-doped $NaAlH_4$ (4 [29] and 2 mol.% [2]; wet chemical doping). SEM images made after the 17th dehydrogenation showed that the material is highly porous and

composed of particles of less than 5 μm in size. Elemental mapping of Na and Al suggested that the doped material in the dehydrogenated state is separated into NaH and Al phases. According to TEM micrographs and EDS analyses of the 2 mol.% doped material, the same two phases were identified in the dehydrogenated sample. In this case, use of TEM demonstrated that Al is crystalline (crystallite size about 10 −1 μm), while NaH is amorphous. According to EDS analysis, Ti is present in the Al phase only and its distribution varies in the range of 0 to about 6 at %.

17b.3.3 $Ti(OBu^n)_4/Zr(OPr)_4$ Precursor

$NaAlH_4$ doped with a tandem catalyst (2 mol.% $Ti(OBu)_4$ and 2 mol.% $Zr(OPr)_4$) by high-energy ball milling (Spex mill, milling time 2 min or 3 hours) was subjected to SEM [20, 30]. Microscopy and compositional analyses were performed in different stages of the decomposition process within the first desorption cycle, which means: fully hydrogenated $NaAlH_4$, partly dehydrogenated to the Na_3AlH_6 composition and fully dehydrogenated to the NaH phase. EDS analysis clearly indicates the presence of a large amount of residual oxygen introduced by the alkoxide process used to dope $NaAlH_4$. Absorption and desorption cycles at elevated temperature reduce the oxygen content, but do not eliminate the residue. As for the $Ti(OBu)_4$ dopant, it was found that mechanical ball milling did not break up particles, but induced the formation of clusters. Absorption and desorption cycles of hydrogen significantly altered the particle morphology, but particle break-up or fragmentation was not noticed even after 5 cycles, in contrast to intermetallic hydrides. At last, decomposition between Al and Na was observed and a correlation between the Ti catalyst and the Al-rich surfaces was noticed after 5 cycles only.

17b.3.4 Ti_{13}.6THF Cluster Precursor

$NaAlH_4$ doped with Ti_{13}6THF [2] (2 mol.% Ti by ball milling 3 hours in stainless steel vial) was investigated in the first dehydrogenated state by TEM. Particles had a globular shape and were occasionally fused with each other. Ti_{13}6THF-doped alanate was characterised by a lower degree of crystallinity in contrast to $Ti(OBu)_4$-doped samples. EDS analyses confirmed the dispersed nature of this material and showed a homogeneous distribution of Ti in the Al phase. Similar results were obtained with dehydrogenated $TiCl_3$-doped $NaAlH_4$ [2] (2 mol.% Ti by ball milling 3 hours in stainless steel vial using a Spex ball mill). In this case, the distribution of Ti in the Al phase was found to be less uniform in comparison to the Ti colloid dopant. The authors pointed out that the amorphous character of the dehydrogenated doped compound could be the result of ball milling. The crystalline Al phase was obtained in the case of $Ti(OBu)_4$ doped by a wet chemical

method. They concluded that both the ball-milling method and the high and homogeneous dispersion of the Ti species due to the use of Ti clusters as dopant might contribute to the extraordinarily high hydrogen discharge and recharging rates observed.

Felderhoff et al. [2] systematically studied the dehydrogenated state. More recently, to supply complementary information on the distribution of Ti in the material in the dehydrogenated state as well as in the hydrogenated case, Léon et al. [23] performed a SEM and (S)TEM characterisation of Ti colloid-doped alanates with 5 mol.% Ti_{13}6THF cluster by ball milling in a silicon nitride vial during hydrogenation/dehydrogenation cycling, during and after the first desorption, during and after the first absorption, and after 2, 8, and 9 hydrogenation cycles. Figures 17b.13 and 17b.15 display the corresponding STEM micrographs. As can be seen, the material is of highly porous character with pores randomly distributed inside the particles, their size ranging from 50 nm–3 µm. This indicates that a decomposition process occurs after ball milling already. Globally, the chemical maps and the elemental line scans displayed in Figs. 17b.13–17b.16 show a strong correlation between the different elements after the ball-milling process. At some points shown in Fig. 17b.14 for the ball-milled sample, however, an increase of sodium can be observed, which is associated with a decrease of Al and Ti. After 2 cycles, HRTEM showed the presence of both Na_3AlH_6 and Al. After the ninth cycle, Ti and Al were not systematically correlated in all grains, as indicated by the EDS analyses displayed in Figures 17b.17 and 17b.18. The analyses always reveal the presence of oxygen within the compounds. It is important to note that the Na content obtained from the quantitative EDS analyses is always underestimated. This is most probably due to the evaporation of Na occurring during the acquisition time necessary to obtain a good counting statistics. Another reason may be the specimen morphology which is far from meeting the requirements of the Cliff-Lorimer method (thin and homogeneous specimen).

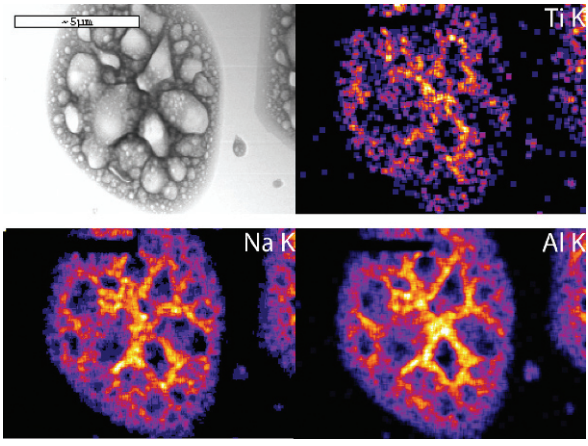

Fig. 17b.13 X-ray maps of 5 mol.% Ti_{13}.6THF-doped $NaAlH_4$ ball-milled 30 min at 600 rpm

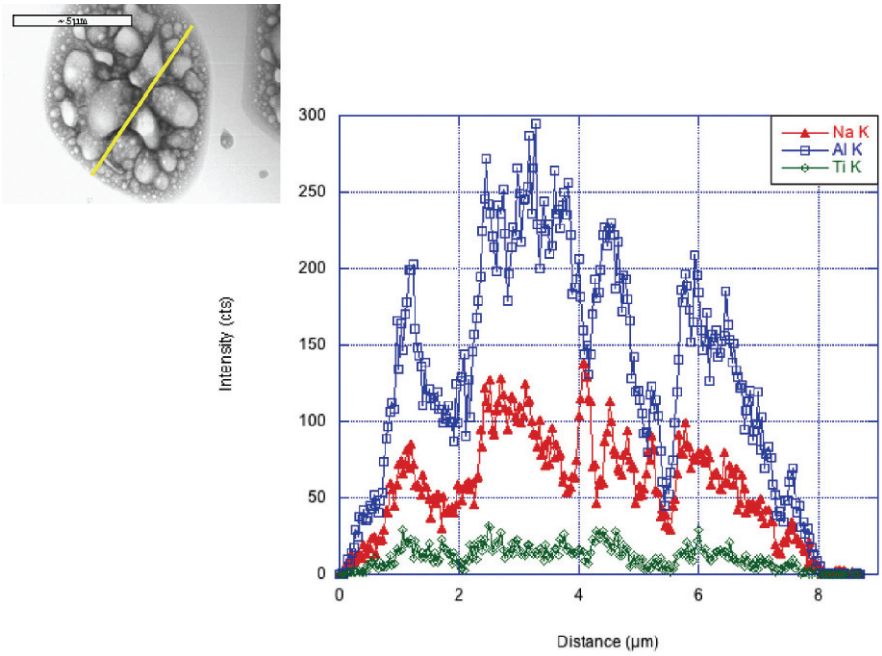

Fig. 17b.14 Elemental line scan on the particle shown in Fig. 17.13

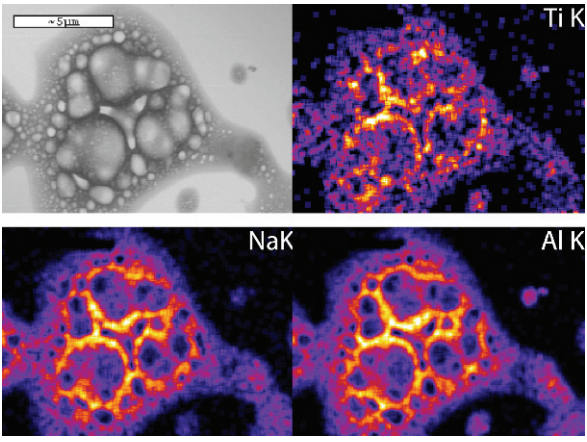

Fig. 17b.15 X-ray maps of 5 mol.% Ti_{13}.6THF-doped $NaAlH_4$ ball-milled 30 min at 600 rpm, then quenched once. 2.6 wt.% of hydrogen are released (T = 150°C, P_{H2} = 0.3 bar)

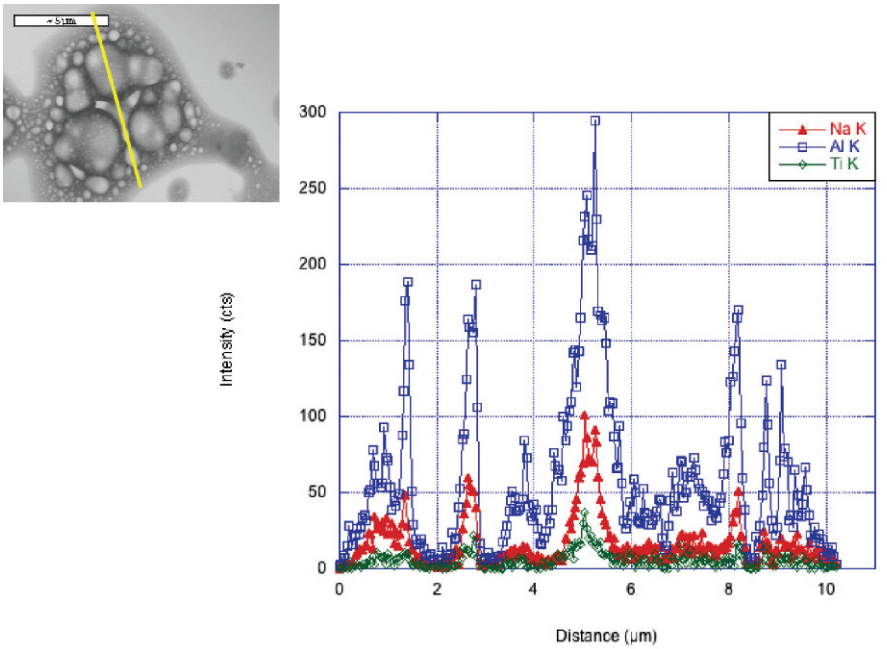

Fig. 17b.16 Elemental line scan on the particle shown in Fig17b.15

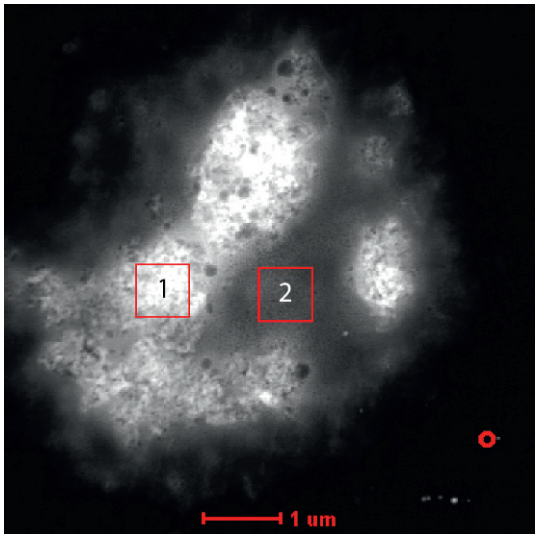

Fig. 17b.17 STEM image of $NaAlH_4 + 5$ mol.% Ti_{13}.6THF, ball-milled 30 min at 600 rpm, after the ninth desorption ($T = 150°C$, $P_{H2} = 0.3$ bar)

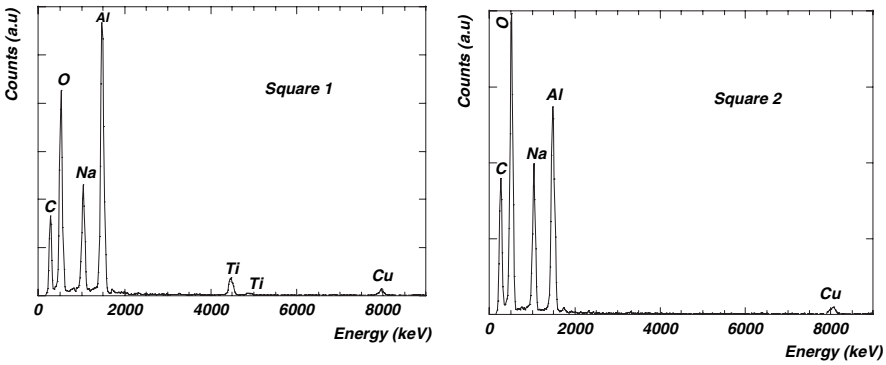

Fig. 17b.18 EDS spectra of zones 1 and 2 highlighted in Fig. 17b.17

17b.3.5 $TiCl_3$ Precursor

Felderhoff et al. performed a TEM study on dehydrogenated $TiCl_3$-doped alanate, which was similar to that done on Ti clusters [2]. Again, lacking crystallinity was recorded and EDS measurements revealed that the distribution of Ti in the Al phase was less uniform that in the case of a Ti cluster dopant.

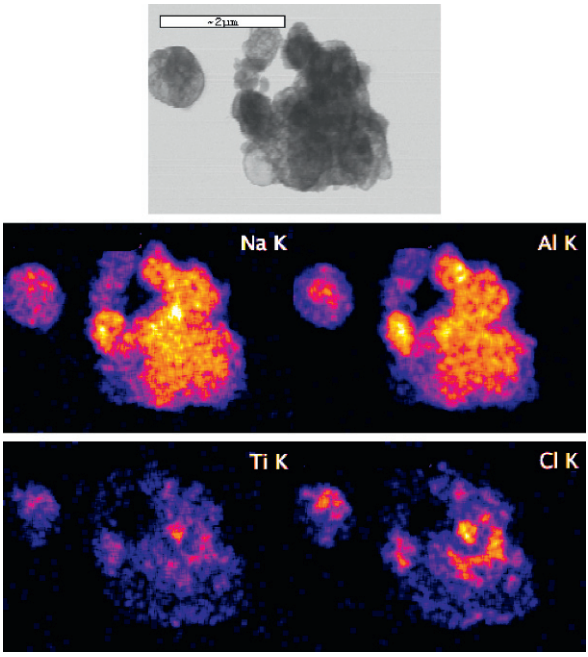

Fig. 17b.19 X-ray maps of 5 mol.% $TiCl_3$-doped $NaAlH_4$ ball-milled 30 min at 600 rpm, showing the inhomogeneous repartition of $TiCl_3$ in the sample

On the other hand, Léon et al. [23] compared 5 mol.% $TiCl_3$-doped alanate during and after the first desorption, during and after the first absorption, and after 2, 8, and 9 hydrogenation cycles. For a direct comparison with Ti clusters, the STEM images and elemental maps recorded at the same step of the hydrogenation/dehydrogenation cycle are displayed in Figs. 17b.19–17b.24. After ball milling, Fig. 17b.19, the morphology of the material is very different from that of the Ti colloid-doped sodium alanate. In the present case, the particles have a dense structure. Then, during desorption, Figure 17b.21, and during absorption, Fig. 17b.23, a porous morphology is found similarly to what has been reported above for Ti clusters. Pores are embedded in the matrix with a size varying from about 20 nm to 7 µm.

The elemental mappings performed on the material showed a less homogenous repartition of the elements in contrast to what had been reported for Ti clusters (Figs. 17b.20, 17b.22, 17b.24). The repartition of the elements constituting the alanate on the one hand and $TiCl_3$ on the other hand is not well correlated, showing an inhomogeneous repartition of the dopant in the material. A closer examination of the repartition of Ti and Cl reveals some local decorrelations indicating an inhomogeneous repartition of these two elements.

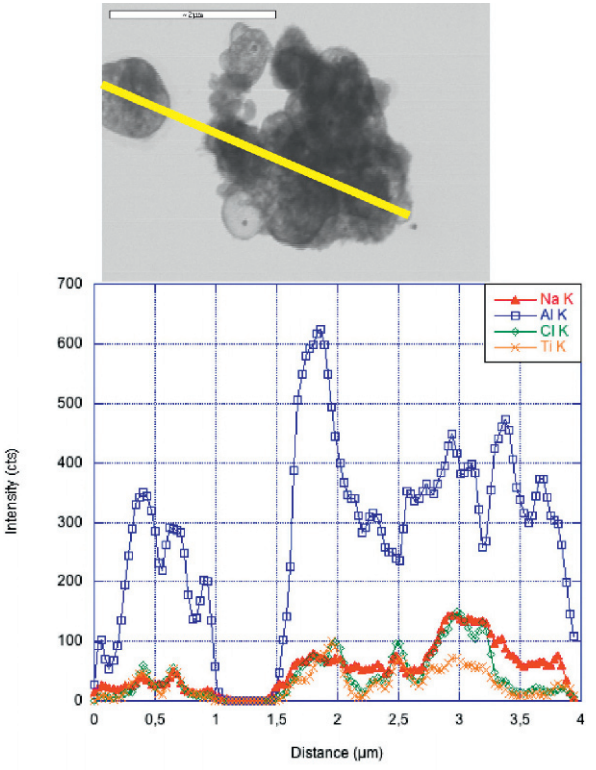

Fig. 17b.20 Elemental line scan on the particle shown in Fig. 17b.19

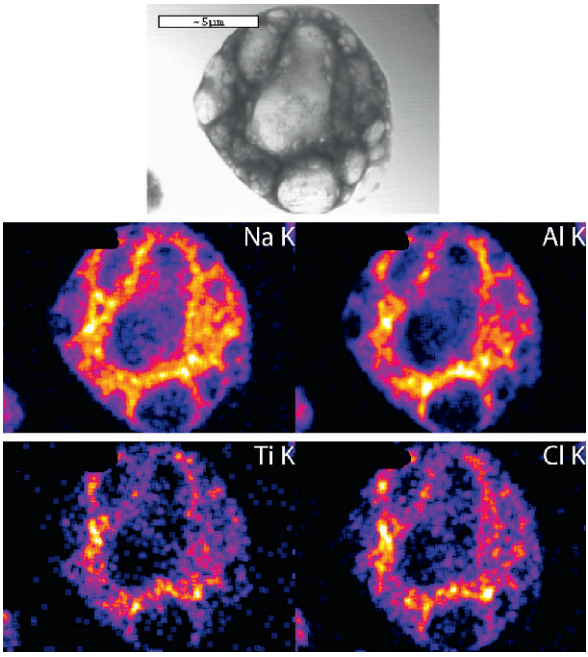

Fig. 17b.21 $NaAlH_4 + 5mol.\%\ TiCl_3$, ball-milled 30 min at 600 rpm, then quenched once. 2.6 wt.% of hydrogen are released (T = 150°C, P_{H2} = 0.3 bar)

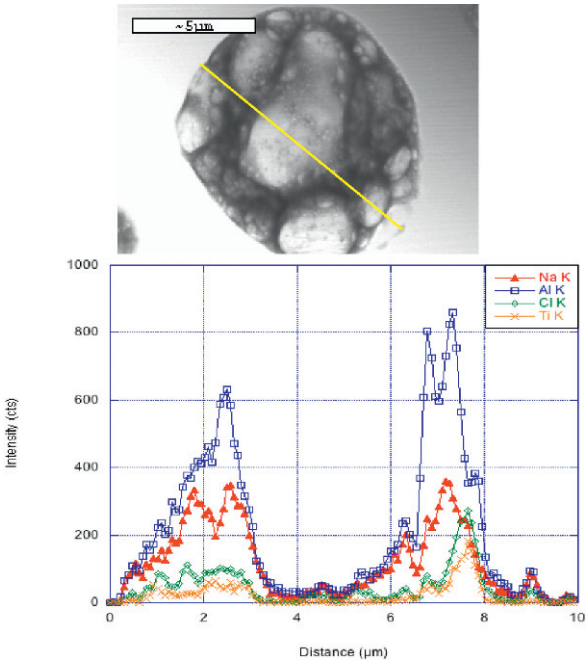

Fig. 17b.22 Elemental line scan on the particle shown in Fig. 17b.21

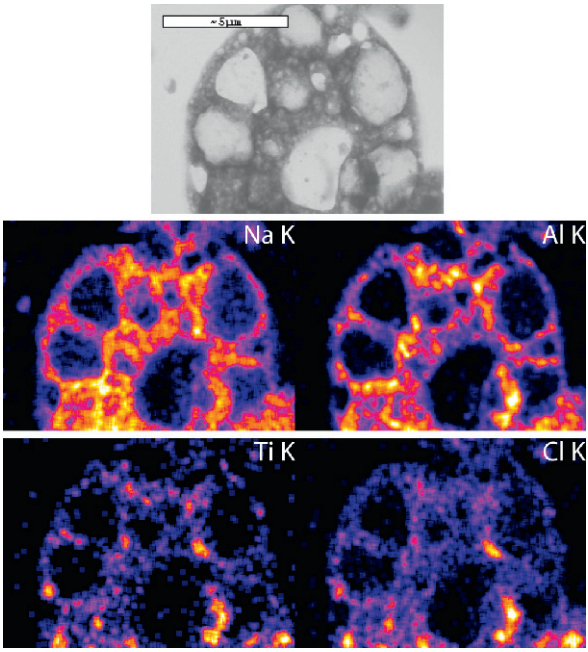

Fig. 17b.23 X-ray maps of $NaAlH_4 + 5mol.\%\ TiCl_3$, ball-milled 30 min at 600 rpm, desorbed, then quenched once. 2.6 wt.% of hydrogen are absorbed (T = 100°C, P_{H2} = 100 bar)

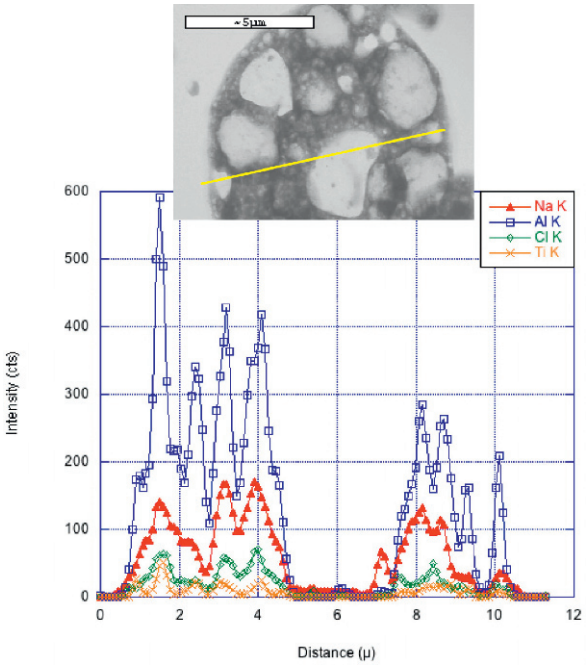

Fig. 17b.24 Elemental line scan on the particle shown in Fig. 17b.23

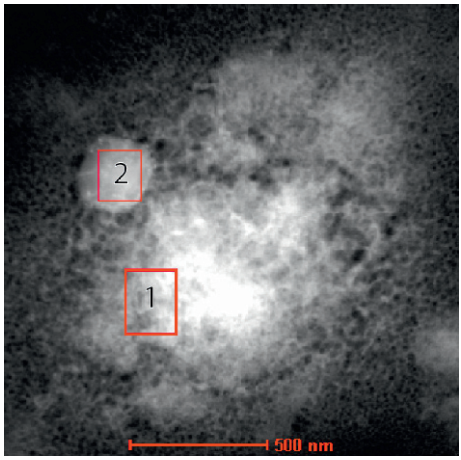

Fig. 17b.25 STEM image of $NaAlH_4 + 5\,mol.\%\ TiCl_3$, ball-milled 30 min at 600 rpm, after the ninth desorption ($T = 150°C$, $P_{H2} = 0.3$ bar)

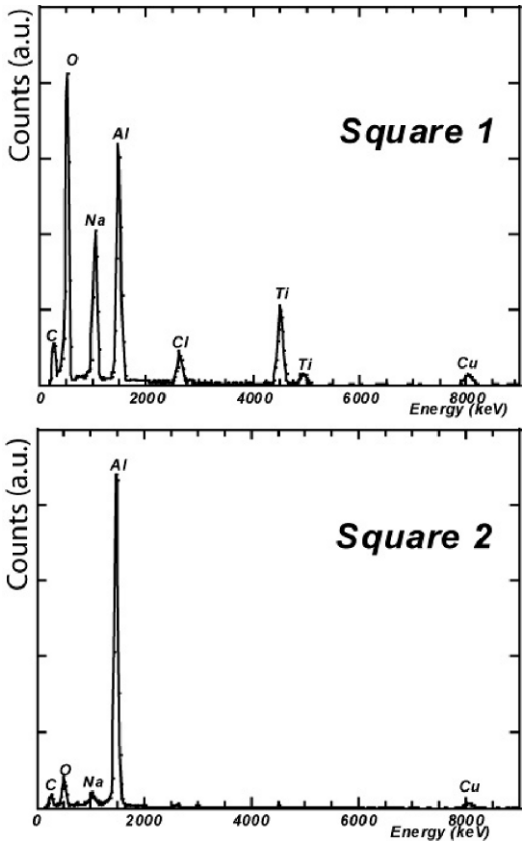

Fig. 17b.26 EDS spectra of zones 1 and 2 highlighted in Fig. 17b.25

After the ninth cycle, a correlation between the Ti species and the elements constituting the alanate is evident from the STEM EDS analyses, as displayed in Figs. 17b.25 and 17b.26. Moreover, spherical crystallites of a few nanometres of an aluminium phase are embedded in the particles, as can be seen in Fig. 17b.25 and in square 2 of Fig. 17b.26. It should be noted that the analyses always reveal the presence of oxygen in the compounds as it is the case for Ti cluster-doped samples.

17b.4 Conclusions

The combination of SEM/(S)TEM and EDS was applied to study Ti-based precursor-doped Na-alanate. In particular, it was shown that Ti is present in the Al phase for most of the Ti precursors. On this basis, it is probable that the location of reaction events (Eqs. 17b.1 and 17b.2) is at the phase boundary between Al and NaH, Na_3AlH_6 or $NaAlH_4$ phases [2, 31]. As mentioned by Felderhoff et al. [2] and Thomas et al. [20], this view is supported by the clean analogy between the $NaAlH_4$ (Eqs. 17b.1 and 17b.2) and Mg_2FeH_6 [32, 33] (Eq. 17b.6) reversible systems.

$$Mg_2FeH_6 \longrightarrow MgH_2\,(Mg) + Fe + H_2\,(3H_2) \qquad (17b.6)$$

In both cases, formation of a homogeneous ternary hydride phase ($NaAlH_4$ or Mg_2FeH_6) takes place via a heterogeneous reaction of a metal (Al or Fe) with a binary metal hydride phase (NaH or MgH_2) and hydrogen. (Instead of MgH_2, also Mg can be used). For the case of Mg_2FeH_6 formation, it was indeed demonstrated by means of TEM-EDS investigations that the reaction takes place at the phase boundary between Fe nucleation sites and the growing Mg_2FeH_6 phase via insertion of a newly formed Mg_2FeH_6 between the two phases [33].

Further information concerning the state of the Ti in the Al phase was obtained by X-ray absorption fine-structure spectroscopy (XAFS) investigations [2, 27, 34]. But there are discrepancies between the interpretations. While Felderhoff et al. [2] conclude that Ti forms an alloy with Al, Léon et al. [27, 34] state that there are no hints indicating the formation of an alloy. More recently, Léon et al. [35] revealed the presence of Ti-Al clusters having a local structure very different from the $TiAl_3$ phase. These divergent results may be due to the fact that XAFS is a global measurement technique. The EELS technique mentioned above may be a tool for the exploration of the local chemistry. This type of study was performed on lithium aluminium hydrides doped with Ti- and V-based additives by Andrei et al. [36]. Thanks to the fingerprint technique, the authors were able to obtain maps not only in terms of elements, but also in terms of chemical bonding. As an example, it was found that Ti is oxidised and also that Ti and Al are not correlated. Such a study on Ti-doped sodium alanates would be of great interest.

References

1. Bogdanovic, B. and M. Schwickardi, *Ti-doped alkali metal aluminium hydrides as potential novel reversible hydrogen storage materials.* Journal of Alloys and Compounds, 1997. **253–254**: pp. 1–9.
2. Felderhoff, M., et al., *Combined TEM-EDX and XAFS studies of Ti-doped sodium alanate.* Physical Chemistry Chemical Physics, 2004. **6**(17): pp. 4369–4374.
3. Loretto, M.H. and R.E. Smallman, *Defect analysis in electron microscopy*. 1975, London; New York: Chapman and Hall; Wiley : distributed by Halstead Press. ix, 134 p.
4. Edington, J.W., *Practical electron microscopy in materials science*. 1976, New York: Van Nostrand Reinhold Co. xii, 344 p.
5. Hirsch, P.B., et al., *Electron microscopy of thin crystals*. 2nd edition ed. 1967, London: Butterworth.
6. Thomas, G. and M.J. Goringe, *Transmission electron microscopy of materials*. 1979, New York, Chichester, Brisbane and Toronto: John Wiley & Sons.
7. Williams, D.B. and C.B. Carter, *Transmission electron microscopy : a textbook for materials science*. 1996, New York: Plenum Press. xxvii, 729 p.
8. Oxford, *Energy dispersive X-Ray microanalysis hardware explained*, in *Technical briefing*. 2002, Oxford Instruments Analytical Ltd. 5 p.
9. Cliff, G. and G.W. Lorimer, *The quantitative analysis of thin specimens.* Journal de Microscopie, 1975. **103**: pp. 203–207.
10. Horita, Z., T. Sano, and M. Nemoto, *Determination of the Absorption-Free kANi Factors for Quantitative Microanalysis of Nickel Base Alloys.* Journal of Electron Microscopy (Tokyo), 1986. **35**(4): pp. 324–334.
11. Horita, Z., T. Sano, and M. Nemoto, *A new form of the extrapolation method for absorption correction in quantitative X-ray microanalysis with the analytical electron microscope.* Ultramicroscopy, 1991. **35**(1): pp. 27–36.
12. Morris, P.L., M.D. Ball, and P.J. Statham. *The correction of thin foil microanalysis data for X-ray absorption effects*, in *Electron microscopy and Microanalysis* Editor: T. Mulvey. 1979. London: Institute of Physics.
13. Van Cappellen, E., *The parameterless correction method in X-Ray microanalysis* Microscopy, Microanalysis, Microstructures, 1990, **1**: p. 1–22.
14. Van Cappellen, E. and A. Schmitz, *A simple spot-size versus pixel-size criterion for X-ray microanalysis of thin foils.* Ultramicroscopy, 1992. **41**(1–3): pp. 193–199.
15. Ahn, C.C., *Transmission Electron Energy Loss Spectrometry in Materials Science and the EELS Atlas*. 2004, Berlin: Wiley-VCH. pp. 1–19.
16. Egerton, R.F., *Electron energy-loss spectroscopy in the electron microscope*. 2nd ed. The language of science. 1996, New York: Plenum Press. xi, 485 p.
17. Gatan, *EELS Imaging & analysis training school*. 2005, Gatan Inc Pleasanton, Ca, USA,. April, 12–15 pp.
18. Ahn, C.C. and O.L. Krivanec, *EELS Atlas*. 1983: Gatan Inc.
19. Schüth, F., B. Bogdanovic, and M. Felderhoff, *Light metal hydrides and complex hydrides for hydrogen storage.* Chemical communications, 2004: pp. 2249–2258.
20. Thomas, G.J., et al., *Microstructural characterization of catalyzed $NaAlH_4$*. Journal of Alloys and Compounds, 2002. **330**: pp. 702–707.
21. Andrei, C.M., et al., *Electron microscopy studies of lithium aluminium hydrides.* Journal of Alloys and Compounds, 2005. **395**(1–2): pp. 307–312.
22. Andrei, C.M., et al., *Electron microscopy studies of $NaAlH_4$ with TiF_3 additive: hydrogen-cycling effects.* Applied Physics A Materials Science Processing, 2005. **A80**(4): pp. 709–15.
23. Léon, A., et al., *SEM and TEM characterization of sodium alanate doped with $TiCl_3$ or small Ti clusters (Ti_{13}-6THF).* Journal of Alloys and Compounds, 2006. **414**(1–2): pp. 190–203.

24. Jones, W., et al., *Evidence for the formation of single crystals of sodium metal during decomposition of sodium aluminium hydride: an electron microscopic study.* Materials Letters, 1984. **2**(5A): pp. 377–379.
25. Herley, P.J. and Jones, W., *Transmission Electron Microscopy of Beam-sensitive Metal Hydrides*. Zeitschrift für Physikalische Chemie Neue Folge, 1986. Bd. 147, S. 147–159, pp. 785–797.
26. Vesely, D. and D. Finch. *Methods for the evaluation of the beam damage*. in *Electron Microscopy and Analysis*. Editor: Dr. G.J. Patlock. 1985: Institute of Physics. pp. 7–14.
27. Léon, A., D. Schild, and M. Fichtner, *Chemical state of Ti in sodium alanate doped with $TiCl_3$ using X-ray photoelectron spectroscopy.* Journal of Alloys and Compounds, 2005. **404–6**: pp. 766–770.
28. Pukazhselvan, D., et al., *Investigations on hydrogen storage behavior of CNT doped $NaAlH_4$*. Journal of Alloys and Compounds, 2005. **403**(1–2): pp. 312–317.
29. Bogdanovic, B., et al., *Metal-doped sodium aluminium hydrides as potential new hydrogen storage materials.* Journal of Alloys and Compounds, 2000. **302**(2000): pp. 149–208.
30. Gross, K.J., G.J. Thomas, and C.M. Jensen, *Catalyzed alanates for hydrogen storage.* Journal of Alloys and Compounds, 2002. **330–332**: pp. 683–690.
31. Bogdanovic, B., et al., *Investigation of hydrogen discharging and recharging processes of Ti-doped $NaAlH_4$ by X-ray diffraction analysis (XRD) and solid-state NMR spectroscopy.* Journal of Alloys and Compounds, 2003. **350**: pp. 246–255.
32. Gennari, F.C., F.J. Castro, and J.J. Andrade Gamboa, *Synthesis of Mg_2FeH_6 by reactive mechanical alloying: formation and decomposition properties.* Journal of Alloys and Compounds, 2002. **339**(1–2): pp. 261–267.
33. Bogdanovic, B., et al., *Thermodynamics and dynamics of the Mg-Fe-H system and its potential for thermochemical thermal energy storage.* Journal of Alloys and Compounds, 2002. **345** (1–2): pp. 77–89.
34. Léon, A., et al., *Chemical State and Local Structure around Titanium Atoms in $NaAlH_4$ Doped with $TiCl_3$ Using X-ray Absorption Spectroscopy.* Journal of Physical Chemistry B, 2004. **108**: pp. 16372–16376.
35. Léon, A., et al., *Evolution of the local structure around Ti atoms in $NaAlH_4$ doped with $TiCl_3$ or Ti_{13}.6THF by ball milling using X-ray absorption and X-ray photoelectron spectroscopy.* Journal of Physical Chemistry B, 2006. **110**(3): pp. 1192–200.
36. Andrei, C.M., et al., *Analytical Electron Microscopy Studies of Lithium Aluminum Hydrides with Ti- and V-Based Additives.* Journal of Physical Chemistry B, 2005. **109**(10): pp. 4350–4356.

Chapter 17c
X-ray Photoelectron Spectroscopy

Dieter Schild

List of Abbreviations

a	Mean atom size or monolayer thickness
A	Mean atom weight ($g\,mol^{-1}$)
ADXPS	Angle-dependent XPS
AES	Auger electron spectroscopy
bm	Ball-milled
CHA	Concentric hemispherical analyzer
d	Layer thickness
d_{esc}	Escape depth
E	Electron energy (eV)

Dieter Schild
Institut für Nukleare Entsorgung, Forschungszentrum Karlsruhe, P.O. Box 3640, D-76021 Karlsruhe, Germany, e-mail: dieter.schild@ine.fzk.de

A. Léon (ed.), *Hydrogen Technology*,

E_B	Binding energy (eV)
E_F	Fermi level
E_V	Vacuum level (free electron level)
ESCA	Electron spectroscopy for chemical analysis
FAT	Fixed analyzer transmission
h	Planck constant ($6.6260693 \times 10^{-34}$ J s)
I	Intensity of elemental line (counts eV s^{-1})
IMFP	Inelastic mean free path
L	Langmuir (10^{-6} Torr · s, equal to 1.334×10^{-4} Pa · s)
M	Molecular weight (g mol^{-1})
N_A	Avogadro constant (6.0221415×10^{23} mol^{-1})
p	Absolute pressure (Pa, N m^{-2}), 1 Torr equals 133.4 Pa
R	Molar gas constant (8.314472 J mol^{-1} K^{-1})
S	Sensitivity factor of elemental line
T	Temperature (K)
UHV	Ultra-high vacuum
V	Molar volume of a gas at standard pressure and temperature
W	Angular distribution factor of photon-electron interaction
XPS	X-ray photoelectron spectroscopy
XRF	X-ray fluorescence
Z	Nuclear charge
β	Asymmetry parameter for atomic orbital
δ	Angle of photon to photoelectron direction
ϕ	Sample work function (eV)
ϕ_S	Spectrometer work function (eV)
λ	Attenuation length
Θ	Emission angle (angle of photoelectron direction to sample surface normal)
ν	Frequency (s^{-1})
ρ	Bulk density (kg m^{-3})

Chemical interaction of a solid material with its environment takes place at its surface, which mostly results in the formation of an interface phase or a layer with a chemical composition differing from that of the bulk. Examples are oxide passive layers on metals, hydroxides on oxides or coatings. To identify elements and chemical bonding in the outermost atomic layers, surface-sensitive techniques like electron spectroscopy for chemical analysis (ESCA), also called X-ray photoelectron spectroscopy (XPS), are applied. Elemental detection and the chemical shifts of elemental lines resulted in the initial term ESCA for X-ray photoelectron spectroscopy. Knowledge of surface and bulk chemistry among others is a prerequisite for improving materials, thin film systems or production processes. XPS gives information about the composition and chemical state of the outermost atomic layers of a sample. Hydrogen dissociation and material performance during hydrogenation/dehydrogenation cycles can be affected by the chemistry of the actual surface. Therefore, knowledge of the state of the surface of highly reactive hydrogen storage materials is of importance in the development of new material.

This chapter will introduce in a first part the XPS method, its theory, and the necessary instrumental setup. A broad range of reviews of XPS theory and applications is available [1, 2, 3] and further reading about this widely used method is encour-

aged. In a second part, to illustrate the type of information which can be extracted from XPS, this technique will be applied to the surface analysis of sodium alanate ($NaAlH_4$) doped with 5 mol% Ti based on $TiCl_3$ or $Ti_{13} \cdot 6THF$ by ball milling in different stages of the desorption and absorption of hydrogen. In the case of Na alanate, $TiCl_3$ [4] and $Ti_{13} \cdot 6THF$ [5, 6] up to now have been the most efficient precursors for the desorption and absorption reaction of hydrogen. However, several questions remain open, such as the way Ti affects the hydrogen absorption and desorption kinetics in doped Na alanate (why are the fastest kinetics and the higher storage capacity obtained with Ti colloid-doped Na alanate only?), the location of titanium (is it at the surface or in the bulk?). It will be shown that XPS helps to understand the reaction to a certain extent at least. For example, it will be demonstrated that the concentration of Ti at the surface decreases with increasing milling time or increasing number of cycles and tends to a constant value of 0.5 at.%. This indicates that titanium does not remain at the surface of the material. Moreover, it will be pointed out that the chemical state of Ti is in the zerovalent state after several cycles under hydrogen. Thus, the results obtained from X-ray absorption spectroscopy will be confirmed and complemented.

17c.1 XPS Technique

In the late 1960s, Kai Siegbahn and his group at Uppsala University of Sweden pioneered X-ray photoelectron spectroscopy (XPS) [7]. In 1981, Siegbahn was awarded the Noble Prize for Physics for his work. Today, XPS is routinely used for analyzing the outermost atomic layers of solid materials. Chemical state properties of the bulk material are also accessible by XPS analysis, if pristine surfaces are prepared by scraping or fracturing solid samples in the ultra-high vacuum of the spectrometer.

17c.1.1 Basics and Definitions

Surface analysis by XPS is performed by irradiating the sample surface using monoenergetic soft X-rays, usually Mg K_α (1253.6 eV) or Al K_α (1486.6 eV), and analyzing the photoelectrons emitted from the atomic core levels. Figure 17c.1 displays the energy level scheme for the photo-ionization of a core shell and subsequent relaxation of the ion by emission of characteristic X-rays and Auger electron. Once the photo-ionization has occurred, the kinetic energy of the ejected photoelectrons is determined by the analyzer. The kinetic energies of the photoelectrons are defined by Eq. (17c.1):

$$E_K = h\nu - E_B - \Phi_S \tag{17c.1}$$

where E_K is the measured energy of the photoelectron, $h\nu$ is the X-ray energy, E_B is the binding energy of the core shell electron in relation to the Fermi level, and

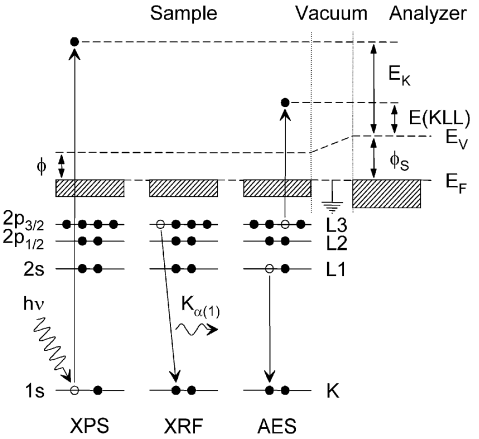

Fig. 17c.1 Energy level scheme for photo-ionization and subsequent relaxation by emission of characteristic X-rays and Auger electron. Electron energy is determined by the analyzer. The hatched areas represent the conduction bands

XPS: photoelectron generation by X-ray photo-ionization of a core level
XRF: emission of characteristic X-rays
AES: emission of an Auger electron
Φ: sample work function
Φ_S: spectrometer work function
E_F: Fermi level
E_V: vacuum level (free electron level)

Φ_S is the spectrometer work function. The work function represents the energy necessary to promote electrons from the uppermost occupied electronic level of a solid ($T = 0\,\mathrm{K}$) to the unbound state of zero kinetic electron energy, termed vacuum level.

The Fermi levels of conducting samples and of the spectrometer couple in electric contact. Electrons emitted from the sample surface and detected at the analyzer finally experience the vacuum level of the spectrometer (Fig. 17c.1). The Fermi level thus is the appropriate reference for the binding energies of elemental lines and corresponds to zero binding energy by definition. Experimentally, the binding energy scale of the spectrometer is adjusted to the zero point by measuring the conducting band of a metal with well-defined Fermi edge, for example Ag.

The photo-ionized atom can relax either by filling the hole with an electron from a higher level associated with emission of characteristic X-rays, for example $E(K_{\alpha(1)}) = E(K) - E(L_3)$, or by the Auger process as illustrated in Fig. 17c.1. Emission of characteristic X-rays dominates for heavy elements, and the Auger process occurs preferentially with light elements. The Auger process consists of filling the core hole by an electron from a higher level without emission of radiation, with the surplus of energy leading to the ejection of an electron, the Auger electron, from an outer shell or from the valence band. If the initial core hole is generated by excitation without ionization, say from core level to valence band, a single charged ion is

generated after Auger electron ejection. If the Auger electron is emitted from an ion, a twofold charged ion is left and X-ray excited Auger electron lines are observed in the spectra with the following kinetic energy:

$$E(\mathrm{KLL}) = [E(K) - E(L_1)] - E^*(L_{2,3}) - \Phi_S \tag{17c.2}$$

where E(KLL) is the measured energy of the Auger electron, $E(x)$ are binding energies of the electron levels involved in relation to the Fermi level, E^* denotes binding energy of an electron level of the ion, and Φ_S is the spectrometer work function. Due to the multitude of electronic transitions allowed, for example up to nine for the KLL type, Auger lines result in extended features in the spectra.

XPS spectra are plotted in terms of electron intensity versus binding energy E_B. In this way, the elemental lines have the same binding energy, irrespective of the exciting X-ray energy used. Electronic core level energies are different for each element according to their nuclear charge. Therefore, the elements that compose a material can be identified by measuring the binding energy of photoelectron lines. The binding energy represents the energy difference between the initial and the final state of the photo-ionization process. Each final state has its own probability or cross section defining different sensitivities for each of the elemental lines.

In XPS, the photoelectron and Auger electron lines can be distinguished by recording spectra at two different X-ray energies. Indeed, Auger electron lines are identified by their shift according to the difference of X-ray energies used.

17c.1.2 Determination of Atomic Concentration

Atomic concentrations are calculated from elemental line intensities using their peak areas after background subtraction and relative sensitivity factors which are proportional to the photo-ionization cross section of the core level electrons. The relative percentage C of an element i is given by Eq. (17c.3):

$$C_i = \frac{I_i}{S_i} \Big/ \sum_n \frac{I_n}{S_n} \times 100 \tag{17c.3}$$

where S_x are the sensitivity factors and I_x are the intensities of elemental lines (counts eV s^{-1}). Experimentally determined sensitivity factors are usually tabulated in relation to the sensitivity of the 1s line of fluorine set to one. All elements can be determined semi-quantitatively, except for H and He, as their photo-ionization cross sections are too low to be detected by XPS. The detection limit is around 2 and 0.02 at.% for light and heavy elements, respectively.

Moreover, quantification requires the asymmetry parameters of the photon-electron interaction and the analyzer transmission function.

Interaction of unpolarized X-rays with randomly oriented atoms is given by the angular distribution factor W which describes the geometric asymmetry of the photoemission. W for core levels is independent of the molecular structure and defined as follows:

$$W = \left(4\pi\left[1 - \frac{\beta}{4}\left(3\cos^2\delta - 1\right)\right]\right)^{-1} \quad \text{(17c.4)}$$

where β is the asymmetry parameter describing the anisotropy of photo-emission and δ is the angle between photon, i.e. X-ray source, and the photoelectron direction, i.e. the analyzer.

Reilman et al. [8] calculated the asymmetry parameters for atomic orbitals. For *S* orbitals, $\beta = 0$ and the photoemission is isotropic. For $\delta = 54.7°$ in angle between the X-ray source and analyzer direction (photoelectron detection), W is $(4\pi)^{-1}$ for all orbitals and no asymmetry correction is needed ("magic angle"). For angles different to 54.7° the asymmetry parameter is taken into account in the calculation of the atomic concentrations by multiplying the sensitivity factors S_x for 54.7° by W_x.

Transmission of electrons through the analyzer depends on electron energy, the type of analyzer, and operating parameters. Consequently, the sensitivity factors are adjusted according to the transmission characteristics of the individual analyzers. Semi-quantitative results (within 10–20%) of atomic concentrations are achieved without additional standards.

17c.1.3 Spectral Features

Figure 17c.2 displays the XPS survey spectra of Na alanate doped with Ti based on $TiCl_3$ by ball milling for 2 minutes, measured using Al K_α mono, Fig. 17c.2(a),

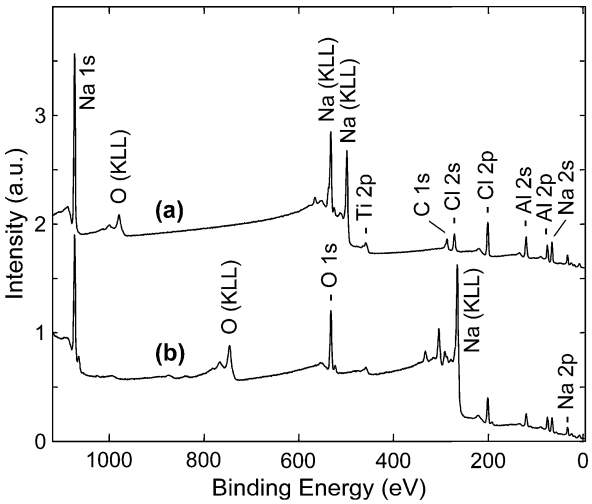

Fig. 17c.2 XPS survey spectra of $NaAlH_4$ doped with 5 mol% Ti on the basis of $TiCl_3$ by ball milling for 2 minutes, measured using Al K_α mono (a) and Mg K_α (b). Photoelectron lines have same binding energies in (a) and (b), Auger lines are shifted by the difference of X-ray energies, i.e. 233 eV in this case. Na (KLL) lines superpose the O 1s line at (a), C 1s and Cl 2s at (b)

and Mg K_α, Fig. 17c.2(b). They are composed of photoelectron lines of core levels like Na 1s or Ti 2p, X-ray excited Auger lines like O (KLL) or Na (KLL), and the valence band near to zero binding energy.

17c.1.3.1 Elemental Lines and Chemical Shifts

Core level ionization of p, d, or f levels results in spin-orbit splitting into $p_{1/2}$, $p_{3/2}$, $d_{3/2}$, $d_{5/2}$, $f_{5/2}$, and $f_{7/2}$ doublets with relative intensity ratios of 1:2, 2:3, and 3:4, respectively. Each ratio is determined by the degeneracy factor (2J+1), where J is the total spin of the electronic core level. Thus, binding energy, splitting energy, and intensity ratios of the doublets provide for a distinct elemental identification.

Small variations in binding energies (typically <10 eV) of photoelectron lines, called chemical shifts, are due to the differences in the chemical potential and the polarizability of the compounds. Chemical shifts often are dependent on the valence state, electronegativity, proton affinity, electron density, and final state effects, i.e. electronic relaxation. For example, enhanced electron density on the atom that is being photo-ionized will decrease the measured binding energy and vice versa. Chemical shifts are detected by narrow scans of the elemental line spectra at high-energy resolution of the analyzer. If various bonding types of an element are present simultaneously, curve fits to the spectra yield chemical shift values and the fraction of each bonding. By comparing the chemical shifts with the references, the chemical states may be identified. Well-established compilations of chemical shift data can be found in [9, 10].

17c.1.3.2 Satellites, Plasmons, and Multiplet Splitting

Upon core level ionization and subsequent relaxation of valence electrons, the ion may be left in an electronically excited state some eV above ground state. The kinetic energy of photoelectrons is then reduced by the excitation energy, generating discrete structures, called shake-up satellites, on the high binding energy side of the main photoelectron peak. Spacing between the main peak and satellite corresponds to the excitation energy of the ion, ranging up to 15 eV.

Electrons passing through a conducting material can excite quantized collective oscillations of the conducting electrons, called plasmons. Additional lines separated by the excitation energy of one or more plasmons, called plasmon loss lines, are located at equidistant spacings higher than the main lines binding energies. Plasmons confined close to the surface result in surface plasmon loss lines with lower intensity and excitation energies smaller by a factor of 0.71 compared to the bulk plasmons.

Ionization of atoms with spin due to unpaired valence electrons can create holes in several ways. Coupling of unpaired electrons results in numerous final state configurations of different energies due to splitting of the multiple. Photoelectron lines become asymmetric and consist of multiple components which are unresolved in conventional XPS.

17c.1.3.3 Valence Band

Narrow scans of the valence band, typically in the range of (0-20) eV, are measured preferably using monochromatic X-ray excitation. Photo-ionization cross sections at the X-ray energies used in XPS are lower for the valence electrons than for the core level electrons.

The valence band spectra recorded by XPS represent closely the initial filled density of valence states, molecular orbitals, and energy bands (i.e. energies of the photo-ionized valence electrons are within the continuum). However, energy resolution actually is not high enough to resolve the multitude of valence states.

The valence band spectra are often used as fingerprint spectra in addition to core level spectra. The presence or absence of conducting bands at the Fermi level helps to identify conductors and insulators. Elements cannot be identified by analysis of the valence band spectra. All valence states of the elements present within the probed depth contribute to the valence band. To prevent interference with contributions from surface contamination, clean and well-defined samples are mandatory for valence band investigations.

17c.1.3.4 X-ray Satellites and Ghost Lines

Apart from the characteristic $K_{\alpha 1,2}$ main line, use of non-monochromatic X-ray sources results in less intense $K_{\alpha 3}$, $K_{\alpha 4}$, $K_{\alpha 5}$, $K_{\alpha 6}$, K_{β} X-ray lines at higher photon energies, termed X-ray satellites. The intensities and spacings of X-ray satellites in relation to the main line are well known and photoelectron lines caused by X-ray satellites are subtracted from the spectrum directly by the software for XPS data analysis.

Occasionally, electrons from the cathode of the X-ray source may excite characteristic X-rays of materials near the anode. Low-intensity photoelectron spectra due to spurious X-ray excitation, so-called ghost lines, superpose the main spectrum with a displacement equal to the difference in X-ray energies. For example, Mg K_{α} and Al K_{α} excited photoelectron spectra at dual anode (Mg, Al) X-ray sources differ by 233 eV.

17c.1.4 Surface Sensitivity

Soft X-rays in the range of 1 keV used in XPS penetrate into a solid by up to some micrometers in depth and ionize atoms within this volume. In this volume, the interaction of electrons with atoms of the solid is higher than the interaction of photons having the same energy. Therefore, electron intensity passing through a thin solid layer at discrete electron energy decreases nearly exponentially with layer thickness. The Lambert-Beer law describes homogeneous attenuation:

$$I = I_0 \cdot \mathrm{e}^{-d/\lambda \cos\Theta} \tag{17c.5}$$

where I_0 is the incident intensity of electrons (energy E_0), I the emergent intensity, d the layer thickness, λ the attenuation length determined by the material, and Θ the angle of electron direction to surface normal.

The angle Θ is termed emission angle and d/cosΘ is the path length. In XPS, the fraction F of electron intensity leaving the surface at an angle Θ under the depth z is given by integration of Eq. (17c.5): $F = 1 - e^{-z/\lambda \cos\Theta}$. Within $z = \lambda \cdot \cos\Theta$, termed escape depth d_{esc}, 63% of spectral information are generated. From a depth of $3d_{esc}$ which is the sampling depth or information depth, 95% of the spectral information originates.

In the range of kinetic electron energy common to XPS (> 150 eV), λ varies roughly as $E^{0.5}$, giving an attenuation length of a few nanometers. Initially, Seah and Dench (1979) [11] proposed empirical relationships derived from experimental data to describe the dependence between attenuation length, electron energy, and material properties:

$$\lambda_m = 538E^{-2} + 0.41(a \cdot E)^{0.5} \qquad \text{(for elements)} \tag{17c.6}$$

$$\lambda_m = 2170E^{-2} + 0.72(a \cdot E)^{0.5} \qquad \text{(for inorganic compounds)} \tag{17c.7}$$

where λ_m is in units of monolayers or may be expressed in units of nanometers by $\lambda_n = a \cdot \lambda_m$. E is the electron kinetic energy (eV) in the range of up to 6 keV and a denotes the monolayer thickness or mean atomic size:

$$a = \left(\frac{A}{\rho \cdot N_A}\right)^{1/3} \times 10^8 \text{ (nm)} \tag{17c.8}$$

where A is the mean atomic weight (g mol^{-1}), ρ the bulk density (kg m^{-3}), and N_A the Avogadro constant.

First, attenuation was interpreted only by means of inelastic scattering of the electrons. Consequently, the attenuation length λ was the equivalent of the inelastic mean free path (IMFP). Detailed analyses in subsequent years revealed that attenuation does not exactly follow an exponential law. It was shown that elastic and inelastic scattering processes contribute to electron intensity attenuation [12]. The inelastic mean free path (IMFP) is defined by the mean distance that an electron with a given energy travels until inelastic scattering occurs and changes its energy. Elastic scattering redirects travelling electrons and the attenuation of intensity occurs along the initial direction of propagation. Thus, attenuation length λ in reality is smaller than the 'real' IMFP value by around 10 to 25%.

Based on Monte-Carlo simulations, Cumpson and Seah [13] developed a semi-empirical formula for λ, termed CS2 (Eq. 17c.9), which takes in account the elastic electron scattering in the range from 50 eV to 2 keV

$$\lambda = 0.316 \cdot a^{3/2} \left[\frac{E}{Z^{0.45}\,[\ln(E/27) + 3]} + 4\right] \quad \text{nm} \tag{17c.9}$$

where a is the mean atom size, Z is the mean nuclear charge, and E electron energy.

If the average lattice parameter is not known, a formula termed CS1 in units of monolayers can be used as follows:

$$\lambda = 0.16\left[\frac{E}{Z^{0.45}\left[\ln\left(E/27\right)+3\right]}+4\right] \quad \text{monolayer} \qquad (17c.10)$$

At an emission angle Θ of 45°, errors in the measurement of overlayer thickness due to elastic scattering are minimized and the Lambert-Beer law gives useful results. Moreover, if the mean atom size is known, CS2 produces more accurate results than CS1.

Only electrons that are unscattered or underwent elastic scattering leave the top surface without energy loss and contribute to intensities of elemental lines in the spectra. Consequently, XPS is intrinsically surface-sensitive, irrespective of sample roughness. Electrons that have experienced energy loss by inelastic processes contribute to the background arising at the high binding energy side of elemental lines.

Information depth can be changed by variation of the emission angle, i.e. tilting the sample. This technique is used in angle-dependent XPS (ADXPS) for non-destructive depth profiling of the outermost atomic layers. Alternatively, depth information can be obtained in a non-destructive manner by varying the photoelectron energy by changing the X-ray energy or by analyzing elemental lines of the same element from different core levels.

17c.1.5 Charge Referencing

Insulator surfaces are charged positively during XPS analysis due to the emission of photo- and Auger electrons. This effect apparently increases the binding energies of elemental lines. In addition, elemental lines may broaden by differential or non-uniform charging of rough or inhomogeneous surfaces. Samples irradiated by monochromatic X-rays may easily be charged up to some 100 eV without neutralization. The charging process reaches a steady state either by the gain of conduction electrons or thermal electrons from the vacuum or by application of a neutralizer. The standard setup for neutralization uses either an electron flood gun with adjustable intensity and energy (<5 eV) or a combination of flood gun with low-energy ions. Over-compensation by an electron flood gun leads to negative charging of the surface repelling the emitted electrons. The enhanced kinetic energy of the electrons results in a shift of the elemental lines to lower binding energies. Optimum charge compensation is achieved, if sharp peaks are attained. However, absolute neutralization of the surface resulting in true binding energy values cannot be ensured.

The standard, non-monochromatic (dual-anode) X-ray source adjacent to the sample is equipped with an Al window of micrometer thickness for definition of the electric potential within the X-ray source and prevention of stray-electron escape. The intensity of secondary electrons leaving the Al window proportionally to the X-ray flux allows for a reduction of sample charging.

Charge correction of spectra during data processing is performed by referencing to a line of known binding energy. A common method is to use the *C* 1s line of adventitious hydrocarbons sorbed at nearly all surfaces from the laboratory environment or vacuum pump oil vapors. Determination of the apparent binding energy of *C* 1s (C_xH_y) indicates the amount of charging with respect to the reference value of 284.8 eV. Alternatively, an elemental line with known binding energy can be used as internal standard, either directly from the sample or by addition of a moiety of reference material to the surface [14, 15].

17c.1.6 XPS Sputter Depth Profiling

XPS sputter depth profiles are measured by cycling of material removal from the sample surface by ion beam sputtering and subsequent recording of spectra. Chemical states and elemental composition are likely to be changed by sputtering, but still a lot of information can be obtained.

The etch rates, expressed in $nm \cdot s^{-1}$, are dependent on the sample material, ion energy, ion type, ion current density, and ion incidence angle (surface normal to incident ion beam). Sputter depth profiles are usually presented versus sputter time, as the etch rate varies with actual surface composition. In order to convert the sputter time to the depth scale, knowledge of the etch rates at each step of the profile is required. Most of the ion beam parameters are known by the instrumental setup and the ion beam density is measured using a Faraday cup. The etch rate and depth resolution can be estimated by depth profiling of thin films of known composition and thickness under the same experimental conditions than the investigated sample, like Ta_2O_5 on Ta, SiO_2 on Si, or Ni/Cr multilayers. Using elemental sputter yields [16, 17, 18], defined as the ratio of the number of atoms removed from the surface to the number of incident ions, etch rates can be calculated according to the actual surface composition. Depth resolution is defined by the step width at the interface in relation to film thickness. The step width is the difference in depths, for example, with the oxygen elemental line intensity being 84% and 16% of the initial value.

Extended depth profiling results in an artificial elemental composition caused by the different elemental sputter yields. Elements lighter than the incident ions are preferentially sputtered from the surface.

In practice, a focused beam of low energy ions (500 eV–3 keV) scans the sample surface during sputtering. To avoid signal contribution from the edge of the sputter crater, the scan area has to be more extended than the XPS analysis area. Due to the relatively large sputtered area necessary for XPS depth profiling, the etch rates typically amount to a few nanometers per minute and depths of profiles are limited to about 1 μm.

Sample rotation during ion beam sputtering, termed Zalar rotation [19], with about one revolution per minute around the center of the analysis area, ensures uniform removal of material. Zalar rotation diminishes preferential sputtering and

improves depth resolution especially for rough surfaces. Depth resolution is optimum at an ion incidence angle of about 50°–60° and a similar angle of photoelectron emission for low information depth.

17c.2 Instrument

17c.2.1 The Need for Ultra-high Vacuum

Experimental techniques using electrons or ions are operated at pressures below 10^{-4} Torr (1.3×10^{-2} Pa) to increase the mean free path in order to allow the photoelectrons to reach the analyzer, for example, without scattering.

From the kinetic theory of gases, the flux Z, i.e. the number of molecules striking a surface of 1 m^2 per second, is given by the Herz-Knudsen equation:

$$Z = \frac{N \cdot \bar{u}}{4V} \tag{17c.11}$$

where N/V is the number of gas molecules per molar volume and $\bar{u}$ is their mean thermal velocity. Using the Maxwell-Boltzmann distribution, the mean thermal velocity $\bar{u}$ becomes

$$\bar{u} = \sqrt{\frac{8RT}{\pi M}} \tag{17c.12}$$

where R is the molar gas constant (8.314 J mol^{-1} K^{-1}), T the absolute temperature (K), and M the molecular weight of the gas molecules (g mol^{-1}). By combining Eqs. (17c.11) and (17c.12) with the ideal gas equation $pV = nRT$, the flux Z can be written as follows:

$$Z = \frac{N_A \cdot p}{\sqrt{2\pi MRT}} \approx 2.6 \times 10^{24} \frac{p}{\sqrt{MT}} \quad [\mathrm{m^{-2}s^{-1}}] \tag{17c.13}$$

where p is the gas pressure in units of Pa (N m^{-2}) and $N = nN_A$. 1 Torr is equal to 133.4 Pa. N_A is the Avogadro constant equal to 6.022×10^{23} mol^{-1}.

For example, a monolayer of water (M = 18 g mol^{-1} and T = 300 K) with about 10^{19} molecules per square meter results in a flux of $Z \approx (3.5 \times 10^3) \cdot p$ monolayer per second. This indicates that a monolayer is formed in 3 seconds at 10^{-4} Pa, if every impinging water molecule sticks to the surface. At 10^{-7} Pa, a monolayer can therefore be built up within three quarters of an hour. This is the upper pressure limit for XPS analysis of a pristine surface.

A convenient dosage unit often used for gas exposure measurements is Langmuir (L). 1 Langmuir represents a pressure-time integral of 10^{-6} Torr·s, equal to 1.334×10^{-4} Pa · s, which is roughly equivalent to the formation of an adsorbate coverage of one monolayer, if every impinging gas molecule sticks to the surface. For example, one monolayer of water is formed in 3 seconds at 10^{-4} Pa corresponding to the dosage of 2.2 L of water vapor.

In the ultra-high vacuum regime (UHV), the residual gas usually is composed of H_2, H_2O, CO, CO_2, and hydrocarbons according to the experimental setup. Moreover, the samples that are not prepared in situ under ultra-high vacuum are often covered to some extent by adventitious hydrocarbons, oxides or hydroxides and, hence, less reactive to further adsorption of residual gas molecules. Therefore, samples with low vapor pressure only can be analyzed by the standard XPS technique, while frozen or liquid samples require specially designed spectrometers. In addition, clean preparation and handling of samples is mandatory due to the high surface sensitivity of XPS in order not to contaminate the surface with ubiquitous hydrocarbons or dust particles.

17c.2.2 Energy Resolution and Instrument Calibration

High-energy resolution for detailed chemical information by XPS is affected by several sources of peak broadening. Peak widths, given by the full-width-at-half-maximum (FWHM), are a convolution of X-ray line width, width of photoelectron lines, possible broadening by surface charging, and analyzer resolution.

Characteristic $K_{\alpha 1,2}$ X-rays of light elements have low full-width-at-half-maxima (FWHM), a prerequisite for good energy resolution. The natural FWHM is 0.70 eV for Mg K_α (1253.6 eV) and 0.85 eV for Al K_α (1486.6 eV). For comparison, the natural FWHM of Cu K_α (8048 eV) is 2.6 eV. In general, a twin-anode X-ray source with Mg and Al anodes placed at an angle of $\delta = 54.7°$ between the X-ray source and analyzer direction is used in XPS, as can be seen in Fig. 17c.3. All elements have core levels that can be ionized by Mg K_α or Al K_α X-rays. Additionally, the kinetic energy of photoelectrons induced by the low energy of Mg K_α or Al K_α X-rays gives the surface sensitivity of XPS.

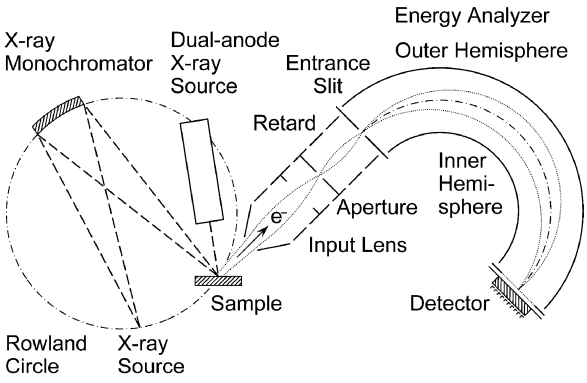

Fig. 17c.3 Scheme of XPS spectrometer equipped with a concentric hemispherical analyzer and additional monochromatic X-ray source. Before entering the analyzer, electrons are retarded to pass energy. Spectra are essentially generated by scanning the retard voltage

For high-energy resolution, an X-ray monochromator is used to cut out a section from the Al K_α main line, which is composed of $K_{\alpha 1}$ and $K_{\alpha 2}$. Additionally, an X-ray monochromator allows eliminating unwanted X-ray satellites, ghost lines, photoelectrons produced by bremsstrahlung contributing to the background, and Auger transitions excited by bremsstrahlung. Thus, low background in the spectra and enhanced elemental sensitivity can be achieved.

The natural width Γ of a photoelectron line is linked to the mean lifetime τ of the core hole state by $\Gamma \geq h/2\pi\tau$, where $h = 4.136 \times 10^{-15}\,\mathrm{eV \cdot s}$ is the Planck constant. Typical lifetimes of core hole states in XPS are in the range 10^{-13} to 10^{-15} s. Holes at inner core levels have shorter lifetimes than holes at outer levels. In addition, broadening due to vibration may contribute to the widths of elemental lines.

The type of analyzer and operating parameters determine analyzer resolution. The concentric hemispherical analyzer (CHA) has been established in XPS due to its double-focusing characteristic, convenience of construction, and high resolution. For a given CHA geometry, resolution depends on the pass energy, i.e. the kinetic energy at which electrons are able to pass the CHA. The pass energy is defined by the potentials at the inner and outer hemisphere of the CHA. At low pass energy, energy resolution is high, but electron transmission low. At high pass energy, resolution is low and transmission is high. Spectra are generated by scanning the retard voltage of the electron optics in front of the hemispherical analyzer to decelerate the electrons to the specified pass energy and detecting the electrons that have passed the CHA. This mode of operation allows for a high resolution of elemental lines also at high kinetic electron energies, termed fixed analyzer transmission (FAT).

Instrument calibration at regular intervals may be divided into mechanical alignment of instrument components, determination of the etch rate of the actual ion gun settings, and calibration of intensity and binding energy scales. Of these calibration procedures, binding energy calibration is most important to the determination of chemical states. Therefore, further details concerning the binding energy scale will be given below. Elemental lines of pure metals (Mg $K\alpha$: Cu $2p_{3/2}$ at 932.62 eV, Ag $3d_{5/2}$ at 368.22 eV, Au $4f_{7/2}$ at 83.95 eV) with well-established binding energies are used to calibrate the binding energy scale of the spectrometer [20]. Before measurement, the reference samples are cleaned by ion beam sputtering until impurities like oxygen or carbon can no longer be detected. The difference of binding energies between Cu $2p_{3/2}$ and Au $4f_{7/2}$ is adjusted by the electronics to coincide with the reference value of 848.67 eV within ±0.1 eV. The spectrometer work function is then set to meet the reference binding energy of the Ag $3d_{5/2}$ line and the Fermi edge at the conduction band. Standard deviation of binding energies is within ±0.1 eV for conductors and within ±0.2 eV for non-conducting samples. A linear regression function between reference data and measured values from the calibration is useful for fine adjustment of binding energies from samples. In addition, survey spectra are measured of each reference sample to check consistency of spectral intensity. In order to maintain the calibration settings, appropriate circuits are energized in the stand-by mode at constant temperature.

17c.3 Application to $NaAlH_4$ Doped with Ti-based Precursor

Surface composition and chemical bonding of Ti-doped sodium alanate ($NaAlH_4$) upon ball milling and subsequent cycling under hydrogen were analyzed by X-ray photoelectron spectroscopy. Using Al $K\alpha$ X-ray excitation, XPS information depth (95% of signal) for $NaAlH_4$ (density 1250 kg m^{-3}) is about 11 nm for Al 2*p* and Na 2*s* lines.

Under vacuum, the hydrides are expected to be dissociated, if thermodynamic equilibrium is achieved. However, the hydrogen desorption rate is low at room temperature. For example, desorption rates of $NaAlH_4$ and Na_3AlH_6 doped with 4 mol.% $TiCl_3$ [4] estimated by means of Arrhenius diagrams are 10^{-3} wt.% h^{-1} and 10^{-5} wt.% h^{-1}, respectively. Moreover, the hydrogenated and de-hydrogenated state of the sample can be differentiated, as the Al 2*p* photoelectron spectra present significant differences in these two states.

17c.3.1 Experimental Setup

17c.3.1.1 Sample Preparation

All sample preparations were done in an argon-filled glove box equipped with a recirculation system to keep the water and oxygen concentrations below 10 ppm. Table 17c.1 displays the descriptions of the samples investigated at different stages of the reaction. Na alanate samples doped with 5 mol% of Ti based on $TiCl_3$ or Ti_{13}·6THF were prepared using different milling times (2, 30, 60, and 180 minutes), labelled (bm2), (bm30), (bm60), and (bm180), respectively. For comparison, samples of pure $NaAlH_4$, $TiCl_3$, and Ti_{13}·6THF were also investigated. Na alanate samples doped with $TiCl_3$ or Ti_{13}·6THF and ball-milled for 30 minutes were used for decomposition/absorption cycles. Desorption was carried out at 150°C under

Table 17c.1 Sample descriptions

Labels	Sample description
$NaAlH_4$	(Chemetall, Frankfurt) purified by Soxhlet extraction with THF [5]
$TiCl_3$	as received (99.999%, Sigma Aldrich)
Ti_{13}·6THF	as synthesized (purity 74%) [5]
$TiAl_3$	as received (99.5%, Alfa Aesar)
TiH_2	as received (99%, Alfa Aesar)
(bmx)	$NaAlH_4$ + 5 mol% of Ti based on $TiCl_3$ or Ti_{13}·6THF, ball-milled x min at 600 rpm
(a1d)	(bm30) stopped after the 1st desorption (T = 150°C, p_{H2} = 0.3 bar)
(a1a)	(bm30) stopped after the 1st absorption (T = 100°C, p_{H2} = 100 bar)
(a8a)	(bm30) stopped after the 8th absorption (T = 100°C, p_{H2} = 100 bar)
(a9d)	(bm30) stopped after the 9th desorption (T = 150°C, p_{H2} = 0.3 bar)

a residual hydrogen pressure of 0.3 bar. Absorption took place at 100°C under a hydrogen pressure of 100 bar. The samples are labelled (a1d), (a1a), (a8a), and (a9d) for sample after the first desorption, after the first absorption, after the eighth absorption, and after the ninth desorption, respectively.

For XPS analysis, small portions of the powder samples were pressed onto indium foil and mounted on the sample holder. By means of a transfer vessel, samples were transported from the glove box into the XPS instrument without exposing them to air.

17c.3.1.2 Instrument Setup

XPS measurements were carried out under an ultimate pressure of 7×10^{-8} Pa with a PHI 5600ci spectrometer (Physical Electronics Inc.) equipped with a concentric hemispherical analyzer and a multi-channel plate (MCP) detector, as displayed in Fig. 17c.3. XPS spectra were acquired using Mg K_α or monochromatic Al K_α X-ray sources. Narrow scans of elemental lines were recorded at 11.75 eV pass energy of the analyzer, yielding an FWHM of the Ag $3d_{5/2}$ line of 0.85 eV and 0.62 eV, respectively.

The angle of the dual-anode X-ray source to electron analyzer was 54.7, and 90° in the case of the X-ray monochromator displayed in Fig. 17c.3. The angle of emission (sample surface normal to analyzer direction) was 25° for all measurements except for depth profiling. The area of analysis on the sample surface, selected by the aperture of the analyzer electron optics, was about 0.8 mm in diameter.

The monochromatic Al K_α X-ray source is windowless and an electron flood gun is required for the necessary charge compensation of insulating samples. If elemental lines have same binding energies acquired either by the standard X-ray source or by the monochromator without additional neutralization, the sample is likely conducting, and reference binding energies may be determined. For analyzing the hydrides, the *C* 1s line of adventitious hydrocarbons was not used as charge reference, as hydrocarbons may react at the surface, leading to a change of the *C* 1s binding energy. Instead, the Cl $2p_{3/2}$ line (binding energy 200.7 eV) observed with some conducting samples (bm2) was used as an internal reference line for the non-conducting samples. In addition, binding energy differences of elemental lines can help to identify chemical states.

17c.3.2 XPS Survey Spectra and Atomic Concentrations

During acquisition, the surfaces of $TiCl_3$ and $NaAlH_4$ samples were charged, whereas the Na alanate sample doped with $TiCl_3$ (bm2) was conducting. To identify the lines, two survey spectra at different X-ray energies were measured to discriminate between photoelectron and Auger lines, as was shown in Fig. 17c.2. All elements composing the material, except H, could be detected, including the Ti 2p lines.

Atomic concentrations were calculated from peak areas of elemental lines after Shirley background subtraction taking into account asymmetry parameters, sensitivity factors, and the transmission function of the analyzer measured at same instrumental parameters. Table 17c.2 displays the atomic concentrations of the different elements at the surface of Na alanate doped with 5 mol.% of Ti based on $TiCl_3$ or Ti_{13}·6THF after different milling times, different decomposition/absorption cycles, and after sputter depth profiling.

It is obvious that Si is present at the surface in samples (a1a), (a1d), (a8a), and (a9d), regardless of whether the precursor used is $TiCl_3$ or Ti_{13}·6THF. This is due to a potential contamination of the material with small amounts of silicon oil (into which the reactor is immersed during the cycling experiments) when the reactor is opened between the cycles to remove the material for the spectroscopic measurements. The main contaminants at the surface of the samples are carbon and oxygen. In addition, K, B, N, and Br are present in the case of Ti colloid-doped alanate due to its synthesis procedure.

In the case of Na alanate doped with Ti on the basis $TiCl_3$, the concentration of oxygen and carbon increases at the surface with increasing milling time. It is evident that there is no significant evolution of the atomic concentration of Na. The concentration of Ti at the surface decreases significantly between a milling time of two

Table 17c.2 Atomic concentrations obtained from XPS surveys of Na alanate, $TiCl_3$, Ti_{13}·6THF, and $NaAlH_4$ doped with 5 mol.% of Ti based on $TiCl_3$ or Ti_{13}·6THF after different times of ball milling and different cycles under hydrogen. AD: After depth profiling. Relative error ± (10–20)%

Sample	C	O	Na	Al	Al^{3+}	Al^0	Ti	Cl	Si	K	B	N	Br	Ref.
$NaAlH_4$	4.7	32.4	28.1	34.0	*34.0*	–		0.5	0.3					[21]
$TiCl_3$		8.4					25.7	65.9						[21]
Ti_{13}·6THF	46.2	28.0					3.1		18.3	2.0	1.2	1.2		[22, 23]
$NaAlH_4$ doped with 5 mol.% $TiCl_3$ by ball milling														
(bm2)	7.3	32.9	24.9	21.5	*18.1*	*3.4*	2.8	10.6						[21]
(bm30)	8.4	35.6	25.4	24.7	*20.1*	*4.6*	0.6	5.3						[21]
(bm60)	9.9	34.6	25.5	25.4	*21.1*	*4.3*	0.5	4.1						[21]
(bm180)	11.6	36.6	26.2	21.6	*20.2*	*1.4*	0.4	3.6						[23]
(a1d)	8.3	43.3	26.5	16.0	*12.6*	*3.4*	0.3	4.6	1.0					[22]
(a1a)	9.3	40.7	27.9	16.5	*14.4*	*2.1*	0.4	4.4	0.8					[22]
(a8a)	13.5	40.6	25.0	16.0	*13.8*	*2.2*	0.4	2.8	1.7					[22]
(a9d)	13.1	40.6	25.4	15.9	*11.1*	*4.8*	0.4	3.9	0.7					[22]
$NaAlH_4$ doped with 5 mol.% Ti_{13}·6THF by ball milling														
(bm2)	25.9	34.8	13.6	13.5	*13.5*	–	3.4		6.7	0.8		1.1	0.2	[23]
(bm30)	20.1	36.6	20.6	16.3	*16.3*	–	3.0		1.6	0.3		1.2	0.3	[23]
(bm60)	13.0	41.4	25.4	15.6	*15.6*	–	2.3		1.0	0.3		0.7	0.3	[23]
(bm180)	9.3	46.5	27.7	14.3	*14.3*	–	1.3		0.2	0.2		0.4	0.1	[23]
(a1d)	8.8	45.8	29.5	12.8	*7.4*	*5.4*	1.7			0.2	0.9	0.3		[22]
(a1a)	9.1	44.1	28.0	16.4	*15.4*	*1.0*	0.8	0.1	0.3		1.1	0.1		[22]
(a8a)	11.9	42.7	33.0	11.2	*9.3*	*1.9*	0.5		0.3			0.4		[22]
(a9d)	23.8	34.6	24.6	12.2	*6.6*	*5.6*	0.6		3.4			0.8		[22]

and thirty minutes and remains constant around 0.5 at.% with further milling. The evolution of the Cl concentration follows the trend of the Ti concentration, but also indicates the small-scale formation of a salt (NaCl) other than $TiCl_3$. Additionally, metallic Al is detected at the surface after 2 minutes of milling. The concentration of both species Al^{3+} and Al^0 at the surface increases during the first 60 minutes of ball milling and then decreases with increasing milling time.

In $NaAlH_4$ doped with Ti_{13}·6THF by ball milling, the atomic concentration of oxygen at the surface increases, whereas the carbon concentration decreases, probably due to stripping of THF molecules from the colloid particles. In contrast to $TiCl_3$-doped samples, the relative amount of Na increases significantly with milling time. Moreover, the atomic concentration of Ti decreases with increasing milling time, but in a less pronounced way as observed for the $TiCl_3$-doped samples. As far as Al is concerned, the significant difference between the two precursors is that Al^{3+} and Al^0 are present at the surface in $TiCl_3$-doped samples after a milling time of 2 minutes already, whereas in Ti colloid-doped samples, the valence state of Al does not change and Al^0 is absent irrespective of the milling time.

17c.3.3 Binding Energies

17c.3.3.1 Reference Materials

Table 17c.3 presents the binding energies of elemental lines obtained from the references. For pure Na alanate, the Al 2p line is observed at 75.4 eV, while the binding energy of oxygen (O 1s) at the surface is at 532.7 eV. The difference between these

Table 17c.3 XPS binding energies (in eV) of reference samples. Charge reference lines for insulating samples are printed in italic, *) conductors, **) C 1s line superimposed with the plasmon loss line of Cl 2s. Error: ±0.1 eV for conductors, ±0.2 eV for insulators

Reference samples	Na 1s	Ti $2p_{3/2}$	O 1s	C 1s	Cl $2p_{3/2}$	Al 2p	Na 2s	Ref.
Al*						72.9		[10]
Al_2O_3			531.0			74.4		[10]
AlO(OH)			531.5			74.2		[10]
Ti*		454.0						[24]
TiH_2^*		454.6						[22]
TiO_2		458.6	529.8					[24]
$TiCl_3$		458.5			199.5			[24]
$TiCl_3$		459.8		**	*200.7*			[21]
$TiAl_3$*		453.8				72.4		[21]
$NaAlH_4$	1073.9		532.7 / 80%	**	*200.7*	75.4	65.6	[21]
			534.2 / 20%					
Ti_{13}·6THF* ~Ti(0)		456.1 / 21%	530.9 / 10%	286.0				[23]
~Ti(I)		457.5 / 24%	532.0 / 10%					
~Ti(III)		459.3 / 55%	533.7 / 80%					

two energies is 457.3 eV which is comparable to 457.3 eV of AlO(OH), but not to 456.6 eV of Al_2O_3 [10].

The Ti 2p spectrum of $TiCl_3$ is well fitted by one doublet, i.e. Ti $2p_{3/2}$ and Ti $2p_{1/2}$. The Ti $2p_{3/2}$ line of $TiCl_3$ has a binding energy of 459.8 eV when referenced to the Cl $2p_{3/2}$ line at 200.7 eV. In a previous work, the reported binding energies of Ti $2p_{3/2}$ and Cl $2p_{3/2}$ in $TiCl_3$ [24] were 458.5 eV and 199.5 eV, when charge-referenced to C 1s at 284.8 eV. The differences in binding energies between Ti $2p_{3/2}$ and Cl $2p_{3/2}$ lines are 259.0 eV [24] and 259.1 eV (this work). This confirms that the sample is $TiCl_3$. As the reference binding energy of Ti $2p_{3/2}$is 458.5 eV and 458.6 eV [10] for $TiCl_3$ and TiO_2, respectively, it was concluded that the oxygen present at the surface of $TiCl_3$ is bound as TiO_2.

17c.3.3.2 $NaAlH_4$ Doped with Ti Based on $TiCl_3$ or Ti_{13}·6THF by Ball Milling

Table 17c.4 shows the binding energy positions of elemental lines obtained for Ti-doped samples.

Figure 17c.4 displays the evolution of the Ti 2p line with milling time of $NaAlH_4$ doped with $TiCl_3$. Comparison of the Ti 2p spectra of pure $TiCl_3$ and of Ti-doped $NaAlH_4$ based on $TiCl_3$ ((bm2), (bm30), and (bm60)) shows that ball milling induces shoulders on the low binding energy side of the Ti 2p lines. The binding energies of Ti $2p_{3/2}$ indicate that a partial reduction of $TiCl_3$ occurs after 2 minutes of ball milling already. This is evident from the presence of lines with binding energies of 459.4 eV (Ti^{3+}) and the shoulder at 454.2 eV (Ti^0). A complete reduction is observed after 30 minutes and this state remains with increasing milling time (presence of the metallic component only with binding energy of the Ti $2p_{3/2}$ line

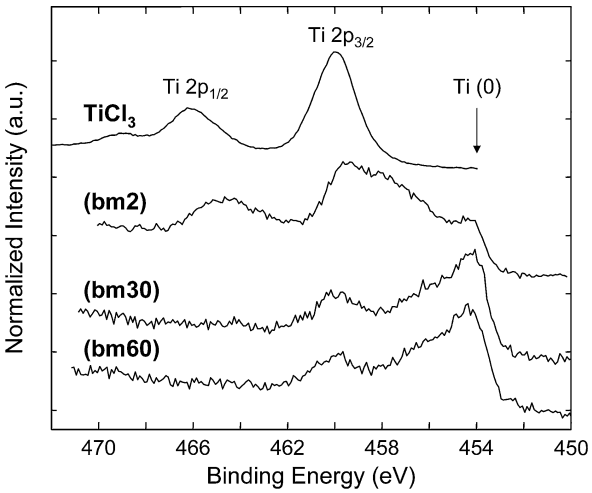

Fig. 17c.4 Ti 2p spectra of samples (bm2), (bm30), and (bm60) of Na alanate doped with $TiCl_3$ by ball milling. For comparison, the spectrum of pure $TiCl_3$ is added

Table 17c.4 XPS binding energies (in eV) of doped Na alanate after a milling time of 2 and 30 minutes, respectively, and in different stages of the decomposition/absorption reaction. [ ]: FWHM of elemental lines in units of eV, determined by narrow scans (Al $K\alpha$ mono.). Binding energies of most abundant species are printed in bold if multiple binding energies are given. Charge reference line of insulating samples is is printed in italic. *) Conductors. Error: ±0.1 eV for conductors, ±0.2 eV for insulators

Sample	Na 1s	Ti $2p_{3/2}$	O 1s	C 1s	Cl $2p_{3/2}$	Al 2p	Na 2s	Ref.
$NaAlH_4$ doped with 5 mol.% $TiCl_3$ by ball milling								
(bm2)*	1073.7 [1.71]	454.2 **459.4**	**531.9** 533.4	**287.0** 290.8	200.7 [1.38]	72.9 **75.2** [1.68]	65.5 [1.51]	[21]
(bm30)	1073.6 [1.76]	454.2	**531.9** 533.4	**287.0** 290.8	200.7 [1.15]	72.8 **75.1** [1.75]	65.3 [1.54]	[21]
(a1d)*	1074.0 [2.06]	454.2	**532.6** 534.0	**287.5** 290.4 292.1	201.3 [1.36]	72.7 **75.7** [1.79]	65.7 [2.08]	[22]
(a1a)	1073.4 [2.14]	454.5	**532.6** 534.1	**286.6** 288.6 291.2	201.4 [1.47]	73.0 **75.6** [1.85]	65.3 [2.07]	[22]
(a8a)*	1073.7 [1.88]	454.2	**532.5** 533.8	**287.1** 289.1 291.5	201.5 [1.46]	72.9 **75.5** [1.72]	65.4 [1.89]	[22]
(a9d)*	1073.6 [1.89]	454.2	**532.7** 534.1	286.0 **287.3** 288.9 291.5	201.6 [1.58]	72.9 **75.7** [1.81]	65.1 [1.87]	[22]
$NaAlH_4$doped with 5 mol.% Ti_{13}·6THF by ball milling								
(bm2)	1073.6 [1.90]	456.4 457.7 **459.4**	530.8 **532.1** 533.8	286.6		75.4 [1.63]	65.5 [1.75]	[23]
(bm30)*	1073.6 [1.83]	456.2 457.8 **459.5**	530.7 **532.1** 533.5	286.8		75.4 [1.56]	65.5 [1.77]	[23]
(a1d)*	1073.2 [1.55]	455.2 456.9 **459.0**	531.1 **532.7** 534.3	286.0 **287.2** 288.5 291.1		72.7 **75.2** [1.87]	64.9 [1.50]	[22]
(a1a)*	1073.3 [1.77]	455.3 457.0 **459.0**	530.8 **532.4** 533.9	286.0 **287.2** 288.5 291.1		72.8 **75.2** [1.60]	65.1 [1.81]	[22]
(a8a)*	1073.2 [1.53]	453.9	530.9 **532.4** 534.0	285.9 **287.1** 288.4 290.9		72.7 **75.2** [1.60]	64.8 [1.53]	[22]
(a9d)*	1073.5 [1.59]	453.9	531.1 **532.6** 534.2	**286.7** 288.3		72.8 **75.3** [1.76]	65.0 [1.51]	[22]

at 454.2 eV). Accordingly, some of the Al in the sample is reduced to the metallic state with the Al 2p line at 72.9 eV (Al^0). As far as the non-metallic part of Al is concerned, it can be observed that the binding energy of the Al 2p line decreases from 75.4 eV (initial $NaAlH_4$ sample) to 75.2 eV after ball milling. The difference in the binding energy between the most intense O 1s line at 531.9 eV and the Al 2p line of (bm2) assigned to the non-metallic state is 456.7 eV. This value is comparable to the binding energy difference observed for Al_2O_3 [10]. Moreover, ball milling shifts the Na 1s and Na 2s lines by 0.3 eV towards lower binding energy. This and the decrease of the binding energy of the Al 2p line after ball milling suggest an enhanced electron density within the alanate induced by the presence of metallic Ti and Al (i.e. by the introduction of $TiCl_3$ precursor).

When Ti_{13}·6THF is used as precursor, no significant change in the binding energies of Ti $2p_{3/2}$, Al 2p, Na 2s, Na 1s, O 1s, and C 1s is observed after various ball milling times. The Al 2p binding energy is always equal to 75.4 eV (Al^{3+}), and a Ti $2p_{3/2}$ signal at 454.2 eV (Ti^0) is absent even after 60 minutes of milling. The results indicate that besides the possible stripping of THF molecules, the Ti cluster does not chemically react with Na alanate during the ball milling process, in contrast to the $TiCl_3$ precursor.

17c.3.3.3 Cycling of Ti-doped $NaAlH_4$ Based on $TiCl_3$ or Ti_{13}·6THF

In the following section, results obtained for samples (a1a), (a1d), (a8a), and (a9d) with both precursors shall be compared with those of the initial sample (bm30). Cycling under hydrogen was performed after ball milling of the mixture of Na alanate and precursor for 30 minutes. The surface concentration of carbon increased with the number of cycles in $TiCl_3$-doped samples, whereas in the case of Ti colloid-doped samples, the initial carbon concentration decreased during the first cycle and then increased with increasing number of cycles, similar to the $TiCl_3$-doped samples. In both cases, the concentration of oxygen at the surface increased in the first cycle.

Evolution of the Ti concentration at the surface upon cycling was not significant in the case of $TiCl_3$-doped Na alanate. From 0.6 at.% in sample (bm30), it decreased and remained at 0.4 at.% between the first and the eighth absorption cycles. In the case of Ti_{13}·6THF-doped alanate, however, the concentration of Ti at the surface decreased with an increasing number of dehydrogenation/ hydrogenation cycles, from 3.0 at.% in sample (bm30) to 0.6 at.% in sample (a9d). This indicates that the amount of Ti present at the surface after eight cycles is around 0.5 at.%, irrespective of the Ti-based precursor used to activate the reversible decomposition reaction of Na alanate.

Upon cycling, the valence state of titanium remains in the metallic state when using the $TiCl_3$-doped Na alanate, whereas $Ti_{13} \cdot 6THF$ reacts with Na alanate during the first dehydrogenation and reduction of Ti to the metallic state occurs. After eight cycles, all titanium is in the zero-valent state, irrespective of whether the precursor used is $TiCl_3$ or $Ti_{13} \cdot 6THF$, as can be seen in Table 17c.4.

Metallic Al appears at the surface during the first decomposition of Ti colloid-doped samples. Moreover, binding energies of Al 2p remain at about 75.4 and 72.9 eV during the cycles under hydrogen, which correspond to $NaAlH_4$ and metallic Al, respectively. The evolution of the Al^{3+}/Al^0 ratio reflects the transformation taking place. In case of both precursors, metallic aluminum remains at the surface in samples (a1a) and (a8a), thus confirming that the back reaction from NaH, Al, and hydrogen to $NaAlH_4$ is incomplete (Fig. 17c.5).

Independently of the precursor used, the binding energies of Ti $2p_{3/2}$ and O 1s lines of samples (a8a) and (a9d) are similar. The significant difference between samples (a8a) and (a9d) results from the binding energy differences between the Al 2p and the Na 2s lines. Comparison of the binding energy differences between the Al 2p and the Na 2s lines reveals that the difference is smaller for pure alanate and solely ball-milled samples than for samples (a8a) and (a9d). This indicates that the Al and Na lines are more sensitive to the dehydrogenation/hydrogenation reaction than the Ti line. Comparison of the differences between the lines Na 1s and Na 2s, Al 2p and Na 2s, and Al^{3+} 2p and Al^0 2p of pure alanate and Ti colloid- or $TiCl_3$-doped samples after eight absorption cycles suggests that the Na environment is similar, while the Al environment undergoes changes. Furthermore, binding energies of Al 2p and Na 2s lines of the (a8a) Ti colloid-doped samples are lower than those of the (a8a) $TiCl_3$-doped samples or those of pure alanate. This suggests that the surface of Ti colloid-doped alanate has a higher electron density than that of the $TiCl_3$-doped Na alanate.

Analysis of atomic concentrations and binding energies indicates that TiO_2 or TiH_2 are not present at the surface of the samples. However, presence of a Ti-Al alloy at the surface cannot be excluded by XPS.

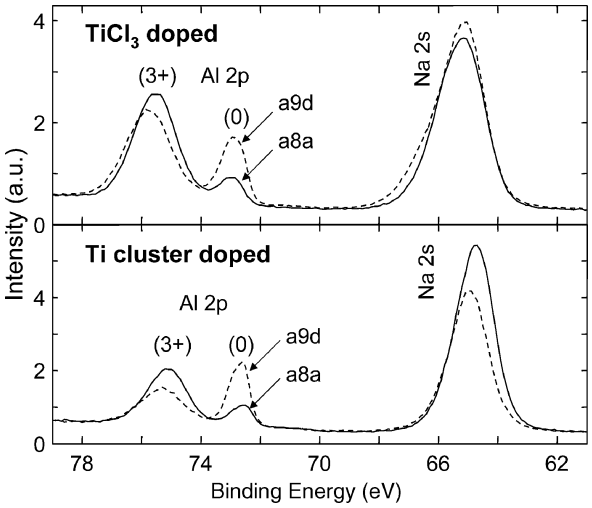

Fig. 17c.5 Narrow scans of the Al 2p and Na 2s lines of Ti-doped Na alanate on the basis of $TiCl_3$ or $Ti_{13} \cdot 6THF$ after the eighth absorption (full line) and after the ninth desorption (broken line). In Na alanate doped with $TiCl_3$, the presence of NaCl contributes to the Na 2s line

17c.3.4 XPS Depth profiles of Ti-doped $NaAlH_4$ Based on $TiCl_3$

XPS depth profiles were acquired for sodium alanate doped with 5 mol.% $TiCl_3$ by ball milling for 2 and 60 minutes by means of alternate ion beam sputtering (Ar^+, 3 keV, current density 15.4 $\mu A/cm^2$) followed by XPS (Mg $K\alpha$) acquisition of elemental lines, except for the C 1s line which is superposed with the Na (KLL) line (cf. Fig. 17c.2). The angle of the sample normal to the ion gun was 43° and the emission angle for photoelectrons 60°. During sputtering, the ion beam of about 0.2 mm in diameter scanned over an area of $3 \times 3\ mm^2$ with Zalar rotation applied to the sample. The area of analysis and the rotation axis were aligned to the center of the sputtered area. In the low binding energy region, the conducting band and the Fermi edge were more pronounced after sputtering, indicating that the sputtering process itself induces changes, i.e. a reduction of the samples.

Figure 17c.6a represents the depth profiles of samples (bm2) and (bm60). It is obvious that once the reacted surface layer has been removed, the atomic concentrations of all elements vary in a different manner. The Al signal steadily increases and the O signal decreases during sputtering.

The Ti signal, Fig. 17c.6b, depends on the milling time of the sample. Indeed, a fast initial increase of the Ti concentration is observed in the (bm2) sample, followed by an almost constant concentration (in the range of 5 mol.%), whereas it increases slowly in the (bm60) sample. Table 17c.5 shows the atomic concentrations obtained after sputtering. For both samples, the depth profiles indicate that the concentration of titanium is higher in the bulk than at the surface. This is in accordance with SNMS depth profiles obtained with similarly prepared samples [25]. Moreover, the amounts of Ti, Cl, and Al increase, while the amounts of Na and oxygen decrease. Both samples exhibit similar depth profiles for Na and oxygen. The initial surface then seems to be enriched by NaCl and Al_2O_3 and it is evident that carbon contamination of the samples only is a surface effect (Table 17c.5). Portions of the initial surface layers always contribute to the elemental intensities during depth profiling of such nanopowders in contrast to plane solid samples.

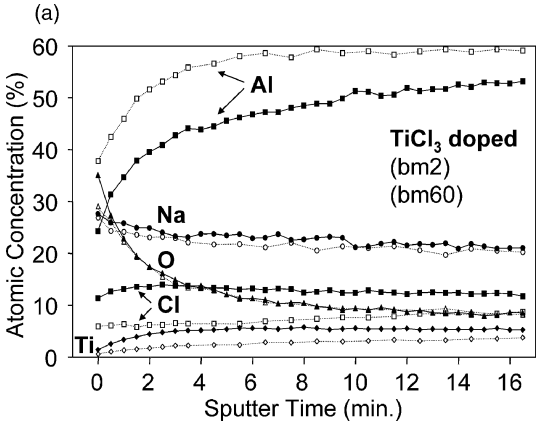

Fig. 17c.6a XPS sputter depth profiles of Na alanate doped with 5 mol% $TiCl_3$ ball-milled for 2 (filled symbols) and 60 min (non-filled symbols)

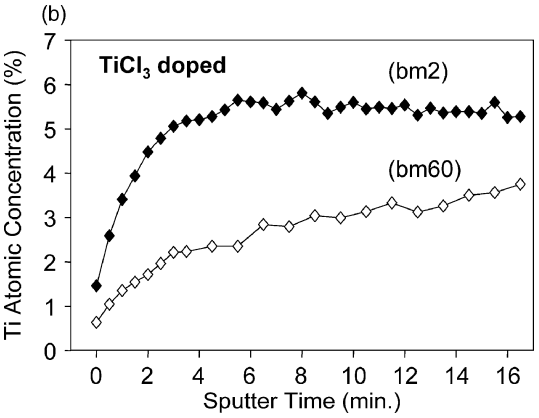

Fig. 17c.6b Detailed view of the Ti atomic concentrations of the depth profiles of Fig. 17c.6a

High-resolution scans of elemental lines acquired directly after depth profiling show similar spectra for the two samples (Table 17c.6). After sputtering, no alteration of the Cl 2p signal can be observed, whereas the Na 1s line shows two Components with a difference of about 1.6 eV in the binding energies. Moreover, curve fits to Al 2p spectra show that about 60% of Al are present in the metallic state, whereas all the Ti is in the zero-valent state within the detection limit of the method.

Table 17c.5 Atomic concentrations obtained from XPS surveys of $NaAlH_4$ doped with 5 mol.% of Ti on the basis of $TiCl_3$ after different milling times and after depth profiling. AD: After depth profiling. Relative error ± (10–20)%

Sample	C	O	Na	Al	Al^{3+}	Al^0	Ti	Cl	Ref.
(bm2)	7.3	32.9	24.9	21.5	*18.1*	*3.4*	2.8	10.6	[21]
(bm60)	9.9	34.6	25.5	25.4	*21.1*	*4.3*	0.5	4.1	[21]
(bm2)AD		6.9	16.5	60.3	*21.6*	*38.7*	5.3	11.0	[21]
(bm60)AD		7.5	17.4	63.1	*19.8*	*43.3*	4.2	7.8	[21]

Table 17c.6 XPS binding energies (in eV) of doped Na alanate after a milling time of 60 min and after sputter depth profiling of samples ball-milled for 2 and 60 minutes. AD: After depth profiling. [ ]: FWHM of elemental lines in units of eV, determined by narrow scans (Al $K\alpha$ mono.). *) Conductors, error: ±0.1 eV

Sample	Na 1s	Ti $2p_{3/2}$	O 1s	C 1s	Cl $2p_{3/2}$	Al 2p	Na 2s	Ref.
$NaAlH_4$ doped with 5 mol.% $TiCl_3$ by ball milling								
(bm60)*	1073.6 [1.74]	454.2	**532.0** 533.4	**287.0** 290.7	200.7 [1.17]	72.9 **75.1** [1.66]	65.3 [1.52]	[21]
(bm2) AD*	1072.3 **1073.9** [1.84]	454.0	**531.9** 533.0	–	200.7 [1.17]	**72.8** [0.86] 74.6	64.1 **65.6** [1.59]	[21]
(bm60) AD*	1072.3 **1073.9**	454.0	**532.0** 533.3	–	200.7	72.8 74.8	64.0 **65.5**	[21]

17c.3.5 Gained Knowledge

17c.3.5.1 Location of Ti

XPS depth profiling of $TiCl_3$-doped $NaAlH_4$ showed that with increasing ball milling time, the Ti migrates into the bulk and contaminants like O and C are located at the surfaces only.

Surface concentration of Ti tends to a value of about 0.5 at.% after the first cycle already and is nearly invariant during hydrogen cycling. In contrast to this, the concentration of Al^0 at the surface varies significantly with dehydrogenation and subsequent hydrogenation (for example, for Ti colloid-doped Na alanate, values of 5.4 at.% are measured in the sample (a1d) and 1.0 at.% in sample (a1a)). This indicates that the metallic Al phase migrates under hydrogen cycling, whereas the metallic Ti phase does not segregate. A detailed analysis of the kinetics of absorption and decomposition data also showed that a diffusion-like growth process most likely governs the phase transformations in Ti-doped $NaAlH_4$.

Either once Ti is reduced to the zero-valent state by ball milling, i.e. in the case of $TiCl_3$ precursor, or by cycling, it remains in the zero-valent state, although oxygen traces are present, i.e. during handling within the inert gas glove box. This suggests that Ti^0 and Al^0 are present within the information depth of XPS, but not present within the topmost atomic layer, where oxidation will take place readily even at trace level. Oxides on the surface usually represent a significant hydrogen permeation barrier, but may be overcome by the high specific surface of the nanoscaled material.

After the eighth absorption, Ti colloid-doped Na alanate exhibits lower binding energies of Na, Al, and Ti elemental lines than $TiCl_3$-doped Na alanate. Concurrently, the samples are conducting and the C 1s and O 1s lines related to surface contamination have similar binding energies. This suggests that the surface of Ti colloid-doped alanate has a higher electron density than the $TiCl_3$-doped Na alanate.

17c.3.5.2 Insights into the Reaction

According to the XPS and XAS analyses [26], a certain molar fraction of the initial charge of sodium alanate reacts with the $TiCl_3$ during the milling process according to the following reaction:

$$3\ NaAlH_4 + TiCl_3 \rightarrow 3\ NaCl + 3\ Al^0 + 6H_2 + Ti^0 \qquad (17c.14)$$

When the sodium alanate is doped with 5 mol.% of $TiCl_3$, 15 mol.% of the initial sodium alanate are drawn off for the reduction of $TiCl_3$. Thus, the fact that the theoretical capacity of 5.6 wt.% is never reached experimentally with doped sodium alanate (which was also observed in [4]) is explained by the reduction of $TiCl_3$, which is taking place during the milling process already.

Reduction of $TiCl_3$ during ball milling results in three Al^0 atoms for one reduced Ti atom, which give the stoichiometry of $TiAl_3$. Several studies assumed the

formation of $TiAl_3$ [27, 28, 29, 30]. It should be noted, however, that even though it is possible to check the presence or the absence of $TiAl_3$ at the surface with XPS, the experimental conditions in this study (milling vial, milling time, number of cycles, etc...) are different from the previous ones. Knowledge of the atomic concentrations and the binding energies of Ti $2p_{3/2}$ and Al 2p lines allows statements to be made with respect to a possible alloying effect between Al and Ti at the surface. Table 17c.4 reveals that the binding energy of the elemental lines of the (bm) samples without sputtering is not comparable to $TiAl_3$. The 2p line of zero-valent Al of doped Na alanate is close to the reference value of Al metal and not to the measured value of the $TiAl_3$ sample. From the present data, it can be concluded that $TiAl_3$ is not present at the surface after ball milling. Its presence in the bulk, however, cannot be confirmed or ruled out strictly by XPS.

Comparison with kinetic data reveals the fastest kinetics for Ti colloid-doped samples having the lowest concentration of Ti at the surface after ball milling. Concerning the storage capacity, 5.5 wt.% of H_2 are released from sample (bm2), (bm30), or (bm180) after the first decomposition, suggesting that the hydrogen capacity likely is independent of the surface concentration of Ti. This result may correlate with the fact that, upon milling, the Ti colloid does not react chemically with the Na alanate. During the first cycle, oxygen atoms are stripped off from the Ti core and a shift to the Ti metallic state occurs. At a certain point, the presence of metallic Ti and metallic Al favors the formation of a Ti-Al phase binding a fraction of Al. The incomplete back reaction would explain why the reversible hydrogen storage capacity decreases during the first cycles and then stabilizes around 4.5 wt.% after subsequent cycles.

These results may give a first explanation why the kinetics is faster and why the hydrogen storage capacity is higher during the first cycle in the case of the Ti cluster-doped sample compared to the $TiCl_3$-doped alanate.

References

1. D. Briggs, M.P. Seah (eds.): "Practical Surface Analysis. Vol. 1: Auger and X-ray Photoelectron Spectroscopy", John Wiley & Sons, Chichester, 1990, ISBN 0-471-92081-9.
2. D. Briggs, J.T. Grant (eds.): "Surface analysis by Auger and X-ray photoelectron spectroscopy", IM Publications and SurfaceSpectra Limited, 2003, Cromwell Press, Trowbridge, UK, ISBN 1-901019-04-7.
3. S. Hüfner: "Photoelectron Spectroscopy, Principles and Applications", Springer-Verlag, Berlin, Heidelberg, New York, 2003, ISBN 3-540-41802-4.
4. G. Sandrock, K. Gross, G. Thomas: J. Alloys Compd. 339 (2002) 299–308.
5. M. Fichtner, O. Fuhr, O. Kircher, J. Rothe: Nanotechnology 14 (2003) 778–785.
6. B. Bogdanović, M. Felderhoff, S. Kaskel, A. Pommerin, K. Schlichte, F. Schüth: Adv. Mater. 15 (2003) 1012–1015.
7. K. Siegbahn, C. Nordling, A. Fahlman, R. Nordberg, K. Hamrin, J. Hedman, G. Johansson, T. Bergmark, S.-E. Karlsson, I. Lindgren, B. Lindberg: "ESCA: Atomic, Molecular and Solid State Structure Studied by Means of Electron Spectroscopy" Almqvist & Wiksells, Uppsala, Sweden, 1967.

8. R.F. Reilman, A. Msezane, S.T. Manson: J. Electron Spectrosc. Relat. Phenom. 8 (1976) 389–394.
9. C.D. Wagner, A.V. Naumkin, A. Kraut-Vass, J.W. Allison, C.J. Powell, J.R. Rumble: "NIST Standard Reference Database 20", National Institute of Standards and Technology, Gaithersburg, Maryland, USA, http://www.nist.gov/srd/surface.htm.
10. J.F. Moulder, W.F. Stickle, P.E. Sobol, K.D. Bomben: "Handbook of X-ray Photoelectron Spectroscopy" (ed. J. Chastain), Perkin-Elmer Corporation, Physical Electronics Division, Eden Prairie, Minnesota 55344, United States of America, 1992, ISBN 0-9627026-2-5.
11. A. Jablonski, C.J. Powell: Surf. Sci. Reports 47 (2002) 33–91.
12. M.P. Seah, W.A. Dench: Surf. Interface Anal. 1 (1979) 2–11.
13. P.J. Cumpson, M.P. Seah: Surf. Interface Anal. 25 (1997) 430–446.
14. W.E.S. Unger, T. Gross, O. Böse, A. Lippitz, T. Fritz, U. Gelius: Surf. Interface Anal. 29 (2000) 535–543.
15. M.C. Burrell, J.C. Chera: Surf. Interface Anal. 27 (1999) 811–815.
16. H.H. Andersen, H.L. Bay: "Sputtering Yield Measurements" in "Topics in Applied Physics, Vol. 47: Sputtering by particle bombardment I, physical sputtering of single-element solids", (R. Behrisch ed.), Springer-Verlag, Berlin, Germany, 1981, pp.145–218.
17. G. Betz, G.K. Wehner: "Sputtering of multicomponent materials" in "Topics in Applied Physics, Vol. 52: Sputtering by particle bombardment II, sputtering of alloys and compounds, electron and neutron sputtering, surface topography", (R. Behrisch ed.), Springer-Verlag, Berlin, Germany, 1983, pp.11–90.
18. D. Briggs, M.P. Seah (eds.): "Practical Surface Analysis. Vol. 2: Ion and Neutral Spectroscopy", John Wiley & Sons, Chichester, 1992, ISBN 0-471-92082-7.
19. S. Hofmann, A. Zalar: Surf. Interface Anal. 21 (1994) 304–309.
20. M.P. Seah, I.S. Gilmore, G. Beamson: Surf. Interface Anal. 26 (1998) 642–649.
21. A. Léon, D. Schild, M. Fichtner: J. Alloys Compd. 404–406 (2005) 766–770, and 407 (2006) 340.
22. A. Léon, O. Kircher, M. Fichtner, J. Rothe, D. Schild: J. Phys. Chem. B 110 (2006) 1192–1200.
23. A. Léon, J. Rothe, D. Schild, M. Fichtner: Chem. Eng. Trans. 8 (2005) 171–176.
24. Ch. Sleigh, A.P. Pijpers, A. Jaspers, B. Coussens, R.J. Meier: J. Electron Spectrosc. Relat. Phenom. 77 (1996) 41–57.
25. M. Fichtner, P. Canton, O. Kircher, A. Léon: J. Alloys Compd. 404–406 (2005) 732–737.
26. A. Léon, O. Kircher, J. Rothe, M. Fichtner: J. Phys. Chem. B 108 (2004) 16372–16376.
27. M. Felderhoff, K. Klementiev, W. Grünert, B. Spiethoff, B. Tesche, J.M. Bellosta von Colbe, B. Bogdanović, M. Härtel, A. Pommerin, F. Schüth, C. Weidenthaler: Phys. Chem. Chem. Phys. 6 (2004) 4369–4374.
28. B. Bogdanović, M. Schwickardi: J. Alloys Compd. 253–254 (1997) 1–9.
29. C. Weidenthaler, A. Pommerin, M. Felderhoff, B. Bogdanović, F. Schüth: Phys. Chem. Chem. Phys. 5 (2003) 5149.
30. J. Graetz, J.J. Reilly, J. Johnson, A. Yu. Ignatov, T.A. Tyson: Appl. Phys. Lett. 85 (2004) 500.

Chapter 17d
X-ray Absorption Fine Structure (XAFS) Spectroscopy

Jörg Rothe and Aline Léon

List of Abbreviations

μ	absorption coefficient
μ_0	absorption coefficient of an isolated atom
$\chi(k)$	EXAFS function
ANKA	ANgströmquelle KArlsruhe (Angström source Karlsruhe)
d	crystal plane spacing
DCM	double-crystal monochromator
E and $h\nu$	photon energy
E_0	ionization energy
E_{kin}	photoelectron kinetic energy
EXAFS	Extended X-ray Absorption Fine Structure

Jörg Rothe
Institut für Nukleare Entsorgung, Forschungszentrum Karlsruhe, P.O. Box 3640, D-76021 Karlsruhe, Germany, e-mail: rothe@ine.fzk.de

Aline Léon
Institut für Nanotechnologie, Forschungszentrum Karlsruhe, P.O. Box 3640, D-76021 Karlsruhe, Germany, e-mail: aline.leon@int.fzk.de

A. Léon (ed.), *Hydrogen Technology*,

$f(k)$	backscattering amplitude function
FZK	Forschungszentrum Karlsruhe
$\Phi(k,R)$	total phase shift
FT	Fourier Transform
hcp	hexagonal closed packed structure
$\hbar$	Planck's constant, reduced
I_0	incident photon intensity
I_1	transmitted photon intensity
INE	Institut für Nukleare Entsorgung (Institute for Nuclear Waste Disposal)
INT	Institut für Nanotechnologie (Institute for Nanotechnology)
k	photoelectron wave vector
k_{bn}	beat node k-value
ℓ	angular momentum quantum number
λ	Wavelength
$\lambda(k)$	photoelectron mean free path length
m_e	electron mass
MS	multiple scattering
N	coordination number
Θ	Bragg angle of reflection
R	interatomic distance between absorber and backscatterer
R-Δ	apparent distance in the FT plot due to photoelectron wave phase shift
${S_0}^2$	amplitude reduction factor
σ^2	mean square average displacement (Debye-Waller factor)
SR	synchrotron radiation
SS	single scattering
THF	tetrahydrofuran
XAFS	X-ray Absorption Fine Structure
XANES	X-ray Absorption Near Edge Structure

For the development of new, high-efficiency hydrogen storage materials, the principles controlling hydrogen release and uptake are of special importance. A better understanding of the nature of the active catalyst in these materials is needed in order to optimize their storage properties. For this purpose, X-ray absorption fine structure (XAFS) spectroscopy is chosen as a well-suited local structure technique to investigate the chemical state and local atomic environment of an element in the material. Indeed, this method yields element-specific information on the number, type, and distance of neighboring atoms surrounding the selected absorber atoms. Due to the high penetration strength of X-rays, measurements to determine bulk properties are performed easily on sealed samples or even *in situ* under reaction conditions.

Section 17d.1 of this chapter will introduce the fundamentals of the XAFS method, including experimental aspects. This description will provide a general overview of the experimental method, theory, and data analysis. Further details concerning XAFS techniques can be found in the book edited by Koningsberger et al. [1]. In Sect.17d.2, it shall be demonstrated how XAFS has been applied successfully to investigate the atomic-scale properties of Ti in sodium alanate doped with a Ti-based precursor by ball milling. It will be shown how XAFS spectroscopy has elucidated the chemical state and local atomic environment of Ti dopants in Ti-activated sodium alanate and contributed to gaining additional insight into the absorption/desorption reaction of this hydrogen storage material.

17d.1 X-ray Absorption Fine Structure (XAFS)

X-rays are absorbed by matter primarily through the photoelectric effect, as a result of which electrons from inner core states are excited into empty outer-lying states at energies above the ionization threshold. Figure 17d.1 depicts the X-ray absorption spectrum of a Ti metal foil recorded at the Ti K-edge, where the product of absorption coefficient and sample thickness, μd, is shown as a function of photon energy. A sharp rise is observed at the absorbing element core state threshold or ionization energy, E_0, which renders this technique element-specific. According to the principle quantum number of the electron excited, these abrupt changes are referred to as K, L, M, etc. absorption edges.

Figure 17d.1 displays the oscillatory structure of μ. Based on the scattering processes responsible for the oscillatory structure, the photon energy range in an X-ray absorption spectrum generally is divided into two parts: The X-ray absorption near-edge structure (XANES, cf. inset in Fig. 17d.1) at lower energies and the extended X-ray absorption fine structure (EXAFS) at higher energies.

In the EXAFS region, the wave function of the excited photoelectron in the core region is modulated by interference of the outgoing wave function with a fraction backscattered by the neighboring atoms. In this sense, the EXAFS oscillatory pattern literally is an interferogram of the atomic arrangement surrounding the absorbing atoms. Consequently, it contains metrical parameters characterizing this

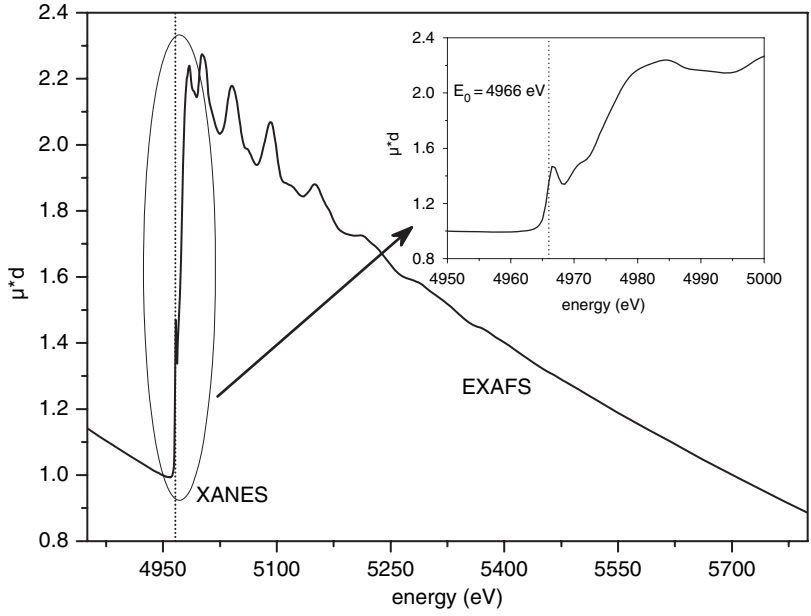

Fig. 17d.1 Ti K-edge XAFS spectrum of Ti metal (5 μm foil). The XANES region is enlarged in the inset. E_0 corresponding to the Ti(0) 1s-energy is indicated by a dotted line

arrangement, such as the number and type of neighboring atoms and their distance to the absorbing atom.

The XANES region itself can sometimes be divided into two parts: The pre-edge region at energies below E_0 and the XANES region extending from the threshold up to energies 50–100 eV above it. Pre-edge structures result from transitions of the photoelectron to bound excited states of the absorbing atom. For the K-edges of transition metal compounds, the pre-edge region generally exhibits structures reflecting the local symmetry around the absorber atoms. As in the EXAFS regime, the changes in μ within the XANES region also result from the scattering of the excited photoelectron at the outlying, neighboring atoms. However, the photoelectron is not simply backscattered, but undergoes multiple scattering (MS) at the outlying atoms as will be described in Sect. 1.4.

17d.1.1 Experimental Setup and Data Reduction

A generic experimental setup of the optics and instrumentation used in an XAFS experiment is shown in Fig. 17d.2. Synchrotron radiation from an electron storage ring is used as the light source. Synchrotron radiation is emitted from centripetally accelerated charged particles (an overview of synchrotron radiation can be found elsewhere, e.g., [2]). It is a very intense, highly collimated, polarized beam of electromagnetic radiation having a continuous band of wavelengths from around the μm (infrared) to the pm (hard X-ray) range. The selection and variation of the photon energy E around E_0 of the element of interest is accomplished by means of a monochromator. The incoming synchrotron beam is diffracted on the crystal planes of the monochromator. According to Bragg's law of diffraction, the wavelength of the exiting photons is

$$n\lambda = 2d \cdot \sin\Theta \qquad n = 1,2,3\ldots \tag{17d.1}$$

where d is the spacing between diffracting planes. Different types of monochromator crystal pairs exist. At the XAS and INE beamlines of the ANKA synchrotron source

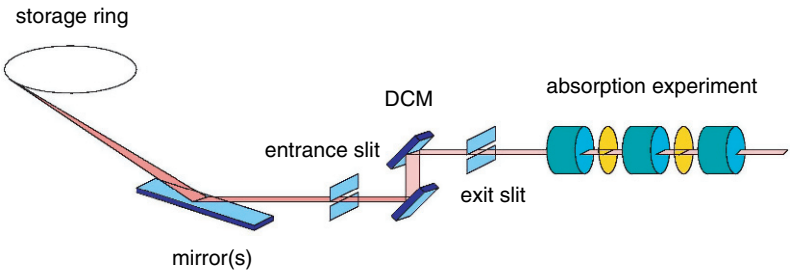

Fig. 17d.2 Schematic diagram of a generic X-ray absorption experiment using a synchrotron radiation source and standard transmission geometry

[3], e.g., Si<111> (d = 3.135 Å), Si<311> (d = 1.638 Å), Ge<220> (d = 2.000 Å), and Ge<422> (d = 1.155 Å) are available to cover a wide energy range. The photon wavelength is selected by varying the angle of reflection, Θ. The photon energy E in keV is related to λ in Å by the following equation:

$$E[keV] = 12.398/\lambda[\text{Å}] \tag{17d.2}$$

Most commonly, a double-crystal monochromator (DCM) is used to keep the beam propagating in the same direction following two reflections. This has the advantage of suppressing higher harmonic reflections ($n > 1$ in Eq. 17d.1) by detuning slightly the parallel alignment of the crystal pair. To offset the vertical movement of the beam as Θ is varied, either the sample is simultaneously moved vertically or the second crystal is translated during the movement to maintain a fixed beam exit height.

An absorption spectrum is obtained by measuring the photon intensity in front of the sample (I_0) and behind the sample (I_1) as a function of the incident photon energy E using ionization chambers as X-ray detectors (Fig. 17d.3a). The absorption for a given sample length is given by Lambert-Beer's law

$$\mu(E) \cdot d = \ln[I_0(E)/I_1(E)] \tag{17d.3}$$

where μ is the absorption coefficient and d the thickness of the sample. The absorption of a reference with known E_0 placed upstream of the sample and measured simultaneously ($\ln[I_1(E)/I_2(E)]$) is used for energy calibration. For K-edge

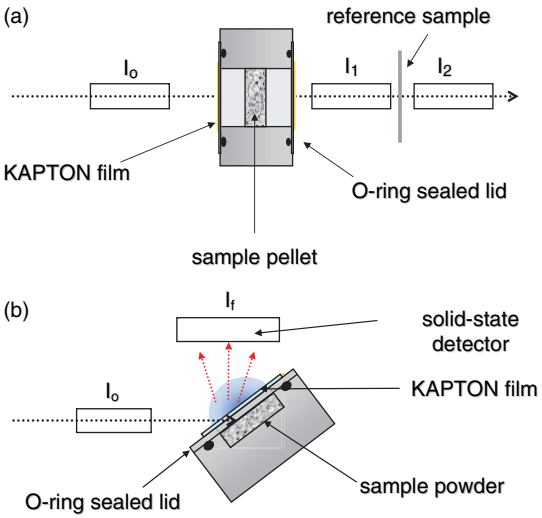

Fig. 17d.3 Schematic representation of an XAFS transmission experiment using ionization chambers (Fig. 17d.3a) and a fluorescence yield detection experiment using a solid-state detector (Fig. 17d.3b). Sealed sample cells are designed to prepare, transfer, and measure oxygen-sensitive materials without exposure to air

measurements of transition metal compounds, the corresponding pure elements generally are used as thin reference foils of adequate thickness (optimized to give an absorbance step around one: $(\mu(E > E_0)–\mu(E < E_0) \cdot d \sim 1)$.

In addition to recording the transmission of photon intensities, proportional secondary processes can be detected, which occur when atoms relax following inner-shell electron excitation by the X-rays, such as fluorescence photon emission or emission of secondary electrons. Fluorescence detection as displayed in Fig. 17d.3b is required for diluted samples (i.e. where the element concentration is less than around 5 mol%) and for samples which are totally absorbing or impermeable for X-rays.

The XANES spectrum and EXAFS oscillations must be isolated from the raw XAFS data prior to analysis. For both spectral regions, XANES and EXAFS, the initial steps in data reduction are the same: Background subtraction and normalization of the edge jump to unity. To extract EXAFS oscillations, the energy axis is first converted into photoelectron wave vector (k) values:

$$k = \sqrt{\frac{2m_e}{\hbar^2} E_{\text{kin}}} \; ; \; E_{\text{kin}} = (E - E_0) \tag{17d.4}$$

where m_e is the mass of an electron and $\hbar$ is Planck's constant divided by 2π. E_{kin} is the kinetic energy of the photoelectron (i.e. the difference between the incident X-ray energy E and E_0). To calculate k, E_0 must therefore be defined. The problem in defining E_0 is that errors in its position are coupled to errors in determining bond distances from fits of the experimental EXAFS to the EXAFS equation (see next section). By defining E_0 as an easily identifiable feature in the spectrum and treating E_0 as an adjustable parameter in the fit procedure, this problem can be avoided. For the K-edges of the transition metals, it is very practical to define E_0 as the energy of the maximum derivative of the XANES, as this value is determined easily. For the metal references, the first inflection point in the rising edge can be assigned unambiguously to the corresponding metal atom's 1s-energy. The next steps in EXAFS data reduction (isolation of oscillation with spline polynomial fit, k-weighting, and Fourier transformation) will be covered in the following section.

17d.1.2 EXAFS: Extended X-ray Absorption Fine Structure

It was found that the EXAFS oscillatory pattern is an interferogram of the atomic arrangement surrounding the absorbing atom. The EXAFS function ($\chi(k)$) expresses the modulation of μ by scattering on the surrounding atoms, normalized to the absorption coefficient of an isolated atom of the absorbing atom type (μ_0) as a function of k:

$$\chi(k) = \frac{(\mu - \mu_0)}{\mu_0} \tag{17d.5}$$

Generally, μ_0 is not known. Therefore, fitting an appropriate function to average the oscillatory EXAFS pattern (often splined polynomial functions) allows for an approximation of μ_0. Then, this function is used to calculate $\chi(k)$ according to Eq. 17d.5. The isolated $\chi(k)$ is supposed to oscillate uniformly about the zero axis. $\chi(k)$ is often weighted with k^n, where $n = 1–3$. This accents the oscillations at higher k, where they are considerably dampened (particularly those of low Z elements).

The EXAFS interference processes are illustrated schematically in Fig. 17d.4. Constructive interference between the outgoing photoelectron wave function and backscattered wave leads to maximum EXAFS oscillations, destructive interference corresponds to minima. At the photon energy $h\nu_2$, the relationship between the wavelength of the photoelectron ($\lambda = 2\pi/k$) and the distance between the absorbing atom and the backscattering atom (R) is such that they interfere constructively. At a somewhat lower energy, $h\nu_1$, the wavelength is too long to fulfill this condition and destructive interference with the backscattered wave occurs. It is predicted intuitively that the relationship between R and λ for constructive interference is fulfilled periodically, and this is indeed the case. The EXAFS $\chi(k)$ is derived as the following expression:

$$\chi(k) \propto \sum_{j=1}^{n} N_j \cdot |f_j(k,\pi)| \cdot \sin\left(2kR_j + \Phi_j(k,R)\right) \qquad (17d.6)$$

The sum is over each coordination shell j up to the n^{th} coordination shell. Generally, backscatterers can be identified within distances up to 5 Å. N is the coordination number. $f(k)$ is the backscattering amplitude function for the neighboring atom type. $\Phi(k,R)$ is the total phase shift of the photoelectron, as it passes through the potential of the absorbing atom, through that of the backscattering atom, and back through the absorber potential again after scattering. The functions $f(k)$ and $\Phi(k,R)$ are unknown and must either be extracted empirically using EXAFS data from model compounds of known structure or calculated theoretically. The fact that these functions are dependent on the type of backscatterer allows for an identification of the type of atoms forming a coordination shell from EXAFS analysis. This

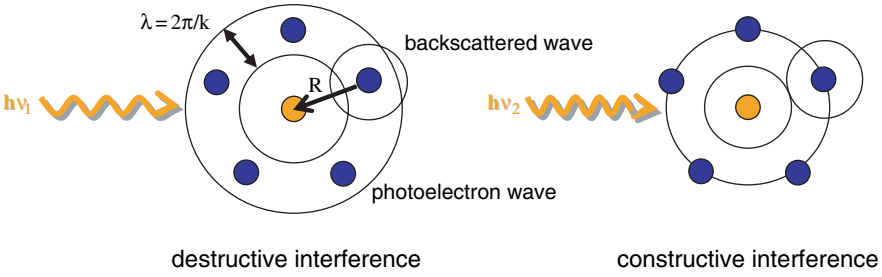

Fig. 17d.4 Illustration of destructive and constructive interference of the outgoing photoelectron wave and backscattered wave, which lead to minima and maxima of the oscillation in μ observed in the EXAFS regime, respectively

is true, provided that the types of atoms differ sufficiently in atomic number (Z). Neighboring atoms have similar functions and it is not possible to differentiate between $Z+1$ types of atoms.

Equation 17d.6 has two terms, a phase term, $\sin(2kR+\Phi(k,R))$, and an amplitude term. The amplitude of $\chi(k)$ is dependent on more parameters than simply N and $f(k)$. Under the assumption of the photoelectron being approximated by a plane wave and the sample having a minimum disorder, the EXAFS equation is given by:

$$\chi(k) = \frac{{S_0}^2}{k}\ell^{-1}\sum_{j=1}^{n} N_j \cdot |f_j(k,\pi)|\frac{e^{-2R_j/\lambda(k)}}{R_j^2}e^{-2k^2\sigma^2}\sin\left(2kR_j+\Phi_j(k,R)\right) \qquad (17d.7)$$

where

S_0^2 = amplitude reduction factor accounting for multi-electron shake-up and shake-off effects,

ℓ = angular momentum quantum number,

σ^2 = mean square average displacement from the mean bond length, and

$\lambda(k)$ = mean free path length of the photoelectron.

By fitting experimental data to the EXAFS equation (Eq. 17d.7) using iterative least square fit techniques, the metrical parameters describing the coordination structure of the absorbing atom can be obtained. Values of R can be obtained with an accuracy of ±0.02 Å. The parameters associated with the amplitude of $\chi(k)$ are obtained with less accuracy of about 20–25%. This is due to the large number of parameters contributing to the EXAFS amplitude and their mutual correlation. In addition, care has to be taken to prevent a number of systematic errors from contributing to the inaccuracy of amplitude measurement. The most important sources of errors include thickness effects of concentrated samples [4], self-absorption effects in fluorescence experiments [5], dead-time effects in fluorescence measurements, radiation leaks in or around a sample, contamination of I_0 with higher harmonics in the beam, and overfitting of the polynomial spline function to μ_0.

The EXAFS oscillations are a sum of contributions from n coordination shells. In order to separate the individual contributions, Fourier filtering techniques are used. By performing a Fourier transformation from wave (k) space into real (R) space, the scattering from each distance (j-shell of atoms) is resolved into a band of Fourier coefficients along the R axis. The magnitude of the transform is a modified radial pair distribution function with peaks corresponding to scattering from atoms located on each coordination shell. The Fourier transform (FT) peaks always appear at distances shorter than R_j, typically around 0.5 Å shorter, due to the Φ phase shift. For this reason, the x-axis is never labeled R, but $R-\Delta$ in the figures displaying the Fourier transform of an EXAFS spectrum. The FT peaks are also broadened, mostly due to a limited transformation range of the data and limited instrumental resolution. The bond length resolution is $\delta R \sim \pi/2k_{\max}$, with $k_{\max}$ being the k-range available. Individual contributions to $\chi(k)$ can be separated using an inverse Fourier transformation. For this purpose, selected regions in the R-space are transformed back into k-space.

A number of ab initio programs are available for calculating theoretical $f(k)$ and $\Phi(k,R)$ functions as well as XAFS spectra. The FEFF code, named after the $f(k)$ function itself (FEFF = $f_{\text{eff}}(k)$, is a notation for the effective curved-wave scattering amplitude [6, 7, 8]). FEFF has interfaces with the codes available for analyzing EXAFS data, such as FEFFIT in the UWXAFS program packages [9] or the interactive FEFFIT version IFEFFIT [10].

17d.1.3 XANES: X-ray Absorption Near-Edge Structure

The fine structures in the XANES spectral region are also due to electron scattering processes. At lower energies near E_0, the outgoing photoelectron is not simply backscattered by the outlying neighboring atoms, but scattered in all directions. The reason is that the $f(k)$ function for photoelectrons of low E_{kin} has significant values at all angles, and not only at 180°. The probability of the excited electron being scattered at all angles at these energies is high. Together with the longer mean free path length $\lambda(k)$ at low energies, this leads to multiple scattering (MS) of the outgoing photoelectron. Where the E_{kin} of the photoelectron is large enough to escape the atomic potential of the central absorbing atom, it is scattered or ricocheted by a neighboring atom at some angle other than 180° into the direction of another near-neighbor atom, where it is scattered again. This process is repeated until the photoelectron eventually returns to the absorbing atom.

It is the MS character of XANES that renders this method sensitive to multi-atom correlation functions, i.e., the XANES region contains information about the coordination geometry of the absorbing atom, including interatomic distances and angles. However, this information is not easily extracted from XANES data. XANES features and their intensity and energy position are observed to be dependent on a number of factors in addition to coordination geometry and interatomic distances. These factors include the absorbing atom valence, orbital occupancy, electronegativity of coordinating atoms, and orientation of anisotropic samples. As the XANES features depend on more parameters than the EXAFS features, theoretical treatment has lagged behind. There is no simple XANES equation, such as the one existing for the EXAFS region (Eq. 17d.7). Generally, two strategies exist to interpret XANES spectra. The first strategy is a comparison of features observed in unknowns with XANES features of known compounds. This is often referred to as “fingerprinting”. The other strategy is to perform theoretical XANES calculations at variable specified parameters, such as sample orientation or atomic cluster size, to explain trends observed in the experimental data.

As the XANES region contains transitions at E_0, the valence state of the absorbing atom can also be determined from XANES data. As shown in Fig. 17d.5, the edge of Ti oxides shifts towards higher energies in the order of Ti, TiO, Ti_2O_3, and TiO_2 due to reduced shielding of the core electrons (i.e. increase in E_0 of the core electrons) associated with an increase in the mean valence state across the series. By

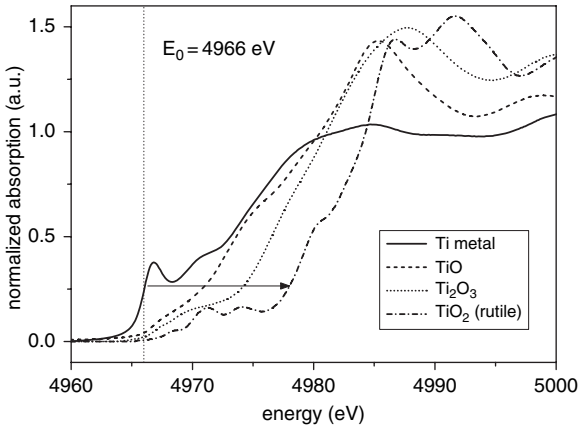

Fig. 17d.5 Normalized Ti K-XANES of Ti metal and different Ti oxides. Note the edge shift to higher energy with increasing Ti valence state (chemical shift), indicated by an arrow. E_0 corresponding to the Ti(0) 1s-energy is marked by a dotted line

comparing XANES edge energies of samples of known oxidation states with that of an unknown, the oxidation of the unknown can be identified.

17d.2 Investigation of Ti-doped $NaAlH_4$ by XAFS

This section is aimed at giving an overview of the application of XAS in hydrogen storage material research, in particular sodium alanate doped with a Ti-based precursor by ball milling. Ti-based precursors were shown to be most efficient in terms of kinetics and hydrogen storage capacity when added to the alanate [11, 12, 13]. However, the nature of the Ti phase present in the activated alanate system still is a matter of debate. In literature, two hypotheses have been suggested: The first speculates that during the doping procedure, Ti(0) species are formed and that the active catalyst is a Ti-Al alloy [14]. The second one claims that the dopant is substituted in the lattice of the bulk hydride [15]. Several research groups investigated the evolution of titanium in doped sodium alanate by XAFS spectroscopy [16, 17, 18]. For more clarity, the following sections will focus on the results obtained by Léon et al. [17, 19]. XAFS measurements at the Ti K-edge were performed in the ANKA XAS and ANKA INE beamlines [20] at Forschungszentrum Karlsruhe (FZK), Germany. Reference samples like Ti metal, Ti alloys, and $TiCl_3$ were measured in the transmission mode. Due to the low concentration of Ti in the doped sodium alanate samples, these spectra were taken in the fluorescence mode at room temperature, collecting Ti K_α radiation ($\sim 4510\,\text{eV}$) by a solid-state detector (5-element Canberra LEGe). Special sample holders as presented in Fig. 17d.3 were used in order to prepare, transfer, and measure the samples without exposing them to air.

17d.2.1 Initial Dehydrogenation/Rehydrogenation with $TiCl_3$ *as Dopant Material*

$TiCl_3$ is one of the most common precursors used to activate sodium alanate for hydrogen storage application. Figure 17d.6 displays the normalized Ti K-edge XANES of $TiCl_3$-doped sodium alanate after ball milling (bm) and at different stages of the reaction. The samples were quenched during the first dehydrogenation (dd = during desorption) and rehydrogenation (da = during absorption). The spectra are compared to those of pure $TiCl_3$ and titanium metal as references. When inspecting the first derivatives of the XANES curves (not shown), it becomes evident that the first inflection point in the spectrum (bm) is lowered from 4972 eV for $TiCl_3$ to 4966 eV, coinciding with the position of Ti metal. This confirms earlier assumptions of $TiCl_3$ being decomposed during ball milling and the valence state of Ti being changed from (+3) to (0). Moreover, the analysis of the first inflection point in spectra (dd) and (da) shows that this valence state does not undergo further changes – neither during desorption, nor during reabsorption of hydrogen. Additionally, the features in the range from 4967 eV to 4973 eV (shoulder marked by an arrow in Fig. 17d.6) and at the edge crest region at around 4990 eV of the absorption curves of samples (bm), (dd), and (da) show a distinct intensity gain. The shoulders in the XANES rising edge region of 3d transition metals are due to 1s → 3d transitions of the excited core electron to the lowest unoccupied states above the Fermi level. The transition probability increases with the degree of 4p/3d hybridization of these states. Hence, it depends on the local absorber site symmetry and – in case of small clusters – on the particle size. [21] The observed evolution indicates the growth or ordering of Ti phases in the alanate, going from sample (bm) to (dd) and (da).

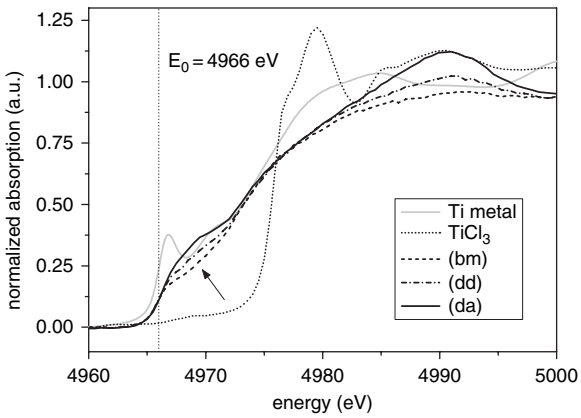

Fig. 17d.6 Normalized Ti K-XANES of $NaAlH_4$ doped with 5 mol% of $TiCl_3$ at different stages: Ball-milled (bm) for 30 minutes, after 2.6 wt.% of hydrogen were released at 150°C under a residual hydrogen pressure of 0.3 bar (dd), and after 2.3 wt.% of hydrogen were reabsorbed at 100°C under 100 bar hydrogen (da). The spectra of $TiCl_3$ and Ti metal are shown for comparison

This interpretation is in agreement with the observation of the edge resonance and EXAFS amplitude increase from sample (bm) to (dd) and (da).

Figure 17d.7 displays the EXAFS functions $\chi(k)$ of the samples corresponding to those of Figure 17d.6. Comparison of the $TiCl_3$ spectrum and (bm) shows that the Ti environment changes significantly during ball milling. The strong reduction of the EXAFS amplitude indicates the strong distortion of the local order in (bm). With the initial alanate decomposition in sample (dd), the oscillations reflecting the new structure in sample (bm) are intensified and become even more pronounced for sample (da) that is quenched during rehydrogenation. EXAFS shows that the local order around Ti in $TiCl_3$ is destroyed during ball milling. This order is replaced by a different local structure during the subsequent hydrogen desorption and absorption cycle.

EXAFS data fit analysis was carried out for $TiCl_3$, Ti metal, and samples (dd) and (da). Analysis of the strongly distorted local Ti environment in sample (bm) was not attempted. The amplitude reduction factor S_0^2 was determined to be about 0.6 in order to reproduce the theoretical coordination number of 12 and 6 for the first Ti neighbor shell in the Ti metal and the first Cl neighbor shell in $TiCl_3$, respectively.

The structural parameters obtained by fitting the $TiCl_3$ EXAFS are in agreement with the crystallographic data (6 Cl with d(Ti-Cl) = 2.45 Å) [22]. The coordination environment in the case of Ti metal is characterized by the distance splitting within the hcp structure (12 next neighbor atoms) between 6 atoms at 2.896 Å in a plane and 6 atoms at 2.95 Å (3 above and 3 below that plane). This slight distance deviation within the first coordination sphere is also visible from the EXAFS beat node in the Fourier-filtered data above 14 $Å^{-1}$ (not shown). However, as the EXAFS bond length resolution is limited to 0.11 Å in these experiments (cf. Sect. 17d.1), the Ti metal's first shell EXAFS fit was carried out with a single distance (2.91 Å) of Ti

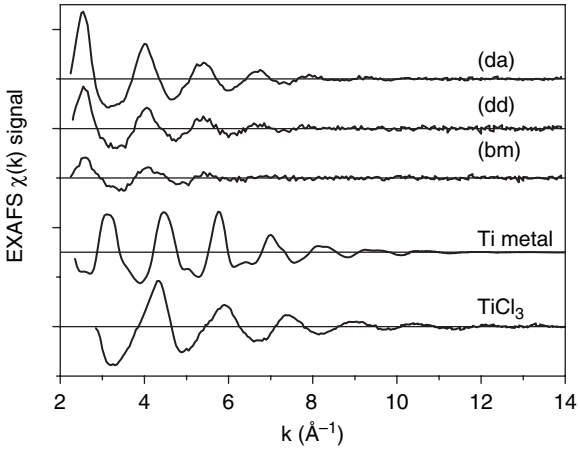

Fig. 17d.7 Ti K-EXAFS spectra $\chi(k)$ of $NaAlH_4$ doped with 5 mol% of $TiCl_3$ at different stages – cf. XANES depicted in Fig. 17d.6. Spectra are vertically shifted for clarity

neighbors. The distance splitting is reflected by the relatively high Debye-Waller factor of 0.0078 Å^2 obtained for the 12 Ti atoms at a mean distance of 2.91 Å.

Figure 17d.8a represents the magnitude and imaginary part of the Fourier transform (FT $k^2\chi(k)$) as well as the fit in R-space of sample (da). Figure 17d.8b displays the corresponding Fourier-filtered data and the fit in k-space. Comparison of the FTs of samples (dd) and (da) (Figs. 17d.8a, 17d.8b) with Ti metal and $TiCl_3$ reveals the much higher asymmetry in the Ti's first coordination sphere of the samples quenched during the decomposition and reabsorption of hydrogen. From the beat node at around 11 Å^{-1} in (dd) and (da) – cf. the arrow in Fig. 17d.8b – the presence of two closely spaced backscatterers with the same atomic number was assumed. The distance separation between the two shells is derived by $\delta R \sim \pi/2k_{\mathrm{bn}}$, where k_{bn} denotes the beat node position in k-space. For sample (dd) a distance separation of 0.154 Å and for sample (da) a distance separation of 0.14 Å was found. Inclusion of two scattering paths is mandatory to model the EXAFS data. The fit results with two

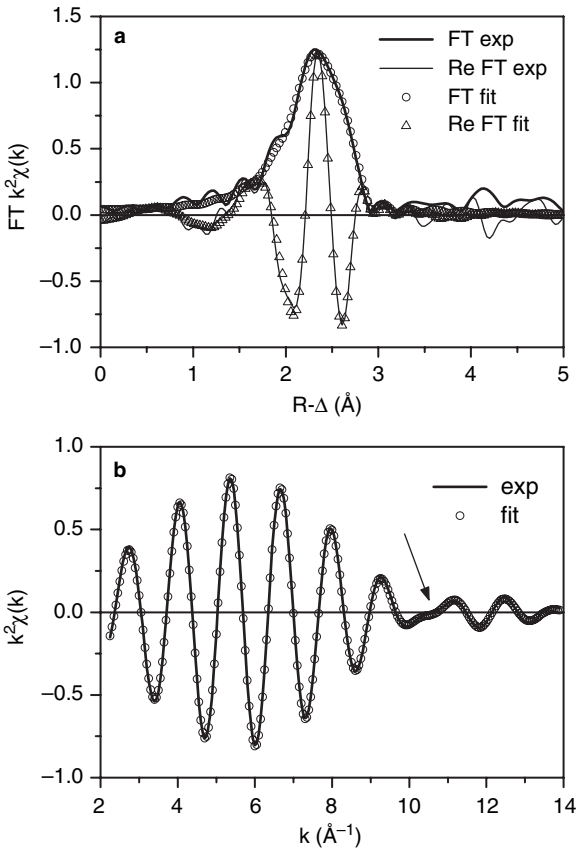

Fig. 17d.8 (**a**) FT magnitude and imaginary part, R-space fit magnitude and imaginary part of sample (da); (**b**) Fourier-filtered data and fit in k-space

Ti backscatterers are in agreement with the estimated distance separation from the beat node position. It should be noted that the fit fails when including Cl backscatterers as well as one or two closely spaced Al shells. These results indicate that neither significant amounts of $TiCl_3$ are present in the samples (bm), (dd), and (da), nor formation of a Ti/Al alloy takes place at this stage of cycling the alanate. As already concluded from XANES, the EXAFS confirms the significantly higher local order around Ti in sample (da) as compared to samples (bm) and (dd), indicating that partial annealing takes place upon the hydrogen exchange. The local order in the ball-milled samples is somehow compatible with a strongly distorted hcp structure, reflecting the strain as a consequence of the mechanical stress resulting from the milling procedure. The formation of an alloy with Al or the formation of TiH_2 in this stage is not supported by our EXAFS data.

17d.2.2 $Ti_{13} \cdot 6$*THF in Comparison to* $TiCl_3$ *as Dopant Material – Further Hydrogen Cycling*

The $Ti_{13} \cdot 6THF$ nanocluster produced by an organo-metallic synthesis route was described for the first time in the mid-nineties. Recently, the cluster was used to prepare a functional nanocomposite by ball-milling with $NaAlH_4$. [23]. The nanocomposite showed superior hydrogen exchange kinetics when compared to the state of the art in literature. EXAFS data and metric parameters obtained from a pure cluster sample were originally published by Franke et al. [24]. The $Ti_{13} \cdot 6THF$ structure comprises a metallic Ti core of icosahedral shape surrounded by six THF ligands with $R_{Ti\text{-}O} = 2.02$ Å and $R_{Ti\text{-}Ti} = 2.89$ Å (schematically shown in the inset of Fig. 17d.9 taken from [23]). Molecular modeling calculations corroborated the proposed structure [25]. The pure $Ti_{13} \cdot 6THF$ cluster is highly reactive to oxygen. The XANES features of a fresh Ti_{13}·6THF sample are compared to a sample placed in the X-ray beam for several hours and to Ti metal in Fig. 17d.9. The aged sample starts to develop the typical oxidation features described in [24] – an edge shift to higher energies, development of a pre-edge peak, and intensity gain at the edge-crest region. In Ti cluster-doped sodium alanate, the valence state of Ti remains unchanged by ball milling – independently of the milling time. The first inflection point stays at 4967 eV as for the pure cluster sample, indicating partial oxidation of some of the outer Ti atoms by interaction with the THF coating. A shift to the metallic state (4966 eV) occurs during the first hydrogenation cycles. Further cycling does not affect the Ti oxidation state as in the case of the $TiCl_3$ precursor.

The EXAFS $\chi(k)$ obtained for the functional nanocomposite and the $TiCl_3$-doped alanate after several hydrogen desorption/absorption cycles is shown in Fig. 17d.10: $TiCl_3$(a8a), i.e. the $TiCl_3$-doped alanate after 8 absorptions, $TiCl_3$(a9d), i.e. the alanate after the 9th desorption, and, correspondingly, $Ti_{13} \cdot 6THF$(a8a) and $Ti_{13} \cdot 6THF$(a9d). The metallic references Ti, $TiAl_3$, and TiH_2 are plotted for comparison. Figure 17d.11a shows the FT magnitudes reflecting the evolution of

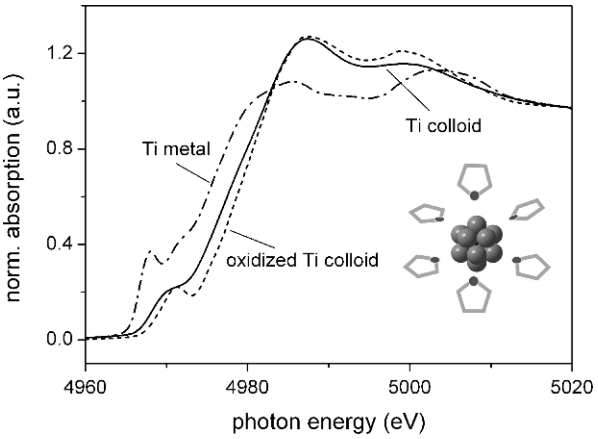

Fig. 17d.9 Normalized Ti K-XANES of the pure $Ti_{13} \cdot 6THF$ sample, an oxidized sample, and a 5 μm Ti metal foil. The inset shows a sketch of the Ti cluster with six THF ligands surrounding the icosahedral metal core

the $TiCl_3$-doped alanate and Fig. 17d.11b the evolution of the $Ti_{13} \cdot 6THF$-doped alanate. EXAFS reveals that after eight hydrogenation cycles, a similar local Ti environment persists for all alanates, no matter which dopant was used. However, the EXAFS amplitude is more pronounced in $TiCl_3$(a8a) and $TiCl_3$(a9d) and significantly dampened in $Ti_{13} \cdot 6THF$(a8a) and $Ti_{13} \cdot 6THF$(a9d). This difference suggests that the local order around Ti in $TiCl_3$-doped samples is better defined than in samples obtained from adding the cluster as Ti precursor. Comparing the $\chi(k)$ of the

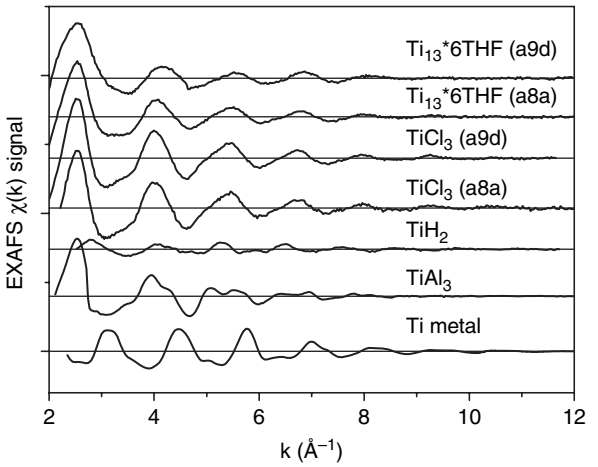

Fig. 17d.10 Ti K-EXAFS spectra $\chi(k)$ of $NaAlH_4$ doped with 5 mol% Ti on the basis of $TiCl_3$ or $Ti_{13} \cdot 6THF$ after eight absorption cycles (a8a) and subsequent desorption (a9d). Spectra of Ti metal, $TiAl_3$, and TiH_2 are shown as references. Spectra are vertically shifted for clarity

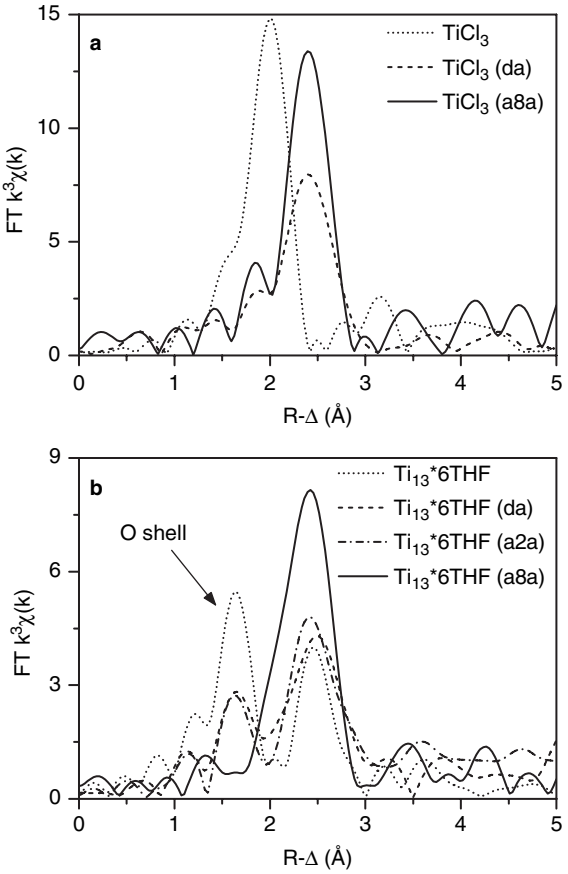

Fig. 17d.11 (**a**) Ti K-EXAFS FT magnitude of $TiCl_3$ and alanate samples doped with 5 mol% Ti on the basis of $TiCl_3$ in different stages of the dehydrogenation/rehydrogenation reaction: (da = during first absorption), (a8a = after 8th absorption); (**b**) corresponding FT magnitude of samples doped with 5 mol% Ti on the basis of $Ti_{13} \cdot 6THF$, (a2a = during second absorption) is shown in addition

recycled alanates to that of the reference samples further suggests that the Ti local structure in the alanates is not the same as in crystalline Ti or TiH_2. The EXAFS signals from the Ti-doped alanates are in phase with the $TiAl_3$ signal only.

EXAFS data fit analysis reveals that upon cycling under hydrogen, the local Ti environment in the $TiCl_3$-doped samples transforms from a distorted hcp structure after ball milling to a structure containing both Al and Ti backscatterers. In samples $TiCl_3$(a8a) and $TiCl_3$(a9d), the first neighbor shell comprises about 10 Al atoms with a Ti-Al distance of 2.8 Å (note that in $TiAl_3$ bulk alloy this shell is split into two Ti-Al distances of 2.74 Å and 2.89 Å, respectively). In addition, EXAFS reveals a small Ti contribution with a Ti-Ti distance of 3.88 Å and an apparent coordination number of 1. The significant reduction of the Ti coordination number compared to

the bulk alloy and the relaxation into a single first shell Al distance indicate the formation of very small intermetallic entities after several hydrogenation cycles. Formation of this alloy phase or Ti-Al "nanocluster" was also suggested by Graetz et al. [26]. The alloy structure is independent of the milling parameters and remains unchanged during subsequent hydrogen cycles.

In the case of the $Ti_{13} \cdot 6THF$-doped alanate samples, the local Ti environment is preserved during ball milling. As shown in Fig. 17d.11b (O shell marked by an arrow), oxygen from the THF coating of the icosahedral metal core is stripped off only after a couple of hydrogenation cycles. After eight cycles, the local structure is similar to the $TiCl_3$-derived samples – with about 9 Al atoms at 2.75 Å and 1 Ti atom at 3.84 Å detected by EXAFS fit analysis.

The formation of the nano-scale Ti-Al alloy detected by XAFS is correlated with the decrease in the hydrogen storage capacity and the alanate desorption/absorption reaction rate. Avoiding the reduction of Ti to the metallic state and the subsequent formation of a bimetallic phase consuming a significant Al fraction that is then missing in alanate reconstruction would therefore increase the efficiency of the material.

17d.2.3 An Alternative Strategy

The structural details obtained from experiments using $TiCl_3$ and $Ti_{13} \cdot 6THF$ as catalyst precursors to activate sodium alanate suggest that Ti should be bound to an element in order to prevent its reduction to the metallic state and, thus, its alloying with Al. A possible solution is to use one of the decomposition products, either NaH or Al, to synthesize a new Ti-containing phase. Chemically and thermodynamically, the most favorable route is the development of an Al-Ti phase at the surface of Al particles. This pre-treated Al is then mixed with an equimolar amount of NaH and ball-milled to form a functional nanocomposite resembling the desorbed state of Ti-doped $NaAlH_4$. The alanate is activated by doping with 2 mol% Ti on the basis of this $NaH–AlTi_{0.02}$ nanocomposite [27].

The decomposition kinetics of the new compound are similar to data obtained after 5 cycles for sodium alanate doped with $TiCl_3$ by ball milling for 30 minutes. Moreover, the kinetics remain stable from the first to the fifth absorption cycle. In contrast to $TiCl_3$-doped $NaAlH_4$, the hydrogen storage capacity remains constant at 4 wt.% of H_2, regardless of the number of cycles.

XAFS investigation of this material reveals that the valence state of Ti does not change during ball milling or cycling under hydrogen. The first inflection point in the XANES remains unchanged at 4967 eV, suggesting that Ti is never fully reduced to the zerovalent state in this new material. Comparison of the corresponding EXAFS $\chi(k)$ functions indicates that the local structure around Ti in the $NaH–AlTi_{0.02}$-doped alanate ball-milled for two hours and Ti in the doped alanate after five absorption cycles is also similar. Therefore, it can be assumed that the local structure around Ti in the novel material persists during the hydrogenation/dehydrogenation cycles. Comparing the EXAFS to that obtained from bulk

$TiAl_3$ indicates that the formation of this crystalline phase can be excluded. Moreover, the local structure of Ti in the new material is also different from that in $TiCl_3$- or Ti cluster-doped sodium alanate after eight absorption cycles.

Figure 17d.12a displays the FT magnitude of the k^3-weighted $\chi(k)$ function of Ti-doped sodium alanate obtained by the hydrogenation of NaH–$AlTi_{0.02}$ after 30 minutes of ball milling. The corresponding Fourier-filtered data and the k-space fit are shown in Fig. 17d.12b. The FT magnitude exhibits three resonances, the best fit is obtained with 6 Al at 2.98 Å, 4 Al at 4.13 Å, and 7–8 Ti at 5.25 Å. The FT reflects the presence of rather large, well-ordered entities. Interestingly, this well-ordered structure is already present after ball milling and not developing slowly – as in the alanate activation process by adding $TiCl_3$ or $Ti_{13} \cdot 6THF$ – after a couple of hydrogenation cycles.

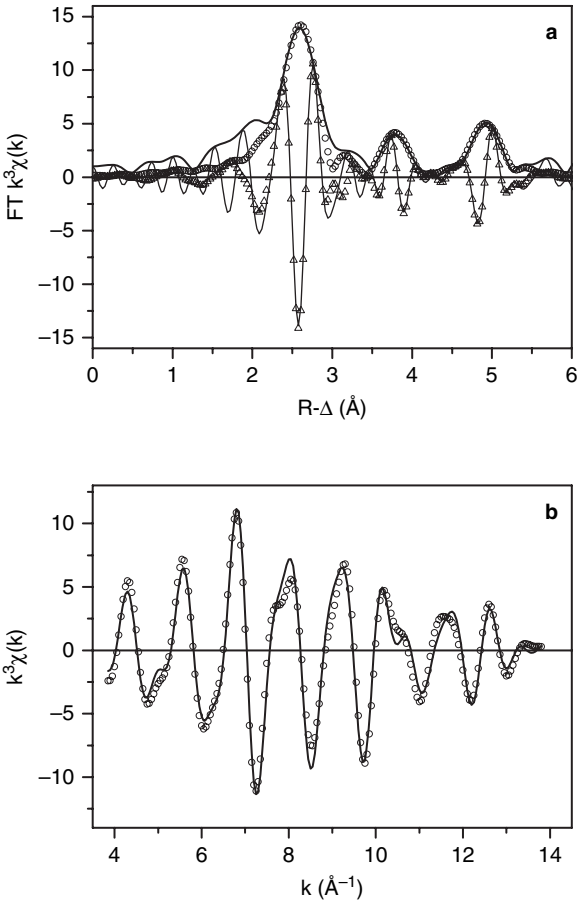

Fig. 17d.12 (**a**) FT magnitude and imaginary part, R-space fit magnitude and imaginary part of $NaAlH_4$ doped with 2 mol% Ti on the basis of the hydrogenation of NaH – $AlTi_{0.02}$ nanocomposite after ball milling; (**b**) Fourier-filtered data and fit in k-space

17d.3 Outlook

Important insights into the evolution of the local atomic environment of Ti atoms in Ti-activated sodium alanate quenched at different stages of hydrogen desorption and absorption were obtained by static Ti K-XAFS investigations. These measurements were performed at room temperature and under ambient pressure conditions. Nevertheless, these measurements may not fully reflect the electronic and structural conditions of the working catalyst, i.e., the active Ti species during the hydrogen uptake and release reaction at increased pressure and temperature. Therefore, a temperature-programmed high-pressure cell was developed and tested successfully at 100 bar hydrogen pressure. The set-up was designed to pursue the decomposition and Na-alanate reconstruction *in situ* with fluorescence yield detection XAFS. This high-pressure cell is equipped with a volumetric system which records the reaction kinetics. The *in-situ* measurement will reveal when and how the Ti-Al phases postulated in Sect. 17d.2.2 are forming. The detailed knowledge of this process is the prerequisite to confirm that the formation of these nano-scale alloy particles is responsible for the decrease of the hydrogen storage capacity.

Furthermore, initial XAFS measurements performed at the Al K-edge (1559 eV) of pure and $TiCl_3$-doped $NaAlH_4$, including Al metal and $TiAl_3$ as references, indicated the feasibility of soft X-ray absorption measurements of alanate-based hydrogen storage materials. [28] According to these initial Al K-XANES results, doping of sodium alanate by $TiCl_3$ also induces modifications of the geometric and electronic structure around the Al sites. After several cycles under hydrogen, a new phase develops, which contains Al in the zerovalent state. The Al K-XANES fingerprint of this phase is similar to that of bulk phase $TiAl_3$. These very recent results fully agree with the identification of nano-scale Ti-Al alloy domains by Ti K-XAFS experiments presented in Sect. 17d.2.2. Measurements on both edges indicate the presence of molecular-scale inhomogeneities within the average alanate framework, which are probably responsible for the deterioration of hydrogen uptake and release properties after a number of hydrogenation cycles.

Acknowledgements Parts of Sect. 17d.1 are based on a manuscript kindly provided by Melissa A. Denecke, INE, Forschungszentrum Karlsruhe.

References

1. D. C. Koningsberger, R. Prins (Eds.), X-Ray Absorption: Techniques of EXAFS, SEXAFS, and XANES, J. Wiley & Sons: New York, 1988.
2. H. Winick, *Scientific American* 1987, November, 72.
3. *http://ankaweb.fzk.de/.*
4. L. G. Parratt, C. F. Hempstead, E. L. Jossem, *Phys. Rev.* 1957, 105, 1228.
5. L. Tröger, D. Arvanitis, K. Baberschke, H. Michaelis, U. Grimm, E. Zschech, *Phys. Rev. B* 1992, 46, 3283.
6. J. M. deLeon, J. J. Rehr, S. I. Z. C. Albers, *Phys. Rev. B* 1991, 44, 4146.

7. A. L. Ankudinov, S. D. Conradson, J. M. deLeon, J. J. Rehr, *Phys. Rev. B* 1998, 57, 7518.
8. J. J. Rehr, R. C. Albers, *Rev. Mod. Phys.* 2000, 72, 621.
9. E. A. Stern, M. Newville, B. Ravel, Y. Yacoby, D. Haskel, *Physica B* 1995, 208&209, 117.
10. M. Newville, *J. Synchr. Rad.* 2001, 8, 322.
11. B. Bogdanovic, M. Schwickardi, *J. Alloys Comp*. 1997, 253–254, 1.
12. C. Jensen, R. Zidan, N. Mariels, A. Hee, C. Hagen, *Int. J. Hydrogen Energy* 1999, 24, 461.
13. M. Fichtner, O. Fuhr, O. Kircher, J. Rothe, *Nanotechnology* 2003, 14, 778.
14. A. G. Haiduc, H. A. Stil, M. A. Schwarz, P. Paulus, J. J. C. Geerlings, *J. Alloys Comp.* 2005, 393(1–2), 252–263.
15. D. Sun, T. Kiyobayashi, H. T. Takeshita, N. Kuriyama, C. M. Jensen, *J. Alloys Comp.* 2002, 337, L8.
16. M. Felderhoff, K. Klementiev, W. Grünert, B. Spliethoff, B. Tesche, J. M. Bellosta von Colbe, B. Bogdanovic, M. Härtel, A. Pommerin, F. Schüth, C. Weidenthaler, *Phys. Chem. Chem. Phys.* 2004, 6, 4369.
17. A. Léon, O. Kircher, J. Rothe, M. Fichtner, *J. Phys. Chem. B* 2004, 108, 16372.
18. J. Graetz, J. J. Reilly, J. Johnson, A. Yu. Ignatov, T. A. Tyson, *Appl. Phys. Let.* 2004, 85(3), 500.
19. A. Léon, O. Kircher, M. Fichtner, J. Rothe, D. Schild, *J. Phys. Chem. B* 2006, 110, 1192.
20. M. A. Denecke, J. Rothe, K. Dardenne, H. Blank, J. Hormes, *Physika Scripta* 2005, T115, 1001.
21. R. Franke, J. Rothe, R. Becker, J. Pollmann, J. Hormes, H. Bönnemann, W. Brijoux, R. Köppler, *Adv. Mater.* 1998, 10, 126.
22. F. Auriemma, V. Busico, P. Corradini, M. Trifuoggi, *Eur. Polym. J.* 1992, 28, 513.
23. M. Fichtner, O. Fuhr, O. Kircher, J. Rothe, *Nanotechnology* 2003, 14, 778.
24. R. Franke, J. Rothe, J. Pollmann, J. Hormes, H. Bönnemann, W. Brijoux, T. Hindenburg, *J. Am. Chem. Soc.* 1996, 118, 12090.
25. P. S. Rudman, *J. Less-Common Met.* 1983, 89, 93.
26. J. Graetz, A. Yu. Ignatov, T. A. Tyson, J. J. Reilly, J. Johnson, *Mater. Res. Soc. Symp. Proc.* 2005, 837, N2.4.1.
27. A. Léon, C. Frommen, J. Rothe, D. Schild, M. Fichtner, WHEC16 2006 proceedings, Lyon, France, 2006.
28. A. Léon, A. Balerna, G. Cinque, C. Frommen, M. Fichtner, *J. Phys. Chem C.*, 2007, 111, 3795.

Part V
Perspectives

Chapter 18
Scientific Scope

Maximilian Fichtner

List of Abbreviations

AER	Absorption enhanced reforming
BET	Brunauer-Emmett-Teller method
GNF	Graphitic nanofibers
MOF	Metal-organic framework
PEMFC	Proton exchange membrane fuel cell
SOFC	Solid oxide fuel cell
SWNT	Single-walled carbon nanotubes
TCWSC	Thermochemical water splitting cycle
THE	High temperature electrolysis

18.1 Introduction

Interest in hydrogen as the future energy carrier has grown in the last few years, mainly because hydrogen economy may be an answer to the two major challenges

Maximilian Fichtner
Institut für Nanotechnologie, Forschungzentrum Karlsruhe, P.O. Box 3640, D-76021, Karlsruhe, Germany, e-mail: fichtner@int.fzk.de

A. Léon (ed.), *Hydrogen Technology*,

facing the future global economy: global warming and the security of energy supplies. While many experts worldwide have considered hydrogen fuel a worthwhile goal since the energy crisis in the early '70s of the last century, a strong interest can be noticed in countries with public strategic plans and significant funding efforts (e. g. USA, Japan, Canada, the European Commission) related to hydrogen. Industry, in particular oil companies, power suppliers and automobile manufacturers, recently has shown increasing interest in new hydrogen-related developments. The need for new, sustainable energy technologies is particularly urgent in the transport sector where energy demand keeps growing while a shortage of oil is expected on a medium term. Also, serious concerns are caused by the significant rise of global temperature due to the increasing amount of fossil CO_2 which is emitted from cars, industry, and households.

The main components of a hydrogen economy encompass production, transport, storage, and end use of hydrogen, e.g. in fuel cells or internal combustion engines. Safety is a crosscutting issue in all areas of hydrogen technology. Considerable technological challenges are encountered in various fields at the moment. Moreover, although steady progress is being made in hydrogen technology, a hydrogen economy is not likely to be introduced soon because there are still major questions to be solved first, such as these:

- How can hydrogen be produced in sufficient amounts, what will be the cost and how is production going to affect the environment?
- Will hydrogen be transported as a gas or as a liquid, and what will be the impact on the global economy?
- How can hydrogen be stored effectively at low cost, low risk, with low energy loss and in a form which makes it readily available for consumer applications?
- How can fuel cells be operated more effectively, over long periods of time, and how can they be produced at lower cost?
- How can severe incidents with hydrogen be avoided?

Hydrogen production and storage undisputedly are the most critical issues at the moment. A global hydrogen economy will not be successful if no satisfactory answers to the key questions have been found in these research areas.

As far as the technical development is concerned, the different techniques of production, transport, storage, and conversion cannot be considered as being independent of each other, if the whole process chain is to be optimized. There may be a certain production method, for example, which leads to a product gas with impurities, such as water, hydrocarbons, CO or sulphuric gases. However, even minor impurities can affect the choice of storage system as not every method is compatible with unpurified hydrogen which may also have a deleterious effect on the catalyst of the fuel cell. On the other hand, severe constraints on the fuel cell and/or the storage method may require the hydrogen to be purified or lead to preferences of certain production methods over others. Another example is the choice of a specific storage method, which will certainly decide whether a distribution infrastructure will be based on gaseous or liquid hydrogen.

Clearly, various options must be considered for technical problems so that an optimum solution of the entire process chain hydrogen technology can be found. A

short overview of the status of, and some of the main challenges in research and development will be discussed below. The focus will be on hydrogen production and storage.

18.2 Production

Producing hydrogen in amounts able to replace current energy carriers and satisfy the growing needs of a global society is one of the biggest challenges at the moment. Currently, it is not envisaged that one method would be able to do the job alone. In fact, the method of choice will depend on the regional situation and the type of energy available. Today, hydrogen is mainly produced from fossil resources (oil (18%), coal (30%), and natural gas (48%)) in processes based on cracking or steam reforming, with only a few percent generated by off-peak electrolysis (4%). In the long run, given the prospect of a lack of fossil resources and limitations on the release of greenhouse gases, only water and biomass are the two candidate raw materials for hydrogen production.

How the hydrogen can be produced from these resources depends on the energy available. When energy is supplied as high-temperature heat (solar thermal or nuclear), the heat can be used directly in a thermochemical process, such as the sulphur-iodine cycle or the so-called Westinghouse or hybrid-sulphur cycle and other, related cycles. In theses cycles, hydrogen and oxygen are produced from water and heat, without the use of electricity which results in an efficiency higher than that of alkaline electrolysis. The main research issues in this field are coupling the heat source (nuclear reactor or solar tower) to the cycle, and assess safety issues and other problem areas such as the selectivity of separation membranes, the flow characteristics in the chemical reactor, and upscale-related issues of the respective process. Moreover, studies are performed to compare the efficiencies of the different cycles for specific heat sources. One additional benefit of a nuclear reactor producing both electricity and hydrogen is that it can shift between the two products. For instance, the plant can produce electricity during the day and hydrogen at night, thus adapting its electricity generation profile to the daily variations in demand.

Solar-driven thermochemical water splitting cycles (TCWSCs) can be an energy efficient and environmentally attractive method of generating hydrogen. Solar-powered TCWSCs can utilize both thermal (i.e. high-temperature heat) and light (i.e. quantum energy) components of the solar resource. A stable conversion cycle is to be developed which utilizes both thermal and quantum energies to increase the solar-to-hydrogen energy conversion efficiency. The cycles under investigation are similar to the thermochemical cycles mentioned above. There are a number of open questions and challenges in this new field mainly related to unwanted side reactions, cycle stability, and overall efficiency of the process.

When mechanical energy (hydropower or wind turbines) is used, hydrogen can be generated via electrolysis of water. Although it has been a standard process of water splitting for decades, electrolysis is still a matter of extensive research. The potential for further efficiency improvement (currently >70%) is explored by investigating processes at the electrode surfaces and lowering the kinetic barriers to

the water splitting reaction. Moreover, designing an optimized electrode surface is an issue which includes the development of highly efficient immobilized non-precious metal catalysts in an effort to reduce the production cost of hydrogen. Another area of materials research directly affecting cell efficiency is the electrolyte/separator and its ion conduction. Design parameters determining cell conductance are the intrinsic conductivity of the electrolyte solution and the separation distance of, and current pathways between, electrodes. As electrolysis cells are primarily alkaline, hydroxyl ion-conductive membranes and thin organized membrane structures may lead to decreased electrolyte resistance and higher efficiency of the process.

Compared to conventional low-temperature electrolysis, high-temperature electrolysis (HTE) of water converts more of the initial thermal energy into chemical energy (hydrogen). Some of the energy needed to split the water in HTE is added as heat instead of electricity, thus reducing the overall energy required and improving process efficiency. The efficiency of converting heat to electricity is low compared to direct use of heat, and higher energy efficiency can be achieved by supplying the energy to the system as heat rather than electricity. Generally, the process is only considered in combination with a powerful heat source, e.g. either nuclear power or concentrated solar radiation. HTE has been demonstrated on a laboratory scale, in devices similar to solid oxide fuel cells (SOFC). In the experiment, the feed to the electrolyzer is approximately 50:50 steam and hydrogen, at temperatures around 750–950°C. The output of the electrolyzer typically is 75% hydrogen and 25% steam by volume. The hydrogen can then be separated from the steam in a condensing unit. Crucial issues to be addressed are the durability and reliability of the thin electrolytes and the sealing around the periphery of the electrolyte sheet. Electrodes, corrosion resistance, tolerance to impurities in feed water, and scalability are other important topics of interest at the moment.

One of the most important regenerative hydrogen sources is biomass. The processes for producing H_2 from biomass can be separated into thermochemical and biological routes. While biological processes work at temperatures below 100°C and at ambient pressure, higher temperatures and pressures are needed for the thermochemical routes. A traditional process to convert dry biomass at low pressures is pyrolysis of the biomass combined with a subsequent or direct reforming process. The product gas is cleaned and converted to CO_2 and H_2 by a water gas shift reaction. The process has been tested successfully on a technical scale, optimization and cost reduction being the main issues.

AER (Absorption Enhanced Reforming) is another clean conversion of dry biomass into a gas rich in hydrogen. It allows the single-step generation of a product gas with high hydrogen content for fuel cell application. Shifting of the reaction equilibrium raises the hydrogen concentration significantly to more than 80 vol.%. An interesting characteristic of the process is CO_2 removal in the reaction zone of the gasifier. As CO_2 absorption is a highly exothermic reaction, the heat released is integrated directly into the endothermic gasification/reforming process. The spent absorbent must be regenerated in a subsequent process step. The technology uses a fluidized bed reactor containing a CO_2 absorbent, e. g. dolomite or limestone. The

development of a catalytic absorbent material with high tar cracking efficiency is another key aspect of the AER process. Hence, work is currently focused on the investigation of various natural and synthetic absorbent materials with regard to their CO_2 absorption capacity and chemical and mechanical stability under real process conditions with repeated absorption-regeneration steps. Circulating fluidized bed systems are the next development step allowing a continuous production of hydrogen parallel to absorbent regeneration.

Hydrogen can also be produced out of wet biomass, which is more abundant. In the supercritical water process, biomass slurry reacts with water under supercritical water conditions to generate a gas rich in hydrogen. The reaction of the organic substances with water proceeds at temperatures of 600°C and pressures of 25 MPa at residence times on the order of 1–4 min. Carbon gives rise to CO_2 and small amounts of methane. Efficient heat exchangers can be employed to regenerate the heat also under high-pressure reaction conditions. Electricity consumption in generating the high-pressure is low due to the low compressibility of the slurry. These factors ensure high-energy efficiency even for diluted feed. The process has been tested experimentally on a pilot scale with an efficiency of 90% for corn silage, for example. Further optimization of the reaction conditions, of slurry conditioning, and of the hardware components is still needed. A particular issue is the formation of salts which may precipitate and lower the efficiency or even block the process. Furthermore, supercritical water is highly corrosive; materials development is in progress for this particular application.

Microbial hydrogen production or hydrogen production by biological reactions from renewable organic waste sources could represent an important area of hydrogen production if the space-time yield of the reaction can be increased considerably. Hydrogen can be produced by micro-organisms either through splitting of water by photosynthesis, or by ”dark” fermentation of low-cost substrates or waste. Producing hydrogen by the dark process is much simpler than the photo process on technical grounds; the dark process generates hydrogen from a large number of carbohydrates frequently obtained as refuse or waste products. Anaerobic bacteria use organic substances as their sole source of electrons and energy, converting them into hydrogen. Moreover, biohydrogen production from waste takes comparatively less time than methane fermentation, which implies a lower capacity of the bioreactor and lower capital costs for construction. However, natural organisms of convenient species examined so far show rather low rates of hydrogen production because of the complicated reaction systems needed to overcome the large free energy requirements (+237 kJ/mol hydrogen).

Photosynthetic bacteria use organic substrates rather than water as the starting compound for hydrogen production. Compared to algal hydrolysis, photosynthetic bacteria require much less free energy to produce hydrogen and can completely decompose organic substances. However, this process requires high activation energies to drive hydrogenase with the consequence of low solar conversion efficiencies, typically not much higher than those of algal biophotolysis systems. Research and development in this field mainly focus on raising the production rates of hydrogen. Nutrient constraints can be used to arrest growth, reducing metabolic energy

requirements, for example. Operation at higher temperatures would shift thermodynamics in favour of H_2 production. In particular, more knowledge must be acquired before genetic modification and metabolic engineering can be used to redirect bacterial metabolism efficiently toward H_2 production.

Direct water splitting by sunlight can also be accomplished on the basis of inorganic systems. Current photocatalysts are mainly oxide semiconductors, such as metal-doped TiO_2 and perovskites ($SrTiO_3$, KNb_6O_{17} and $NaTaO_3$). If irradiated by sunlight, the oxides can split the water into hydrogen and oxygen at quantum yields of lower than 1%. To improve the yield, a fine dispersion of the material is essential; nanotechnological methods have been applied to produce the catalyst. However, very fine dispersion may cause stability problems in the water and looking for means to improve long term stability is an important issue. Moreover, the photocatalysts mentioned above are effective only in the ultraviolet range due to their wide band gap which is detrimental to the efficiency of the process.

Unlike metal oxide photocatalysts, many metal sulfides have narrower band gaps and thus can absorb light also in the visible range. Ternary sulfides have strong absorption in the visible region and may be good candidates for photocatalytic water splitting to produce hydrogen; however, many of them are unstable during the photocatalytic reaction. Improving the stability of metal sulfide catalysts such as CdS for water splitting therefore is another important issue. It has been reported recently that multicomponent metal sulfide and oxysulfide show stable photocatalytic activity for water reduction and oxidation. Thus, multicomponent metal sulfides may be an interesting new class of stable photocatalyst for water reduction. In general, the number of photocatalysts working under exposure to visible light is still limited and more materials research is needed to identify more promising photocatalysts for direct water splitting.

A new and challenging approach to hydrogen production is to biomimetically reproduce successful mechanisms in nature. A breakthrough was achieved in this field recently when the crystal structure of the photosystem II was solved. The spatial configuration of the tetramanganese complex responsible for water splitting in plants is now known and chemists can try to build artificial molecules which may split water catalytically by the same mechanism. Thus, water would be split into oxygen, protons, and electrons. Recombination of the protons and electrons could be used to either produce molecular hydrogen or enable endergonic chemical reactions to proceed in order to produce energetically rich chemical compounds. This could lead to an interesting and efficient combination of solar energy with hydrogen production and storage.

18.3 Storage

Figure 18.1 is an overview of the physical limits of hydrogen storage by three different methods: pressurized hydrogen (1 bar, 350 bar, 700 bar), liquid hydrogen, and H in metal hydrides. On a materials basis, metal hydrides are seen to have a potential

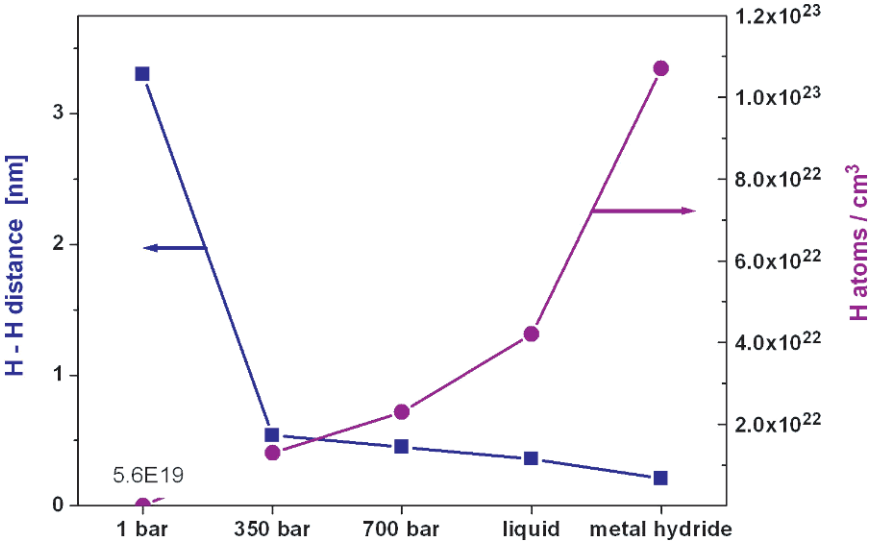

Fig. 18.1 Mean distances of hydrogen molecules (pressurized and liquid hydrogen) or atoms (metal hydride, according to the Westlake criterion) and resulting physical limits for volumetric hydrogen densities in different storage methods [1]

to overcome the already reached physical limits of pressurized and liquefied hydrogen. However, none of the three storage methods is currently able to provide a sufficient storage density, e.g., for applications in vehicles, at acceptable cost and suitable operating temperatures and pressures. Each storage method has its peculiarities making it more or less convenient for a specific application. Hence, the decision in favour of a storage method will always depend on the requirements of the systems environment. Liquid storage tanks, for example, are well suitable for storing large amounts of hydrogen, starting from the size of a car tank. However, they are not suitable to supply small portable devices, such as laptop computers etc. In this case, reversible or non-reversible metal hydride systems may offer application potential.

In the automotive area, pressurized and liquid hydrogen will not be able to meet the long term goals of storage density of the system (e.g. as established by the US Department of Energy for the year 2015). Moreover, despite considerable progress was made in the last years none of the international goals concerning gravimetric and volumetric storage density and operating temperatures and pressures has been reached also with reversible solid storage materials. Although hydrogen storage has progressed significantly in recent years, further progress is needed to meet the technical and economic requirements. These research efforts will require new materials and solutions and, in the case of solid storage materials, significant improvements in current technologies.

18.3.1 Pressurized Hydrogen

Storing hydrogen in pressure vessels is a technique which has reached a high degree of maturity. However, if larger amounts of hydrogen are to be stored for an acceptable driving range, very high pressures are needed. The development of viable 700 bar composite tanks therefore is one of the greatest challenges at the moment. While feasibility has already been demonstrated, there are many challenges concerning lower manufacturing cost, optimization of stability, hydrogen diffusivity, and safety of the vessels. The development of low-cost, lightweight composite materials is essential. Moreover, it is imperative that they withstand the varying high mechanical forces. Pressure vessels must maintain long-term stability also at low temperatures and after many loading cycles. Therefore, novel fibre materials need to be developed and tested, and detrimental reactions between the vessel materials and hydrogen must be investigated in order to be avoided. Such effects may lead to embrittlement of the materials in contact with hydrogen and increase the risk of sudden failure of the tank, for example. As the composite structure is not gastight enough, cost-effective liner materials with a very low diffusion coefficient for hydrogen must be developed which maintain their properties under the mechanical and thermal loads, prevailing over the life of the vessel.

18.3.2 Liquid Hydrogen

Since the early twentieth century liquid hydrogen has been stored in vacuum-insulated tank systems. The liquefaction process consumes much energy and more than 30% of the energy content of hydrogen is needed to cool the hydrogen to the boiling point of 20.3 K, which reduces efficiency considerably. However, there may be an economic advantage over pressurized hydrogen in a logistics chain, because of lower delivery frequencies. The high volumetric density (70.8 kg/m^3) makes the method particularly applicable to vehicles with high fuel consumption.

One basic disadvantage of liquid storage is the gradual evaporation of hydrogen, due to the inevitable heat transfer from the environment as a result of heat conduction, convection, and radiation. Once evaporated, hydrogen cannot be liquefied again by pressure because of its low critical temperature (32 K). The resultant overpressure must be released at 6–10 bar to avoid damage to the tank. Thus, 2–4% of the stored amount is lost per day by evaporation. Sophisticated multilayer insulation systems have been developed to keep evaporation losses as low as possible. Moreover, also active cooling of the cryoliquid can reduce losses, but current systems have low efficiencies and are too expensive. Conventional designs are cylindrical which is unsuitable for use in cars. The development of lightweight free-form tanks therefore is one of the current activities in this field.

In summary: Although important parameters, such as long term stability, robustness, refuelling time, crash safety, and recyclability have been tested successfully,

current tank systems are still expensive. It needs to be demonstrated whether large-scale production can decrease fabrication costs to an acceptable level.

18.3.3 Solid Storage

Hydrogen storage in solids is based on weak interaction of hydrogen molecules with a materials surface (physisorption) or strong binding of hydrogen atoms to a carrier compound (chemisorption). Again, each principle has its own prospects and constraints. Chemisorption materials may provide high volumetric and gravimetric storage capacities, but there is always the need to split or recombine hydrogen molecules and chemically bind or release atoms while the compounds are being formed. A basic parameter of both physisorption and chemisorption materials is the reaction enthalpy, ΔH_r for binding and releasing the hydrogen which sets the operating temperatures and pressures for storage. The equilibrium condition for the Gibbs free energy ΔG_r, is

$$\Delta G_r = \Delta H_r - T\Delta S_r = 0 => \Delta H_r = T\Delta S_r$$

The standard entropy for hydrogen, 130 J/mol $H_2 \cdot$ K, can be used as a good estimate of ΔS_r. Hence, there is an "optimum" reaction enthalpy, ΔH_r, for operation at room temperature which is in the range of 30–40 kJ/mol H_2.

Splitting hydrogen for chemisorption is a process inherently involving large enthalpies, which must be handled in a tank system. Typical binding energies of 50 kJ/mol H_2 lead to high demands for the heat management system of the storage. For example, several 100 kW of heat transfer power have to be provided to remove the binding energy released during a refuelling cycle of 5 minutes. However, only 50 kW is needed to release 2g of H_2 per second from the storage material during the driving cycle. Storing hydrogen by physisorption is not subject to this technical (and economic) challenge because the hydrogen stays in its molecular form, and the binding energies involved are weak. The problem instead is to provide lightweight materials with a sufficient number of binding sites for hydrogen per volume. Moreover, physisorption interaction between the H_2 molecule and the surface of an organic molecule typically is in the range of 5–8 kJ/mol, as a result of which very low working temperatures must be applied. Most data therefore exist for 77 K, the temperature of liquid nitrogen.

Nanostructured carbon materials, such as graphitic nanofibers (GNF), multi-walled carbon nanotubes (MWNT), single-walled carbon nanotubes (SWNT), and carbon nanohorns, exhibit novel properties and produce unusual scientific phenomena and it had been hoped that they would also be able to store large amounts of hydrogen. However, no particular interaction of hydrogen molecules with carbon nanomaterials has been demonstrated up to now, and some initial reports about unusually high storage capacities of graphitic nanofibers and carbon nanotubes were not reproduced by other groups. The data published so far rather indicate that the

amount of hydrogen adsorbed is proportional to the specific surface area (BET) of the carbon material and is limited to 2 wt.% hydrogen at 1 bar H_2 and 77 K. Attempts to modify the materials by doping with noble metal atoms or nanoparticles have led to some improvement. However, the storage capacities reported are still low compared to those of activated carbon or other nanomaterials.

The main line of research in this field is to reach higher operating temperatures by increasing the interaction energy of H_2 and the sorbent and raising the storage capacity by increasing the number of binding sites per volume. Void size of microporous materials is an important parameter in this context because unnecessarily large void diameters reduce volumetric storage capacity. A bottom-up design strategy to improve storage capacity of microporous systems should therefore include

– a framework consisting of light elements,
– avoidance of non-essential free space in the structure,
– improving the interaction energy between hydrogen and the framework.

The systems investigated most thoroughly at the moment therefore are self-organizing metal-organic frameworks (MOFs), microporous organic frameworks, and microporous inorganic frameworks. While the binding energies of hydrogen and organic supports seem to be limited to levels comparable to carbon, higher interaction energies were found with metal partners in MOFs and inorganic frameworks.

The highest hydrogen storage densities can be attained with chemisorption materials, typically metal hydrides. There has been significant development in the past starting with the "classical" or interstitial metal hydrides based on hydrogen absorbing metals or alloys. Their advantage is the very high volumetric storage density achievable with several alloys (AB_5 and AB_2 type) working at ambient temperature and pressure. However, due to the heavy transition metal content of the base structure, gravimetric storage density is comparatively low, limited to some 2 wt.% H. Progress has been made when it was found that the saltlike complex hydrides based on aluminum (so-called alanates) can desorb and absorb hydrogen reversibly when small amounts of transition metal based dopants are thoroughly mixed with the H carrier material. Thus, more than 4 wt% H can be exchanged at temperatures between 100 and 150°C with a $NaAlH_4$ based storage material. At the moment, there is little hope of finding reversible Al based hydrogen carrier materials with higher hydrogen contents which would work at ambient temperature or at the operating temperature of a PEMFC. Hence, development focuses on other light metal systems. Boranate ($M_x(BH_4)_y$) and amide ($M_x(NH_2)_y$) based solid state reaction systems are under investigation at the moment. The systems contain even larger amounts of hydrogen, i.e. up to 18 wt.%. Appropriate reaction partners allow systems with suitable thermodynamic properties and high hydrogen contents of up to 16 wt.% to be designed. Currently, reversibility is a problem with some of the boron-based materials, probably due to the formation of stable boron structures on the low-hydrogen side of the reaction. Another challenge is the prevention of small amounts of volatile by-products, such as B_2H_6 and NH_3 which would have a detrimental effect on the noble metal catalyst of a fuel cell.

In the search for other ways of storing hydrogen, it was recently demonstrated by Japanese researchers that hybrid systems consisting of a pressure tank (350 bar H_2) filled with a conventional Ti-Cr-Mn bcc alloy offer higher storage capacities of up to 7.3 kg per 180 l volume at 350 bar [2]. These promising results have given rise to new ideas in this field about combining different storage methods and thus achieving high storage capacities.

A new, interesting approach to overcome the need for expensive thermal management in mere hydride tanks is the use of kinetically stabilized hydrides, i.e. hydrides with a decomposition reaction thermodynamically favourable under ambient conditions because of the low reaction enthalpy. The reaction does not occur, as there are kinetic barriers slowing down transformation considerably. Gamma-AlH_3, for example, has a hydrogen content of 10 wt% and a reaction enthalpy of only $\Delta H_r = 7.1\,\mathrm{kJ/mol}$, which is low compared to reversible metal hydrides. However, the method would require an exchange system for the fuel at gas stations, and external regeneration of the hydrogen carrier.

References

1. M. Fichtner, Editorial: Preface to the viewpoint set: Nanoscale hydrogen storage materials, Scripta Materialia 56 (2007) 801.
2. D. Mori et al., Journal of the Japanese Institute of Metals 69 (2005) 308–311.

Chapter 19
Environmental Scope

Maurizio Fermeglia

List of Abbreviations

APUs	Auxiliary power units
EOR	Enhanced oil recovery
GHGs	Greenhouse gases
GWP	Global warming potential
IEA	International Energy Agency
IPCC	International Panel on Climate Change
NG	Natural gas
OE	Oil equivalent energy consumption

19.1 Introduction

In the third millennium "sustainability" is increasingly becoming a social, political, scientific, and engineering key issue. Indeed, there are growing signs of sustainability becoming a major new paradigm influencing the society of tomorrow and the

Maurizio Fermeglia
ICS UNIDO, Area Science Park, 34100 Padriciano, Trieste, Italy; University of Trieste, DICAMP-MOSE, Piazzale Europa 1, 34127 Trieste, Italy,
e-mail: Maurizio.Fermeglia@dicamp.units.it

A. Léon (ed.), *Hydrogen Technology*,

engineering it requires. The sustainable development, which can be defined very simply as a process, in which it is tried not to take more from nature than nature can replenish, can be achieved without sacrificing the many benefits that modern technology has brought. The only problem is that technology respects the imposed constraints. Engineers are asked to do this by designing new processes and/or by modifying existing processes aiming at using less energy and renewable resources and producing by-products that can be safely returned to the earth.

Driving the global energy system on a sustainable path increasingly represents a major concern and policy objective [1, 2]. The emergence of a sustainable global energy system is a long-term process that will require a deep transformation of its current structure. In fact, energy resources play a major technical role in sustainable industrial development, and energy-related issues and hydrogen, its production, storage, transportation, and utilization are key elements in a sustainable industrial development. Today, the world's economy is based on fossil fuel, as it covers around 80% of the world energy consumption, the remainder 6.5% and only 13.5% being met by nuclear and renewable resources, respectively [3]. Emissions from industry and fossil fuel energy use constitute the man-made part of the greenhouse gas emissions and result in heavy local and regional air pollution. The price to pay appears in the form of natural disasters, unreliable access to food, the spread of tropical diseases, and severe health and ecosystem impacts.

To remedy this situation, the ultimate goal must be to establish an energy system based on clean and renewable energy sources, such as solar, wind, hydro, geothermal, and bio. An integrated approach to meeting these demands is to find energy carriers that do not pollute during distribution or usage and, at the same time, ensure flexibility with regard to energy sources. Energy carriers with such characteristics are hydrogen, electricity, and thermal systems (such as district heating and cooling systems) as illustrated in Fig. 19.1 [4]. Of the energy carriers, hydrogen is a newcomer in the scene and going to be by far the most important in the future. Hydrogen is not an energy source, but an energy carrier. Accordingly, it is not available

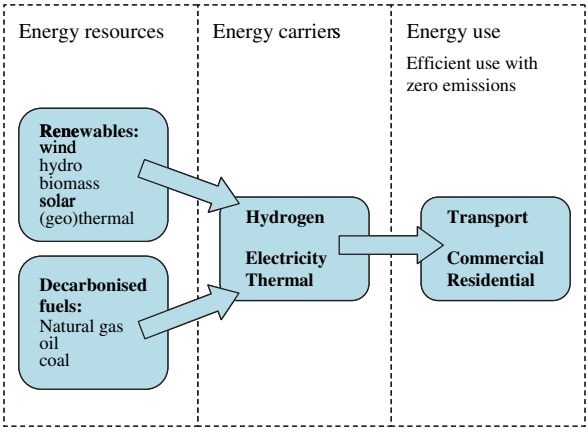

Fig. 19.1 Vision of a clean energy chain in hydrogen society

in nature as it is, but must be produced from a raw material, transported, and finally utilised for the production of energy. Production and storage of hydrogen certainly are important in this chain, but the utilization device, namely, the tool that transforms the chemical energy of hydrogen into electrical energy, plays a crucial role. This piece of equipment is a fuel cell and its efficiency and operating condition is of paramount importance in the hydrogen-based energy scenario.

The pollutants emitted by fossil energy systems (e.g. CO, CO_2, C_nH_m, SO_x, NO_x, radioactivity, heavy metals, ashes, etc.) are by far larger in quantity and more damaging than those that might be produced by a renewable hydrogen energy system. Worldwide reduction of CO_2 emission to limit the risk of climate change (e.g. greenhouse effect) requires a major restructuring of the energy system, and the use of hydrogen as an energy carrier is a long-term option to reduce CO_2 emissions.

In this chapter, environmental issues related to hydrogen technology will be presented and discussed briefly. Particular attention will be devoted to the benefits of the introduction of hydrogen technology for energy production. Direct positive effects of the production, storage, and utilization of hydrogen are perceived immediately in terms of carbon dioxide emission reduction and, hence, the reduction of global warming. This, in turn, will result in a cascade of benefits to the climate, biodiversity, agriculture, and in general to the quality of life and world economy.

The chapter will start by illustrating the issue of global warming and its relation with carbon dioxide handling. In particular, current figures summarizing the impact of carbon dioxide emission on climate changes and on ecosystem changes shall be reported and strategies will be discussed to reduce the carbon dioxide emissions. Subsequently, issues related to hydrogen and the energy market shall be presented in order to depict some possible scenarios for the future. The state of the art of hydrogen production and utilization industries and devices will be highlighted. In the end, some conclusions will be drawn in line with many researchers and scientists, who agree that the future in energy production is hydrogen [4, 5, 6, 7, 8]. The question is not whether, but only when this will happen. And we all hope that this will be soon.

19.2 Global Warming and CO_2 Handling

19.2.1 Current Figures

Global primary energy consumption amounted to 10.54 billion tons of oil equivalent (OE) in 2005 and is projected to increase by 1.3% per year for the industrialised countries and by up to 9.2% per year for the developing countries [9]. With such a large oil consumption predicted, great care should be given to oil reserves, but this issue definitively is one of the most controversial aspects of the discussion for several reasons: (i) there is no universally accepted definition of reserves, nearly everybody has his own version, (ii) most reserve estimates are unverifiable, as they tend to be state secrets, and (iii) reserves reported in open publications tend to increase

with time in spite of extensive production. Despite this uncertainty in determining the amount of oil available for energy production, fossil energy will remain the number-one energy source until far into this century.

Since 1751, roughly 305 billion tons of carbon have been released into the atmosphere from the consumption of fossil fuels and cement production. Half of these emissions have occurred since the mid-1970s. The 2003 global fossil fuel carbon dioxide emission estimate – 7303 million tons of carbon – represents an all-time high and a 4.5% increase compared to 2002 [10]. Globally, liquid and solid fuels accounted for 76.7% of the emissions from fossil fuel burning in 2003. Combustion of gas fuels (e.g., natural gas) accounted for 19.2% (1402 million tons of carbon) of the total emissions from fossil fuels in 2003 and reflects a gradually increasing global utilisation of natural gas. Emissions from cement production (275 million tons of carbon in 2003) have more than doubled since the mid-1970s and now make up 3.8% of global CO_2 release. On the other hand, gas flaring which accounted for roughly 2% of global emissions during the 1970s now accounts for less than 1% [10].

Preliminary figures calculated in compliance with the International Panel on Climate Change (IPCC) directives show that the amount of carbon dioxide, the most common of the greenhouse gases (GHGs), emitted in 2005 was 177 billion kg, a reduction by 4 billion kg (2%) compared to 2004. Other greenhouse gas emissions remained stable or decreased [11].

The most remarkable CO_2 emission reduction was reported in the energy sector. In electricity production the emission of CO_2 caused by combustion of fossil fuels was reduced by approximately three billion kg. The use of natural gas and coal, for example, was cut by 3 and 7%, respectively. In spite of the reduction, the amount of electrical energy available remained on the same level due to the promotion of renewable energy sources and extra imports of electricity. The use of renewable energy sources increased by approximately 40% in 2005 compared to the previous year; net imports increased by 13% [11].

Despite the good news of a minor reduction or stabilisation of CO_2 emissions, it is estimated that continued use of fossil energy will lead to an increase of the average global temperature in the next century by up to 3.4°C [12]. On 2nd February 2007, the fourth assessment report of IPCC [13] was presented, where this prediction has been updated to a more dramatic value of 4.0°C as the best estimate corresponding to an interval of 2.4–6.4°C as a likely range in the next 100 years. In the same report this temperature increase is said to correspond to an average sea level rise of 0.26 to 0.59 m.

19.2.2 Impact of CO_2 *Emissions*

19.2.2.1 Change in the Climate

The most important impact of carbon dioxide emission will be on the **climate**. Although the forecasts of future CO_2 emissions from fossil energy use as well as the magnitude of their influence on global warming are much disputed and there is

much dissent on the climatic consequences of global warming, the impact of CO_2 emissions on global warming itself is widely admitted.

On 29th August 2005, the hurricane Katrina ravaged New Orleans, Louisiana, and Mississippi, leaving a trail of destruction in its wake. It will take some time until the full toll of this hurricane can be assessed, but the devastating human and environmental impacts are already obvious. If Earth's climate will warm steadily in coming decades, as many scientists predict, heavy smog and extreme weather events could increase health risks around the world. Warmer temperatures could bring increased rainfall to some regions as well as heat waves and drought. The possible reduction in cleansing cold fronts is based on known aspects of the interconnected global climate. Low-pressure systems transfer heat from the tropics and bring cold air away from the poles. If the planet warms, the poles are expected to warm more quickly. This would decrease the temperature difference between the poles and the equator and the atmospheric "engine" that moves heat around would slow down. A report in the Journal of Medical Entomology warned that a warmer climate would bring increased mosquito populations and also allow for disease-spreading pests to propagate into new terrain. Most of the increase in diseases is due to numerous environmental factors (including infectious microbes, pollution by chemicals and biological wastes, and shortages of food and nutrients) and global warming will only make matters worse [14].

The fourth assessment report of IPCC [13] says that warming is expected to be greatest over land and at highest northern latitudes and least over the Southern Ocean and parts of the North Atlantic ocean. Snow cover is projected to contract and widespread increases in thaw depth are foreseen for most permafrost regions. Sea ice is projected to shrink in both the Arctic and Antarctic and in some predictions Arctic late-summer sea ice will disappear almost entirely by the later part of the 21st century. It is very likely that hot extremes, heat waves, and heavy precipitation events will continue to become more frequent and, based on a range of models, it is likely that future tropical cyclones (typhoons and hurricanes) will become more intense, with larger peak wind speeds and heavier rainfalls. Moreover, extra-tropical storm tracks are projected to move towards the poles, with consequent changes in wind, precipitation, and temperature patterns to continue the broad pattern of trends observed over the recent half of the last century.

19.2.2.2 Change in the Ecosystem (i.e. Agriculture)

Changes in the climate will turn to changes in the ecosystem, in particular **agriculture**. The situation in Europe is evident. Recent data [15] show clearly that the amount of rain has decreased slightly, but the number of rainy days in Europe has decreased strongly. This fact which is particularly evident in south Europe caused a high number of dramatic changes in the territory, sometimes enhanced by a questionable policy of constructions in highly populated areas. Another destructive effect of global warming is on agriculture. South Europe climate is increasingly changing towards a "tropical climate" and the first sign of this change can be seen in the fact

that hundreds of animal and vegetal species from lower latitudes have colonised south Europe, sometimes replacing indigenous species. The Mediterranean Sea is the most invaded sea of the planet with its 750 alien species, mostly tropical and subtropical species coming with ship traffic to the Mediterranean and settling due to favourable conditions. Similar phenomena are observed also for animals and plants on dry lands in Italy, Spain, and Greece: a tropical squirt from Thailand is a typical example as far as animal species are concerned. In 2005, Italian production of corn, soy, and milk was reduced by 30, 25, and 20%, respectively, due to climate changes. To balance such losses, Italian farmers are switching the production to less heat-sensitive species, such as peanuts [15].

19.2.3 Strategies to Reduce the CO_2 Emissions

19.2.3.1 De-carbonisation of the Fuels

With the scenario depicted in the previous paragraphs, it becomes mandatory to agree on common strategies for reducing the emission of carbon dioxide and other greenhouse gases: **decarbonisation** of the fuels is the main issue in this effort. Renewable energy sources only constitute a very small part of today's energy production and, compared to fossil fuel, renewable pathways to hydrogen are currently scarce and costly. Decarbonised fossil fuel may therefore play a key role in the transition to an all-renewable energy economy. Figure 19.2 summarises the concept of decarbonisation and indicates the future trend. In this scenario, it is expected that the fuel cells tomorrow will play the same role that the internal combustion engines played in the past transition from the coal to the oil age, thus facilitating the first step towards decarbonisation. Today, feeding fuel cells with natural gas could be considered an unsatisfactory compromise and perhaps, it is not the best solution in terms of global warming and carbon dioxide emission. Nevertheless, while the shares of fuel cell engines and fuel cell-based stationary energy production are far from

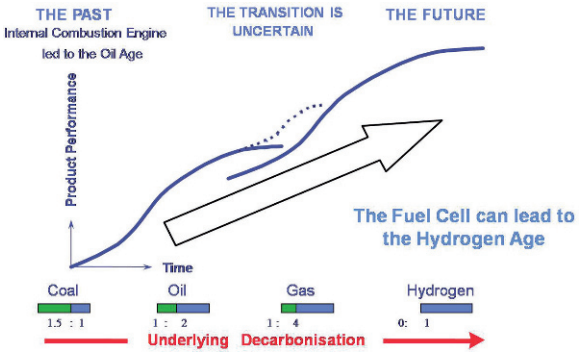

Fig. 19.2 Decarbonisation and product performances

substantial, the transition to the full hydrogen age will be rather difficult, if possible at all.

The transition is further complicated by the fact that, since producing renewable energy sources, such as solar panels and windmills is energy-intensive, replacing polluting energy production by renewable alternatives will require an increased use of energy during the transition period. A key challenge is to accelerate this transition as quickly as possible and without a parallel increase in emissions.

Harmonised worldwide implementation of CO_2 reduction strategies is, however, far from being realised. Many countries have made substantial progress in applying these strategies. Nevertheless, the contribution of industrialised countries to worldwide CO_2 emissions still is over-proportionally large. The costs of developing and applying CO_2 reduction technologies are tremendous, if not prohibitive for most of the emerging economies. There are serious obstacles, though, to reducing CO_2 emissions while satisfying the energy needs of our world, e.g. lacking international harmonisation, national needs and egotisms, rapid growth of world population, and a strongly increasing energy demand of emerging economies. Summing up, though an anthropogenic contribution to global warming cannot be proved for the time being, it cannot be ruled out forever. Therefore, internationally harmonised measures for CO_2 reduction have to be taken in the sense of a no-regret policy to avert potential damage from mankind and, thus, contribute to a sustainable development with fossil energy [16].

A hydrogen economy based on fossil fuels (including natural gas) without CO_2 handling will at best have limited benefits due to continued emissions of GHGs. This calls for identifying practical and environmentally sound CO_2 handling strategies. It is important to develop safe long-term solutions for CO_2 in parallel with work for a more efficient use of energy and increased use of renewable sources. Europe is in a position to implement a clean hydrogen economy by taking advantage of the availability of fossil resources, combined with the large storage potential of CO_2 in the North Sea basin.

Today, natural gas and water are being injected into oil reservoirs for oil recovery. In old oil fields the use of CO_2 for enhanced oil recovery (EOR) may increase the total amount of oil recovered. Moreover, by creating a demand for CO_2, petroleum companies would be willing to pay for it, which could pave the way for a large-scale CO_2 infrastructure. More importantly, in particular from an environmental perspective, petroleum companies could invest in emptying existing reservoirs rather than embarking on new oil exploration in sensitive areas like the Arctic. Paradoxically, the problem is to provide enough CO_2 in order to meet the demand for EOR in existing and future oil fields in the North Sea. CO_2 can be collected by capture from existing power plants and non-energy industries. With a common infrastructure for transportation and injection of CO_2 in the North Sea region, economies of scale and profitability can be achieved.

CO_2 storage beyond EOR and deposition in salt water-filled formations (saline aquifers) has a considerable potential. Studies suggest there is a capacity to store 100–150 years of EU's present CO_2 emissions. This capacity could help to further reduce GHG emissions beyond the first Kyoto protocol. In fact, combining CO_2

handling technology with the bio-based generation of energy will enable a negative net emission of CO_2, thus opening up the possibility of mitigating or even reversing climate change tendencies in the longer run.

19.2.3.2 Energy Efficiency

An important issue when discussing global warming and carbon dioxide emission is **energy efficiency**. Any discussion of energy policy deals with three issues: energy supply (and, hence, security), climate change, and costs or prices. Energy efficiency is an obvious win-win-win approach. Every barrel of oil or ton of coal that we do not burn means less carbon dioxide in the atmosphere and a higher efficiency. Fortunately, many leading businesses are taking practical steps towards reducing their contribution to climate changes. US energy intensity is already improving by 1.5% per year. If we could accelerate this rate to 2% per year, energy use in 2050 would be nearly 50% lower than it would be otherwise, but still 60% higher than current levels: clearly not, where we should be, if our energy sources are not carbon-friendly. So what these figures tell us is that energy efficiency is an essential component, but not the only one, of any long-range effort to protect the climate.

With the use of natural gas, for example, emissions of greenhouse gases can be limited, but there are real challenges to be overcome in terms of supply and costs. With coal, by contrast, it is climate and not costs or supply that we need to worry about (unless we put real effort into carbon capture and sequestration and can make it work at an affordable price). Costs, of course, are an important challenge for nuclear power, as are considerations of waste and weapons proliferation. Costs also are a challenge with renewables: a challenge that clearly influences the supply and use of these technologies. When looking at oil, challenges are faced in all three areas. The world may have ample supplies overall, but the security of these supplies is an obvious concern, as are prices and climate.

Energy efficiency will reduce the demand of fossil fuels and, thus, constitutes an effective way to reduce emissions of GHGs. However, it must be very clear that electricity savings alone cannot contribute to the clean production of hydrogen, as long as the electricity is generated from fossil and nuclear sources. If this is the case, the performance of hydrogen vehicles would be very poor in terms of both energy efficiency and GHG emissions, as compared to other alternatives. Figure 19.3 [6] reports the energy consumption from well to wheel, expressed in MJ/km, and the GHGs reduction in 100 g/km: note the "H2 from EU el. mix" performances as compared to other alternatives in Fig. 19.3. The fossil fuels (typically natural gas) resulting from energy efficiency measures should rather be converted into hydrogen directly, combined with CO_2 handling. This will ensure efficient production and near-zero emissions of GHGs as shown in the column "H2 from NG+CO2 handling" in Fig. 19.3.

When discussing the efficiency of the different devices for the production of electrical energy (independently of the source of energy), it is clear from Fig. 19.4 that fuel cells are among the best devices reaching efficiencies of about 70%.

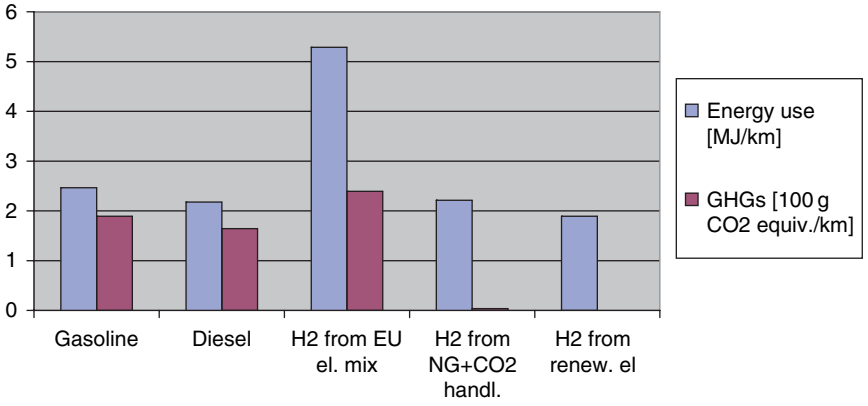

Fig. 19.3 Performance of different vehicles (fuel cycle included), based on [6]

This is another reason why fuel cells should be used now to generate electricity, with fossil fuels serving as feed material. This once more confirms the conception of the fuel cell being the winner technology to be used in the transition to hydrogen age. In the hydrogen era, however, great care should be devoted to the storage and transportation of hydrogen. Since hydrogen reacts with tropospheric hydroxyl radicals, emissions of hydrogen into the atmosphere disturb the distributions of methane and ozone, the second and third most important greenhouse gases after carbon dioxide. Hydrogen therefore is an indirect greenhouse gas with a global warming potential GWP of 5.8 over a 100-year time horizon. A future hydrogen economy will therefore have greenhouse consequences and not be free from climate perturbations. If a global hydrogen economy replaced the current fossil fuel-based energy system and exhibited a leakage rate of 1%, then it would produce a

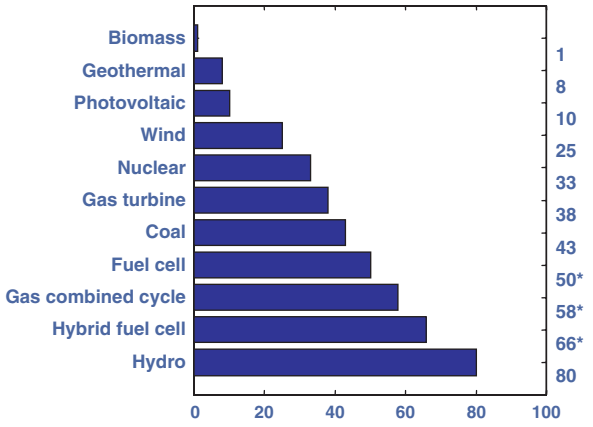

Fig. 19.4 Efficiency of energy production systems; (*) efficiencies improve with heat recovery

climate impact of 0.6% of the current fossil fuel-based system. If the leakage rate was 10%, then the climate impact would be 6% of the current system. Attention must be devoted to reducing to a minimum the leakage of hydrogen from its synthesis, storage, and utilisation processes in a future global hydrogen economy, if the full climate benefits are to be achieved in comparison to fossil fuel-based energy systems.

19.2.3.3 Government Policies of Industrialized and Developing Countries

Governments should facilitate the creation of a CO_2 market by establishing infrastructure and fiscal incentives that will make CO_2 for EOR purposes commercially viable. The introduction and future strengthening of the CO_2 emissions trading directive will clearly affect the energy markets and could result in favouring the use of nuclear energy. The European Commission's high-level group report also recommends the use of nuclear energy for hydrogen in the middle and long terms. Nuclear power for hydrogen may achieve a market advantage over fossil energy in this situation. It is not in the interest of the environment to increase nuclear capacity as long as the challenges related to nuclear waste handling remain unsolved. It is thus urgent to promote the use of decarbonised fuels with a view to counteracting this situation.

Solutions of the global warming problem – renewable energy, energy efficiency, and new environmentally sound technologies – already exist. The latest report from the IPCC [13] confirms that hundreds of technologies are now available at very low costs to reduce climate-damaging emissions and that government policies need to remove the barriers to these technologies.

The good news is that we can slow down and eventually stop global warming, but we must act today. The most important step we can take to curb global warming is to improve energy efficiency. Our cars and light trucks, home appliances, and power plants could be made much more efficient by simply installing the best current technology. Energy efficiency is the cleanest, safest, and most economical way to begin to reduce global warming.

No global warming solution will succeed, unless we can control emissions from cars. While there is no technology to remove carbon dioxide from a car's exhaust, we can make cars less polluting by making them more fuel-efficient. By using today's best technology, car producers could dramatically increase the fuel economy of their cars and trucks.

We also need to clean up our electrical power plants. Most utilities still use coal to produce electricity; part of the problem could be solved by converting these plants to burning cleaner natural gas. We could do much more to save energy in our homes and office buildings. More energy-efficient lighting, heating, and air conditioning could keep millions of tons of carbon dioxide out of our air each year. Harnessing the clean, abundant energy of the sun and wind is critical to solving the global warming problem. Today, the costs of wind and solar power are becoming competitive with dirty coal-fired plants.

19.3 Hydrogen and the Energy Market

19.3.1 Status of Hydrogen Economy

What is the status of hydrogen economy? There are only a few industrial sectors, where hydrogen is undisputedly used for energy production. The space business is one, which would even be inexistent without the highly energetic combination of hydrogen and oxygen in the space launchers' power plants. Hydrogen is also used in submarines, where high-efficiency hydrogen/oxygen fuel cells guarantee extended underwater travel and low to zero detection, because the condensed water steam exhaust has no contours. Hydrogen is used in refineries for the production of reformulated hydrogenated gasoline and the desulphurisation of diesel and in the cooling of large electrical generators.

There are areas in which hydrogen use still is in the phase of research and development or, at most, in the demonstration phase. Examples are (i) fuel cells to replace short-life batteries in portable electronics, such as laptops, camcorders, cellular phones, and the like, energised with the help of hydrogen or methanol cartridges; (ii) natural gas or hydrogen-supplied fuel cells in distributed electricity and heat supply or to replace boilers in central heating systems in buildings; (iii) fuel cells for auxiliary power units (APUs) in vehicles or airplanes; (iv) hydrogen and internal combustion engines or fuel cells on board of buses or automobiles; (v) liquefied cryogenic hydrogen instead of kerosene in aviation [17]. The technologically driven hydrogen energy economy is at its very beginning and will have to face many years or even decades before commercialisation.

In automotive industry, the Toyota engine is powered by a 90-kW fuel cell in combination with a nickel–metal hydride battery and regenerative braking, with the energy of braking being used to recharge the battery. Running on high-pressure hydrogen, the vehicle achieves a top speed of nearly 153 km per hour, has a range of more than 250 km, and reaches twice the tank-to-wheel fuel efficiency of a regular gasoline-powered car. Ford believes that the vehicle can help to establish a hydrogen infrastructure, while fuel cells continue to be developed. Hydrogen-fuelled vehicles became a step more feasible, as many car producers have opened hydrogen fuelling stations in the US (California) and Germany for their fuel cell-powered vehicles. Honda's station uses solar power to extract hydrogen from water: solar panels on the station generate enough hydrogen to power one fuel cell vehicle, but additional electrical power from the power grid is used to increase the hydrogen production capacity [18].

19.3.2 Innovative Technologies to Facilitate Hydrogen Penetration in the Market

Sustainable development requires innovation to reduce the so-called "ecological footprint" [19]. Such innovation may transform the way energy and energy carriers

are produced, gradually shifting the emphasis away from the traditional hydrocarbon–based energy and ultimately yielding a sustainable mix of energy carriers and energy markets.

Beyond any doubt, hydrogen and fuel cells are the bridging technology to a renewable energy system: they must be introduced as rapidly as possible with full market penetration in an early stage already. Hydrogen produced exclusively from renewables is, and remains, the overall goal. However, there is a substantial gap in supply and demand of renewable energy for the production of hydrogen. Moreover, state-of-the-art renewable production of hydrogen is accomplished by electrolysis, one of the most costly sources of hydrogen at present. This certainly is a barrier for the deployment of hydrogen and fuel cell technology and will cause serious delays in the transition to the large-scale all-renewable hydrogen society. As shown in Fig. 19.5, the International Energy Agency (IEA) has established two future scenarios for the supply of electricity based on renewable energy [20]. The first scenario encompasses all current policy measures for producing renewables and referred to as scenario A. In scenario B future policy measures for renewables are added. Finally, scenario C indicates the energy demand of an entirely hydrogen-driven transport sector in the EU. The gap in Fig. 19.5 is equivalent to about 1.3 million 1-MW windmills. Today, 24000 MW of wind power are installed in the EU – it would meet only 1.8% of the total hydrogen demand.

Even in the most optimistic hypothesis of increasing energy efficiency and introducing further renewable sources of energy compared to IEA's scenarios, a huge imbalance between supply and demand of renewable energy will remain.

There are other ways to produce renewable hydrogen apart from electricity-based pathways, such as directly from biomass. However, the potential of these resources may constitute between 15 and 50% of total hydrogen demand, still leaving a significant gap.

Fortunately, producing hydrogen today is not terribly expensive. Figure 19.6 reports the relative costs of energy from different sources, including hydrogen

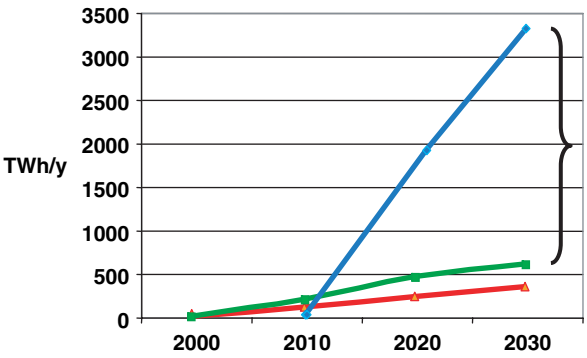

Fig. 19.5 Calculated annual electricity demand for hydrogen as a function of the expected renewable generation (wind, solar, biomass, tide, wave, geothermal), based on [6, 21]: scenario A lower curve in red, scenario B middle curve in green, and scenario C in blue

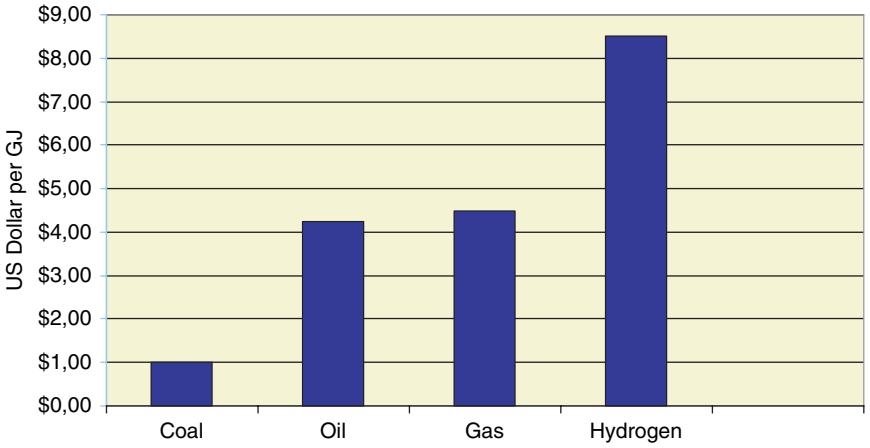

Fig. 19.6 Comparison of costs of energy from coal, oil, gas, and hydrogen (hydrogen from natural gas)

reformed from natural gas [21]. The costs of hydrogen from renewables (solar, wind,. . .) are much higher at present. To enter the transition period as soon as possible, however, it seems that the best way is to produce hydrogen from natural gas: the process is well known and has been technologically available since many decades in the petrochemical industry. This, in turn, will enable car manufacturers to introduce hydrogen and fuel cell vehicles. Fuel cell vehicle stocks and hydrogen infrastructure will then develop. Such hydrogen infrastructure will lay the foundation for the distribution and widespread use of hydrogen fuel from renewables in the long term.

Figure 19.7 shows the trend of the costs of energy obtained with fuel cells fed with natural gas per kW produced versus time [22]. In 2005, the costs are approximately $1,500 per kW. By contrast, a diesel generator costs about $800 per kilowatt

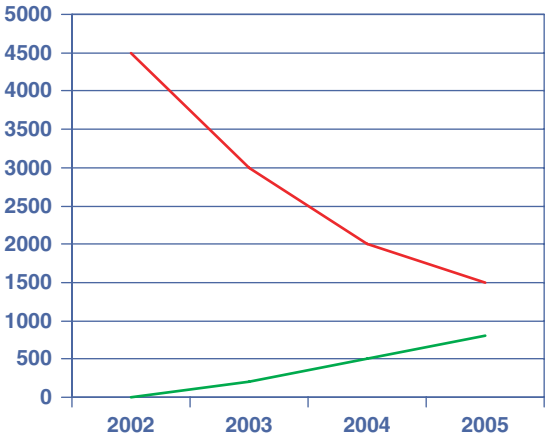

Fig. 19.7 Costs of energy [$/kW] (in red) and energy production (in green) versus time (fuel cell with hydrogen from natural gas)

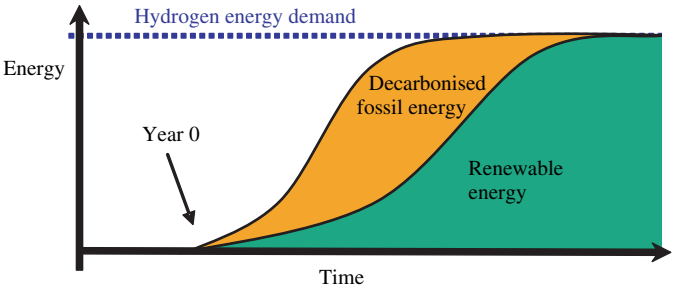

Fig. 19.8 The transition period to hydrogen

and a natural gas turbine even less. The costs will decrease with increasing the total energy produced due to economy of scale.

Figure 19.8 illustrates how this transition to a full hydrogen economy based on renewable resources will evolve in time. Production of hydrogen from fossil and renewable resources starts in year zero in Fig. 19.8 [23]. Fossil energy boosts hydrogen in transportations, giving benefits to the environment and society in an early stage. At the same time, it is extremely important to work as fast as possible for the development and implementation of renewable solutions. Over time, renewables can replace fossil resources in order to ensure a sustainable long-term hydrogen economy. Increasing hydrogen production from decarbonised fossil energy in the short term will accelerate the transition towards commercial and common use of hydrogen and, at the same time, safeguard the commitment to struggling against climate change.

When considering the energy situation realistically, renewable electricity generation, such as photovoltaics, wind and tide power, and so forth, still has a long way to go before it constitutes any significant share in terms of electricity supply. These sources must displace an enormous generation capacity in order to dominate the markets. In this situation, society can choose to use renewable electricity to replace either (i) conventional electricity generation or (ii) conventional fuels for vehicles in the short term. For both pathways, benefits will become manifest in terms of increased sustainability and reduced emissions. By choosing the second option, converting energy from electricity into hydrogen via electrolysis will considerably increase the relative energy costs compared to conventional road fuels. Renewable generation will suffer, as the increased competitiveness with conventional generation built up over several decades will be lost. In the short term, it is therefore necessary to use decarbonised fossil energy for hydrogen to accelerate the development towards a sustainable energy system.

At present, direct conversions of biomass and bio-waste into hydrogen are the only renewable sources of hydrogen that come close to competing with fossil sources. Improving the competitiveness of these renewable energy sources through the introduction of proper fiscal and other framework conditions will be necessary.

Although optimism for hydrogen economy is virtually universal, it is improbable that hydrogen will become a major fuel source in the short term. This is not

because the various obstacles will not be overcome, but because hydrogen is an energy carrier and not an energy source. In fact, whatever energy sources may be exploited in the future, it could be put to more effective use directly, without a significant involvement of hydrogen or fuel cell technology in general. The real costs of fuel cell engines currently are still rather high and the total GHGs release from hydrogen vehicles per km is comparable to that of fossil-diesel hybrids. In the short term, bio-diesel from bio-methanol or other bio-options could compete with fossil diesel within 4 years, and the efficiency of the diesel hybrid will exceed that of the practical fuel cell.

19.4 Conclusions

Energy, economic and political crises as well as the health of man, animals, and plant life are all critical concerns. Environmental protection issues show that there is an urgent need for expediting the process of implementing the hydrogen economy, since a worldwide conversion from fossil fuels to hydrogen would eliminate many problems. The optimal end point for the turn to hydrogen economy will be the substitution of the present fossil fuels by clean hydrogen. The production of hydrogen from non-polluting sources (such as solar energy) is the ideal way [17].

Hydrogen has an outstanding potential for being the key factor in driving the energy market to a sustainable system. Hydrogen can deliver high-quality, highly efficient energy services, while contributing to reducing local, regional, and global environmental impacts.

In this scenario, versatile, clean, and flexible fuel cells play a central role, since they provide for transportation services and supply heat and electricity for a wide range of applications. Together with other distributed-generation alternatives, they contribute substantially to the shift to a more flexible, cleaner, and less vulnerable distributed electricity generation system. In addition, fuel cells are a strategic component of the transition to a less polluting and less oil-dependent transportation system.

Hydrogen production, initially fossil-based (steam reforming of natural gas), will develop towards renewable resources (solar and biomass) in the long run, contributing to driving the global energy system towards sustainability. In addition, hydrogen is produced close to the demand centres, mainly from indigenously available resources, and this dispersed hydrogen supply brings tangible benefits in terms of security of supply for a number of regions. This local production of hydrogen contributes to reducing the reliance on imported energy carriers and the dependence on long-distance transportation infrastructures, thus mitigating the vulnerability to geopolitical uncertainties.

Although the global hydrogen production system progressively shifts towards renewable sources, significant differences exist in the hydrogen production in different regions with time. Industrialised countries mainly rely on steam reforming of natural gas to satisfy their hydrogen needs, while developing and emerging countries,

where a higher demand for hydrogen occurs, rely on a more diversified supply system with a higher share of renewable-based hydrogen production (biomass, solar, wind...).

The main result of hydrogen-based energy production is decarbonisation. This is combined with substantial improvements of energy intensity, resulting in considerable reductions of emissions and, consequently, in relatively low climate change impacts. This highlights the key role that hydrogen could play to "hedge" against the risks of uncertain climate change. Pursuing the penetration of hydrogen within the current hydrocarbon-based energy system while being compatible with the dominant technologies could pave the way for the long-term transition to an energy system with a low release of carbon into the atmosphere [23].

Clearly, a number of technological, institutional, political, and social obstacles remain on the way of a transition towards a sustainable hydrogen-based global energy system. Achieving the large-scale transformations that would result in a clean and sustainable hydrogen-based energy future requires substantial efforts in a number of fields and the involvement of many different social actors. In particular, the combination of government measures and business actions is necessary to stimulate the growth of a sustainable hydrogen energy industry, the commercialisation of the technologies, and the development of a supporting infrastructure [24]. Among other actors, current energy supply companies could become prime players in the transition, if they recognise the challenges and are able to harness the opportunities that hydrogen-based technologies bring along.

Together with other activities, international partnerships on research, development, demonstration, and deployment [25] are necessary for a successful development of hydrogen technologies and their commercialisation. International public–private collaboration in research and development will contribute to sharing costs and risks, identifying and exploiting niche market opportunities, and implementing buy-down strategies to ensure that these technologies will move along their learning curves. They could also facilitate technology transfer and access to attractive markets, key issues for speeding up the global deployment of a cluster of cleaner and more efficient hydrogen-based technologies.

The time of action is now. We cannot leave the decision to the next generation and we have to move to an environmentally friendly energy system. We cannot wait for the oil reservoirs to empty to use hydrogen as an energy carrier. After all, the Stone Age did not end, because they ran out of stones...

References

1. IEA (International Energy Agency), Towards a Sustainable Energy Future, Paris, France, 2001.
2. Riahi K, Roehrl RA, Schrattenholzer L, Miketa A, Technology clusters in sustainable development scenarios. Progress Report of Environmental Issue Groups, International Forum of the Collaboration Projects in Spring, 2001, Tokyo, Japan.

3. IEA (International Energy Agency), Key World Energy Statistics 2006, CD-ROM, Paris, France, 2006.
4. The Bellona Foundation, Hydrogen: Status and possibilities (Report 6: 2002), available at: www.bellona.org/en/energy .
5. European Commission High Level Group on Hydrogen and Fuel Cell Technologies: A Vision for Our Future, 2003, available at: europa.eu.int/comm/research/energy/pdf/hydrogen_summary_report.pdf.
6. GM Well-to-wheel analysis of energy use and greenhouse gas emissions of advanced fuel/vehicle systems, A European study, GM 2002, available at: www.lbst.de/publications/studies__d/2002/TheReport_Euro-WTW_27092002.pdf.
7. Zittel W, Wurster R, 2002, The prospects for a hydrogen economy based on renewable energy, L-B systemtechnik, available at: www.hyweb.de/Wissen/pdf/ireland2002.pdf.
8. Kruger P, Electric power required in the world by 2050 with hydrogen fuel production – Revised, International Journal of Hydrogen Energy, 2005, 30:1515–1522.
9. BP Statistical Review of World Energy June 2006, available at: www.bp.com/statisticalreview.
10. Marland G, Boden TA, Andres RJ, 2006, Global, Regional, and National CO_2 Emissions. In Trends: A Compendium of Data on Global Change. Carbon Dioxide Information Analysis Center, Oak Ridge National Laboratory, U.S. Department of Energy, Oak Ridge, Tenn., U.S.A.
11. Intergovernmental Panel on Climate Change (IPCC), available at: www.mnp.nl/mnc/i-nl-0170.html.
12. Intergovernmental Panel on Climate Change (IPCC), "The IPCC Third Assessment Report", 2001 Geneva, Switzerland, available at www.grida.no/climate/ipcc_tar/.
13. Intergovernmental Panel on Climate Change (IPCC), "Climate Change 2007: The Physical Science Basis", Contribution of Working Group I to the Fourth Assessment Report of the IPCC, 2007, Geneva, Switzerland.
14. Britt RR, Health warning issued for global warming, Live Science, web, 2006 available at: LiveScience.com.
15. Bergamaschi W, Greco D, Iadicicco R, Palombo F, Relazione sullo Stato Sanitario del Paese, 2006 Ministry of Health, Rome, Italy, available at: www.ministerosalute.it/normativa/sezNormativa.jsp?id=380.
16. Kessel DG, Global worming: Facts, assessment, countermeasures, Journal of Petroleum Science and Engineering, 2000, 26:157–168.
17. Winter CJ, Electricity, hydrogen: competitors, partners? International Journal of Hydrogen Energy, 2005, 30:1371–1374.
18. Momirlan M, Veziroglu TN, The properties of hydrogen as fuel tomorrow in sustainable energy system for a cleaner planet, International Journal of Hydrogen Energy, 2005, 30:795–802.
19. Gosselink JW, Pathways to a more sustainable production of energy: Sustainable hydrogen a research objective for Shell, International Journal of Hydrogen Energy, 2002, 27:1125–1129.
20. IEA (International Energy Agency), World Energy Outlook 2002, Paris, France, 2002.
21. Samuelsen S, Medrano Martorell M, Wojciechowski J, Fuel Cells Economic Analysis Report, UCI Advanced Power and Energy Program, 2004, available at http://www.casfcc.org/2/ResourceCenter/pdfs/FinalFuelCellsEconomicAnalysisReport.pdf
22. Azar C, Lindgren K, Andersson BA, Global energy scenarios meeting stringent CO2 constraints: Cost-effective fuel choices in the transportation sector, Energy Policy, 2003, 31:961–976.
23. Barreto L, Makihire A, Riahi K, The hydrogen economy in the 21st century: a sustainable development scenario, International Journal of Hydrogen Energy, 2003, 28:267–284.
24. NHA (National Hydrogen Association), Strategic plan for the hydrogen economy: The hydrogen commercialization plan, 2000, available at: http://www.hydrogenus.com/commpln.htm.
25. PCAST (President's Committee of Advisors on Science and Technology), Powerful partnerships: The federal role in international co-operation on energy innovation, Panel on International Co-operation in Energy Research, Development, Demonstration and Deployment, Washington, USA, 1999.

Chapter 20
Political and Economic Scope

Teresa Malyshev

List of Abbreviations

IEA	International Energy Agency
OECD	Organisation for Economic Co-Operation and Development
R&D	Research & Development
RD&D	Research Development & Demonstration
WEO	World Energy Outlook

20.1 Introduction

Hydrogen offers significant prospects as the transportation fuel of the future and also a generator of electricity to heat and power homes and businesses. But its potential is still to be proven. Hydrogen must be produced, stored, transported, and utilized in

Teresa Malyshev
International Energy Agency, 9, rue de la Fédération, 75015 Paris,
e-mail: teresa.malyshev@iea.org

A. Léon (ed.), *Hydrogen Technology*,

energy conversion devices. All these operations are currently routinely performed, but further progress from the cost point of view is badly needed. As a consequence, hydrogen research and development presently is a top priority in several nations of the world. This is so in order to maintain and improve our quality of life, to ensure security and diversification of energy supply, to protect the environment, to provide sustainable solutions to transfer to the developing world. However, coherent long-term energy policy decisions are necessary as regards the contribution of hydrogen and fuel cells to the realization of sustainable energy systems in the future.

Technology development and international cooperation are part of the solution to address the energy security and environmental concerns that affect our current energy system. Along with other energy technologies, hydrogen as an energy carrier and fuel cells as a conversion technology are emerging as high-potential options to ensure a carbon dioxide (CO_2)-free, secure energy future. The expectation is that in some decades from now fuel cells and CO_2-free hydrogen produced from fossil, renewable and nuclear energy sources will be entering the power generation market as well as the transport, industrial, and residential sectors, thus playing a significant role in reducing emissions and enhancing global energy security. But this development requires extensive public and private R&D efforts to achieve technology breakthroughs and bring these technologies to commercial maturity.

The goal is to achieve a step-by-step shift towards a fully integrated hydrogen economy, based on renewable energy sources by the middle of the century. This will depend on a stronger commitment on the part of governments to adopt and implement policies promoting research and development as well as demonstration projects. Moreover, increased international cooperation only will speed-up the advancement of scientific knowledge and technology in the energy area and allow for an optimal development of hydrogen economy. In addition, an important research effort is needed to overcome technical barriers and to reach the necessary levels of economic competitiveness and safety. Indeed, hydrogen production, storage, and distribution require energy-consuming and costly processes and specific infrastructure, which does not exist today. Similarly, fuel cell performance and cost are far from economic competitiveness, and fuel cell use is currently confined to niche market applications.

In the following sections, the policy priorities will be first identified. Then, a description of the 2006 IEA analysis will be given with the projected scenario by 2030 in the absence and in presence of new policies for a better energy future. According to this analysis, urgent and aggressive policies are necessary. The current RD&D initiatives as well as the challenges for the governments will be described. Finally, the economics of hydrogen energy systems which will actually play a major part in determining the time frame for hydrogen's adoption will be outlined.

20.2 Identifying Policy Priorities

The adoption and implementation of policies and measures in order to increase energy efficiency and to promote RD&D in cleaner technologies, including hydrogen, need to begin immediately, as they would be a major step on the road to a more

sustainable global energy system. These policies would begin to steer the world onto a markedly different energy path from the one we are on today – a path that could lead, well beyond 2030, to a truly sustainable energy future in which energy supplies are secured and climate change is arrested.

There are many different possible paths leading to this more sustainable future, involving a myriad of technology options and fuel choices. A policy approach that promotes a portfolio of technologies would greatly reduce the risk and potentially the cost of accelerating technological solutions, because one or more technologies might fail to make the expected progress.

R&D efforts need to be technology-specific and there would be competition for a limited pot of money. A wide range of policies needs to be adopted urgently, including the sensitive and progressive removal of subsidies that encourage the wasteful use of energy, more programs on technology research, development, demonstration, and deployment, and additional economic incentives to encourage energy users and producers to switch to low-carbon technologies. Any delays would compound the problems associated with rising energy use and emissions by extending the legacy of inefficient energy systems, increasing the costs of meeting targets, and generating greenhouse gas emissions that will reside in the atmosphere for decades or centuries to come.

Aggressive policies are needed and a single one would not be sufficient. Even synergies between policies are encouraged, as for example a price on carbon will promote investments in research and development.

There are many companies and actors involved in the energy sector. Therefore, one should take care that policies which may give advantage to one part of that community may damage another one. Interventions by policy-makers to allocate the costs and the benefits may be necessary to maximize the effectiveness of the policies and, even, to make them politically feasible.

20.3 2006 IEA Analysis

In the *World Energy Outlook 2006*, the International Energy Agency explored the extent to which energy savings and emissions reductions might be achieved by 2030. This scenario responds to requests by policy-makers to illustrate the potential for achieving ambitious emissions reductions through stronger policies and more favorable technological development.

20.3.1 Projected Scenario by 2030 in the Absence of New Policies

World primary energy demand will grow by more than half over the next quarter of the century with coal use rising most in absolute terms. The annual increase in coal demand is mainly driven by China. Indeed, the coal demand in China increased from 120 to 300 million tons in 2002 and 2005, respectively, while for the rest of the

world it increased from 30 to 50 million tons within these 3 years. However, oil will remain the dominant fuel in 2030. Global gas trade will expand by 1.5 times, with two thirds of the increase coming from Russia, the Middle East, and North Africa. Furthermore, developing Asia will become more dependent on oil and gas imports from fewer countries, mainly Middle East and Russia.

Fuel analysis estimates an increase in energy-related CO_2 emissions by 14.3 Gt (55%) with half of the projected increase in emissions coming from new power stations using mainly coal in China and India. A large population in the world has no access to electricity and most of them are located in south Asia and sub-saharan Africa. The number of people using traditional "dirty biomass" for cooking is set to grow from 2.5 billion now to 2.7 billion, which subsequently will increase the annual deaths from indoor air pollution.

20.3.2 Alternative Policy Scenario

The goal adopted in this scenario, as a proxy for more diverse energy objectives, is to ensure that global energy-related carbon dioxide emissions in 2030 are not higher than the 2004 level of 26.1 Gt. This scenario is not constrained by the criterion that only policies already under consideration by governments are adopted. Accordingly, this scenario assumes even faster and more widespread deployment of the most efficient and cleanest technologies, such as hydrogen, beyond those which have already been applied commercially today.

The WEO maps out a cleaner, cleverer, and more competitive energy future based on alternative policies. They consist mainly of more efficient oil-consuming equipments, more efficient electrical appliances, an improved end-use efficiency for fossil fuels and electricity, a renewed interest in nuclear power and biofuels. Many of these measures and technologies would enhance energy security. Greater diversity in the fuel mix serves a diversity of purposes. Oil and gas demand would be reduced. Lower oil and gas demand and imports in developing countries would boost the disposable incomes of households and businesses and the potential for more rapid economic and human development. This would be of benefit to all importing nations. Recognition of the mutual energy security benefits of such policies would facilitate the establishment of cooperative arrangements between developing and OECD countries. It is estimated that the economic cost of these policies would be more than outweighed by the economic benefits. Moreover, the investment payback periods of new policies are very short, especially in non-OECD countries for policies introduced before 2015.

However, achieving the goal in this scenario would require major changes in energy supply and use. Technologies exist today that could permit radical changes over the next 30–40 years, but there are many barriers to their deployment, including the following ones:

- The life span of the existing capital stock limits commercial opportunities for new plant construction.

- Even existing highly-efficient technologies still remain to be widely adopted.
- The costs are, in some cases, likely to be considerably higher than those of established technologies.

Therefore, strong political will and urgent government action is needed to create clear incentives to change existing investment partners.

20.4 Government RD&D Initiatives and Challenges

20.4.1 Current RD&D Initiatives

Current RD&D efforts are focused on developing improved processes for smaller-scale hydrogen production systems, based on established industrial production processes or innovative reactor designs. These include industry-led, cost-shared development and deployment of small-scale autothermal reformers and steam methane reformers. Process improvements may have limited impact on greenhouse gas emissions due to the focus on using conventional fossil fuels to keep the level of costs as low as possible.

RD&D efforts are also focused on large-scale production using coal gasification technologies with carbon sequestration and storage. Such an approach provides flexibility to the investor, since the amount of electricity and hydrogen produced could vary depending on power and fuel demands. Support is also needed for accelerated materials research and systems development for ceramic/membrane reactors and microchannel reformers to meet the growth in demand for distributed and centralized hydrogen generation at lower capital cost and increased efficiency.

Hydrogen and fuel cells may have a significant role in the energy system, if current targets for reducing their costs can be met and also if governments give high priority to policies for reducing CO_2 emissions and oil dependence. In the next few decades, hydrogen costs need to be reduced by a factor of 3 to 10 and fuel cell costs by a factor of 10 to 50. Substantial improvements will then be needed in hydrogen transportation and storage as well as fuel cell performance. At the same time, governments need to implement decisive policies and incentives to promote energy savings and diversify the energy supply.

Governments and industry should therefore continue to sustain current research effort with a focus on fuel cell costs and performance together with new concepts for hydrogen transportation, distribution, and on-board storage for vehicles. Sufficient attention should also be paid to some high-risk/high-potential technologies, such as photo-electrolysis and biological production of hydrogen that are presently in their early stage.

Because of the global nature of the energy market and transport industry, international co-operation and harmonization of codes and standards for hydrogen and fuel cells remain to be of vital importance. Deploying fuel cell vehicles in niche

markets where the economics are more attractive could start reducing costs through larger-scale production and familiarize the public with these technologies.

20.4.2 Necessity of a Technology Shift for Mass Deployment

A technology shift would represent a very severe challenge in terms of the speed of deployment. Technology development typically is a slow process: Decades often elapse between the initial invention and mass application. Without sustained research and development efforts, many technologies will remain too expensive to be used outside niche applications. But this level of achievement will also need technologies which are, as yet, far from commercial application.

Hydrogen technologies could make a significant contribution to energy supply after 2030. But they are unlikely to be commercialized and deployed rapidly in the absence of determined policy intervention. These technologies are inhibited by a combination of institutional and technical barriers. It will take considerable resource commitments, as well as policy intervention, to bring them into widespread use.

Beyond 2030, the production of hydrogen from low-carbon and zero-carbon sources could expand and the consumption of hydrogen, in distributed uses, could grow substantially. However, this will require huge infrastructure investments. Hydrogen-powered fuel cell vehicles could make a significant contribution, even by 2030, if there are breakthroughs in hydrogen storage and the infrastructure develops. The use in fuel cell vehicles of hydrogen from low-carbon or zero-carbon sources could ultimately largely decarbonize oil use in transport.

20.5 Economics of Hydrogen

Hydrogen is more expensive than conventional fuels partly because of relatively high distribution and retail costs. These costs depend on the configuration of the hydrogen supply system and on the scale of hydrogen demand. If there is low demand (such as in a transition period), decentralized production and/or delivery of hydrogen by trucks to refueling stations may be the best option: The transition cost is one of the key problems for the future hydrogen economy. Over the longer term, a hydrogen pipeline distribution system would be a less costly solution. The energy efficiency of central production would be significantly higher and the investment costs lower.

Similarly, the fuel cells cost significantly more compared to conventional alternatives for both automotive and stationary applications. Their high cost actually limits their mass deployment. Consequently, more RD&D are needed together with financial incentives, better information, better public awareness, standardization, and certification.

20.5.1 Fuel Cell Vehicles

Per unit of energy, hydrogen is more expensive than gasoline. Because of the high efficiency of fuel cell vehicles, however, the fuel costs are the same or even lower than gasoline per kilometer driven.

Of all fuel cell technologies, proton exchange membrane (PEM) fuel cells are particularly suited for powering passenger cars and buses, and have now been installed in demonstration vehicles. Buses may be the most promising market. Although current production volumes are very low (10 buses a year), market developments could increase production volumes and help drive down the costs of fuel cell technology. If such cost reductions would occur, PEM fuel cells could be used more widely in passenger cars as well.

Current fuel cell vehicles already are competitive in terms of efficiency, emissions, silent driving, and acceleration. The efficiency of hydrogen fuel cell vehicles is proven compared to standard internal-combustion-engine cars, but fuel cell cars are not yet ready for commercialization. They need cost reductions and improvements in their durability and reliability. In addition to the cost of the fuel cell stack, the final price of a fuel cell vehicle depends on the cost of other components, such as the electric engine and the hydrogen storage system. All these items need to be less expensive. More R&D is needed in order to develop vehicle designs that can meet the economic and technical criteria. It is unlikely that market forces alone will result in the development of a hydrogen economy. Hydrogen fuel cells will only achieve their full potential, if ambitious supply security policies and CO_2 emission reduction incentives will be implemented.

Distribution and retail sales are an important planning problem in a transition to a hydrogen energy system. A difficult transition period will exist, where there either will be too few vehicles to justify widespread refuelling infrastructure or strong consumer resistance to buy hydrogen vehicles because of insufficient fuel availability. Without government intervention, it is unlikely that this dilemma would be overcome. Even then, substantial investment will be needed to produce the large volumes of hydrogen needed for an expanding fleet of fuel cell vehicles. Moreover, the problems associated with the costs of storing hydrogen on-board the vehicle need to be solved, as existing on-board storage options do not yet meet the technical and economic requirements to make them competitive. Thus, such a system will require huge investments in three major components: Fuel cell vehicles, hydrogen production facilities, and a system for transporting hydrogen between production facilities and vehicles. Investors in each component may be reluctant to commit, if it is uncertain whether the other components will be developed in time to achieve profits.

Before full-scale development of hydrogen production and infrastructure begins, international quality and safety standards must be established for the use of hydrogen as a fuel. An appropriate on-board storage system also must be chosen, as it will have a particular impact on the characteristics of the refueling infrastructure.

20.5.2 Buildings Applications

Several types of fuel cells that are appropriate for buildings are under development, although some versions have already been deployed commercially or in demonstration projects. But fuel cells for both commercial and residential applications will be competitive only when capital costs are reduced.

Fuel cell technology still is under development in this sector, and barriers related to reliability, cost, and effectiveness must be overcome. Most of these technologies do not guarantee a minimum length of operation, require specialized personnel for operation, and cost much more (often by an order of magnitude) than competing technologies on the same markets. Moreover, the technology has not yet accumulated a substantial number of operating hours and an increase in operating knowledge and number of demonstration units will be necessary before investors are willing to purchase fuel cells.

20.5.3 Power Applications

An advantage of fuel cells is their flexibility, as they exist in different sizes, from a few watts to many megawatts. Fuel cells can be readily adapted to power generation systems. Natural gas is easily reformed into hydrogen and, in the case of molten carbonate fuel cells or solid oxide fuel cells, natural gas can be used without external reforming. Integrated gasification combined cycle technologies can be used to produce hydrogen from coal. While the use of fossil fuels releases CO_2 emissions into the atmosphere, the expected high efficiency of fuel cells will result in lower CO_2 emissions compared to conventional coal or gas plants. Moreover, the CO_2 produced is in concentrated form which makes its capture and sequestration much easier.

As for the other applications, factors that limit their use now are their high capital cost compared to conventional alternatives, and their relatively unproven status in this sector.

20.6 What Future for Hydrogen?

Hydrogen production, storage, and distribution require a specific infrastructure, which does not exist today and, hence, needs heavy investment. A multi-faceted, aggressive set of initiatives is necessary.

Demonstration activities will require significant public funding by international, national, and regional authorities, because they do not offer attractive returns on investment in the short to medium term. However, industry and end users should be encouraged to contribute an increasing proportion of the costs with a view to ensure their motivation and close involvement.

The agreement on common codes and standards for fuel cell systems is an important enabler for future mass markets. Such codes and standards are needed to minimize the costs and risks associated with installing fuel cell systems in buildings, allowing fuel cell vehicles to enter public garages and car parks, etc. This will be a lengthy process, because different trade and regulatory organizations on international, national, and local levels have developed the existing codes and standards.

Education is important for two reasons. Firstly, it will be necessary in the longer term to educate the public to understand fuel cell technology due to the perceived safety problems with hydrogen. This can be started early by maximizing public awareness of demonstration projects and early products. Secondly, motor mechanics and boiler technicians must be educated in the installation and maintenance of fuel cell systems.

Hydrogen and fuel cells could help us cope with our energy security and environmental concerns. Clean, emission-free hydrogen could be produced from natural gas and coal and – in the longer term – from renewable and nuclear energy sources. It could be used for distributed generation, transport, residential, industrial applications, and electricity storage. Hydrogen and fuel cells together hold the promise to become an alternative to oil and combustion engines, thus significantly reducing emissions in transport. However, the high cost of hydrogen and fuel cell technology at present is the most important barrier to the widespread introduction of hydrogen. Significant technological and economic challenges need to be overcome before fuel cell vehicles will become viable for mass production.

Developing cost-effective hydrogen and fuel cell technologies requires time and public/private research. Technology breakthroughs are needed to achieve commercial maturity and infrastructure investment. All over the world, several programs and initiatives have been started to develop the network for the mass deployment of hydrogen. Efficiently organized, evaluated, and coordinated multinational research and development programs should advance the transition to a global hydrogen economy.

Acknowledgements The author would like to gratefully acknowledge Dr. Fatih Birol, Chief Economist at the IEA, for his expert review.

References

1. International Energy Agency (2006), Energy Technology Perspectives: Scenarios & Strategies to 2050, OECD/IEA, Paris.
2. International Energy Agency (2006), World Energy Outlook 2006, OECD/IEA, Paris.
3. International Energy Agency (2005), Prospects for Hydrogen and Fuel Cells, OECD/IEA, Paris.

Index